BUREAU OF STANDARDS

NBS SPECIAL PUBLICATION 462

U.S. DEPARTMENT OF COMMERCE / National Bureau of Standards

Laser Induced Damage in Optical Materials: 1976

ASTM

STP 622

NATIONAL BUREAU OF STANDARDS

The National Bureau of Standards[1] was established by an act of Congress March 3, 1901. The Bureau's overall goal is to strengthen and advance the Nation's science and technology and facilitate their effective application for public benefit. To this end, the Bureau conducts research and provides: (1) a basis for the Nation's physical measurement system, (2) scientific and technological services for industry and government, (3) a technical basis for equity in trade, and (4) technical services to promote public safety. The Bureau consists of the Institute for Basic Standards, the Institute for Materials Research, the Institute for Applied Technology, the Institute for Computer Sciences and Technology, and the Office for Information Programs.

THE INSTITUTE FOR BASIC STANDARDS provides the central basis within the United States of a complete and consistent system of physical measurement; coordinates that system with measurement systems of other nations; and furnishes essential services leading to accurate and uniform physical measurements throughout the Nation's scientific community, industry, and commerce. The Institute consists of the Office of Measurement Services, the Office of Radiation Measurement and the following Center and divisions:

Applied Mathematics — Electricity — Mechanics — Heat — Optical Physics — Center for Radiation Research: Nuclear Sciences; Applied Radiation — Laboratory Astrophysics[2] — Cryogenics[2] — Electromagnetics[2] — Time and Frequency[2].

THE INSTITUTE FOR MATERIALS RESEARCH conducts materials research leading to improved methods of measurement, standards, and data on the properties of well-characterized materials needed by industry, commerce, educational institutions, and Government; provides advisory and research services to other Government agencies; and develops, produces, and distributes standard reference materials. The Institute consists of the Office of Standard Reference Materials, the Office of Air and Water Measurement, and the following divisions:

Analytical Chemistry — Polymers — Metallurgy — Inorganic Materials — Reactor Radiation — Physical Chemistry.

THE INSTITUTE FOR APPLIED TECHNOLOGY provides technical services to promote the use of available technology and to facilitate technological innovation in industry and Government; cooperates with public and private organizations leading to the development of technological standards (including mandatory safety standards), codes and methods of test; and provides technical advice and services to Government agencies upon request. The Institute consists of the following divisions and Centers:

Standards Application and Analysis — Electronic Technology — Center for Consumer Product Technology: Product Systems Analysis; Product Engineering — Center for Building Technology: Structures, Materials, and Life Safety; Building Environment; Technical Evaluation and Application — Center for Fire Research: Fire Science; Fire Safety Engineering.

THE INSTITUTE FOR COMPUTER SCIENCES AND TECHNOLOGY conducts research and provides technical services designed to aid Government agencies in improving cost effectiveness in the conduct of their programs through the selection, acquisition, and effective utilization of automatic data processing equipment; and serves as the principal focus within the executive branch for the development of Federal standards for automatic data processing equipment, techniques, and computer languages. The Institute consists of the following divisions:

Computer Services — Systems and Software — Computer Systems Engineering — Information Technology.

THE OFFICE FOR INFORMATION PROGRAMS promotes optimum dissemination and accessibility of scientific information generated within NBS and other agencies of the Federal Government; promotes the development of the National Standard Reference Data System and a system of information analysis centers dealing with the broader aspects of the National Measurement System; provides appropriate services to ensure that the NBS staff has optimum accessibility to the scientific information of the world. The Office consists of the following organizational units:

Office of Standard Reference Data — Office of Information Activities — Office of Technical Publications — Library — Office of International Relations — Office of International Standards.

---

[1] Headquarters and Laboratories at Gaithersburg, Maryland, unless otherwise noted; mailing address Washington, D.C. 20234.

[2] Located at Boulder, Colorado 80302.

Laser Induced Damage In Optical Materials: 1976

Proceeding of a Symposium Sponsored by:
National Bureau of Standards
American Society for Testing and Materials
Office of Naval Research
Energy Research and Development Administration
Defense Advanced Research Project Agency

July 13-15, 1976
NBS Boulder, Colorado 80302

Edited by

Alexander J. Glass
Lawrence Livermore Laboratory
Livermore, California 94550

and

Arthur H. Guenther
Air Force Weapons Laboratory
Kirtland AFB, New Mexico 87117

U.S. DEPARTMENT OF COMMERCE, Elliot L. Richardson, Secretary
Edward O. Vetter, Under Secretary
Dr. Betsy Ancker-Johnson, Assistant Secretary for Science and Technology
NATIONAL BUREAU OF STANDARDS, Ernest Ambler, Acting Director

Issued December 1976

Library of Congress Catalog Card Number: 76-600074

National Bureau of Standards Special Publication 462

Nat. Bur. Stand. (U.S.), Spec Publ. 462, 410 pages (Dec. 1976)

CODEN: XNBSAV

U.S. GOVERNMENT PRINTING OFFICE
WASHINGTON: 1976

For sale by the Superintendent of Documents, U.S. Government Printing Office, Washington, D.C. 20402
(Order by SD Catalog No. C13.10:462). Stock No. 003-003-01729-9 Price $4.60
(Add 25 percent additional for other than U.S. mailing)

Foreword

The Proceedings contain the papers presented at the 8th Annual Symposium on Optical Materials for High Power Lasers held at the National Bureau of Standards in Boulder, Colorado, on July 13-15, 1976. The Symposium was jointly sponsored by the National Bureau of Standards, the American Society for Testing and Materials, the Office of Naval Research, the Defense Advanced Research Projects Agency, and the Energy Research and Development Administration. The Symposium was attended by about 160 scientists from the United States, the United Kingdom, France, Canada, and Brazil. It was divided into half-day sessions devoted to the following topics: bulk material properties and thermal behavior, mirrors and surfaces, thin film properties, thin film damage, and scaling laws and fundamental mechanisms. The Symposium Co-chairpersons were Dr. Alexander J. Glass of the Lawrence Livermore Laboratory and Dr. Arthur H. Guenther of the Air Force Weapons Laboratory, who also served as Editors of this report.

The Editors assume full responsibility for the summary, conclusions, and recommendations contained in the report, and for the summaries of discussion found at the end of each paper. The manuscripts of the papers presented at the Symposium have been prepared by the designated authors, and questions pertaining to their content should be addressed to those authors. The interested reader is referred to the bibliography at the end of the summary article for general references to the literature of laser damage studies.

The 9th Annual Symposium on this topic will be held in Boulder, Colorado, from October 4 to 6, 1977. It is anticipated that there will be more extensive foreign participation than in previous years. Also, a concerted effort has been made to ensure closer liaison between the practitioners of high peak power and the high average power community.

The principal topics to be considered in 1977 do not differ drastically from those enumerated above. We expect to hear more about improved scaling relations as a function of pulse duration, area, and wavelength, and see a continuing transfer of information from research activities to industrial practice. New sources at shorter wavelengths continue to be developed, and a corresponding shift in emphasis to short wavelength damage problems is anticipated. Fabrication and test procedures will continue to advance, particularly in the micro-machined optics and thin film areas.

The purpose of these Symposia is to exchange information about optical materials for high power lasers. The Editors will welcome comment and criticism from all interested readers relevant to this purpose.

A. H. Guenther

A. J. Glass

CONTENTS

Section		Page
	Foreword A. H. Guenther and A. J. Glass	iii
	Summary and Conclusions A. J. Glass and A. H. Guenther	viii
0.1	Introduction and Welcome A. J. Glass	1
0.2	SI Conversion Units	3
0.3	Advanced Optical Materials for Laser Fusion J. W. Weiss	4
	BULK PROPERTIES and THERMAL BEHAVIOR	
1.1	Thermal Distortion Thresholds for Optical Trains Handling High Pulse Powers H. E. Bennett	11
1.2	Electric Fields and Power Dissipation in Windows at Oblique Incidence J. H. Apfel	25
1.3	Analysis of Laser-Induced Thermal Stresses in Laser Windows R. E. Rondeau & D. Ford	29
1.4	Interferometric Measurements of Laser Heated Windows E. Bernal G. & J. S. Loomis	36
1.5	New Materials for Chemical Laser Windows J. A. Harrington	45
1.6	Studies of Absorption in Mid IR Laser Window Materials A. Hordvik, B. Bendow, H. G. Lipson, L. H. Skolnik, & R. N. Brown	50
1.7	Effect of Temperature and Stress on the Refractive Index of Window Materials A. Feldman, D. Horowitz, & R. M. Waxler	58
1.8	Refractive Index and Temperature Coefficient of Refractive Index of Hot-Forged Calcium Fluoride M. J. Dodge	64
1.9	Fabrication and Properties of Laser Window Materials R. M. Cannon, H. K. Bowen, A. M. Glaeser, H. J. Mayson, F. A. McClintock, W. M. Sherry, J. B. VanderSande, & M. F. Yan	69
1.10	Double-Doped Alkali Halide Laser Windows H. Posen, N. Klausutis, J. Bruce, J. A. Adamski, J. R. Weiner, & S. A. Kulin	82
1.11	Intermediate Temperature (0.5 to 0.7 T_{mp} °K) Forging of Calcium Fluoride Crystals. R. H. Anderson, B. G. Koepke, & E. Bernal G.	87
1.12	Forging Finished Halide Optical Components R. H. Anderson, E. Bernal G., & R. J. Stokes	95
1.13	Vapor Deposition and Mechanical Properties of CdTe H. L. Tuller, K. Uematsu, J. B. VanderSande, E. L. Hall, & H. K. Bowen	100
1.14	Absorbing Tellurium Inclusions in Polycrystalline Cadmium Telluride: Estimates for Extrinsic Damage Thresholds H. S. Bennett & C. D. Cantrell	119
1.15	Hot-Pressed $CdCr_2S_4$ for Faraday Effect Isolation at 10.6 μm: Preliminary Damage Tests. S. D. Jacobs & K. J. Teegarden	126
1.16	Pulsed Laser Induced Damage at the DF Laser Wavelength M. Bass, K. M. Leung, C. Tang, & M. J. Soileau	136

MIRRORS and SURFACES

2.1 Naval Weapons Center Diamond Turned Optics Facility 145
D. L. Decker & R. E. Cram

2.2 10.6 μm Pulsed Laser Damage Studies of Diamond Turned KCl Window Surfaces 149
M. J. Soileau, J. M. Bennett, J. O. Porteus, W. Faith, J. Jernigan, & T. T. Saito

2.3 Surface, Optical and Laser Damage Characteristics of Diamond-Turned Metal Mirrors 158
D. L. Decker, M. J. Soileau, J. O. Porteus, & J. M. Bennett

2.4 Character of Pulsed Laser Damage to Al at 10.6 μm Inferred from Single-Crystal Targets in Vacuum 165
J. O. Porteus, M. J. Soileau, & C. W. Fountain

2.5 Measurements at 10.6 μm of Damage Threshold in Germanium, Copper, Sodium Chloride, and Other Optical Materials at Levels up to 10^{10} W/cm^2
J. J. Hayden & I. Liberman

2.6 Laser-Induced Damage of Mirror and Window Materials at 10.6 μm 181
R. Gibbs & R. M. Wood

2.7 Absorption of Dielectric Enhanced Mirrors at 5.3 μm 189
P. Kraatz, J. R. Buckmelter, & S. J. Holmes

2.8 Optical Properties of Mirrors Prepared by Ultraclean dc Sputter Deposition 195
P. A. Temple, D. K. Burge, & J. M. Bennett

THIN FILM PROPERTIES

3.1 Materials for High-Power Window and Mirror Coatings and Multilayer-Dielectric Reflectors. 203
M. Sparks

3.2 Alternate Materials for Infrared Window Coatings. 214
A. D. Baer, T. M. Donovan, A. K. Green, & G. Turner

3.3 Design of Three-Layer Antireflectance Coatings. 221
A. D. Baer

3.4 Characteristics of Plasma Polymerized Ethane for Laser Window Coating 230
T. A. Reis, H. Hiratsuka, A. T. Bell, & M. Shen

3.5 Epitaxy and Optical Scattering in T&I Films 239
R. A. Skogman

3.6 Thin-Film Coating Evaluation by Attenuated Total Reflection 246
R. T. Holm & E. D. Palik

THIN FILM DAMAGE

4.1 ZnSe Sputtered Coatings 253
D. A. Walsh & J. A. Detrio

4.2 Laser Damage Studies of Low Index Coating Materials at 10.6 μm 264
M. J. Soileau, A. D. Baer, J. O. Porteus, J. L. Jernigan, W. N. Faith, T. M. Donovan, & A. K. Green

4.3 The Use of Rare Earth Fluorides as 10.6 μm Antireflective Coatings 271
A. Golubovic, J. Fitzgerald, I. Berman, J. Bruce, R. Bradbury, J. J. Comer, W. S. Ewing, & H. G. Lipson

4.4 Performance of $Ge_{0.45}Se_{0.55}/As_2S_3$ Antireflection Coatings at 3.8, 5.3, and 10.6 μm . . . 279
J. F. Lewis & M. C. Ohmer

4.5 AR-Coated KCl Damage at 10.6 μm 283
J. A. Detrio, R. D. Petty, M. C. Ohmer, & O. F. Swenson

4.6 Spectral Dependence of Damage Resistance of Refractory Oxide Optical Coatings 292
B. E. Newnam & D. H. Gill

4.7 The Role of Electric Field Strength in Laser Damage of Dielectric Multilayers 301
J. H. Apfel, J. S. Matteucci, B. E. Newnam, & D. H. Gill

4.8 Preparation Techniques and Hydroxyl Concentration vs Surface Damage Threshold 310
R. A. House, J. R. Bettis, & A. H. Guenther

4.9 Laser Induced Damage to Thin Films Immersed in Liquids 315
A. Balbin-Villaverde & L. G. DeShazer

4.10 Dielectric Coatings on Metal Substrated 331
S. S. Glaros, P. Baker & D. Milam

SCALING LAWS and FUNDAMENTAL MECHANISMS

5.1 Spot Size and Pulse Duration Dependence of Laser-Induced Damage 338
J. R. Bettis, R. A. House II, & A. H. Guenther

5.2 Re-Examination of Laser Induced Breakdown in the Alkali Halides at 10.6 μm 346
C. C. Tang, K. M. Leung, & M. Bass

5.3 Can a Model Which Describes Gas Breakdown also Describe Laser Damage to the Bulk and Surfaces of Solid Dielectrics 350
D. Milam

5.4 Laser Damage to Semiconductor Materials from 10.6 μm CW CO_2 Laser Radiation 357
S. K. Gulati & W. W. Grannemann

5.5 Phototransport Damage of Optical Materials 365
S. M. Wong & D. L. Olson

5.6 Resonant Defect Enhancement of the Laser Electric Field 371
P. A. Temple & M. J. Soileau

APPENDIX I

Participants 379

Laser Induced Damage in Optical Materials

8th ASTM Symposium

July 13-15, 1976

The Eighth Annual Symposium on Optical Materials for High Power Lasers, the Boulder Damage Symposium, was held at the National Bureau of Standards in Boulder, Colorado, from July 13th to 15th. The Symposium was held under the auspices of ASTM Committee F-1, Subcommittee on Laser Standards, with the joint sponsorship of NBS, the Defense Advanced Research Project Agency, the Energy Research and Development Administration, and the Office of Naval Research.

About 160 scientists attended the Symposium, including representatives of the United Kingdom, France, Canada, and Brazil. The Symposium was divided into five half-day sessions, concerning Bulk Material Properties and Thermal Behavior, Mirrors and Surfaces, Thin Film Properties, Thin Film Damage, and Scaling Laws and Fundamental Mechanisms.

As in previous years, the emphasis of the papers presented at the Symposium was directed towards new frontiers and new developments. Particular emphasis was given to new materials for use at 10.6 μm in mirror substrates, windows, and coatings. New techniques in film deposition, and advances in diamond turning of optics were described. The scaling of damage thresholds with pulse duration, focal area, and wavelength were discussed.

Alexander J. Glass of Lawrence Livermore Laboratory and Arthur H. Guenther of the Air Force Weapons Laboratory were Co-chairpersons of the Symposium. The Ninth Annual Symposium is scheduled for October 4-6, 1977, at the National Bureau of Standards, Boulder, Colorado.

Key words: Avalanche ionization; infrared windows; laser damage; metal mirrors; optical fabrication; optical materials; thin films.

1. Principal Conclusions

The Eighth Annual Symposium on Optical Materials for High Power Lasers, the Boulder Damage Symposium, was held as in previous years at the National Bureau of Standards in Boulder, Colorado, from July 13 to noon on July 15, 1976. The Symposium was held under the auspices of the ASTM Committee F-1, Subcommittee on Laser Standards, with the joint sponsorship of NBS, the Defense Advanced Research Projects Agency, the Energy Research and Development Administration, and the Office of Naval Research. This year for the first time an effort was made to coordinate the Damage Symposium with the DARPA Laser Window Conference. The Window Conference was held on Monday, July 12, with the majority of the attendees remaining in Boulder for the entire week. Working sessions of the Committee F-1 Subcommittee on Lasers were held on Thursday afternoon and Friday, July 15 and 16. About 160 scientists attended the Symposium, including representatives of the United Kingdom, France, Canada, and Brazil. The Symposium was divided into five half-day sessions concerning bulk material properties and thermal behavior, mirrors and surfaces, thin-film properties, thin-film damage, and breakdown theory and experiments. For the first time in the eight year history of the Symposium two poster sessions were held. The general consensus of both those presenting poster papers and those viewing them was highly favorable. In all, approximately 50 technical presentations were made. Alexander J. Glass of Lawrence Livermore Laboratory and Arthur H. Guenther of the Air Force Weapons Laboratory were co-chairpersons of the Symposium. The Ninth Symposium is scheduled for October 4 through 6, 1977, at the National Bureau of Standards, Boulder.

As in previous years, one of the major concerns of the Symposium was recent advances in fabrication and testing of optical elements. Concern was expressed over the capacity of the special optics industry to supply the large volume of high quality optical elements that would be needed if influences like various DoD laser programs or the laser fusion program continue to increase at its present rate. Several new fabrication techniques have been proposed in order to remedy this problem. One of these is diamond turning or micromachining. Diamond turning of metal optics has been reported in previous years at the Damage Symposium and a number of high quality reflecting flats and ellipsoids of large aperture have been made by this process. This year for the first time reports were presented on the diamond turning of dielectrics. Of particular interest is the diamond turning of the following materials: NaCl; KCl; CaF_2, SrF_2, BaF_2, ZnS, ZnSe, and MgF_2. Among the metals which have been diamond turned are Pb, Ni, Al, Au, Cu, and various Cu alloys. To date, certain materials, most notably glasses and ferrous materials, have not been successfully diamond turned. New facilities have been established, most notably at the Naval Weapons Center, for investigation of diamond turning technology and the extension of the process to new materials. Large scale, volume production facilities have been set up at the Y-12 plant in Oak Ridge, Tennessee. Another process that has been advanced for volume production of transparent dielectric optics is hot forging. This technique has recently been applied to divalent fluorides for the fabrication of both lenses and windows.

There is increased emphasis on the importance of process control in the fabrication of both windows and thin-film coatings. It is now relatively well known that it is essential to use ultra-pure materials, such as those fabricated by chemical vapor deposition, and to insure reduced surface absorption by paying particular attention to substrate cleaning. The chemistry or chemical activity of the substrate surface is also of paramount importance in controling surface absorption. If substrates are subjected to optical polishing, it is, of course, important to use an appropriate cleaning or even etching technique in order to remove the residual polishing material. In the thin-film optics area the use of ultra-high vacuum techniques in the film deposition is one way of achieving high purity in the film structure. Because of the frequently reported observations that sputtered films exhibit higher damage thresholds than do vacuum deposited films, there is continuing interest in both rf and dc sputtering for metals, dielectric films, and even polymerized organics. However, great care must be exercised in the sputtering process due to the fact that the surface can be contaminated by the sputtering gas.

Another area of continuing advance is the introduction of new materials for a variety of purposes in high power laser optics. The Proceedings of the Damage Symposium continue to record the expansion of the data base regarding new materials. The development of new materials can have a significant impact on system performance; thus in the high power glass program of the Energy Research and Development Administration the introduction of materials of low index nonlinearity and high damage resistance, both in active and passive elements, can lead to significant improvement in the output and efficiency of large glass lasers. In considering the advantages resulting from the introduction of a new and improved material in a large laser system, it is essential that a total system evaluation be carried out, rather than simply an evaluation of an individual element. The presence or absence of a correlation of figure errors and laser-induced distortion between system elements must be considered in evaluating the benefit which accrues from the introduction of a new material.

With these caveats in mind we can review the new materials which are currently under investigation. Silicon carbide was introduced at this year's symposium as a useful substrate material for 10.6 μm mirrors. SiC can be electroplated with a metal such as copper to yield a highly reflective surface with a high damage threshold. Thresholds as high as 11 joules per square centimeter have been observed in 1.4 nanosecond 10.6 μm pulses on copper-plated SiC mirrors. These mirrors exhibited surface roughnesses as low as 5 Å rms. In previous years speakers had expressed concern over the high absorption values seen in ThF_4 coatings used at 10.6 μm. This year several new coating materials were described for possible use as low index materials at 10.6 μm. These include monovalent and divalent fluorides which exhibit low refractive indices. NaF is especially attractive as an alternative to ThF_4 since it exhibits low absorption, a high damage threshold, and can be used as a single layer anti-reflection coating on NaCl. Novel designs for anti-reflection coatings, such as a three-layer coating consisting of only low index materials (BaF_2, NaF) can lead to a greatly increased damage resistance due to the absence of normally encountered high index coating materials. Thus, not only new materials, but new designs are leading to improved performance. Additionally, rare earth fluorides, including SmF_3, EuF_3, and NdF_3, can be used in conjunction with higher index substrates in single layer anti-reflection coatings and in two-layer designs along with a higher index material. The properties of these materials are just beginning to be investigated. It has been observed that they are particularly sensitive to the presence of water, even at very low pressures in the deposition process. Considerable interest is evident in the use of TlI as a high index coating material for use at 10.6 μm. This material exhibits an index of 2.3 at 10.6 μm, is insoluble in water, and adheres well to KCl.

A totally new class of materials was introduced this year for the first time as an optical coating material. Plasma polymerized ethane (PPE) coating has been discussed as a possible protective coating for alkali halide windows. A substantial amount of research is still required in order to reduce the residual absorption in this material. Another attractive option which has been presented is that of using mixed films of germanium and selenium in order to create films of continuously variable refractive index. Finally, the use of hot pressed chalcogenides as Faraday rotator materials at a variety of wavelengths in the infrared has been suggested. The hot pressing process offers the possibility of developing large aperture components.

Advances in the laser damage field have generally required corresponding advances in the area of diagnostic instrumentation technology. The use of Auger spectroscopy to probe the concentration of impurities near surfaces is an example of a sophisticated research tool being brought to bear on an optical materials problem with great effect. This year saw an increasing use of Auger techniques in diagnosing surface contamination, thin film deposition phenomena and the role of impurities. Another technique advanced for thin-film studies was attenuated total reflection (ATR) spectroscopy. By depositing thin film specimens on ATR witness plates it is possible to probe for the effects of surface absorption with a very high sensitivity, and to distinguish near surface absorption in the bulk of the film or substrate. Another technique advanced for distinguishing between surface and bulk absorption was photo-acoustic spectroscopy.

In order to provide the systems designer with useful relationships concerning the utility of specific materials in a variety of laser systems, there has been a tendency to organize data in the form of empirical scaling relations. This year has seen an advance in the sophistication and in the scope of these scaling laws. It has been pointed out that a significant amount of relevant work exists in the literature, particularly in the literature of the Soviet Union, on such scaling relations. This year at the Damage Symposium scaling laws for both the area dependence and time dependence of laser damage were put forth. It has been observed that the power density at which damage occurs increases as the reciprocal of the diameter of the focal spot size and as the reciprocal of the square root of the pulse duration. These scaling laws have been seen to apply over a wide range of pulse durations from 10^{-10} to 10^{-2} seconds and over a range of spot sizes from 9 to 140 μm in the bulk and 180 to 10^{4} μm on surfaces. The fundamental mechanisms underlying these simple scaling laws and the reasons for the extensive range of applicability of these relationships are not immediately apparent. Nevertheless, within this range of parameters the use of the scaling laws as an empirical guide seems fully justified. Another parameter which can be varied in order to obtain scaling laws is the wavelength or frequency of the incident light. However, in this case great care must be exercised because of the existence of resonant phenomena. Thus, it has been observed that in a number of oxides of refractory materials the damage threshold increases as the operating wavelength goes from 1 μm to 0.5 μm, but that the damage threshold is further reduced by moving the operating wavelength further into the ultraviolet. The reason for this is undoubtedly the onset of direct absorption in the material, either by one photon process or possibly by a two-photon process. There are other cautions that must be observed regarding the application of scaling laws. One of these relates to the Achilles Heel nature of damage phenomena. Damage at a surface or in a thin film structure, or even in bulk material, typically occurs at a weak point in the material. Scaling laws.of necessity,typically relate to average properties of the material. It is not always expected that failure at a weak point will follow a simple scaling relation, and therefore, it is only expected that empirical scaling laws will be obtained for relatively pure homogeneous and well characterized materials. Additionally, other factors such as standing electric waves from constructive and destructive interference must be taken into account. This is most evident, of course, in multi-layer dielectric films, and experiments were described in this year's symposium which bear out both the Achilles Heel nature of laser damage and the importance of calculating the detailed local electric field in more fully understanding damage phenomena.

Finally, advances continue to be made in the fundamental understanding of damage processes. The role of impurities is continually being elucidated. An abundance of data has been generated regarding such properties as bulk absorption in transparent dielectrics. Good care must be excerised in the intercomparison of these data due to the mediating effect of impurities in determining bulk absorption. The damage threshold of hard drawn copper mirrors, for example, was found to be much lower than the damage threshold of OHFC copper mirrors. The cause of this discrepancy was identified as the presence of oxide impurities at grain boundaries in the hard drawn material. Impurities often play an important role in improving the quality of laser materials. The introduction of divalent impurities in alkali halides, for example, increases their fracture strength and also stabilizes micro-crystals preventing the migration of grain boundaries. So, for example, the use of strontium chloride, $SrCl_2$, in stabilizing KCl. The presence of impurities, either those introduced on purpose or those that come into the material accidentally, greatly complicates the problem of materials characterization.

The avalanche ionization process continues to be investigated. It has been observed that ionization damage in the subnanosecond regime appears to be deterministic while in the nanosecond time range the process appears to be statistical in nature. As in gas breakdown at high pressures, avalanche ionization appears statistical when it occurs at a lower field strength. In short pulse experiments in solids or low pressure experiments in gases, breakdown occurs at high field values where the generation of the initial electrons is highly deterministic. Whereas, at low pressures in the gas or at long pulses in solids where low field values are involved the statistical nature of the initial electron generation is more in evidence. Other points of fundamental interest that come to the fore in this year's discussion include the identification of an interference of the electric wave with near-field scattering from dielectric or metallic inclusions giving rise to a ripple-like damage pattern oriented along the electric vector of the incident light wave. This effect has been noticed by several observers in the past, but it was only this year that a coherent explanation of the observation has been provided. Finally, a note of caution has been introduced in regard to the role that defects play in determining the damage process. No matter what the fundamental nature of the damage phenomenon is, whether it is avalanche ionization, thermal, multi-photon absorption, or field intensification, all of these processes are enhanced in the vicinity of a defect or discontinuity in the material. Therefore, the fact that damage occurs in the vicinity of a discontinuity or defect in no way indicates that mechanism is responsible for the damage. Uncovering of the intrinsic damage process must thus be accomplished in the absence of extrinsic influences.

2.0 Summary of Papers

The 1976 Symposium was divided into five sessions, each occupying roughly half a day. The formal presentations were supplemented by poster sessions, at which several papers, either of special interest or consisting primarily of data tabulation, were presented. The general topical areas were (1) Bulk Material Properties and Thermal Behavior, (2) Mirrors and Surfaces, (3) Thin Film Properties, (4) Thin Film Damage, and (5) Scaling Relations and Fundamental Damage Mechanisms. In the following summary a concise statement of the principal results of each paper is presented. Readers are thereby directed to the topics of their particular interest, and at the same time, presented with an overall view of the principal concensus of the Symposium.

2.1 Bulk Properties and Thermal Behavior

In high average power systems, thermal effects are the dominant damage considerations. At average power densities of tens of kW/cm^2, absorptance values of $10^{-4}cm^{-1}$ can easily lead to an unacceptable deterioration in system performance. Accordingly, one of the topics of principal interest in this session was weak absorption and its consequences on overall system performance. Thermal effects can also be important for high peak power systems, leading to transient optical distortion or even thermal fracture.

In the first paper of the Symposium H. E. Bennett of the Michelson Laboratories at the Naval Weapons Center presented a detailed multi-component system oriented discussion centered about thermal distortion thresholds for optical trains handling high pulse powers. A diffraction approach based on the Marechal criterion for the multi-element system was employed. This analysis included the role of figure errors, thermal distortion in windows and mirrors, energy transmission limits for optical trains and a comparison of the influence of window and mirror material properties. In this presentation emphasis was placed not on the catastrophic damage limit, but rather on the allowable degradation in beam focusability and the impact of this latter limit on optical tolerances based upon fabrication specification and material properties. Detailed consideration of the utility of adaptive optics to correct or ease these constraints was not discussed, but rather the development of frequency dependent figures of merits which would ease the correction requirements, by allowing for optimum material selection and component specification.

He concluded that for most multi-component optical trains, thermal distortion, initial figure error and optical homogeneity must be considered with initial figure errors frequently a fraction of a visible wavelength even at infrared wavelengths. Thus for materials of low index (alkali halides and alkaline earth fluorides),tolerances can be set at much more relaxed levels than for high index materials such as ZnSe. However, correlation of errors must be considered in assigning an error budget to each element in a multi-element system. For example, initial figure errors and homogeneity error are usually uncorrelated with each other or with thermal distortion, while figure errors resulting from thermal distortion are correlated. The sign of the variation must also be considered.

From the materials selection standpoint, calculations suggest that selected window materials can handle much higher single pulse energy densities than mirrors, while for high average power cw or repetitively pulsed systems metal mirrors are easier to cool. For the materials considered, coated molybdenum is preferred for mirrors used in microsecond or larger pulsed systems, while uncoated mirrors are best for shorter pulse lengths where catastrophic damage evolved. Here copper is preferred over molybdenum or aluminum.

J. H. Apfel of the Optical Coating Laboratory presented formulas for calculating the polarization dependent electric field strength and power dissipation due to weak absorption in transparent optical elements at non-normal incidence. Although not of an exact description, power dissipation per unit value can be assumed to vary as the cosine of the incident angle.

Of obvious interest to individuals concerned with the system design and performance of high power cw gas laser systems is the induced thermal stress in laser window elements. This subject was the topic of a paper by R. E. Rondeau of the Air Force Materials Laboratory and Dale Ford of the University of Dayton Research Institute. Their paper discussed in detail several coupled two-dimensional computer programs which model in-depth optical absorption, resulting heat transfer, and induced stress in disc geometries. The effect of window thickness, incident power level, absorptance and duration of exposure of a ZnSe output coupler employed in a 15 kW CO_2 laser was studied. Stress resulting from radial and axial temperature distortions was calculated and compared to experimental results. Although not conclusive, this comparison indicated the possible degradation of ThF_4 coatings by hydroscopic action which led to increased surface absorption resulting in intolerable thermally induced tangential tensile stresses occuring near the edge of the beam. This possibly was suggested by the abnormally high value measured for the coating absorption.

In their continuing exploration of improved techniques for interferometric analysis of laser heated windows E. Bernal of the Honeywell Corporate Research Center and J. S. Loomis of the University of Arizona reported on several new developments. In particular, they investigated the contributions of anisotropic aberrations, due to a polarization dependence, to resultant window response. Results indicated this dependence to be quite small for many normally employed materials. In order to make the requisite measurements with accuracy and facility, elegant techniques involving the generation of synthetic interferograms and semi-automatic digital analysis were reported.

Their results concluded that signified anisotropic effects are present in BaF_2, SrF_2, and CaF_2 at 10.6 μm while alkali halides (of considerably less absorption at 10.6 m) exhibited essentially insignificant anistropic effects. In fact, these materials are ∿ 50 times less sensitive than the alkaline earth fluroides at 10.6 μm.

As laser technology develops and new laser wavelengths become the center of interest, a search for transparent materials exhibiting desirable characteristics and damage resistance evolves. Such was the subject of a report by J. A. Harrington of the University of Alabama in which he assessed the potential of several alternate optical materials for use with HF (2.8 μm) and DF (3.8 μm) chemical lasers. The main thrust of his investigation concentrated on an evaluation of the optical absorption at the chemical laser wavelengths of $LiYF_4$, Yttralox [Y_2O_3(90%):ThO_2(10%)], Zns, CdTe, KBr, SrF_2, and KRS-5 window materials. Unfortunately, the optical absorption of all the materials studied was in a limited range. However, Yttralox and LiF_4 should be investigated for achieving lower absorption through improved materials processing because of their otherwise appealing physical properties (strength and environmental resistance). As an ancillary to this study, water repellent polymeric coatings were evaluated as a protection for hydroscopic materials such as KCl. Initial tests relating to film absorption are sufficiently encouraging to warrant further investigation using higher quality KCl substrates.

The group at Hanscom Air Force Base has been a vital contributor to the development and assessment of low loss infrared optical materials, particularly windows and coatings. In a continuation of their work A. Hordvik, B. Bendow, H. G. Lipson, L. H. Skolnik, and R. N. Brown have recently completed a rather thorough and comprehensive investigation of bulk and surface optical absorption in several mid IR laser window materials at CO and HF laser wavelengths. The materials investigated included ZnSe, Al_2O_3, MgO, LiF, MgF_2, CaF_2, SrF_2, and BaF_2. Experimental techniques included emittance and Fourier transform spectroscopy as well as laser calorimetry and a new photo-acoustic technique which allowed simultaneous determinations of both bulk and surface absorption to be made. The latter technique, with an estimated sensitivity of $10^{-6}cm^{-1}$determines the resultant expansion of a material after short duration exposure to an appropriate wavelength optical pulse. Any material absorption leads to the generation of an acoustic or elastic wave, which is measured and related to the absorption coefficient. Tabulations of both the bulk and surface values as a function of wavelength were presented. Interestingly at 2.7 μm, surface absorption may become dominant over bulk losses. Sapphire emerged as an excellent candidate at the HF laser wavelength providing its large surface absorption can be substantially reduced. Included in the presentation was an indication of success in calculating the intrinsic absorption level in ZnSe from first principles.

In their continuing program on establishing quantitative values for optical and mechanical properties of important optical materials, the group at the National Bureau of Standards consisting of A. Feldman, D. Horowitz, and R. M. Waxler reported on the temperature and stress dependence of the refractive index of CaF_2, BaF_2, CVD ZnSe, and fused silica at 632.8 nm, 1.15 μm, 3.39 μm, and 10.6 μm, typically over the range -180° to +200°C. This information is coupled with thermal expansion data to allow a quantitative evaluation of the response of these materials in window form to high laser intensities. Thermal expansion is normally measured by the method of Fizeau interferometry while piezo-optical constants are made using a modified Dyson polarizing interferometer, exhibiting a precision of $\lambda/500$ at 632.8 nm. Expansion parameters from -100°C to +120°C are as follows: for CVD ZnSe $\Delta t/t = (7.29 \pm 0.02) \times 10^{-6} T + (5.26 \pm 0.17) \times 10^{-9} T^2 - (1.45 \pm 0.07) \times 10^{-11} T^3$, for BaF_2 the coefficients are $+ (18.1 \pm 0.1) \times 10^{-6} T + (11.5 \pm 0.3) \times 10^{-9} T^2 - (2.0 \pm 0.3) \times 10^{-11} T^3$ and for CaF_2 $+ (18.4 \pm 0.1) \times 10^{-6} T + (16.4 \pm 0.3) \times 10^{-9} T^2 - (3.7 \pm 0.3) \times 10^{-11} T^3$. At 632.8 nm the dn/dT of CVD ZnSe ranges from $9.3 \times 10^{-5} T$ at -100°C to $11.2 \times 10^{-5} T$ at 120°C. The piezo-optic coefficients are in essential agreement with earlier investigations.

In a closely allied paper M. J. Dodge also of the National Bureau of Standards investigated the refractive index and the temperature coefficient of refractive index of hot-forged CaF_2. Using a minimum deviation method and precision spectrometer, she reported the refractive index from 0.25 μm to 8.0 μm at 21°C and 34°C. Data was fitted to a three term Sellmeier-type dispersion formulation

$$n^2 - 1 = \sum [A_j \lambda^2 / (\lambda^2 - \lambda_j^2)]$$

which permits interpolation within a few parts in 10^{-5}. The index of refraction is n, λ is the wavelength of interest, λ_j's are the calculated wavelengths of maximum absorption, and the A_j's are the calculated oscillator strengths. At 20.8°C the constants are $A_1 = 0.98584551$, $A_2 = 0.05290246$, $A_3 = 4.2816899$, $\lambda_1 = 0.07218116$, $\lambda_2 = 0.14114719$, and $\lambda_3 = 36.465937$, while $\Delta n/\Delta T(°C)^{-1}$ in the stated temperature range varies between -2.2×10^{-6} and -4.5×10^{-6} over the wavelength range studies. These values for the hot forged polycrystalline CaF_2 are between one-third and equal to the corresponding values for single crystal CaF_2.

New materials and fabrication processes are continually evolving as laser technology progresses. Recent interest in the hot forging process as a technique for fabricating laser windows with high strength and low absorption was evidenced by four papers relating to this process.

Some critical questions relating to the use of hot forged monovalent and divalent halides as laser window materials were addressed in a paper by R. M. Cannon, H. K. Bowen, A. M. Glaeser, H. J. Mayson, F. A. McClintock, W. M. Sherry, J. B. VanderSande, and M. F. Yan, all of the Massachusetts Institute of Technology. They concerned themselves with two aspects of hot forged crystalline materials, micro-structure formation during the forging process, and microcrack coalescence, leading to mechanical failure. They observed that dynamic recrystallization is significant in CaF_2 at temperatures as low as half the melting temperature, while in monovalent halides, it generally is limited to temperatures greater than 80% of the melting temperature. An analytical model has been developed for grain boundary mobility in alkali halides, which relates the strengthening effect of divalent impurities to the increased electrostatic interaction between the impurity and the grain boundary. Techniques for microcrack detection using both acoustic emission and light scattering were discussed.

Due to the untimely illness of Harold Posen of Hanscom Air Force Base, the paper by him, N. Klausutis, J. Bruce, J. A. Adamski, and J. R. Weiner on double doped halide laser window materials was not formally presented at the Symposium; however, it is included in the Proceedings proper. In this interesting discourse, the grain boundary stability of alkali halide materials alloyed with 1.75% RbCl was investigated. RbCl is usually added to RAP (reactive atmosphere processing) grown KCl to produce a considerably strengthened polycrystalline window material by hot forging with little degradation in other important optical properties. However, instabilities in the micro-structure of these KCl-RbCl alloys is usually observed, leading to secondary recrystallization and grain growth. Thus these materials tend to revert to a single crystal state causing a considerable reduction in material strength. To prevent this undesirable state of affairs, the addition of 10 ppm to 250 ppm $SrCl_2$ as a stabilizing agent was studied. Results of this investigation led to the following conclusions: polycrystalline KCl-RbCl alloys stabilized with low concentrations of $SrCl_2$, yield forged billets which (1) have small grain size (< 10 μm), (2) have high strength when complete recrystallization is achieved (5840 psi), (3) have low 10.6 μm optical absorption ($2\text{-}6 \times 10^{-4} cm^{-1}$), and (4) show greater grain boundary stability with increasing ppm $SrCl_2$. Billets containing 50 ppm $SrCl_2$ or greater show no secondary recrystallization or grain growth after a 350°C anneal.

In an additional contribution from the Honeywell group, R. H. Anderson, B. G. Koepke, and E. Bernal G. discussed a related subject, namely, the intermediate temperature (0.5 to 0.7 T_m) isostatic forging of calcium fluoride crystals. Their results conclude that isostatic forging is a viable process for producing crack-free fine grained (< 10 μm) material from CaF_2 single crystals with significantly improved fracture energies, providing forging is done at temperatures greater than 500°C. However, from birefringence measurements there resides a considerable internal stress. This problem will require further study. If a positive result can be attained without increased grain size, an additional increase in the fracture energy is expected. Observations of the present developmental forgings indicate a certain amount of "veiling" (internal cloudiness). Higher temperature forging should greatly reduce this annoying feature.

In a poster paper R. H. Anderson, E. Bernal G., and R. J. Stokes of the Honeywell Corporate Research Center discussed an evaluation they performed on the forging of completely finished halide optical components. This investigation was initiated to address the possibility of eliminating or reducing optical shaping and finishing operations. In this work employing KCl billets (3.81 cm in diameter x 3.81 cm in height), forging is done isotatically using a closed $\lambda/10$ quartz die technique to produce the desired surface shape and finish at 275°. Normally two separate forging operations are necessary, one to produce uniform strain distribution and then, after a small amount of preshaping by water polishing, the major shaping operation is accomplished by a second forging. A major conclusion of this work was that the forged surfaces appeared superior to mechanically prepared surfaces as far as coatability is concerned, particularly for protective and thin films of thallium iodide. Work on this interesting approach to volume production of high quality optical elements is proceeding.

Two papers were presented concerning the properties of CdTe, a promising material for infrared windows. Other papers dealt with new materials in the infrared for use as isolators and windows.

H. L. Tuller, K. Uematsu, J. B. VanderSande, E. L. Hall, and H. K. Bowen of the Massachusetts Institute of Technology presented results from a detailed materials study of the mechanical properties of vapor deposited CdTe. The intent of this study was to evaluate the feasibility of growing large, high quality plates of CdTe for laser window applications. Heretofore, previous attempts have results in material whose absorption coefficients were greatly in excess of theoretical expectations ($\sim 10^{-4} cm^{-1}$). It was pointed out that this difficulty can arise because (CdTe) exists over a range of compositions around the stoichiometric composition, and thus the concentration of defects will be very sensitive to the original growth conditions, e.g., substrate temperature and Cd/Te ratio, and to the cooling path followed after growth. For this reason vapor deposition from elemental Cd and Te sources was chosen as the best approach.

Several important results were obtained. Mechanical tests indicate that CdTe undergos a considerable amount of plastic strain at 300°C before failure, thus forging is immediately suggested for preparing large blanks. Additional effort on the development of large sized, high optical quality, strong CdTe elements are contemplated.

From the previous paper it is obvious that when substances are proposed as new candidate optical materials, growth and fabrication procedures together with resultant optical and mechanical properties must be assessed and correlated to fully appreciate the details of failure modes. Frequently the specifics of the failure mechanism and an appropriate line of analysis have previously been detailed for another related case. Cubic CdTe, as studied by H. S. Bennett of the National Bureau of Standards and C. D. Cantrell of the Los Alamos Scientific Laboratory, is a promising infrared material which frequently fails extrinsically due to the deleterious heating of absorbing, tellurium-rich inclusions. Resulting thermal expansion leads to the production of unacceptable stresses within the host materials. This is not at all unlike the care of absorbing Pt or Sb inclusions in laser glass as studied by Hopper and Uhlman, as well as Feldman and detailed in the Proceedings of the 1970 Symposium on Damage in Laser Materials. In that case $\sim$ 1 μm spheres were most susceptible to damage in $\sim$ 40 ns pulsed 1.06 μm irradiations. Here for Te conclusions, computations suggest that heating of 0.1 μm to 10 μm Te aggregates when subjected to power densities of $\sim$ 100 MW/cm^2 and pulse widths of 200 ns could produce stresses comparable to the fracture strength of the CdTe host.

Because of the great advantages of using a saturated ferromagnetic material in a Faraday rotator, the material $CdCr_2S_4$, a ferromagnetic spinel, has attracted attention as an isolator material at 10.6 μm. As reported by S. D. Jacobs and K. J. Teegarden of the University of Rochester, large aperture components can be made by hot-pressing polycrystalline $CdCr_2S_4$ material. Unfortunately, the observed absorption in the spinel is high, typically $\sim$ 1 cm^{-1} in the most favorable spectral range. However, the authors feel that this absorption is principally due to impurities, and that it can be reduced by purifying the starting material. Due to the high Verdet constant of the material, only thin samples need be used. Thus, in a saturating field of 3.5 KOe, a thickness of 0.375 cm will yield 45° rotation, providing from 20 to 30 dB isolation with a 30% insertion loss. Preliminary damage tests on the material indicate that under 50 ns, multimode irradiation at 10.6 μm, the damage threshold is about 6.5 J/cm^2, about half that of Germanium under similar test conditions.

There is a paucity of information regarding laser damage in the midrange of the infrared from 3 to 6 μm. M. Bass, K. Leung, and C. Tang of the University of Southern California, along with M. J. Soileau of the Naval Weapons Center, have made a first attempt at remedying this deficiency. They investigated laser damage in a variety of midrange window materials, namely, divalent and monovalent fluorides and sapphire, using a multiline, transverse-excited DF laser. The output pulse shape of the laser was not simple, but an equivalent pulse width was about 75 ns.

The samples irradiated were commercially prepared, and specified as having "high power laser" finishes but showed surface damage thresholds typically a factor of ten below the corresponding bulk values. Surprisingly, although Al_2O_3 exhibited a bulk absorption of 4×10^{-2} cm^{-1}, 100 times that of the fluorides, its bulk damage threshold was 1.6 times that of NaCl, and within 20% of the highest values obtained for any material. The authors feel that the observed bulk damage was impurity-mediated. The high value obtained for sapphire is undoubtedly correlated with its very high melting temperature, which is 1.5 to 2.0 times that of the fluorides. This is especially valid if the bulk absorption in Al_2O_3 is actually of the order of 10^{-4} cm^{-1} rather than 10^{-2} cm^{-1} as is reported elsewhere in these Proceedings by investigators at Hanscom Field. The discrepancy in reported absorption values may be due to high surface absorption for sapphire.

2.2 Mirrors and Surfaces

As in last year's Symposium, there was considerable interest evidenced in diamond turning, both of metals and new dielectrics. An extensive catalogue of materials successfully finished by this process is presented below. The high optical quality and damage resistance shown by micro-machined mirrors has generated strong interest in metal mirrors for laser use, as well as in diamond-turned dielectric windows.

D. L. Decker and R. E. Cram of the Michelson Laboratories reported on a highly precise diamond turning facility for the machining of optics now under development at the Michelson Laboratories. A brief review of the advantages of diamond turning for optics was given, with special emphasis on the requirements for a compatibility between tool and work piece for successful machining. The current capabilities of diamond turning were summarized as follows: mechanically polished metal surfaces are accurately fabricated to a random surface error of 25 to 40 Å rms. Small diamond-turned pieces (< 15 cm diameter) are fabricated to a surface finish of < 40 Å rms for flat pieces, 50 to 100 Å rms for figured pieces. Large pieces display surface finish of the order of 180 Å rms, typically. Diamond turned optics shows lower surface absorption, and higher laser damage values than conventionally polished optics. Among the materials successfully diamond-turned to date are metals; including Cu, Cu-alloys, brass, Au, Ag, Al, Al-alloys, Pb and electrodless nickel; insulators, such as NaCl, KCl, CaF_2, SrF_2, BaF_2, ZnS, ZnSe, MgF_2, and acrylic plastics.

The proposed machine at NWC incorporates an air bearing spindle, and air bearing slide ways in both X and Y directions, mounted on an air suspension isolated, block granite layout plate. A slide position interferometer is mounted at tool height, thereby reducing the offset errors. Work pieces up to 35 cm in diameter and 100 pounds weight can be accommodated. The machine is viewed as a research facility to explore both the machine technology itself and the capabilities of diamond turned optics. The facility will be operational by February 1977.

A detailed investigation of the surface properties of diamond-turned KCl windows was reported by M. J. Soileau, J. M. Bennett, J. O. Porteus, W. Faith, and J. Jernigan of the Michelson Laboratories, and T. T. Saito of the Lawrence Livermore Laboratories. They examined specimens of polycrystalline KCl, doped with EuCl and RbCl, hot-forged into laser window blanks. The windows were diamond turned at the Oak Ridge Y-12 facility, using an off-center fly cutter without lubricant, to generate a smooth surface free of contamination. The off-center cutting produces grooves which are relatively straight and parallel. The samples were then sent to the Naval Weapons Center, Michelson Laboratories for characterization and laser damage tests.

Among the tests carried out were laser absorption calorimetry, total integrated scattering, surface profilometry, using a Talystep instrument and CO_2 laser damage threshold measurement. Surface roughness was measured to be $\sim$ 135 Å rms, by Talystep profilometry, 180-200 Å rms by use of a polarization interference microscope, and over 300 Å as measured by total integrated scattering at 10.6 μm. Similar discrepancies are seen between TIS and Talystep measurements of mechanically polished surfaces, and may be due to the contribution of bulk scattering to the TIS value.

Surface absorption was estimated to be about 3.7×10^{-4} per surface, obtained by measuring total absorption before and after etching. This measurement was made on the KCl: EuCl sample; no satisfactory etching could be obtained with the KCl: RbCl sample. The high value of surface absorption may have been due to atmospheric contamination or poor handling after machining, rather than to the machining process itself. Laser damage thresholds were observed to be as high or higher than on conventionally polished and etched surfaces.

A further investigation into the properties of diamond-turned metal mirror surfaces was reported by D. L. Decker, M. J. Soileau, J. O. Porteus, and J. M. Bennett of the Michelson Laboratories. The samples investigated included diamond turned copper surfaces from the Lawrence Livermore Laboratory, and from a commercial source (Heliotrope) as well as electroplated silver and gold mirrors from LLL. Surface roughness, laser damage, and surface composition were studied. The surfaces were all very smooth, with rms roughness is from 30 to 40 Å. Profilometry revealed a regular topographical structure corresponding to the tool advance. Light scattering measurements did not correlate with the measured roughness, and measured scattering in the visible was much lower than the measured surface roughness would imply. No explanation for this discrepancy was advanced. Laser damage tests implied that damage was due to absorbing centers congregated at grain boundaries, or in isolated particulates. Laser-induced delamination was observed in electroplated samples.

Damage at optical surfaces remains a significant problem in high power laser systems. Due to the prevalence of defects and impurities of exposed surfaces, from both environmental contamination and the polishing process, surfaces fail more readily than does the bulk material.

A detailed study of laser-induced thermal damage on single-crystal, Al targets, irradiated in vacuum with 100 ns pulses of 10.6 μm radiation, was carried out by J. O. Porteus, M. J. Soileau, and C. W. Fountain of the Michelson Laboratories. The objective of their study was to differentiate between stresses generated by thermal gradients in the material and compressions resulting from the vaporization of target material. Both ion and neutral particle emission from the targets were monitored. The authors concluded that evaporative compression is responsible for stress generation at illumination levels above the threshold for local melting, while below that threshold, surface roughening can be generated by thermally induced stresses. Thresholds for damage by melting were about 14 J/cm^2 on these single-crystal targets, which is almost twice the threshold observed on polished 2024 polycrystalline targets. This apparent inconsistency is probably due to a variation (reduction) in surface absorption.

Damage at 10.6 μm resulting from plasma formation was studied by J. J. Hayden of the Los Alamos Scientific Laboratory and I. Liberman of the Westinghouse Research Labs. Using a mode-locked TEA laser emitting pulses of 1.4 ns FWHM, they measured the threshold for plasma formation on OFHC copper mirrors, both micro-machined and conventionally polished, on NaCl windows, with and without single layer CaF_2 AR coatings, and on a variety of other window and mirror samples. Their principal results are summarized as follows.

Micro-machined Cu mirrors showed slightly higher damage thresholds than conventionally polished samples, when tested both in air and in vacuum. At both 90° and 45° angles of incidence, damage thresholds varied from 7 to 10 J/cm^2 in the indicated pulse duration. The morphology of the damaged surface was different for the two methods of preparation; conventionally polished surfaces showed damage in the form of small pits, while micro-machined surfaces showed a more uniform surface melting.

AR-coated, NaCl windows showed damage thresholds almost twice as high as uncoated surfaces probably due to the significantly lower index of refraction of the coating material. The threshold at the coated surfaces varied from 7 to 10 J/cm^2, typically. These were very good, single crystal specimens of NaCl. Among the other materials tested, copper-electroplated SiC mirrors were of great interest. Repeated exposures at 11.4 J/cm^2 failed to produce damage on these surfaces.

Another damage study at 10.6 μm was reported by R. Gibbs and R. M. Wood of the General Electric Company, Ltd. Laboratory in Wembley, England. Operating at a pulse duration of 60 ns FWHM, they observed thermal damage in metal mirrors, ir window materials, and dielectric coatings. They also observed comparable thresholds in conventionally polished and diamond-turned Cu. They reported, however, that hard-drawn Cu showed a much lower threshold than OFHC Cu due to oxide formation at the grain boundaries. In metal mirrors, damage thresholds were shown to correlate with surface absorption, and with surface scratches from the polishing process. On coated elements, the presence of absorbing defects was shown to reduce the damage threshold significantly. Plated gold surfaces showed significantly higher thresholds than evaporated gold surfaces, as well as higher reflectivity and greater durability.

A method for the measurement of the absorptivity of dielectric-enhanced mirrors was presented by P. Kraatz, J. R. Buckmelter, and S. J. Holmes of the Northrop Corporation. They investigated a number of dielectric coatings on Mo, Cu, CerVit, and CaF_2 substrates, using 5.3 μm radiation from a cw CO laser. Measurements were made calorimetrically from measurements of the energy reflected by and transmitted through the sample, and a direct measurement of the sample's temperature rise. The calorimetrically determined absorption was compared to reflectometer values obtained at the Naval Weapons Center. Agreement in three samples was within 4×10^{-4}, while in a fourth sample the discrepancy was 2×10^{-3}. The reasons for this discrepancy were unclear. Absorptivities on the order of 1 to 5×10^{-3} were measured for ThF_4/ZnS multilayer coatings on bare Mo, Ag-plated Mo, Cr-plated Mo, Ag-plated CerVit and CaF_2.

Absorptivity values of 1×10^{-3} or lower were observed in multilayer ThF_4/ZnSe coatings on all of the above substrates. Coatings of SiO/Si and SiO/Ge exhibited absorptivities of $1 - 9 \times 10^{-3}$ on most substrates. Al_2O_3/Si multilayers exhibited much higher absorptivities. The best overall combination appeared to be ThF/ZnSe, with 3 or 4 pairs of layers. Several vendors provided reflectors with absorptivities less than 1×10^{-3} and reflectivities of 0.999 on numerous substrate materials.

The effect of sputtering gas entrapment on the reflectance of metallic films was studied by P. A. Temple, D. K. Burge, and J. M. Bennett of the Michelson Laboratories. Cu, Au, Ag, and Al films were deposited via dc sputtering, using Ar and Xe sputtering gases. Films were prepared using various combinations of gas type, gas pressure, and sputtering rate. The best films prepared compared favorably with those prepared by UHV evaporative deposition. In general, in accord with the model advanced by Lee and Oblas, higher gas pressure led to lower gas entrapment, and consequently higher reflectance films. However, effects due to the reactivity of the metal, as in the case of Al, and the presence of residual impurities, especially oxygen, can greatly outweigh the direct deleterious effect of sputtering gas entrapment.

2.3 Thin Film Properties

Thin film multilayers represent the weakest link in any high power laser systems. Whatever weaknesses surfaces are heir to are manifested many times over in multilayer dielectric coatings. Such coatings, however, are essential ingredients of the laser system. A continuing effort to find new materials, characterization tools, methods, and designs for thin film optics is underway, especially in the infrared, where thin-film optics is less advanced than in the visible.

Multilayer dielectric coatings for polarizers, reflectors, beam splitters, and AR coatings, remain a critical area at 10.6 μm. Currently, there are significant problems encountered in obtaining satisfactory coatings for high-power, infrared laser use. These problems, their elucidation, and potential resolution in the next few years, were the subject of a report by M. Sparks of Xonics, Inc. Sparks identified a set of guidelines for the selection of materials for thin film use at 10.6 μm, including; bulk absorption less than 0.5 cm^{-1}, appropriate refractive indices, non-hygroscopic character, appropriate mechanical characteristics, and good properties in the thin film state, such as high packing density, good adhesion, stable stoichiometry, and chemical inertness. Materials satisfying most, if not all of these criteria, include ThF_4, NaF, NaCl, KCl, BaF_2, SrF_2, and $KGaF_4$ for low-index layers, and As_2S_3, As_2Se_3, ZnS, ZnSe, and TlI for high index layers. Specifically excluded were materials containing elements lighter than flourine since they generally exhibit a fundamental resonance near 10.6 μm. This exludes oxides, carbon compounds, and some fluroides (LiF, CaF_2, MgF_2, AlF_3, and cryolite) which absorb at 10.6 μm. Polymer films, discussed elsewhere in this Symposium (see paper by Reis, Hirtsuka, Bell, and Shen) have a potential as protective coatings for hygroscopic materials, assuming the problems of pinholes and H_2O vapor transmission can be solved.

One of the major problems of thin films today is the presence of H_2O in the film. Water is absorbed on the surface of the film, and also forms as liquid H_2O in the pores of the film. The latter has a doubly deleterious effect in high index materials, since the index of H_2O is low, and the absorption coefficient for liquid H_2O is uniformly high at all $\lambda > 4.5$ μm. Film porosity is a problem of major importance in improving thin film performance at all wavelengths, not only at 10.6 μm. Other impurities can be equally deleterious. Sparks suggests a near-term process development program, using only ultra-pure materials, UHV vapor deposition (although sputtering, for example, is still interesting as an alternative process), careful characterization of the films, calorimetric measurements of film absorption (spectroscopic measurements are not sufficiently sensitive) and standardized use of attenuated total reflection spectroscopy (ATR) to probe the location of absorbing layers in multilayer films. Laser damage measurements could complete an appropriate characterization program.

Sparks report represents an effort to delineate a near-term development program, carefully bounded for maximum effect, to achieve a particular goal, better coatings at 10.6 μm. As will be seen elsewhere in this Symposium, the ideas he presents represent the consensus of informal opinions among researchers in the field. Sparks has drawn these ideas together, along with their supporting arguments, in a concise summary.

Realizing the need for better anti-reflection coating materials in the infrared, A. D. Baer, T. M. Donovan, A. K. Green, and G. Turner of the Michelson Laboratory studied several dielectric materials for this application. Specifically addressed were films of NaF, SrF_2, and As_2Se_3. Correlation of optical and other physical properties, such as absorption at 10.6 μm, scattering, structure, index of refraction, and laser induced damage thresholds,with processing variables are reported. General conclusions were that NaF is a very promising low index ($n = 1.23$) material since it has relatively low absorption and high damage threshold which is quite suitable as a single layer anti-reflection on NaCl at 10.6 μm. Furthermore, its solubility is only 0.12 of NaCl, which, however, would still be a concern under high humidity. SrF_2 films exhibit higher absorptions, but compared to the previously proposed material BaF_2, it is more damage resistant. Finally As_2Se_3 appears to be worse than As_2S_3 for IR coating applications. Compared to the solubility of NaCl,SrF_2 is only 3×10^{-4}, while As_2Se_3 is insoluble. Measured absorption coefficients of $\lambda/4$ films of NaF, ThF_4, SrF_2, and BaF_2 on KCl were 6.0, 10-12, 25 and 15 cm^{-1}, respectively, while corresponding films of As_2S_3 on KCl and As_2Se_3 on NaCl were 1.2 and 1.1, respectively. Reported damage thresholds for 100 ns pulses of a CO_2 TEA laser indicated levels of 38 ± J/cm^2 for the NaF films and 194 and 76 J/cm^2 for the SrF_2, and BaF_2 films, respectively, while for the above described films of As_2S_3 and As_2Se_3 the values were 38 and 12 J/cm^2, respectively.

The problem of designing 3-layer antireflectance coatings was analyzed by A. D. Baer of the Michelson Laboratories. He wrote down the conditions which must be satisfied by the thicknesses and indices of the materials used in the various layers of the coating in order for maximum transmission to occur. The effect of losses was also examined. Solutions were presented for both combinations of high index- low index- high index materials, such as $As_2Se_3/NaF/As_2Se_3$ on CaF_2, which is currently used at 10.6 μm, and for low index - medium index - low index combinations, such as $NaF/ThF_4/NaF$ on KCl, which represents a novel class of coatings. The latter type of coating has no two-layer solution, while two-layer versions of high-low-high coatings (where one layer goes to zero thickness) do exist. The low index coatings are attractive due to the possibility of higher damage thresholds.

In the search for high performance, high quality damage resistant thin films in the infrared, an intriguing approach is being pursued by T. A. Reis, H. Hirtsuka, A. T. Bell, and U. Shen of the Department of Chemical Engineering at the University of California at Berkeley. They reported on an investigation of plasma polymerized ethane (PPE) as a possible organic coating material. The films are prepared by passing ethane gas through a radio frequency glow discharge. Infrared absorption properties havebeen correlated with deposition conditions, and as expected, 3.5 μm and 7.0 μm are regions of high absorption due to C-H stretching and bending motions. Outside of these regions film absorption is encouragingly low, exhibiting about 4 - 7 cm^{-1} at 10.6 μm when PPE is deposited on KCl substrates. PPE has an index of refraction of 1.51 at the sodium D line. Films of $\sim$ 1 μm thickness have not shown any marked deterioration when exposed to a relative humidity of 55% - 60% for 100 hours. Deterioration, however, was noted over the same duration at 84% RH, when moisture attack was confined to regions of scratches or other imperfections on poor quality KCl substrates. Microscopic results indicate that PPE can coat surfaces of high quality and of gentle variations while sharp edges and small holes cannot be suitably coated. In all cases, high humidity deterioration was noted on elements containing these later type of characteristics. Polymerized coating is a promising avenue of approach which demands additional and increased attention.

It has long been noted that a need exists for a durable high index coating material at 10.6 μm for use both in multilayer designs or as a protective coating for the alkali halides, such as KCl. R. A. Skogman of the Honeywell Research Center addressed this quest reporting on a study of epitaxy and scattering in the TlI films. It had been reported that TlI has an absorption coefficient of less than 1 cm^{-1} at 10.6 μm, and in addition is insoluble, while exhibiting excellent adhesion to KCl surfaces. This tenacious adhesion is primarily due to its epitaxial growth on KCl. He reported that the TlI film structure was strongly dependent upon the specific KCl crystalline orientation. The correlation of film structure on KCl orientation has allowed an understanding of the optical scattering in TlI films. It was reported that the alignment of the TlI b_o axis parallel to the KCl <110> direction determined the epitaxial growth habit. As a consequence, on a <100> crystal surface, two <110> directions lie in the plane and thus TlI nucleates in two orientations 90° from one another. The resulting film structure manifests itself as increased light scattering from diffraction of light passing from one biaxially birefringent orientation to another. Since this epitaxial occurrence is not amenable to solution for coating polycrystalline materials an alternate solution (opposed to only using that crystal orientation which did not produce birefringent behavior) had to be found. This was accomplished as follows: TlI was condensed in its cubic (β) phase on KCl and allowed to transfer to its stable orthorhombic (α) phase resulting in a clear polycrystalline, randomly oriented film independent of substrate orientation. This is done by maintaining the substrate at 140°C or above during deposition. The phase change occurs during substrate cooling with the resulting α grain size dependent upon the condensation temperature and cooling rate. High evaporation rates are necessary (∿ 2000 Å/min).

It is now abundantly clear that much of the near-term effort in the field of laser induced damage to optical materials will concentrate on the multi-faceted area of thin-film coatings. To aid in unraveling the details of the response of thin films to high power laser irradiation, improved film characterization is necessary. One technique which is receiving considerable attention as an evaluation aid is attenuated total reflection (ATR) spectroscopy. This subject was discussed in detail by R. T. Holm and E. D. Palik of the Naval Research Laboratory. Normally, thin films are in part evaluated by either single or double pass transmission, absorption or reflection spectroscopy. However, with the need for producing very low absorption coatings a much more sensitive technique was demanded. ATR is one such promising alternative, which is both sensitive and frequency dependent as opposed to the normal non-spectroscopic calorimetric or non-sensitive simple spectroscopic techniques. Consider the investigation of AR coatings. Typically a trapezoid is made from the laser window material, then thin films of thickness d, are deposited on both sides. Light is then multiply-reflected down the trapezoid at an appropriate angle θ which results in total reflection. If there were no absorption in the film the reflection would be unity. If, however, there is some absorption the reflection is reduced, in other words attenuated. By changing the frequency of light, absorption bands in the film can be identified. This technique has the sensitivity of determining thin film absorption coefficients of ∿ 1 cm^{-1} or less by increasing the number of internal reflections. Furthermore, by changing the angle of incidence, probing of a thin film in depth (cross section) is possible, thus thin film homogeneity, etc., can be evaluated. This technique should become an important adjunct to the science of the film characterization.

2.4 Thin Film Damage

As indicated above, the need for new materials for dielectric coatings is most strongly felt at 10.6 μm. A number of alternative materials, both for high and low index coatings, were proposed at this year's Symposium, together with quite encouraging preliminary damage test results. In addition, the well-known dependency of damage threshold on the method and circumstances of deposition was explored in greater detail. Extensive use of Auger spectroscopy continues to be of great value in elucidating the role played by impurities.

D. A. Walsh and J. A. Detrio of the University of Dayton Research Institute (URDI) reported results of a detailed study of rf-sputtered ZnSe films. Single-layer films of ZnSe were deposited on both ZnSe and KCl substrates. Two target materials were used for the sputtering, being hot-pressed (HP) Kodak Irtran IV ZnSe, and chemical vapor deposited (CVD) Raytheon ZnSe. Calorimetric measurements indicated three to six times greater absorption in films deposited from HP material. Auger analysis revealed a measurable sulfur impurity in the HP ZnSe, which was absent in the CVD material. Another observation was the presence of impurities in the sputtering gas, in this case, argon. Using as-received argon, deviations from stoichiometric composition were observed, while using gettered argon, stoichiometric films resulted.

The sputtered films showed excellent environmental stability, when deposited on CaF_2. Using a water immersion test, sputtered films were found to be more stable than e-gun deposited films. Films deposited on a freshly cleaned surface showed the greatest durability.

An exploration of the use of NaF, SrF_2, and BaF_2 monolayer films as opposed to the normally employed ThF_4, as low index coatings on KCl and NaCl windows was presented by M. J. Soileau, A. O. Baer, J. O. Porteus, J. L. Jernigan, W. N. Faith, T. M. Donovan, and A. K. Green of the Michelson Laboratories. NaF is of particular interest, since at 10.6 μm, its refractive index is very nearly the square root of that of NaCl, allowing a simple single-layer AR coating to be made.

Films of the materials indicated were vacuum-deposited on NaCl and KCl substrates. Bulk absorption of the coating materials was measured, as was the absorption of the coating substrate and the final coated element. Film absorption values were typically 10 to 200 times bulk values. In the bulk, each of these low index materials showed a higher damage threshold than the substrate materials, as expected. The coated elements failed under intense CO_2 laser illumination due to delamination of the coating in the vicinity of surface defects at the coating-substrate interface. Ostensibly, these defects could be prevented by suitable substrate preparation and handling.

As part of a continuing search for materials to use as alternatives to ThF_4 in multilayer dielectric coatings at 10.6 μm, A. Golubovic, J. Fitzgerald, I. Berman, J. Bruce, R. Bradbury, J. J. Comer, W. S. Ewing, and H. G. Lipson of the Deputy for Electronic Technology of RADC reported on the properties of several rare earth fluoride films. The films studied were deposited as single-layer coatings on ZnSe, and in combination with ZnSe layers as two-layer films on KCl. Both vacuum evaporation and rf sputtering were used. Detailed parametric studies of the film deposition process were carried out. Starting materials were carefully analyzed, and resulting film morphology was correlated with deposition parameters.

Sputtered ZnSe films were deposited in cubic form with a preferred orientation of the {111} planes parallel to the substrate surface. Thermally deposited ZnSe showed the same preferred orientation. The quality of the thermally deposited films was strongly dependent on the deposition rate. High deposition rate films produced coloration, and crazed immediately when removed from the deposition chamber, while the sputtered films showed good adhesion, and resisted crazing.

The fluoride films were deposited on ZnSe with cubic, orthorhombic, or hexagonal structure, depending on the coating material. Hexagonal films showed the greatest OH absorption, as evidenced by absorption bands at 3 and 6 μm. The effect of adsorbed OH was reduced under ultra-high-vacuum (UHV) deposition, for LaF_3, which exhibited pronounced OH absorption. SmF_3 and CeF_3 films, which showed only weak OH bands, did not improve perceptibly under UHV deposition.

These films were damage tested at 10.6 μm, using pulses of 100 ns FWHM from a TEA laser. Absorptances of 3 to 6 percent were observed. Observed damage thresholds were generally high. In combination with ZnSe, on KCl substrates, all the materials showed damage at the same level, about 6-7 J/cm^2, probably corresponding to failure of the high index material. The fluoride single layers on KCl damaged at 10 to 15 J/cm^2. Sputtered ZnSe on KCl damaged at 20 J/cm^2, comparable to values obtained from thermal deposition.

John Lewis and M. C. Ohmer of the Air Force Materials Laboratory discussed the use of variable index films of the form Ge_xSe_{1-x} in combination with Ag_2Se_3 for AR coatings at 3.6 μm, 5.3 μm, and 10.6 μm. A two-layer film, deposited on substrates of Eu-doped KCl (10.6 μm), BaF_2 (5.3 μm), and CaF_2 (3.8 μm) with an $x = 0.55$ composition. Absorption, transmission, and laser damage thresholds were measured. No evidence of H_2O or OH absorption bands was observed. The films were deposited by vacuum evaporation and were observed to be physically robust. At 10.6 μm, the film showed the lowest absorption the investigators had ever seen on coated KCl substrates,on the order of 0.1% per surface. A possible disadvantage of these films is their poor transmission in the visible. The 10.6 μm coating had an opaque, metallic appearance and the thinner coatings were observed to be reddish in color. The 3.8 μm coating exhibited an optical density of 1.0 in the visible.

In the continuing search for materials to use as dielectric coatings at 10.6 μm, J. A. Detrio and R. D. Petty of the University of Dayton Research Institute, and M. C. Ohmer and O. V. Swenson of the Air Force Materials Laboratory reported on a study of TlI coatings. These coatings, either in monolayers or in combination with ThF_4, were deposited on KCl windows by vacuum deposition. Samples were irradiated at increasing power levels with cw CO_2 laser radiation at 10.6 μm. The damage threshold, either identified by disruption of the film or severe stress-induced birefringence, was defined as the lowest power at which damage was visually observed. Single layer TlI films generally exhibited damage levels in excess of 100 kW/cm^2. Under similar test conditions ThF_4 films damaged at levels of 30 - 50 kW/cm^2. Auger scans of the ThF_4 films showed significant oxygen impurities, whereas no impurities were detected in the TlI films.

The art of optical coating at near-visible wavelengths is further advanced than in the infrared, but studies of the damage mechanisms at shorter wavelengths continue to be of great value. In fact, the greater reproducibility of coatings prepared with established methods and materials leads to more meaningful results in damage studies, as well as forming an important data base as laser activity moves to shorter wavelengths. This year studies were reported of the effects of wavelength, standing wave effects, substrate preparation, and liquid immersion on film damage thresholds. Finally, the totality of design considerations for a dielectrically enhanced, diamond turned, metal mirror for high power laser use was presented.

Brian Newnam and Dennis Gill of the Los Alamos Scientific Laboratory presented a study of the spectral dependence of sub-nanosecond damage in refractory oxide optical coatings. Quarter-wave thick films of TiO_2, ZrO_2, HfO_2, and SiO_2 were deposited on fused silica substrates using electron-gun evaporation. The first three materials were chosen as representative of high-index materials used in laser coatings, while SiO_2 is frequently used as a low-index component. These films were tested at 1.064 μm, 0.532 μm, and 0.355 μm, using the fundamental, second and third harmonic of the output of a mode-locked, Nd-YAG laser. The pulse duration was 30 ps at 1.064 μm, 20 ps at 0.532 μm, and 17 ps at 0.355 μm. Forty exposures on a sample were used to determine damage thresholds. Damage was identified by spark emission detection at the longer wavelengths and by laser-induced scattering. Since all the tested materials fluoresced under 0.355 μm irradiation, spark detection could not be used at this wavelength. No significant spot-size dependence was observed for focal spots from 70 to 500 μm in radius at these pulse lengths.

Damage thresholds were corrected for the standing wave pattern in the coated samples. All of the materials showed the same general behavior, an increase in threshold electric field from 1.064 μm to 0.532 μm, and an abrupt reduction of threshold at 0.355 μm. This reduction in threshold was especially pronounced for TiO_2. Absorption spectra were taken on thin film samples of the four oxides tested. TiO_2 showed a strong absorption edge at 0.350 μm, while HfO_2 and ZrO_2 showed an edge between 0.220 and 0.230 μm. Good transmission was seen for SiO_2 to 0.200 μm. Thus, one-photon absorption is expected to dominate in TiO_2 films at 0.355 μm, sharply reducing the damage threshold. Two-photon absorption is identified as leading to reduced damage thresholds in HfO_2, SiO_2, and ZrO_2 at short wavelengths. The slight increase in threshold from 1.064 μm to 0.532 μm is consistent with the electron avalanche picture of laser damage.

An elegant experimental study on damage in dielectric multilayers was reported by J. H. Apfel and J. S. Matteucci of OCLI, and B. E. Newnam and D. H. Gill of LASL. Nine-layer stacks of alternating quarter-wave layers of TiO_2 and SiO_2 were deposited on fused silica substrates, with the high index (TiO_2) layer always at the substrate-film interface. Similar stacks were prepared with the fourth, fifth, and sixth layers respectively eliminated, resulting in half-wave thicknesses of low or high index material in the middle of the stack. The standing-wave pattern in each design was then analyzed, to relate the peak field inside the stack to the external field associated with the incident light wave.

Damage studies were carried out using a 30 ps, 1.064 μm mode-locked Nd:YAG laser. The observed damage thresholds provide strong confirmation for the hypothesis that multilayer coatings fail in the high index material, when the local field in that material exceeds its damage threshold. Failure in TiO_2 occurred at about 8 MV/cm local field strength. The SiO_2 coating withstood damage to field strengths as high as 12 MV/cm, a value comparable to that previously reported for bulk fused silica. This study strongly supports the guideline that multilayer coatings should be designed to keep the field strength in the high index material as low as possible as a means of raising the damage threshold.

The effect of substrate contamination on coating performance is generally considered to be deleterious. The fact that this is not always the case was demonstrated in a report given by R. A. House, J. A. Bettis, and A. H. Guenther of the Air Force Weapons Laboratory. They studied the effect of the hydroxyl impurity content in fused silica on damage threshold of films of SiO_2 and MgF_2, deposited on these substrates. The principal effect of the OH lies in the chemistry of the film. For SiO_2 films, the oxidizing action of the OH greatly reduces the formation of SiO which damages more easily than SiO_2. For MgF_2, the presence of OH leads to the formation of some MgO, lowering the damage resistance of the film. In short, the presence of OH is deleterious in these cases where the desired film composition is in competition with the simple oxide.

In these experiments, OH concentration was monitored by absorption spectroscopy at 1.4 and 2.23 μm. As these absorption bands, associated with the OH radical, increased in strength, the damage threshold of the SiO_2 films increased, while that of MgF_2 films decreased. The effect of surface roughness on the damage threshold was taken into account by normalizing the damage threshold electric field to $\sqrt{\sigma}\,E$, where σ is the rms surface roughness. This allowed a detailed comparison of results from samples of different surface character to be made.

A. Balbin-Villaverde of the Universidade Estadual de Campinas in Brazil and L. G. DeShazer of the University of Southern California reported on laser-induced damage in thin film immersed in liquids of varying dielectric and optical properties. Samples included a variety of quarter- and half-wave monolayers, multilayer reflectors, and AR "vee" coatings. Eight different liquids, with visible light indices ranging from 1.32 (methanol) to 1.71 (di-iodomethane) were used. Damage testing was carried out with a pulsed ruby laser, operating in a single longitudinal and transverse mode with a pulse duration of 12 ns FWHM.

In general, one might expect the damage threshold to be affected by the alteration of the internal field distribution brought about by immersion in the liquid. The authors calculated the exact field distribution throughout the liquid-film-substrate system, and searched for correlation between observed thresholds and calculated field strengths. This correlation was not generally found. A correlation was observed between laser damage threshold and low frequency dielectric constant. The authors propose that this effect may be due to a change in the photoemission barrier (work function) at the immersed surface, or due to a filling-in of the cracks, pores, and defects at the surface, reducing the field intensification effect. An extensive tabulation of data is given.

Large aperture, highly damage resistant reflective optics are required for the laser fusion program. S. S. Glaros, P. Baker, and D. Milam of the Lawrence Livermore Laboratory reported on the choice of material and processes for the fabrication of 50 cm aperture reflecting optics for use with the Argus laser. Three design decisions were considered, the choice of the substrate material, the choice of the surface coating, and the choice of the dielectric overcoating of the optical surfaces. An analysis of the relative merits of BK-7, CerVit, and beryllium led to a choice of beryllium for the mirror substrates. Beryllium is favored over the glassy materials due to its greater strength, stiffness, thermal conductivity, and convenience of figuring. The substrates were chemically plated with copper and nickel layers. The copper plated substrates were diamond turned to the desired shape, and the final nickel plated surfaces were lapped to the requisite optical figure. Various dielectric multilayer coatings were tested for laser damage and maintenance of optical figure. A 12-layer stack of TiO_2/SiO_2 was the final choice, exhibiting a damage threshold of 6.5 J/cm^2 at 1.064 μm, in 125 ps pulses.

2.5 Scaling Laws and Fundamental Mechanisms

In recent years, a number of simplified empirical scaling relations have evolved for the evaluation of materials for use in high power lasers. The expected dependence of nonlinear index and damage threshold on the linear index, for example, represent useful rules-of-thumb of this type. Such scaling laws are of great use to the laser designer in selecting materials for particular applications, and also represent intriguing simplifications of an otherwise overwhelming abundance of experimental data, challenging the theorist for a cogent explanation.

In a continuing effort to establish empirical scaling laws for laser damage, J. R. Bettis, R. A. House, and A. H. Guenther of the Air Force Weapons Laboratory presented a model for the pulse length dependence and spot size dependence of surface damage thresholds. The model was also extended to bulk damage. The starting point is the assumption that the surface damage threshold corresponds to the investment of a critical amount of energy in a plasma layer at the surface of the material. Using the expression for the classical inverse bremsstrahlung absorption, they argue that the plasma absorption increases linearly with increasing laser power density, so the heating rate goes like I^2, where I is the incident power density. Thus they arrive at a scaling law (assuming the evolving plasma fills the entire beam) that at threshold, t_pAI^2 is constant for a given material. Here t_p is the pulse duration and A is the beam area. Considerable evidence is adduced from the literature showing that for a large class of materials, both bulk and surface damage thresholds vary according to the rule, t_pI^2 is constant. Evidence for the area scaling rule is somewhat less convincing.

As is pointed out elsewhere in these Proceedings (see, for example, the paper by Gibbs and Wood), any diffusion model, like absorption heating, will yield a relation, t_pI^2 is constant. This scaling law appears to hold from 30 ps to 100 ns pulse durations, and is a useful rule-of-thumb, as long as new phenomena do not come into play. Thus, scaling from the realm of avalanche ionization to that of thermal damage may be erroneous.

Further explanation and justification of scaling relations remains to be done. It is important to establish the realm of validity of such relations, due to their potential use in scaling up large laser systems or correlating damage testing results.

The question of spot size dependence was further investigated by C. C. Tang, K. M. Leung, and M. Bass of the University of Southern California. They re-examined the bulk breakdown threshold of alkali halides, both RAP- and conventionally grown, using a CO_2 laser emitting 92 ns bursts of mode-locked pulses of about 2.5 ns duration, spaced 8 ns apart. The pulses were focused to two spot diameters, 59 μm and 89 μm. Damage thresholds were recorded both for single shots and for "N on 1" experiments. In the latter, the pulse energy is incrementally raised from far below threshold until damage fully appears. The difference between single-shot and N on 1 thresholds is taken as evidence of a pre-conditioning of the material. It is not clear what the mechanism of pre-conditioning in bulk damage entails, unless it is the dispersal of electrons from shallow traps. However, in the samples studies, damage was highly impurity-mediated, as evidenced from the spot-size dependence. Thus, these samples for which the N on 1 threshold was significantly greater than the single-shot threshold also showed strong spot-size dependence, and exhibited defects upon subsequent mophological investigation.

An interesting side light of this investigation was the fact that RAP-grown materials used in this study showed high concentrations of defects and inclusions. Apparently, the phrase "RAP-grown" does not automatically assure high quality in alkali-halide materials.

The fundamental mechanism for intrinsic failure of optical materials at high flux levels is avalanche ionization. This subject has been widely explored in recent years, but discrepancies remain in the model generally proposed for this process.

The subject of avalanche ionization was further explored by D. Milam of the Lawrence Livermore Laboratory who proposed to explain essentially all features of existing avalanche ionization experiments on the basis of a three-part model. In his model, one distinguishes three phases of the avalanche process, the initiation, by photoionization of defects or impurities, or multiphoton ionization, the generation of a dense plasma, by the avalanche process itself, and the damage of the material, by the deposition of heat in the dense plasma. By analogy with gas breakdown at various pressures, Milam argues that short pulse avalanche ionization (t_p < ns) differs from long pulse ionization primarily, because in order to have enough energy in a short pulse to heat the plasma, the electric field strength must be very high. At high field strength, the initiation process is highly probable, and behaves in a deterministic fashion. For longer pulses, however, where the requisite energy density can be achieved with a low electric field value, the initiation process becomes statistical in nature, depending on the availability of "seed charge" in the focal volume. Evidence of this is the appearance of explosive damage on carefully prepared surfaces, such as those prepared with ion-etching, chemical etching or flame-polishing. On such surfaces, the sites for the initiation of the avalanche at low field strength are widely spaced. Thus, the pulse will rise well above the threshold for the avalanche buildup before the plasma is initiated, and an explosive avalanche will ensue. Milam offers corresponding explanations of many other observations relating to both bulk and surface damage. He addresses himself to the questions of breakdown times (why are there no breakdowns on the tail of the pulse?), damage statistics, and micro-pit formation. The arguments he presents and the data he introduces are very convincing, although some contradictory evidence does exist. Milam's careful reasoning suggests that overly simplified models of the avalanche process, such as Bettis et al., had earlier proposed, may only be approximate guidelines and must be applied with considerable caution.

In an intriguing report which generated considerable discussion, S. K. Gulati and W. W. Grannemann of the Department of Electrical Engineering and Computer Science at the University of New Mexico presented results on 10.6 μm cw laser induced damage in Si, Ge, GaAs, GaAsP, and GaP semiconductors. Laser induced lattice damage was ascertained from the alteration of low temperature carrier mobility measurements. This modification was analyzed on the basis of a parametric instability in solid-state plasmas previously formulated by DuBois and Goldman, after discounting possible competing processes such as two stream instability, avalanche breakdown, and simple Drude absorption or joule heating. While their experimental damage results are not in exact numerical agreement with analytical predictions based on the proposed parametric instability, they do approximate the correct order of damage sensitivity.

An intriguing hypothesis was put forward for the consideration of the Symposium by S. M. Wong and D. L. Olson of Rockwell International. They described the phenomenon of electro-transport, well-known in electrical conductors, in which the transfer of momentum from dc current carriers such as electrons, to atoms in the conductor can lead to the migration of selected species of atoms or even of vacancies towards one of the electrodes of the circuit. In situations in which the current density is nonuniform, localized concentrations of vacancies, and even macroscopic voids can be formed.

The authors propose a corresponding effect, photo-transport, where in a light-carrying medium the transfer of momentum from photons to the medium, either through absorption or dielectric polarization can lead to a migration of ions or defects along the direction of light flow. Although no detailed calculations were presented in support of this hypothesis, it is interesting as a possible source of progressive deterioration of an optical material under prolonged use. Further investigation of this effect is, of course, only warranted if calculations indicate that the magnitude of the effect is observable.

A number of investigators have reported that in the vicinity of small defects at optical surfaces, the occurrence of laser damage is accompanied by the formation of a pettern of ripples extending away from the damage site in the direction of the electric field vector of the incident light wave. In a paper by P. A. Temple and M. J. Soileau of the Michelson Laboratories, this ripple pattern is attributed to the interference of the incident light wave with the electrostatic field induced in the vicinity of the polarizable defect. This hypothesis is given support by the fact that the ripple spacing is observed to be λ', the optical wave length in the medium rather than $\lambda'/2$, which would be the spacing if the effect were purely due to the radiation field and oriented along the E-vector where no dipole radiation can propagate. The authors propose that the effect should be a maximum for defects of an odd number of half-wavelengths in size due to resonant enhancement of the field. In the discussion of the paper, it was suggested that tests with circularly polarized light would be of interest. It is expected that circular ripples would occur in this case.

Recommendations

Over the last ten years, the subject of laser damage has moved steadily from primarily a reporting of empirical observations to one of genuine scientific study. The major phenomena of laser damage have been catalogued, and are understood to varying degrees. Scaling laws of increasing sophistication provide the system designer with convenient and generally reliable rules-of-thumb governing the selection and employment of materials for windows, coatings, and laser media as well as pointing the way for material development. The study of laser materials closely parallels other aspects of materials science, with the added complications imposed by the interaction of intense light with optical materials.

If there is any one word which describes the essence of studies of this kind, it is characterization. This encompasses the detailed description of the material, the conditions of the experiment, and a full diagnosis of the results. All of these are essential in any laser damage study carried out today. The characterization of bulk material for optical use should be in terms of its residual absorption. Materials of interest for laser components are generally used in the region of high transparency, between the intrinsic Urbach tail and the reststrahl edge, in a spectral region dominated by extrinsic impurity absorption. The absorption in this region, like the resistivity of semiconductors, is a direct measure of the impurity level in the material. In order for reported results to be compared, or applied to device design, such a characterization is essential.

A comparable characterization of the structural homogeneity of bulk material is provided by optical scattering measurements. Scattering may be due to particulate inclusions and voids, or to the presence of micro-crystallites or phase separation. A scattering measurement provides the same overall description of the quality of a sample, from the standpoint of structural homogeneity, as is provided by absorption data for compositional homogeneity. If it is necessary to characterize the actual source of the scattering or absorption, microprobe analysis of some variety is generally required.

The characterization of the optical surface is even more demanding than the bulk description. Surface contamination, either from embedded polishing materials or environmental factors, greatly influences the damage properties of the materials. Surface roughness is now well established as a factor in damage studies. Consequently, where optical surfaces are involved, in addition to bulk properties, surface absorption and scattering data are required to complete the characterization of the experiment. Again, if it is necessary to detail the origin of the absorption or scattering, microprobe analysis, Auger spectroscopy for example, and profilometry, either mechanical or by optical means, must be carried out.

When one considers the characterization of thin film structures, to the degree indicated above, the mind boggles. The identification of bulk vs surface properties becomes difficult in layers of material of thickness less than one μm. A full characterization of even a single, quarter-wave layer goes beyond a simple statement of absorption and scattering. The means and rate of depositing, substrate temperature and background environment during deposition, substrate preparation, composition and morphology of the film, porosity, complex index, residual stress, electric field distribution, film and substrate roughness and aging or film stability have all been shown to influence the damage resistance of the film. If a multilayer structure is involved, the list of relevant parameters grows accordingly.

Clearly, it is not possible to specify all of these parameters for every study of laser damage on thin films. Parametric studies must be carried out to isolate the effects of each of the relevant variables, holding the other factors constant as far as possible. This requires carefully controlled deposition conditions, specified as fully as possible, extreme cleanliness, care in preparation and handling, and relevant film characterization. Damage tests on production films, although of empirical value in defining the current state of the industrial art, are of minimal value in isolating the factors responsible for the failure of the film. The reluctance of manufacturers to characterize their products even in terms of composition must be overcome, and a policy of full disclosure instituted, if not in production films, at least on samples supplied for damage testing. In this way, variations in the parameters of the film fabrication process can be related to variations in observable properties, such as absorption, scattering, structure, and residual stress, and these, in turn, to the observed damage phenomena. These remarks apply to both vacuum-evaporated films and sputtered films.

At present, given the intense, goal-oriented pressures in the large laser programs, no one has the time and money to pursue basic research on optical films for high power laser use, with the instrumentation and detail of investigation required for full fundamental understanding. However, if laser fusion, for example, becomes a reality, and systems with hundreds of coated surfaces proliferate, the demands of the market will be sufficient to warrant the kind of heavily instrumented, highly detailed research that characterizes the study of metallic films in the electronics industry today. Basic research investigations, and funding agencies, should be moving in that direction now, trying to develop a first principles understanding of the relation between deposition parameters and the physical, chemical, mechanical, structural, and optical properties of the finished dielectric film.

As indicated above, characterization of samples is all important. No less important is the full characterization of the laser output used in the experiment. The actual profile of the beam at the sample and its Z direction variation should be reported, wherever possible, in conjunction with damage results. This goes beyond the description, "TEM_{oo}", since aberrations due either to high power propagation effects in the laser, or figure errors in the lenses can change the focal distribution significantly. With this emphasis on characterization, the subject of diagnostics must be addressed. The relation of light scattering to the nature of the surface remains unsatisfactory. Discrepancies among different methods of measuring surface profiles remain, and should be understood. Measurements must be correlated with exact vector theory, and wherever possible, scalar approximations for light scattering should be developed. There is an extensive literature of radar scattering which should be valuable in guiding this work.

In the damage area, the reason for the correlation between surface roughness and damage threshold remains open to speculation. It has been proposed that increased roughness yields a larger effective surface area, or higher electric field values, or increased electron scattering below the surface. Experimental investigations of these hypotheses are needed. The use of ATR and ellipsometry can provide a sensitive tool for these investigations.

Improved calculations of thermal stresses in windows are also required, taking account of the antistropy of crystalline materials in an exact way. The analysis of thermally induced stress-birefringence may yield a sensitive measure of bulk absorption for transparent materials.

Much remains to be done in the development of scaling laws. The recently enunciated scaling with area and pulse duration, apparently valid over many orders of magnitude, must be understood on a more fundamental basis. The sensitivity of these scaling relations to material quality (impurities, defects, etc.) is also in need of investigation. The scaling of avalanche ionization with frequency is still largely unresolved. Resonant processes, including multi-photon absorption, complicate the picture, where frequency scaling is involved, and must be taken into account, as reported at this year's Symposium. The temperature dependence of avalanche ionization should be further investigated, to elucidate the role of phonon processes. Some investigations of the temperature dependence of avalanche ionization have been carried out by Manenkov and co-workers in the USSR.

A new kind of scaling relation is needed. One needs to know, how long can an optical element be expected to last if operated at a certain fraction of the normal damage level? This kind of information is known for capacitors, flashlamps, and other high voltage equipment. High power laser components need to be characterized in the same way. This area is closely related to aging or film stability under a variety of environmental conditions. It may be due to effects, such as H_2O entering the porous regions of the film, or structural effects, such as from growth, or some other cause.

There are a few practical questions which need immediate attention. One is the problem of surface contamination during substrate preparation for thin films. Diamond turned metal surfaces must be entirely free of oil or other contaminants to ensure adequate adherence of dielectric over-coatings. More investigations of novel coating designs, such as that presented by Baer this year are needed, especially in the uv, where the variety of available coating materials is limited.

Finally, a need remains for the consolidation of data on window and coating materials, along the lines of that presented in the Handbook of Military Infrared Systems, but extended to high power laser uses. Wide gap materials such as alkali halides are useful from the uv to the IR, and new materials are continually evolving. Some effort of this kind of compilation has been made by the DARPA laser window program, but a broader compilation of data is needed, with a provision for continuing expansion, a sort of laser materials documentation project.

4. Acknowledgment

The editors would like to acknowledge the invaluable assistance of Dr. Harold S. Boyne, Mr. Wilbur J. Anson, and Ms. Florence M. Indorf and the other involved staff members of the National Bureau of Standards in Boulder, Colorado, for their interest, support, and untiring efforts in the professional operation of this Symposium and in the preparation and publication of the Proceedings. The continued success of the Damage Symposia would not have been possible without the enthusiastic support of those named above.

5. Bibliography

[1] "Damage in Laser Glass," A. J. Glass and A. H. Guenther, Editors, ASTM Special Technical Publication 469, ASTM, Philadelphia, PA (1969).

[2] "Damage in Laser Materials," A. J. Glass and A. H. Guenther, Editors, NBS Special Publication 341, U.S. Government Printing Office, Washington, D.C. (1970).

[3] "Fundamentals of Damage in Laser Glass," N. Bloembergen, National Materials Advisory Board Publication NMAB-271, National Academy of Sciences, Washington, D.C. (1970).

[4] "High Power Infrared Laser Windows," N. Bloembergen, National Materials Advisory Board Publication NMAB-292, National Academy of Sciences, Washington, D.C. (1972).

[6] "Laser Induced Damage in Optical Materials: 1972," A. J. Glass and A. H. Guenther, Editors, NBS Special Publication 372, U.S. Government Printing Office, Washington, D.C. (1972).

[7] "Laser Induced Damage of Optical Elements, A Status Report," A. J. Glass and A. H. Guenther, Applied Optics 12, pp. 637-649 (1973).

[8] "Laser Induced Damage in Optical Materials: 1973," A. J. Glass and A. H. Guenther, Editors, NBS Special Publication 387, U.S. Government Printing Office, Washington, D.C. (1973).

[9] "Laser Induced Damage to Optical Materials, 1973: a Conference Report," A. J. Glass and A. H. Guenther, Applied Optics 14, pp. 74-88 (1974).

[10] "Laser Induced Damage in Optical Materials: 1974," A. J. Glass and A. H. Guenther, Editors, NBS Special Publication 414, U.S. Government Printing Office, Washington, D.C. (1974).

[11] "Laser Induced Damage in Optical Materials: 6th ASTM Symposium," A. J. Glass and A. H. Guenther, Applied Optics 14, pp. 698-715 (1975).

[12] "Laser Induced Damage in Optical Materials: 1975," A. J. Glass and A. H. Guenther, Editors, NBS Special Publication 435, U.S. Government Printing Office, Washington, D.C. (1975).

[13] "Laser Induced Damage in Optical Materials: 7th ASTM Symposium," A. J. Glass and A. H. Guenther, Applied Otpics 15, No. 6, pp. 1510-1529 (1976).

A. J. Glass

A. H. Guenther

0.1 INTRODUCTION AND WELCOME

Alexander J. Glass
Lawrence Livermore Laboratory
P.O. Box 808
Livermore, CA 94550

On behalf of Dr. Guenther and myself I'd like to extend a personal welcome both to our old friends and new acquaintances here at the Symposium on Optical Materials for High Power Lasers. The meeting is subtitled the Eighth Annual Boulder Damage Symposium, a name which evokes images of people involved in crushing rocks. This image may not be entirely inappropriate to the task before us.

The previous speakers have alluded to the fact that we've made outstanding progress over the last eight years in the field of laser damage and I heartily agree with that. I am, however, somewhat unnerved to look at our agenda which breaks down into the following five topics: (1) Bulk Absorption, (2) Surfaces and Mirrors, (3) Thin Film Properties, (4) Thin Film Damage,and (5) Avalanche Ionization. This is hardly a radical departure from previous years. The only difference is that we have, at least for the time being, set aside self-focusing and the nonlinear index. It behooves us to ask ourselves why the same subjects year after year. In part it may be because those who fail to study history are doomed to repeat it. Certain problems continually re-emerge in new guises, and for those who have been coming to Boulder every year for eight years there is a familiar ring to some of the papers. From time to time we ask ourselves, didn't that come up in '69 or '70 in a slightly different form? It's true, we do continually work away at the same old problems in some ways, but that's because these problems are difficult and because they are important. Our concern in this Symposium is the limitations imposed by optical materials, real optical materials, on high energy laser systems. These limitations are what stand between the brilliant conception of the device and its realization. Somehow we all come out of graduate school imbued with the concept of ideal materials, materials which are perfectly transmitting dielectrics and perfectly reflecting metals. We need to be continually reminded of the limitations that real materials impose on us. Nature takes care of that; the reminders are ever present. We continually report progress at this Symposium even though the agenda doesn't change, and it doesn't always look like progress. It takes a long view to recognize progress in its various forms.

The Talmudic scholars have a metaphor for the truth, which is that truth appears like an onion. If you peel away one layer, there's another layer that looks just like it underneath and if you peel away that layer, still another appears. Our onion, unfortunately, exists in Hilbert Space. Problems which are simply stated at first, upon subsequent investigation turn out to be much more complex than anyone originally thought, and on further investigation seem to be totally unclear. The best example of that which comes to mind in our present agenda is the question of avalanche ionization. At least two papers have appeared in the literature in the last five years which purported to be the last word in avalanche ionization, summing up and stating the received opinion on what was now a well understood and relatively simple phenomenon. Of course, subsequent investigation showed that was indeed not the case and more work remained to be done. Thus, the old subjects continue to be unraveled and sometimes look more complex for having been investigated.

As Harry Winsor just mentioned, we also keep moving into new operating ranges and new wavelength regions and introducing new materials in the systems. The advent of the carbon monoxide, HF, or DF lasers for long wavelength applications, and the advent of shorter wavelength systems both in the ARPA applications and in laser fusion and laser isotope separation keep confronting us with new aspects of the old problem areas. These subject headings are so general that they essentially comprise the total subject of laser materials for high energy use; bulk absorption, surface effects, thin film properties, and of course, the ultimate limitation of dielectrics, avalanche ionization. We have made continuing progress in this field and can look forward to further progress being made as long as someone is interested in what we have to say.

We must ask ourselves the burning question, "Who cares"? The answer is to take a look at our ever expanding list of sponsors to get some idea of who cares. I feel that the work of this Symposium continues to be relevant because it continues to be supported, and the day when it ceases to be supported is the day when the Symposium will be out of business. We're very happy this year to acknowledge the expanded support that we have received and I want to acknowledge the continuing support of the ASTM and thank Haynes Lee for his efforts on behalf of the ASTM in helping us move this Symposium along. From NBS, whose hospitality we enjoy and from whom we receive tremendous administrative support, we have to thank Hal Boyne. The Office of Naval Research has supported the Symposium for several years now, and we are indebted to Hershel Pilloff for his help, cooperation,and support. We are very pleased this year to have a speaker on our agenda from ERDA, Joel Weiss from the Washington office, who will review some aspects of the laser materials program in ERDA. Let me again thank Harry Winsor for his support and cooperation in coordination

with the laser window program. I am particularly glad to see full participation by ERDA, because I work for ERDA and I consider it a good sign for continuing employment to see a manifestation of interest from on high. I think everyone is aware of the fact that Martin Stickley, who has a long and abiding interest in optical materials, is now in ERDA leading the new laser division. If you are a reader of portents, you might consider that a good sign for those of us who are interested in further investigation of optical materials.

We're trying a number of innovations this year. The first and most important one is that we are trying to coordinate this meeting with the ARPA Window Conference. I want to give my particular thanks to Bob Andrews and Patsy Collins, who organized the agenda for the Window Conference and with whom Art Guenther and Harry Winsor worked very closely in setting up dual agendas for these two meetings. Secondly, we are trying something new in the way of having poster papers. From the response to the poster papers yesterday and the response I anticipate for the two poster sessions we have in this meeting, I think that will turn out to be a very nice vehicle for allowing us to present a large number of papers without having recourse either to ten minute papers or multiple sessions. The poster papers, I want to make clear, are not intended to be a form of second class citizenship in this meeting. Some papers are more appropriately given as poster papers. By the way, Art Guenther and I would welcome comments and yes, even criticism (if properly tendered) with regard to all aspects of the Symposium, but particularly with regard to the poster sessions. Any suggestions you might have of how these can be improved, expanded, or deleted will be received with interest.

Once again, we're enjoying the hospitality of NBS. I want to acknowledge the steadfast support we have received from Florence Indorf, Wilbur Anson, and the staff of the Bureau in making these superb facilities available to us, for helping us in the preparation of the manuscripts, and in making the whole enterprise both enjoyable and productive.

0.2 SI CONVERSION UNITS

In view of present accepted practice in this technological area, U. S. customary units of measurement have been used throughout this report. It should be noted that the U. S. is a signatory to the General Conference on Weights and Measures which gave official status to the metric SI system of SI units in 1960. Readers interested in making use of the coherent system of SI units will find conversion factors in ASTM Standard Metric Practice Guide, ASTM Designation E 380-76 (available from American Society for Testing and Materials, 1916 Race Street, Philadelphia, Pennsylvania 19103). Conversion factors for units used in this paper are:

Length

1 in = 0.0254* meter

1 ft = 0.3048* meter

1 microinch = $2.5400^{*} \times 10^{-8}$ meter

Area

1 in^2 = $6.4516^{*} \times 10^{-4}$ $meter^2$

1 ft^2 = 9.2903×10^{-2} $meter^2$

Force

1 lb (lbf) = 4.448 newton

1 kip = 4448 newton

Pressure Stress

1 psi = 6895 pascal

1 psf = 47.88 pascal

1 torr (mmHg.0°C) = 133.32 pascal

Energy

1 ft-lbf = 1.3558 joule

Moment

1 lbf-ft = 1.3558 newtonmeter

Temperature

$T_{°C} = 5/9 (T_{°F} - 32)$

Heat

Thermal conductivity, K

1 cal (thermochemical) cm.s. °C = 418.40* watt/meter kelvin

specific heat, C

1 cal (thermochemical)/gm.°C = 4184.00* joule/kilogram-kelvin

---

*Exact Value

0.3 ADVANCED OPTICAL MATERIALS FOR LASER FUSION

Joel A. Weiss
Division of Laser Fusion
U.S. Energy Research and Development Administration
Washington, D.C. 20545

I appreciate the opportunity to make a few remarks this morning about the optical materials needs of the laser fusion program. ERDA's Division of Laser Fusion has the distinction of being not only the newest of the sponsoring organizations for this symposium, but also the newest of the sponsoring organizations in terms of length of time of existence. As Alex Glass mentioned in his remarks, Dr. C. Martin Stickley has been appointed the Director of the newly created Division which became a full division in ERDA on March 22, 1976. The Division has the mission of demonstrating, developing, and utilizing inertial confinement fusion, which includes laser, e-beam, and ion-beam fusion processes. The laser isotope separation program, which had been coupled with the fusion program is now part of the Division of Nuclear Research and Applications, under Dr. Richard Roberts the Assistant Administrator for Nuclear Energy.

From talking with people over the past several days I have noticed that to many of you ERDA is a large amorphous organization. I would like to take a moment to point out some of the features of this new and evolving agency because there are divisions other than my own to which some of you may wish to submit research proposals.

The basic ERDA structure is as follows: There are six scientific Assistant Administrators who report to the Administrator, Dr. Seamans. Of these six there are three who would be of interest to this audience. Dr. Robert Hirsch is responsible for the Division of Physical Research, ERDA's basic research unit as well as for solar, geothermal, and magnetic confinement fusion research. I have already mentioned Dr. Roberts whose domain includes all nuclear energy research. Lastly, there is the Assistant Administrator for National Security, Alfred D. Starbird, whose responsibilities include the Division of Military Application, the parent organization of the present Division of Laser Fusion, which remains under his direction.

At present our division has an extremely small staff, something that will most probably change over the next year. My area of responsibility is solid state laser development and related optical materials research. This area covers the full range of materials and coatings for use in high power pulsed lasers for fusion.

Because the laser fusion program is a young and evolving program, in contrast to the mature program which Harry Winsor discussed yesterday, the projected needs and experimental objectives of the research have continued to change over the past few years. This behavior is probably typical of most state-of-the-art technology efforts in their early stages where the direction of the program is continually being driven by the results of ongoing experiments and calculations. However, our program has now matured to the point where we feel we can map out a well-coordinated plan for development over the next 25 years and can attempt to guide a research program to meet our program objectives.

Because the program has needs in both the near and long term time frames, the materials research efforts sponsored by the Division have two relatively distinct facets. We are currently supporting efforts to develop materials needed to bring on-line laser systems now in the planning stages and at the same time we are sponsoring research on more basic, long term efforts required to permit realization and development of the next generation of laser fusion facilities, such as a materials test reactor or an experimental power reactor. As an example of this two-fold approach, we will be supporting research on dielectric coatings for use on glass lasers at Livermore while at the same time we are interested in supporting some efforts oriented towards developing a fuller understanding of coating science.

Yesterday, Walt Reichelt gave an overview of the materials program as it affects the Los Alamos CO_2 laser program. Today, I plan to limit my remarks to the materials effort at 1.06 μm and visible wavelengths. However, let me point out that the Division of Laser Fusion has prime responsibility for coordinating all aspects of inertial confinement fusion be they Nd:glass, CO_2, e-beam, or ion beam. So my omission of CO_2 from my discussion does not indicate a lack of interest in that subject.

In his talk Walt mentioned that at 10 μm laser design is limited by intrinsic materials breakdown considerations. These limitations drive the laser designer to develop large aperture systems. At 1 μm the laser designer is also materials limited, but not principally, by intrinsic breakdown,

but rather by nonlinear propagation effects, that is, small scale self-focusing (the B-integral). Considerable progress over the past several years in controlling small scale self-focusing through spatial filtering has permitted development of lasers such as the ARGUS system at Livermore which has recently begun operation at better that 1 TW per beam line. This technology is basically the same as will be used in the SHIVA laser now under construction at Livermore which will have 20 such beam lines.

However, despite the fact that spatial filtering can reduce small scale self-focusing and thereby reduce point-to-point variations in laser intensity across the aperture the overall limitations imposed by the nonlinear index of refraction still force the laser designer to ever larger apertures. An example of this trend can be seen on the first slide (fig. 1).

This slide is a picture of a Livermore D-size disk amplifier. This device has a 30cm clear aperture and is the largest disk amplifier ever built. Although not planned for use on the present ARGUS or SHIVA laser systems this amplifier is being considered for use on an upgraded SHIVA laser.

Obviously, when one gets to lasers of this size, it is clear that a better way must be found to increase power or else things will soon get completely unmanageable. One approach to achieving more laser power would be simply to increase the number of beam lines without increasing apertures,but this is an extremely expensive way to go and leads to complexities in the area of pointing and focusing. A much simpler and cheaper approach to higher power laser systems would be to increase the power that can be obtained from any one beam line. If this can be achieved in an existing system by replacement of the optical glass, there can be substantial savings since the cost of glass for a "glass" laser is usually less than 25% of the total outlay.

This then represents the central theme of the present DLF materials program: To develop low n_2 optical materials and related technologies, such as coatings, to improve the performance of solid state laser systems.

One might ask at this point: Why spend all this money on glass lasers since they can never be used as practical fusion lasers. One answer is that glass lasers are the most advanced high power short wavelength ($<< 10$ μm) lasers now in existence,and therefore, represent the most direct,and probably least expensive approach to demonstrating the scientific feasibility of laser ignited thermonuclear fusion. These lasers are the only type of short wavelength laser capable of being brought to the 100-200 TW level in the next five years.

Another answer to the question of why pursue glass development is that only about one-half of the glass in a "glass laser" is actually laser glass. The remainder goes into lenses, polarizer substrates, Faraday rotators, etc. Even when we discard glass lasers, we will not discard all of the glass.

Furthermore, there is no question but that when we discard glass lasers we will still be every bit as concerned with reducing the n_2 of the glass that remains as we are now. In fact, if it proves to be true that n_2 increases as we go toward shorter wavelengths, we will be even more interested in reducing it in the future.

For these reasons then, we are pursuing a program to develop low n_2 optical materials.

The next slide (fig. 2), which is courtesy of Alex Glass and Marv Weber at LLL, is a plot of refractive index versus Abbe number for a number of common optical materials. The dotted lines are lines of constant n_2. Notice that all presently available laser glasses fall in the upper right region of the plot. A tremendous reduction in n_2 can be achieved by developing glasses that lie in regions toward the lower left. Notice also that some of the most attractive materials, from an n_2 standpoint, are the alkali halide and alkaline earth fluoride materials with which many of you here have been dealing as DoD window materials.

Although the basic parameter of importance in our research program is the nonlinear index, n_2, the actual figure of merit for an optical material may, in addition, be independent on other parameters and the functional dependence may vary depending on the role played by the material in the laser system. The next slide (table 1) shows the functional form of the figure of merit for laser rods, disks, lenses, polarizer substrates, and Faraday rotators. As you can see, the choice of a material is highly dependent on where it is in the laser system and what purpose it will serve. For example, laser disks operating in the parasitic-limited regime have a figure of merit which is equal to n^2/n_2, whereas, if parasitics are not a problem, the figure of merit includes gain and can be written as $n^2\sigma/n_2$. Notice also that it is difficult to improve the figure of merit for a lens because of the $n(n-1)$ dependence since n decreases with decreasing n_2. The data is valid for 1 ns pulses.

On this table are also given representative figures of merit for silicate, phosphate, fluorophosphate and fluoroberyllate glasses, and for fluoride crystalline materials. It is apparent that the use of fluoroberyllate glasses and crystalline materials is the most attractive course to follow even if it is a somewhat more difficult path.

In our research program we are obviously not assuming that one class of materials will be suitable for all purposes in a laser system. The next slide (table II) is an outline of the roles as we see them for the various optical materials on which we are supporting research. We are counting on fluorophosphate materials to be available as laser hosts, polarizer substrates, and rotator hosts. Crystalline materials will be used principally for lenses, possibly for rotator hosts and almost certainly as oscillator materials. (The Nd laser wavelength for fluorophosphate and beryllate glasses lies at 1.047 μm, requiring the development of new oscillator materials.) Lastly, as a high risk, high payoff option we are supporting research on fluoroberyllate glasses to be used in the same roles as the fluorophosphates.

As we support research designed to increase the power output per unit area for a laser beamline we find ourselves suddenly pressing another area of technology to the limit--dielectric coatings. The next slide (table III) shows typical coatings requirements for an upgraded SHIVA laser operating at the 100-200 TW level. As you can see we are seriously deficient in the area of AR coatings while the situation is not nearly bad for polarizers and dielectric reflectors. Notice that even with such a laser we are still operating well below the intrinsic bulk damage level for the optical glasses themselves. Although we can dispense with some coatings in these laser systems we can do so only with a loss of output power. For this reason we are interested in supporting development of improved coatings for high power applications.

We are attempting to have the materials which I have discussed today developed within 2-2½ years to the point where purchase orders can be placed for production quantities and sizes. This will require that pre-production prototypes be produced by the end of this time period. This is a big job, but we are getting responses of interest from many of the major glass manufacturers and from quite a few companies that have been involved in the ARPA window program. We feel that this is an important job and one which can and will be accomplished.

I appreciate the opportunity to speak here this morning to present our program and our needs, and I encourage you to contact me if you have any questions about our materials research effort.

Table I. Figures of merit of laser system materials.

COMPONENT	Figure of Merit	HOST MATERIAL				
		Silicate Glass	Phosphate Glass	Fluorophosphate Glass	Fluoroberyllate Glass	Fluoride Crystal
LASER ROD Pump Limited	$\frac{\sigma n}{n_2}$	1.0	1.8	1.9	3.1	--
LASER DISK Pump Limited	$\frac{\sigma n^2}{n_2}$	1.0	1.7	1.8	2.7	--
LASER DISK Parasitic Limited	$\frac{n^2}{n_2}$	1.0	1.4	1.8	2.7	--
WINDOW	$\frac{n}{n_2}$	1.0	1.3	1.7	2.7	2.0
LENS	$\frac{n(n-1)}{n_2}$	1.0	1.3	1.7	2.2	1.7
ROTATOR	$\frac{Vn}{n_2}$	1.0	0.5	1.2	2.1	5.0

Table II. Roles for candidate optical materials.

FLUOROPHOSPHATE GLASSES

- LASER HOSTS
- SUBSTRATES, FOCUSING LENSES, WINDOWS
- FARADAY ROTATOR HOSTS

CRYSTALLINE MATERIALS

- FOCUSING LENSES (CaF_2)
- WINDOWS (CaF_2)
- OSCILLATOR MATERIALS (Nd:YLF)
- FARADAY ROTATORS

FLUOROBERYLLATE GLASSES

- LASER HOSTS
- FOCUSING LENSES
- FARADAY ROTATORS

Table III. Coating requirements for an upgraded shiva laser.

100 ps performance	Antireflection	High reflection	Polarizers	Substrates
Past Experience	2 J/cm^2	2 J/cm^2	3 J/cm^2	15 J/cm^2
Best Today	4 to 6 J/cm^2	4 to 9 J/cm^2	4 to 7 J/cm^2	30 J/cm^2
Upgrade Requires	10 J/cm^2	8 J/cm^2	8 J/cm^2	15 J/cm^2

Figure 1. 30-cm aperture disk amplifier.

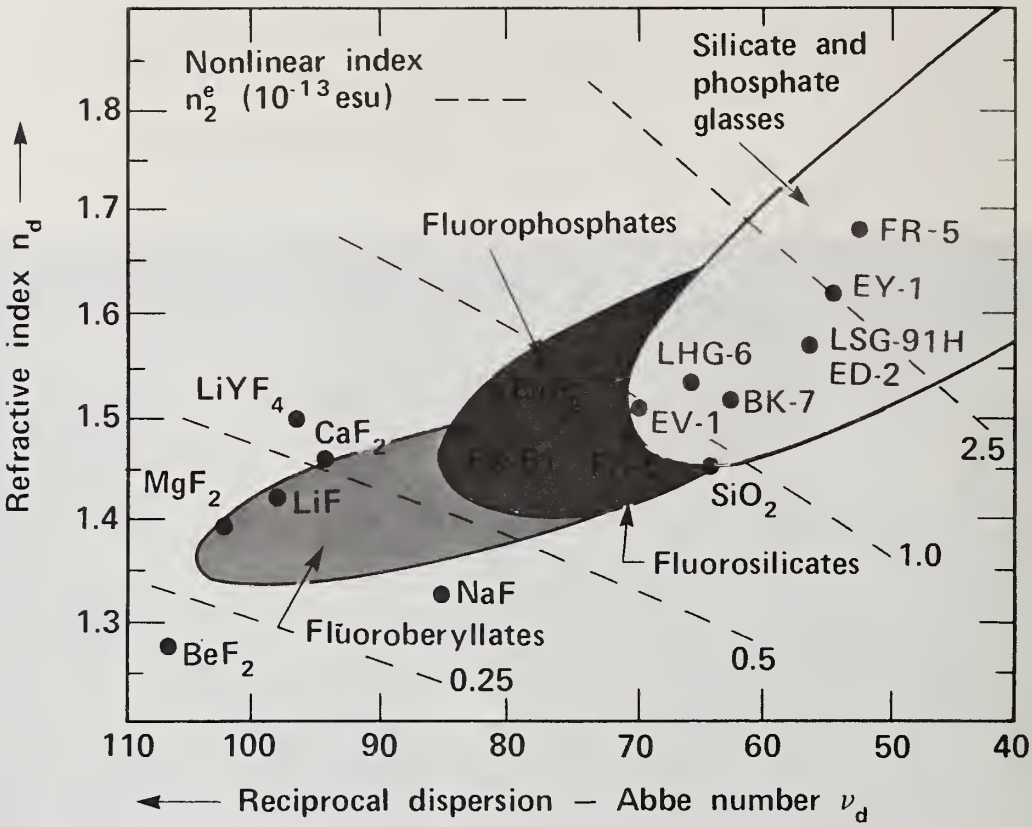

Figure 2. Refractive indices of laser system optical materials.

COMMENTS ON PAPER BY WEISS

No discussion on this paper.

1.1 THERMAL DISTORTION THRESHOLDS FOR OPTICAL TRAINS HANDLING HIGH PULSE POWERS

H. E. Bennett
Michelson Laboratories, Naval Weapons Center
China Lake, California 93555

The maximum pulse power level which components in the optical train of a high energy laser can pass is determined by the catastrophic damage threshold for the system. Before that level is reached, however, thermally induced optical distortion may make the beam unfocusable and hence for most practical purposes unusable. The amount of thermally induced optical distortion which may be tolerated depends strongly on the initial optical figures of the various components, and in the case of windows, on their optical homogeneity. Requirements for these parameters in a multicomponent infrared optical train can be surprisingly severe, and are frequently comparable to those commonly used for high quality optics designed for the visible region of the spectrum. Figure requirements for mirrors are more severe than for windows unless their index of refraction is above about 2.4. Adaptive optics may be used to remove some of the resultant wave front error, but the lower the requirements made by the optical train the more easily the adaptive optics system can correct for wave front distortions arising from the laser medium and from the optical path. A detailed analysis is required to set optimum tolerances for the various components in the optical path of a particular system. Simple relations can be developed, however, which can be used to predict the approximate pulse power handling capability of the optical train for short periods of time in terms of the material parameters of the various components in the system, their optical figures, and in the case of windows, their homogeneity. These relations can be used as figures of merit to select between materials and preliminary calculations for system design.

Key words: Laser windows and mirrors; optical figure; pulsed laser; thermal distortion.

Introduction

In an optical train handling high intensitites such as those generated by lasers the maximum power levels windows and mirrors can pass are limited by the catastrophic damage threshold of the materials. Before that level is reached, however, thermally induced optical distortion may make the optical beam unfocusable and hence in many cases unusable. The amount of thermally induced optical distortion which may be tolerated depends in part on the initial optical figure of the component; figure requirements for multicomponent optical trains can be surprisingly severe even at infrared wavelengths. In an actual optical system it is necessary to assign an error budget to each component. If a large error is allowed for one component, it may make the tolerances on the other components impossibly tight. The practice of calculating allowable figure distortions for individual windows or mirrors as if they were the only component in the optical system is thus quite unrealistic. Some of the resultant wave front errors may be removed by using adaptive optics. However, the lower the requirements made on the adaptive optical system by the optical train, the more easily it will be able to correct for wave front distortions arising from the laser medium and the optical path. In this paper only the allowable optical distortion is considered. A diffraction approach is used based on the Maréchal criterion for a multielement system. Optical distortion limits for individual windows using a geometrical optics approach have been discussed previously in a classic paper by Sparks, who has also discussed fracture thresholds [1][1]. He has shown that when only single windows are considered the fracture threshold rather than the thermal distortion threshold usually limits window performance. However, as discussed in this paper, unless adaptive optics are used, optical trains consisting of many components each with a practical initial optical figure will usually have a thermal distortion threshold for high intensity beams which is lower than the fracture threshold.

The first section of this paper discusses allowable figure errors for both windows and mirrors based on the Maréchal criterion. The second, third, and fourth sections discuss thermal distortion limits for windows and mirrors in optical trains. The analytical expressions developed there are used in the last two sections to provide figures of merit for evaluating various window and mirror materials.

Figure Errors

More stringent tolerances are required to focus diffraction limited intensities than are required to give diffraction limited resolution [2]. The ratio of the intensity I (at the center of a focused

1. Figures in brackets indicate the literature references at the end of this paper.

spot produced by an optical train which introduces an rms wave front error σ) to the intensity I_o (which would be obtained if $\sigma = 0$) is given approximately by the Strehl relation [3]

$$\frac{I}{I_o} = 1 - \left(\frac{2\pi}{\lambda}\right)^2 \sigma^2 \tag{1}$$

where λ is the wavelength. The accuracy of the Strehl relation for differing values of I/I_o and also that of an exponential relation which reduces to the Strehl relation for large intensity ratios but gives a closer approximation to the exact calculation for small intensity ratios, has been discussed by Loomis [4]. In deriving eq. (1) the limiting apertures in the optical train are assumed to be uniformly illuminated. In practice the intensity will vary across the aperture, modifying eq. (1) to some extent. Modifications in the Strehl relation for the case of a truncated Gaussian beam profile have been considered by Lowenthal [5]. When the half-width of the beam profile is much smaller than the aperture radius, the error introduced by assuming a uniform illumination can be very large. However, if the Gaussian intensity falls to $1/e^2$ of its maximum value at the edge of the aperture, an intensity ratio of 0.8 given by eq. (1) is low by only about 6%. Maréchal has suggested [3] the criterion that the rms wave front errors not exceed $\lambda/14$, giving $I/I_o = 0.8$. This criterion is more quantitative, but similar to the well known Rayleigh $\lambda/4$ criterion for allowable peak-to-valley wave front distortions [3]. Equation (1) is a good approximation to the exact calculation of I/I_o when the Maréchal criterion is met. If it is relaxed, for example, by doubling the loss in *on-axis* intensity so that only 60% of the theoretical intensity is achieved rather than 80%, the allowable distortion only increases by about a factor of 1.4. The Maréchal criterion is thus a good objective to strive for in a multielement optical system.

The total rms wave front distortion σ is the sum of contributions from the N components in the optical train. If these contributions are uncorrelated, then we can add intensities rather than amplitudes and σ^2 is the sum of the squares of the contributions from the individual components [6]. Thermally induced wave front errors in different components are often correlated; in some cases the wave front errors are of different sign and correlation between components results in partial cancellation. We will assume thermally induced wave front errors between components are correlated. However, unless similar figure errors were developed by the lap on the different components or on the two sides of a polished window there will be no correlation between figuring errors in different components. In the case of windows, wave front errors caused by optical inhomogeneity in the window material are also assumed to be uncorrelated in different components. For an equal error budget per component the resultant intensity decrease caused by figuring errors and by inhomogeneities in the bulk of the window materials are each then simply N times the square of the respective wave front distortions per component.

The contribution from each component will be caused partly by the initial figure and optical inhomogeneity errors and partly by the thermally induced figure error resulting from absorption. Assuming that the initial figure and optical inhomogeneity errors are uncorrelated with each other or with the thermally induced figure errors so that the squares will be additive, assigning the same figure error budget to each component and using the Maréchal criterion, we then have

$$\frac{I}{I_o} = 0.8 = 1 - \left(\frac{2\pi}{\lambda}\right)^2 \left(N\sigma_f^2 + N\sigma_i^2 + \sigma_T^2\right) \tag{2}$$

where σ_f is the rms wave front error introduced by initial figure errors in a single component, σ_i, that introduced by optical inhomogeneity if any in a window component and σ_T is the thermally induced rms wave front error. If δn is the rms variation in the value of the index of refraction across the window and ℓ is its thickness, then $\phi_i = \delta n \ell$. The peak to peak wave front errors introduced by figuring are approximately $2\sqrt{2}$ times the rms values (an exact relation if the wave front errors are sinusoidal) and the wave front error introduced by a mirror is twice the physical displacement τ_{fm} of the mirror surface so that $\sigma_f = \tau_{fm}/\sqrt{2}$. Substituting in eq. (2) we then obtain a relationship for the allowable peak to peak initial figure error τ_{fm} for a mirror

$$\tau_{fm} = \sqrt{\frac{\lambda^2}{10\pi^2 N} - \frac{2}{N}\sigma_T^2}\ . \tag{3}$$

In air for windows with index of refraction n the change in optical path caused by a physical path difference will be (n - 1) times the physical path difference. The contribution to the rms wave front distortion arising from initial peak to peak figure errors of τ_{fw} at each of the two surfaces will be $\sigma_f^2 = (1/2\sqrt{2})^2\ 2(n-1)^2\tau_{fw}^2$ or

$$\sigma_f = \frac{1}{2}(n-1)\tau_{fw} \tag{4}$$

assuming that the figuring errors are uncorrelated. From eq. (2) an expression relating the magnitude of the allowable errors for a window on an equal error per component basis is then

$$\tau_{fw} = \frac{1}{n-1}\sqrt{\frac{\lambda^2}{5\pi^2 N} - \frac{4\sigma_T^2}{N} - 4\sigma_i^2} \quad . \tag{5}$$

By comparing eqs. (3) and (5) and letting $\sigma_T = \sigma_i = 0$, we see that for windows whose index of refraction is less than 2.414, the maximum figuring error per surface can be larger for a window than for a mirror. In other words, when initial figure errors are uncorrelated, the initial figure requirements for a homogeneous window ($n < 2.414$) are not as stringent as those for a mirror. If we had assumed [7] that the initial figure errors on the two sides of the window were correlated, windows whose index of refraction was less than 2.0 would have less stringent figure requirements than for mirrors, but those with higher indices would have more stringent figure requirements. Uncorrelated initial figures appear to be the more realistic assumption in most cases. Dueweke *et al.* [8] have experimentally verified that initial figure errors on different windows in one typical infrared optical train were uncorrelated and hence that the resultant wave front error was given by the sum of the squares of the figure errors for each window.

If the sum of the squares of the maximum allowable initial figure and homogeneity errors are restricted to one-half of the square of the thermally induced error, the maximum allowable initial figure error can be calculated for mirrors from eq. (3) and for windows from eq. (5). Results for homogeneous windows of ZnSe, KCl, CaF_2, and SrF_2 and for mirrors are shown in figure 1 for a 10-component system. For KCl a full wave of figure error is permissible at 10.6 μm, as compared to slightly over a quarter-wave for ZnSe and for a mirror. At CO and DF wavelengths about an eighth-wave figure is required for ZnSe and for mirrors, which is a very severe tolerance for components of appreciable size. Figure tolerances for ZnSe and for mirrors coincide because the index of ZnSe is 2.4, the crossover value as discussed above. For KCl and both CaF_2 and SrF_2 the figure tolerance is about one-half to three-eighths wave at CO and DF wavelengths. In the general case the figure tolerances on homogeneous windows are a factor of $\sqrt{2}/(n-1)$ larger than those of mirrors. Inhomogeneities in the window will tighten these figure tolerances since under the above error budget the allowed peak to peak figure error per surface for a window is

$$\tau_{fw} = \frac{1}{(n-1)}\sqrt{\frac{\lambda^2}{15\pi^2 N} - 4\sigma_i^2}. \tag{6}$$

Thermal Distortion in Windows

The thermally induced wave front distortion a window can contribute without serious degradation of the optical image can be calculated approximately from eqs. (2) and (5) for either pulsed or CW operation. Calculation of the energy in a single pulse which can be passed without violating the Maréchal criterion for the optical train is simplest since lateral thermal diffusion effects can be neglected. In one second the thermal diffusion lengths for typical window materials are 2-3 mm, so the calculated maximum single pulse energies represent approximately the maximum amount of energy the window can pass without significant optical distortion over periods as large as a few seconds. Even if we neglect lateral diffusion, however, the relation between the heating of the window and thermally induced optical distortion is strongly dependent on the beam profile. Since the thermally induced wave front distortion results from differences in optical path length across the component, not from the total thermally induced change in optical path lengths, the beam profile is very important. If a homogeneous window were heated uniformly, for example, the optical path length might change significantly without introducing any wave front distortion. To calculate representative wave front distortion values some model of the beam profile must thus be made. A convenient model is a top hat beam profile which occupies the center half of the area of the aperture. In calculating the wave front distortion, however, the changes in optical path length in all equal areas of the mirror or window are weighed equally. This approximation will in most cases result in overestimating the resultant wave front distortion somewhat. The effect of a similar assumption using Gaussian beam profiles has been studied by Lowenthal [5].

The top hat function described above is a first approximation to a Gaussian beam profile whose $1/e^2$ points coincide with the component aperture. The power P passing through an aperture of radius b when the beam profile is Gaussian is

$$P = \int_0^{2\pi}\int_0^b I_o e^{-2r^2/b^2}\, r dr d\theta \cong I_o \pi b^2/2 \tag{7}$$

which may be approximated by a top hat beam profile with maximum intensity I_o and radius $b/\sqrt{2}$.

In actual applications the beam profile is often neither flat-topped nor Gaussian. For example, in the near field of an unstable resonator the intensity profile is donut shaped with a minimum at the center as well as near the edge of the aperture. Asymmetric energy profiles are commonly observed. Thus the limiting energy levels calculated assuming the top hat beam profile described above are at best only approximate for an actual system. They provide a useful figure of merit for various window or mirror materials, but more detailed calculations involving the actual beam profile are required to establish maximum permissible power levels in an actual system.

For a window the energy absorbed per unit area of the beam is, for a temporally square pulse of incident intensity I_o and pulse length t, $I_o t(\beta\ell + 2A_s)$ where A_s is the surface absorption per surface, ℓ the thickness of the window and β the bulk absorption coefficient. Both $\beta\ell$ and $A_s \ll 1$ and we are neglecting the window reflection loss. Let the thickness of the surface absorption layer be ℓ_s. Then the increase in surface temperature T_s will be

$$T_s = \frac{I_o t\, A_s}{\rho c_p \ell_s} \tag{8}$$

where c_p is the specific heat at constant pressure of the window material and ρ is its density. Similarly the temperature increase T in the interior of the window, neglecting thermal diffusion, will be

$$T = \frac{I_o t \beta}{\rho c_p} \quad . \tag{9}$$

The change in optical path length caused by thermal heating depends both on the window material, how it is polished, the beam profile and the window mounting configuration. Assume that the dominant source of thermal heating is volume absorption. If the window were uniform in absorption, uniformly heated and unconstrained, the change in optical path length would be simply

$$\frac{d[(n-1)\ell]}{dT} T = \left[(n-1)\frac{1}{\ell}\frac{d\ell}{dT} + \frac{dn}{dT}\right] \ell T \quad . \tag{10}$$

However, if nonuniform heating occurs, stresses will be set up in the window. The cool window material at the rim will constrain the expansion of the hotter window center in the plane of the window and this stress will cause the window to bulge and grow somewhat more normal to its surface than it would if thermal expansion in a radial direction were unconstrained. Making the simplifying (and incorrect) assumption that the window is isotropic in all crystalline directions, we can calculate the resultant axial growth caused by this constraint from Hooke's law. Consider a thin circular disk with an axisymmetric temperature distribution, but with no temperature variation normal to the disk surface. If z is the normal coordinate and r and θ the cylindrical coordinates in the plane of the disk, Hooke's law including thermal expansion for the differential strain ε_z in the z direction may be written

$$\varepsilon_z - \alpha T = \frac{1}{E}\left[\sigma_z - \nu(\sigma_r + \sigma_\theta)\right] \tag{11}$$

where E is Young's modulus, ν Poisson's ratio, α the linear expansion coefficient and σ_z, σ_r, and σ_θ are the differential stresses in the z, r, and θ directions, respectively. Similar expressions hold for ε_r and ε_θ, the differential strains in the r and θ directions. If we assume the stress is entirely in the plane of the disk (plane stress approximation) then $\sigma_z = 0$. If the disk is simply supported so that there are no external body forces then [9]

$$\sigma_r = \alpha E\left(\frac{1}{b^2}\int_o^b Tr\, dr - \frac{1}{r^2}\int_o^r Tr\, dr\right) \tag{12}$$

$$\sigma_\theta = \alpha E\left(-T + \frac{1}{b^2}\int_o^b Tr\, dr + \frac{1}{r^2}\int_o^r Tr\, dr\right) \tag{13}$$

where b is the disk radius. The axial displacement $w(r) = \ell\varepsilon_z(r)$ is then

$$w(r) = \alpha\ell T(r)\left[1 + \nu \quad 1 - \frac{2}{b^2 T(r)}\int_o^b T(\xi)\xi\, d\xi\right] . \tag{14}$$

For the "top hat" function $T(r) = T$ for $r \le b/\sqrt{2}$ and $T(r) = 0$ for $r > b/\sqrt{2}$. In the heated area the axial displacement w_1 is then

$$w_1 = \alpha\ell T[1 + \nu/2] \quad . \tag{15}$$

The compressive radial stress exerted by the heated area on the unheated area causes a small compressive stress radially and a larger tangential hoop stress which is tensile. The resultant axial displacement w_2 is thus negative in the unheated area. From eq. (14)

$$w_2 = -\alpha\ell T\nu/2 \quad . \tag{16}$$

The relative axial displacement of the heated area with respect to the unheated area is then

$$w_1 - w_2 = \alpha\ell T(1 + \nu) \quad . \tag{17}$$

Another effect of thermally induced stress in a heated window is to introduce strain birefringence. A pressure differential across the window will also produce this effect, which is quite pronounced in materials such as the alkaline earths and to a lesser extent in the alkali halides. Representing the contribution of strain birefringence by ϕ, we then have for τ_T, the maximum thermally induced change in optical path length for a window,

$$\tau_T = \frac{I_o t}{\rho c_p} (2A_s + \beta\ell) \left[(n - 1)(1 + \nu)\ \alpha + \frac{dn}{dT} + \phi\right] \quad . \tag{18}$$

The rms change in optical path length for the "top hat" beam profile is then $\tau_T/\sqrt{2}$. In deriving eq. (18) we have neglected the temperature dependence of the material parameters, a good approximation since the allowable temperature rise of most windows is only a few degrees centigrade.

Thermal Distortion in Mirrors

In windows surface absorption occurs on both sides in approximately the same amount and bulk absorption occurs more or less uniformly so that little or no asymmetric bowing of the window occurs. However, in mirrors absorption occurs on only one face. The thermal expansion of this face is restricted by the colder body of the mirror and a bowing occurs at the mirror surface distorting the optical figure. In addition, the heated center of the mirror expands normal to the surface distorting the optical figure further. As a first approximation consider only the heated center of the mirror and add the expansion and bowing terms to obtain the resultant wave front distortion.

Let the thermal expansion of the mirror center normal to its surface be w_3 where

$$w_3 = \int_{-\ell/2}^{\ell/2} \alpha T(z,r,t)dz \quad . \tag{19}$$

But the energy absorbed by the mirror per unit area is

$$I_o(1 - R)t = \int_{-\ell/2}^{\ell/2} \rho c_p\ T dz \tag{20}$$

so that

$$w_3 = \frac{\alpha I_o(1 - R)t}{\rho c_p} \tag{21}$$

which is independent of the thermal conductivity of the substrate.

To calculate the bowing of the mirror surface we utilize the derivation for a thin circular shell of diameter $\sqrt{2}$ b which is uniformly irradiated on one side with a flux of intensity I_o. The axial deflection w_4 caused by bowing of such a shell simply supported is [10]

$$w_4 = \frac{6\alpha}{\ell^3}\left(\frac{b^2}{2} - r^2\right) \int_{-\ell/2}^{\ell/2} T(z,t)z\ dz \tag{22}$$

where [11]

$$T(z,t) = \frac{2I_o(1 - R)}{K}\left[\left(\frac{kt}{\pi}\right)^{1/2} e^{-z^2/4kT} - \frac{z}{2}\left(1 - \frac{2}{\sqrt{\pi}}\int_o^{z/2(kt)^{1/2}} e^{-\xi^2}\ d\xi\right)\right] \tag{23}$$

and K is the thermal conductivity of the mirror. The thermal diffusivity k is

$$k = \frac{K}{\rho c_p} \tag{24}$$

and the thermal diffusion depth ℓ_d is given by

$$\ell_d = (kt)^{1/2} \quad . \tag{25}$$

For typical substrate metals the thermal diffusion depth in cm is approximately equal to the square root of the pulse length in seconds. Thus even for honeycomb mirrors,cooling will be ineffective during the pulse even for pulse lengths as long as ten milliseconds. At a depth ℓ_d below the surface of the mirror the temperature is seen from eq. (23) to be 80% of that at the surface and it falls rapidly at greater

depths. A simple model of the surface is then a thin slab of thickness ℓ_d which has been raised to the surface temperature T(0,t) and is restrained by the unheated body of the mirror. If $\ell_d \ll \ell/2$, the integral in eq. (22) then becomes

$$\int_{(\ell/2)-\ell_d}^{\ell/2} T(0,t)z\, dz \cong \frac{T(0,t)\ell\ell_d}{2} \quad . \tag{26}$$

Evaluating T(0,t) using eq. (23) the axial displacement of the simply supported thin shell is seen to be parabolic [12] in this approximation and is given by

$$w_4 = \frac{3I_o(1 - R)\alpha t}{\sqrt{\pi}\ \rho c_p \ell^2} (b^2 - 2r^2) \quad . \tag{27}$$

The rms displacement over the mirror surface is then

$$\left[\frac{1}{\pi b^2}\int_o^{2\pi}\int_o^{b/\sqrt{2}} (w_1 + w_2)^2\ r dr d\theta\right]^{1/2} = \frac{I_o(1 - R)\alpha t}{\sqrt{2}\ \rho c_p} (1 + 3\chi + 3\chi^2)^{1/2} \tag{28}$$

where $\chi = (1/\sqrt{\pi})(b/\ell)^2$. Equation (28) has been derived on the basis of the thin shell model and hence will become less accurate as the mirror becomes thicker relative to its diameter. To estimate the magnitude of this error a finite element analysis was performed on aluminum shells of various thicknesses which were simply supported and had a temperature distribution which did not vary with lateral position on the surface. The calculated maximum axial displacements were higher than the values predicted by the shell model by 15% or less for diameter to thickness ratios up to 3 and the 2:1 thickness ratio differed by only 34%. Equation (28) should thus be usable even when $b/\ell \sim 1$. It predicts that the surface distortion and thus the change in optical path length for a mirror caused by thermal heating is independent of the thermal conductivity of the mirror substrate and depends only on the absorbed flux, the mirror's linear expansion coefficient, its heat capacity per unit volume and its diameter to thickness ratio.

Energy Transmission Limits for an Optical Train

Since the figuring errors, bulk inhomogeneities and thermally induced wave front distortions are assumed to be uncorrelated but the thermal distortion between components is correlated, eq. (2) gives

$$\sigma_T = \left[\frac{\lambda^2}{20\pi^2} - N\sigma_f^2 - N\sigma_i^2\right]^{1/2} . \tag{29}$$

The thermally induced changes in optical path length can be calculated from eq. (18) for windows and will be positive if dn/dT is positive. For mirrors it will be negative since expansion of the mirror decreases the optical path length by twice the axial movement of the mirror surface. The change in optical path length for mirrors is twice the physical displacement of the mirror surface and hence can be calculated from eq. (28). Since the thermal distortion is proportional to the energy density striking each component, an accurate calculation of thermal distortion must involve an analysis of the beam diameter and profile at the surface of each optical component. Some components will have greater energy densities incident on them than others and the trade-offs which can be made are only revealed by detailed analysis of the entire system. To obtain a rough approximation of the power levels which may be involved and to obtain an approximate figure of merit for comparing different materials assume an equal error budget for each component and assume the "top hat" beam profile just discussed. Then σ_T is given by

$$\sigma_T = \sum_{p=1}^{N_w} \frac{I_{op}t}{\sqrt{2}\rho c_p} (2A_s + \beta\ell) \left[(n - 1)(1 + \nu)\alpha + \frac{dn}{dT} + \phi\right] - \sum_{q=1}^{N_m} I_{oq}t(1 - R)\frac{\sqrt{2}\alpha}{\rho c_p} (1 + 3\chi + 3\chi^2)^{1/2} \tag{30}$$

where the first summation gives the contribution from the N_w windows in the optical train, and the second summation the contribution from the N_m mirrors, where $N_w + N_m = N$. The peak beam intensity at a given window p is I_{op} and at a given mirror q, I_{oq} where p and q are running indices specifying the individual mirrors and windows. The values of I_{op} and I_{oq} for the various components will depend on the design of the optical train. If the wave front error produced by the window is positive, as it is for ZnSe for example, it will cancel some of the negative wave front error produced by the mirrors, perhaps allowing greater powers to be transmitted by the optical train than would be possible if the window were not present. The assumption that the allowed thermal distortion per component is 1/N times the total allowed thermal distortion will thus often be unduly conservative. It does, however, give a useful figure of merit for mirror or window performance. For mirrors the limiting energy density using this criterion is, from eqs. (29) and (30)

$$I_{oq}t = \frac{\rho c_p \left(\frac{\lambda^2}{5\pi^2 N} - 2\tau_f^2\right)^{1/2}}{2(1 - R)\alpha[2N(1 + 3\chi + 3\chi^2)]^{1/2}} \tag{31}$$

and for windows

$$I_{op}t = \frac{\rho c_p \left[\frac{\lambda^2}{5\pi^2 N} - (n - 1)^2 \tau_f^2 - 4\sigma_i^2\right]^{1/2}}{\sqrt{2N}(2A_s + \beta\ell)\left[(n - 1)(1 + \nu)\alpha + \frac{dn}{dT} + \phi\right]} . \tag{32}$$

The limiting pulsed energy density which the component can pass is thus inversely proportional to its absorption and directly proportional to its specific heat. For mirrors it is inversely proportional to the expansion coefficient of the mirror substrate. For windows it is inversely proportional to $[(n - 1)(1 + \nu)\alpha + dn/dT + \phi]$, which is a particularly important term when dn/dT is negative, as it is for alkali and alkaline earth halides. A pole may occur in this case, making it possible for the window to handle very large energy densities without significant optical distortion.

Comparison of Window Materials

Equation (32) furnishes a convenient figure of merit for the optical performance of a window material. Other material properties must also be considered, however, including physical strength, type of fracture, polishability, surface microroughness, achievable optical figure, hygroscopicity, coatability, etc. In the intermediate infrared the alkaline earth fluorides are promising laser window materials with low indices of refraction and high strengths. Unfortunately they do exhibit brittle fracture so that their engineering strength is significantly lower than their breaking strength. They are not hygroscopic and are nearly as easy to work as optical glass. Quarter or even eighth wave figures can be obtained routinely. One CaF_2 sample examined at Michelson Laboratory had an rms roughness under 10 Å, but commercially polished CaF_2 samples typically have roughnesses of 50-60 Å and SrF_2 is slightly higher. The microroughness determines the scattered light level in the visible region and to some extent in the infrared region and also is related to the laser damage threshold [13].

Zinc selenide, a leading candidate for windows for carbon dioxide lasers, is a soft but very brittle material which is fairly difficult to polish and has a high index of refraction. Optical figures of one quarter-wave in the visible on 15 cm diameter windows have been reported [14,15] with microroughnesses under 25 Å rms. KCl, another leading candidate for carbon dioxide lasers, is the softest and most difficult to polish of the four materials discussed. However, quarter-wave figures have been obtained while minimizing surface absorption [16]. Microroughnesses as low as 27 Å have been obtained on KCl [17], but more typical values are in the 100-200 Å range. The low index of refraction of KCl is a very important asset for laser applications.

A comparison of experimentally observed minimum surface and bulk absorption values for various window materials is shown in figure 2. KCl has the lowest absorption coefficient in the 5-10 μm wavelength range. The volume absorption coefficient value of 8×10^{-5} cm^{-1} for KCl at 10.6 μm was reported for single crystal material [18]; the best forged polycrystalline material is 2-4 times higher. The increase in absorption in the vicinity of 9.6 μm has been reported by several authors [19-21], its origin is obscure but may be associated with impurity levels of less than 0.1 ppm [22]. Values of surface and bulk absorption at CO wavelengths for KCl are those reported by Deutsch [23], and for SrF_2 and CaF_2 by Newberg and Pappis [24] for cast material. Comparable values were reported for single crystal material by Larkin et al., [25]. Volume absorption data at DF and HF wavelengths are as reported by Harrington et al., [26]. They report surface absorption values in the 10^{-3} range for both SrF_2 and ZnSe, lower values for CaF_2 and KCl. However, Miles [27] has reported a value of 2.5×10^{-5} for surface absorption of SrF_2 at DF wavelengths. The quality of the surface finish is usually not reported, but it is safe to assume that the surfaces were all etched. Other material properties [28] were taken from table 1.

We may conclude from figure 2 that the minimum surface absorption per surface is usually comparable in magnitude to the minimum volume absorption coefficient in cm^{-1}. Unless extreme care is taken in producing the bulk material and the polishing process, however, either bulk or surface absorption values may be orders of magnitude higher than the values quoted. Both the surface absorption and the bulk absorption coefficient tend to be lower at CO wavelengths than for either CO_2 or HF/DF. The short dashed lines indicate the intrinsic multiphonon absorption edges. KCl and ZnSe at CO_2 wavelengths and CaF_2 and SrF_2 at CO wavelengths are thus nearly at intrinsic levels. At the shorter wavelengths the absorption appears to be extrinsic and, as pointed out by Hass [29], is much higher than would be expected at the HF/DF wavelengths. The surface absorption at these wavelengths may thus not continue to track the volume absorption coefficient, as Miles' data for SrF_2 indicates.

The product of the absorption term and the term giving the change in optical thickness with temperature in the denominator of eq. (32) determines to a large extent the energy density which a window can transmit without excessive thermal distortion. Values calculated from eq. (32) for a ZnSe, KCl, CaF_2 or

SrF_2 window in a 10-component system using the material parameters given in table 1, are shown in figure 3. The surface absorption per surface shown in figure 2 was doubled to account approximately for the minimum increase in surface absorption which can be expected because of polishing. A 2-cm thick window was assumed with an initial figure error per surface of a quarter-wave. A figure error of this magnitude is not significant except for ZnSe, but a larger figure error could drastically reduce the calculated energy levels. Since data exist only at the laser wavelengths, the curves connecting the points are not significant.

Table 1. Material parameters for window materials used to calculate figure 3 as referenced in text. Symbols are λ wavelength, n index of refraction, T temperature, β bulk absorption coefficient, A_s surface absorption coefficient, α linear expansion coefficient, ν Poisson ratio, c_p specific heat at constant pressure, and ρ density.

	Optical Parameters					Non-Optical Parameters			
Material	λ (μm)	n	$dn/dT(°K^{-1})$	$\beta(cm^{-1})$	$2A_s$	$\alpha(°K^{-1})$	ν	c_p(J/gm°K)	$\rho(gm/cm^3)$
KCl	10.6	1.454	-2.7×10^{-5}	8×10^{-5}	2.4×10^{-4}	36.8×10^{-6}	0.11	0.6895	1.9893
	5.25	1.470	-3.15×10^{-5}	1.5×10^{-5}	2×10^{-5}	---	---	---	---
	3.8	1.473	-3.26×10^{-5}	3.12×10^{-4}	2×10^{-5}	---	---	---	---
ZnSe	10.6	2.40	6×10^{-5}	4.1×10^{-4}	11×10^{-4}	7.2×10^{-6}	0.30	0.3	5.265
	5.25	2.43	9×10^{-5}	1.5×10^{-4}	10^{-3}	---	---	---	---
CaF_2	5.25	1.3952	-7.2×10^{-6}	4.2×10^{-4}	4×10^{-5}	18.2×10^{-6}	0.26	0.854	3.18
	3.8	1.4122	-7.8×10^{-6}	2.67×10^{-4}	---	---	---	---	---
SrF_2	5.25	1.40	-1.19×10^{-5}	7.6×10^{-5}	2.5×10^{-5}	17.5×10^{-6}	0.26	0.556	4.18
	3.8	1.44	-1.19×10^{-5}	5.0×10^{-5}	2.5×10^{-5}	---	---	---	---

Although zinc selenide has the lowest pulse energy threshold for optical distortion of the four materials examined, it should pass over 100 J/cm^2 at 10.6 μm without significant optical distortion. When used in an optical train containing several mirrors it may pass significantly higher energy densities than this since the thermal distortion produced in the window will be largely cancelled by that produced by the mirrors. Potassium chloride windows exhibit less than 1/30th the optical distortion found in ZnSe windows at 10.6 μm and hold particular promise as internal windows in lasers where flux densities tend to be higher than at the output window.

At the shorter wavelengths CaF_2 and SrF_2 may be able to operate at even higher flux levels than KCl. The advantage of the alkali halides and alkaline earth fluorides lies not so much in the low absorption of these materials, but in the magnitude of their negative dn/dT values, which cause a pole to occur at some wavelengths. The predicted distortion threshold near this pole can depend strongly on the assumptions made in the calculations. The most extreme example is CaF_2. If the Poisson ratio correction $(1 + \nu)$ in eq. (32) is neglected, the calculated pulsed energy density threshold increases by over two orders of magnitude at 5.25 μm. For SrF_2 the threshold decreases by a factor of 1.6 if $(1 + \nu)$ is neglected and for KCl by less than a factor of 1.2. The uncertainty in the optical constants of the material and the contribution from the strain birefringence term ϕ, which has been neglected in these calculations make the calculated threshold values near the pole very questionable. For the alkaline earths strain birefringence, which may cause slewing as well as defocusing [30], is probably comparable in the region of the pole to the sum of the other terms [31]. The alkaline earths are more sensitive to mechanically and thermally induced strain birefringence than is KCl, which is more sensitive than ZnSe. An analysis of thermally induced strain birefringence has been given by Flannery and Marburger [32] and more recently by Loomis and Bernal G. [33], but it is difficult to calculate the magnitude of ϕ accurately using present theory.

Fracture may limit the energy density which the window can withstand even though the optical distortion is acceptable. An approximate value for the energy density at which pressed polycrystalline KCl 2-cm thick and having a breaking strength of 4000 psi would be expected to fracture [34] is indicated by the dashed line in figure 3. In practice the fracture level would depend strongly on the beam profile, diameter and thickness of the window and the differential pressure which it must withstand.

Fracture resulting from laser induced damage to the window becomes increasingly important as the pulse length decreases, particularly for pulse lengths shorter than a microsecond. If the energy density per pulse is to remain constant, the beam intensity must increase as the pulse length decreases. The limiting damage mechanism for very pure single crystal or amorphous window materials is thought to be dielectric breakdown, which depends on the local electric field strength at optical frequencies and hence on the beam intensity rather than the energy density. The maximum field strength occurs at the exit surface of the window [35,36] and in the case of the best etched KCl, damage there occurs [37,38]

at a beam intensity in excess of 8 GW/cm^2 at a pulse length of 100 ns. For polished samples the surface damage threshold is between [38] one and two GW/cm^2. At longer pulse lengths damage would be expected at this same beam intensity, but at significantly shorter pulse lengths the incomplete data available suggests that it may increase inversely as the fourth root of the pulse length [13,39]. Extrinsic effects such as impurities, surface absorption and probably lattice irregularities can decrease the threshold values by an order of magnitude or more [38]. In the example shown in figure 3 the limiting energy density for KCl is $\sim 10^3$ J/cm^2; we may conclude that for submicrosecond pulse lengths the threshold for catastrophic damage to the KCl window, rather than that for thermal distortion, determines the maximum energy density which an actual KCl window may transmit. A similar argument can be made for the other window materials. Surface damage thresholds of 5 to 70 MW/cm^2 have been reported [40, 41] for ZnSe at 10.6 μm. For CaF_2 and SrF_2 at 3.8 μm the surface damage thresholds are lower than that of KCl by a factor of two or three [42].

Comparison of Mirror Materials

The limiting energy density for mirrors may be determined from eq. (31) if equal density per mirror is assumed. Results for a 10-component system are shown in figure 4 for silicon carbide, molybdenum, copper, and aluminum mirror substrates with a 0.998 reflection coating and a diameter to thickness ratio of three. Material parameters used in calculating data shown in figures 4-7 are given in table 2.

Table 2. Material parameters for mirror materials used to calculate figures 4-7 as referenced in text. Symbols are λ wavelength, R reflectance, ρ density, c_p heat capacity, α linear expansion coefficient, K thermal conductivity and $T_{melting}$ the melting temperature of the material. The values of R are optimum values measured at Michelson Laboratories on various samples.

	Optical Parameters			Non-Optical Parameters				
Material	λ(μm)	R	R_{coated}	$\rho(g/cm^3)$	$c_p(J/gm°K)$	α	K(W/cm/°K)	$T_{melting}(°K)$
Mo	10.6	0.9814	0.998	9.01	0.2477	5.0×10^{-6}	1.4	2890
	8	0.9792	0.998	---	---	---	---	---
	5.25	0.9754	0.998	---	---	---	---	---
	3.8	0.972	0.998	---	---	---	---	---
Cu	10.6	0.9919	0.998	8.993	0.3851	16.8×10^{-6}	4.0	1356.5
Al	10.6	0.9814	0.998	2.70	0.9024	23.2×10^{-6}	2.38	933.2
SiC	10.6	0.85	0.998	3.2	0.75	4.3×10^{-6}	1.8	2000

Coatings are often the limiting parameter, but if these are adequate silicon carbide would be predicted to handle the maximum energy. Molybdenum is slightly (20%) lower. It can handle over twice the energy density of copper, which itself can handle nearly twice the energy density of aluminum. An eighth wave optical figure in the visible is assumed for each substrate material. A perfect figure would result in less than a 3% improvement over the eighth wave mirror in energy density at 10 μm. However, at 3.8 μm the eighth wave mirror decreases the allowable energy density by nearly 20% as compared to a mirror with a perfect figure. The shorter wavelength also reduces the allowable thermal distortion the mirror can have and hence its energy handling capability. In the example given the allowable energy density at a wavelength of 3.8 μm is less than one-third that at 10.6 μm. In figure 5 the energy density threshold of well polished molybdenum mirrors having various initial figure errors is compared to the theoretical performance of a hypothetical molybdenum mirror with no figure error coated with a very high reflectance coating. The importance of a high reflectance is evident. The reflectance is often strongly influenced by the polishing technique used; polished molybdenum mirrors with twice the absorption assumed here for the uncoated mirror are not uncommon. The distortion threshold for these mirrors would be lower than that shown in figure 5 by a factor of two.

The increasing importance of a good optical figure with decreasing wavelength is also illustrated in figure 5. At 10.6 μm there is relatively little difference between the energy density threshold for a perfectly figured mirror and one with eighth and quarter-wave figure errors. However, as the wavelength decreases these differences become pronounced and at 3.8 μm the Maréchal criterion cannot be met at any energy density if the figure error is as large as a quarter-wave.

The effectiveness of substrate cooling between pulses and hence the allowable energy densities for multipulse operation are influenced by substrate conductivity and thickness. However, the energy density threshold for a single pulse is not a function of the thermal conductivity of the mirror until pulse lengths approach the tenth microsecond range and the threshold is determined by catastrophic damage to the mirror rather than by optical distortion. The maximum energy density which the mirror can pass without being damaged can be obtained from eq. (23) by letting z = 0, giving

$$I_o t = \frac{(\pi K \rho c_p)^{1/2}(T_m - T_o)t^{1/2}}{2(1 - R)} \qquad (33)$$

where T_o is the initial temperature of the mirror and T_m its melting temperature. The heat of fusion does not appear in eq. (33) since the heat taken up by melting depends on the mass of material melted, which at threshold is very small [43]. As before we are assuming that temporally the pulse is flat-topped and of duration t. More complicated pulse shapes would require that the pulse intensity be integrated over its duration.

For a pulse length of 100 ns the catastrophic damage threshold for a diamond turned copper mirror would be calculated from figure 6 to be about 110 J/cm^2. Flux densities of optical beams are often averaged spatially over the beam diameter so care must be taken to use peak values rather than average values when computing thresholds using eq. (33). For a Gaussian spatial beam profile the peak energy density is twice the average energy density over the $1/e^2$ diameter of the beam, the quantity usually specified as the beam energy density. For example, the catastrophic damage threshold for a diamond turned copper mirror in terms of conventional beam densities for a Gaussian beam profile would then be about 55 J/cm^2, a value in good agreement with experimental results for diamond turned copper mirrors. Results of several other threshold studies of laser damage in metals [43] are also in reasonable agreement with eq. (33).

Figure 6 gives a comparison of threshold values [44] for uncoated and coated copper mirrors prepared using various surface finishing techniques with the theoretical value predicted by eq. (33). The experimental values are a factor of two higher than those initially reported by Soileau and Wang because of a calibration error which was discovered after the paper was published [42]. Several points should be emphasized. First the maximum experimentally measured threshold value for an uncoated copper sample is within 6% of the theoretical value. Second, if a different preparation technique is used, damage can occur at one-fourth the theoretical threshold level. Finally, the coated copper substrates tested had a lower damage threshold than the best uncoated samples even though the absorption of the coated samples was lower than that of the uncoated samples by about a factor of two. The best sputtered coating was higher than the best evaporated coating, possibly because of improved adhesion in the sputtered film. Significant gains in damage threshold resulting from improved coating techniques may thus be possible.

Figure 7 shows the calculated threshold values of peak energy density for uncoated Cu, Mo, and Al mirrors in a 10-component system at a wavelength of 10.6 μm as a function of pulse length. Eighth wave optical figures are assumed for each mirror and reflectances are assumed to be 0.9918 for copper (achievable for good diamond turned surfaces), 0.9814 for aluminum, and 0.9814 for mechanically polished molybdenum. At pulse lengths longer than 10 to 40 ns the threshold value is determined by optical distortion and is over four times as high for molybdenum and copper as it is for aluminum mirrors. For shorter pulse lengths it is determined by the catastrophic damage threshold for the mirrors. Copper would be expected to be a better choice than molybdenum in this region since its higher thermal conductivity and higher reflectance make its damage threshold higher than that of molybdenum by nearly a factor of four.

Conclusion

In multicomponent optical trains handling intense beams of light the limiting parameter is frequently the optical figure. Both thermal distortion, initial figure error, and optical homogeneity must be considered. If there are many components in the optical train, initial figure error tolerances are typically a fraction of a visible wavelength even for optical trains used at infrared wavelengths. For materials with low indices of refraction such as the alkali halides and alkaline earth fluorides, tolerances can be significantly lower than for mirrors and high index window materials such as ZnSe. Although the initial figure errors and homogeneity errors are usually uncorrelated with each other and with thermal distortion, figure errors caused by thermal distortion typically are correlated. The allowed thermal distortion tolerances are thus lower than if the thermally induced figure errors were uncorrelated. An exception is when they are of opposite sign, as is the case when mirrors are used with windows such as ZnSe which have positive values of dn/dT. On the other hand, window materials with negative dn/dT can develop resonances in some wavelength regions which should practically eliminate their contribution to thermal distortion.

Calculations suggest that selected window materials can handle much higher single pulse energy densities than can mirrors. On the other hand, metal mirrors are much easier to cool than are windows, an important consideration for multiple pulsed operation. To satisfy the Maréchal criterion in a multicomponent system used in the 3-5 μm wavelength region, optical figures for mirrors may have to be as good as an eighth wave in the visible. In the ten μm wavelength region tolerances can be relaxed significantly. Coated molybdenum is clearly the best choice of the mirror materials considered here for use for pulse lengths in the microsecond range or longer. Uncoated molybdenum or copper will have a significantly lower pulsed energy density threshold than coated samples provided the catastrophic damage threshold of the coating is high enough to avoid limiting mirror operation. Uncoated mirrors are probably the best choice at shorter pulse lengths where catastrophic damage becomes important. At these pulse lengths copper mirrors should perform better than mirrors of molybdenum or aluminum.

Acknowledgments

The author would like to thank Dr. Jean M. Bennett, W. R. Compton, R. G. Purcell and Dr. J. B. Patton of Michelson Laboratory, NWC; Dr. T. G. Bergman, presently at the Navy High Energy Laser Office, Washington, D. C; and Major J. L. Stapp and Lt. Col. R. F. Prater of the Air Force Weapons Laboratory, Albuquerque, New Mexico, for helpful discussions.

References

[1] Sparks, M., J. Appl. Phys. 42, 5029 (1971); Sparks, M. and Chow, H. C., J. Appl. Phys. 45, 1510 (1974).

[2] Conrady, A. E., *Applied Optics and Optical Design* (Dover Publications, Inc., New York, 1960), pp. 139-141 and 627.

[3] Born, M. and Wolf, E., *Principles of Optics*, 1st ed. (Pergamon Press, New York, 1959), p. 468.

[4] Loomis, J., in *Proceedings of Fourth Annual Conference on Infrared Laser Window Materials, 1974*. C. R. Andrews and C. L. Strecker, eds. (Defense Advanced Research Projects Agency, Arlington, Va., 1975), pp. 281-297.

[5] Lowenthal, D. D., Appl. Opt. 13, 2126 (1974).

[6] Winsor, H. V., in *Proceedings of Third Conference on High Power Infrared Laser Window Materials, 1973*. C. A. Pitha and B. Bendow, eds. (AFCRL-TR-74-0085, Special Report 174, 1974), pp. 1069-1082.

[7] Bennett, H. E. and P. C. Archibald, in *Laser Induced Damage in Optical Materials: 1974*, A. J. Glass and A. H. Guenther, eds. (NBS Spec. Publ. 414, 1974), pp. 23-29.

[8] Dueweke, P. W., Kester, J. M., McBroom, R. J., and Preonas, D. D., in *Proceedings of Fourth Annual Conference on Infrared Laser Window Materials*, op. cit., pp. 789-802.

[9] Boley, B. A. and Weiner, J. H., *Theory of Thermal Stresses* (John Wiley and Sons, Inc., New York, 1960), p. 290.

[10] ibid, p. 402.

[11] Carslaw, H. S. and Jaeger, J. C., *Conduction of Heat in Solids* (Oxford University Press, London, 1959), p. 75.

[12] Timoshenko, S. and Woinowsky-Krieger, S., *Theory of Plates and Shells*, 2nd ed. (McGraw-Hill Book Co., New York, 1959), p. 43.

[13] House, R. A., Bettis, J. R., Guenther, A. H. and Austin, R., *Laser Induced Damage in Optical Materials: 1975*, A. J. Glass and A. H. Guenther, eds. (NBS Spec. Publ. 435, 1976), pp. 305-319.

[14] Austin, R. R., in *Proceedings of Fourth Annual Conference on Laser Window Materials*, op. cit., pp. 97-98.

[15] Braunstein, M. and Rudisill, J. E., op. cit., pp. 23-39.

[16] Soileau, M. J., Bennett, H. E., Bethke, J. W., and Shaffer, J., in *Laser Induced Damage in Optical Materials: 1975*, op. cit., pp. 20-28.

[17] Shaffer, J. J., Martin, E. C., Soileau, M. J., and Bennett, H. E., in *High Energy Laser Mirrors and Windows* (Semi-Annual Report No. 4, ARPA Order 2175, Naval Weapons Center, March 1974), pp. 103-110.

[18] Hass, M., Davisson, J. W., Rosenstock, H. B., and Babiskin, J., in *Proceedings of Fourth Annual Conference on Laser Window Materials*, op. cit., pp. 231-239.

[19] Hass, M., Davisson, J. W., Klein, P. H., and Boyer, L. L., J. Appl. Phys. 45, 3959 (1974).

[20] Deutsch, T. F., Appl. Phys. Letters 25, 109 (1974).

[21] Stierwalt, D. L. and Hass, M., in *Proceedings of the Fourth Annual Conference on Laser Window Materials*, op. cit., pp. 8-11.

[22] Duthler, C. J. and Sparks, M., in *Laser Induced Damage in Optical Materials: 1974*, op. cit., pp. 219-226.

[23] Deutsch, T. F., in *Proceedings of Third Conference on High Power Infrared Laser Window Materials*, op. cit., pp. 13-29; P. Kraatz and P. J. Mendoza, *Proceedings of Fourth Annual Conference on Infrared Laser Window Materials*, op. cit., pp. 213-230.

[24] Newberg, R. and Pappis, J., in *Proceedings of Fifth Annual Conference on Infrared Laser Window Materials: 1975*, C. R. Andrews and C. L. Strecker, eds. (Defense Advanced Research Projects Agency, Arlington, Va., 1976), pp. 1065-1078.

[25] Larkin, J., Klausutis, N., Hilton, R. and Adamski, J., in *Proceedings of Fifth Annual Conference on Infrared Laser Window Materials*, op. cit., pp. 1079-1085.

[26] Harrington, J. A., Gregory, D. A. and Otto, W. F., in *Proceedings of Fifth Annual Conference on Infrared Laser Window Materials*, op cit., pp. 871-886.

[27] Miles, P., in *Proceedings of Fifth Annual Conference on Infrared Laser Window Materials*, op. cit., pp. 7-15.

[28] Dickinson, S. K., "Infrared Laser Window Materials Property Data for ZnSe, KCl, NaCl, CaF_2, SrF_2, BaF_2." Air Force Cambridge Research Laboratories AFCRL-TR-75-0318, Physical Sciences Research Papers, No. 635 (1975); C. S. Sahagian and C. A. Pitha, "Compendium on High Power Infrared Laser Window Materials." Air Force Cambridge Research Laboratories AFCRL-72-0170, Special Reports, No. 135 (1972).

[29] Hass, M., in *Proceedings of Fifth Annual Conference on Infrared Laser Window Materials*, op. cit., pp. 849-858.

[30] Skolnik, L. H., Bendow, B., and Gianino, P. D., in *Proceedings of Third Conference on High Power Infrared Laser Window Materials*, op. cit., pp. 967-1009.

[31] Miles, P., Raytheon Corporation (private communication).

[32] Flannery, M. and Marburger, J., in *Laser Induced Damage in Optical Materials: 1974*, op. cit., pp. 31-38.

[33] Loomis, J. S. and Bernal G., E., in *Laser Induced Damage in Optical Materials: 1975*, op. cit., pp. 126-141.

[34] Sparks, M. and Duthler, C. J., J. Appl. Phys. 44, 3038 (1973).

[35] Crisp, M. D., Boling, N. L., and Dubé, G., Appl. Phys. Letters 21, 364 (1972); Crisp, M. D., in *Laser Induced Damage in Optical Materials: 1973*, op. cit., pp. 80-83.

[36] Boling, N. L., Dubé, G., and Crisp, M. D., in *Laser Induced Damage in Optical Materials: 1973*, op. cit., pp. 69-79.

[37] Braunstein, M., in *Proceedings of Third Conference on High Power Infrared Laser Window Materials*, op. cit., pp. 863-890.

[38] Soileau, M. J., Bennett, H. E., Porteus, J. O., Temple, P. A., and Bass, M., in *Proceedings of Fifth Annual Conference on Infrared Laser Window Materials*, op. cit., pp. 391-417.

[39] Sparks, M., in *Laser Induced Damage in Optical Materials: 1975*, op. cit., pp. 331-345.

[40] Wang, V., Rudisill, J. E., Giuliano, C. R., Braunstein, M., and Braunstein, A., in *Laser Induced Damage in Optical Materials: 1974*, op. cit., pp. 59-65.

[41] Shatas, R. A., Smith, J. L., Tanton, G. A., and Meyer, H. C., in *Proceedings of Fourth Annual Conference on Infrared Laser Window Materials*, op. cit., pp. 53-62.

[42] Leung, K. M., Tang, C. C., Bass, M., and Soileau, M. J., "Damage Resistant Optical Components for 2-5 μm Laser Systems," this conference.

[43] Sparks, M., J. Appl. Phys. 47, 837 (1976).

[44] Soileau, M. J. and Wang, V., Appl. Opt. 13, 1286 (1974).

Figures

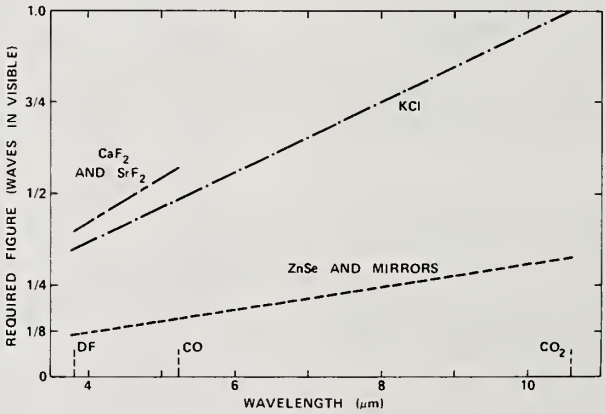

Figure 1. Initial optical figure required for each component in a ten component optical train when the thermal contribution to wave front distortion is twice the contribution from the initial figure error and the Mare'chal criterion is met.

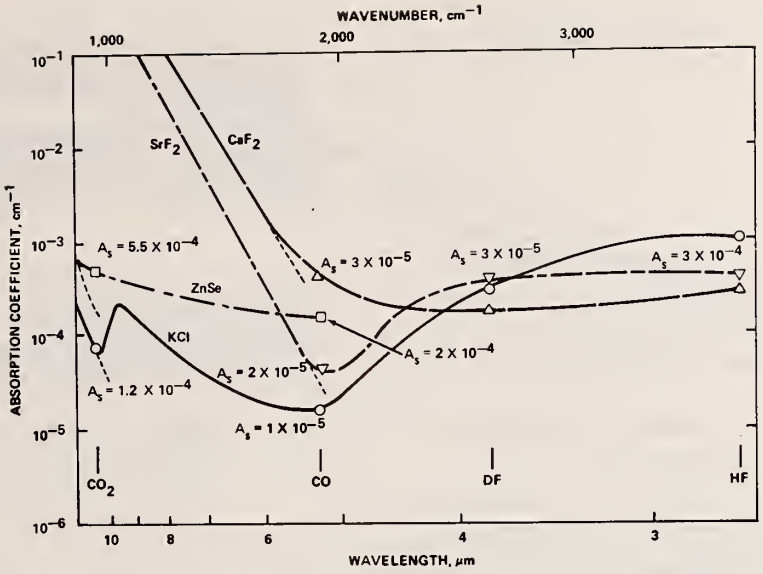

Figure 2. Best reported surface and bulk absorption values for various laser window materials. The circles, squares, and triangles are bulk absorption values and the numerical values of A_s are surface absorption values. Values of A_s at DF and HF wavelengths are for SrF_2. All values for ZnSe were reported by M'les [23].

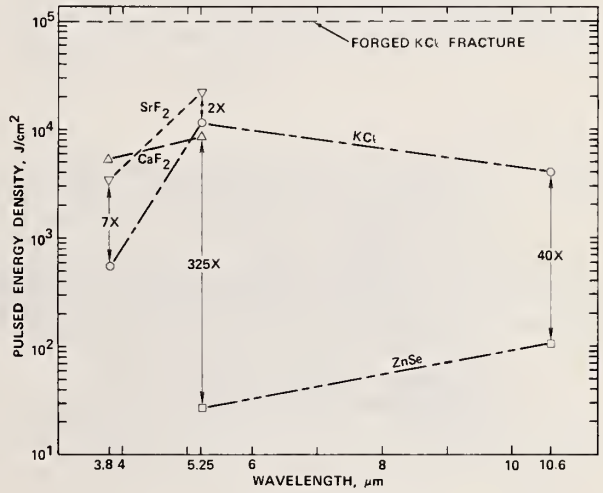

Figure 3. Calculated distortion threshold for a 2-cm thick window of CaF_2, SrF_2, KCl, and ZnSe as one component of a ten component optical train. Assumptions are an equal energy density budget per component and an initial figure error of a quarter-wave in the visible, and a resultant wave front distortion which does not violate the Mare'chal criterion.

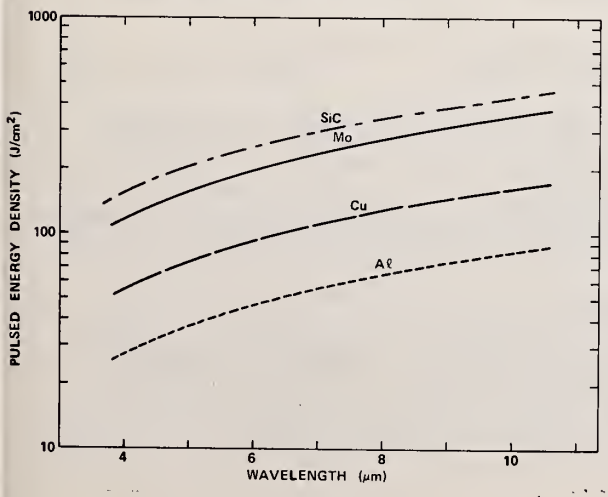

Figure 4. Calculated distortion thresholds for SiC, Mo, Cu, and Al mirrors with a 0.998 reflectance coating in a ten component optical system. Assumptions are an equal energy density budget per component, an initial figure error of an eighth-wave in the visible, and a resultant wave front distortion which does not violate the Mare'chal criterion.

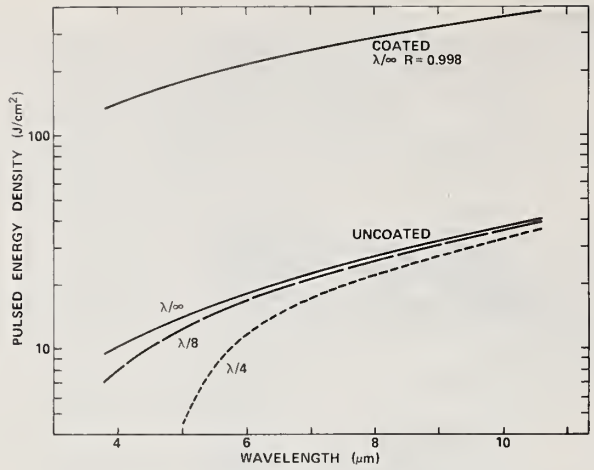

Figure 5. Calculated distortion threshold for polished molybdenum mirrors having various initial figure errors compared to the theoretical performance of a hypothetical molybdenum mirror with no figure error and coated with a 0.998 reflectance coating. Results are for a ten-component system, equal error budget per component, and a resultant wave front distortion which does not violate the Mare'chal criterion.

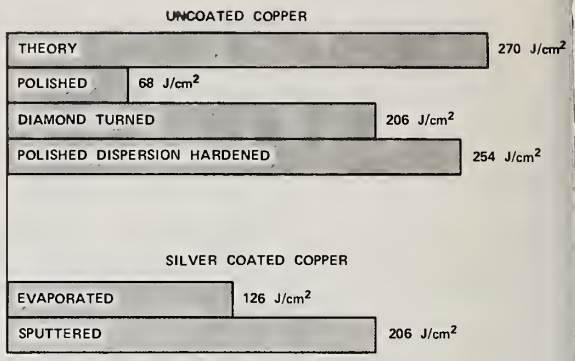

Figure 6. Damage threshold of copper for 10.6 μm radiation, 600 ns pulse length. The theoretical value was calculated from eq. (33), the experimental results are taken from [44].

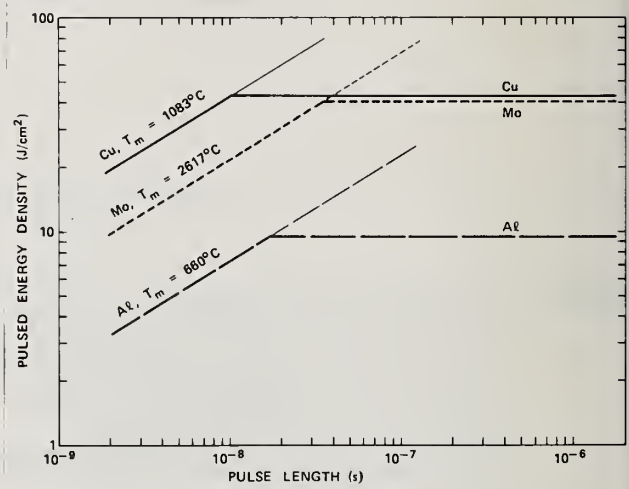

Figure 7. Calculated threshold values of peak energy density for uncoated Cu, Mo, and Al mirrors in a ten-component system at a wavelength of 10.6 μm as a function of pulse length. Eighth-wave optical figures are assumed. At pulse lengths longer than 10 to 40 ns the threshold value is determined by optical distortion as in previous figures. At shorter pulse lengths it is determined by the catastrophic damage threshold for the mirrors.

COMMENTS ON PAPER BY BENNETT

The analysis presented here is admittedly pessimistic. In a specific system, it is generally possible to improve the performance above the levels indicated by this analysis, by use of refocusing, adaptive optical correction, and other specific measures. Also, in the treatment of thermal distortion of mirrors, heat conduction into the mirror was neglected, while for pulses longer than 10 ms, conduction cooling can be an important factor. The goal here was to obtain an analytic tool, capable of providing a basis for choice among different materials for use in mirrors or windows, and for estimating safe levels of operation.

A great deal of interest was expressed in the use of SiC as a mirror substrate material. The speaker indicated that SiC samples tested at the Michelson Laboratories were among the best mirror surfaces they had ever seen, with rms surface roughness of about 5 Å. The material was prepared by Dr. Choyke at the Central Research Laboratories of Westinghouse. It is machinable in the uncured form, and thus is prepared to an approximate figure. It is then cured, and a surface of SiC is deposited on it by chemical vapor deposition. The final surface is then polished to the desired figure. The potential for extending this approach to the fabrication of large mirrors appears to be straightforward.

1.2 ELECTRIC FIELDS AND POWER DISSIPATION IN WINDOWS AT OBLIQUE INCIDENCE

Joseph H. Apfel
Optical Coating Laboratory, Inc.
Santa Rosa, California 95402

Formulas are provided for calculating the strength of the electric fields and the power dissipation due to weak absorption in a window illuminated by a collimated beam at non-normal incidence. For a glass window the power dissipation per unit volume varies approximately as the cosine of the incident angle.

Key words: Electric fields; laser damage; oblique incidence; standing waves

Introduction

The power of a collimated beam of radiation which is intercepted by a flat sample surface varies as the cosine of the incident angle. One intuitively expects, therefore, that the electric field and the volumetric power dissipation in the window due to weak absorption will vary similarly. Exact formulas are derived and shown to predict the angular dependence which is only slightly different from cosine θ_0.

Theory

A collimated plane polarized monochromatic beam of intensity M_0 measured in W/cm^2 propagating in a non-absorbing media of index n_0 is composed of sinusoidally varying electric and magnetic fields. The peak amplitude of the electric field measured in V/cm and the intensity are related by the formula

$$M_0 = .0013\, n_0 E_0^2 \tag{1}$$

and the time average square of the electric field strength is

$$\overline{E_0^2} = \tfrac{1}{2} E_0^2. \tag{2}$$

If a sample of surface area A is placed within the beam so that its normal makes an angle θ_0 with the beam axis, the total power intercepted by the sample is $M_0 A \cos\theta_0$ (watts). This energy will be reflected or transmitted through the sample (assuming no absorption).

Assuming there is no reflection from the second surface of the sample, the electric field within the sample of index n is given by [1][1]

$$n\,\overline{E^2}\cos\theta = T\; n_0\,\overline{E_0^2}\cos\theta_0 \tag{3}$$

where T is the conventional transmittance of the surface and θ is the propagation angle in the sample.

If there is absorption within the sample the volumetric power dissipation is

$$P = C\, n\, \alpha\, \overline{E^2}\ \ (W/cm^3), \tag{4}$$

where C = .0027 for field strength in units of V/cm, and $\alpha = 4\pi k/\lambda$ is the absorption coefficient (cm^{-1}). Assuming that the absorption is very weak, the attenuation of the electric field within the sample can be ignored. Combining all the

1. Figures in brackets indicate the literature references at the end of this paper.

numbered equations above, we have

$$\frac{P}{M_0} = \alpha \frac{n}{n_0} \frac{\overline{E^2}}{\overline{E_0^2}} = \alpha T \frac{\cos\theta_0}{\cos\theta} \tag{5}$$

which describes the volumetric power dissipation as a function of incidence angle. Equation (5) merely states that power dissipation is proportional to the local intensity.

The transmittance T of a single interface is given by

$$T = \frac{4nn_0}{(n_0 + n)^2} \tag{6}$$

where the indices must be replaced by effective indices at non-normal incidence. Combining (6) with Snell's Law we have, for the two polarizations with $n_0 = 1.0$

$$T_p \frac{\cos\theta_0}{\cos\theta} = \frac{4n^3\cos^2\theta_0}{\left[n^2\cos\theta_0 + \sqrt{n^2 - \sin^2\theta_0}\right]^2}$$

$$T_s \frac{\cos\theta_0}{\cos\theta} = \frac{4n\cos^2\theta_0}{\left[\cos\theta_0 + \sqrt{n^2 - \sin^2\theta_0}\right]^2} \tag{7}$$

which, from equation (5) are seen to equal the ratio of beam intensities within and incident on the sample.

Numerical example

Figures 1 and 2 are profiles of the time average square of the electric field along the normal to a glass (n = 1.51) surface as a function of incidence angle for and *s* polarizations. From equation (5) we expect the volumetric power dissipation within the glass due to weak absorption to vary as the height of the field profiles in the glass multiplied by the index ratio (1.51).

Figure 3 is a graph of formulas (7) for n = 1.51 and $n_0 = 1.0$ which shows how nearly the volumetric power dissipation follows a cosine dependence (broken curve).

Conclusion

The electric field strength and the intensity of a refracted beam in a transparent medium vary with incidence angle according to stated formulas. For glass windows the angular dependence can be approximated by the cosine θ_0 curve.

Reference

[1] J.H. Apfel, "Electric Fields in Multilayers at Oblique Incidence," to be published in Applied Optics, October 1976.

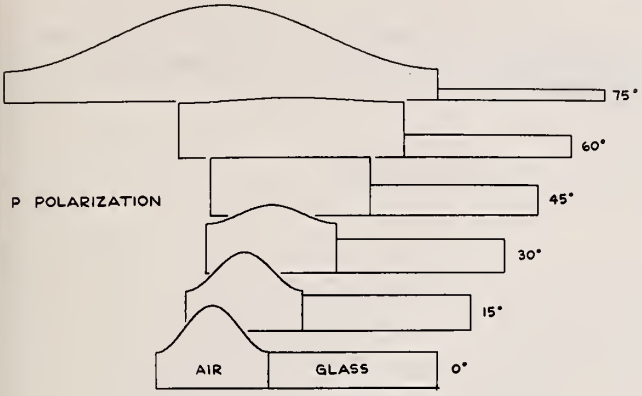

Figure 1. Time averaged square of the electric field strength for p radiation incident from the left on a surface of glass (n = 1.51). The abscissa is metric distance along a normal to the surface.

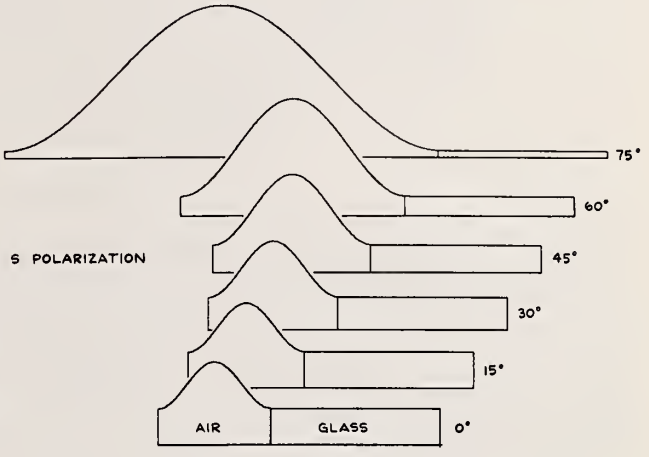

Figure 2. Same as figure 1 for s polarized radiation.

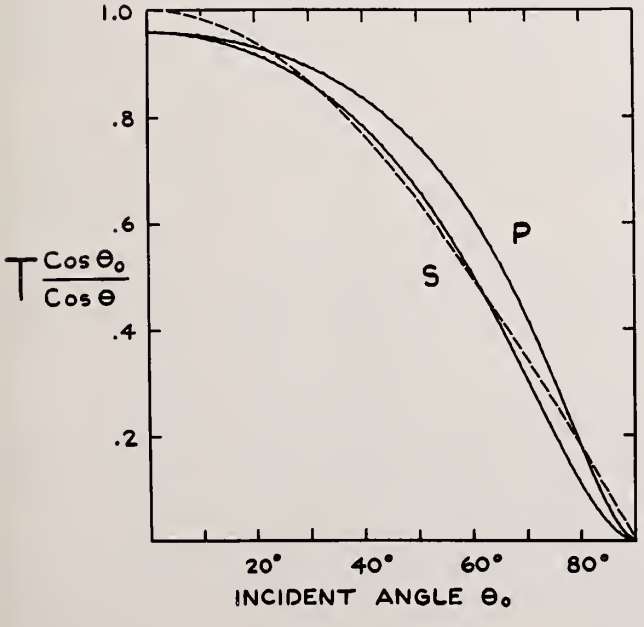

Figure 3. Angular dependence of the volumetric power dissipation for p and s radiation compared with cosine θ_0 (broken curve).

COMMENTS ON PAPER BY APFEL

It was pointed out that the angular dependence of the damage threshold, as discussed in this paper, may be of consequence in the analysis of surface damage experiments using short focal length lenses, where a variety of effective angles of incidence are present.

1.3 ANALYSIS OF LASER-INDUCED THERMAL STRESSES IN LASER WINDOWS

Roger E. Rondeau
Air Force Materials Laboratory
Wright-Patterson AFB, Ohio 45433
and
Dale Ford
University of Dayton Research Institute
Dayton, Ohio 45469

Laser induced damage in the ZnSe output coupler of a 15 kilowatt cw CO_2 coaxial electric discharge laser has been investigated. An analytical technique has been developed for predicting thermal stresses from in depth absorption of laser energy in laser window materials. A two-dimensional transient heat transfer code, APPLE, (Aerotherm Prediction Procedure for Laser Effects) was used to obtain the temperature histories of the irradiated window. The effect of window thickness, transmitted power level, absorptance and exposure time were investigated. The stress distribution in the circular disk was computed from radial and axial temperature distributions obtained from the APPLE code. This analytical technique has been used to determine maximum power levels and exposure times to prevent window damage in laser experiments.

Key words: Computer analysis; laser induced stresses; stress analysis; thermal analysis; zinc selenide window.

1. Introduction

In the fall of 1975, the Air Force Materials Laboratory realized its goal of constructing a 10 kilowatt laser facility capable of producing a uniform intensity beam. With consultant support from the Air Force Weapons Laboratory, the "flat-top" device was modeled after the AFWL Electric Discharge Coaxial Laser (EDCL) system which has recently been described [1][1]. Both of the above systems are continuous wave carbon dioxide lasers which emit a circular, uniform, temporally stable, and easily characterized beam. Both systems are equipped with a zinc selenide output coupler - a solid, transparent window at the muzzle of the laser. To maintain the inherently high power capacity of these optimized gas laser systems and to insure a high quality output beam the window must not only be transparent at 10.6 μm, but must absorb very little energy at the thin film coatings. Excessive absorption of radiant energy within the window leads to degraded beam quality, optics misalignment, and if the absorption is high enough, to catastrophic thermally-induced fracture. For these reasons, considerable time and effort have gone into the development of laser window materials [2,3]. Thus far, zinc selenide fabricated by chemical vapor deposition has emerged as one of the leading materials for this application and is used as the output coupler in both of the above laser devices.

On the 25th of March 1976, an AFML output coupler developed cracks and failed. Although the cause of the failure is not known for sure, we believe moisture attacked the multilayered thin film coatings of thorium tetrafluoride on zinc selenide causing an increase in absorption and introducing temperature gradients. The resultant, nonuniform temperature distribution produces stresses which, if large enough, can lead to mechanical failure of the window.

Replacement windows have recently been obtained, which from witness plate measurements, exhibit total absorptances of less than 0.8% [4,5]. These new windows are also much thicker than the old ones. The use of analytical techniques for computing in depth temperature profiles and stress distributions in both the old and new laser windows is the subject of this paper.

This study was undertaken in order to find answers to the following questions: How hot did the old window get and how large were the induced stresses? How much heat and stress are generated in the new window? How long a cool-down time is required between shots? What is the effect of thickness on window performance? Assuming that with time, some degradation will occur within the window, how much of an increase in total absorptance can be tolerated before the fracture limit of the window is reached?

The answers to these questions will not only shed light on revealing a failure mechanism for the old window, but also provide valuable information that can be used to prevent recurrence of window failure. Moreover, parametric analyses can be used to project approaching damage levels and to monitor window performance.

1. Figures in brackets indicate the literature references at the end of this paper.

2. Analytical Approach

The codes used in this analysis are shown in figure 1. The coupled codes, ACE and ASTHMA, are part of a family of codes called APPLE (Aerotherm's Prediction Procedure for Laser Effects), which treats the transient response of a solid subjected to radiative and convective environments [6]. APPLE evolved from a DoD-sponsored program for developing a unified analysis of laser-heated metals and nonmetals. The procedure is based on well-verified aerospace codes originally written for reeetry ablation studies and extensively modified for radiant heating at flux levels of current laser sources. Some other features and capabilities of the APPLE codes include: arbitrary axisymmetric incident radiant flux; one- or two-dimensional solid heat conduction; temperature dependent thermophysical properties; in-depth charring and pyrolysis; multilayer, multimaterial capability; coupling to aerodynamic environment; and in-depth absorption of radiant energy. This last feature is based on a linear absorption coefficient and has been included in the ASTHMA code (Axi-Symmetric Transient Heating and Material Ablation). Different absorption coefficients can be used at different depths extending the computational capability to multilayered, partially transparent materials.

The ACE code (Aerotherm Chemical Equilibrium) is a general thermochemistry code which performs a set of calculations of surface mass balances to determine a parametric relationship between surface temperature, pressure and other information needed to perform an energy balance on the surface. Thus ACE output is in the form of a series of tables which include all the surface mass transfer and chemical relationships. Computation of surface temperatures requires the ASTHMA solution of the surface energy balance. For transient heating response, the surface energy balance is intimately coupled to the in-depth material response and is solved simultaneously with the in-depth code. Besides providing ablation, recession, and surface energy flux data, ASTHMA also furnishes the data needed for the thermal analysis; that is, surface and nodal temperatures as a function of time and position.

The next step in the analysis requires using the output from ASTHMA as input for DISC [7]. DISC treats axisymmetric heating of thin plates and computes the stress distribution in a circular disk exposed to a radial and axial temperature distribution. Using plane stresses and the assumption that radial temperature gradients are much greater than the axial gradients, the code computes radial and axial displacements as well as radial and circumferential stresses as a function of distance from the center.

3. Analytical Modeling

The model used in the analysis is shown in figure 2. A flat-top beam with 8.9 cm diameter enters the 11.4 cm wide window from the cavity side where, for the new window, 71% of the energy is reflected. Since the window is wider than the beam, two radiation tables were needed, one having zero flux for the surface of the window outside the beam. Three absorption coefficients were used: for the reflective coating, the bulk material and the anti-reflective coating at the exit face. The old (fractured) window absorption coefficients used were front to back: 5.239, .0075, and .295 cm^{-1} while the respective new window values were .012, .0026, and .088 cm^{-1} [8]. Although model thicknesses of 0.0254 cm were held constant for the two surfaces, the overall window thickness was varied systematically. Other parameters varied include the transmitted power (5-15 kilowatts) radiation time (0-20 seconds) and total absorptance (0.5%). Window thickness was changed from 0.635 to 2.1 cm in six steps. It should be noted that using more realistically thin surface nodes did not change the computed surface temperatures and served only to drastically increase the computational time.

The first step in the analysis involves a closed system, mass balance calculation of the laser gas mixture of 13.5% nitrogen, 4.5% carbon dioxide and 82% helium (by volume) on the cavity side of the window. This solution was obtained from the ACE code. ACE also computed the cavity wall enthalpies for surface temperatures ranging from 25° to 800°C and generated input tables for ASTHMA which relate the surface temperatures to the rate of energy conduction into the material. Free convection heat transfer coefficients were calculated for the cavity and output sides from Kreith [9]. The ASTHMA option used in this analysis couples the film coefficient boundary condition to the in-depth solution.

For specifying sample geometry, a 7X13 nodal scheme was drawn, sectioning one half of the axisymmetric flat plate. Thin nodes were used at the front and rear of the window for better thermal definition at the surfaces. For the same reason, narrow nodes were employed at the beam edge where the temperature gradients were expected to be large. The nodal temperatures generated by ASTHMA were used as input data for the DISC code. However, since the latter code calls for a 3X6 nodal temperature grid, six temperatures were taken from each of the first, fourth, and seventh row of nodes. In addition to the temperature input, the mechanical properties of CVD (chemical vapor deposition) zinc selenide were taken from [2] for use in the stress analysis code.

4. Results

The maximum temperature rise computed by ASTHMA for the damaged coupler is plotted as a function of time for three transmitted power levels in figure 3. In operating the laser facility, the majority of tests are in the 5 to 10 kW power level range for 5 to 10 seconds. The shaded area covers this range and shows a temperature rise in the window of approximately 40° to 150° C.

Figure 4 illustrates the nodal network and the temperature distribution across the window at the 10 kilowatt, 10 second point of figure 3. The thermal profile was obtained by writing the 91 (7X13) nodal temperatures into their respective nodes and connecting isothermal points. Near the center of the beam, the axial temperature gradient is approximately 80°C. Radiating out from the center toward the edge, the temperature drops 155° with most of the drop occurring near the edge of the beam. This thermal gradient at the window surface is shown in figure 5.

A stress analysis was first performed on the damaged coupler using 18 of the temperature points from figure 4. For each DISC run, stresses and displacements were computed for 50 locations in the window: 10 radial points on each of 5 axial planes. Radial stresses were compressive and relatively small. On the other hand, the tangential stresses were compressive only near the center and became increasingly tensile toward the edge of the window, reaching a maximum near the edge of the beam. Maximum stresses were computed at the surface plane, Z=O, where the greatest thermal load is imposed. Thus, in order to obtain only the largest induced stresses, the analyses were performed only for the thin plane section at the surface with no axial gradients specified. Radial stresses at the outer radial boundary were also assumed to be zero. The effect of these assumptions and simplifications will be evaluated with a much more sophisticated analysis procedure called DOASIS, a computer code for the Deformation plastic, Orthotropic, Axisymmetric (and plane) Solution of Inelastic Solids [10].

As noted above, the largest computed stresses are tangential tensile stresses which occur near the edge of the beam - and these are the stresses (in megapascals) plotted in figure 6 as a function of time and for three output power levels. The superimposed box shows the ultimate tensile strength of the zinc selenide window with the percentages indicating the cumulative fraction of samples failing at that imposed stress [2]. Based on this data, the analysis predicts that during operation at the 10 kW output power level, the probability of fracture increases to 50% within 8 seconds. It is interesting to note that window fracture did occur while operating under conditions very close to those just mentioned. Another important piece of information in the stress analysis plot is the 100 kilojoule curve drawn as a dotted line. Setting an operational laser output energy limit of say, 100 kilojoules, can be misleading because of the power dependence shown here. Operation at 15 kilowatts for 5 seconds, for example, while well below the 100 kilojoule limit is also well above the 95% failure level.

Thermal and stress analyses were also performed on the new window and the results compared with those of the damaged window analysis. Assuming laser beam transmission at a 10 kilowatt power level, the maximum temperature rise and stress at times between 0-20 seconds were computed to be approximately only 3% of the old window values. For example, after 10 seconds the greatest temperature increase and tensile stress were 5.6°C and 1.7 megapascals for the new output coupler as opposed to 169° and 50.8 MPa for the old window.

In addition to the large optical difference, there also exists a significant physical difference between the two laser windows - the new window is significantly thicker. Since thickness is a relatively easily controllable material parameter, its effect on window performance deserves attention. A parametric study was made using the high absorption data of the damaged window, whereby material thickness was varied from .635 cm to 2.05 cm while all other material parameters and properties were left unchanged. The results, in terms of time rates of temperature rise during 10 kilowatt operation, are shown in figure 7. Similar studies were made at 5 and 15 kilowatts, again indicating a heat sink effect in the windows — the thicker the window the more heat it can dissipate. At the 10 kilowatt/10 second point the maximum temperature generated in the thinnest window is 32% higher than in the thickest window. The differences increase with time and power. Incidentally, whereas the damaged coupler was 1.05 cm thick, the new window is nearly twice as thick at 2.05 cm. Therefore, neglecting any of the dramatic optical differences, the new window should be capable of handling appreciably more heat simply on the basis of its greater bulk.

Recognizing the fact that laser windows degrade with time, another parametric analysis was performed to study performance as a function of total absorptance. Although the total absorptance of the new output coupler is now only 0.8%, there is no doubt that this value will eventually increase. Figure 8 is a plot of the increase in window tem-

perature as a function of total absorptance. Assuming that degradation is most likely to occur at the reflective surface – as it did in the case of the damaged window – the increase in absorptance is assumed to be due entirely to the increase taking place at that surface. The arrow points to the current absorptance of the window. Based on data from the thermal analysis, the parameterization study was extended to a stress analysis – and this is shown in figure 9. Again using the 10 kilowatt/10 second point of reference, this study shows that even after more than a six-fold increase in window absorptance, the maximum stress induced is approximately 19 megapascals which is still well below the point where only 1% of the samples would be expected to fail.

5. Conclusion

The analytical procedure described above represents a convenient method of assessing damage in partially transparent laser materials and of monitoring the performance of an installed laser window. Used in the latter sense, periodic measurements of a window's absorptance and checks against the predicted stresses may reveal progressive or incipient damage. Thus, through the combination of thermal and stress analyses, sufficient information is provided to predict damage thresholds, guide laser experiments,and guard against unexpected window failure.

6. Acknowledgments

The authors are indebted to Edmund Rolinski (AFML) for encouraging and promoting this study, to Kurt Suchsland (Aerotherm/Acurex) for his help in the use of the ASTHMA code and to Henry Tong (Aerotherm/Acurex) for his help in using the DISC code.

7. References

[1] Carlson, R. L., Air Force Weapons Lab. TR-76-115, June (1975).

[2] Wurst, J. C. and Graham, T. P., Air Force Materials Lab. TR-75-28, April (1975).

[3] Dickinson, S. K., Air Force Cambridge Research Lab. TR-75-0318, June (1975).

[4] The optical data for the damaged window was obtained from University of Dayton Research Institute.

[5] The new window was purchased from II-VI, Inc., 207 Garden Lane, Glenshaw, PA 15116.

[6] Tong, H., et.al., Air Force Materials Lab. TR-73-190, June (1975).

[7] The DISC code was obtained from the Aerotherm Division of the Acurex Corp.

[8] The witness plate optical measurements were performed by U.D.R.I.

[9] Kreith, F., "Principles of Heat Transfer," International Textbook Co., August (1960).

[10] Weiler, F. C., Air Force Materials Lab. TR-75-37, Vol I, October (1975).

8. Figures

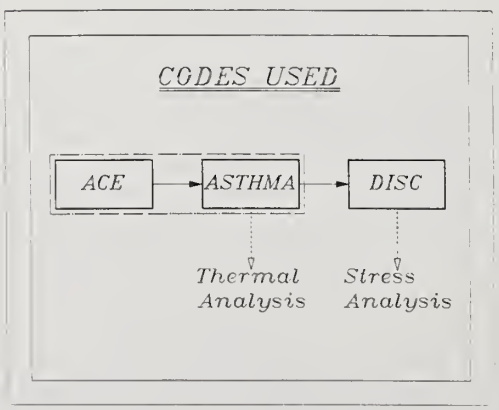

Figure 1. Codes used and their coupling for the thermal and stress analyses.

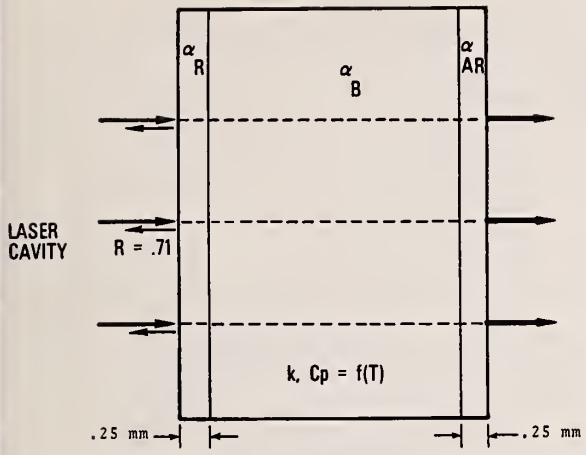

Figure 2. Analytical model of the coated zinc selenide.

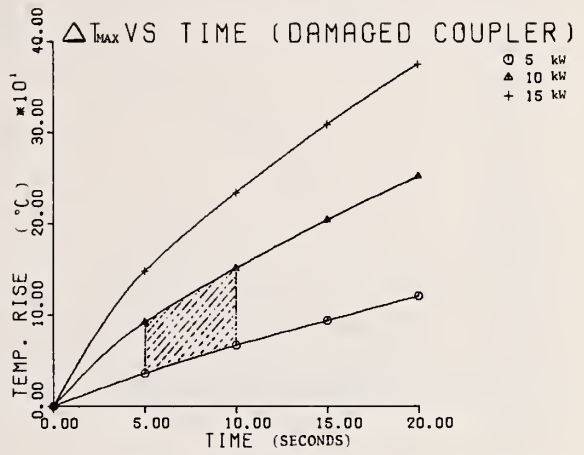

Figure 3. Plot of maximum temperature increase in the irradiated window as a function of time.

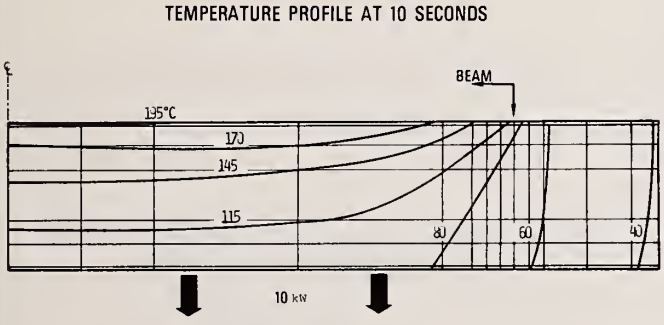

Figure 4. Nodal grid and temperature profile of the window at 10 kilowatts output power and 10 seconds.

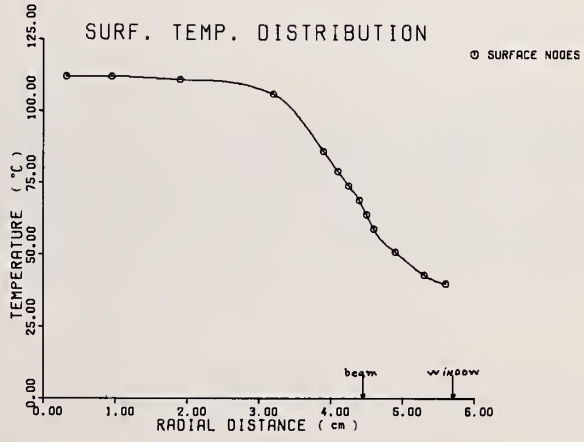

Figure 5. Surface temperature distribution at 10 kilowatts and 10 seconds.

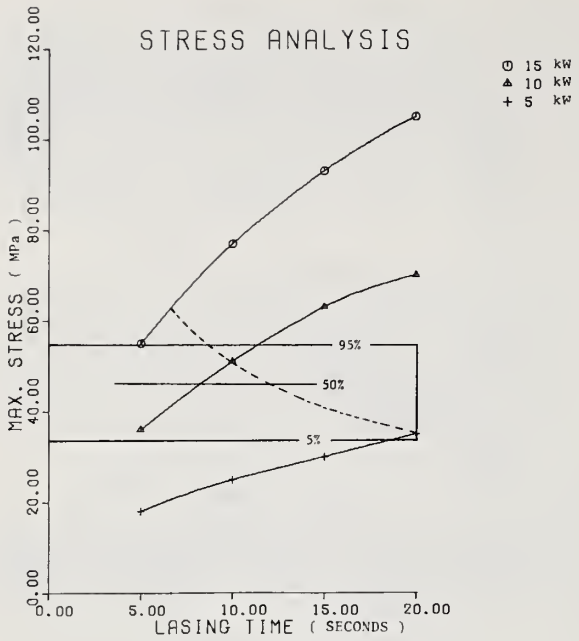

Figure 6. Maximum induced tensile stress as a function of time.

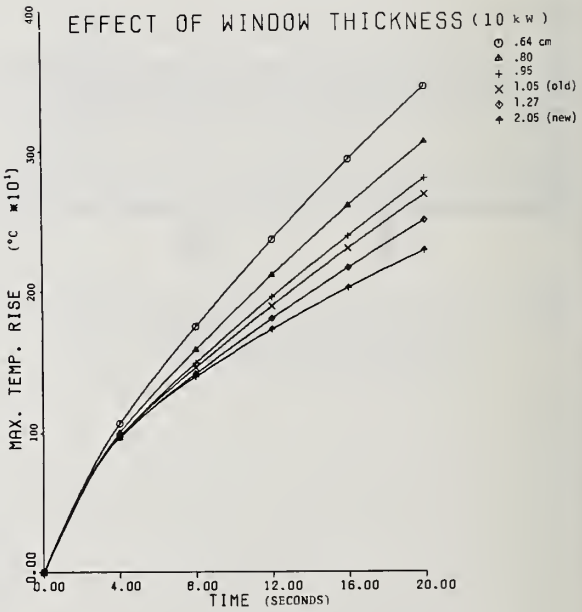

Figure 7. Maximum temperature rise as a function of time for six window thicknesses.

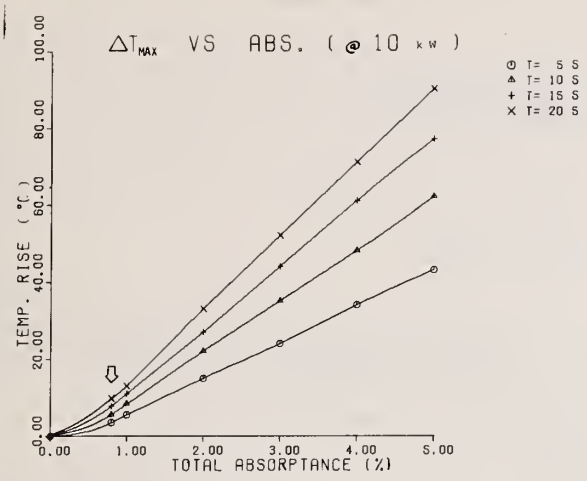

Figure 8. Maximum window temperature rise as a function of total window absorptance at 10 kW transmitted power.

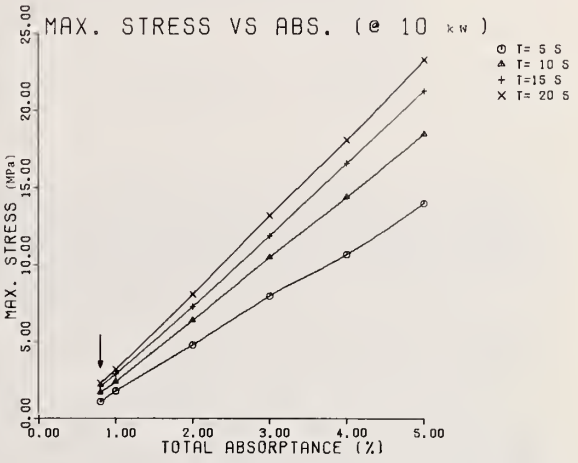

Figure 9. Maximum thermally induced stresses as a function of total absorptance at 10 kW.

COMMENTS ON PAPER BY RONDEAU AND FORD

It was pointed out by J. Zar of AVCO-Everett that the treatment of the window as a thin plate is not sufficient. Tri-axial stresses must be considered as well as planar stresses. Windows generally fail due to shear, of which axial stress is the strongest component. The speaker remarked that although the DISC code assumed only planar stresses, the results are being checked with a more complete code.

The question was raised as to why these windows failed, when windows of similar design at the AFWL had withstood higher radiative levels. The speaker attributed the difference to water absorbed from the humid atmosphere into the ThF_4 coating. Questions were raised about the very high value reported for the coating absorption.

1.4 INTERFEROMETRIC MEASUREMENTS OF LASER HEATED WINDOWS†

Enrique Bernal G.
Honeywell Corporate Research Center
Bloomington, Minnesota 55420

and

John S. Loomis
University of Arizona
Tucson, Arizona 85721

The optical aberrations in infrared window materials irradiated with a CO_2 laser have been measured at 0.6328 μm. The contributions of anisotropic aberrations due to polarization dependence were examined and found to be small for several materials of interest. Techniques for the semi-automatic digital analysis of our interferometric data will be discussed. The results will be applied to figure-of-merit characterization of window performance and calculation of far-field irradiance degradation.

Model calculations of the thermal profiles in irradiated windows and the resulting optical aberrations will be reviewed. Synthetic interferograms generated from these calculations were used to exhibit many of the experimentally observed features and to test the digital analysis techniques mentioned earlier.

Key words: Interferometry; laser windows; optical materials; thermal distortion.

1. Introduction

Efforts to improve infrared transmitting materials have been directed for the most part toward decreasing the absorption coefficient and increasing the strength of the material. The success of these efforts is measured by the steady decline in absorption coefficients to nearly intrinsic levels and substantial increases in the fracture strength of the alkali halides and fracture energy of alkaline earth fluorides. The very fact that measurement techniques were available contributed significantly to the success of the development program. Without measurements of absorption and strength, progress would have had to be defined by qualitative factors or measurements (such as infrared spectrophotometric transmission) which were relevant, but not sensitive enough.

We believe that the measurement problem is most difficult in the area of optical testing, especially laser-induced optical distortion. One approach to the problem is to measure individual parameters which contribute to thermal distortion and combine them with calculations of optical performance such as far-field irradiance distributions. This is unsatisfactory because errors of the individual terms accumulate when they are combined. Our approach is to use calculations to identify the important combinations of parameters which affect optical performance and then try to relate these in a meaningful way to optical measurements which can be made in a laboratory. By measuring one or two lumped parameters which characterize optical performance using a laboratory laser, one can then predict how large components, with the same parameters, will behave in a large laser system.

Interferometric methods are unique among the many techniques for characterizing infrared optical properties because they directly measure wavefront distortion, and are more sensitive than measurements of far-field profiles. However, the interpretation of interferometric results is time consuming and may become very complicated. Furthermore, making the measurements at the wavelength of interest is difficult because of the lack of suitable techniques for recording interferograms in the infrared with high enough spatial resolution.

In this paper we address the problem of interpretation of interferometric tests. We use a theoretical model of laser distortion developed earlier [1]¹ to generate synthetic interferograms. These can be compared with experimental results and are shown to demonstrate good qualitative agreement. We then discuss some of the details of interferogram analysis procedures and illustrate some of the preliminary results obtained.

---

†This work is partially supported by Defense Advance Research Projects Agency under contract #DAHC15-73-C-0464 and by Honeywell Independent Research and Development Funds.

1. Figures in brackets indicate the literature references at the end of this paper.

2. Synthetic Interferograms

Generation of synthetic interferograms based on an analytic model of window distortion is a useful tool for exploring the effects observed in the interferometry of laser-heated optical materials. Such a model provides a common basis for comparison of the response of various materials to laser irradiation as a function of combinations of their physical properties. Once the parameters involved have been obtained for laboratory lasers with small beams and relatively low powers, the model can be used directly to predict the performance of these materials at large apertures and high powers. Synthetic interferograms are also useful in previewing the effects of experimental parameters such as beam shapes, interferometer bias pattern, and sample geometry. Finally, synthetic interferograms can be used to verify that data reduction procedures yield correct results.

Generation of a synthetic interferogram can be divided into three separate processes. First, the temperature distribution produced by the absorption of energy from the laser must be calculated. Second, expressions for the optical path differences (OPD) as a function of temperature and thermally-induced stress must be found. Third, the intensity variations in the interferogram must be calculated and displayed photographically. We shall describe each of these processes in turn.

2.1. Temperature Rise

The window is assumed to be in the form of a disc heated by a laser with only radial variations in intensity referred to the center of the window and uniform absorption of energy in the axial direction. The temperature is then only a function of the r, z cylindrical spatial coordinates and time and is obtained by solving the heat conduction equation

$$\nabla^2 T + (Q/k) = (1/\kappa)(\partial T/\partial t)$$

where Q is the heat generation function

k is the thermal conductivity

κ is the thermal diffusivity.

This equation, with the appropriate boundary conditions, has been solved by an eigenfunction series [2] or by finite-difference techniques [3]. Both methods have produced very adequate numerical results and are applicable to a variety of beam profiles. We shall not dwell on the details of the numerical analysis, but make some general remarks on the nature of the solution.

It is easily shown for the sample dimensions used in the laboratory that after a few seconds the temperature distribution within the sample is almost stationary in time, but that the edge temperature rises uniformly [3]. This corresponds to the well-known linear rise period in calorimetric measurements of absorption. One can conclude from this observation that long irradiation times are not necessary in making interferometric measurements. Once the edge temperature increase becomes linear with time, the temperature distribution and hence the optical distortion does not change significantly. Note also that the heat conduction equation suggests that the temperature distribution scales as Q/k. Any measure of optical distortion will likewise scale proportionally. Finally, the heat generation term used in solving the heat conduction equation is assumed to have a Gaussian intensity profile to simulate the laser beam profile for a laboratory laser.

2.2. Optical Path Differences

Changes in optical path arise because the index of refraction and the sample thickness depend on temperature and thermally induced stress in the sample. The thermal stresses are calculated using thin-plate theory for isotropic, elastic media [4]. This approach, which has been extensively used by others, is somewhat unsatisfactory because several window materials of interest exhibit stress anisotropy, even though they possess a cubic structure. A general solution, however, violates our assumption of cylindrical symmetry. The results of thin-plate theory for radial and azimuthal stresses are

$$\sigma_r = \frac{1}{2} \alpha E \left[\overline{T}(b) - \overline{T}(r) \right]$$

$$\sigma_\theta = \frac{1}{2} \alpha E \left[\overline{T}(b) + \overline{T}(r) - 2T(r) \right]$$

where α = thermal expansion coefficient

E = Young's modulus

and $\overline{T}(r) = \frac{2}{r^2} \int_0^r T(r)\, r\, dr.$

The latter integral evaluated at the edge reduces to the average temperature rise of the window.

The change in optical path for radial and azimuthal polarizations can now be calculated. The results are then expressed as an isotropic OPD ϕ and anisotropic OPD δ given by [1].

$$\phi\ (r) = \tfrac{1}{2}\ (\phi_r+\phi_\theta) = \chi_I d\ [T(r) - \overline{T}\ (b)]$$

$$\delta\ (r) = \tfrac{1}{2}\ (\phi_r-\phi_\theta) = \chi_A d\ [T(r) - \overline{T}\ (r)]$$

where $\chi_I = dm/dT + (n-1)(1+\nu)\alpha + \tfrac{1}{2}\ \alpha n^3\ [(1-\nu)P_{11} + (1-3\nu)P_{12}]$

$$\chi_A = \tfrac{1}{2}\ \alpha n^3(1+\nu)(P_{11}-P_{12})$$

n = index of refraction

ν = Poisson's ratio

and P_{11}, P_{12} are stress-optic coefficients.

Figure 1 shows the radial dependence of $T(r)$, $\overline{T}(r)$, $\phi(r)$, and $\delta(r)$ for a Gaussian intensity with $1/e^2$ radius = $b/4$, and an irradiation time of 10 seconds. The isotropic OPD is proportional to the deviation of temperature from average temperature and resembles the original intensity distribution. The anisotropic OPD, however, is zero at the center of the window and attains its maximum value at a radius which is typically larger than that of the incident laser beam.

2.3. Intensity Variations

The intensity distribution in the image of the interferometer is calculated [1] for an interferometer linearly polarized in the y-direction (vertical). The intensity is given by

$$I = I_o\ [1+\cos(\phi+\omega)\cos\ \delta + \sin\ (\phi+\omega)\ \sin\ \delta\ \cos^2\theta].$$

Factors of $2\pi/\lambda$ have been omitted for simplicity. $\omega(r,\theta)$ is the bias OPD contributed by the reference beam of the interferometer. The bias produces reference fringes which are typically either equally spaced straight lines obtained by introducing a wedge into one arm of the interferometer or unequally spaced circular fringes introduced by changing the curvature of the reference beam relative to the sample beam.

The effect of the window on the interferogram can be understood as resulting first, from changes in the OPD for the y-direction,

$$\phi_y = \phi + \delta\ \cos\ 2\theta,$$

which deforms the shape of the fringes and, second, from changes in polarization of the sample beam which reduces fringe contrast, especially along the 45^o directions. When P_{11} and P_{12}, the anisotropic OPD vanishes and $\delta = 0$. Then the azimuthal variations in the intensity distribution disappear and the fringe deformation retains circular symmetry. When the anisotropic OPD is not small, the deformed fringes resemble ellipses whose eccentricity varies with radius.

A synthetic interferogram is a pictoral representation of the intensity distribution just presented. Figure 2 is an example of such a process. An array of printed characters was used to display the intensity distribution. The "finesse" was adjusted by only printing characters where the relative intensity exceeded a predetermined threshold. Contract was then enhanced by blackening the printed area with india ink. This method has the advantages of speed and low cost. Another type of synthetic interferogram is shown in Figure 3. Here a laser beam was used to expose an array of points on a sheet of photographic film. The intensity of the laser at any point on the film is controlled to produce the appropriate exposure. The array used in Figure 2 consists of approximately 2000 x 2000 points. The results closely approximate the ideal interferogram, but are time-consuming and expensive to produce.

3. Actual Interferograms

Interferometric measurements of materials heated by a CO_2 laser were made using a holographic interferometer operating at 0.6328μm. The primary advantage of the holographic method is that it allows interferometric measurements on samples that do not have optically flat surfaces because holographic recording permits one to combine the wavefront from a heated window to that previously recorded for the unheated window. The holographic interferometer also has more flexibility in the introduction of bias fringes.

The experimental arrangement is shown in figure 4. It consists of a two-beam interferometer using a thermoplastic holographic recording material [5]. Prior to irradiation by the CO_2 beam, a hologram is recorded on the thermoplastic recording material. The hologram can be developed in situ and it can be erased and used for repeated tests. Once the hologram is recorded and developed, the CO_2 laser is used to heat the window material. The interference pattern between the new wavefront and a holographic reconstruction of the old wavefront from the window is imaged on a diffuse screen where it is observed by a video camera and recorded onto magnetic tape. Recently [6] a video data processing system has been built which will allow us to analyze numerically the distortion detected by these interferometric tests.

4. Comparison of Real and Synthetic Interferograms

A crucial question in judging the usefulness of the theoretical model for window distortion which has been developed is whether it can reproduce qualitatively the effects which are observed in actual interferometric tests. We have found that this is the case, and will illustrate with examples of interferograms published earlier [1].

4.1. Isotropic Materials

As a working definition of an isotropic material we offer the criterion that an azimuthally uniform fringe pattern (circular fringes) remain uniform during heating by a laser at the center of the pattern. As shown by the synthetic interferogram in figure 3, the magnitude and sign of the bias fringes will charge the spacing and width of the fringes for the heated window. However, the fringes remain circular. A good example of an isotropic material is ZnSe, see figure 5. The fringe motion observed during the course of heating is proportional to the average temperature of the window, which is rising more or less linearly in time. The distortion introduced by the window is revealed by changes in the spacing of the fringes during heating.

Other materials which have been observed to be isotropic in practice are KCl and NaCl. That these materials have some anisotropic contribution to the OPD is indicated by observing the window samples between crossed polarizers [3]. The absorbed power needed to produce an observable change in the polarization of visible light is an order of magnitude higher than the power needed to produce significant optical distortion. Thus, while birefringence can be observed, its magnitude is much smaller than the isotropic distortion and can be ignored in most applications.

4.2. Anisotropic Materials

The materials in which we have observed significant anisotropic effects are BaF_2, SrF_2, and CaF_2. Figure 6 shows synthetic interferograms which have the same isotropic OPD function. Figure 6A, in fact, is the same function shown in figure 1. Figure 6B has an anisotropic factor χ_A equal to 20 percent of the isotropic factor χ_I. The original circular fringes are deformed into ellipses except for the innermost fringe. For comparison interferograms of BaF_2 are shown in Figure 7. Note that the innermost fringes retain circular symmetry while the outer fringes exhibit a strong elliptical appearance.

For these materials, of course, the CO_2 laser was adjusted to very low power because of their high absorption at 10.6μm. The purpose of the CO_2 laser is solely to produce the appropriate heating mechanism in these tests.

The degree of anisotropy present in the alkaline earth fluorides compared to the alkali halides is shown by the differences in $P_{11}-P_{12}$ for these materials [7]. The values of $P_{11}-P_{12}$ for KCl, NaCl, and KBr at 0.589μm are reported to be approximately - 0.02 whereas the values for CaF_2 and BaF_2 are approximately unity, an increase of a factor of fifty. Thus it is really not surprising that anisotropic effect are significant for the alkaline earth fluorides.

5. Interferogram Analysis

The fringes in an interferogram represent contour levels of optical path difference (OPD) between a reference wavefront and an optical system under test. The positions of these fringes are the basic raw data for analysis of the wavefront of the optical system. This section will describe some of the results obtained using FRINGE, a computer program for the analysis of interferometric test data, and the techniques used by that program.

For numerical analysis of wavefront information it is desirable to have as uniform a sampling of the wavefront over the pupil as practical. This is best achieved by using straight line bias fringes as in the synthetic interferogram in figure 3. Furthermore, it is useful to conduct the test to generate well-defined patterns without closed fringes. This is illustrated by figure 8, which shows the optical distortion for synthetic interferograms with increasing absorbed heat.

The wide dark areas shown in the bottom two interferograms do not accurately define the contour line for data reduction purposes. Fringes in the top two interferograms are much better suited for manual or semi-automatic location of fringe peaks. Manual location of fringes involves setting a cursor at the desired point as the interferogram and pressing a button to digitize the coordinates of the cursor. Typically 300-500 points can be located in 1-2 hours. With semi-automatic operation using a video digitizer [6], a minicomputer assists in locating the fringes. Approximately 1200 points can be located in 20-30 minutes.

Auxiliary information about the interferogram must also be provided for the proper scaling and definition of the pupil, by locating the edges of the pupil and measuring the magnification of the image. A reference wavefront can be subtracted from the data to improve the resolution of the measurement of thermally induced effects. Then the analysis proceeds in two stages. The first stage is a global fitting of the data by a polynomial series. The second is a calculation of the diffraction intensity spread function (point spread function) which is the expected intensity profile in the far field, of light imaged through the system.

5.1. Global Fit

The program fits a 37 term series of Zernike polynomials to the wavefront data and uses this series expansion to represent the wavefront in later calculations. Using a global function to represent the distortion has the advantage of smoothing the original data and simplifying the process of averaging several wavefronts to assess the consequences of combining several distorting elements into the optical train. Zernike polynomials were selected for several reasons. The polynomials are orthogonal and form a complete set of functions over the domain of the unit circle. Each member of the series minimizes the rms deviation for that order. Finally, the Zernike polynomials are easily understood in terms of optical aberrations, so that tilt and defocus and, if necessary, coma and astigmatism can be removed from the wavefront.

The Zernike polynomial series is fitted to the data using the Gram-Schmidt method with a least-squares minimization. A statistical characterization of the wavefront from the original data is compared to that obtained for the polynomiol fit. This information provides a measure of optical quality (rms values, Strehl definition) and a judgement on the goodness-of-fit of the polynomial series (how many terms were adequate). Other useful information includes a contour map of the wavefront after all corrections have been applied.

Figure 9 shows a typical contour plot from a test on BaF_2. The elliptical distortion pattern is clearly visible in the contour map, but was not apparent in the original interferogram [1], which incorporated straight line bias fringes. Subjecting a synthetic interferogram, such as shown in figure 3, to the data reduction process provides a measure of the adequacy of the process. Typically a synthetic interferogram such as this can be analyzed to an absolute precision of about 1.5 percent compared to the original wavefront - if the original is smooth enough. The rms deviation of the wavefront can be matched to the original within 0.5 percent. Problems arise when the heating beam is much smaller than the size of the pupil and when anisotropic effects are significant. Then 37 terms are not sufficient to adequately represent the wavefront. This deficiency will be corrected by using the calculated temperature distribution itself as the basis function and fitting the parameters with a non-linear least-squares minimization algorithm.

5.2. Far Field Analysis

Interferometric data can be used to calculate the degradation in far field irradiance of light imaged through the optical system under test. The complex pupil function is obtained by taking measurements of the intensity across the pupil and interferometric measurements of the optical phase. The amplitude and phase of the light is then calculated for a 31 x 31 mesh of points on the pupil. This mesh is embedded in the center of a 64 x 64 matrix of zeros, and the Fast Fourier Transform [FFT] algorithm is applied. The modulus squared of the resultant matrix is the point spread function [PSF] of the pupil function, which gives the intensity distribution in the far field.

As an example of the results of this analysis, we considered the situation where the heated window is used in a visible light imaging system simultaneously with the incident CO_2 laser beam. Such a situation is realistic in experiments on beam degradation because light in the visible wavelengths is more sensitive to optical distortion and is easier to photograph than is infrared imaging. Figure 10 shows the Airy pattern produced for an undistorted beam. Figure 11 is the result obtained for a distorted BaF_2 window, using the optical phase shown in figure 9. The peak intensity in each case was normalized to the same value. The principal observation is that the relative contribution of the ring structure is greatly enhanced,but that the size of the central spot does not change significantly.

6. Conclusions

It has been possible to generate synthetic interferograms which display most of the characteristics of actual interferograms. Only two optical parameters were required (χ_T and χ_A) to describe the optical pathlength change per degree of temperature rise once the temperature distribution is known. For isotropic materials the OPD is proportional to the deviation of temperature in the window. Knowledge of these parameters and the geometry of a high power laser beam profile makes possible the prediction of far field patterns for realistic systems. Measurements of χ_T and χ_A are expected to provide useful information for the optical design of high power laser systems.

7. References

[1] Loomis, J. S. and Bernal G., E., in "Laser Induced Damage in Optical Materials: 1975", NBS Special Publication 435, U.S. Government Printing Office, p. 126 (1975).

[2] Bernal G., E., Appl. Optics 14, 314 (1975).

[3] Loomis, J. S. and Huguley, C. A., in "Laser Induced Damage in Optical Materials: 1974", NBS Special Publication 414, U.S. Government Printing Office, p. 94 (1974).

[4] Boley, B. A. and Wiener, J. H., "Theory of Thermal Stresses", Wiley, New York, p. 290 (1960).

[5] Lee, T. C., Applied Optics, 13, 888 (1974).

[6] Bernal G., E., Anderson, R. H., Koepke, B. G., Loomis, J. S., Skogman, R. A., Stokes, R. J., Wertman, D., Honeywell Semiannual Technical Report #5, ARPA Contract #DAHC-73-C-0464, July 1976.

[7] Flannery, M. and Marburger, J. in "Fifth Annual Conference on Infrared Laser Window Materials", Defense Advanced Research Projects Agency, Washington, D.C., p. 782 (1976).

8. Figures

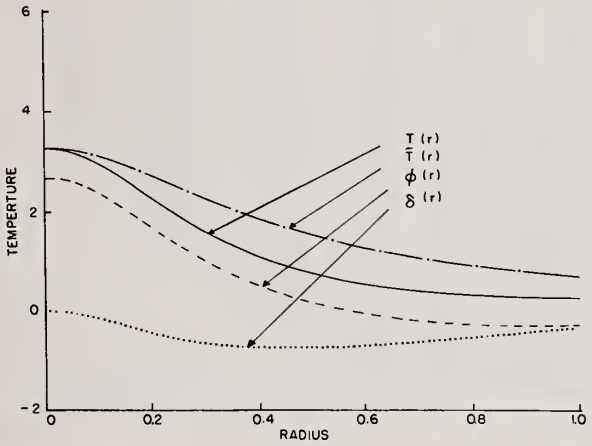

Figure 1. Temperature and related distributions as a function of radius.

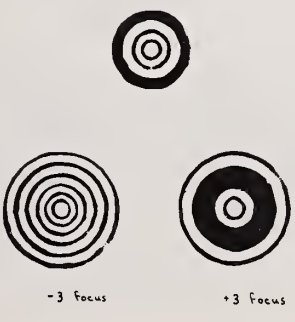

Figure 2. Synthetic interferograms showing the effect of focal shift bias fringes. The top picture is an unbiased interferogram.

Figure 3. Synthetic interferogram generated on pictoral output device.

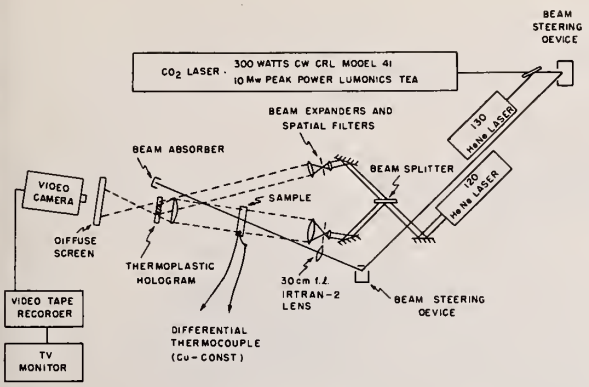

Figure 4. Layout of experimental apparatus.

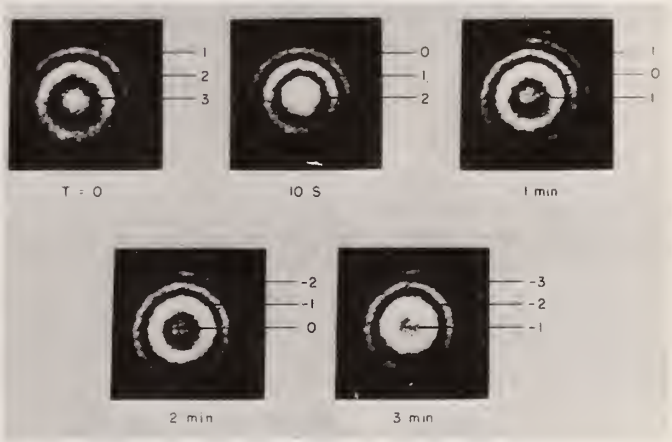

Figure 5. Interferogram of laser-induced optical distortion in polycrystalline CVD zinc selenide. Upper left photo shows reference fringe bias.

Figure 6. Synthetic interferograms for isotropic (A) and anistropic (B) effects. $\chi_A = 0$ for (A) and $\chi_A = 0.2$ for (B). $\chi_I = 1$ for both cases.

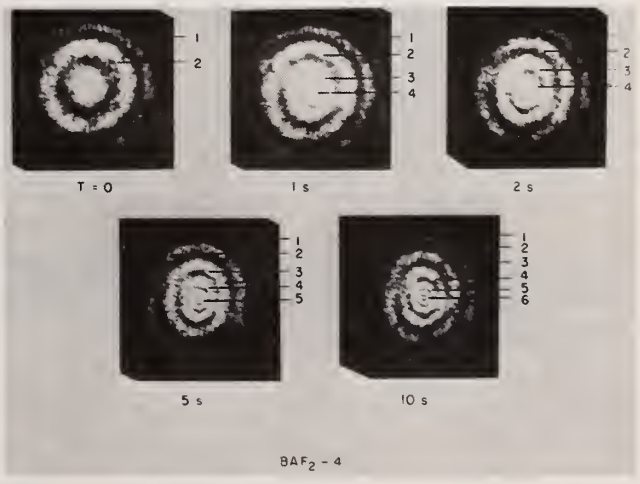

Figure 7. Interferogram of laser-induced optical distortion in single crystal barius fluoride. Upper left photo shows reference fringe bias.

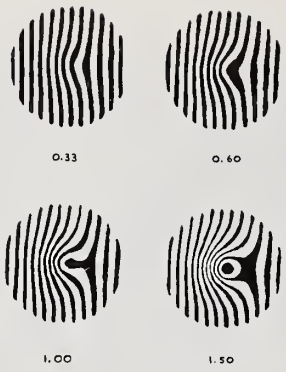

Figure 8. Synthetic interferograms showing effect of changing χ_I. The reference fringe bias was a simple wedge (straight line fringes).

Figure 9. OPD contours for optical distortion in barius fluoride. Contour step is fractions of He-Ne laser wavelength (.6328 μm).

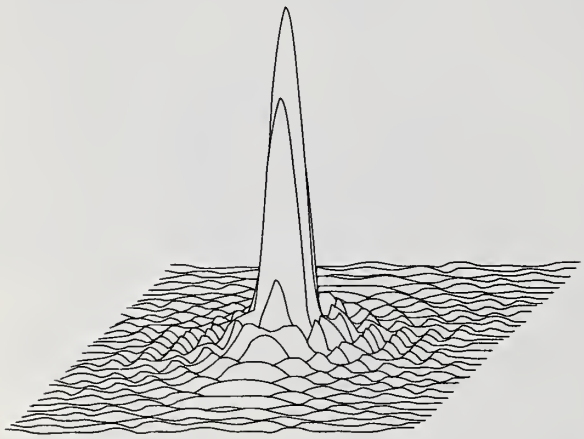

Figure 10. Point spread function (PSF) showing Airy disc for unaberrated pupil.

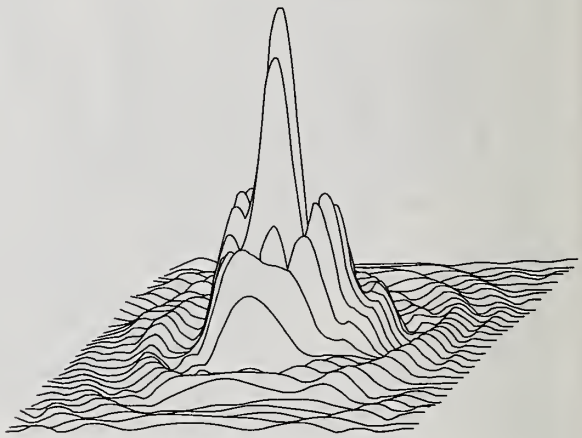

Figure 11. Point spread function (PSF) for optical distortion in barium fluoride.

COMMENTS ON PAPER BY BERNAL AND LOOMIS

No discussion.

1.5 NEW MATERIALS FOR CHEMICAL LASER WINDOWS*

James A. Harrington
Physics Department
University of Alabama in Huntsville
Huntsville, Alabama 35807

Many of the more common materials such as the alkaline earth fluorides, ZnSe, and the alkali halides have been studied for use as low loss windows on DF-HF chemical lasers yet there remain others which have received little or no attention at these wavelengths. We have begun to investigate some of these other materials in hopes of finding additional low absorbing materials which show potential as laser windows. Specifically, our measurements of the optical absorption in $LiYF_4$, Yttralox, ZnS, CdTe, KBr, SrF_2, and KRS-5 will be discussed and related to the intrinsic absorption in these hosts. In all cases, the measured absorption has been found to be greater than the intrinsic value. In addition to the absorption measurements on these substances, some recent optical absorption measurements on water repellent coatings on KCl will be discussed.

Key words: Chemical lasers; infrared materials; laser windows; multiphonon absorption; optical absorption; water repellent coatings.

1. Introduction

During the past several years, a wide variety of materials have been studied for use as low loss windows on high powered infrared lasers. At DF/HF chemical laser wavelengths, the range of potentially low loss materials is particularily wide and the optical absorption in the most common hosts such as the alkali halides, alkaline earth fluorides, ZnSe, Si, Ge, Al_2O_3, and MgO has been previously discussed [1,2][1]. There remain, however, other promising materials which have received little or no attention at these wavelengths. In this investigation, we report the results of our optical absorption measurements at DF and HF wavelengths on some less studied substances (Yttralox, KRS-5, ZnS, CdTe, and $LiYF_4$) as well as on some improved KBr and polycrystaline SrF_2. In addition to these measurements, the optical absorption in polymeric (water repellent) coatings on KCl will be presented.

2. Experimental Procedure and Techniques

The optical absorption was measured using standard laser calorimetric techniques [3]. In order to minimize surface contamination, all samples were measured in a vacuum calorimeter. In the case of SrF_2, a special vacuum calorimeter was used so that the samples could be baked out under vacuum and then measured without moving the samples (cf section 3.2). The cw DF/HF chemical laser used as a source was constructed from our own design and delivered from 5 to 10 watts of multiline power.

Samples were supplied for measurement from a variety of laboratories engaged in state-of-the-art materials preparation. Each sample was cleaned with spectrograde CCl_4 just prior to measurement. In instances when the surface quality looked particularly bad as viewed under a Nomarski microscope, the surfaces were mechanically polished, cleaned, and then remeasured. When this was done, the absorption was always less than the initial value. Examples of this behavior are noted in the next section.

3. Experimental Results

3.1 Semiconductors

Two semiconductors, which had previously not been measured, were studied. Single crystal CdTe obtained from II-VI, Inc. was found to have an absorption coefficient β at DF (3.8 μm) and HF (2.8 μm) wavelengths of:

CdTe β (DF) = 4.8×10^{-3} cm^{-1}
β (HF) = 5.3×10^{-3} cm^{-1}

These values are approximately an order of magnitude higher than the values reported by Deutsch [4] at CO_2 and CO wavelengths. A sample of CVD ZnS was obtained from Raytheon. In the past this has been a high loss material with a measured $\beta(CO_2)$=0.15 cm^{-1} [4]. At chemical laser wavelengths, however, we

*Work supported by DARPA and ONR.

[1]Figures in brackets indicate the literature references at the end of this paper.

measured smaller absorption as follows:

ZnS β (DF) = 0.049 cm^{-1}
β (HF) = 0.024 cm^{-1}

3.2 Raytheon Cast SrF_2

Three samples (VHP 597) of the most current, polycrystaline SrF_2 material were obtained from Raytheon. The three pieces enabled us to obtain β for four different lengths L ranging from 0.5 to 2 cm and thus to plot βL vs L for separation of bulk and surface absorption contributions from the total absorption.

The first measurements performed on the as-received samples are shown at 3.8 μm in figure 1. It can easily be seen from the figure that the absorption data (●) are quite scattered and therefore no reliable surface and bulk separation is possible. A similar result, not shown, was obtained at 2.7 μm. This scatter in the data is often due to unequal preparation or contamination of the sample surfaces. In order to minimize this problem, each sample was cleaned in trichloroethylene and then mounted in a special vacuum calorimeter for a bakeout at 200°C for several hours under vacuum. The samples were then cooled and β remeasured without breaking vacuum. These remeasured absorptions, which are plotted in figure 1 (▲), yield more consistent data and thus a least squares fit to the data was made. From the slope and intercept of this fit the following bulk (β_B) and surface (β_S) absorption coefficients are obtained:

$$\beta_B = 5.4 \times 10^{-5}\ cm^{-1}$$
$$\beta_S = 5.3 \times 10^{-5}/\text{surface}$$

The bulk value of $5.4 \times 10^{-5} cm^{-1}$ represents the smallest absorption of any sample measured to date at 3.8 μm. Unfortunately, the results after bakeout at 2.7 μm were again quite scattered and it was not possible to fit the data. A summary of all data for these samples is given below in table 1.

Table 1. Optical absorption in SrF_2 (Raytheon VHP 597)

Sample Condition	Wavelength	$\overline{\beta}_T (cm^{-1})$	$\beta_B (cm^{-1})$	β_S/surface
As-received	DF	1.6×10^{-4}	--	--
	HF	4.7×10^{-4}	--	--
Vacuum bakeout	DF	1.6×10^{-4}	5.4×10^{-5}	5.3×10^{-5}
	HF	4.1×10^{-4}	--	--

The total absorption coefficient $\overline{\beta}_T$ is the average β obtained from the three samples.

3.3 Alkali Halides

KRS-5 is an attractive substance for a laser window because of its resistance to environmental attack. It has received little attention, however, due to its relatively high loss at CO_2 frequencies [4]. At DF and HF wavelengths we have measured the following absorption in a sample of Harshaw KRS-5:

KRS-5 β (DF) = $2.3 \times 10^{-3}\ cm^{-1}$
β (HF) = $3.5 \times 10^{-3}\ cm^{-1}$

Recently grown single crystal KBr was obtained from Dr. Phil Klein of NRL for our absorption studies. This material was RAP processed [5] and represents some of the best KBr we have measured to date. Table 2 summarizes our absorption coefficient measurements on the samples as-received and after a mechanical polish. It can be seen that polishing just prior to measurement lowers the ab-

Table 2. Optical Absorption in KBr

Sample No.	Surfaces	β_T (DF) $[cm^{-1}]$	β_T (HF) $[cm^{-1}]$
B-324	As-received	3.6×10^{-4}	4.2×10^{-4}
	Mech. Polish	2.2×10^{-4}	3.2×10^{-4}
B-326	Mech. Polish	1.3×10^{-4}	4.1×10^{-4}

sorption as might be expected for a hydroscopic material yet the absorption still remains well above the intrinsic value for KBr. Further surface treatment such as chemical etching should be done to try to minimize surface absorption.

3.4 Yttralox

Yttralox [Y_2O_3(90%): ThO_2(10%)] is an oxide with many attractive features as a potential low loss laser window. It has the usual strength and environmental resistance typical of oxides while at the same time exhibiting lower absorption than, for example, sapphire [1]. The Yttralox obtained for this study was supplied by General Electric [6].

The infrared absorption spectrum for Yttralox is shown in figure 2. An extrapolation of the multiphonon edge to $\beta_{int}(DF)=2.6\times10^{-5}cm^{-1}$ and $\beta_{int}(HF)=4.6\times10^{-9}cm^{-1}$ indicates the very low intrinsic values for this material at the chemical laser wavelengths. However, an extrinsic band is present in the as-received material. This band, unfortunately, appears directly between the DF and HF frequencies and is responsible for the higher absorption in this region.

In order to improve this material it is necessary to reduce the extrinsic absorption band centered near 3 μm. One method used to minimize this band is a reheating of the sample in a small amount (∿10 ppm) of oxygen at high temperature (∿1700°C). In reheating the sample whose absorption is shown in figure 2, the extrinsic band completely disappeared. In this treatment, oxygen is presumably being forced into the Yttralox and the likely OH^- contaminant removed. On remeasuring β calorimetrically, the DF β in one sample (not shown in figure 2) decreased by a factor of 6 and the HF β by a factor of 4 [1].

It would seem that the most likely contaminant would be OH^- and that it is being at least partially removed in the retreatment process described above. Sulfur containing compounds, however, are also a possible source of contamination. In some cases the starting powder is ball-milled and in some cases this step is eliminated from the processing procedure. Ball-milling can introduce sulfur and, therefore, we have looked at different samples which are identical in processing except for the ball-milling operation. For those samples which involved the ball-milling operation, the absorption was always less at both DF and HF wavelengths than the corresponding samples which did not include ball-milling in their processing. Therefore, we cannot conclude that sulfur is definitely an impurity contributing to the extrinsic band near 3 μm.

3.5 Li YF_4

Li YF_4 is a potentially low loss material with good environmental resistance, a low index of refraction (1.46), and relatively high thermal conductivity ($0.044\ ^{W}/_{cm\,^oK}$). The infrared absorption of undoped, single crystal Li YF_4 obtained from Sanders Assoc., Inc. is shown in figure 3. Included on the figure are our calorimetrically measured absorption coefficients

Li YF_4 $\quad \beta\ (DF) = 6.3\times10^{-3}\ cm^{-1}$

$\beta\ (HF) = 4.1\times10^{-3}cm^{-1}$

along with the much smaller extrapolated intrinsic values. Again it can be seen that the measured absorptions lie well above the multiphonon edge indicating that the absorption is extrinsically limited.

3.6 Polymeric coatings

Water repellent coatings have been produced to protect hydroscopic materials such as KCl. These coatings have, as well, to be evaluated in terms of optical absorption. To study the DF and HF absorption, Research Triangle deposited a water repellent,polymer coating on one-half of a KCL substrate. Our absorption measurements on this half-coated substrate are given in table 3. Unfortunately, the total absorption in the uncoated half is essentially the same as the coated half, within experimental

Table 3. Polymeric coatings on KCl

Sample Section	$\beta_T(DF)\ [cm^{-1}]$	$\beta_T(HF)\ [cm^{-1}]$
Uncoated	1.9×10^{-3}	1.3×10^{-2}
Coated	2.1×10^{-3}	1.6×10^{-2}

error, so that it is impossible to extract from the data the absorption in the polymeric coating alone. All that can be said is that the coating material may have a low absorption but reliable coating absorptions cannot be obtained until better KCl substrate material is used.

4. Conclusions

The optical absorption in all of the materials studied has been found to be extrinsically limited. In the case of some materials such as Yttralox, the extrinsic bands are visible and methods have been attempted to reduce these bands near 3 μm. Yttralox, as well as, $LiYF_4$, and CdTe are previously little studied materials which could be improved through further materials processing. This would be especially profitable for Yttralox and Li YF_4 since they have appealing physical properties. Other materials such as ZnS and KRS-5 have absorption coefficients too high to be viable alternatives for low loss windows.

5. Acknowledgments

The author gratefully acknowledges the assistance of D.A. Gregory and W. Otto, Jr. for technical assistance in these measurements.

6. References

[1] Harrington, J.A., Gregory, D.A., and Otto, W.F., Appl. Optics, Aug., 1976 (to be published).

[2] Harrington, J.A., Gregory, D.A., and Otto, W.F., Fifth Conference on Infrared Laser Window Materials, Las Vegas, NV, 1975, p. 871.

[3] Hass, M., Davisson, J.W., Klein, P.H., and Boyer, L.L., J. Appl. Phys. 45, 3959 (1974).

[4] Deutsch, T.F., J. of Elect. Mat. 4, 663 (1975).

[5] Klein, P.H., Fifth Conference on Infrared Laser Window Materials, Las Vegas, NV, 1975, p. 983.

[6] Greskovich, C. and Woods, K.N., Amer. Cer. Soc. Bull. 52, 473 (1973).

7. Figures

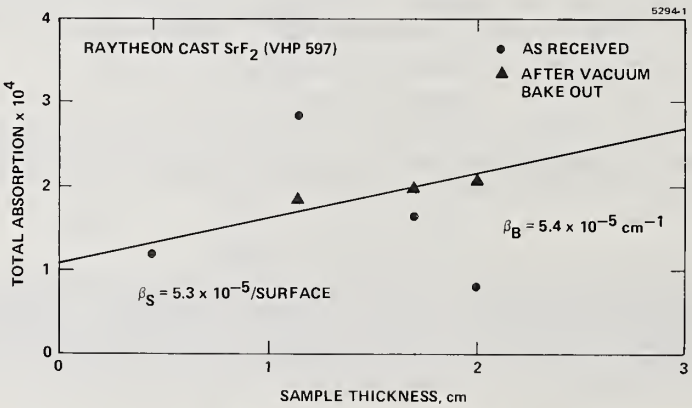

Figure 1. Intrinsic absorption in Raytheon cast Sr F_2 at DF laser frequencies.

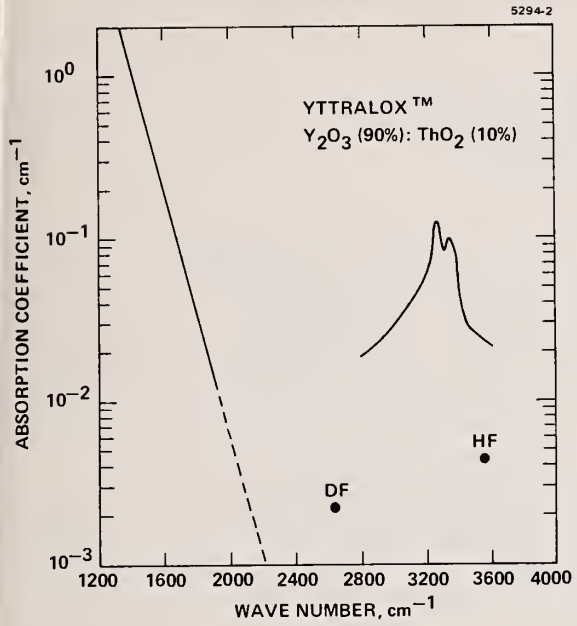

Figure 2. Infrared absorption in Yttralox. Note the extrinsic band near 3 μm and the extrinsically limited DF and HF absorption coefficients.

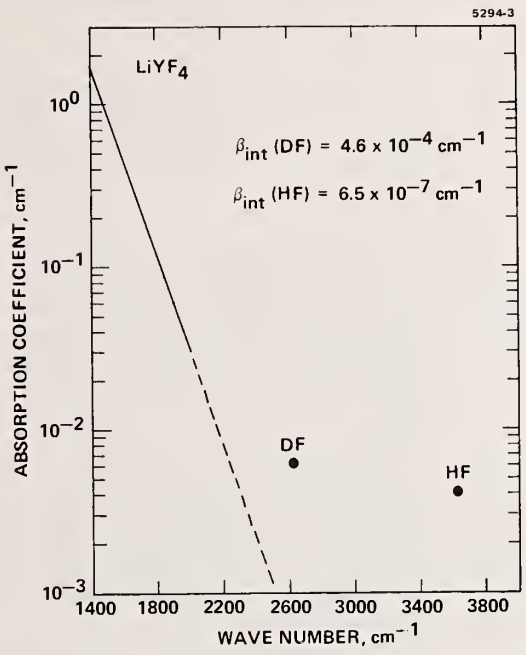

Figure 3. Infrared absorption in Li YF_4.

COMMENTS ON PAPER BY HARRINGTON

The speaker pointed out that the calorimetric analysis included a correction for the Fresnel reflection at the surface, and for standing wave effects in parallel surfaces. J. Johnston of UDRI stated that his measurements made on fluoride materials at the CO laser wavelength confirmed the observation that veiled surfaces often show lower infrared absorption than clear surfaces, i.e., that the visible appearance of the surface is not a reliable guide to its infrared characteristics.

1.6 STUDIES OF ABSORPTION IN MID IR LASER WINDOW MATERIALS

A. Hordvik, B. Bendow, H. G. Lipson,
L. H. Skolnik, and R. N. Brown
Rome Air Development Center
Deputy for Electronic Technology
Hanscom AFB, MA 01731

An investigation has been made of the absorption properties of various potential laser window materials in the wavelength ranges of the CO_2, CO, and HF lasers. Various experimental techniques were utilized including emittance spectroscopy, Fourier spectroscopy, laser calorimetry, and a new photoacoustic technique which allowed both bulk and surface absorption to be determined simultaneously. The materials investigated were ZnSe, Al_2O_3, MgO, LiF, MgF_2, CaF_2, SrF_2, and BaF_2. At both the CO and HF laser wavelengths it was found that surface absorption was substantial in most cases and particularly so in the HF laser region. Among the materials tested, sapphire emerged as an excellent candidate for use with the HF laser provided its large surface absorption can be reduced substantially. Preliminary theoretical calculations have been made of the intrinsic absorption in ZnSe to interpret the measurements.

Key words: Bulk absorption; CO laser; HF laser; infrared laser window materials; multiphonon absorption; surface absorption.

Introduction

Materials suitable for use in high power infrared laser windows have been the subject of considerable research in the last 5-6 years [1-5][1]. In general, candidate materials must possess very low optical absorption coefficients at the laser wavelength of interest in order to avert unacceptable optical distortion and catastrophic mechanical failure. A large number of absorption measurements have been performed at the CO_2 laser wavelengths [1-5], but the work at the CO and HF laser frequencies has been more limited [6-8], and in particular only a few attempts have been made to distinguish between bulk and surface absorption [7,8].

We report here a number of measurements of both bulk and surface absorption at CO and HF laser wavelengths. Various experimental techniques were used including emittance spectroscopy, Fourier spectroscopy, and laser calorimetry. In addition, a new photoacoustic method was utilized whereby both surface and bulk absorption can be measured simultaneously. Finally, to determine the intrinsic value of the absorption coefficient in semiconductors, multiphonon calculations of the type carried out previously for ionic crystals have been modified to provide preliminary theoretical results for the optical absorption in ZnSe.

Experimental Procedure

The various experimental techniques utilized for measuring absorption have all been described in the literature [9]. But since the use of the photoacoustic effect for measuring absorption in solids is rather new [10, 11, 12], a short description of this method will be given.

When a periodically interrupted light beam is incident on an absorbing medium, heating and subsequent expansion occurs resulting in the generation of an acoustic or elastic wave. Since the amplitude of the elastic wave is proportional to the absorbed energy, the effect can be used to measure absorption coefficients. The technique can be viewed as a variation of the standard laser calorimetric method, but since an elastic wave propagates much faster than a thermal wave, one can use ac instead of dc detection. In principle, the absorption coefficient can be

1. Figures in brackets indicate the literature references at the end of this paper.

calculated from the measured amplitude of the acoustic wave, however, the calculation is difficult. Instead, each sample is calibrated at a wavelength of known absorption. The calibration is usually done at a frequency where the absorption is large enough to be measured accurately by transmission. Once the calibration constant has been established at one wavelength, the number can be used to determine the absorption coefficient at other wavelengths. The technique has been found to be quite sensitive and should be able to measure absorption coefficients in the 10^{-6} cm^{-1} range using laser powers of about one watt [12].

A schematic of the experimental arrangement used in the photoacoustic absorption measurements is shown in figure 1. It consists of a cw laser, a beam chopper, a sample with transponder attached for measuring the amplitude of the generated acoustic wave, a power meter, and a lock-in amplifier. The transponder is made of a piezoelectric ceramic. An unattached transponder (see fig. 1) serves to detect any signal generated by scattered radiation. If necessary, one can then compensate for scatter contribution to the signal generated by the attached transponder. Typical sample dimensions are 5 x 10 x 12.5 mm where the beam passes through the 5 x 12.5 mm surfaces, and the transponder is attached to one of the 10 x 12.5 mm surfaces.

With this experimental configuration it is possible to determine both surface and bulk absorption [13]. By measuring the transducer output as a function of distance between beam and transducer for pure bulk absorption and for pure surface absorption one finds that the two generated curves have quite different shapes. The functional dependence of the two curves is independent of the absorbed power and can be found experimentally. If both surface and bulk absorption are present, the magnitude of each can be found by curve fitting provided the signals generated by the two types of absorption are within one to two orders of magnitude of each other. Calibration is done at a wavelength of known surface absorption, for instance in the opaque region.

Experiments were performed on ZnSe, MgO, Al_2O_3, LiF, MgF_2, CaF_2, SrF_2, and BaF_2. The ZnSe (CVD) was obtained from Raytheon [14] and polished by Man Labs. The MgO sample was grown by Norton Research Corp. (Canada) Ltd. and polished by Man Labs. All the other samples were obtained from A. Meller Co. in finished form, and the material was of standard commercial quality. The samples were stored in a desiccator, but otherwise no particular care was taken to protect the surfaces. Any surface contamination that might occur during mounting of transponder or during the experiment was removed with acetone.

For measurement and calibration we had available a CO_2, CO, HF, and Ar-laser. The CO laser was tunable to a large number of discrete lines in the 5.2 to 6.5 μm region. The HF laser oscillated on several wavelengths simultaneously with most of the power being in the 2.7-2.8 μm range. Typically, laser powers of a few hundred mW or less was used in the various experiments.

Results and Analysis

The results of bulk absorption measurements on CaF_2, SrF_2, and BaF_2 performed with the tunable CO laser are shown in figures 2, 3 and 4 and in table 1. The straight, dashed line in each figure is drawn through the measured absorption coefficient at 10.6 μm and with the slope determined by Deutsch [15]. For CaF_2 the absorption decays exponentially with frequency as predicted by the multiphonon theory [15,16], although the slope is slightly lower than that measured by Deutsch [15]. For both SrF_2 and BaF_2 the absorption coefficient clearly levels off at the higher frequencies. Lower absorption values have been reported in specially prepared samples [6]. The higher absorption levels observed here may be caused by impurities, dislocations and/or inclusions.

Results of surface absorption measurements are also given in table 1. CaF_2 had high bulk absorption and this made it difficult to determine the surface absorption accurately, and it was measured at only two wavelengths. Surface absorption was found to be strongly dependent on wavelength. In the shorter wavelength regions surface losses will in some cases be larger than bulk absorption for windows less than 1-2 cm thick. Surface losses for the materials in table 1 have previously only been reported for the 5.2-5.3 μm region [17]. Our results are in general agreement with the former measurements.

Bulk absorption for MgO, MgF_2, Al_2O_3, and LiF is plotted versus frequency in figure 5. The curves have been extrapolated down to the 1 x 10^{-4} cm^{-1} level assuming an exponential decay. Measurements at the HF laser wavelength were done with the photoacoustic technique. For MgO, the high absorption level at 2.7 μm is probably caused by the closeness to the bands indicated in the figure. The absorption coefficient for Al_2O_3 at 2.7 μm is near the predicted intrinsic level.

Data for both bulk and surface absorption are given in table 2 for the above materials and also for ZnSe, CaF_2, SrF_2, and BaF_2. Note that at 2.7 μm surface absorption may become dominant over bulk losses for most of the materials depending on sample thickness.

Both bulk and surface absorption are larger than expected in the 2.7 μm region. The data for SrF_2, CaF_2, and ZnSe are consistent with the measurement by Haas et al. [8], and Harrington et al. [9]. Sapphire is the only material with bulk absorption close to the expected value. It has been suggested that the higher than predicted absorption is due to carbon containing compounds which have contaminated the materials during fabrication and polishing [3, 18].

To compare the optical performance of the various materials as an HF laser window the figure of merit for optical distortion at 2.7 μm has been calculated for each sample. The figure of merit has been defined as follows [19, 20]:

$$\left[\beta + \frac{2\beta_s}{L}\right]^{-1} \times \left\{\frac{dn}{dT} + \alpha\,(1+\nu)\,(n-1) + \alpha\,\frac{n^3}{2}\left[(1-\nu)p_{12} - \nu p_{11}\right]\right\}^{-1} \times \begin{bmatrix} C \\ or \\ K \end{bmatrix} \qquad (1)$$

Here β is the bulk absorption coefficient, β_s the surface absorption, L the window thickness, n the index of refraction, T temperature, α the thermal expansion coefficient, ν Poisson's ratio, p_{ij} the strain optic coefficient, C the heat capacity, and K the thermal conductivity. For the short time response appropriate to pulsed laser conditions the heat capacity is used. The thermal conductivity is used for the equilibrium response under cw laser irradiation. It should be noted that the stress optics term used in eq. (1) is really only applicable to isotropic materials, but in most cases this simplification does not give a large error. It will be assumed that L = 2 cm for all materials. The values of the absorption coefficients used in the calculations are from table 2. The values of various physical constants in eq. (1) have been taken from [6 and 21]. Results are listed in table 3. In the column labeled "total" both surface and bulk absorption have been included. In the column labeled "bulk" the surface losses have been neglected. All values have been referenced to ZnSe. CaF_2, SrF_2, and BaF_2 have high figure of merit since dn/dT is negative for these materials while the two other terms in the bracket are positive resulting in some degree of cancellation. In this case the stress-optic effect contributes significantly to the optical distortion, and when comparing the figure of merit for the various materials, it should be remembered that we have used an approximate stress-optic term. Sapphire also looks like a promising candidate if the surface absorption could be reduced substantially. In addition sapphire has mechanical, chemical, and thermal properties which are well suited for an external window.

Theoretical Considerations

The absorption spectrum of ZnSe (CVD) in the 500-1000 cm^{-1} range is shown in figure 6. The solid curves are experimental, and the dashed line is the result of preliminary calculations. A variant of the non-interacting cell approach has been used [22] in which full phonon spectral properties have been retained, but multicell dynamic interactions have been neglected. All k-selection rules have been suppressed, and only linear moments are included. One multiplicative parameter was adjusted to make the theoretical and experimental curve coincide at one frequency. The calculated rate of decrease in absorption with increasing frequency is too rapid at the higher frequencies, but it should be noted that the experimental curve was determined from a sample with somewhat high absorption. Recently, we have acquired a lower absorbing sample. The result of a calorimetric measurement at 10.6 μm (943 cm^{-1}) on this sample has been indicated on figure 6, and it is much closer to the calculated curve. It is also possible that by

including nonlinear moments the calculated absorption might become somewhat enhanced.

Conclusion

A study has been made of the absorption properties of a variety of potential window materials suitable for the mid IR region. It was found that both bulk and surface absorption were generally higher than expected and that at the HF laser frequency in particular, surface absorption was dominant in several materials. A preliminary attempt to calculate the absorption level in ZnSe from first principles has yielded encouraging results which account for various trends observed experimentally.

References

[1] "Conference on High Power IR Laser Window Materials, 27-28 Oct. 1971", edited by C. S. Sahagian and C. A. Pitha. AFCRL-71-0592, Spec. Rep. No. 127, (AFCRL, Bedford, Mass.).

[2] "Conference on High Power IR Laser Window Materials, 30-31 Oct, 1 Nov. 1972", edited by C. A. Pitha. AFCRL-TR-73-0372, Spec. Rep. No. 162, (AFCRL, Bedford, Mass.).

[3] "Third Conference on High Power IR Laser Window Materials, 12-14 Nov. 1973", edited by C. A. Pitha and B. Bendow. AFCRL-TR-74-0085, Spec. Rep. No. 174, (AFCRL, Bedford, Mass.).

[4] "Proc. of the Fourth Annual Conf. on IR Laser Window Materials", compiled by C. R. Andrews and C. L. Strecker. AFML-TR-75-9. (AFML, Wright-Patterson AFB, Ohio)

[5] "Proc. of the Fifth Annual Conf. on IR Laser Windows Materials", compiled by C. R. Andrews and C. L. Strecker. (AFML, Wright-Patterson AFB, Ohio).

[6] A listing of many of these measurements can be found in "Infrared Laser Window Materials Property Data for ZnSe, KCl, NaCl, CaF_2, SrF_2 and BaF_2", by S. Dickinson, AFCRL-TR-75-0318, Phys. Sc. Res. Paper No. 635 (AFCRL, Bedford, Mass.).

[7] J. Harrington, D. Gregory, and W. Otto, in Ref. 5 p. 871 (1975).

[8] M. Hass, J. A. Harrington, D. A. Gregory, and J. W. Davisson, Appl. Phys. Lett. 28, 610 (1976).

[9] For a review see L. H. Skolnik in "Optical Properties of Highly Transparent Solids", edited by S. S. Mitra and B. Bendow, p. 405, (Plenum Press, New York, N.Y., 1975).

[10] A. Hordvik and H. Schlossberg, J. Opt. Soc. Am. 65, 1165 (1975).

[11] A. Hordvik and H. Schlossberg, in [5], p. 639.

[12] A. Hordvik and H. Schlossberg, to be published in Applied Optics.

[13] A. Hordvik, to be presented at the OSA 1976 Annual Meeting, 18-22 Oct. 1976, Tucson, Ariz.

[14] We are grateful to Mr. Donadio of Raytheon for providing us with this sample.

[15] T. F. Deutsch, J. Phys. Chem. Solids 34, 2091 (1973).

[16] T. C. McGill in "Optical Properties of Highly Transparent Solids", edited by S. S. Mitra and B. Bendow, p. 3 (Plenum Press, New York, N.Y., 1975).

[17] T. F. Deutsch, [3], p. 13.

[18] P. H. Klein, paper presented at Infrared Laser Window Materials Meeting, Boulder, Col., 12 July 1976.

[19] B. Bendow and P. D. Gianino, Appl. Opt. 12, 710 (1973).

[20] P. Miles in [5], p. 8.

[21] C. S. Sahagian, C. A. Pitha, "Compending on High Power IR Laser Window Materials", AFCRL-72-0170, Spec. Report No. 135 (AFCRL, Bedford, Mass. 1972).

[22] B. Bendow, S. P. Yukon and S. C. Ying, Phys. Rev. B10, 2286 (1974).

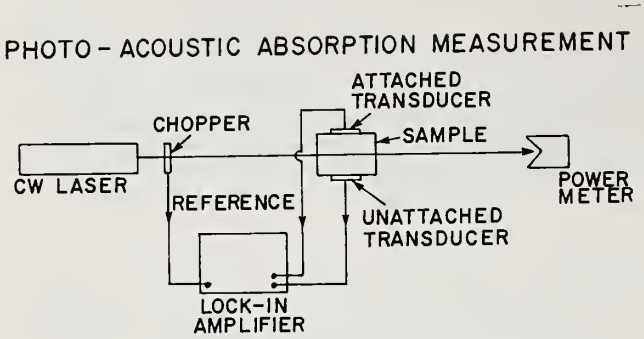

Figure 1. Schematic of the experimental arrangement for the photoacoustic absorption measurements.

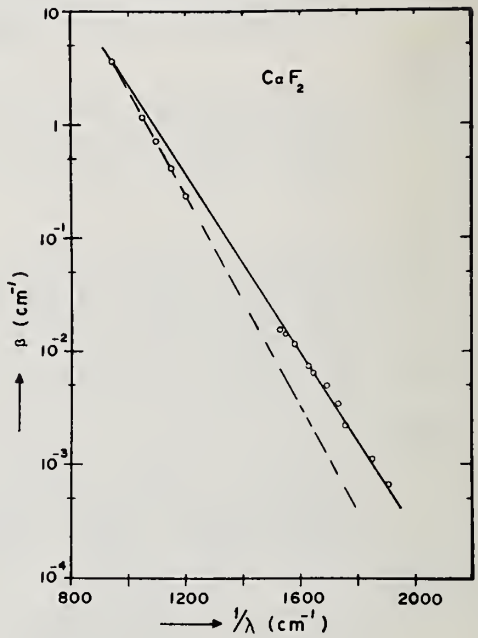

Figure 2. Bulk absorption coefficient versus wavenumber for $Sr F_2$.

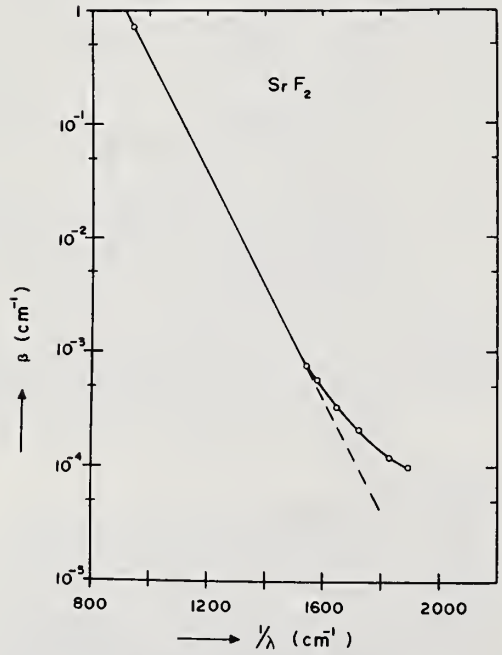

Figure 3. Bulk absorption coefficient versus wavenumber for SrF_2.

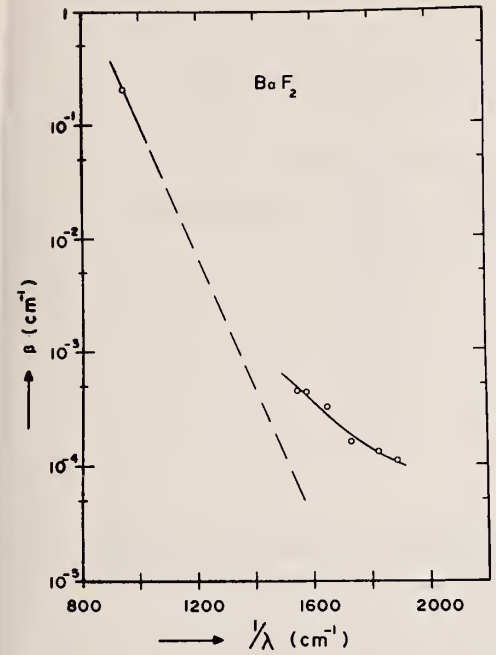

Figure 4. Bulk absorption coefficient versus wavenumber for BaF_2.

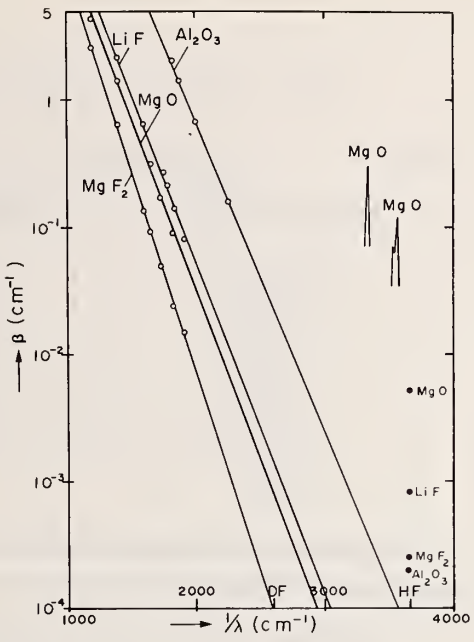

Figure 5. Bulk absorption coefficient versus wavenumber for MgO, MgF_2, Al_2O_3, and LiF.

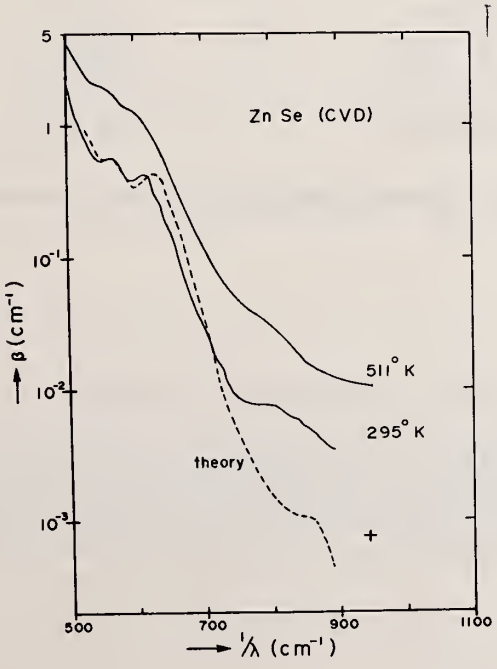

Figure 6. Bulk absorption spectrum for ZnSe. The fully drawn curves are experimental. The dashed curve is theoretical. The point marked (+) is a calorimetric measurement at 10.6 μm.

Table 1. Bulk and surface absorption of CaF_2, SrF_2 and BaF_2

CaF_2

Wavelength (μm)	Bulk abs. (cm^{-1})	Abs. per surface
10.6	3.60	-
6.546	1.5×10^{-2}	-
6.466	1.4×10^{-2}	-
6.330	1.2×10^{-2}	2×10^{-3}
6.137	7.3×10^{-3}	-
6.085	6.3×10^{-3}	-
5.906	4.9×10^{-3}	-
5.782	3.4×10^{-3}	6×10^{-4}
5.700	2.2×10^{-3}	-
5.424	1.1×10^{-3}	-
5.257	6.7×10^{-4}	-

SrF_2

Wavelength (μm)	Bulk abs. (cm^{-1})	Abs. per surface
10.6	0.71	-
6.466	7.4×10^{-4}	3×10^{-3}
6.330	5.7×10^{-4}	3×10^{-3}
6.058	3.2×10^{-4}	9×10^{-4}
5.782	2.1×10^{-4}	7×10^{-4}
5.488	1.2×10^{-4}	8×10^{-5}
5.280	9.8×10^{-5}	9×10^{-5}

BaF_2

Wavelength (μm)	Bulk abs. (cm^{-1}	Abs. per surface
10.6	0.21	-
6.466	4.4×10^{-4}	1×10^{-3}
6.330	4.3×10^{-4}	1×10^{-3}
6.058	3.2×10^{-4}	5×10^{-4}
5.782	1.6×10^{-4}	5×10^{-4}
5.488	1.3×10^{-4}	6×10^{-5}
5.280	1.1×10^{-4}	5×10^{-5}

Table 2. Absorption at HF laser wavelength

Material	Bulk (cm^{-1})	Surface
MgO	5.2×10^{-3}	9×10^{-4}
LiF	8.3×10^{-4}	3×10^{-4}
ZnSe	5.8×10^{-4}	1×10^{-3}
BaF_2	3.0×10^{-4}	4×10^{-4}
SrF_2	2.7×10^{-4}	6×10^{-4}
MgF_2	2.5×10^{-4}	1×10^{-3}
Al_2O_2	2×10^{-4}	2.4×10^{-3}
CaF_2	1.9×10^{-4}	5×10^{-4}

Table 3. Figure of merit at HF*

	CW		Pulsed	
Material	Total	Bulk	Total	Bulk
ZnSe	1	3.1	1	3.1
MgO	1.2	1.4	2.3	2.7
LiF	2.2	2.9	17.5	24
Al_2O_3	4.7	61	7.8	100
MgF_2	10.6	53	55	280
CaF_2	21	75	78	278
SrF_2	37	117	126	420
BaF_2	192	416	685	1420

* All values normalized to the ZnSe figure of merit

COMMENTS ON PAPER BY HORDVIK, BENDOW, LIPSON, SKOLNIK, AND BROWN

Several points regarding the experimental apparatus were clarified in discussion. The speaker mentioned that the photoacoustic measurement was carried out in a range where the photoacoustic signal was simply proportional to the chopping frequency (low frequencies). It was suggested that better coupling might ensue if the acoustic signal in the sample was coupled through the surrounding gas rather than contacting the transducer directly to the sample. The speaker estimated that the sensitivity of the present method should enable the measurement of absorptions as low as 10^{-6} cm^{-1}.

1.7 EFFECT OF TEMPERATURE AND STRESS ON THE REFRACTIVE INDEX OF WINDOW MATERIALS*

Albert Feldman, Deane Horowitz and Roy M. Waxler
National Bureau of Standards
Washington, D. C. 20234

Windows subjected to high average power laser radiation experience a rise in temperature due to residual absorption. The temperature distribution, which is non-uniform, will distort the wavefront of the beam. The distortion results both from changes of refractive index with temperature and from changes of refractive index with stress induced by the temperature gradients. We are presently measuring dn/dT and the photoelastic constants of laser window materials at 632.8 nm, 1.15 μm, 3.39 μm, and 10.6 μm. Two new experimental arrangements have been constructed. The first permits measuring dn/dT and thermal expansion from -180 °C to +200 °C. The second is a highly stable and sensitive interferometer for measuring photoelastic constants in the visible, the near infrared, and the near ultraviolet. Thermal expansion data are obtained on CVD ZnSe, CaF_2 and BaF_2 between -100 °C and +120 °C and fitted to a third degree polynominal in temperature. We obtain dn/dT for CVD ZnSe at 632.8 nm over the same temperature range. The piezo-optic constants of fused silica and CVD ZnSe obtained with the new interferometer at 632.8 nm are in excellent agreement with values obtained by other methods.

Key words: BaF_2; CaF_2; fused silica; interferometry; photoelasticity; piezo-optic constants; thermal coefficient of refractive index; thermal expansion coefficient; ZnSe.

Introduction

When high-power radiation propogates through a laser window the residual absorption causes a temperature rise in the window. The temperature distribution in the window is, in general, non-uniform and hence will distort the wavefront of the beam. This distortion arises from three sources: the direct change of the refractive index due to a change in temperature; the change of optic path due to a change of thickness with temperature; and the change of refractive index due to stresses induced by thermal gradients. If the distortion is sufficiently severe, the laser window becomes unusable [1][1]. In order to predict the distortion of a laser beam wavefront from the laser energy deposited in a window, one requires certain material parameters. These parameters include absorption coefficient, refractive index, n, change of refractive index with temperature, dn/dT, the piezo-optic constants, q_{ij}, thermal expansion coefficients, α, and elastic constants, S_{ij} or c_{ij} [1]. It is the purpose of the Optical Materials Characterization Program at the National Bureau of Standards to measure n, dn/dT, q_{ij}, α, and if necessary S_{ij} [2].

In this paper we describe two new apparatuses constructed under this program. The first apparatus consists of a cryogenically cooled furnace that permits us to measure α and dn/dT interferometrically from -180 °C to +200 °C. The second apparatus consists of a polarizing interferometer that is capable of measuring fringe shifts to within a precision of λ/500 at 632.8 nm. This precision is useful for measuring the piezo-optic constants of materials at low stresses. The use of the interferometer is limited in the ultraviolet by the cutoff of calcite which is at about 300 nm, and in the infrared by the useful range of the Soleil-Babinet compensator which is at about 1.15 μm. The Soleil-Babinet compensator is used for measuring fringe shifts.

We present data obtained with the two new instruments. We have measured the photoelastic constants of chemical vapor deposited (CVD) ZnSe and fused silica and found excellent agreement with previously reported values [3,4,5]. We have measured the linear expansion coefficient of CVD ZnSe, CaF_2, and BaF_2 from -100 °C to +120 °C and the data were fitted to a third degree power expansion in temperature. The fit for CaF_2 and BaF_2 agrees with available published data to within about 1% [6]. There was a slightly poorer agreement of our fit for CVD ZnSe to single crystal values of ZnSe [7], however, the observed difference is not necessarily significant because of the different materials measured. We have also measured dn/dT of CVD ZnSe at 632.8 nm and have found a value 2% smaller than our previously reported value [8]. We attribute this difference to our improved measurement technique; however, our value differs significantly from Mukai et al. [9].

---

*Research supported in part by Defense Advanced Research Projects Agency.

[1]Figures in brackets indicate the literature references at the end of this paper.

For brevity we do not discuss the phenomenological theory of photoelasticity, because this theory has been described adequately in the literature [10].

Apparatus and Experimental Method

The thermal expansion coefficient and dn/dT are measured by the method of Fizeau interferometry. The general method for making these measurements has been described in the literature [11].

To measure thermal expansion we measure as a function of temperature the shift of Fizeau fringes between two optical flats separated by the specimen. To measure dn/dT we measure as a function of temperature the shift of Fizeau fringes formed from reflections from the front and back surfaces of a specimen polished plane parallel. We have constructed a compact apparatus for obtaining α and dn/dT from -180 °C to +200 °C. A schematic of the apparatus is shown in figure 1.

The furnace is constructed from a cylinder of copper 37 mm in diameter by 75 mm high with walls 6 mm thick to permit rapid transfer of heat. A commercial band heater, which is clamped around the furnace, generates 175 W with an input of 120 VAC.

The furnace rests at the bottom of an evacuable chamber 100 mm in diameter by 150 mm tall. Protruding from the bottom is a copper rod, 12 mm in diameter by 150 mm long, that conducts heat away from the furnace to the liquid nitrogen reservoir. Thus, we can stabilize the temperature in the furnace at an arbitrary point by balancing the heat input from the heater with the heat leak to the liquid nitrogen.

The specimen rests within the furnace over a depression that is milled at an angle of 1° with respect to the furnace axis in order to deflect laser beam reflections to the side. Holes are drilled at several locations within the furnace to allow placement of thermocouples in contact with the specimen and to allow the pressure within the furnace to equalize with the pressure outside the furnace. Two thermocouples measure the temperature at the top and at the bottom of the specimen. A copper cover with a window allows access of laser radiation to the specimen in the furnace while maintaining a uniform thermal environment around the specimen. All windows in the system are tilted at a 1° angle to eliminate unwanted reflections.

We find that the system operates well when filled with a helium exchange gas of several millimeters pressure. The helium environment has several advantages over air or vacuum. During cooldown, products in the air condense on the system optics and hence interfere with the laser beam. With vacuum, the thermal response of the system is sluggish because of poor heat transfer between the furnace, the heat leak, and the specimen. In addition, there is a large temperature difference between the two thermocouples. With the helium present, the maximum temperature differential measured with the two thermocouples across a 12 mm thick specimen is less than 1 K at a given temperature.

The procedure used for measuring dn/dT or α consists of first cooling the specimen to approximately liquid nitrogen temperature. Sufficient time is allowed for the two thermocouple readings to agree to within 1 K. The furnace is then heated very slowly until a fringe minimum is observed on a strip chart recorder monitoring the Fizeau fringe intensity. The temperature is then recorded. Subsequently, the furnace is heated rapidly and after a convenient number of fringes has been observed, power to the furnace is cut back to allow the thermocouple readings to equilibrate while the temperature is slowly rising. At a fringe minimum, the temperature is recorded. The heating process is repeated until the maximum desired temperature is achieved.

The fringe counts and their corresponding temperatures are punched onto computer tape and the fringe count, ΔN is then obtained as a power series expansion of the temperature by computer. For thermal expansion measurements, we obtain an expression for the relative incremental thickness change of the specimen

$$\frac{\Delta t}{t_o} = A_1 T + A_2 T^2 + A_3 T^3 \qquad (1)$$

where t_o is the specimen length at room temperature, Δt is the incremental length, and A_1, A_2, A_3 are the expansion parameters. The derivative of eq. (1) with respect to T gives α.

We obtain dn/dT by calculating first the incremental change of refractive index Δn as a function of temperature with the formula

$$\Delta n = \left(\frac{\Delta N \lambda}{2t_o} - n_o \frac{\Delta t}{t_o}\right)\left(1 + \frac{\Delta t}{t_o}\right)^{-1} \qquad (2)$$

where n_o is the room temperature refractive index and ΔN and $\Delta t/t_o$ are representations of power series in temperature. The slope of the curve gives dn/dT, which we tabulate at a variety of temperatures.

The polarizing interferometer we have constructed for measuring piezo-optical constants is shown in figure 2. This interferometer is based on a design by Dyson [12], which was further modified by Green [13] for measuring thermal expansion and dn/dT. Our design, which is a slight modification of Green's, is capable of measuring fringe shifts to within a precision of $\lambda/500$ at 632.8 nm. The modification involves a change of position of the quarter wave plate within the interferometer.

The output of a helium-neon laser is propogated through a Glan-Thompson polarizer and is focused into a Wollaston prism. The prism splits the beam into two orthogonally polarized beams. The intensities of the two beams are balanced by a rotation of the polarizer. The beams are then collimated and made parallel to each other by passing through a second lens. The outer beam is intercepted by the specimen. Both beams are now brought to a focus at a rear mirror after propogating through a quarter wave plate. The two beams then return through the system; the central beam retraces its path while the outer beam propogates along the opposite side of the interferometer. Double passage through the quarter wave plate interchanges the states of polarization of the two beams. Thus, when the two beams are rejoined at the Wollaston prism, they exit as a combined beam at an angle with respect to the incident beam. A spatial filter and beam expander are placed in the exit beam to eliminate spurious laser radiation. A Soleil-Babinet compensator and a second Glan-Thompson prism are then used to analyze the state of polarization of the exit beam. The output fringe patterns are observed with a silicon matrix vidicon camera and a television monitor.

This interferometer has several advantages over conventional Twyman-Green interferometers: It is highly stable with respect to motion of system elements because both beams traverse the same optics, hence the optic path changes in both arms tend to be equal. In addition, the close proximity of the arms minimizes the effect of thermal currents, which are further reduced by placement of a cover over the interferometer part of the apparatus. Moreover, the fringe shifts are analyzed with ellipsometric techniques which have great inherent precision.

At the position of the specimen shown in figure 1, the radiation is polarized in the horizontal plane, hence, the fringe shift per unit applied uniaxial stress, $\Delta N/\Delta P$, for an isotropic material will depend on the piezo-optic constant q_{12}. If we shift the specimen to the outer return beam, where the radiation is vertically polarized, the fringe shift will depend on q_{11}. The expression for the piezo-optic constant is

$$q = \frac{2}{n^3}\left(\frac{\lambda}{t_o}\frac{\Delta N}{\Delta P} + (n-1)\, S_{12}\right) \qquad (3)$$

where $q = q_{11}$ for vertical polarization, $q = q_{12}$ for horizontal polarization, λ is the wavelength of the radiation and S_{12} is the elastic compliance component. In this equation t_o lacks a factor of two present in the equation for the Twyman-Green interferometer because the modified Dyson interferometer is used only as a single pass instrument.

Sample preparation and the method of applying stress have been described in the literature and so will not be discussed here [14]. The direction of stress is always vertical.

Results

In table 1, we list the thermal expansion parameters (eq. 1) of CVD ZnSe that we have obtained with seven runs on three specimens. The bottom row gives a statistically weighted average of the coefficients and the errors are the standard deviation of the mean. These values permit us to calculate the linear thermal expansion coefficient between -100 °C and +120 °C. These coefficients differ from our earlier reported values [8], however, we believe our present values are better because of our improved experimental technique. The thermal expansion coefficients calculated with these parameters are slightly higher than values obtained by Novikova [7], however, the type of material we have used differs from that used by Novikova. Moreover, Zhdanova and Sergeev report that the thermal expansion coefficient of ZnSe varies with free carrier and impurity content [15].

In table 2, we list the thermal expansion parameters we have obtained for CaF_2 and BaF_2 between -100 °C and +120 °C. When these parameters are used to calculate α, we find agreement within about 1% with values published in the literature [6].

The expressions we have obtained for the thermal expansion facilitate our measurement of dn/dT by the interferometric method. In table 3, we list the values of dn/dT we have obtained for CVD ZnSe at 632.8 nm from -100 °C to +120 °C. The value we obtain at 25 °C is $1.06 \times 10^{-4}\ K^{-1}$ which is 2% smaller than our previously reported values. We attribute this difference to an improvement of our measurement technique; however, we cannot explain the discrepancy of our value with that of Mukai et al. [9].

The piezo-optic constants of fused silica and CVD ZnSe have been measured at 632.8 nm with the modified Dyson interferometer. The results obtained for fused silica, given in table 4, agree extremely well with those of Primak and Post [5]. The standard deviation we give in the table represents the deviation from a linear least squares fit of optic path change as a function of stress. The actual accuracy is not as good because of possible systematic errors in the system, but these we believe to be less than 2%. Such systematic errors would include stress gradients.

The results we have obtained for CVD ZnSe are given in table 5. The agreement obtained with our previously reported values [3] is remarkably good, where the errors in the table are attributed mainly to the uncertainty in S_{12}. The data also agree, within experimental error, with the results of Goldstein et al. [4].

Acknowledgment

We thank the Raytheon Company for the CVD ZnSe.

References

[1] Sparks, M., J. Appl. Phys. 42, 5029 (1971); Jasperse, J. R., and Gianino, P. D., J. Appl. Phys. 43, 1686 (1972); Bendow, B., and Gianino, P. D., Applied Physics 2, 1 (1973); Bendow, B., Gianino, P. D., Hordvik, A., and Skolnik, L. H., Optics Comm. 7, 219 (1973).

[2] Feldman, A., Malitson, I., Horowitz, D., Waxler, R. M., and Dodge, M., in *Laser Induced Damage in Optical Materials*, edited by A. J. Glass and A. H. Guenther, National Bureau of Standards Special Publication 414 (1974) pp. 141.

[3] Feldman, A., Waxler, R. M., and Horowitz, D., in *Optical Properties of Highly Transparent Solids*, edited by S. S. Mitra and B. Bendow (Plenum Publishing Corp., N.Y., 1975) pp. 517.

[4] Goldstein, L. F., Thompson, J. S., Schroeder, J. B., and Slattery, J. E., Applied Optics 14, 2432 (1975).

[5] Primak, W., and Post, D. J., J. Appl. Phys. 30, 779 (1959).

[6] Baily, A. C., and Yates, B., Proc. Phys. Soc. 91, 390 (1967); Sharma, S. S., Proc. Indian Acad. Sci. A31, 261 (1950).

[7] Novikova, S. I., Soviet Physics-Solid State 3, 129 (1961) [Fizika Teverdogo-Tela 3, 178 (1961)].

[8] Feldman, A., Malitson, I. H., Horowitz, D., Waxler, R. M., and Dodge, M., in *Proceedings of the 4th Annual Conference on Infrared Laser Window Materials*, (1974) pp. 117.

[9] Mukai, H., Krok, P., Kepple, G., Harris, R., and Johnston, G., in *Proceedings of the Fifth Conference on Infrared Laser Window Materials* (1975) pp. 225.

[10] Nye, J. F., in *Physical Properties of Crystals* (Oxford University Press, London, 1957) pp. 243-254.

[11] Waxler, R. M., Cleek, G. W., Malitson, I. H., Dodge, M. J., and Hahn, T. A., J. Res. Nat. Bur. Stand. (U.S.) 75A, 163 (1971).

[12] Dyson, J., *Interferometry as a Measuring Tool* (The Machinery Publishing Co., Ltd., Brighton, 1970).

[13] Green, F., in *Optical Instruments and Techniques, 1969*, edited by J. H. Dickson (Oriel Press Limited, New Castle upon Tyne, England, 1970) pp. 189-198.

[14] Feldman, A., and McKean, W. J., Rev. Sci. Instrum. 46, 1588 (1975).

[15] Zhdanova, V. V., and Sergeev, V. P., Soviet Physics-Solid State 14, 1859 (1973) [Fizika Tverdogo Tela 14, 2153 (1972)].

Figures

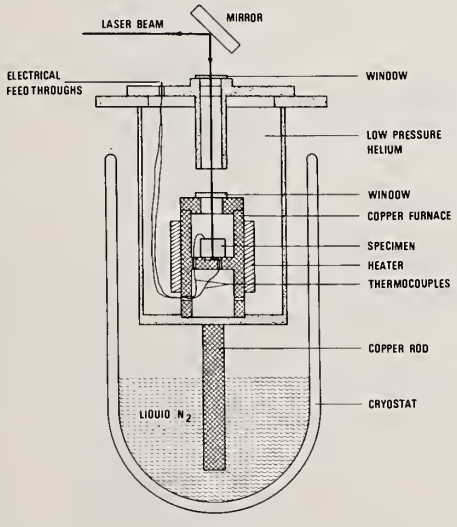

Figure 1. Cryogenically cooled furnace for measuring thermal expansion and change of refractive index with temperature. The specimen shown is for dn/dT.

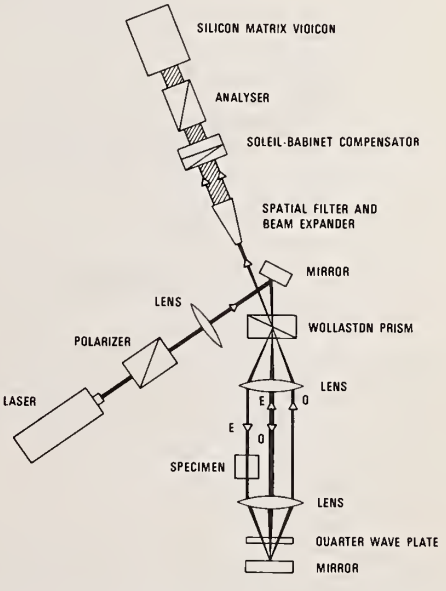

Figure 2. Modified Dyson interferometer for measuring piezo-optic constants.

Table 1. Tabulation of expansion parameters of CVD ZnSe for
$-100\ °C < T < +120\ °C$

$$\Delta t/t_o = A_1 T + A_2 T^2 + A_3 T^3$$

Run #	Specimen #	$A_1 (10^{-6}\ K^{-1})$	$A_2 (10^{-9}\ K^{-2})$	$A_3 (10^{-11}\ K^{-3})$
1	1	7.23 ±.08	5.24 ±.31	-1.40 ±.30
2	1	7.35 ±.03	4.62 ±.16	-1.67 ±.15
3	1	7.33 ±.05	4.80 ±.17	-1.47 ±.22
4	1	7.23 ±.04	5.19 ±.17	-1.26 ±.17
5	2	7.24 ±.05	5.51 ±.25	-1.53 ±.22
6	3	7.28 ±.04	5.94 ±.13	-1.44 ±.13
7	3	7.30 ±.04	5.27 ±.15	-1.34 ±.16
Weighted Average		7.29 ±.02	5.26 ±.17	-1.45 ±.07

Errors are the standard deviation of the mean.

Table 2. Expansion parameters of CaF_2 and BaF_2 for
$-100\ °C < T < +120°C$

$$\Delta t/t = A_1 T + A_2 T^2 + A_3 T^3$$

	$A_1 (10^{-6}\ K^{-1})$	$A_2 (10^{-9}\ K^{-2})$	$A_3 (10^{-11}\ K^{-3})$
CaF_2	18.4 ±.1	16.4 ±.3	-3.7 ±.3
BaF_2	18.1 ±.1	11.5 ±.3	-2.0 ±.3

Table 3. dn/dT of CVD ZnSe at 632.8 nm

Temperature	dn/dT (10^{-5} K^{-1})
-100	9.3
- 80	9.6
- 60	9.8
- 40	10.0
- 20	10.2
0	10.4
20	10.6
40	10.7
60	10.9
80	11.0
100	11.1
120	11.2

Table 4. Piezo-optic constants of fused silica at 632.8 nm

	Present Work	Primak and Post[a]
q_{11}	0.42 ±.002[b]	0.44
q_{12}	2.70 ±.006[b]	2.71

Units - 10^{-12} m^2/N

[a]Reference [5]

[b]Errors represent the standard deviation of the experimental data to a straight line least squares fit. Accuracy is believed to be within 2%.

Table 5. Piezo-optic constants of CVD ZnSe at 632.8 nm

	Present Work	Previous Work	
q_{11}	0.17 ±.04	0.17 ±.05[a]	0.22 ±.05[b]
q_{12}	-1.44 ±.04	-1.44 ±.04[a]	-1.48 ±.05[b]

Units - 10^{-12} m^2/N

[a]Reference [3]

[b]Reference [4]

COMMENTS ON PAPER BY FELDMAN, HOROWITZ, AND WAXLER

No discussion.

1.8 REFRACTIVE INDEX AND TEMPERATURE COEFFICIENT OF REFRACTIVE INDEX OF HOT-FORGED CALCIUM FLUORIDE*

Marilyn J. Dodge
Optical Physics Division, Institute for Basic Standards, National Bureau of Standards
Washington, D.C. 20234

The refractive index of a sample of hot-forged CaF_2 was measured from 0.25 μm to 8.0 μm by means of the minimum-deviation method on a precision spectrometer. Data were obtained near 21°C and 34°C. Each data set was fitted to a three-term Sellmeier-type dispersion equation, which permits interpolation of refractive index as a function of wavelength within a few parts in 10^{-5}. Using the index values obtained at the two temperatures, the change in index with temperature, $\Delta n/\Delta T(^{o}C)^{-1}$ was calculated. The refractive index and $\Delta n/\Delta T(^{o}C)^{-1}$ values obtained for this specimen are compared with data previously published.

Key words: Calcium fluoride; refractive index; temperature coefficient of refractive index.

1. Introduction

Optical distortion as a result of temperature gradients can occur in transparent or semi-transparent components of high-power laser systems at powers below that which would be required to melt or fracture the component [1-2][1]. Knowledge of the refractive index, n, and temperature coefficient of refractive index, dn/dT of a candidate material to be used in a high-power laser system is necessary before the amount of optical distortion which might occur can be predicted. The study of these parameters is a part of an optical materials characterization program [3] which is currently in progress at NBS.

The increased use of high-power lasers in the 2-6 μm wavelength region has resulted in a need for improved transparent component materials to be used in large, high-resolution optical systems. Ideally, the materials should be stronger, exhibit less scatter, and have lower absorption coefficients than the materials which are currently available [4]. Hot forging of alkali halides and alkaline-earth fluorides is one fabrication technique being developed to achieve these goals. Alkaline-earth fluorides are the materials of choice for use in the 2-6 μm range [5]. If the new manufacturing technique does induce changes in the optical absorption of these materials, corresponding changes in the refractive index and dn/dT would also be expected from dispersion theory [6] and need to be determined.

John R. Fenter of the Air Force Materials Laboratory provided a large finished prism of hot-forged CaF_2 manufactured by Harshaw Chemical Corp.[2]. This specimen has a refracting angle near 60°, with one polished face about 4 cm x 5 cm and the other polished face about 4 cm x 6.5 cm. Unlike the synthetic single crystal CaF_2 which is commercially available, the new material is polycrystalline.

The index of refraction was determined by means of the minimum-deviation method using a precision spectrometer shown schematically in figure 1[7]. From the ultraviolet to 2.0 μm, the index was determined at known emission wavelengths of mercury, cadmium, helium, and zinc. Beyond 2 μm, a glo-bar was used for the radiant-energy source, and measurements were made at known absorption bands of water, carbon dioxide, polystyrene and 1,2-4 trichlorobenzene. A series of narrow-band interference filters was also used between 3.5 μm and 6.5 μm. A thermocouple with a cesium iodide window was used for the detector. The scale of this spectrometer can be read to 1.0 second of arc. The accuracy of this scale permits the determination of the refractive index of good optical quality material to within 2×10^{-5} over a wide wavelength range.

---

*This work was supported in part by the Defense Advanced Research Projects Agency.

1. Figures in brackets indicate the literature references at the end of this paper.

2. The use of company and brand names in this paper are for identification purposes only and in no case does it imply recommendation or endorsement by the National Bureau of Standards, and it does not imply that the materials used in this study are necessarily the best available.

The index was determined from 0.2483 to 8.03 μm and at average controlled room temperatures of 20.8°C and 33.6°C. Each set of experimental data was fitted to a three-term Sellmeier-type dispersion equation [8] of the form $n^2-1 = \Sigma[A_j\lambda^2/(\lambda^2-\lambda_j^2)]$. The index of refraction is represented by n, λ is the wavelength of interest, the λ_j's are the calculated wavelengths of maximum absorption and the A_j's are the calculated oscillator strengths corresponding to the absorption bands. The λ_j's and A_j's are not intended to have any physical significance. Primary emphasis is given to procuring a mathematical fit of the measured data useful for interpolation.

2. Index Data

The constants calculated for each dispersion equation, the number of wavelengths fitted and the average absolute residual (the average difference between the experimental values and the calculated values) are given in table 1.

Table 1: Constants for Dispersion Equations

Constant	20.8°C	33.6°C
A_1	0.98584551	0.97066991
A_2	0.05290246	0.06792205
A_3	4.2816899	4.1634415
λ_1	0.07218116	0.07115659
λ_2	0.14114719	0.13670627
λ_3	36.465937	35.984292
No. of Wavelengths	69	47
Average Absolute residual of index x 10^5	1.9	1.9

It should be emphasized that these constants refer specifically to this sample of hot-forged CaF_2, at the stated temperatures, and should be used for interpolation only within the wavelength range of the experimental data, or approximately 0.25 to 8.0 μm. The average absolute residual is an indication of the overall accuracy of the experimental data. Generally, the largest residuals were in the IR beyond 5 μm, where 35 strong atmospheric absorption bands existed between 5.0 and 7.3 μm. Because of the large size of the prism and the apparent excellent quality of the material, these bands were sharp and the minimum was easily determined. Therefore, the index determinations are not considered to be any less accurate than in the UV or near IR. The wavelengths of these atmospheric bands were assigned from values in the literature [9,10]. The uncertainties in the wavelength values would be difficult to define due to differences in the laboratory conditions and the existence of many weak bands which could affect the wavelengths of nearby strong bands. An error of 0.1% in wavelength would result in an index residual of 9×10^{-5} in this particular sample.

The refractive index was calculated at regular wavelength intervals for each temperature using the appropriate fitted parameters. The results of the 20.8°C data are plotted as a function of wavelength in figure 2.

The index values obtained for this specimen are compared in figure 3 with those obtained by I. H. Malitson on single crystal CaF_2[11]. The single crystal data is represented by the "zero" line. The differences reach a minimum between 0.7 and 0.9 μm where the hot-forged CaF_2 is only -0.5×10^{-5} less than the single crystal. A maximum difference of -6.6×10^{-5} between the two types of CaF_2 exists at 0.28 μm and 4.8 μm. The index variance at 0.28 μm is probably the result of a weak absorption band near 0.3 μm. The Harshaw catalog [12] shows transmission runs for two grades of CaF_2, the UV grade in which this band does not appear, and the optical grade, sold for use in IR components, in which the band does exist. Assuming this band did not exist in the single crystal studied previously, the differences in index would become more negative, reaching the maximum Δn, then receding as the index of the new CaF_2 approaches that of the single crystal in the red region of the spectrum.

The maximum magnitude of Δn at 4.8 μm is not as easily explained. The absorption bands and interference filter used for index measurements between 4 and 5 μm generally yield low residuals in highly transmitting materials such as CaF_2 when fitted to the dispersion equation. The Sellmeier equation will fail completely in an area of strong absorption in the material, but will attempt to fit data through a region of weak absorption yielding larger residuals in the area of the band. In this study, the residuals between 4 and 5 μm were an order of magnitude higher than the ones immediately on either side of the region where they agreed well with the overall average of 1.9×10^{-5}. The Sellmeier fit called for higher wavelengths in this region, indicating that the experimental index values were lower than what would be expected in a region of normal dispersion. From dispersion theory, this could be an indication of a weak absorption band near 5 μm. There are indications of a weak absorption band in the 3-4 μm region of ionic crystals including fluorides [13]. Most absorption studies which have been made on the polycrystalline material have been done at the specific laser wavelengths of HF (2.7 μm), DF (3.8 μm) and CO (5.25 μm). To get a clear picture of the absorption characteristics in this area it would be necessary to run an absorption curve as a function of wavelength.

3. Temperature Coefficient of Index

The index values calculated using the fitted parameters at the two temperatures were used to determine $\Delta n/\Delta T(^{o}C)^{-1}$ as a function of wavelength and are indicated in figure 4 by the solid line. Also shown in this figure for comparison purposes, is the $\Delta n/\Delta T$ curve for the single crystal material referenced previously. Generally the hot-forged CaF_2 shows much smaller $\Delta n/\Delta T$ values than the single crystal. The maximum $\Delta n/\Delta T(^{o}C)^{-1}$ of the new material over the wavelength range studied is -4.5×10^{-6} between 0.5 and 0.6 μm, or a little less than half the $\Delta n/\Delta T(^{o}C)^{-1}$ reported for the single crystal in the same region. The ratio is about the same at 2 μm where $\Delta n/\Delta T(^{o}C)^{-1}$ of the hot-forged sample is a -3.9×10^{-6}, but at 6 μm $\Delta n/\Delta T$ of the polycrystalline material is only about a third of that given for the single crystal material, or a -2.2×10^{-6}. Beyond 6 μm, $\Delta n/\Delta T(^{o}C)^{-1}$ increases to a -4.3×10^{-6} at 8.0 μm. The negative $\Delta n/\Delta T$ indicates that the effect of thermal expansion on the change in refractive index is greater than the effect of the frequency contributions. Because of this, $\Delta n/\Delta T$ is expected to increase as either the ultraviolet or infrared limits of transmittance are approached [14]. The deviations from this expected behavior could be another indication of some type of absorption in the 5 μm region. The $\Delta n/\Delta T(^{o}C)^{-1}$ values which were calculated from the measured data are shown as data points in figure 4. The magnitude of the values between 3 and 4 μm increase to almost 1.5×10^{-6} higher than those calculated from the smoothed data, but then decrease to about 2×10^{-6} less than the smoothed values at about 4.5 μm, giving an anomalous appearance. The smoothed $\Delta n/\Delta T$ values are considered accurate within 1×10^{-6}. Other investigators have stated that when determining $\Delta n/\Delta T$ by the technique used in this study fourth decimal place accuracy in index is required to achieve a 10 percent accuracy in $\Delta n/\Delta T$[15].

4. Conclusions

This is the first detailed study of the refractive properties of hot-forged CaF_2. From the standpoint of the reduced temperature coefficient of refractive index, it appears that components fabricated from this material could produce less optical distortion then those made from synthetic single crystal CaF_2. However, since the hot-forged manufacturing technique is still in a stage of development and improvement, and in light of the refractive index anomaly which appeared in the 4 to 5 μm region of primary interest to laser systems designers, further studies on other samples of this material should be considered. It should not be assumed that the refractive properties of this sample are necessarily typical of what can be expected of future production runs of hot-forged CaF_2.

5. Acknowledgments

The author expresses sincere appreciation to Warren K. Gladden for his technical assistance in this study.

6. References

[1] Sparks, M., J. Appl. Phys. 42, 5029 (1971).

[2] Loomis, J. S. and Bernal, E. G., "Laser Induced Damage in Optical Materials: 1975," p. 126, NBS Special Publication 435, US Govt. Printing Office, Wash. (1976).

[3] Feldman, A., Malitson, I., Horowitz, D., Waxler, R. M. and Dodge, M., "Laser Induced Damage in Optical Materials: 1974," NBS Special Publication 414, p. 141, US Govt. Printing Office, Wash. (1974).

[4] Newberg, R. T., Readey, D. W., Newborn, H. A., and Miles, P. A., Proceedings, Fourth Annual Conference on Infrared Laser Window Materials, p. 445, AFML (Jan. 1975).

[5] I.B.I.D.

[6] Jenkins, F. A. and White, H. E., Fundamentals of Optics, 3rd ed. McGraw-Hill Book Company, Inc., 1957).

[7] Rodney, William S. and Spindler, Robert J., J. Res. Nat'l. Bur. Stds. (US), 51, 123, (1953).

[8] Sutton, Loyd E. and Stavroudis, Orestes N., J. Opt. Soc. Am. 51, 901 (1961).

[9] Downie, A. R., Magoon, M. C., Purcell, Thomasine and Crawford, Bryce Jr., J. Opt. Soc. Am. 43, 941 (1953).

[10] Benedict, W. S., Claassen, H. H. and Shaw, J. H., J. Res. NBS 49, 91 (1952).

[11] Malitson, I. H., Applied Optics 2, 1103 (1963).

[12] Harshaw Optical Crystals, The Harshaw Chemical Co., 22, (1967).

[13] Hass, Marvin, Proceedings, Fifth Annual Conference on Infrared Laser Window Materials p. 850, UDRI (Feb., 1976).

[14] Krishnan, R. S., Progress in Crystal Physics, Vol. 1, Ch V, p. 146 (Viswanathan, S. at the Central Art Press; Chetput, Madras 31, 1958).

[15] I.B.I.D., p. 144.

7. Figures

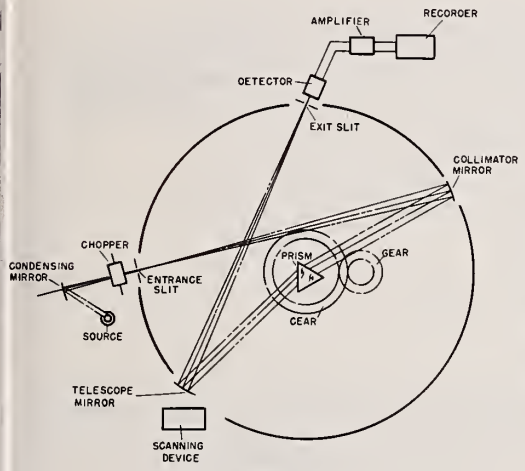

Figure 1. Schematic diagram of the modified Gaertner precision spectrometer showing optical path. The prism is rotated at one-half the rotation rate of the telescope assembly by gear system, thus maintaining the condition of minimum-deviation for any wavelength. The scanning device drives the assembly which scans the spectrum to identify lines or bands and determine their approximate scale positions.

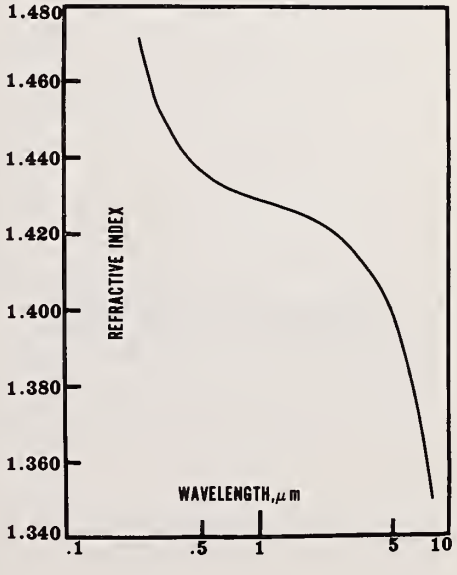

Figure 2. Refractive index of hot-forged CaF_2 as a function of wavelength (logarithmic scale). Data at 20.8°C were calculated from the dispersion equation of form $n^2-1 = \Sigma A_j\lambda^2/\lambda^2-\lambda_j^2)$.

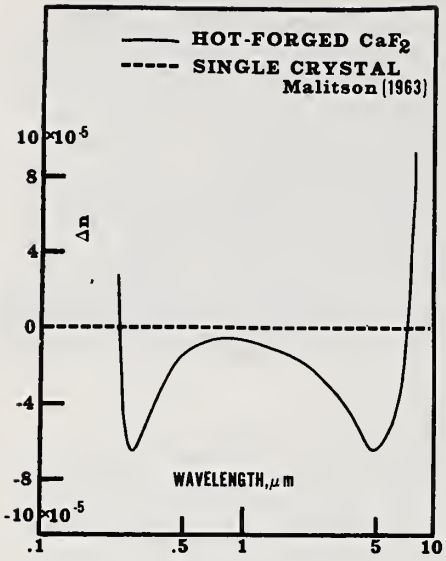

Figure 3. The differences in index of hot-forged CaF_2 from single crystal CaF_2 at 20.8°C as a function of wavelength (logarithmic scale). The index of the single crystal is represented by the zero line.

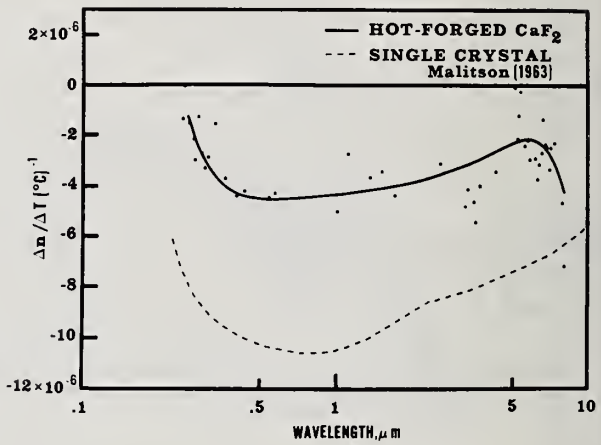

Figure 4. Temperature coefficient of index as a function of wavelength (logarithmic scale) of CaF_2. The solid line represents $\Delta n/\Delta T(°C)^{-1}$ calculated from the fitted values at 20.8°C and 33.6°C for the hot-forged CaF and the data points (x's) represent $\Delta n/\Delta T$ values calculated from the measured index values. The dashed line shows $\Delta n/\Delta T$ for single crystal CaF_2 from the literature.

COMMENTS ON PAPER BY DODGE

No discussion on this paper.

1.9 FABRICATION AND PROPERTIES OF LASER WINDOW MATERIALS*

R. M. Cannon, H. K. Bowen, A. M. Glaeser,
H. J. Mayson, F. A. McClintock, W. M. Sherry,
J. B. Vander Sande and M. F. Yan
Massachusetts Institute of Technology

Cambridge, Massachusetts 02139

In hot forged CaF_2, as in forged alkali halides, fine subgrains develop and the subgrain size varies inversely with the forging stress. Dynamic recrystallization is more of a problem than for KCl or KBr; it results in very coarse grained regions in which the subgrains are poorly developed. In alkali halides aliovalent impurities exert a significant drag on grain boundaries causing large reductions in grain boundary migration rates and significant retardation of recrystallization and grain growth. Theoretical results for the boundary mobility and for the conditions under which a boundary may escape from the segregated impurity cloud are presented.

Theory of the macroscopic fracture behavior resulting from failure by coalescence of subcritical cracks shows the extent of detectable precracking and the effects of biaxial stresses, specimen size, and the distribution of microstrengths. The ultimate strengths do not fit an extreme value distribution even if the microscopic strengths do; this makes statistical design more difficult and may necessitate proof testing or inspection. Flaw strength distribution curves can be determined from acoustic emission measurements during microhardness testing. Crack openings as small as 0.1μm have been nondestructively detected using scattered light. Better resolution is required for stronger materials for which crack openings as small as 0.01μm must be detected.

Key words: CaF_2; crack coalescence; flaw detection; flaw distribution; forging; grain boundary mobility; subgrains.

Introduction

In recent years, alkali halides have been forged both to shape them and to produce the strengthening necessary for use in high power laser windows. The desirable fine subgrain microstructures can be formed by forging under appropriate conditions of temperature and stress. However, it has been found, that impurities must be added in order to inhibit recrystallization and stabilize these microstructures [1][1]. Theory has been developed for the effects of impurities on grain boundary mobility and on the conditions under which boundaries can breakaway from the impurity cloud resulting in much faster rates of recrystallization [2]. The first part of this paper presents the results of similar experimental work on forging and substructure development in CaF_2 and summarizes some of the more recent results of the analysis of impurities on boundary mobility and breakaway during recrystallization.

The second part of the paper deals with the problem of designing with brittle ceramics in applications such as laser windows. It is often assumed, frequently without sufficient justification, that a simple analytical form can be used to describe the distribution of flaws, this simplifies the statistical design and prediction of size effects and probability of failure. This paper presents the results of some analytical models based on failure from coalescence of subcritical cracks in which the effects of specimen size and loading mode on the stress for initial cracking and for final failure are investigated. Finally, methods for determination of flaw distributions are presented. A partially destructive method involves indentation tests and acoustic emission monitoring from which complete distribution curves of flaw density can be determined. Nondestructive methods of detection of worst flaws by light scattering are also discussed.

* Work sponsored by ARPA and monitored by RADC/ET.

1. Figures in brackets indicate the literature references at the end of this paper.

Forging of CaF_2

Undoped single crystals of CaF_2 with random initial orientations have been forged within the temperature range of 475-1229°C. The samples were typically forged to 60% reduction by which time they had reached a steady state condition. The temperature dependence of the steady state flow stresses is shown in figure 1. For forging at temperatures greater than 1100°C oxide contamination was apparently a problem as manifest by a cloudy condition of the crystal and microstructural evidence of second phase precipitates which may have been calcium oxide. This occurred despite the reducing atmosphere which can be expected from forging in vacuum in a graphite die. For specimens which were hot ejected and air quenched in order to preserve the forging microstructure cracking frequently resulted from thermal shock; this could usually be eliminated by proper cooling. At temperatures below about 600°C there was evidence for cracking during forging usually starting as edge cracks, although nearly crackfree pieces could sometimes be obtained. Anderson, et al [3] reported that crack free specimens in this temperature range can be achieved by forging with an additional hydrostatic constraint to suppress fracture.

The microstructures generally exhibited subgrains resulting from recovery during forging as is shown in figures 2a and 2b. At the lowest forging temperature, 475°C, which is $0.45T_m$, the microstructures have a cellular pattern. The boundaries themselves are rather poorly resolved suggesting that at these temperatures the dislocations are not knit into tight subgrains, but perhaps are still better characterized as loose dislocation cell boundaries. At higher temperatures, the subgrain boundaries are much sharper, figure 2a. Examination by transmission electron microscopy, figures 3a and 3b, also indicated that at low temperature the subboundaries do not reach an equilibrated structure as is found at higher temperatures. Within these subgrains finer dislocation cells can often be seen as shown in figure 4. The subgrain boundaries have a low misorientation angle and the samples have a strong crystallographic texture.

The subgrain size varies inversely with the forging stress, figure 5, similar to that previously reported in forged KCl and KBr [1]. The data suggest that in CaF_2 a somewhat stronger σ stress dependence may result than the $d\alpha\sigma^{-1}$ dependences typically found after creep of metals and alkali halides.

Recrystallization

In many of the CaF_2 samples dynamic recrystallization occurred during forging, figure 6. Areas essentially free of subgrains or with poorly defined subgrain boundaries were observed in samples forged at temperatures as low as 580°C or about half the melting point. Apparently these are sub-boundaries in which the misorientation angle is much lower than in those cases in which recrystallization has not occurred. Similar behavior has been reported in KCl and KBr, but was not usually seen at temperatures below $0.8T_m$ for pure specimens and at even higher temperatures for doped crystals [1,2]. In CaF_2 forged at temperatures above 800°C and quenched to room temperature, the interior was frequently largely recrystallized and well developed subgrain deformation structures were only found around the edges.

This results from nucleation of new grains during forging which as they grow produce strain free regions in which the subgrain structure is largely removed. Sometimes these new grains grow until they impinge with other similar grains leaving occasional high angle boundaries within the crystal, whereas in other cases they apparently slow down and leave regions of essentially un-recrystallized material between the new grains. Within these strain free grains transient creep starts again and new substructures develop with continuing strain. The degree of development of the new subgrains depends on the amount of strain which has occurred between recrystallization and the end of forging.

In KCl the extent of recrystallization during forging or subsequent annealing is very sensitive to impurities due to the effect of impurity drag on grain boundary mobility and to the effect of impurities on nucleation [1,2]. The nucleation problem per se is currently not well understood. Very likely it does not involve discreet nucleation in the classical sense, but instead may result from the occasional development of a subgrain boundary of higher than average misorientation angle which has a higher mobility; it then acts as a nucleus and grows through the crystal rapidly leading to the strain free region. Thus the breakaway of a portion of the boundary or sub-boundary from the impurity cloud may be important in its formation as an nuclei.

Modeling of the effects of impurities on the steady state boundary mobility and on the process of breakaway of the boundary from the impurity cloud has been done particularly with emphasis on doped KCl [2]. Previously reported experimental work showed that there is a much greater drag force from divalent impurities than from

monovalent impurities; divalent materials such as Ca or Sr give greater drag at the 100 ppm dopant level than do Br or Rb at concentration levels of approximately 5% [1,2]. Consequently, calculations of the impurity segregation and the effect on the boundary mobility are based primarily on the electrostatic interaction. It has been found theoretically that the size misfit or any other interaction energies between the aliovalent impurities and the boundary are coupled to and modify the electrostatic effect in an important way, particularly at temperatures near the isoelectric temperature.

A calculation of the theoretical mobility vs reciprocal temperatures for Sr doped KCl is shown in figure 7. Those curves with the full line represent a set of calculations for one plausible functional dependence of the strain interaction energy which would be typical of Sr doped KCl. Those with the dashed line represent the results of the calculations for another plausible strain energy interaction. For both cases, the maximum interaction energy is presumed the same, and is calculated from the size misfit; the difference is in the functional dependence of the interaction energy on distance from the boundary. The results for either assumption show similar important characteristics. There are two solutions to the steady state impurity drag problem over much of the temperature range. At very low velocities typified by the lowest curves shown, the impurities drag along with the boundary and the concentration of impurity near the boundary, although somewhat less, is approximately equal to that for a static boundary. The highest mobilities shown are those which would result for a grain boundary which has broken away from its impurity cloud. This mobility is typically many orders of magnitude higher than that when the boundary is moving with its impurity cloud. The points represent experimental data obtained from discontinuous recrystallization in Sr doped KCl. Agreement is encouraging although not perfect at this time. Both the modified theory and the experimental results suggest that even at temperatures very near the isoelectric temperature, which for figure 7 is 444°C, the additional small strain energy interactions lead to coupled electrostatic interactions. This yields electric fields of changing sign near the boundary and distributions of the impurity concentration near the boundary which result in greater drag than would be predicted from purely electrostatic considerations. At temperatures well away from the isoelectric the calculated drag is similar to that based on purely electrostatic considerations.

At high temperatures, boundaries can move rapidly enough even when dragging the impurity cloud to give experimentially observable recrystallization rates although these rates may be much slower than those for pure samples. At low temperatures the boundary velocity when moving in the impurity drag region is much too slow to account for any observable grain growth. However, in KCl grain growth has been reported in pure specimens at temperatures as low as room temperature [2,4]. In these cases, the few ppm impurity which exist in available crystals would be sufficient to prevent recrystallization if the boundaries were constrained to move in the low velocity regime. The observed mobilities are frequently very high and are consistent with those to be expected for the high velocity intrinsic regime.

The question then is under what conditions does a boundary moving at very low velocities breakaway from its impurity cloud and move at much higher velocities? If the driving force is sufficiently high the low velocity regime will not be stable and boundaries will all be torn away from the impurity clouds and only the high velocity regime will be observable. As can be seen from the calculations both regimes are stable over wide ranges of conditions. The method of breakaway is thought to involve a spontaneous growth of small velocity fluctuations along the length of a boundary. Small fluctuations may of course occur for a boundary even if the driving force and impurity distribution are uniform. In the real case they will no doubt be accentuated by non-uniform distributions of impurity and of strain energy or sub-boundary energy.

The results previously discussed were for a 1-dimensional problem in which the boundary was assumed to remain planar. It can be extended by considering the conditions for unstable growth or decay of perturbations as compared to those for stable or spontaneous growth of perturbations of an infinitesimally fluctuating boundary [2b,5], as sketched schematically in figure 8. The instability results in part from convective motion of impurities which results because the local direction of migration is not exactly equal to the average direction for the entire boundary, and it is further effected by the ability of impurities to diffuse preferentially along grain boundaries. Finally it results from the fact that as the boundary velocity increases the steady state concentration of impurities decreases and so impurity should be evaporated from the boundary. An analysis which incorporates the first of these two features explicitly and only partially incorporates the last one by using the non-linear drag velocity relation calculated from the steady state, has been used to indicate the conditions under which an initially sinusoidal boundary would grow spontaneously. It is found that for wave lengths longer than the critical value, λ_c, any perturbations would grow, but smaller wavelength perturbations would

decay. The critical wavelength is

$$\lambda_c^2 = \frac{4\pi^2 D\gamma\alpha C_\infty}{F^2(1+\beta^2 V_o^2)}$$

where D is the impurity diffusivity parallel to the boundary, γ is the grain boundary energy, α is proportional to the impurity drag in the low velocity regime, C_∞ is the average dopant concentration, β is an additional parameter from the impurity drag theory which is equal to the drift velocity of impurity atoms across the boundary, and V_o is the nominal velocity. The critical wavelength increases with dopant level, but decreases strongly with applied driving force, F.

The behavior to be expected is shown schematically in figure 8. Similar effects have been seen in very irregular grains in KCl and are suggested in the isolated grain in CaF_2 in figure 5. It is thought that the growth of one of the perturbations into a bulge can eventually, by lateral expansion of that bulge, lead to an entire segment of a boundary shedding its impurity cloud and moving at high velocity.

To summarize, an analytical model has been developed to the extent that calculations of grain boundary mobility as a function of temperature or driving force can be done for divalent doped alkali halides. These results incorporate measured diffusional activation energies and impurity vacancy interaction energies and best estimates of the individual energies of formation of the two types of vacancies. The electrostatic calculations require no additional unspecified or arbitrary parameters. Strain calculations are based on the ion size misfit to give the maximum interaction energy and require an arbitrary assumption about the form of the strain function. Because of the dominance of the electrostatic requirements near the boundary the calculated mobilities apparently are not strongly dependent on the assumed form of the strain energy. Limited progress has been made in predicting the conditions under which a boundary can breakaway from the impurity cloud and migrate at high rates. This is thought, at least in some situations, to be an important part of the nucleation process for recrystallization.

Fracture by Crack Coalescence

As the fracture in brittle ceramic materials is statistical, proper design requires knowledge or control of the flaw distribution and of the crack dynamics in order to design adequate lifetimes or probability of failures. Techniques which have variously been considered include nondestructive evaluation to determine pre-existing flaws and flaw distributions, determinations of flaw distributions from strength or other destructive tests, proof test techniques to eliminate those specimens with particularly severe flaws and monitoring by acoustic emission in order to detect fracture prior to the critical failure. Frequently failure statistics considerations utilize an assumed extreme value function for the flaw or strength distributions, and then predict the size dependence and the probability of failure for a particular loading mode. However, an analytical model for crack propogation by coalescence as well as measurements of particular flaw distributions in materials with optical polished surfaces indicate that such an assumption is often inappropriate.

A numerical model [6] has been used to suggest assumptions for and to test approximate analytical solutions for the problem of calculating the effects of applied stress state and of part size on failure stress. A hexagonal net is assumed to represent grain boundaries and grain boundary strengths have been taken to satisfy an extreme value function. The part is loaded until the first weakest segment under the applied stress cracks. The stress distribution is recalculated to include the modification from this crack and the loading is increased until an additional segment cracks. This process is repeated until a critical crack is formed from coalescence of several fractures or from fracture ahead of a particular flaw which develops into a flaw that limits the load to a maximum.

Some typical results are shown in figures 9 and 10. The cracked segments are numbered in order of cracking. Those that cracked after a maximum load had been attained are denoted by dashed lines. Two different orientations were considered for the hexagonal array relative to the direction of the maximum principal component of applied stress, S_1. In the "vertex" orientation, one of the vertices of the hexagons is in the direction of maximum principal stress component; in the "face" orientation one of the faces of the hexagon is in that direction.

Approximate analytical solutions for the two orientations have been developed. They first find the density of unit cracks as a function of applied stress level and then the probability of coalescence of these cracks is estimated. Maximum strength is assumed to have been attained when the crack lengths and the applied stresses are high enough to cause crack extension even with median strengths at the crack tip.

The effect of the biaxial stress state which is applied is shown in figure 11.

In this case the solid lines represent the analytic solution whereas the data points each represent the result of five numerical calculations on the computer. The stress for instability is considerably less sensitive to the biaxial tensile condition or to a compressive stress for one of the principal stresses than is the stress for first cracking. The vertex case is somewhat more sensitive to the stress state than is the face case. The coefficient m which, for example, is taken equal to 3 is the so-called Weibull modulus. For larger values of m the difference between the stresses for first cracking and failure is reduced.

The effect of part size is shown in figure 12. The stress for first cracking is very much more strongly sensitive to the part size than is the stress for final cracking. This difference is of course smaller for higher values of m. The results shown are for embedded fracture and have neglected any surface effects on the stress around a particular flaw. The numerical model has been extended to enable calculations for a semi-infinite array in which the stress field has been modified as a result of the free surfaces. The results are relatively insensitive to the presence of the surface assuming that the distribution of strength near the surface is the same as that in the interior. The strength of the individual grain boundary facets have been assumed to follow an extreme value function. As a result the size dependence shown for first cracking is that to be expected for such a function. It can be seen however, from figure 12, that the size dependence for the final cracking or instability condition is much weaker than that predicted for an extreme value function. This means that when the first crack is not critical, designing on the assumption that the final strength satisfies an extreme value function will not be correct in its predictions on size dependence. Although the predictions would be desirably conservative in that larger pieces would not be weakened as much as would be predicted, the degree of error can be seen to be large enough to be appreciable for the larger sizes of particular interest here and would lead to considerable overdesign which is also undesirable.

Flaw Detection

For more realistic design techniques it is desirable to know the actual distribution of strength impairing flaws to be expected within or on the surface of a brittle material. This can be inferred from macroscopic strength tests. However, to enable reliable failure rate predictions to be made requires testing an impractical number of samples. Alternative techniques that yield large amounts of data from only a few samples have been developed for determining the distribution of surface flaws [7,8]. This is appropriate for those materials in which the density and severity of surface flaws if greater than that for volume flaws so that failure largely originates at the surface, which is a frequent situation in brittle materials. The distribution obviously depends in detail on a particular surface treatment. Such a technique involves making a series of hardness indent measurements and monitoring the cracks formed using acoustic emission transducers. This technique increases the sensitivity particularly for opaque materials in which detection of surface flaws is much more difficult. In addition, a computer program has been developed for determining the actual flaw density distribution from the distribution of experimentally observed failure loads at which cracking occurs [8]. Some typical results for flaw densities on sheet glass surfaces before and after etching with an HF solution are shown in figure 13. In this case it can be seen that in the untreated condition a smooth extreme value distribution is completely inappropriate. The results indicate there are two low strength peaks in addition to a rapidly rising region of high strength. Most of these low strength flaws are removed by the HF treatment and the flaw distribution fits a more regular distribution function.

Experiments have also been undertaken to detect the most severe flaws from light scattering. It is expected that the intensity of scattered light from a columnated beam will be proportional to the square of the ratio of the width or crack opening of the flaw to the wavelength of the light. For small crack opening displacements, the scattered intensity will be very small. Experiments have been conducted using optical white light and glass slides with various flaws. To date, cracks as small as about 0.1μm have been detected by this technique. However, for most brittle ceramics the critical flaws may be much narrower than this if they are sharp cracks. For a perfectly sharp crack the crack is virtually closed under no load, and some prior load must be applied in order to open it. This displacement will increase with the load, but it is desirable to apply small enough loads so significant numbers of specimens are not destroyed in order to detect flaws. Figure 14 represents a typical calculation expected for a material such as ZnSe [9], with $K_{IC} = 0.75$ MN/m$^{3/2}$, in which the crack opening displacement for an elastic crack is plotted against the applied stress for various assumed crack lengths. The lengths are presented in terms of the final failure stress which would be expected. It can be seen that for a sensitivity or detection limit of about 0.1μm that median strength specimens as strong as 45 Mpa (6600 psi) would have to be stressed to loads, in general, greater than 1/3 of the fracture stress in order to reach this detection limit. Consequently, it would be

highly desirable to reduce the detection limit by up to another order of magnitude for inspection using visible light. However, the results look encouraging for the use of a light scattering technique as a means of detecting the critical, but relatively rare, low strength cracks. Further work in this direction is underway. Scattered intensities will be reduced by a factor of about 100 for materials transparent only to longer wavelengths and in this case proof testing must be used.

Summary and Conclusions

Fine grained microstructures can be obtained in CaF_2 by forging at the appropriate stresses and temperatures. These grains are in fact subgrains resulting from a recovery microstructure rather than from actual recrystallization and the size of the subgrains varies inversely with the applied stress. However, dynamic recrystallization is a significant problem in undoped CaF_2 at temperatures as low as half of the melting point. Modeling of the recrystallization process, is in progress. Theory for the grain boundary mobility in divalently doped KCl shows a strong drag results from the electrostatic interaction of divalent impurities with the boundary. This is consistent with experimental results which show that divalent impurities are much more effective than monovalent ones in reducing boundary mobility. The theory further predicts that additional drag will result from those divalent impurities with a greater size misfit or other secondary interactions with the boundary. Preliminary modeling has been accomplished on the problem of breakaway of the grain boundary from the impurity cloud. Further work is continuing on this and other problems relevant to the nucleation problem.

Numerical and analytical modeling has been carried out on the failure of brittle materials by the coalescence of subcritical microcracks and subsequent formation of a macrocrack that limits the load to a maximum. These models have been used to predict the effects of applied stress state, surfaces and of part size on the failure stress. A significant result is that for such materials an extreme value function is not found to be appropriate for the final fracture behavior. Two schemes have been investigated for detecting actual strength impairing flaws. A hardness indent-acoustic emission method capable of determining the flaw density curves has been discussed. Limited success has been achieved with detecting more severe flaws with a non-destructive light scattering technique. Further work in both of the areas is underway.

Acknowledgments

This work has been sponsored by ARPA contract F19628-75-C-0191, under the direction of Dr. C. M. Stickley and has been monitored by Dr. H. Posen of RADC/ET. The continued assistence and support of both are gratefully acknowledged.

References

[1] Cannon, R. M., Yan, M. F. and Bowen, H. K., "Substructure Formation During Halide Processing", in Proc. of the Fifth Conf. on Infrared Laser Window Materials, ed. Andrews, C. R., and Strecker, C. L., (Feb., 1976).

[2] (a)Grant, N. J., et al., "Research on Materials for High Power Laser Windows", Final Report, ARPA Contract F19628-75-C-0304, (Dec., 1975).

(b)Yan, M. F., "Grain Boundary Mobility at KCl", Sc.D. Thesis, M.I.T., (1976).

[3] Anderson, R. H., Koepke, B. G., Bernel G., E., "Intermediate Temperature (0.5 to 0.7 T_{mp}) Forging of Alkaline Earth Fluorides", this volume.

[4] Koepke, B. G., Anderson, R. H., Bernel G., E., and Stokes, R. J., "Room Temperature Grain Growth in Potassium Chloride, J. Appl. Phys., 45, 969, (1974).

[5] Roy, A. and Bauer, C. L., "Effect of Impurities on the Stability of a Moving Grain Boundary", Acta Met. 23, 957 (1975).

[6] (a)McClintock, F. A., and Zaverl, F., Jr., "A Computer Model of the Mechanics and Statistics of Brittle Crack Initiation", to be published, Int. J. of Fract.

(b)McClintock, F. A., and Mayson, H.J. "Principal Stress Effects on Brittle Crack Statistics", ASME Applied Mech. Conf., (June, 1976). Salt Lake City.

[7] Argon, A. S., "Distribution of Cracks on Glass Surfaces", Proc. Roy Soc. 250, 482 (1959).

[8] Matthews, J. R., McClintock, F. A., Shack, W. J., "Statistical Determination of Surface Flaw Density in Brittle Materials", J. Am. Ceram. Soc. 59, 304 (1976).

References

9] McClintock, F. A., and Hahn, W., "Design of Brittle Components Using Flaw Analysis", in ref. 1.

Figures

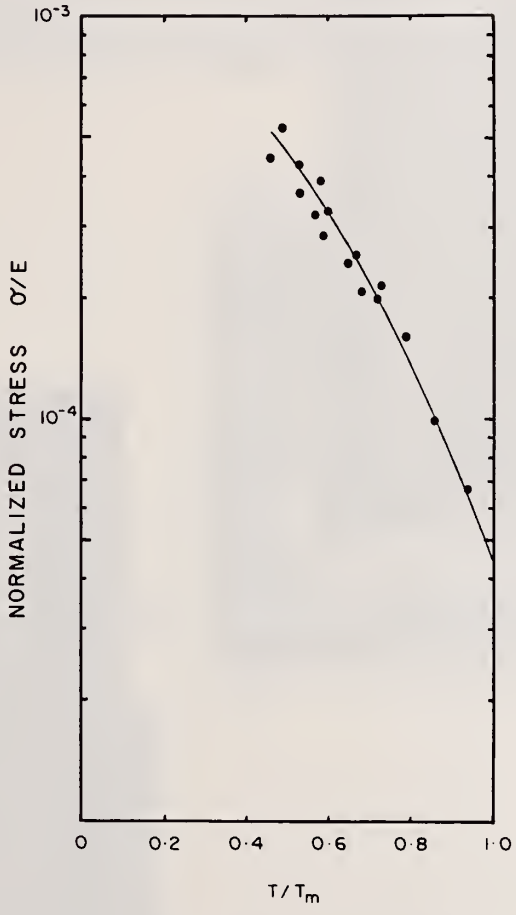

Figure 1. Steady state flow stress versus temperature for forged CaF_2 samples.

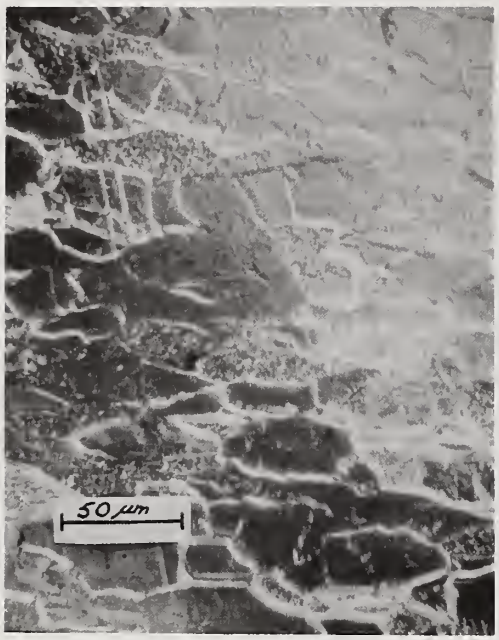

2(a)

2(b)

Figure 2. Subgrain structures in CaF_2 forged at 795°C (a) and 475°C (b).

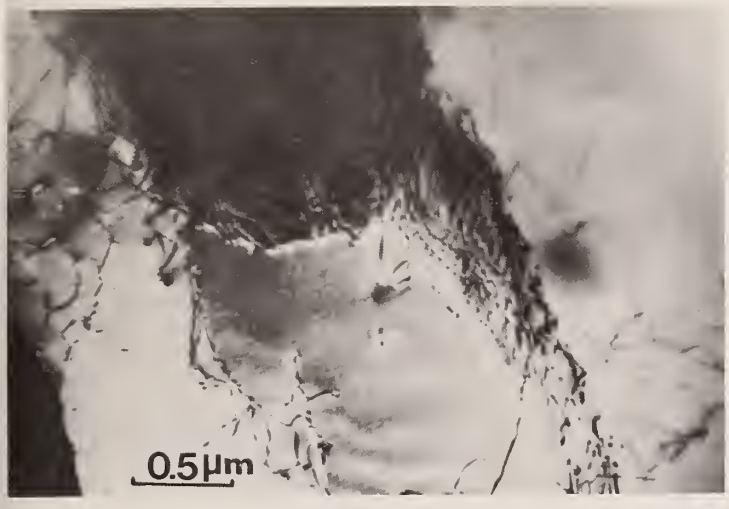

3(a)

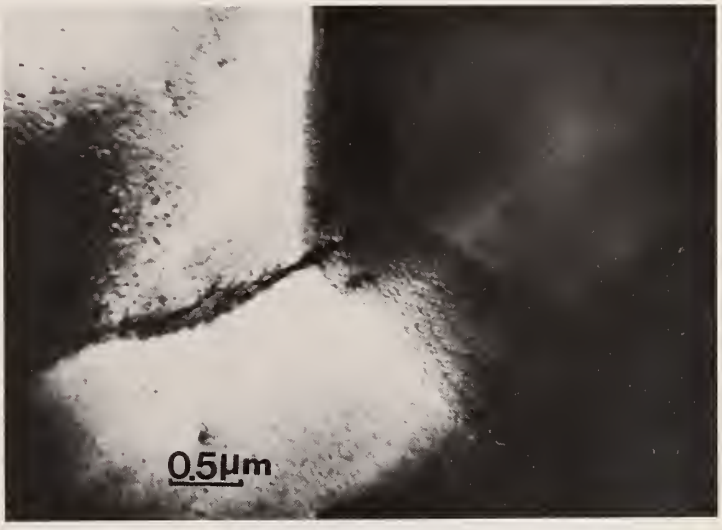

3(b)

Figure 3. Transmission electron micrographs of sub-boundaries in CaF_2 forged at 590°C (a) and 817 C°(b).

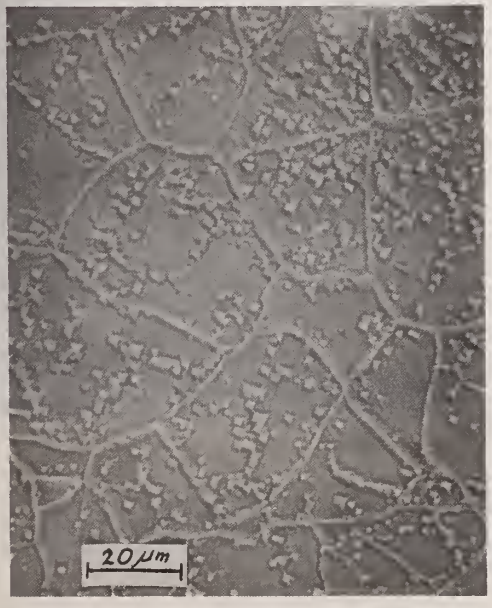

Figure 4. Dislocation cells within sub-grains in CaF_2 forged at 795°C.

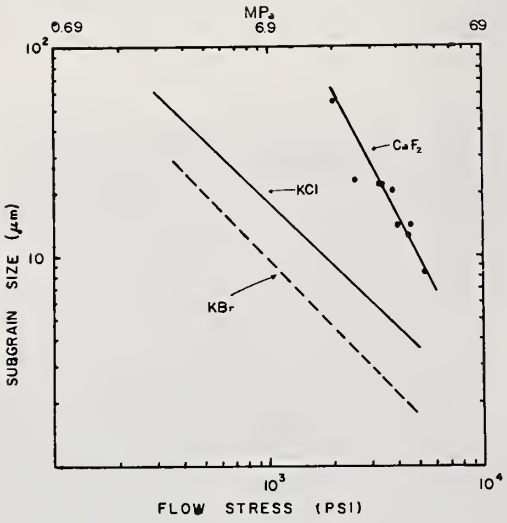

Figure 5. Subgrain size versus stress for forged CaF_2.

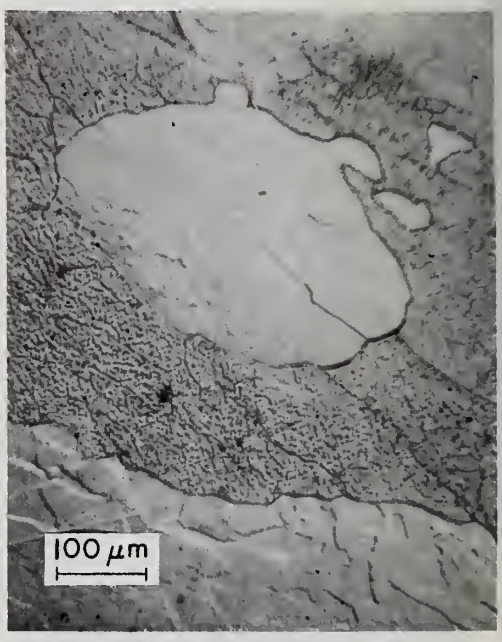

Figure 6. New grains with incompletely developed subgrains resulting from dynamic recrystallization in CaF_2 at 1018°C.

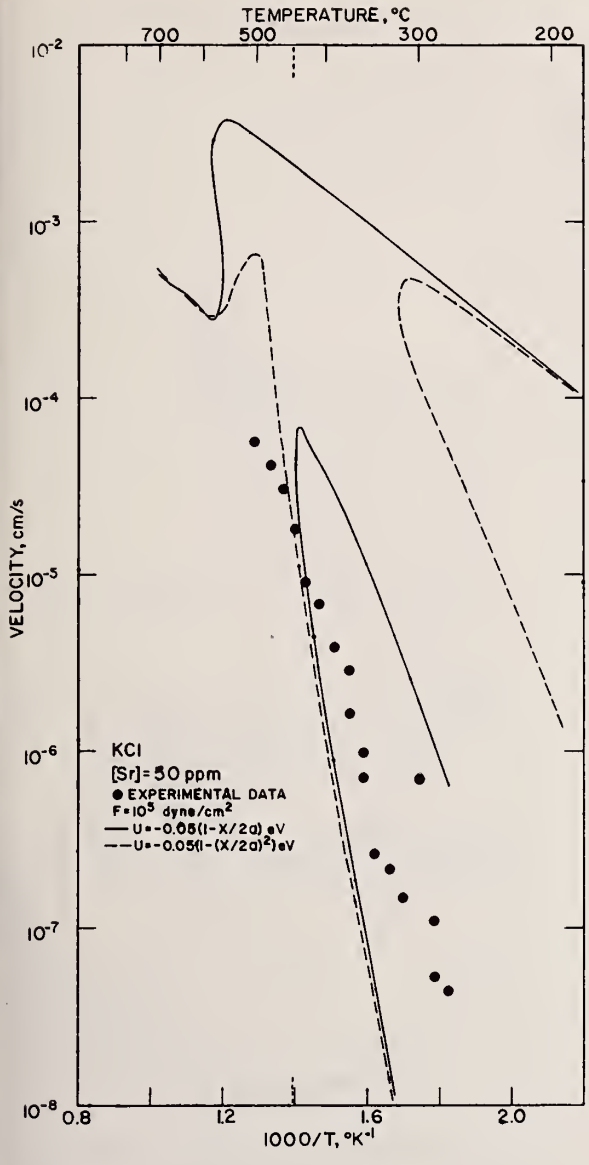

Figure 7. Comparison of calculated and experimental grain boundary velocity for Sr doped KCl.

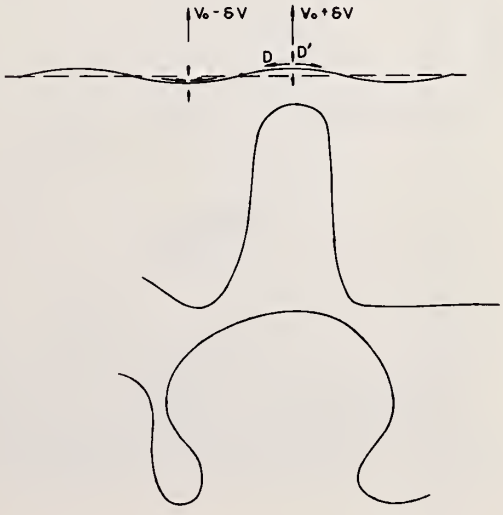

Figure 8. Schematic of breakaway of a grain boundary from its impurity cloud by growth of unstable velocity perturbations.

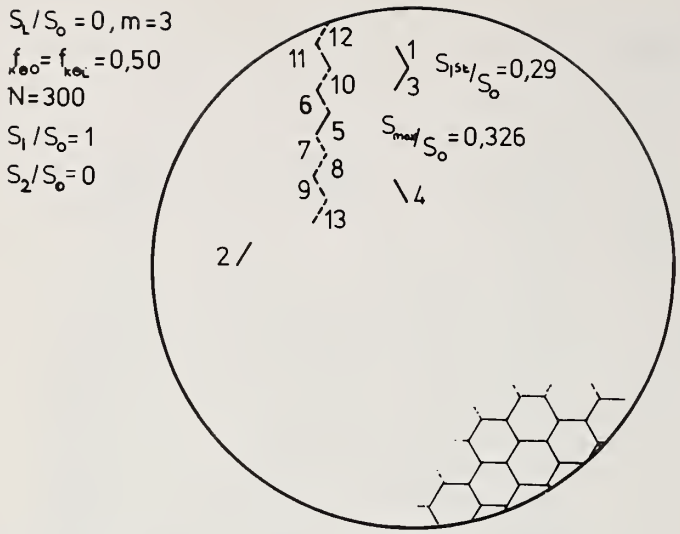

Figure 9. Sample cracking pattern for a vertex orientation.

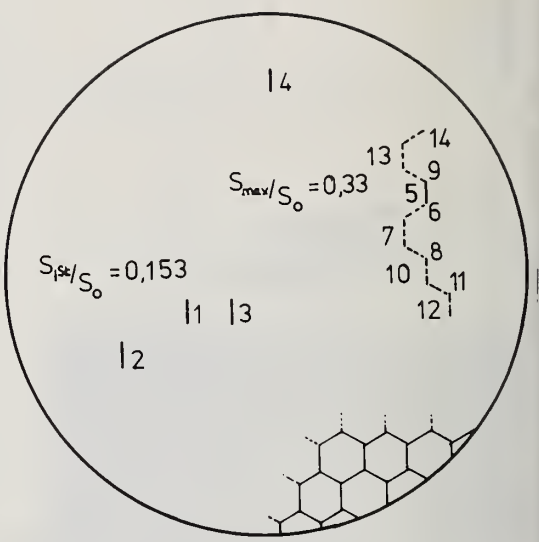

Figure 10. Sample cracking pattern for a face orientation.

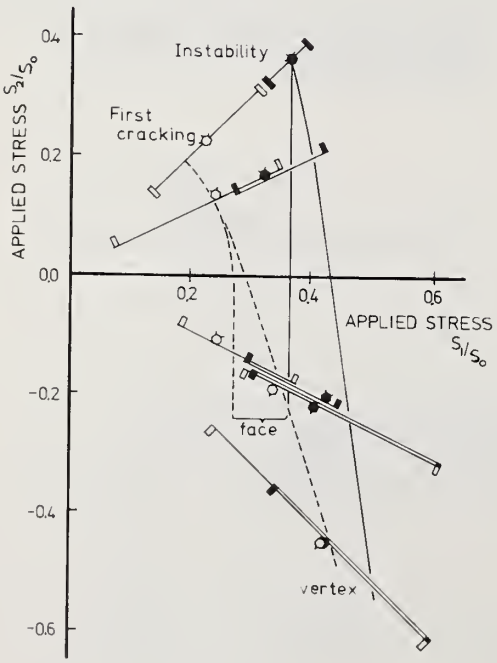

Figure 11. Principal stress fracture loci for first cracking and instability for an extreme value distribution of microstrengths with m = 3, S_L/S_0 = 0, part size N = 100.

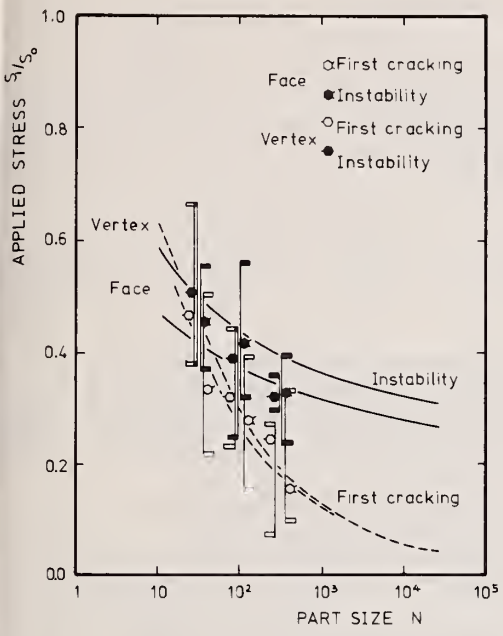

Figure 12. Statistical strength as a function of part size for a strength distribution with m = 3, S_L/S_0 = 0. Samples of 5, giving 93.75% confidence for the median.

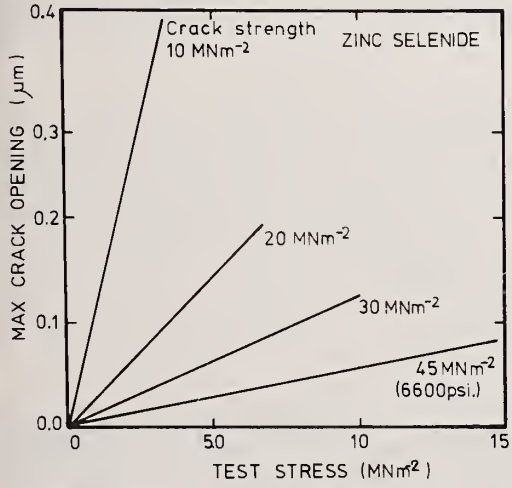

Figure 14. Predicted maximum openings of cracks having different strengths under different test loads for ZnSe.

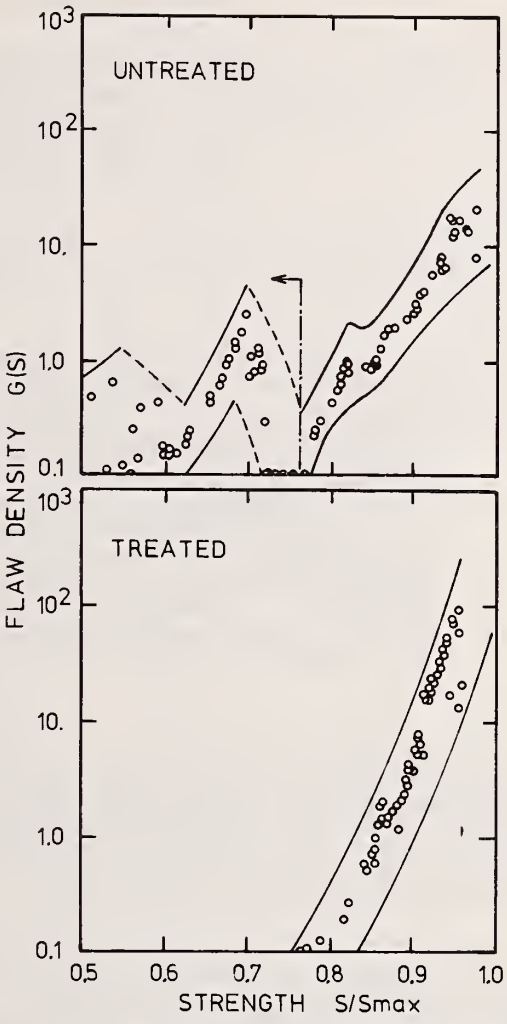

Figure 13. Flaw density distributions obtained from indentation tests for sheet glass before and after treatment with HF solution (S_{max} ≃ 225,000 psi) [8].

COMMENTS ON PAPER BY
CANNON, BOWEN, GLAESER, MAYSON, McCLINTOCK, SHERRY, VANDERSANDE, AND VAN

The speaker was questioned regarding the values of ion mobilities used in this analysis. A range of values exists in the literature for ionic mobilities in crystals, and the calculation of the diffusion process is complicated. The speaker indicated that in his opinion, the literature values were sufficiently reliable to provide a valid basis for the computation.

1.10 DOUBLE-DOPED ALKALI HALIDE LASER WINDOWS

Harold Posen, Normantas Klausutis, Jane Bruce,
Joseph A. Adamski, Joseph R. Weiner
Solid State Sciences Division
Deputy for Electronic Technology (RADC)
Hanscom AFB, MASS 01731

and

S. Andrew Kulin
Manlabs, Inc.
Cambridge, MASS

We have observed grain boundary instability in alloys doped with 1.75% RbCl. Theoretical studies have indicated that doping with divalent ions can provide some strengthening, and at the same time provide grain boundary stability. In an attempt to provide both solid-solution strengthening and grain-boundary stability, we have studied a series of double-doped RAP-grown KCl crystals. The primary dopant is fixed at 1.75 mole %RbCl, while the secondary dopant is varied from 10 ppm to 250 ppm $SrCl_2$. Polycrystalline discs were forged under constant strain rate. The strength, texture, 10.6 μm absorption,and grain boundary stability were studied as a function of $SrCl_2$ dopant level. Our studies indicate that double doping with a divalent ion enhances grain boundary stability without degrading other desirable window properties.

Key words: Double doped KCl laser windows; grain boundary stability; hot forging; KCl; mechanical strength; microstructure; optical absorption; RbCl; $SrCl_2$.

Introduction

The alkali halide materials, as a class, have for many years been considered as promising candidate materials for high energy laser window applications. In particular, KCl has received extensive study and has responded well to optimization of mechanical and optical parameters. Purification and growth techniques using reactive atmosphere processing (RAP) has reduced the 10.6 μm optical absorption to the 10^{-4} cm^{-1} range. Alloying with a few percent of RbCl coupled with hot forging to produce a polycrystalline microstructure has dramatically increased the strength of these materials without adversely affecting the optical properties.

However, one of the problems which has been observed in hot-forged Rb-doped KCl is instability of the microstructure. Secondary recrystallization and grain growth have been found to occur in materials processed both by us and by other laboratories. This phenomena, of materials returning to their single crystal state causes these materials to become weaker. They no longer have the desirable property of high strength provided by the polycrystalline microstructure. This paper defines a new 10.6 μm laser window material composition which appears to satisfy both the optical and mechanical requirements of high energy laser optics coupled with increased grain boundary stability.

In this study, we explore the use of double doping of KCl in order to simultaneously enhance the mechanical strength and microstructural stability of hot forged billets without degrading their optical properties. A nominal composition of 1.75 mole % RbCl-KCl was selected in order to correlate with forgings being conducted under AFML contract with Honeywell. To this composition were added various small amounts, on the order of parts per million, of $SrCl_2$. The RbCl serves primarily to enhance mechanical strength, while the divalent Sr^{2+} has been shown by theory [1]¹ to be a much more effective stabilizing impurity than the monovalent Rb^{+}. Thus the ultimate objective of this study was to find some low Sr^{2+} doping level which stabilized microstructure without introducing optical scattering problems in the forged billets.

Hot Forging

All forgings were carried out in a Vacuum Hot Pressing System* using an automatic strain rate control system capable of true-strain rate or ram rate control. This system achieves smoother strain rate control than the manual technique used formerly. Sample deformation takes place inside a Poco Graphite punch and die set using Graphoil as a lubricant. This technique differs from that used by some investigators in that no constraining rings or hydrostatic forces are applied to the sample during deformation. The sample undergoes a fully unconstrained deformation without contacting the die wall. It has been shown [2] that when a deforming billet does contact a constraint, residual strain is

---

*This apparatus was procured with financial support from AFWL.

1. Figures in brackets indicate the literature references at the end of this paper.

introduced in the finished billet in the area of contact.

All forgings were conducted in vacuum and at a true-strain rate of less than 0.01 cm/cm/min. Deformation is begun very slowly, gradually accelerated over a 20-30 minute period to the desired strain rate, then maintained at constant strain rate until the required total deformation is achieved. The forging stress is then removed and the sample is allowed to cool in-situ for approximately 16 hours. This technique produces forgings free of any edge tearing, cracking, or veiling. The residual strain in forged billets depends in part on the quality of strain rate control achieved.

All of the starting material used was grown at RADC/ET from J. T. Baker reagent grade KCl, RbCl, and $SrCl_2$ using the Bridgman technique with a reactive atmosphere of CCl_4-Argon. The resulting crystals had a random crystallographic orientation and were forged in the growth direction. Forging blanks were prepared from the single crystals by cutting with a wet string saw and water lapping to the desired size and shape. Due to time limitations, these crystals were not annealed prior to cutting and forging.

Forgings were carried out on a series of KCl crystals nominally doped with 1.75 mole % RbCl and with $SrCl_2$ in amounts varying from 10-250 ppm. A summary of the forging data for each composition is presented in table 1. Also included is data on the resulting grain size and microstructure. With $SrCl_2$ doping levels of 50 ppm or greater, complete recrystallization was not achieved and the grain size could not be measured. Typical examples of these microstructures are shown in figure 1.

Table 1. Summary of forging data for a series of KCl crystals doped with 1.75 mole % RbCl and varying ppm $SrCl_2$

Sample No.	ppm $SrCl_2$	Forging Temp °C	Strain Rate cm/cm/min	Grain Size μm	% Height Reduction
	0	300	<0.01	7.6	55-60
LQ-652	10	300	<0.01	6.2	60
LQ-666	50	300	<0.01	I*	55-60
LQ-661	100	300	<0.01	I*	55-60
LQ-665a	200	300	<0.01	I*	55-60
LQ-665b	200	330	<0.01	I**	70

*Insufficient height reduction caused incomplete recrystallization.

**Microstructure more fully developed than LQ-665a.

These results indicate that for low $SrCl_2$ levels of 10 ppm, the same forging conditions apply as for the Rb singly doped KCl. However, as the $SrCl_2$ content is increased to 50 ppm or greater, it becomes necessary to increase the total deformation up to 80 per cent or higher and also increase the forging temperature in order to achieve fully developed microstructures. Failure to produce total recrystallization results in a decrease in strength. The underdeveloped microstructures did not reveal themselves clearly upon polishing and etching, hence it was difficult to evaluate them accurately.

Optical Absorption

The total optical absorption at 10.6 μm of the RAP grown Bridgman double doped single crystals was measured using laser calorimetry. The results of these measurements, shown in table 2, list optical absorption coefficients in the range of $2\text{-}6 \times 10^{-4}$ cm^{-1}. These values are similar to those measured by Klausutis [2] and Larkin [3] on KCl doped with RbCl only. The data does not show any trend in optical absorption with Sr content. In fact, the crystal with the highest $SrCl_2$ content gave the best value. These results indicate that the addition of small amounts of $SrCl_2$ to Rb doped KCl has no appreciable deleterious effect on the optical absorption. These measurements were on samples cut from boules prepared during early growth runs, where the quality was somewhat questionable. However, the quality of the boules is continually improving, and measurements on samples taken from more recent boules should yield consistently lower absorption values.

Mechanical Strength

The mechanical strength of the forged double doped KCl specimens was evaluated using four-point bend measurements. Mechanical test bars were cut from the as-fabricated disks with the longitudinal beam axis parallel to the radial direction of the disk. Typical dimensions were approximately 0.25x0.5x3.0 cm. Sample surfaces were prepared by grinding followed by polishing with magnesia or ceria powder in alcohol on billiard cloth.

Table 2. Summary of 10.6 μm absorption and strength data vs $SrCl_2$ content

Sample No.	ppm $SrCl_2$	β (cm-1) @ 10.6 μm*	Ultimate Strength (psi)**
LQ-652	10	6.4×10^{-4}	5840
LQ-666	50	5.5×10^{-4}	4650
LQ-661	100		3850
LQ-665a	200		3020
LQ-664	250	2.5×10^{-4}	

*Calorimetry data obtained from single crystals only.

**Average of several measurements, on forged bars.

Specimen loading was accomplished using a Manlabs Inc. constant strain rate Polani-type tensile tester. In these tests a specimen deflection of approximately 3.8×10^{-4} cm/s was employed. Maximum stress, σ, was calculated from the equation

$$\sigma = \frac{3Pa}{bh^2} \quad (1)$$

where P is the applied four-point (total) bending load, a is the moment arm, b is the specimen width and h the specimen height. A typical load deflection curve is shown in figure 2. The curve indicates that failure was by brittle fracture with very little plastic deformation prior to failure.

The results of the four-point bend tests are presented in table 2 in terms of ultimate strength (psi). Each value is an average of 3-4 measurements. The highest value was obtained for the fully recrystallized sample containing a nominal 10 ppm $SrCl_2$. Strength values were found to decrease with increasing $SrCl_2$ content. It was noted earlier that the degree of recrystallization after forging also decreased with increasing $SrCl_2$ content. It follows that those specimens with underdeveloped microstructure have lower ultimate strength.

Microstructure Stability

The microstructure of the forged double doped KCl was, at 10 ppm $SrCl_2$, very fine with well-defined grains. However,as the $SrCl_2$ content was increased to 50 ppm or more, the grains coarsened and were not well defined.

In order to investigate the stability of the microstructure, accelerated lifetime tests were performed. Samples, in the form of unstrained ends of the mechanical test bar samples, were vacuum annealed in a globar tube furnace. The furnace was maintained at temperature and the samples were slowly moved into the hot zone, held at temperature for one hour, and then slowly removed. Annealing temperatures of 350, 400,and 450°C were used. Samples were then water polish-etched on billiard cloth, examined and photographed immediately.

The results of the annealing studies are best demonstrated by the micrographs of figures 3, 4,and 5. At 350°C, some areas of the 10 ppm $SrCl_2$ specimen had undergone complete secondary recrystallization with 50 ppm and above, no secondary recrystallization was observed. At 400°C, both the 10 ppm and the 50 ppm specimens had undergone complete secondary recrystallization; the 100 ppm specimen showed some grain growth, while the 200 ppm specimen remained unchanged. Finally at 450°C, the 100 ppm specimen showed partial secondary recrystallization, and the 200 ppm sample showed some grain growth, but no secondary recrystallization.

Conclusions

These preliminary experiments have demonstrated that the addition of a few ppm of $SrCl_2$ to KCl doped with 1.75 mole % RbCl can yield forged billets which

1. have small grain size (less than 10 μm)
2. have high strength when complete recrystallization is achieved (5840 psi)
3. have low 10.6 μm optical absorption ($2\text{-}6 \times 10^{-4}$ cm^{-1})
4. show greater grain boundary stability with increasing ppm $SrCl_2$ (billets containing 50 ppm $SrCl_2$ or greater showed no secondary recrystallization or grain growth after 350°C anneal).

Crystals containing more than 10 ppm $SrCl_2$ are now being forged, but as $SrCl_2$ content is increased, forging conditions must be adjusted to higher temperatures and greater % height reduction in order to achieve complete recrystallization. However, increasing these parameters may cause inhomogeneities in the optical path length of such specimens. So it appears that the minimum $SrCl_2$ content which would improve grain boundary stability without adversely affecting optical and mechanical properties is probably in the range of 0-50 ppm $SrCl_2$.

In conclusion, the technique of double doping of an alkali halide as described in this paper is capable of producing a material with the required optical and mechanical properties for HEL applications and with greater microstructural stability than singly doped alkali halide materials. Such a material should receive very serious consideration for use in 10.6 μm high energy laser window applications.

References

[1] K. Bowen (private communication).

[2] N. Klausutis et al.,"High Strength Forgings of RbCl doped KCl", Proc. of Fifth Annual Conf. on IR Laser Window Materials, 1-4 Dec 1975, pp 1037-1050.

[3] J. Larkin et al.,"Mechanical and Optical Properties of RbCl-KCl Solid Solutions", presented at Preparation and Properties of Electronic Materials Conf., 9-11 Sep 1974, Boston MA, sponsored by AIME.

Figures

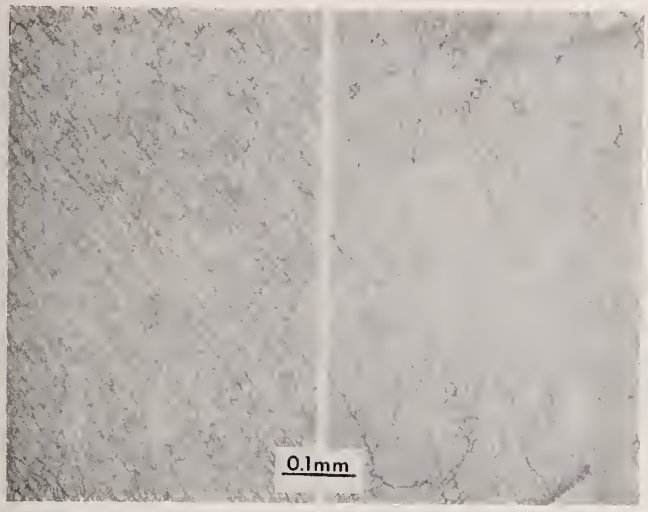

Figure 1. Microstructure of forged double doped KCl crystals illustrating full recrystallization (left) and incomplete recrystallization (right).

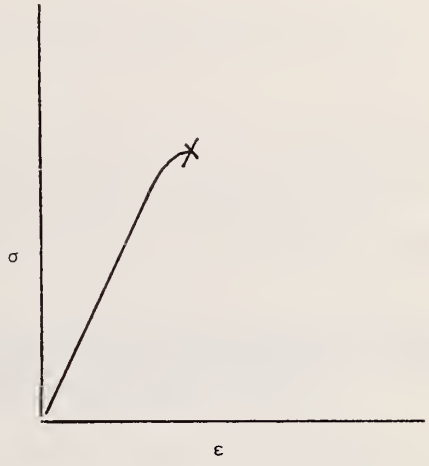

Figure 2. Typical σ-ε curve for 4-point bend test of double doped KCl.

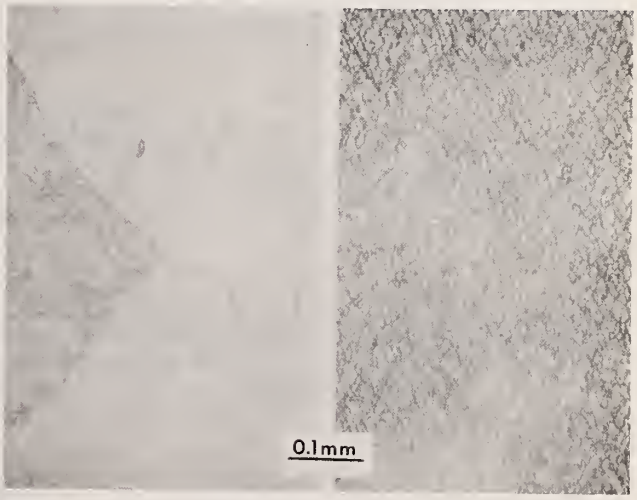

Figure 3. Microstructure after annealing at 350°C for 1 hour: (left) 10 ppm $SrCl_2$ - shows some areas of complete secondary recyrstallization; (right) 50 ppm $SrCl_2$ - no secondary recrystallization.

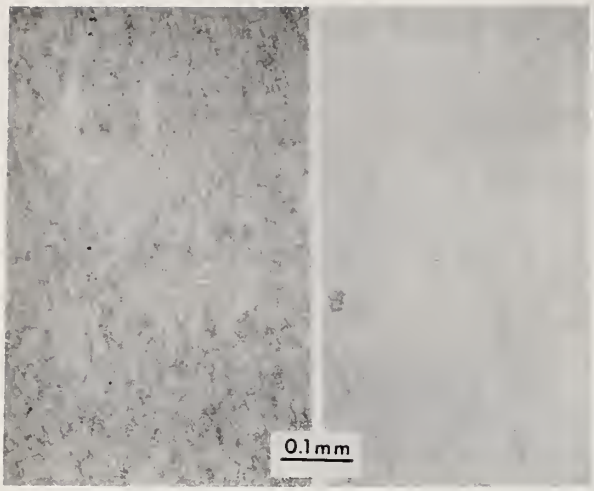

Figure 4. Microstructure of 100 ppm specimen as fabricated (left) and after 450°C anneal (right) - shows partial recrystallization.

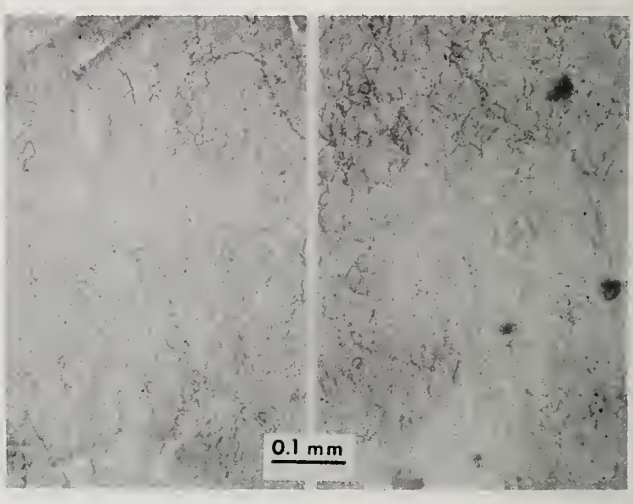

Figure 5. Microstructure of 200 ppm $SrCl_2$ specimen as fabricated (left) and after 450° anneal (right) indicating grain growth, but no secondary recrystallization.

COMMENTS ON PAPER BY POSEN, KLAUSUTIS, BRUCE, ADAMSKI, WEINER, AND KULIN

No discussion on this paper.

1.11 INTERMEDIATE TEMPERATURE (0.5 TO 0.7 T_{mp} ^{o}K) FORGING OF CALCIUM FLUORIDE CRYSTALS*

R. H. Anderson, B. G. Koepke, and E. Bernal G.
Honeywell Corporate Research Center
Bloomington, Minnesota 55420

Crack free forgings have been successfully produced from CaF_2 crystals at temperatures as low as 0.5 T_{mp} (^{o}K) using an isostatic forging technique. Forging temperatures and isostatic pressures have ranged from 500^{o} to 750^{o}C and to 28 MN/m^2 respectively. Most forging has been along <111> directions. The resulting microstructures varied from highly deformed structures with barely recognizable subgrains to structures with subgrain sizes of around 10μm in crystals forged at higher temperatures. Annealing for long times at 720^{o}C resulted in recrystallization and a large grained polycrystalline structure. Internal cloudiness or "veiling" is observed in all <111> oriented forgings. The extent of the veiling decreases with increasing forging temperature. The fracture energies of several forgings are compared with the fracture energies of single crystals and large grained polycrystalline material.

Key words: Annealing; fracture energy (γ_c); isostatic forging; kinking; microstructures; recrystallization temperature; veiling.

1. Introduction

Hot press forging is a technique that has been quite successful in producing infrared laser window blanks from alkali halide single crystals [1][1]. The forging operation introduces a fine grained microstructure that accounts for considerable strengthening at little expense to the absorption at 10.6μm. By forging at lower temperatures (i.e., <200^{o}C for KCℓ) material can be produced with acceptable mechanical properties [2,3]. To eliminate fracturing of the billet during the lower temperature working, isostatic forging techniques have been adopted [2,4].

To produce laser window blanks for operation in the 3-5μm range, alkaline earth fluoride crystals can be hot forged in ways identical to those used for alkali halides. The biggest difference is that the working temperatures are increased due to the differences in melting points. For instance, KCℓ crystals isostatically forged at 250^{o}C (.5 Tmp (^{o}K)) show strength increases of an order of magnitude. The equivalent working temperature for CaF_2 is 550^{o}C.

Calcium fluoride crystals have been forged without constraints to large reductions at temperatures ranging from 550^{o}C (.5 Tmp(^{o}K)) to 1000^{o}C (.8 Tmp (^{o}K)) by workers at Hughes [5-7]. The material forged at the lower temperatures exhibited fine grain sizes, but cracked during or after hot working [7]. These workers have since found that crack free CaF_2 forgings can be routinely made at 900^{o}C (.7 Tmp^{o}K), but that the grain sizes of these forgings are fairly large (i.e., .5 to 4mm) [6]. This material exhibits rupture strength of about 69 MN/m^2.

The high yield strength (i.e. 15 times that of KCℓ) and the limited number of slip systems available at temperatures lower than about 300^{o}C dictate that the predominant mode of mechanical failure in CaF_2 laser windows will be brittle fracture [8,9]. This is further evidenced from the above quoted value of rupture strength which is clearly less than the extrapolated room temperature single crystal yield strength of CaF_2 of 97 MN/m^2 [8, 10].

It is important, therefore, to characterize the fracture resistance of CaF_2 laser windows and to determine if deformation processing can improve the fracture resistance. The fracture resistance of a material is given by its critical fracture energy, γ_c. γ_c is the energy required to create a unit area of crack during rapid fracture. Freiman et. al., [10] have determined γc for {111}<110> cleavage in CaF_2 crystals to be 0.51 J/m^2. They further showed that hot worked, transparent large grain CaF_2 (Polytran) exhibited a fracture energy of 1.6 J/m^2 [10].

In this paper we address the question of whether the fracture resistance of forged CaF_2 can be increased over that of large grained samples. To do this we have adapted an isostatic forging technique that can produce fine grained, crack free forgings at working temperatures of 0.5 to 0.7 Tmp ^{o}K(500^{o} to 750^{o}C). Fracture energy measurements made to date on these forgings have, in fact, shown that a 67% increase in γc is observed when compared to large grain size polycrystalline material.

*Work supported by Defense Advanced Research Projects Agency under contract DAHC15-73-C-0464.

1. Figures in brackets indicate the literature references at the end of this paper.

2. Experimental Procedure

2.1 Isostatic Forging

A schematic showing the isostatic forging technique is given in Figure 1. The equipment is essentially identical to that used to forge halides [2,4], but has been modified to operate at higher temperatures. Crystals are forged in a closed chamber which is pressurized with helium gas to pressures up to 34.5 MN/m^2. Pressures are maintained during forging by a water cooled O-ring seal and spring actuated pressure release valves. Forging is carried out with a 3450 MN/m^2 hand pumped hydraulic press. Deformation rates are monitored with a dial gauge mounted on the press. Two thermocouples inside the chamber are used to note the temperature. Forging temperatures up to 800°C can be reached with this equipment. Typical heating and cooling times during a run were 3 hours to heat and 16 hours to reach room temperature after forging.

Cylindrical single crystals* 2.54 and 3.81 cm in diameter with an aspect ratio of unity were used as starting material. In most cases the crystals were forged along <111> at a constant true strain rate of 6×10^{-3} min^{-1} under isostatic pressures of 10.3 to 27 MN/m^2. Lower pressures were used at higher forging temperatures to minimize chances of permanent deformation of the chamber. Each starting crystal was carefully polished with 6 micron diamond paste to eliminate any surface imperfections that could initiate a crack during forging.

2.2 Fracture Energy Measurements

Fracture energy measurements were made using the modified double cantilever beam technique of Freiman et. al. [11]. A schematic of the sample and loading geometry is shown in Figure 2. Loading arms cemented to a precracked specimen apply a constant moment to each half of the specimen, thereby propagating the crack to failure. The fracture energy is given by

$$\gamma_c = \frac{AM_c^2}{E}$$

where A is a geometrical term, E is Young's modulus and M_c is the applied moment at failure. Fracture energy specimens were cut from forgings with a diamond cut-off wheel to typical dimensions of 1cm. wide, 1.9cm. long, and 0.1cm. thick. A groove was cut half way through the thickness of specimens cut from forgings to guide the crack. No groove was necessary to measure the fracture energy of single crystal specimens. Samples were cut from forgings such that the crack ran parallel to the top and bottom surfaces of each forging about midway through the thickness.

The microstructures of the forged samples were revealed by polishing through No. 1 alumina and etching for 1/2 hour in concentrated sulphuric acid.

3. Results and Discussion

3.1 Forging Results and Microstructures

Table 1 lists forging conditions and heat treatments of a number of calcium fluoride single crystals isostatically forged at temperatures ranging from 515°C to 750°C. In all cases the crystals were forged to 60% reduction in thickness at a constant true strain rate of 6×10^{-3} min^{-1}.

*Purchased from Optovac and Hawshaw

Table 1. Forging conditions and heat treatment of CaF_2 crystals forged to 60% reduction at different temperatures at a constant true strain rate of 6×10^{-3} min^{-1}.

Sample	Forging Temp. (°C)	Chamber Pressure (MN/m^2)	Final Forging Stress (MN/m^2)	Heat Treatment
A	510	27.6	*	Not annealed after forging.
B	515	27.6	*	Annealed in situ 1 hour at 720°C.
C	520	27.6	*	Not annealed after forging.
D	600	20.7	66.9	Annealed in situ 1 hour at 600°.
E	650	17.2	56.6	Annealed in situ 2 hours at 800°C. Removed from press and annealed 24 hours at 720°C.
F	700	13.8	45.5	Annealed in situ 2 hours at 800°C.
G	750	10.3	40.7	Annealed in situ 2 hours at 800°C.

Without exception, crystals isostatically forged at temperatures greater than 500°C come out of the press crack free. We have further determined that the forged billets can have their top and bottom surfaces polished for examination without introducing cracks. Examination between crossed polarizers indicates, however, that even forgings produced at 750°C contain significant internal stresses. Attempts to cut the forgings with a diamond wheel for mechanical property tests always result in the introduction of one or more large cracks. Further cutting is then possible because the long range internal stresses are relieved by the fractures. Crystals forged at 500 to 600°C and subsequently polished, fractured during room temperature storage as a result of subcritical growth of surface flaws. Subcritical crack growth in single crystal and forged CaF_2 has been fully documented by Freiman et. al. [10] who showed water to be a major cause. Crystals forged at 700 and 750°C have survived long storage periods at room temperature. Our observations that the samples fractured during storage prompted the incorporation of the post forging anneals listed in table 1. Although the residual stresses are relieved somewhat by these treatments, an acceptable annealing schedule has not been determined at this point.

A photograph of crystals forged along <111> to 60% reduction at 650°, 700°, and 750°C is shown in Figure 3. As the forging temperature is increased the shape of the deformed crystals becomes more uniform. Note particularly that the serrations visible on the sides of the 650°C forging are absent in the 750°C forging. We attribute this to the increased ease in cross slip at the higher temperatures. Crystals forged along <111> at temperatures below about 700°C apparently deform by both slip and by kinking. The serrations on the side of the crystals indicate regions in which deformation occurred mainly by kinking. The vertical lines at the edges of the billet at which outward flow is impeded appear to be kink boundaries. One observation we have made of a small fracture that propagated along a kink boundary in a highly deformed crystal indicated that the boundary was parallel to a {110} plane in the starting crystal. When the outward flow of material is impeded at these boundaries the tops of <111> crystals forged to large reductions at 650°C or below have a "petal"-like shape.

Photomicrographs of the microstructures of forged CaF_2 crystals are shown in Figure 4. Figures 4a, 4b show a structure typical of a crystal forged at 500°C to 650°C. The structure appears highly deformed with a high dislocation density, but does not contain many regions with recognizable subgrains. The dark lines running across the structure are kink boundaries. Annealing for an hour at 720°C does not alter the appearance of this structure. Forging at 700 or 750°C plus annealing at 800°C for 2 hours produces a structure with recognizable subgrains as shown in Figure 4c. We have not forged a CaF_2 crystal at 700 or 750°C without an 800°C post forging anneal and cannot comment on whether the anneal causes or enhances polygonization. The microstructure of the 650°C forging annealed 24 hours at 720°C is shown in figure 4d. The structure is large grained indicating recrystallization had occurred. The grain size of this material is 0.5mm and is typical of crystals forged at higher temperatures [6].

All <111> crystals forged at 500 to 750°C exhibited internal cloudiness or "veiling" to some extent. As the forging temperatures were increased the amount of veiling decreased. An example of veiling in a crystal forged at 650°C is shown in figure 5. We have noticed a number of things about the veiled regions that suggest they are regions of high void or microcrack density formed as a result of slip band intersection. First, the veils have crystallographic features such as three fold symmetry when viewed from the top of the crystal. Second, the veiling is heaviest in regions where kinking is observed. Finally, veiling decreases at higher forging temperatures due to enhanced ease of cross slip.

Microcracks can form as a result of the plastic deformation of a crystalline solid by a number of mechanisms. Two likely mechanisms are by dislocation pile-ups [12] or by dislocation intersections [13]. In the first case, the dislocations at a pile up become so close they coelesce to form a microcrack. In the second case, glide dislocations on two intersecting slip systems react to form a dislocation on a third slip system which in turn acts as a barrier to further deformation and a microcrack forms. Phillips [8] has pointed out how dislocation reactions of this type can possibly account for both {100} and {110} microcrack formation in CaF_2. At temperatures above 500°C the microcracks would be expected to round out into voids as a result of surface diffusion and be swept along on active slip bands as deformation proceeds. This accounts for the voids being frequently observed in the form of sheets or veils. Since kink boundaries are obstacles to flow, one would expect more slip intersection in these regions.

3.2 Fracture Energy Measurements

As noted in the introduction, a main goal of this study has been to determine if the fracture resistance (as given by the fracture energy, γ_c) of calcium fluoride crystals forged at intermediate temperatures can be raised above that of large grained polycrystalline material forged at temperatures above the recrystallization temperature.

The results of fracture energy measurements on single crystals and hot forged crystals of calcium fluoride are given in table 2. Recall that in the hot forged samples, the crack plane is parallel to the forged surfaces of the billet and about midway through the thickness.

Table 2. Fracture Energies, γ_c, of Hot Forged Calcium Fluoride Crystals

Sample	No. of Tests	γ_c (J/m^2)	Comments
{111}<110> Single Crystal	7	0.45 ± .07	
{111}<110> Single Crystal	-	0.51*	
Harshaw "Polytran"		1.6*	Large grain polycrystal
A	10	2.53 ± .03	Undeveloped microstructure
B	9	2.00 ± .02	Undeveloped microstructure
C	4	1.63 ± .02	Undeveloped microstructure
D		†	
E	9	1.56 ± .03	Large grain polycrystal
F	7	2.03 ± .04	10μm subgrains
G	7	2.67 ± .01	20μm subgrains

*Measured by Freiman et al.,[10].

†Not measured.

We note from table 2 that the single crystal fracture energy measured on the material used in this work compares well with the value measured by Freiman et al., [10]. The value of 1.6 J/m^2 measured on Harshaw Polytran material appears to be about what one should expect for large grained polycrystalline samples since our measurements of fully recrystallized forged CaF_2 (i.e., sample E) gave a comparable value. The fracture energies of crystals forged in the 500 to 700°C temperature range that did not recrystallize were noticeably higher. Material with both fully developed substructures (samples F and G) and with undeveloped substructures exhibited fracture energies over 2 J/m^2. By undeveloped substructures we mean that subgrains are not recognizable at magnifications used with an optical microscope. The forging produced at 750°C had a fracture energy 67% higher than that of large grained polycrystalline material. A number of comments can be made concerning these data. First it would be premature to comment on the relation of the fracture energy to the structures introduced by intermediate temperature forging. More data are needed to determine the effects of residual stresses, subgrain size, etc. Second, the values of γ_c quoted in table 2 for the crystals forged at 500 to 700°C should be taken as

conservative. Pole figures taken on these samples have shown them to have a strong <111> texture. Thus, on the average there is a {111} cleavage plane oriented approximately parallel to the forged surfaces in all regions of the forging. Since this is the crack orientation used in the fracture energy measurements, the measured fracture energies should be a minimum. If samples are cut, on the other hand, such that the crack propagates perpendicular to the forged surface of a <111> textured forging, the fracture energy is expected to be measurably higher. In this case {111} cleavage planes are, on the average, 30.5^{o} from the propagating crack.

Finally, Freiman et al.,[10] determined γ_c for hot pressed CaF_2 (Kodak Irtran) with a grain size of 50 to 100μm to be 3.6 J/m^2. This is clearly higher than the press forged material. This hot pressed CaF_2 is fabricated from powder, however, and does have some porosity.

4. Conclusions

It has been demonstrated that isostatic forging is a viable process for producing crack-free, fine grained material from CaF_2 single crystals. The forgings have been produced below the recrystallization temperature. The fracture energy, γ_c, has been significantly increased over single crystal or large grained polycrystalline materials.

The birefringence observed indicates measurable internal stress. If a suitable heat treatment can be developed to reduce this internal stress without initiating exaggerated grain growth, an additional increase in the fracture energy, γ_c, will probably be noted.

The detrimental effects of "veiling" to the optical properties have not been determined. It is possible that at 3-5μm, the effects may be minimal due to the small size of the imperfections.

5. Acknowledgments

The continued interest and support of Dr. H. V. Winsor, Defense ARPA is gratefully acknowledged. The assistance of W. J. Polzin, J. G. Bruce, and D. W. Woodward is gratefully acknowledged.

6. References

[1] see, for instance, papers in Second, (1972) through Fifth, (1975) Annual Conferences on Infrared Laser Window Materials and papers in Deformation of Ceramic Materials, R. C. Bradt and R. E. Tressler, ed., (Plenum Press, New York, 1975).

[2] B. G. Kopeke, R. H. Anderson, and R. J. Stokes, Deformation of Ceramic Materials, R. C. Bradt and R. E. Tressler ed., (Plenum Press, New York, 1975) p. 497.

[3] P. F. Becher, R. W. Rice, P. H. Klein, and S. W. Freiman, ibid p. 517.

[4] B. G. Koepke, R. H. Anderson, E. Bernal G., and R. J. Stokes, Proc. Fourth Annual Conference on Infrared Laser Window Materials (1974) p. 621.

[5] R. C. Pastor, et al., Proc. Third Annual Conference on Infrared Laser Window Materials (1973) p. 509.

[6] H. V. Winston, et al., Proc. Fourth Annual Conference on Infrared Laser Window Materials (1974) p. 438.

[7] R. R. Turk, Deformation of Ceramic Materials, R. C. Bradt and R. E. Tressler, ed. (Plenum Press, New York, 1975) p. 531.

[8] W. L. Phillips, Jr., J. Amer. Ceram. Soc. 44, 499 (1961).

[9] A. G. Evans, C. Roy and P. L. Pratt, Proc. Brit. Ceram. Soc., No. 6, 173 (1966).

[10] S. W. Freiman, P. F. Becher, R. W. Rice, and K. N. Subramanian, Proc. Fifth Annual Conference on Infrared Laser Window Materials, (1975) p. 519.

[11] S. W. Freiman, D. R. Mulville, and P. W. Mast, J. Mater, Sci., 8, 1527 (1973).

[12] A. N. Stroh, Proc. Roy. Soc. A223, 404 (1954).

[13] A. H. Cottrell, Trans. Met. Soc. Am. Inst. Mining Met. Engrs., 212, 192 (1958).

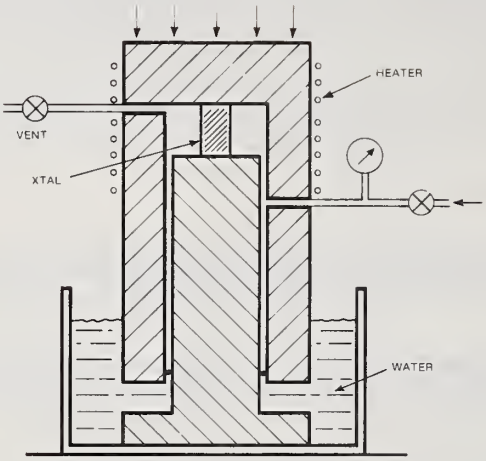

Figure 1. Schematic showing isostatic forging technique. Helium gas is used as the pressurizing medium.

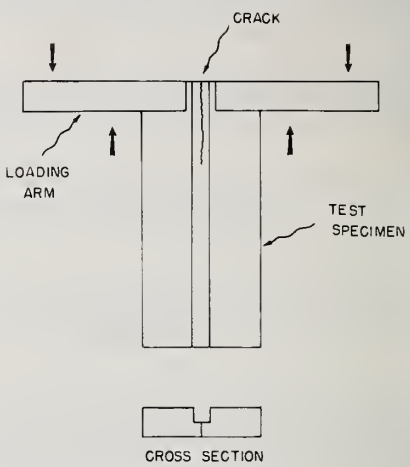

Figure 2. Schematic showing loading and specimen geometry for fracture energy measurements.

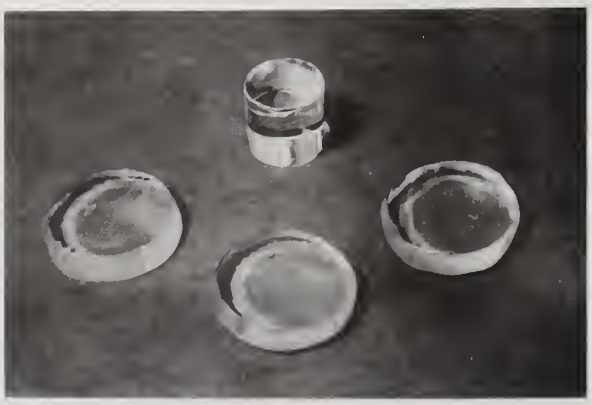

Figure 3. Photographs of CaF_2 crystals forged to 60% reduction at (from left to right in photograph) 650°, 700°, 750°C, respectively, with the single crystal starting material in the background.

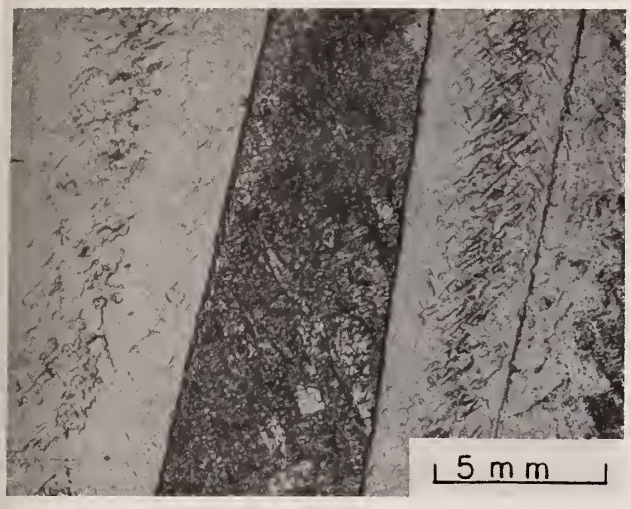

4(a) Sample A

Figure 4. Photomicrographs of forged CaF_2 crystals (a) Sample A, (b) Sample A, (c) Sample G, and (d) Sample E. See table 1 for forging conditions.

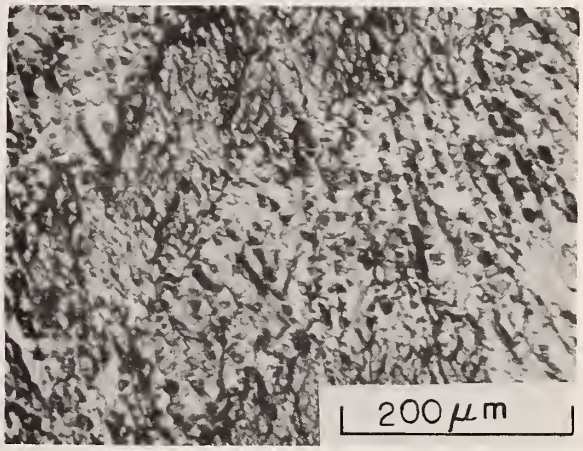

4(b) Sample A

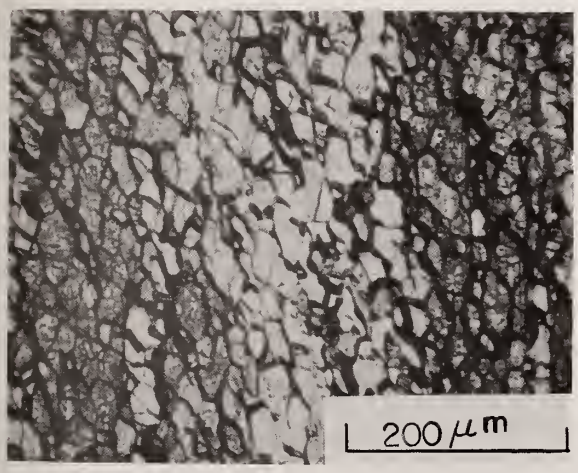

4(c) Sample G

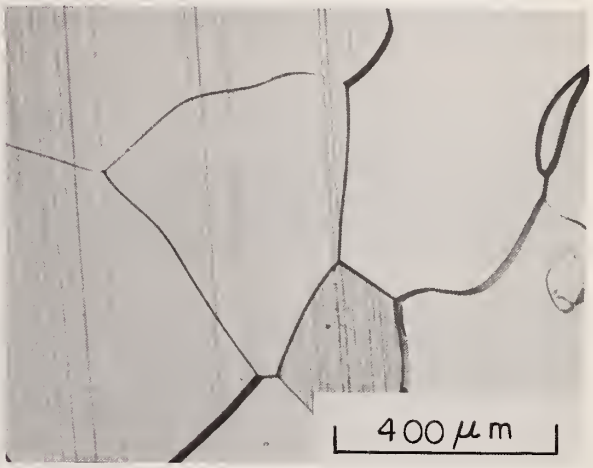

4(d) Sample E

Figure 5. Photograph showing veils in a CaF_2 crystal forged at 650°C.

COMMENTS ON PAPER BY ANDERSON, KOEPKE, AND BERNAL G.

No discussion on this paper.

1.12 FORGING FINISHED HALIDE OPTICAL COMPONENTS*

R. H. Anderson, E. Bernal G. and R. J. Stokes
Honeywell Corporate Research Center
Bloomington, Minnesota 55420

The forging of completely finished halide optical components to eliminate the necessity of shaping and polishing is being evaluated. The forging operation is being done isostatically using a closed die technique. Quartz die faces are being used to produce the desired surface shape and finish. A synthetic oil is being used as the lubricant while the forging is performed at 275°C.

To produce the finished component, two forging operations are being used. The first forging is necessary to produce uniform strain distribution. This pressing is then preshaped by water polishing before the final minor shaping operation.

These, as forged surfaces, appear superior to mechanically prepared surfaces for the deposition of the required protective and optical coating of thallium iodide.

Optical performance results obtained with these lenses will be compared with those obtained with conventionally polished halide and glass lenses.

Key words: Closed die; forging; isostatic; polishing; quartz; shaping.

1. Introduction

The difficulties encountered using either mechanical or chemical methods to attain optical surfaces and specific geometries with alkali halide materials has promoted this investigation. A forging process to produce a finished halide optical component was envisioned as the logical approach to the problem. The method was suggested by the success achieved by injection molding of plastic optical components.

From the outset, it was realized that plastics are amorphous materials while the halides are crystalline. Due to this difference, the techniques associated with injection molding of plastics would not apply directly to the forging of finished halide optical components. In the first place, the plastic deformation of crystalline materials is not isotropic, and second, after the forging operation the halides are subject to nonuniform elastic relaxation. This shape change is related to the crystalline texture developed during the forging process and is a function of the elastic anisotropy of the material.

This research was initiated to determine the fundamental limitations of the forging process in producing finished optical components. It was necessary to identify what physical geometry could be attained and what optical figure was possible.

The following sections will describe, in turn, the forging system as it has evolved to date, the forging process including material preparation and parameters, followed by some optical performance results, and projection for the future.

2. The Forging System

All of the forging operations associated with this program are being done isostatically. A high pressure fluid environment provides the necessary constraint to prevent cracking during deformation as well as to promote lubrication which prevents welding between the halide material and the die surfaces. Figure 1 is a sectional view of the isostatic forging system including the closed die used for the final shaping operation.

A closed die technique is dictated by the necessity to maintain the geometric dimensions associated with optical components. The present closed die fixture consists of a cylindrical steel tube into which close tolerance metal pistons are inserted. The tube maintains the axial alignments while the pistons produce the desired surface shape and finish. The present design uses quartz inserts as die faces on either side of the halide component to produce the final shape and surfaces.

*Work supported by Defense Advanced Research Projects Agency under Contract DAHC15-73-C-0464.

3. The Forging Process

Potassium chloride single crystals 3.81 cm dia. x 3.81 cm high are typically used as the starting material. All three usual orientations with the <100>, <110> and, <111> cylinder axis have been forged to determine the particular forging problems each might pose, and also later to be able to evaluate optical surfaces and geometries as a function of orientation.

The forging process as presently developed is a two stage process. In the initial preforging step the single crystal is deformed by 60%. This amount of deformation has been found necessary to insure uniform strain distribution throughout the bulk of the forging. Intuition might have suggested that the amount of deformation should be kept to a minimum to produce the final forged shape. However, as deformation starts, discrete slip systems begin to operate producing inhomogeneous strain distribution. The interaction of these slip systems at the surface of the crystal produce kink arrays which entrap lubricant as deformation progresses. This orthogonal surface aberration is referred to as "rumpling", and it is essential that it be eliminated by strain homogenization.

To enhance the development of uniform strain distribution during this preforging operation, Teflon sheet is inserted between the crystal faces and the metal forging faces of the isostatic chamber. Figure 2 illustrates the different forged shapes assumed by <100> oriented crystals with and without the introduction of Teflon. On the left, the frictional resistance produced between the crystal and the metal chamber has restrained the contacting crystal faces and produced the "barreling" as well as the rectangular shape. On the right, the vertical sides and circular shape indicate low surface friction with the Teflon and more uniform strain distribution. This forging operation is done at 300°C and an imposed isostatic pressure of 29.655 MN/m^2. This temperature prevents "veiling" within the forging.

The preshaped blank is next placed between the quartz die surfaces which have been finished to an optical figure of $\lambda/10$. The closed die is assembled and placed in the forging chamber. The final forging is done at 275°C with the same isostatic pressure, 29.655 MN/m^2.

The finished alkali halide forging is removed axially from the quartz surfaces to prevent relative movement between the die and the halide surfaces which would otherwise result in scratching.

The lubricant presently being used is a synthetic called Amsoil. It has a di-ester base. Other lubricants have been evaluated, but have proven unsatisfactory due to chemical breakdown or failure to provide the necessary lubrication. Fluids with high vapor pressures which would eliminate rinsing for lubricant removal have failed to provide the necessary lubrication. The Amsoil is removed by rinsing in xylene followed by carbon tetrachloride.

4. Optical Results

Several forgings have been made which appear to have replicated large areas of the quartz die surfaces. Figure 3 is typical of the clarity exhibited by one of these forgings.

A formal evaluation of the surface contours will be made using a (LUPI) Laser Unequal Path Interferometer. However, as a preliminary evaluation, the projection lens of a lantern slide projector was removed and a variety of lenses were substituted. Using various lenses to project a standard resolution target a comparison can be made. All lenses had the same geometry. Figure 4 illustrates four projections comparing glass, "state of the art" mechanically polished (Janos), early forging, and a recent forging. It is apparent that the recent forging compares favorably with the mechanically prepared lens.

It has been noted that forged surfaces appear to be better than those of mechanically prepared surfaces for antireflection coating. It is to be determined if this is a real effect.

5. Future Developments

Surface replication results are encouraging and it is hoped that the process will soon become routine. The effects of elastic anisotropy on the final surface geometry are to be determined as a function of starting orientation. Analysis of these results should yield insight into understanding methods whereby this problem can be overcome such as special shaping of the die surfaces related to forging orientation.

6. Acknowledgments

The continued interest and support of Dr. H. Windsor of Defense ARPA is gratefully acknowledged. The assistance of W. J. Polzin and D. W. Woodward is also gratefully acknowledged.

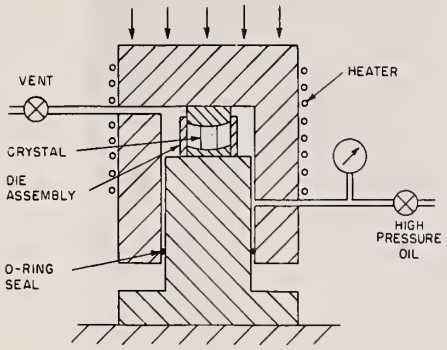

Figure 1. A sectional view of the isostatic forging chamber with the closed die in place.

Figure 2. KCℓ forging <100> orientation deformed 60% without Teflon (left side).

Figure 2. KCℓ forging <100> orientation deformed 60% with Teflon (right side).

Figure 3. Recent KCℓ forging illustrating the clarity achieved.

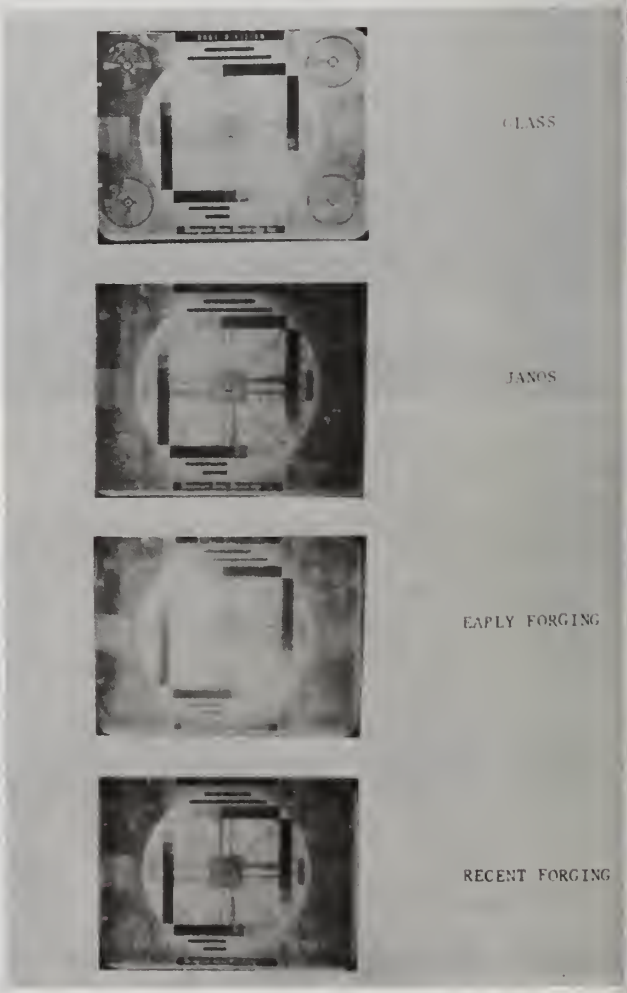

Figure 4. A series of resolution targets to compare various projection lenses.

COMMENTS ON PAPER BY ANDERSON, KOEPKE, AND BERNAL G.

No discussion on this paper.

1.13 Vapor Deposition and Mechanical Properties of CdTe

H. L. Tuller, K. Uematsu, J. B. Vander Sande,
E. L. Hall, and H. K. Bowen

Department of Materials Science and Engineering
Massachusetts Institute of Technology
Cambridge, Massachusetts 02139

The vapor deposition of CdTe from elemental cadmium and tellurium sources was studied as a function of the Cd/Te ratio, the supersaturation, and the substrate temperature. A multisubstrate arrangement was designed to enable simultaneous acquisition of growth data on six CdTe windows under conditions where substrate temperature and radial positioning remained the only variables. Polycrystalline blanks $4cm^2$ x 1mm thick were grown at rates of .02 - .10 mm/h with the growth rate exhibiting sensitivity to all of the above parameters. The affects of varying P_{Cd}/P_{Te_2} ratios during growth, as well as post growth annealing, on surface microstructure, grain size and void density, as observed under SEM and IR microscopy, will be presented.

Shear stress-shear strain results have been obtained from single crystal CdTe deformed in compression at 300°C. The defect microstructures associated with this deformation schedule have been observed by transmission electron microscopy. The macroscopic mechanical behavior will be discussed in terms of the dislocation interactions observed for the various deformation states.

Key words: Cadmium telluride; growth kinetics; mechanical properties; microstructure; stoichiometry; transmission electron microscopy; vapor deposition.

1. Growth and Characterization of CdTe Window Material.

Previous attempts to grow large plates of CdTe for laser window applications have resulted in materials with absorption coefficients at 10.6 m far in excess of that expected theoretically. This can be related to the difficulty in obtaining CdTe windows with desired levels of intrinsic and extrinsic defects. Because CdTe exists over a range of compositions, around the stoichiometric composition, the concentration of defects in a given window will be very sensitive to the original growth conditions (ie., $T_{substrate}$ and Cd/Te ratio) and to the composition-cooling path followed to room temperature.

Since the major factors known to contribute to optical absorptivity include free carrier absorption and absorption due to defects in the structure of the material, it becomes clear that one must be able to control the levels of these defects before one can approach the minimum theoretical absorption limit of $\sim 10^{-4} cm^{-1}$ due to multiphonon absorption [1][1]. Vapor deposition was chosen as the most appropriate means of growing large CdTe windows with controlled composition. First of all, vapor growth affords one the means for close control of the growth parameters which should ultimately result in samples with more precisely controlled stoichiometry. Furthermore since vapor growth can proceed at temperatures considerably below the melting point one can expect to minimize the level of thermally generated intrinsic defect pairs which are said to form agglomerated voids during cooling [2]. Similarly, one also expects the limits of nonstoichiometry to decrease with decreasing temperatures, thus minimizing the number of free carriers necessary to contend with.

1.1. Experimental

The vapor deposition facility constructed at MIT for the growth of 2-inch

1. Figures in brackets indicate the literature references at the end of this paper.

diameter samples has been previously described in detail [3]. This system includes separate temperature controls for the sources (Cd and Te) and for the substrate. In this manner one can control independently the vapor pressures of the Cd and Te sources as well as the deposition temperature. Mass transport is therefore controlled by the level of the source temperatures and the volume flow rates of the carrier gases; He gas for Te and He + 8% H_2 for Cd to prevent oxygen contamination. The actual concentration of Cd and Te vapor at the substrate and therefore the supersaturation, Q

$$Q = \frac{[P_{Cd}P_{Te_2}^{1/2}]_{exp}}{[P_{Cd}P_{Te_2}^{1/2}]_{equil}} \qquad (1)$$

was calculated by making use of previously determined evaporation rate versus temperature curves for cadmium and tellurium measured at fixed flow rates.

Although relatively large polycrystalline windows of 2-inches in diameter and up to 0.5 cm thick were grown with this apparatus, it was often difficult to obtain reproducible results. Since one would ideally like to obtain information about the affects of varying Cd/Te ratios, supersaturation, flow rates, substrate temperature, etc., on the deposition rate, stoichiometry and quality of growth of the CdTe windows in as short a time as possible it was decided to change from a single to a multiple substrate system. The end plate and window at the exhaust side of the reaction chamber was replaced by an end plate with 6 O-ring feed-throughs and a small 2-cm diameter window to enable observation of the reaction chamber. The end plate is shown in figure 1. Through each of the O-ring feed-throughs an 8mm diameter quartz tube, sealed at one end, is fitted. A 2 x 2cm vitreous carbon substrate is cemented to the closed end of each of the quartz tubes with carbon cement. The temperature of each substrate can easily be measured by sliding a thermocouple into the appropriate quartz tube from its open end located outside of the system.

This arrangement has a number of important advantages. First of all, because of the O-ring feed-through arrangement, it is possible to position each of the six substrates independently of each other along the length of the reaction tube. Thus one is able to grow six windows simultaneously under identical growth conditions except for the variable substrate temperature. Secondly, one is able to study the affect of radial positioning of the substrates within the tube and finally it is possible to quench the sample some hundreds of degrees while still within the reaction chamber. Further modifications to this apparatus include the addition of baffles to enhance mixing of the vapors and improved temperature control of the source materials.

1.2. Results and Discussion

A number of deposition runs were made with the multisubstrate system both as a function of P_{Cd}/P_{Te_2} ratio ($1.9 < P_{Cd}/P_{Te_2} < 8.5$) and of the substrate temperatures. Table 1 lists the results for a number of these early runs. The growth rate is observed to be sensitive to the gas composition and the substrate temperature both of which together determine the supersaturation value, Q.

Table 1. Values for the growth rate and supersaturation, Q as a function of the P_{Cd}/P_{Te_2} ratio and the substrate temperature, T_s.

Run#	P_{Cd}(atm)	Te_2(atm)	$P_{Cd}P_{Te_2}^{1/2}$($atm^{3/2}$)	T_s(°C)	Q	GR10^{-2}($^{mm}/_h$)
KU-2	5.01×10^{-3}	1.55×10^{-3}	1.97×10^{-4}	746	11.60	4.16
				771	5.06	4.97
				780	3.65	4.79
				803	1.79	———
KU-3	8.22×10^{-3}	9.67×10^{-4}	2.56×10^{-4}	750	13.45	4.11
				782	4.41	3.80
				785	3.87	3.27
				795	2.84	3.16
				806	1.97	2.11

KU-4 Source material dried up.

KU-5 Deposition time too short.

Table 1. (cont) Values for growth rate and supersaturation, Q as a function of the P_{Cd}/P_{Te_2} ratio and the substrate temperature, T_s.

Run#	P_{Cd}(atm)	Te_2(atm)	$P_{Cd}P_{Te_2}^{1/2}$($atm^{3/2}$)	T_s(°C)	Q	$GR10^{-2}$(mm/h)
KU-6	5.48×10^{-3}	2.90×10^{-3}	2.95×10^{-4}	758	11.8	6.22
				770	7.56	6.42
				785	4.54	3.98
				785	4.54	5.64
				795	3.28	4.35
KU-7	4.12×10^{-3}	4.05×10^{-3}	2.62×10^{-4}	764	7.95	4.78
				782	4.10	4.65
				785	4.03	3.30
				793	3.08	2.87
				805	2.10	———
KU-9	4.40×10^{-3}	4.06×10^{-3}	2.80×10^{-4}	792	3.41	3.91
				795	3.11	2.65
				796	2.98	3.13
				796	2.98	3.52

A simple model is proposed below to predict the growth rate under various experimental conditions. One assumes that when a supersatured gas mixture of Cd and Te reaches the substrate, CdTe deposits so that the vapor pressures of Cd and Te are reduced to the equilibrium values, $P_{Cd}^{eq.}$ and $P_{Te_2}^{eq.}$. The relation between the vapors in the exhaust gas are then given by

$$P_{Cd}^{eq} \times (P_{Te_2}^{eq})^{1/2} = K_{CdTe} \tag{2}$$

while the initial partial pressures of Cd and Te in the reactant gas mixture are described by the relation

$$Q\ K_{CdTe} = P_{Cd} \times P_{Te_2}^{1/2} \tag{3}$$

where Q, the supersaturation is defined as in relation eq. (1). Since each molecule of Te_2 reacts with two molecules of Cd, one requires for mass balance that

$$P_{Cd} - P_{Cd}^{eq} = 2(P_{Te_2} - P_{Te_2}^{eq}). \tag{4}$$

The number of moles of CdTe deposited per unit time is given by the expression

$$n_{CdTe} = \frac{(P_{Cd} - P_{Cd}^{eq})(\nu)}{RT} \tag{6}$$

where ν is the total gas flow rate. One can easily convert this to an expression for the growth rate, GR which is given by

$$GR = \frac{(\nu)}{\frac{\pi r^2}{RT}} \frac{M_{CdTe}}{\rho_{CdTe}} (P_{Cd} - P_{Cd}^{eq}) \tag{6}$$

where r is the reaction tube radius, M_{CdTe} the molecular weight of CdTe and ρ_{CdTe} the density. Figure 2 shows the calculated and observed growth rates as a function of Q for the conditions present in run KU-6. Considering the total duration of each run (heat up and cool down time (~10 h) and deposition period (~30 h)) the experimental scatter is not unreasonable.

An equally important parameter to determine is the affect of gas composition on growth rate. This is particularly important if one desires to grow samples of CdTe off stoichiometry. To separate out the affect of changing gas compositions the growth rate can be calculated as a function of P_{Cd}, for instance, by choosing fixed values of Q and $P_{Cd} \times P_{Te_2}^{1/2}$. The parameters Q~3 and $P_{Cd}P_{Te}^{1/2} \sim 2.7\times10^{-4}$ were chosen to enable comparison of our experimental results with the calculated values. The results of both experimental and calculated values of the growth rate vs P_{Cd} are

plotted in figure 3. The condition of $P_{Cd} = 2P_{Te_2}$ gives the maximum growth rate in the calculated curve as might be expected. It then rapidly decreases as one goes to higher or lower P_{Cd}. The experimental points, as obtained in table 1, fit the predicted curves reasonably well. This indicates the assumption that the vapor over the growing sample is in equilibrium with the sample seems to be well justified.

Since the electrical conductivity, σ is directly proportional to the concentration of free electronic carriers, it can be used as a sensitive measure of the degree of nonstoichiometry existing within a given sample. Table 2 shows the dependence of σ (measured at room temperature) on the gas composition during growth or post growth anneal. It is clear from these results that the level of free carriers in CdTe can be significantly reduced by equilibrating the samples with the appropriate atmospheres. For example, for sample KU7-5, the free carrier concentration was decreased by three orders of magnitude by annealing the sample in a cadmium rich atmosphere. It is expected that even lower values of σ can be achieved by appropriate treatment.

Table 2. Electrical conductivity as a function of growth or annealing atmosphere

	Growth			Annealing		
Sample	Temp(°C)	P_{Cd}(atm)	P_{Te_2}(atm)	Temp(°C)	P_{Cd}(atm)	($ohm^{-1}cm^{-1}$)
KU3-1	785°C	8.22×10^{-3}	9.67×10^{-4}			3.5×10^{-4}
KU6-1	785°C	5.48×10^{-3}	2.90×10^{-3}			5.1×10^{-4}
KU7-1	783°C	4.12×10^{-3}	4.05×10^{-3}			6.7×10^{-4}
KU7-2	763°C	4.12×10^{-3}	4.05×10^{-3}			2.6×10^{-3}
KU8-3	783°C	———	———			1.2×10^{-3}
KU7-5	782°C	4.12×10^{-3}	4.05×10^{-3}			1.5×10^{-3}
KU7-5-A	782°C	4.12×10^{-3}	4.05×10^{-3}	668°C	1.05×10^{-1}	1.5×10^{-6}
KU3-5-A	782°C	8.22×10^{-3}	9.67×10^{-4}	668°C	1.05×10^{-1}	1.5×10^{-6}

To ascertain the microstructures of the samples, as-grown samples were polished and examined under an IR microscope. All samples contained large numbers of dark and semi-transparent platelets assumed to be voids. These were observed both at the grain boundaries as well as inside the grains. The number of voids tended to increase when the samples were grown under near stoichiometric gas compositions of $P_{Cd} \approx 2P_{Te_2}$. Figure 4 shows the significant affect that growth conditions have on both the density and size of voids present in the samples. Generally crystals grown at very large super-saturations tended to have the largest number of voids.

In an attempt to correlate growth conditions with the number and size of macro-voids, the as-grown surfaces were examined under a scanning electron microscope, SEM. An example of a SEM micrograph is shown in figure 5. The samples always exhibit faceted surfaces and pores are often present at the grain boundaries. These pores are assumed to form the voids at the grain boundaries observed previously under the IR microscope. The mechanism of void formation inside the grains is less clear.

High supersaturation [4], constitutional supercooling [5], and turbulance over the substrate generally tend to contribute to void formation in specimens grown from the vapor phase. In order to minimize some of these affects a new arrangement was made in which the substrates were protected by a length of quartz tubing. Thereby mass transport of the vapor species was limited to diffusion through the tubes. Preliminary runs with this arrangement show that specimens can be grown with smaller values of supersaturation, Q. Examination of these specimens under the IR microscope show a decrease both in the concentration and size of voids.

Attempts to eliminate grown-in voids were also made. In preliminary experiments samples were annealed at 668°C for 5 days with $P_{Cd} \approx 0.1$ atm. However, no significant change in the level of macro voids was found under inspection with the IR microscope. Further study is underway to aid in understanding the mechanism of void formation and thus their possible elimination.

In conclusion the above results show that vapor deposition affords one the means for achieving close control over a number of important parameters during growth including composition, free carrier and void density and growth rate. Further experiments are expected to result in specimens with low absorptivities in the 10.6μm range without the need for compensating donor impurities.

2. Mechanical Properties and Dislocation Structure of Single Crystal CdTe Deformed in Compression at 300°C.

When considering the II-VI semiconductor compounds such as CdTe and ZnSe as candidates for low absorptivity window materials for utilization in high power laser optical systems, it is important to insure that the materials possess sufficient mechanical strength and fracture resistance to avoid the possibility of failure while in service. In the as-received condition, these materials just barely meet the minimum standards with regard to mechanical properties, a situation shared with most other laser window candidate materials. The II-VI compounds possess neither the ductility generally associated with metals nor the high hardness characteristic of ceramic materials. Thus far, the solution to the problem of insufficient mechanical strength in these materials has been to increase the thickness of the windows used. But since the ratio of the transmitted intensity to the incident intensity in a laser window is given by the equation

$$\frac{I_t}{I_o} = e^{-\beta t} \tag{7}$$

where β is the optical absorptivity and t is the window thickness, it is clear that the vast effort which has been expended to lower β can be negated if the window thickness must be increased.

The mechanical properties of materials such as CdTe were poorly understood prior to this investigation, and a systematic study of these properties had never been undertaken. In addition, the microstructural basis for the observed mechanical behavior had not been established. The obvious advantages of improving the mechanical strength of laser window materials therefore led to the present study. This paper describes the results of mechanical tests conducted in compression on single crystal CdTe at 300°C. The goal of these experiments was to understand plastic flow in this material and to eventually improve the room temperature mechanical properties.

2.1 Experimental

Single crystal specimens of melt grown CdTe, manufactured by Hughes Research Laboratories and by II-VI Co. Inc., were prepared for mechanical testing as described in a previous paper [6]. After preparation, the orientation of each of the samples was determined by Laue back-reflection X-ray diffraction. The apparatus used to conduct the compression tests was a modified Tinius-Olsen testing machine, which deformed the samples at a constant strain rate. The test temperature was maintained using a radiant-heating furnace, with an accuracy of $\pm 5°$ during the test. Five single crystal CdTe specimens of identical size and orientation were selected for the mechanical tests at 300°C. This temperature was chosen since considerable plasticity was evident in the samples, and at the same time compositional stability was insured and thermal effects on the flow properties were minimized. The samples were compressed at a constant strain rate of .002 inches per minute.

2.2 Results and Discussion

Using the test data and the orientation information obtained from the Laue patterns, a composite shear stress τ versus glide strain γ curve was constructed for the compression of CdTe at 300°C, which is shown in figure 6. The orientation of the compression axis (CA) of the samples is shown in the standard stereographic triangle, and the point of termination of the mechanical tests for each of the five specimens is indicated. The initial portion of the curve, up to approximately 25% glide strain, can be seen to consist of three distinct stages, with a distinct slope or work hardening rate associated with each stage. In addition, a region of negligible work hardening exists beyond this region, and persists to very high strains. Total shear strains as large as 137% have been achieved in this material at 300°C. A distinct yield point was also observed although it is not represented on this curve, occurring at a shear stress level of approximately 125 psi (.862 MPa). As can be seen from the curve, sample 1 was strained just past yield, to 2% glide strain. Sample 2 was strained into the first stage of the curve, with 6% glide strain. Sample 3, with 15% glide strain, is in the second stage of the curve. Sample 4, with a glide strain of 23%, represents the early region of the third stage. Finally, sample 5 was compressed to a large glide strain, 56%.

Additional tests at 300°C showed no effect of changing either the specimen size, length to width ratio, or strain rate on the results shown in figure 6, within reasonable limits. As expected, changing the sample orientation caused a considerable effect, with the existence and extent of various stages of the curve dependent upon the orientation.

The slip band structure caused by the intersection of mobile dislocations with the sample surface was examined for each of the compression specimens in figure 6 using a light microscope operating in a Nomarski interference mode to enhance the contrast due to surface relief. Figure 7 shows the structure of sample 2, and this micrograph is typical of the results obtained from samples 1 and 2 in the first stage of the stress-strain curve. The slip lines do not show great prominence and are generally uniform in distribution. Activity appears to be limited to one set of slip planes.

Figure 8 shows the structure of sample 3, deformed into the second stage region of the τ-γ curve. In this sample some of the slip lines show increased prominence compared to the previous sample. Most striking is the appearance of a second operating slip plane, and the amount of activity on this second plane seems to be roughly equivalent to that of the primary plane. However, dislocation motion appears to be limited to these two sets of planes, and there is no evidence of cross slip.

Figure 9 shows the results obtained from sample 5, compressed far into the third stage of the curve. The slip lines are now greatly accentuated and have lost some of the linearity associated with previous samples. The deformation appears to be much less homogeneous. A total of three active slip planes were observed. The most prominent slip lines were those corresponding to the primary plane, and there was considerable evidence for cross slip associated with this plane. However, although cross slip was most evident on the primary plane, it was also observed on at least one of the secondary planes. The results from sample 4 were similar, although these features were not as pronounced in this sample.

Each of the compression sepcimens was sectioned and polished parallel to the primary slip plane in preparation for transmission electron microscopy, and this microscopy was performed with the electron beam normal to the primary slip plane and the primary dislocations lying in the plane of the foil. This was done in order to insure the accuracy of any quantitative measurements and to simplify the interpretation of results. Since CdTe has the zincblende crystal structure, the slip system is of the type {111} <110> , similar to fcc materials. The microscopy was always performed using one of the three $<2\bar{2}0>$ reflections which exist in the {111} reciprocal lattice plane in fcc as the operating satisfied reciprocal lattice vector ($\vec{g}$). It is important to note that all of the dislocations lying in the primary plane will exhibit contrast in all three reflections. However, the type of contrast displayed using a given $\vec{g}$ will depend upon the Burgers vector of the dislocation ($\vec{b}$). If we define the dot product $\vec{g}\cdot\vec{b} = n$, then a primary dislocation with a fixed $\vec{b}$ will have $n = 1$ for two of the possible $<2\bar{2}0>$ reflections and $n = 2$ for the third. These two conditions produce markedly different contrast. The case $n = 1$ produces a single intensity minima which lies slightly displaced to one side of the dislocation core. The case $n = 2$ exhibits two intensity minima separated by a region which may be as bright as background. In some cases one of the minima may be suppressed. Therefore, the two cases $n = 1$ and $n = 2$ can be distinguished in the electron micrograph. This becomes important since for the case $n = 2$ the dislocation Burgers vector lies parallel to the operating reciprocal lattice vector. This situation does not apply to dislocations lying in planes other than the primary slip plane. The contrast due to these secondary dislocations will become very weak or vanish in one of the $<2\bar{2}0>$ reflections. Therefore, by examining the dislocation images in all three $<2\bar{2}0>$ reflections, the following information can be determined: the density of dislocations on the primary plane, the density on secondary planes, the distributions of co-planar slip systems, the direction of the Burgers vector of the dislocations on the primary plane, and the character (edge vs. screw) of these dislocations.

Figure 10 shows the dislocation structure of sample 1. The dislocation distribution in this sample was extremely heterogeneous, with tangles such as seen in figure 10 lying widely separated in a matrix essentially devoid of dislocations. Figure 11 is a typical area in sample 2. The characteristics of the dislocation structure in these two samples were similar, and therefore they may be discussed together. The increase in dislocation density in sample 2 corresponding to the increase in strain manifested itself not in a change in structural characteristics, but instead by an increase in homogeneity and a decrease in the distance between tangles.

Close inspection shows that in figure 10 the dislocations are displaying $n = 1$ contrast, while in figure 11 the case $n = 2$ is present. The structure in general consists of two types of dislocation: long dislocations and dislocation loops of a widely varied size. Examining the dislocation images in all three $<2\bar{2}0>$ reflections, as is seen in figure 12 taken from sample 2, reveals several important results:

1) since none of the dislocations vanish, both the long dislocations and the loops lie in the primary slip plane.
2) since all of the dislocations display the same contrast features as $\vec{g}$ is changed, then $\vec{b}$ is identical for all of the dislocations and one unique slip system exists.

3) the long dislocations tend to have a mixed character. The direction of b is marked in figure 12.

In these samples some activity on other slip planes can be seen, but it is minimal in comparison to the primary plane. Another striking feature of the structure, most evident in figure 11, is that the large loops are of the dipole type, and the long dislocations tend to form a zig-zag configuration, also a type of dipole. Several mechanisms for the formation of the dipole loops can be postulated, using the dipole segments of the long dislocations as a starting point. One mechanism involves the cutting of primary dislocations formed early in the deformation by dislocations moving on secondary planes. The pinned ends of the dipole segments tend to lie in a <110> direction, which is the trace of the intersection of two {111} planes. However, other mechanisms could be envisioned which do not involve secondary dislocations, but instead can be constructed solely based on minimization of energy and properties of dislocation line segments. In any case, it seems likely that the dipole segments and the dipole loops are related. Stereomicroscopy on these samples also aided in the determination that the dislocation loops lie in the plane of the foil.

Figure 13 shows the dislocation structure typical of sample 3, which represents the second stage in the stress-strain curve. An area of this sample which has been examined using the three possible $<2\bar{2}0>$ reflections is seen in figure 14. Several changes in the dislocation structure are evident as compared with the earlier samples. The obvious dual features of long dislocations and large dipole loops have been replaced by a more densely tangled structure comprised of shorter dislocation segments. These tangles are more homogeneously distributed than in the previous samples. The tangles are beginning to lie along <110> directions in the crystal, suggesting the later possible development of a cell structure. Most importantly, figure 14 shows the existence of dislocations in the primary plane with each of the three possible Burgers vectors, so that three co-planar slip systems are now in operation. Again in this sample the dislocations predominantly lie in the primary slip plane. Increased activity on secondary planes is obvious in figure 14, and several short segments and many small loops can be seen to exist in these planes, but the dislocation density on the primary plane is still much greater than on the secondary planes. The primary dislocations also appear to have a stronger edge character than previously.

Figure 15 shows the structure of sample 4, deformed to a point in the third stage of the τ-γ curve. The scale of the microstructure has decreased significantly, and very short dislocation segments lying in tangles predominate. Again the tangles tend to lie along <110> directions, and the matrix regions between tangles are becoming denuded of dislocations. The structure exhibits greater homogeneity than previous samples. Contrast experiments show that the majority of the dislocations still lie in the primary slip plane and a fairly uniform distribution of the three co-planar slip systems in this plane are seen. The density of secondary dislocations continues to increase, but still does not rival the primary density.

The structure of sample 5, compressed to approximately twice the strain of sample 4, does not vary markedly from the previous sample. Figure 16 shows a typical microstructure, which shows the same general characteristics as figure 15. In some areas of this sample the cell structure was much more highly developed, with the formation of dislocation cell walls with sub-boundary characteristics. Figure 17 shows one of the regions. Figure 18 displays a portion of one of these walls taken under different contrast conditions, and it shows that the density of secondary dislocations in these walls is at least comparable to the primary dislocation density.

Since the image characteristics of the dislocations observed in CdTe in the bright-field transmission electron microscopy mode suggested that these dislocations might exist in a dissociated state, weak-beam dark-field microscopy was utilized to investigate this possibility. The weak-beam dark-field technique makes use of a weakly diffracted reflection to form the image, in contrast to the bright-field mode, which uses the transmitted beam in the presence of one strongly diffracting reflection, or conventional satisfied dark-field, which forms the image using a strongly diffracted beam. Two major advantages are obtained when viewing dislocation images using weak-beam dark-field microscopy. First, the bright-field image of a dislocation, caused by electron interaction with the dislocation strain field, is generally on the order of 200 Å wide, and so fine features associated with the dislocation on a scale smaller than this are lost. The weak-beam dark-field dislocation image is generally from 15-40 Å in width, and so many fine features may be resolved. Secondly, in bright-field the dislocation image is usually displaced to one side of the dislocation core and this shift is difficult to determine. In weak-beam dark-field microscopy, the dislocation image corresponds more closely to the true core position and occurs at a calculable distance.

In materials which have a slip system of the type {111}<110>, it is mechanistically possible and in some cases energetically favorable for the unit dislocations to

dissociate into two partial dislocations with a Burgers vector of the form $\frac{a}{6}$ <112>, separated by a faulted region. A typical dissociation reaction for a unit dislocation on a (111) plane can be represented as

$$\frac{a}{2}[10\bar{1}] \quad \frac{a}{6}[11\bar{2}] + \frac{a}{6}[2\bar{1}\bar{1}].$$

If the diffraction conditions are selected properly, both of the partial dislocations will show contrast and will be visible in the electron image.

Weak-beam dark-field electron microscopy on the dislocations in CdTe showed that the dislocations were indeed in many cases dissociated. In this study, the weak-beam dark-field microscopy was performed using a <2$\bar{2}$0> reflection, with the corresponding <4$\bar{4}$0> reflection satisfied in bright-field. Figure 19 shows a bright-field, weak-beam dark-field pair of micrographs illustrating the dissociation of a dislocation lying in the primary slip plane. This image was taken from sample 2, and both partials are clearly visible in the dark-field view. The observed partial separation, Δ_{OBS}, in figure 19 is 125 Å. An analysis of the dislocation strain field enables the actual separation, Δ, to be calculated. It can be shown that [7]

$$\Delta = \sqrt{\Delta_{OBS} - \frac{4}{C^2}} \tag{8}$$

where

$$C = s_g / \frac{\vec{g}\cdot\vec{b}_p}{2\pi} \left(1 + \frac{1}{2(1-\nu)}\right). \tag{9}$$

Here s_g is the deviation from the perfect Bragg condition for the reflection used, $\vec{b}_p$ is the Burgers vector of the partial, and ν is Poisson's ratio. Using this formula, the actual separation is calculated to be 119 Å.

The dislocation line is also observed to be constricted at irregularly spaced intervals. This type of constriction has been observed in weak-beam images of dissociated dislocations in metals, and was shown to be a real effect [8]. An explanation of the occurrence of these constrictions can be postulated in terms of the reduction of the energy of the dissociation.

Several interesting and potentially important implications can be derived from the results of the experiments to date. The mechanical tests have shown that CdTe samples can undergo a large amount of plastic strain at 300°C before failure. This immediately suggests the possibility of forging as a potential method of preparing large window blanks. Forging large plates from material initially in the form of a cylinder would seem to be economically and mechanistically superior in terms of problems with crystal growth.

The mechanical tests have also shown that a definite increase in strength can be achieved by deformation at elevated temperatures. The problems of utilizing this result to improve the room temperature properties and the effects of deformation on the optical properties will be considered in the future.

It also seems likely that a microscopic explanation for the plastic deformation behavior of CdTe can be developed. At the present time, it appears that the first stage of deformation involves the activity of one slip system exclusively. The onset of the second stage seems to involve the activation of additional slip systems, although it is not clear at the present time whether the key role is played by co-planar systems or by systems on slip planes other than the primary. Finally, in the third stage a number of co-planar and non-coplanar slip systems are activated, and there is considerable evidence for cross slip and cell wall and sub-boundary formation. In the future, additional tests at various temperatures will be performed in order to determine the key process which governs the work hardening behavior in each of these stages, and also to isolate any thermal component of the flow processes involved.

3. References

[1] Sparks, M., Proc. Conf. on High Power Infrared Laser Window Materials, 27, 28, Oct. 1971, C. A. Sahagian, C. A. Ditha, eds., AFCRL-71-0592, Special Report No. 127, Dec. 1971, p. 1.

[2] Shiozawa, L. R., Jost, J. M., and Roberts, D. A., Final Technical Report, AFML-TR-73-163, Sept. 1973, Gould Laboratories, Clevelend, Ohio.

[3] Bowen, H. K., Vander Sande, J. B., Final Technical Report, AFML-TR-75-91, Aug. 1975, M.I.T., Cambridge, Mass.

[4] Ballentyne, D. W. G., Wetwatana, S. and White, E. A. D., J. Cryst. Growth 7, 79 (1970).

[5] Reed, T. B. and LaFleur, W. J., Appl. Phys. Lett. 5, 191 (1964).

[6] Hall, E. L., Nurmikko, A. V., Vander Sande, J. B. and Bowen, H. K., Proc. of the Fifth Annual Conference on Infrared Laser Window Materials (ARPA, Arlington, Va.) Feb. 1976, 715.

[7] Cockayne, D. J. H., Ray, I. L. F., and Whelan, M. J., Phil. Mag., 20, 1265 (1969).

[8] Ray, I. L. F. and Cockayne, D. J. H., Proc. R. Soc. Lond. A., 325, 543 (1971).

4. Figures

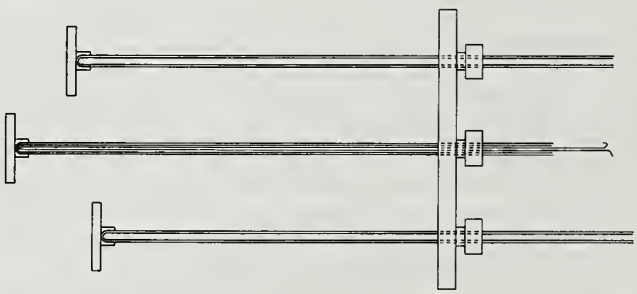

Figure 1. Schematic of end cap with multiple substrates.

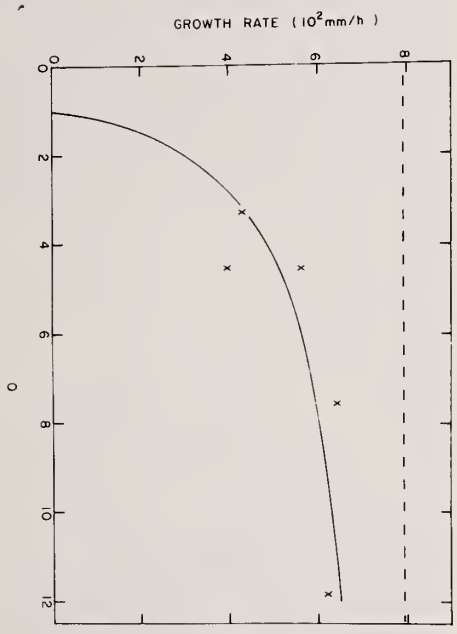

Figure 2. Calculated and observed growth rate as a function of Q for $P_{Cd} = 5.48 \times 10^{-3}$ atm, $P_{Te2} = 2.90 \times 10^{-3}$ atm and flow rate of 600 cc/min at 25°C. Dotted line shows the growth rate at $Q \to \infty$.

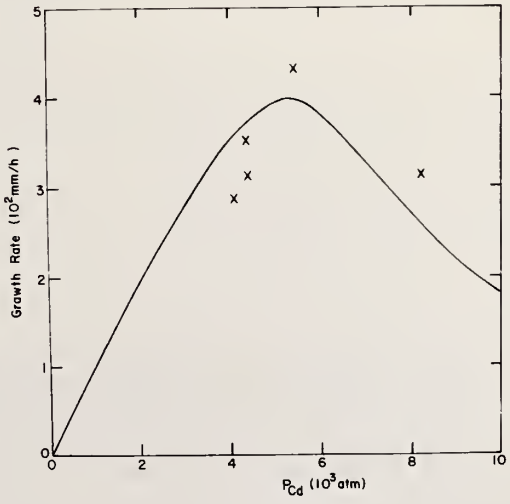

Figure 3. Change of growth rate with P_{Cd} under conditions of $K = 2.7 \times 10^{-4}$ (atm $^{3/2}$) and Q = 3. Observed growth rates are marked by (x).

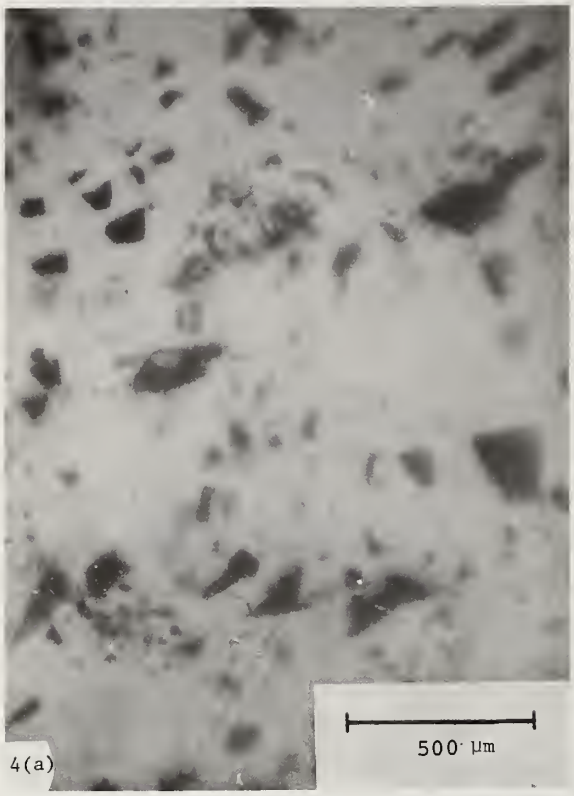

Figure 4. IR photomicrographs of (a) sample KU-6-3 (grown under near stoichiometric conditions) showing significant concentrations of large voids and (b) sample KU-2-2 grown under Cd rich conditions) showing greatly reduced size and concentration of voids.

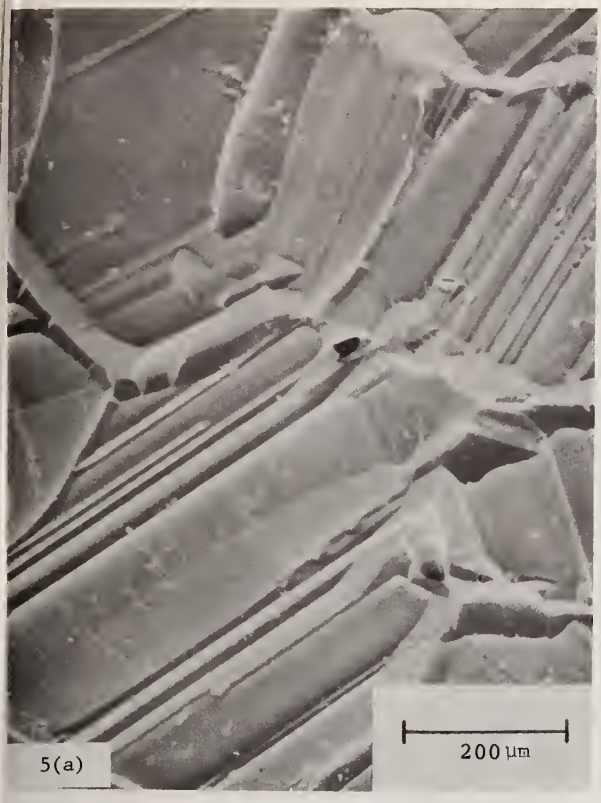

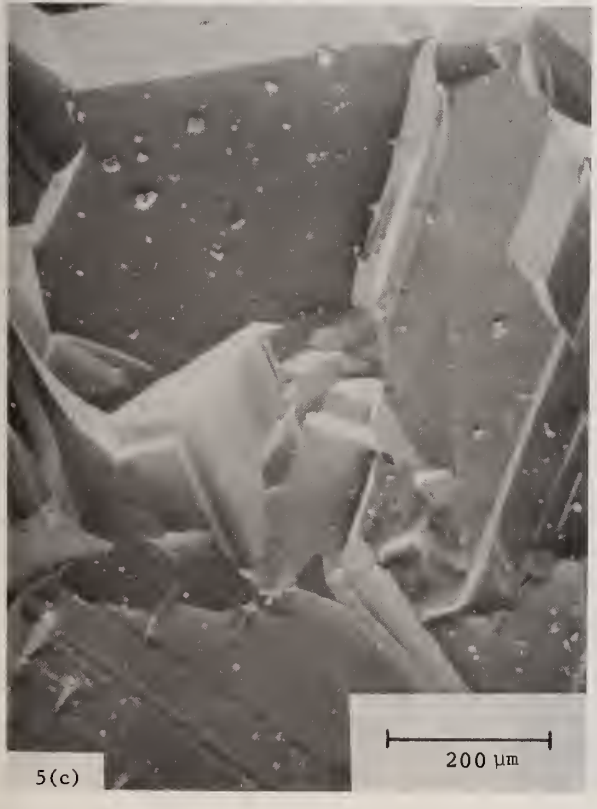

Figure 5. SEM micrographs of as-deposited surfaces, (a) sample KU-8-3 (grown under conditions of high Q) shows high degree of faceting and voids at grain boundaries; (b) sample KU-7-3, and (c) sample KU-13-5 (grown with protective silica tube) both grown under conditions of low Q exhibit lower degree of faceting with no apparent voids at boundaries.

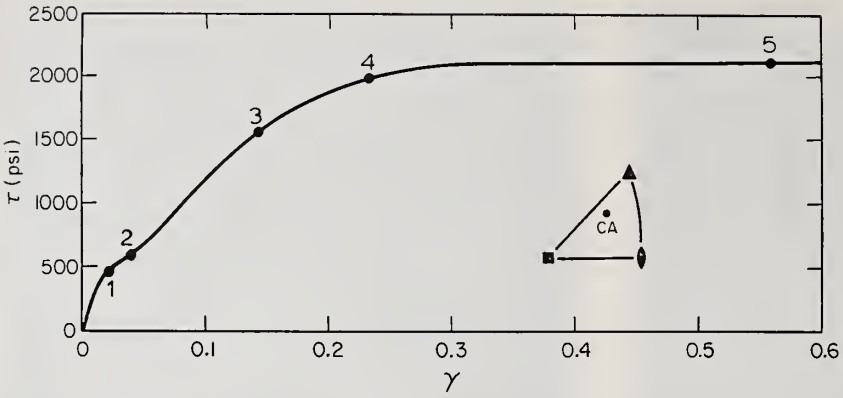

Figure 6. Deformation curve for compression of CdTe single crystal specimens at 300°C, in terms of resolved shear stress τ and glide strain γ. The point of termination of the mechanical test is marked for each of the five samples used in this study.

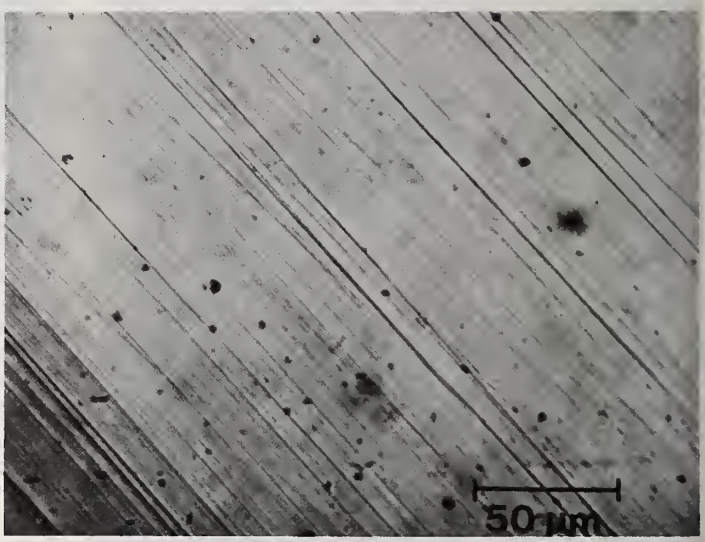

Figure 7. Light micrograph of surface structure of sample 2, γ = 0.06.

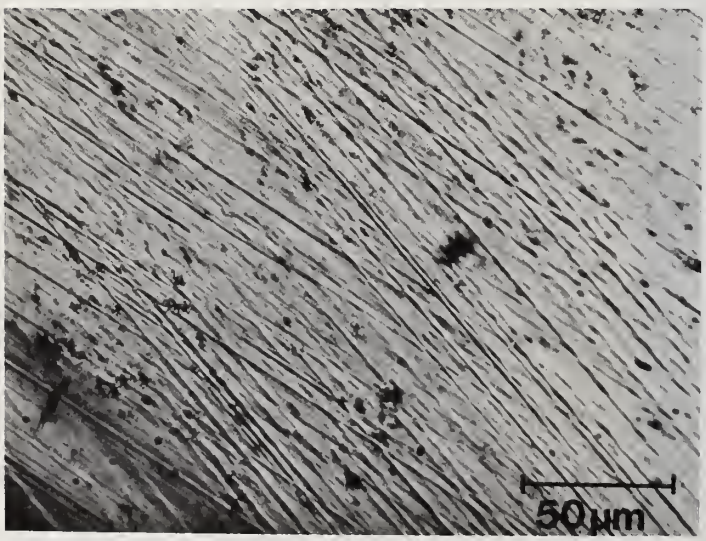

Figure 8. Light micrograph of surface structure of sample 3, γ = 0.15.

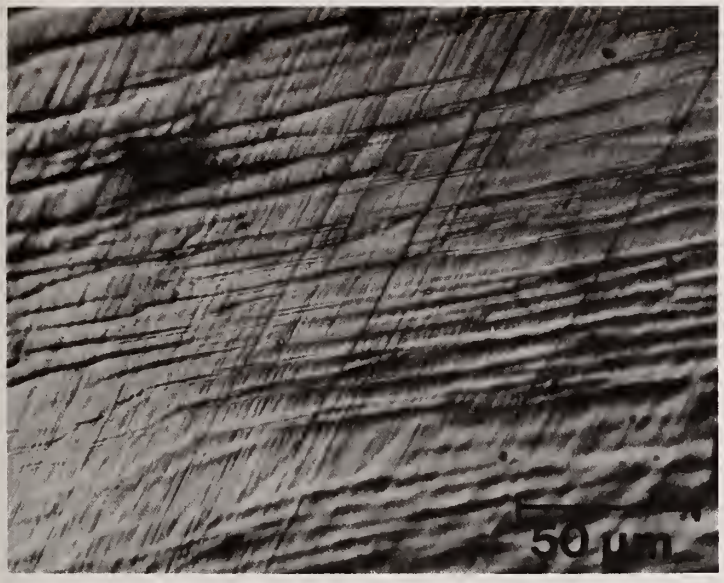

Figure 9. Light micrograph of surface structure of sample 5, $\gamma = 0.56$.

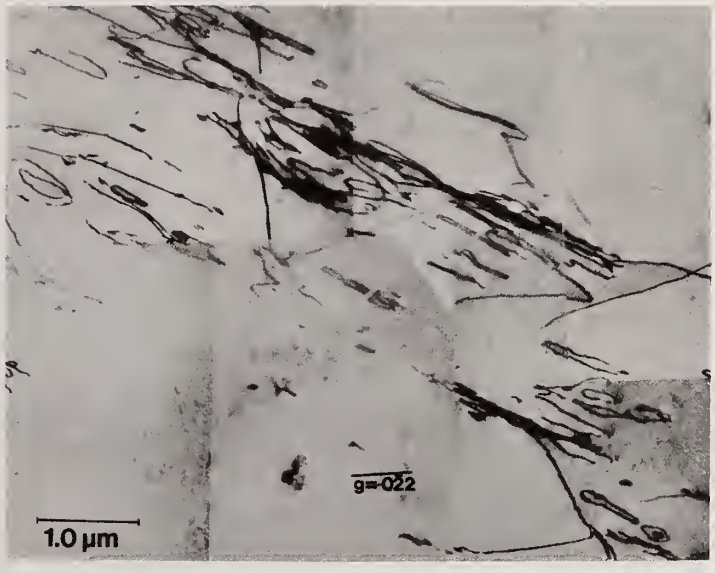

Figure 10. Transmission electron micrograph of the dislocation structure of sample 1, $\gamma = 0.02$. Foil normal [111].

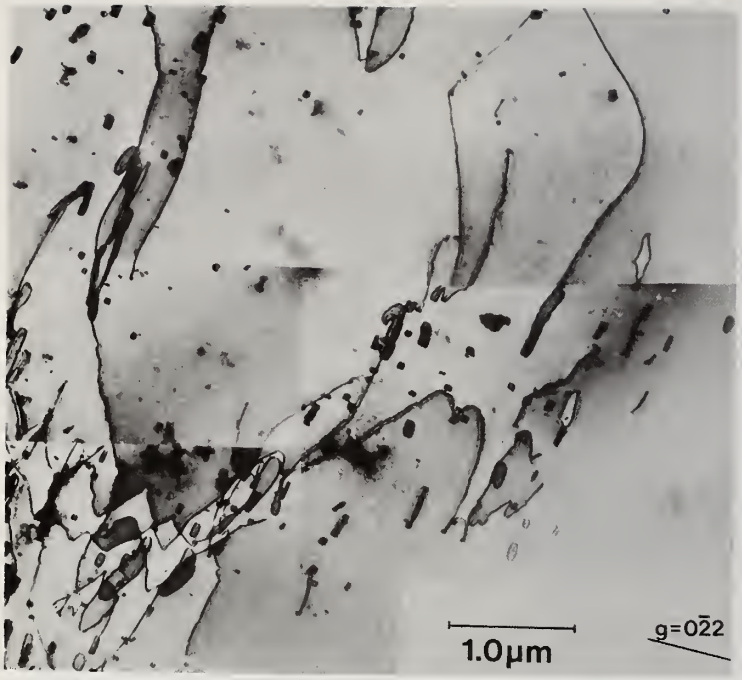

Figure 11. Transmission electron micrograph of the dislocation structure of sample 2, $\gamma = 0.06$. Foil normal [111].

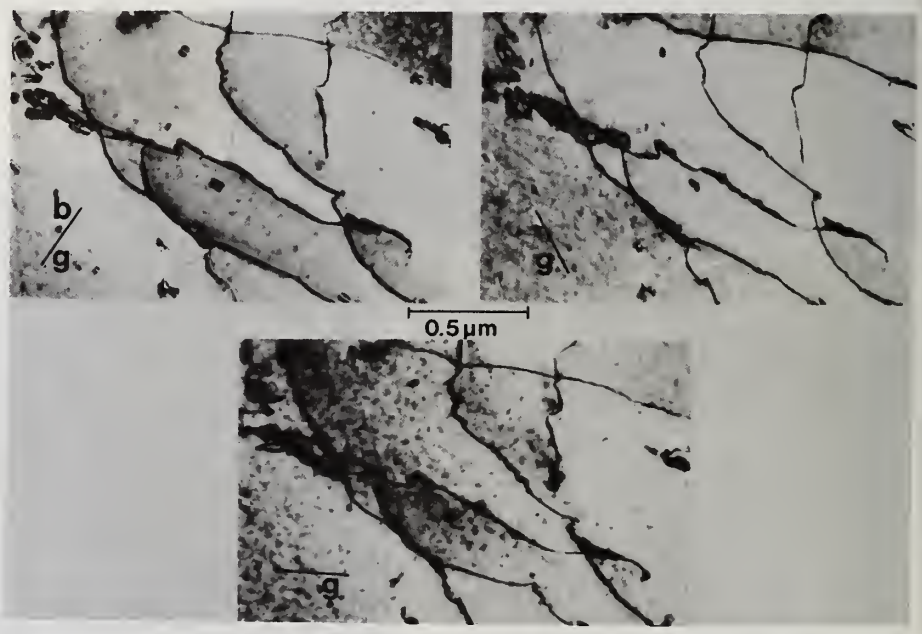

Figure 12. Dislocations in sample 2 imaged under three different diffracting conditions. In each case a unique <2$\bar{2}$0> reflection in the (111) reciprocal lattice plane was strongly excited, and the operating reciprocal lattice vector, $\vec{g}$, is marked on the micrograph. The Burgers vector $\vec{b}$ for the dislocations is indicated on the micrograph where $\vec{g}.\vec{b} = 2$, since in this case $\vec{b}$ is parallel to $\vec{g}$.

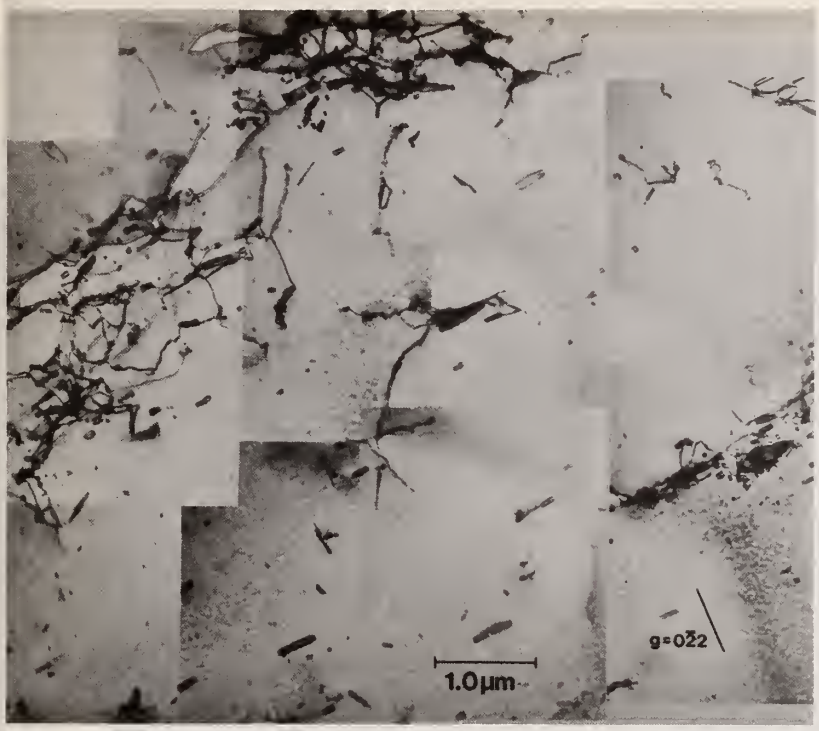

Figure 13. Transmission electron micrograph of the dislocation of structure of sample 3, γ = 0.15. Foil normal [111].

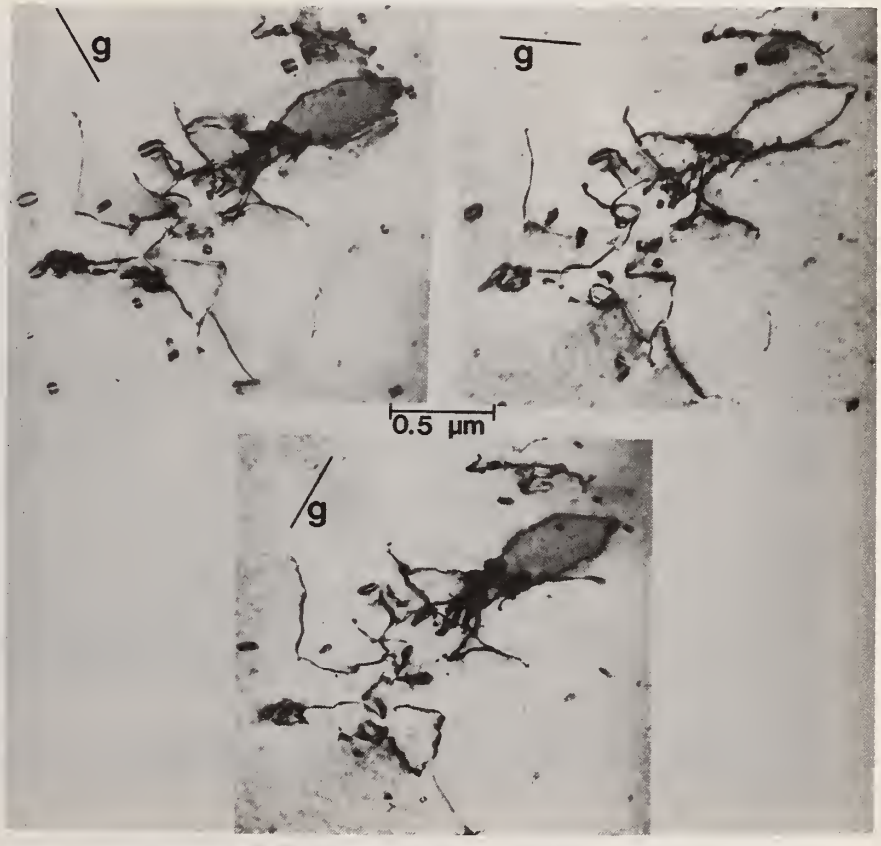

Figure 14. Dislocation images in sample 3 examined using each of the three <$2\bar{2}0$> reflections.

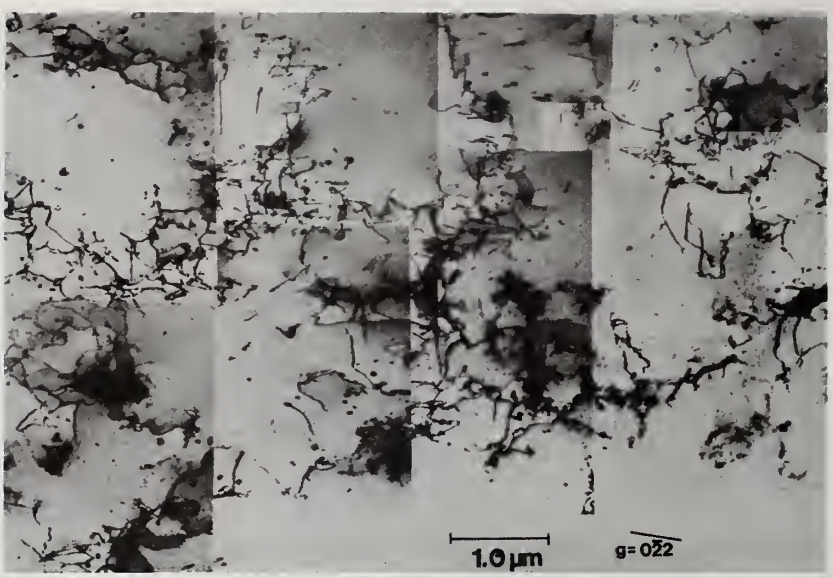

Figure 15. Transmission electron micrograph of the dislocation structure of sample 4, $\gamma = 0.23$. Foil normal [111].

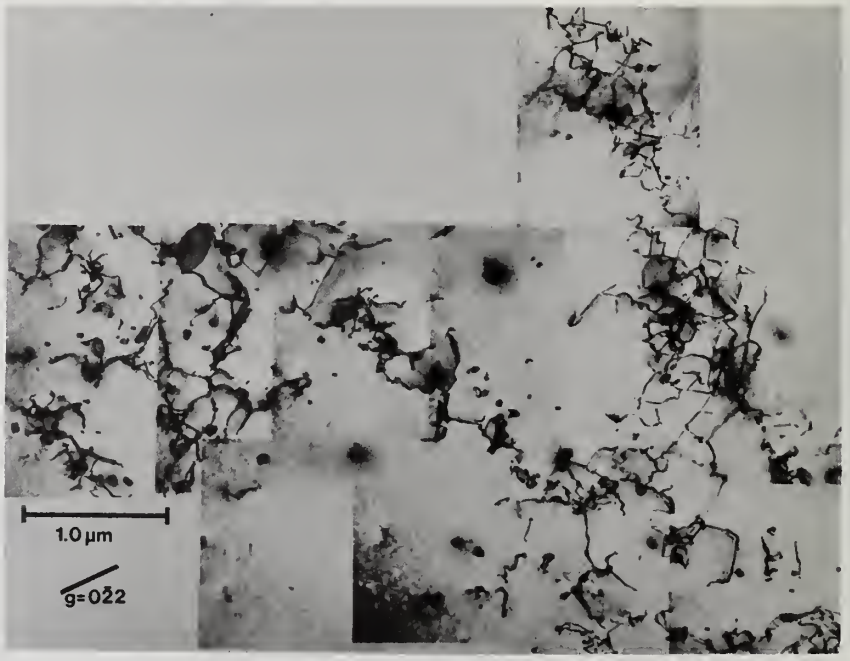

Figure 16. Transmission electron micrograph of the dislocation structure in an area of sample 5, $\gamma = 0.56$. Foil normal [111].

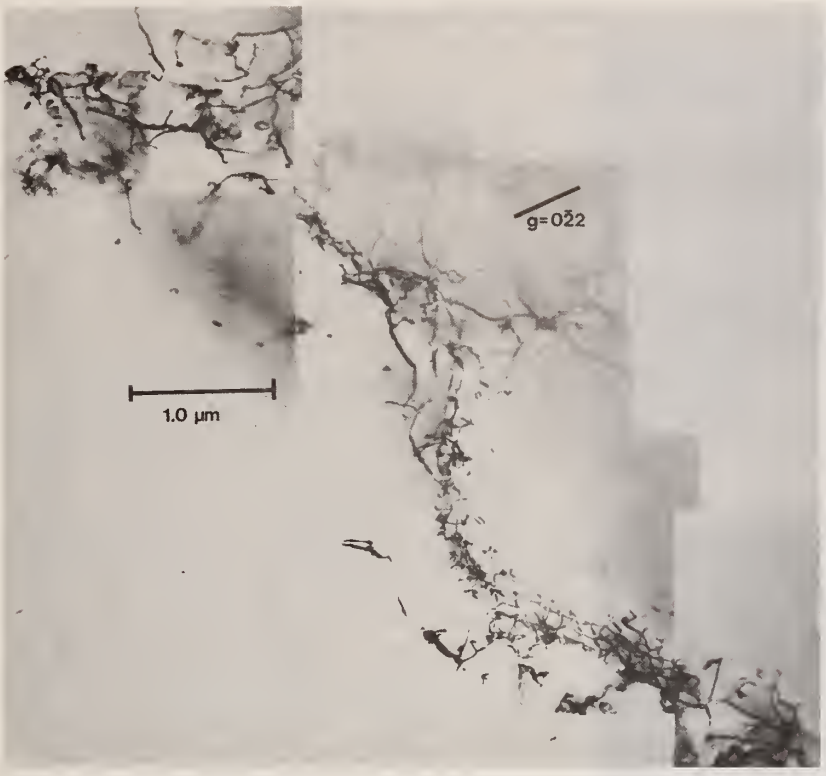

Figure 17. Transmission electron micrograph showing dislocation cell wall in sample 5. Foil normal [111].

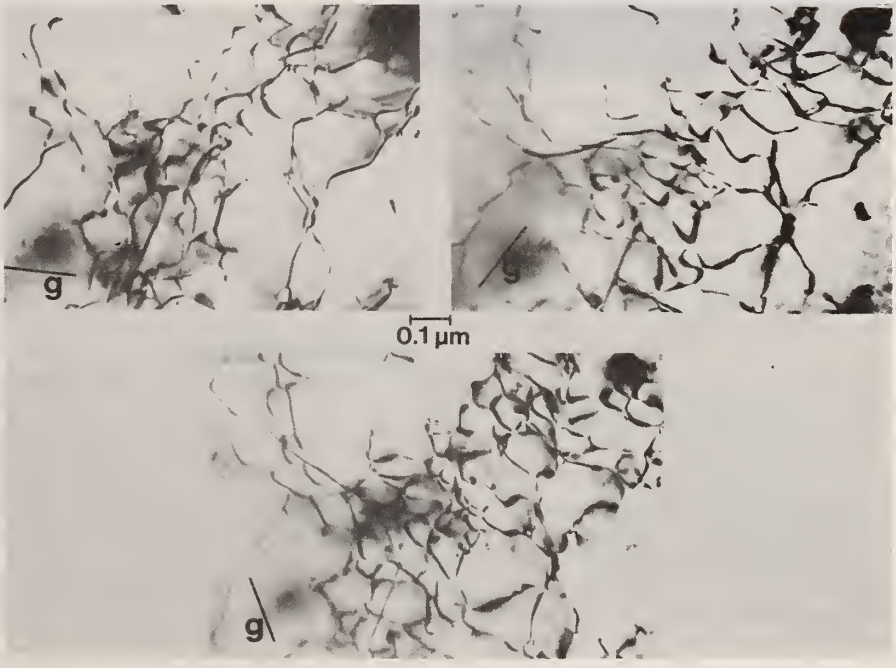

Figure 18. Portion of dislocation cell wall in sample 5 imaged using three different <$2\bar{2}0$> reflections.

Figure 19. (a) Bright-field view of dislocation in sample 2.
(b) Corresponding weak-beam dark-field image showing dislocation dissociation. Diffracting condition is chosen so that both partials are in contrast.

COMMENTS ON PAPER BY TULLER, UEMATSU, VANDER SANDE, HALL, AND BOWEN

No discussion on this paper.

1.14 ABSORBING TELLURIUM INCLUSIONS IN POLYCRYSTALLINE CADMIUM TELLURIDE: ESTIMATES FOR EXTRINSIC DAMAGE THRESHOLDS

Herbert S. Bennett
National Bureau of Standards
Washington, D. C. 20234

and

Cyrus D. Cantrell
Los Alamos Scientific Laboratories
Los Alamos, New Mexico 87544

Cubic cadmium telluride is a promising infrared material for highly transparent windows. However, one problem encountered in high-power laser systems is thermal extrinsic damage to the optical elements which arise from absorbing inclusions. Absorbing inclusions are impurities with physical and optical properties which differ substantially from those of the host material. Such inclusions may absorb an appreciable amount of the incident radiation and thereby may undergo thermal expansion. This produces major stresses within the host. In this paper, we give estimates of the maximum tensile stress as a function of inclusion size, laser pulse width, and laser power for polycrystalline Te spheres in polycrystalline CdTe. Our computations suggest that the heating of 0.1 μm to 10 μm aggregates of Te in CdTe when subjected to power densities of about 100 MW/cm^2 and pulse widths of about 200 ns may produce stresses comparable to or greater than the breaking strength of the CdTe host.

Key words: Cadmium telluride; elastic compliance tensor; elastic moduli; extrinsic damage thresholds; high-power lasers; infrared materials; tensile stress.

1. Introduction

Researchers have shown considerable interest in CdTe as a highly transparent window material for use in high-power infrared laser systems and as a sum and difference frequency generator for use in laser isotope separation processes because of its resistance to environmental influences and reasonably good thermoelastic properties. However, the production of uniform large surface area samples which have infrared absorption coefficients as small as 10^{-4} cm^{-1} at 10.6 μm and which have negligible concentrations of defects poses challenges for the materials scientist [1][1].

Using infrared and optical microscopy, researchers reported macroscopic defects in CdTe which are of the order of one micrometer or greater in size [1-4]. More recent examinations of the microstructural defects by transmission electron microscopy showed that many of the macroscopic defects are aggregations of platelets, precipitates, dislocations, or stacking faults [1,5]. The authors of reference [1] found that the microstructural defects are frequently In_2Te_3 platelets, $CdCl_2$ platelets, and Te precipitates. The densities of such precipitates varied from 10^{14}/cm^3 to greater than 10^{16}/cm^3 and their individual sizes varied from 0.006 μm to 0.015 μm. These authors also reported abnormally high infrared absorption sites of varying morphologies and of sizes from about 1 μm to 6 μm. Annealing at temperatures greater than 500 °C in cadmium vapors reduced substantially the sizes of several of the absorption sites and left other absorption sites essentially unaltered after 48 hours. The latter macroscopic absorption sites were distinct defect aggregations of dislocations, stacking faults, and localized regions of In_2Te_3 or $CdCl_2$ precipitate platelets.

In this paper, we estimate the stresses which occur near localized absorption sites in CdTe samples. Such absorption sites as Te, In_2Te_3, or $CdCl_2$ may absorb sufficient radiation from an incident laser beam to produce deleterious stresses within the CdTe host. To illustrate representative numerical predictions, we compute the stresses near Te absorption sites. Our computations suggest that the heating of Te precipitates when subjected to 100 MW/cm^2 power densities may produce stresses which are comparable to the fracture strength of CdTe. We do not treat the equally important In_2Te_3 and $CdCl_2$ precipitates because literature searches did not provide us with the many optical and mechanical parameters required in the theory. However, the earlier research results of one of us [6,7] showed that the optical, thermal, and mechanical properties of the host dominate in determining the stresses

[1]Figures in brackets indicate the literature references at the end of this paper.

near absorbing inclusions. Hence, even though the quantitative predictions will differ among Te, In_2Te_3, and $CdCl_2$ precipitates, we conclude that all such absorbing sites in the size range from .1 μm to over 10 μm may produce, when subjected to laser power densities of the order of 100 MW/cm^2, thermal stresses which are comparable to or exceed the fracture strength of CdTe.

In section 2, we apply the linear-coupled-quasistatic thermal elastic theory to absorbing polycrystalline aggregates in CdTe to compute the thermal stresses.

In section 3, we introduce approximations by which we reduce the absorbing irregularly shaped aggregate in polycrystalline CdTe to an absorbing polycrystalline sphere in an isotropic host material. The mechanical properties of the sphere and isotropic host are derived respectively from those of Te and CdTe by averaging procedures. We also give the approximations which are necessary to uncouple the linear-thermal-elastic equations [7]. We use this theory in section 3 to formulate the procedure by which we compute estimates for the tangential components of the stress tensor in the vicinity of absorbing Te aggregates in CdTe. The heat diffusion equation with time-dependent boundary conditions for the temperature as a function of time t and of radial distance r was solved by Laplace transforms.

Section 4 contains representative numerical estimates for the stresses around Te aggregates in CdTe and the conclusions which these estimates support.

2. Thermal Elastic Theory

We consider an absorbing site, such as an aggregate of Te, In_2Te_3, or $CdCl_2$ precipitates, in CdTe. An infrared laser beam is incident upon the absorbing aggregate. The resulting heating in the region of the aggregate produces stresses which may become very large. To calculate such stresses, we shall summarize several concepts which together comprise thermal elastic theory [8].

The first concept is that the Newtonian equations of motion apply to any infinitesimal volume element.

The next concept concerns the conservation of energy. The energy balance equation is as follows

$$Q_v - q_{i,i} = \rho C_\varepsilon(\partial T/\partial t) - T(\partial\sigma_{ij}/\partial T)(\partial\varepsilon_{ij}/\partial t) \qquad (1)$$

The quantity Q_v is the internal energy absorption per unit volume; q_i is the i^{th} component of the heat flux vector; C_ε is the specific heat at constant deformation of the elastic solid in question; T is the temperature of the infinitesimal volume element, ε_{ij} is the ij^{th} component of the small-strain tensor, σ_{ij}, is the ij^{th} component of the stress tensor; and ρ is the mass density. Here, we denote partial differentiation with respect to coordinate x_k by ,k and a summation by a repeated index.

For an isotropic material, the heat flux becomes $q_i = -KT_{,i}$, where K is the thermal conductivity. This last equation is called the Fourier law of heat conduction. The internal energy absorption per unit volume is related to the energy density of the local radiation by an absorption equation; that is, $Q_v(\underset{\sim}{r},t) = \gamma I(\underset{\sim}{r},t)$ where the linear absorption coefficient is γ.

The third concept is Hooke's law which expresses the strain ε in terms of the stress σ; namely,

$$\varepsilon_{ij} - \alpha_{ij}(T-T_o) = S_{ijkl}\sigma_{kl}, \qquad (2)$$

where the fourth rank tensor S is called the elastic compliance tensor, and its components S_{ijkl} are the compliances. When a small temperature change $(T - T_0)$ occurs uniformly throughout the material, the resulting deformation is homogeneous and all components $\varepsilon^{\alpha}_{ij}$ which contribute to the total strain ε_{ij} are proportional to $(T - T_0)$; namely, $\varepsilon^{\alpha}_{ij} = \alpha_{ij}(T-T_0)$, where T_0 is the reference temperature for which the material is free of stress and where the coefficients of thermal expansion are α_{ij}. Alternatively, we may use the fourth rank stiffness tensor C_{ijkl} to express the stress σ in terms of the strain; namely,

$$\sigma_{ij} = C_{ijkl}\{\varepsilon_{kl} - \alpha_{kl}(T-T_0)\}. \qquad (3)$$

In order to make these equations amenable to solution, we must simplify them. The approximations to accomplish this simplification are given in the next section.

3. Approximations and Boundary Conditions

Because we seek only estimates for the stresses, we want to simplify the problem. In particular, because a theory for absorbing spheres in isotropic host materials exists [6,7], we shall reduce the problem outlined in section 2 to the problem of an absorbing polycrystalline sphere in an isotropic host material and therby shall apply much of the formalism presented in references [6] and [7] to our present problem.

Our literature survey provides us with complete sets of the essential values for the thermal, elastic, and mechanical properties of Te and of CdTe and only incomplete sets of values for such properties of In_2Te_3 and $CdCl_2$. We therefore consider in the remaining discussion only the Te precipitates in CdTe [9]. However, the concepts presented below apply equally well to In_2Te_3 and $CdCl_2$ precipitates.

Several thermal, elastic, and mechanical properties of the absorbing center and isotropic host enter the linear-uncoupled-quasi-static thermal elastic theory described in references [6] and [7]. Such properties include the density ρ, the specific heat C, the thermal conductivity K, the linear expansion coefficient α, the Young's modulus E, the shear modulus G, the volume compressibility χ, and the Poisson ratio ν.

3.1 Crystalline and Polycrystalline Elasticity

In this subsection we shall discuss the relation between crystalline and polycrystalline elasticity.

The quantities E, G, χ, and ν may be expressed in terms of either the compliances S_{ijkl} or the stiffnesses C_{ijkl}. In general, for crystalline solids, the quantities E, G, and ν depend upon directions relative to the crystalline axes.

We assume that the polycrystalline aggregate contains many grains and is macroscopically homogeneous. This assumption then enables us to use the methods of Hill [10] to compute reasonable values for the elastic moduli of polycrystalline aggregates from a knowledge of the crystalline stiffnesses and compliances. The measured moduli for polycrystalline aggregates invariably lie between the Reuss and Voigt approximations for the moduli of polycrystalline aggregates [10, 11].

The measured values of $\chi = \chi_m$ and $G = G_m$ then have the following limits: $(1/\chi_R) \leq (1/\chi_m) \leq (1/\chi_V)$ and $G_R \leq G \leq G_V$, where the subscripts V and R refer respectively to the Reuss and Voigt approximations. The corresponding values of the Poisson's ratio ν and Young's modulus E for isotropic materials are obtained from the relations,

$$E_m = [(1/3\ G_m) + (\chi_m/9)]^{-1} \tag{4}$$

and

$$\nu_m = (1/2)[1 - \{3\chi_m G_m/(3 + \chi_m G_m)\}] \tag{5}$$

Either the geometric means or the arithmetic means of the Reuss and Voigt values compare well with known experimental values for many polycrystalline materials. Because the experimental values of E, G, χ, and ν for polycrystalline CdTe and Te are incomplete, we calculate $G_g = (G_R G_V)^{1/2}$, $G_a = (1/2)(G_R+G_V)$, $\chi_g = (\chi_R\chi_V)^{1/2}$ and $\chi_a = (1/2)(\chi_R+\chi_V)$, for CdTe and Te. We then assume that $G_{av} = (1/2)(G_g+G_a)$ and $\chi_{av} = (1/2)(\chi_g+\chi_a)$ are reasonable estimates for the measured values G_m and χ_m and use these values in eqs. (4) and (5) to compute estimates for ν_{av} and E_{av}.

Table 1 contains the numerical values of G_{av}, χ_{av}, E_{av}, and ν_{av} for polycrystalline CdTe and Te.

The values for CdTe given in table 1 are reasonable whenever the CdTe host is polycrystalline. The CdTe host may also be a single crystal for which E, G, and ν are functions of directions in the crystal. To simplify the mathematical complexities, we want to approximate the CdTe single crystal by an isotropic material which has properties derived from the single crystal properties. In references [6] and [7] we find that the stress components in the isotropic host are proportional to the Young's modulus of the host. Therefore, we may compute estimated upper and lower limits [12] for the stress components in a single crystal of CdTe by using the respective extremal values for Young's modulus in the isotropic model of references [6] and [7].

The coefficients of thermal expansion for CdTe are isotropic; that is, $\alpha_{ij} = \alpha_h\delta_{ij}$. The thermal expansion coefficient parallel to the c axis of Te, α_3, is not equal to the expansion coefficient perpendicular to the c axis of Te, α_1. Upon averaging over all lattice directions, we obtain an effective thermal expansion coefficient for the polycrystalline Te sphere $\alpha_c = (2/3)\alpha_1 + (1/3)\alpha_3$.

3.2 Isotropic Thermal Elastic Theory

In the previous subsection (3.1), we have simplified the problem of an absorbing, irregularly shaped aggregate of Te in either polycrystalline or single crystal CdTe to a problem involving a polycrystalline sphere of Te in an isotropic host which has properties derived from those of CdTe. This simplification permits us to use the isotropic thermal elastic theory in references [6] and [7]. Using the several approximations given in subsection 3.1, we reduce eqs. (3) and (6) of this paper, respectively, to eq. (2) and eq. (1) on page 250 of reference [7] for the equations of motion and of energy balance. We refer the reader to references [6] and [7] for the details of this theory, of the procedure by which the coupled equations are decoupled, and of the boundary conditions. We summarize here the many assumptions which enter the calculation of the radial stress component $\sigma_{rr}(r,t)$ and the tangential stress component $\sigma_{\theta\theta}(r,t)$:

(a) The absorbing site is a polycrystalline sphere of radius r_0 and is always in good thermal contact with the host. The number of inclusions per unit volume is small so that they do not interact with one another. The effects of shape and orientation to the incident radiation are neglected in the model.

(b) The host material is isotropic, continuous, and of infinite extent. It initially is at an ambient temperature T_0 and free from all stresses and strains. We do not consider the distribution and nature of microcracks and optical imperfections.

(c) The isotropic-linear-thermal-elastic equations give a reasonable description of the processes which ultimately may lead to catastrophic damage when the CdTe host material is approximated by an isotropic continuum with representative properties derived from polycrystalline CdTe.

(d) We neglect the radiation of heat by the absorbing site-host interface and by the host material close to the absorbing site. The laser beams for the examples used here contain energy fluxes much greater than the black body energy flux. In addition, for times less than about one second and for laser pulse widths less than several microseconds, the black body energy flux is very small compared to the energy flux due to thermal conduction.

(e) The coupling term $T_0 C_{ijkl}\alpha_{kl}(\partial\varepsilon_{ij}/\partial t)$ and the inertia term $\rho(\partial^2 u_i/\partial t^2)$ may be neglected whenever three characteristic times which occur in the absorbing site-host system satisfy a set of inequalities. These times are the following. The pulse width τ of the laser beam determines in part the rapidity of heat generation. We shall consider two values of τ: τ = 200 ns and τ = 500 ns. The characteristic relaxation time for temperature equilibration (thermal diffusion) is $t_T \sim (r^2/a_h^2) = 18.6r^2$s for CdTe. In this equation and all subsequent equations the units of r and r_o are centimeters. The thermal diffusivity of CdTe is $a_h^2 = 0.0538$ cm^{2}s and r is a radial distance. The characteristic mechanical time required for the production of stress waves is $t_m \sim (r/v_s) = 6.45 \times 10^{-6}$ rs, where v_s is the speed of propagation of elastic shear waves. Boley and Weiner [8] demonstrate that when $\tau \gg \tau_M$ and $t_T \gg \tau_M$, then the coupling and inertia terms are small compared to the other terms in the equations. The above two inequalities for τ = 200 ns then give us upper and lower limits on the radial distance r; namely, 3.10×10^{-2} cm $\gg$ r $\gg 3.47 \times 10^{-7}$ cm.

(f) The radius of the absorbing sphere is such that the temperature gradients in the sphere are small compared to those in the host material.

The equation which we evaluate is eq. (11) of reference [6]; namely,

$$\sigma_{\theta\theta}(r,t) = \frac{\alpha_h E_h}{(1-\nu_h)r^3}\int_{r_o}^{r} T_h(\rho,t)\,\rho^2 d\rho + \frac{E_h C_{2h}}{(1+\nu_h)r^3} - \frac{\alpha_h E_h T_h(r,t)}{(1-\nu_h)} \tag{6}$$

where $(C_{2h}/r_o^3) = \alpha_c T_h(r_o,t)[1+\{2E_h\chi_c/3(1+\nu_h)\}]^{-1}$. The radial stress component σ_{rr} is not primary to the mechanism for damage considered here.

4. Numerical Examples and Conclusions

The numerical examples which we give here are based on a model whose elastic, thermal, and optical properties are constant independent of temperature. The values for the elastic properties are given in table 1 and are valid for small strains. The values for the thermal properties of density, specific heat at constant volume, thermal conductivity, and effective linear thermal expansion coefficients are given in table 2. Even though the model does not take into account the crystalline aspects, one hopes

that it does give a reasonable description of the actual system. Because we seek here to avoid questions of the value to use for the absorptance $A(\lambda,T)$, we use the value $A(\lambda,T) = 1$ for all numerical examples in this paper. This presents no additional problem because the temperature in the host $T_n(r,t)$ and the stress components σ_{rr} and $\sigma_{\theta\theta}$ are all directly proportional to the absorptance $A(\lambda,T)$. The absorption efficiency for a sphere may be calculated by Mie scattering theory from the complex index of refraction $m = n_1 - in_2$. But the reported values of n_2 in Te vary considerably at 10.6 μm from about 10^{-4} to 10^{-2}. This variation arises partly from impurities. Such values for the imaginary part of the refractive index depend upon the direction of the electric field relative to the c axis and the number of free carriers [13]. For a sphere of radius 10^{-3} cm, Mie scattering theory predicts absorption efficiencies from about 10^{-2} to 0.5. In addition, the theory in reference [7] reveals that the values of the radial and tangential stress components are directly proportional to the incident laser beam power density, E_p. Hence, we shall use for all energies the value $E_p = 100\ MW/cm^2$.

We have used the model outlined in this paper to determine how the maximum tangential stress $\sigma_{\theta\theta}$ varies as a function of the radius r_0 of the spherical absorbing site for fixed power density and pulse width of the laser beam.

Figure 1 contains the dependence upon radius r_0 of the maximum value of the tangential component of stress for polycrystalline Te aggregates in polycrystalline CdTe.

The maximum tensile stresses for In_2Te_3 and $CdCl_2$ precipitates in CdTe are expected to be at least of the same order of magnitude as those for Te in CdTe as given in figure 1. As shown by the asymptotic expressions in reference [7] and the numerical examples in reference [6], $\sigma_{\theta\theta}(max)$ is dominated by the properties of the host and is only slightly dependent upon the absorbing site properties.

CdTe laser windows can be expected to fail when $\sigma_{\theta\theta}(max)$ exceeds the macrocrack formation stress. Macrocrack formation is dependent upon three major factors [14]. (1) the nature of the stresses in three mutually perpendicular directions as a function of distance from the absorbing site host interface; (2) the presence and characteristics of small percursor flaws at the interface and in the host material near the interface; and (3) the size of the precursor flaws, which tend to be larger at the interface. As a result of these factors, macrocracks rarely develop at the theoretical strength σ (theoretical), but may occur at a stress as small as $10^{-2} \times \sigma$ (theoretical), particularly for brittle materials such as CdTe. A general condition by which one may compute σ(theoretical) is to minimize the following quotient Q with respect to orientation of the fracture plane; namely, Q = {square root of (the value of Young's modulus in the direction perpendicular to the fracture plane) times (surface energy for bond rupture)} divided by {the stress normal to the fracture plane}. Calculations [14] show that minimizing Q yields values of σ(theoretical) $\sim 10^{-1} \times$ the Young's modulus. Past experience indicates that the fracture strength which is measured σ(experimental) is probably bounded by $10^{-1} \times$ Young's modulus and $10^{-3} \times$ Young's modulus. In reference [4], Kuhl gives measured values for the fracture strength of CdTe which lie between $1.38 \times 10^7 (N/m^2)$ and $2.75 \times 10^7 (N/m^2)$. Referring to table 1, we see that these measured fracture strengths are of the order of 10^{-3} times the Young's modulus used in the numerical examples of this paper. Figure 1 illustrates the range of r_0 values for which $\sigma_{\theta\theta}(max)$ exceeds $(E_{av}/1000)$. The range of r_0 values is from 10^{-5} cm to over 10^{-2} cm. Hence, we conclude that Te, In_2Te_3, and $CdCl_2$ precipitates in the size range near 10^{-3} cm have the highest probability to produce catastrophic damage in the CdTe host crystals whenever they are subjected to laser power densities of the order of $100 MW/cm^2$.

Even though annealing CdTe at temperatures above 500 °C removes most of the Te precipitates, the In_2Te_3 and $CdCl_2$ precipitates remain and are expected to be equally as troublesome as the Te precipitates for the size range from 10^{-5} cm to over 10^{-2} cm.

In view of the above conclusions, researchers have some options. They may increase the size of the infrared optics and reduce the power density in them; they may devise ways to reduce all damaging precipitates to tolerable sizes; and they may encourage the materials scientists to develop new alternative infrared materials with improved figures of merit when compared with presently available materials such as CdTe.

5. Acknowledgments

The authors wish to thank A. G. Evans, A. Feldman, R. A. Forman, and C. Johnson for several helpful discussions.

6. References

[1] Magee, T. J., Peng, J., and Bean, J., Phys. Stat. Solidi A 27, 557 (1975).

[2] Gentile, A. L., Kiefer, J. E., Kyle, N. R., and Winston, H. V., Proc. Conf. High Power Laser Window Materials, Oct. 30-Nov. 1, 1972, edited by C. A. Pitha, U.S.A.F. Cambridge Research Laboratory Technical Report TR-73-0372, Vol. II, p. 625.

[3] Shiozawa, L. R., Roberts, D. A., and Jost, J. M., ibid., p. 639.

[4] Kuhl, G. E., ibid., p. 607.

[5] Kroger, F. A., Chern, S. S., and Vydyanath, H. R., Proc. Third Conf. on High Power Infrared Laser Window Materials, Nov. 12-14, 1973, edited by C. A. Pitha, A. Armington, and H. Posen, U.S.A.F. Cambridge Research Laboratory Technical Report TR-74-0085(11), Vol. II, p. 437.

[6] Bennett, H. S., J. Appl. Phys. 42, 619 (1971).

[7] Bennett, H. S., J. Res. Natl. Bur. Stand. (U.S.) 75A, 247 (1971); and 75A, 261 (1971).

[8] Boley, B., and Weiner, J., *Theory of Thermal Stresses* (John Wiley and Sons, Inc., New York, 1960).

[9] The authors welcome data on the thermal, elastic, and mechanical properties of In_2Te_3 and $CdCl_2$.

[10] Hill, R., Proc. Phys. Soc. London A65, 349 (1952).

[11] Anderson, O. L., in *Physical Acoustics: Principles and Methods*, edited by W. P. Mason (Academic Press, New York, 1965), p. 43.

[12] Nye, J. F., *Physical Properties of Crystals*, (Oxford University Press, London, 1960), Chap. VIII.

[13] Caldwell, R. S., and Fan, H. Y., Phys. Rev. 114, 664 (1959).

[14] Evans, A. G., *private communication*, Feb. 1976.

7. Figures

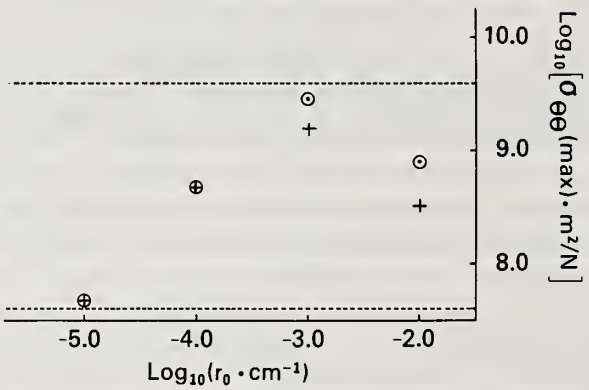

Figure 1. The maximum tensile stress $\sigma_{\theta\theta}$ (max) for Te precipitates in polycrystalline CdTe as a function of radius r_o and pulse width τ for a fixed laser power density E_p = 100 MW/cm^2. The + denotes values for τ = 200 ns and the ⊖ denotes values for τ = 500 ns. The dashed lines are the upper limit ($E_{av}/10$) and the lower limit ($E_{av}/1000$) in MN/m^2 of the estimated fracture strength. The measured fracture strength of CdTe is very close to the lower limit ($E_{av}/1000$).

Table 1. Computed values for the shear modulus G_{av}, volume compressibility χ, Young's modulus E_{av}, and Poisson ratio ν_{av}, for polycrystalline CdTe and Te.

	G_{av} $(N/m^2) \times 10^{10}$	χ $(m^2/N) \times 10^{-11}$	E_{av} $(N/m^2) \times 10^{10}$	ν_{av} (dimensionless)
CdTe	1.4	2.0	4.0	0.37
Te	1.5	5.1	3.7	0.20

Table 2. Values of the thermal properties.[a] The quantities ρ, C, K, and α are, respectively, the density, the specific heat at constant volume, the thermal conductivity, and the linear thermal expansion coefficient. The latter for Te is given by the relation $\alpha = \alpha_c = (2/3)\alpha_1 + (1/3)\alpha_3$.

	ρ (g/cm^3)	C (J/g °C)	K (W/cm °C)	α $(1/°C) \times 10^{-6}$
CdTe	5.85	0.222	0.0699	5.5
Te	6.23	0.164	0.0628	17.8

[a] C. S. Sahagian and C. A. Pitha, Compendium on High Power Infrared Laser Window Materials, U.S.A.F. Cambridge Research Laboratory Special Report No. 135, 9 March 1972.

COMMENTS ON PAPER BY BENNETT AND CANTRELL

No discussion on this paper.

1.15 HOT-PRESSED $CdCr_2S_4$ FOR FARADAY EFFECT ISOLATION AT 10.6μm: PRELIMINARY DAMAGE TESTS

Stephen D. Jacobs
Laboratory for Laser Energetics

and

Kenneth J. Teegarden
Institute of Optics
University of Rochester
Rochester, New York 14627

The ferromagnetic spinel, $CdCr_2S_4$ is considered an attractive candidate for future use in target back reflection isolation of high power infrared lasers for fusion investigations. Used with liquid nitrogen refrigerant in a Faraday rotator configuration, this material demonstrates isolation in excess of 30dB and an insertion loss (due to material attenuation) of 30 percent in saturating magnetic fields of 3500 Oe. Minimal homogeneity requirements for dc magnetic field biasing and the scalability of the hot-pressing process make $CdCr_2S_4$ suitable for large aperture applications. Single crystal growth and hot-pressing procedures are currently being optimized to reduce extrinsic attenuation at 10.6μm.

The threshold for laser induced damage in $CdCr_2S_4$ ($n_{10.6} = 2.84$) is of fundamental importance to the proposed application. Preliminary measurements have been made using a 50ns, TEA CO_2 laser with a multimode output of 20 joules. The results indicate that this material has a damage threshold in excess of 2 J/cm^2.

Key words: $CdCr_2S_4$; chalcogenide spinel; Faraday effect; ferromagnetic semiconductor; hot-pressed; infrared transmission; laser induced damage; optical isolation

1. Introduction

The discovery in 1965 [1][1] of a family of semiconducting ferromagnetic chalcogenide spinels with the potential for optical transmission in the infrared [2] opened up the possibility of their future use for optical isolation. Magneto-optical investigations of these materials progressed slowly at first due to a difficulty in growing large single crystals or large polycrystalline mosaics [3]; but the application of hot-pressing techniques [4,5] and the subsequent fabrication of samples with large cross-sections enabled optical and magneto-optical investigations to rapidly advance. A chalcogenide spinel which received particular attention was $CdCr_2S_4$. By 1971, enough optical and magneto-optical data had been collected for this material [6-8] to indicate that hot-pressed $CdCr_2S_4$ could provide a substantial Faraday effect accompanied by low optical absorption in the infrared. The subsequent acquisition of hot pressed samples of various sizes enabled an investigation of optical isolation to proceed.

This paper is divided into several sections. The first provides an introduction to $CdCr_2S_4$, reviewing the physical, optical, and magneto-optical properties which make it suitable for use as an optical isolator at 10.6μm. Figures of merit measured for breadboard isolator configurations are then presented, and results of a preliminary damage test with high power, short pulse radiation are discussed.

2. Physical Properties and Structure

Single crystals of $CdCr_2S_4$ form in the spinel structure with 8 molecules per unit cell. The sulfur anions are packed in a face-centered cubic arrangement with the various Cd^{+2} and Cr^{+3} cations occupying 24 of the 96 interstitial sites present in the unit cell. The compound considered here is "normal" spinel; only Cd cations are found to occupy A sites (surrounded by a tetrahedron of sulfur

1. Figures in brackets indicate the literature references at the end of this paper.

anions), with Cr cations exclusively on B sites (surrounded by an octahedral arrangement of sulfur anions). Because of the regular ordering of ions, exchange interactions can force $CdCr_2S_4$ into a ferromagnetic state via parallel alignment of spin magnetic moments of Cr^{+3} valence electrons (orbital moments being quenched by the crystal field) at a Curie temperature of T_c = 84.5 K.

It is difficult to grow large, pure, stoichiometric single crystals of $CdCr_2S_4$. The largest single crystals (a few mm in size) have been grown using a liquid-vapor-solid method developed by Shick and Von Neida [9,10]. This fundamental materials acquisition problem was overcome by using the hot-pressing process. The ability to produce a product with useful optical properties depends equally upon spinel powder preparation and hot-pressing technique. Two successful methods of powder preparation [4,5] start with anhydrous chlorides or hydroxide coprecipitates. The former offers a means of working with an oxygen-free system, whereas the latter method produces a finely divided powder. Ideally the prepared powder should have a cubic spinel structure, be stoichiometric, and free of second phase impurities. Powders prepared from C-P grade starting compounds and ground to agglomerate sizes less than 140μm (crystalline sizes of 0.2μm) are sometimes nonstoichiometric (excess Cr^{+3}) and contain such impurities as CdS, Cr_2O_3 and Cr_2S_3. Hot-pressing is done in a vacuum of 10^{-4} torr, between 800 and 900°C, for 10-20 minutes at 50,000 psi.

The objective of this process is the densification of the powder and the preservation of the spinel structure. Densification is thought to occur via plastic flow [4]. The simultaneous application of high pressure and temperature reduce porosity and prevent decomposition. Hot-pressed crystallite grains are 1 to 2μm in size, and show no preferred shape as a result of the hot-pressing process. X-ray diffraction analysis reveals the hot-pressed material to be in the cubic spinel phase, with a density greater than 99.8 percent of the theoretical value [4,5]. Measurement of lattice constants agree with single crystal data. Electron microscopy of fractured surfaces reveals porosity at crystal interfaces of poorly transmitting samples. Pores are not connected and frequently contain impurities. No porosity is observed in samples of good optical transparency [4]. It is not possible to chemically ascertain the stoichiometry of hot-pressed samples of $CdCr_2S_4$ due to their insolubility in nitric acid; but the presence of decomposition products such as CdS or CdO on cold portions of the hot-pressing apparatus indicate a non-stoichiometric excess of Cr^{+3} in some samples. It has been shown, however, that excess Cd^{+2} or Co^{+2} is far more detrimental to optical transmission than excess Cr^{+3} [5].

Hot-pressed samples exhibit good thermal shock resistance, and may be cycled from room temperature to 77 K in minutes without cracking. The materials are easily ground and polished using standard optical techniques, are black in appearance, and exhibit a hardness just under 5.0 on the Moh scale (a value comparable to cerium oxide). Important physical data is summarized in table I.

Table 1. Physical data for h-p $CdCr_2S_4$

Property	Value	Reference
Lattice parameter, Å	10.244[a]	[1]
Theoretical x-ray density, g/cm^3	4.259	[12]
Electrical resistivity		
(300K) ohm-cm	$2x10^3$	[12]
(77K) ohm-cm	$2.86x10^9$	[12]
Curie temperature, K	84.5	[9]
H-p grain size, μm	1 - 2	[4], [5]
Chemical inertness of H-p product	good[b]	
Hardness of H-p product, Moh	5	[11]

[a]Varies less than 0.1 percent from room temperature to 4.2 K [13]

[b]H-p $CdCr_2S_4$ may be etched in boiling concentrated nitric

3. Optical and Magneto-Optical Properties

The index of refraction for $CdCr_2S_4$ at 10.6μm is 2.84 [7]. Typical values of attenuation vs wavelength for an optically good sample are shown in figure 1. The infrared window for $CdCr_2S_4$ extends from 1.0 to 12.0μm with restrahl processes occurring at 26.0 and 28.8μm. Laser calorimetry shows scattering to be unimportant at 10.6μm [8,11], and absorption coefficients less than 1.0 cm^{-1} have been attained with improved hot-pressing techniques. An intrinsic lower limit to absorption has not yet been determined, and the levels depicted in figure 1 are thought to be due to residual absorption. Cr_2O_3 is known to cause absorption at 13.5, 16.1, 17.8, and 18.7μm, and the presence of as little as 0.001 percent oxygen [4] is sufficient to cause the observed structure near 13μm in figure 1.

When cooled below its Curie temperature, $CdCr_2S_4$ exhibits a saturated Faraday rotation at 10.6μm of 120 degrees per cm of material. Rotation is linear with applied field and saturates at 3.5 kOe ($CdCr_2S_4$) in thin disc samples exhibiting maximum demagnetizing effects [11]. The Faraday effect in these materials at long wavelengths is due to magnetic dipole transitions having resonance frequencies in the far-infrared or microwave regions; it is, therefore, essentially independent of optical absorption at 10.6μm. The absolute value of Faraday rotation as a function of wavelength is shown in figure 2.

4. Faraday Effect Optical Isolation

Isolation figures of merit, referred to as the passive extinction ratio (PER) and forward to backward transmitted energy ratio (F/B) have been measured for 12 mm diameter discs of $CdCr_2S_4$. The former gives the amount of extinction that would be obtained for a sample in an unactivated state between crossed polarizers; the latter measures the amount of extinction that would be obtained if the sample were placed between polarizers oriented with pass directions at 45 degrees, under magnetic field biasing sufficient to produce 45 degrees rotation within the activated sample per pass of incident (and reflected) radiation. Measurements on several $CdCr_2S_4$ samples indicate maximum PER and F/B ratios of about 2000/1 [14]. These values are thought to be limited by (a) no prior history of thermal annealing for samples used, and (b) thermally induced strain randomly generated in cool down by a poor sample mounting configuration. Confirmation of depolarization via thermally induced strain birefringence was obtained by measuring the F/B ratio over a 5 mm diameter portion of a 1 cm thick piece of hot-pressed $CdCr_2S_4$ (see figure 3). Two regions exhibiting good isolation (F/B $\geq$ 500) and one region of poor isolation (F/B $\leq$ 200) are well defined. The F/B contour could not be reproduced upon cycling the sample to room temperature and back to 77 K.

Pertinent data for hot-pressed $CdCr_2S_4$ in an isolator configuration is summarized in table 2. At 10.6μm, in a saturating field of 3.5 kOe, an a-r coated $CdCr_2S_4$ isolator element 0.375 cm thick would exhibit a transmittance of 70 percent and provide from 20 to 30 dB isolation. A $CdCr_2S_4$ isolator would require liquid nitrogen coolant.

Table 2: Probable performance characteristics of h-p $CdCr_2S_4$ as an optical isolator at 1.06μm.

Operating temperature, K	77
Element thickness reqd. for 45 degree rotation, cm	0.375
Attenuation coeff., cm^{-1}	<1
A-R coated element transmittance, %	~70
Magnetic field reqd. for saturated operation, kOe	3.5
Optical isolation, dB	20 to 30

Unique possibilities for isolator design are offered by this material and are discussed as follows:

(1) Fabrication of large diameter elements - $CdCr_2S_4$ is easily worked and polished, hard, and insoluble in most chemicals. The progress recently made in understanding the affect of nonstoichiometry upon optical transmittance [5] has made it possible to fabricate one cm diameter $CdCr_2S_4$ discs with

uniformly low attenuation. The hot-pressing process has been well characterized [4] for this material and no new problems should be encountered in producing large discs 20 cm in diameter or greater, possessing good optical quality and uniformity.

(2) Element transmittance -
Because absorption is impurity related and not intrinsic, there are no fundamental limitations to increasing material transmittance at 10.6μm through use of higher purity starting compounds while maintaining large values of Faraday rotation. A reduction in absorption by a factor of 5 for $CdCr_2S_4$, would increase transmittance to greater than 90 percent for AR coated isolator elements of optimum thickness.

(3) Magnetic field requirements -
Because it is ferromagnetic, this material exhibits a saturation of its magnetization and a saturated Faraday rotation. For thin, large diameter discs exhibiting maximum demagnetizing effects, saturation would require low fields of 3.5 kOe. The uniformity of the applied magnetic field throughout the isolator active element volume would not be critical, the Faraday rotation being a maximum uniform value throughout a magnetically saturated ferromagnet.

(4) Optical isolation -
Samples investigated had no history of thermal annealing. Experimental evidence also confirmed that these samples were subjected to additional strains from constriction in cooled mounts. Yet even under such conditions, F/B ratios in excess of 30dB were measured. The uniformity and magnitude of isolation could be expected to improve substantially with annealed samples mounted in an improved manner.

(5) System design -
$CdCr_2S_4$ isolator elements providing 45 degrees of rotation at 10.6μm could be self-supporting discs. Convective edge and face cooling of a $CdCr_2S_4$ element suspended in a helium gas atmosphere at 77 K would provide a set up capable of maintaining the material below its Curie temperature without exerting a large amount of thermal or mechanical stress. The magnetic fields required could be produced by liquid nitrogen cooled solenoids. Modest cooling constraints and minimal magnetic field magnitude and uniformity requirements would permit isolator systems using this material to be fabricated and operated at low cost.

5. Laser Induced Damage Tests

A Lumonics Series 600 TEA CO_2 laser, characterized by a 50ns pulse with an energy density of approximately 0.45 J/cm^2 was used to irradiate a typical disc sample of hot-pressed $CdCr_2S_4$. The sample #16A-53, 12.7 mm in diameter and 0.585 mm thick, had a passive attenuation coefficient of 7cm^{-1} at 10.6μm. The damage test consisted of placing the sample behind a circular aperture and varying the energy density incident upon its surface using a gold coated concave mirror (see figure 4). Beam size at the sample was monitored with thermofax paper.

The results are indicated in table 3 and in the accompanying figures. A total of three shots were taken, the first being unfocussed, and the next two being focussed to average calculated energy densities of 2.3 J/cm^2 and 6.5 J/cm^2, respectively. Burn spots typical of these latter shots are shown in figure 5. The nonuniformity of the energy density within the irradiating beam is readily apparent in figure 5.

Using visual inspection, we observed no damage for the first shot (0.45 J/cm^2). The average energy density in the second shot also failed to cause any visually observable damage except within a 1 mm^2 area accounting for 2 percent of the total irradiated area, where hot-spots did cause significant damage on the entrance surface only (see figure 6). Hot-spot induced damage increased to 30% of the area irradiated in shot 3 and was visually apparent on both entrance and exit surfaces (see figures 7a,b). (Different surface areas were irradiated in shots 2 and 3 so that the damage morphology of each shot could be separated.) Formation of an intense plasma on the entrance surface was noted during this shot.

The Nomarski optical micrographs in figures 6 and 7 indicate several types and stages of damage. Surface cracking, peeling and lifting is apparent, as is the removal of surface material by ablation. The pits in figures 6 and 7b are 2 and 9μm deep, respectively. Numerous scratches visible in these two figures were present on the surface prior to testing, as can be seen in figure 8 which shows an unirradiated portion of the sample near its edge.

It is difficult to draw a definite conclusion as to the damage threshold for hot-pressed $CdCr_2S_4$ at 10.6μm based on the above test results. Repolishing of the sample exit surface did reveal that most of the observed damage was surface related.

Table 3. Damage test results - 50ns pulse irradiation of H-P $CdCr_2S_4$ at 10.6μm

Shot #	Energy on Sample joules	Area Irradiated cm^2	Energy Density J/cm^2	Power Density MW/cm^2	Damage Observed
1	0.5	1.17	0.43	8.6	none
2	1.3	0.56	2.3	46	none*
3	1.3	0.20	6.5	130	Surface+Bulk?†
Uncertainty:	10%	10%	40%	50%	

* Hot spot induced damage was observed over 2% of the irradiated entrance surface

† Hot spot induced damage was observed over 30% of the irradiated entrance and exit surfaces

However, a fundamental limitation to further interpretation is the lack of a TEM_{00} mode energy distribution in the irradiating pulse. The fraction of the average energy which is concentrated in the hot spots of the laser pulse is not known; it is the energy in these hot spots (which may differ from the average energy density) which caused the observed damage. Microscratches on the surfaces of the tested sample also present an obstacle to interpretation of the test results. Such surface defects are known to cause electric field enhancement and surface damage at irradiation levels below those found for defect-free surfaces. This is especially so for high index materials [15] ($n_{10.6}$ = 2.84 for $CdCr_2S_4$).

Given the above it is still useful to pick a rough number for the damage threshold in hot-pressed $CdCr_2S_4$ and make a comparison with thresholds of other high index materials. Table 4 gives $CdCr_2S_4$ data from shot 3 along with 10.6μm induced damage thresholds of ZeSe, GaAs, CdTe, and Ge. It would be useful to scale the data from long to short pulse lengths. One calculation predicts that for inclusion-free dielectrics a 100-fold decrease in irradiation pulse length from 200ns to 2ns would be accompanied by a 4 to 8-fold increase in power density threshold [16]. If electrical breakdown mechanisms hold in the same way for $CdCr_2S_4$, one would predict a damage threshold of 0.4 J/cm^2 for a 1ns pulse. Similar extrapolations, indicated in table 4 for GaAs, CdTe, and Ge, bracket the above value for $CdCr_2S_4$. The data for ZnSe show this extrapolation to agree within a factor of 2 with experimental results.

Table 4. Damage thresholds of high index materials at 10.6μm
(B = Bulk, S = Surface)

Material ($n_{10.6}$)	Pulse Length (mode) ns	Energy Density J/cm^2	Power Density MW/cm^2	Reference	Extrapolated Threshold for 1ns pulse* GW/cm^2 or J/cm^2
ZnSe (2.41)	1_{00}	1.5(B)	1,500	15	1.5
ZnSe (2.41)	600_{00}	55(B)	90	16	3.0
Ge (4.0)	75_{00}	13(S)	173	19	0.8
$CdCr_2S_4$† (2.84)	50_{Multi}	6.5(?)	130		0.4
GaAs (3.3)	$100_{?}$	3(B)	30	17	0.2
CdTe	600_{00}	2(S)	3	18	0.1

* See text

† Based on data from shot #3

Future systems requirements for high power CO_2 laser amplifiers specify that optical components be capable of handling 2 J/cm^2 in 1 ns [20]. From this damage test it may be argued that hot-pressed $CdCr_2S_4$: a) is certainly within a factor of 5 of this specification, and b) warrants continued investigation as an isolator material for 10.6μm.

6. Acknowledgments

The authors would like to acknowledge E. Carnall, Jr., D. Pearlman, and T.W. Martin of the Research Laboratories - Eastman Kodak Company for the provision of hot-pressed material, and J. Wilson from the Laboratory for Laser Energetics, University of Rochester, for assistance in performing the damage tests.

7. References

[1] Baltzer, P.K., Lehmann, H.W. and Robbins, M., "Insulating Ferromagnetic Spinels," Phys. Rev. Lett. 15, 493 (1965).

[2] Harbeke, G. and Pinch, H., "Magnetoabsorption in Single-Crystal Semiconducting Ferromagnetic Spinels," Phys. Rev. Lett. 17, 1090 (1966).

[3] Coburn, T.J., Pearlman, D., Carnall, Jr., E., Moser, F., Lee, T.H., Lyu, S.L. and Martin, T.W., "The Preparation and Magneto-Optical Properties of Hot-Pressings of the Magnetic Semiconductors $Cd_xCo_{1-x}Cr_2S_4$," AIP Conference Proc. on Magnetism and Magnetic Materials in Denver, Colo. 740 (1972).

[4] Pearlman, D., Carnall, Jr., E. and Martin, T.W., "The Preparation of Hot-Pressed Chalcogenide Spinels," J. Sol. State Chem. 7, 138 (1973).

[5] Pearlman, D., Carnall, Jr., E. and Martin, T.W. "The Preparation of Hot-Pressed Chalcogenide Spinels. II. Stoichiometry and Optical Transparency in $CdCr_2S_4$," J. Sol. State Chem. 9, 165 (1974).

[6] Ahrenkiel, R.K., Moser, F., Carnall, E., Martin, T., Pearlman, D., Lyu, S.L., Coburn, T. and Lee, T.H. "Hot-Pressed $CdCr_2S_4$: An Efficient Magneto-Optic Material," Appl. Phys. Lett. 18, 171 (1971).

[7] Moser, F., Ahrenkiel, R.K., Carnall, E., Coburn, T., Lyu, S.L., Lee, T.H., Martin, T. and Pearlman, D., "Optical and Magneto-Optic Properties of Polycrystalline $CdCr_2S_4$," J. Appl. Phys. 42, 1449 (1971).

[8] Coburn, T.J., Moser, F., Ahrenkiel, R.K. and Teegarden, K.J., "Infrared Absorption Spectrum and Faraday Rotation of Hot-Pressed $CdCr_2S_4$," IEEE Trans. Mag., MAG-7, 392 (1971).

[9] Baltzer, P.K., Wojtowicz, P.J., Robbins, M. and Lopatin, E., "Exchange Interactions in Ferromagnetic Chromium Chalcogenide Spinels," Phys. Rev. 151, 151 (1966).

[10] Von Neida, A.R. and Shick, L.K., "Single Crystal Growth of Some Chalcogenide Spinels," J. Appl. Phys. 40, 1013 (1969).

[11] Jacobs, S.D., "Ferromagnetic Isolation and Modulation in the Infrared Using Hot-Pressed $CdCr_2S_4$," Ph.D. Thesis, University of Rochester, 1975.

[12] Lehmann, H.W. and Robbins, M., "Electrical Transport Properties of the Insulating Ferromagnetic Spinels $CdCr_2Se_4$," J. Appl. Phys. 37, 1389 (1966).

[13] Martin, G.W., Kellogg, A.T., White, R.L. and White, R.M., "Exchange-striction in $CdCr_2S_4$ and $CdCr_2Se_4$," J. Appl. Phys. 40, 1015 (1969).

[14] Jacobs, S.D., "Faraday Rotation, Optical Isolation, and Modulation at 10.6μm Using Hot-Pressed $CdCr_2S_4$ and $CoCr_2S_4$," J. Elect. Mater. 4, 223 (1975).

[15] Stark, Jr., E.E. and Reichelt, W.H., "Damage Thresholds in ZnSe, A/R Coated NaCl and Micromachined Mirrors by 10.6μm Multijoule, Nanosecond Pulses," NBS Special Publication 414, p. 53 (1974).

[16] Wang, V., Rudisill, J.E., Giuliano, C.R., Braunstein, M. and Braunstein, A., "Pulsed CO_2 Laser Damage in Windows, Reflectors, and Coatings," NBS Special Publication 414, p. 59 (1974).

[17] Smith, J.L., "Effects of Laser Flux in GaAs," NBS Special Publication 387 - Laser Induced Damage in Optical Materials: 1973, p. 103.

[18] Braunstein, A., Wang, V., Braunstein, M., Rudisill, J. and Wada, J., "Pulsed CO_2 Laser Damage Studies of Windows and Window Coatings," NBS Special Publication 387, p. 151 (1973).

[19] Davit, J., "Damage Threshold in 10.6μm Laser Materials," NBS Special Publication 387, p. 170 (1973).

[20] Figueira, J., LASL: private communication

8. Figures

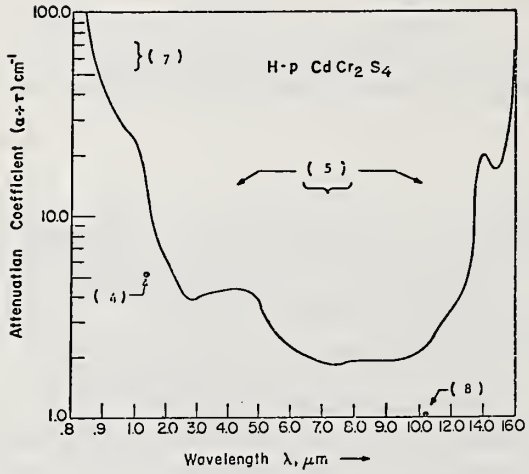

Figure 1. Typical optical attenuation in hot-pressed $CdCr_2S_4$ vs wavelength at 300 K (sources indicated in figure.

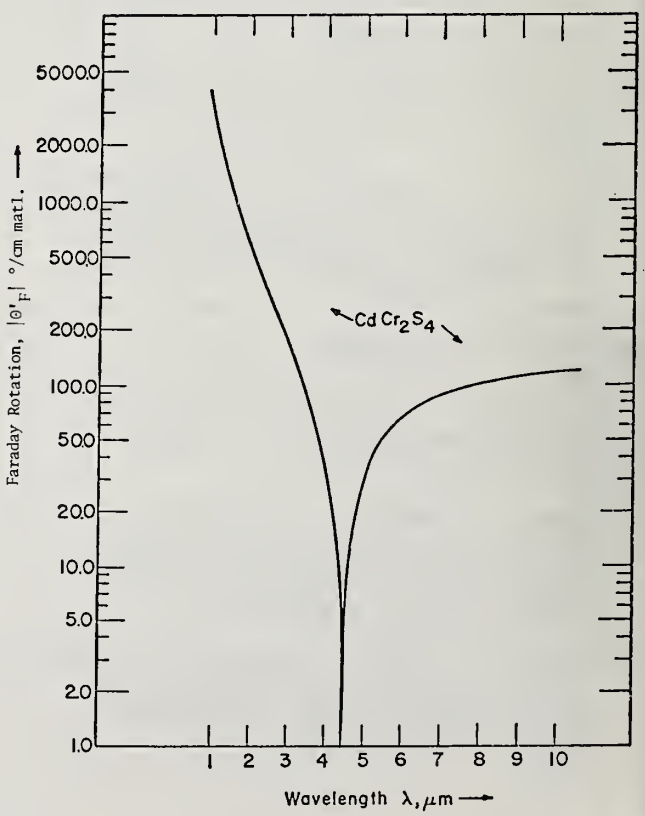

Figure 2. Absolute value of saturated Faraday rotation vs wavelength in hot-pressed $CdCr_2S_4$ at 80 K.

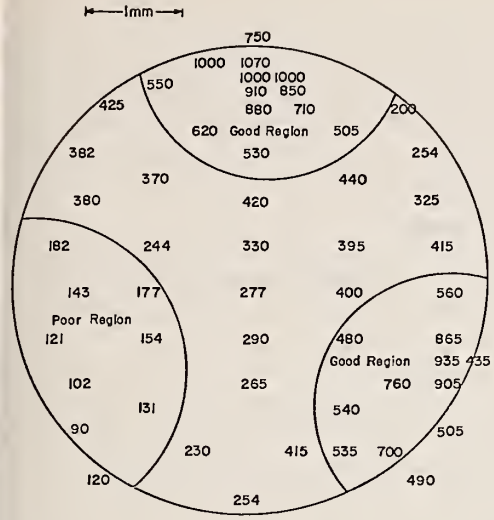

Figure 3. F/B ratio over face of cylindrical sample of hot-pressed $CdCr_2S_3$ 1 cm long by 0.635 cm in diameter, at 80 K. Measurements were made with 10.6 μm radiation from a 0.3 watt cw CO_2 laser focussed to less than 0.5 mm spot size (as measured with thermofax paper) [11].

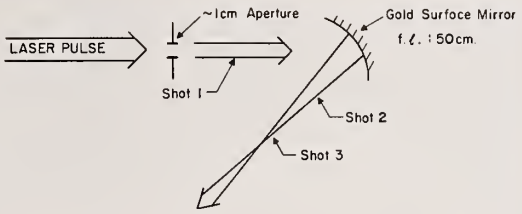

Figure 4. Optical layout for laser induced damage test.

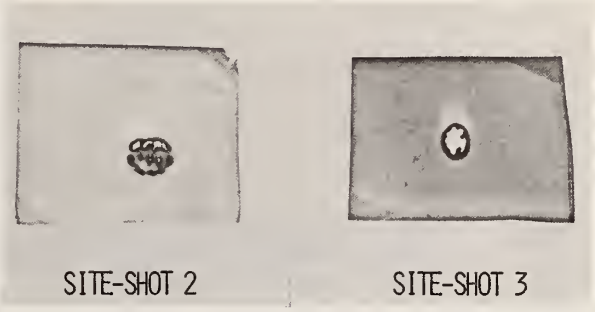

Figure 5. Thermofax burn spots characteristic of 10.6 μm irradiating pulse.

Figure 6. Nomarski micrograph of damage to entrance surface of h-p $CdCr_2S_4$ caused by hot spots in shot 2; 750x - micrograph spans 150 μm of surface.

7(a)

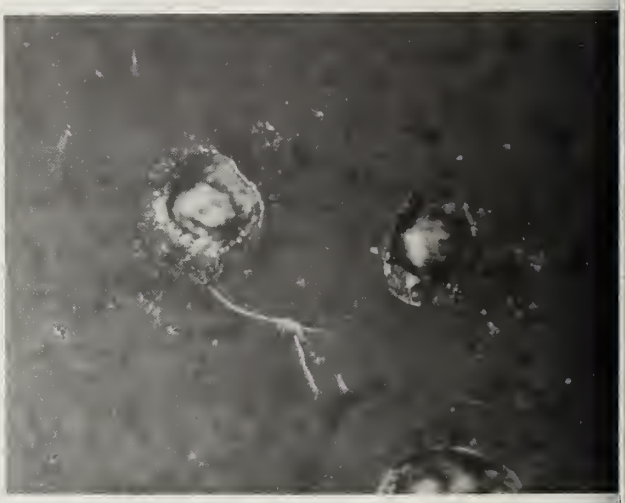

7(b)

Figure 7. Nomarski micrographs of damage to entrance surface of hot-pressed $CdCr_2S_4$ caused by hot-spots in shot 3:

(a) 41x: micrograph spans of 2.8 mm of surface.
(b) 640x: micrograph spans 180 μm of surface.

Figure 8. Nomarski micrograph of a portion of the unirradiated surface of sample, 640x.

COMMENTS ON PAPER BY JACOBS AND TEEGARDEN

No discussion on this paper.

1.16 PULSED LASER INDUCED DAMAGE AT THE DF LASER WAVELENGTH*

M. Bass, K. M. Leung, C. Tang
Center for Laser Studies, University of Southern California
Los Angeles, California 90007

and

M. J. Soileau
Naval Weapons Center
China Lake, California 93555

A pulsed TE DF laser has been used to study the damage phenomenon in materials which are transparent to DF laser light (3.5 - 4.1 μm). We measured the bulk damage threshold in several alkaline-earth fluorides, alkali-halides, and sapphire. The peak on axis intensity which damaged CaF_2 and sapphire was 25 GW/cm^2. Surface damage occurred at intensities less than 1/10 that required for bulk damage. This was attributed to poor surface finish quality and points out the need for improvements in finishing optics for use with DF lasers.

Key words: Alkali-halides; alkaline-earth fluorides; bulk damage; focal spot diameter; inclusion damage; interference ripples; pulsed DF laser damage; sapphire; scattering; waveform distortion.

1. Introduction

In recent years, the development of high power lasers in the infrared region has motivated studies of laser induced damage to infrared transmissive optical materials. Alkaline-earth fluorides have been studied for use in optical components in laser systems operating in the spectral range from 2-5 μm. The damage resistance of optical materials suitable for use in the 2-5 μm region has not yet been systematically evaluated. In this paper we present preliminary measurements of the damage resistance of the best obtainable samples of certain alkaline-earth fluorides, alkali-halides, and sapphire. We also discuss the properties of these materials as they relate to high power 2-5 μm laser systems. The morphology of damage to the surfaces of several samples is described. We found that sapphire has the same bulk damage threshold as that of CaF_2, 25 GW/cm^2. Since sapphire is a mechanically strong material and is also commercially available in large pieces, it is an attractive material for laser windows in the 2-5 μm region.

2. Experimental

The experimental set up and procedures are similar to those described in reference [1][1]. The basic apparatus consists of a pulsed TE DF laser, a beam attenuator, a test chamber, and an energy/waveform monitoring system. The experimental parameters are summarized in table 1. The pulsed

Table 1. Summary of experimental parameters

Laser	TE - DF
Wavelength	30 lines (3.5 - 4.1 μm); 3 dominant lines @ 3.8 μm each separated by ~0.038μm
Waveform	2 leading sharp peaks followed by a long low tail, equivalent pulsewidth is 75 ns
Transverse mode	Lowest order unstable resonator mode
Attenuation	NaCl beam splitter and two ZnSe Brewster angle stacked plate polarizers
Focusing lens	ZnSe, 3.58 cm focal length, AR coated @ 3.8 μm
Focal spot diameter	120 μm at $1/e^2$ in intensity
Detection system	Photon drag detectors and Tektronix 7844 oscilloscope; risetime = 2.5 ns

* Research sponsored by the Defense Advanced Research Projects Agency, Contract No. F19628-76-C-0162, and monitored by Air Force Cambridge Research Laboratories.

1. Figures in brackets indicate the literature references at the end of this paper.

DF laser used in this work has an unstable resonator cavity and a multiline output of ~400 mJ. We have tried to obtain single-line operation by tuning an intracavity grating, but the energy output for the strongest single-line was not sufficient for our damage studies. Two major experimental problems were encountered in this work. Details of these problems and how we attempted to solve them in order to define the damage flux are discussed below.

2.1 DF Laser Pulses

Due to the multiline operation, we observed the two peaked waveform from the DF laser shown in figure 1. If the laser was operated in a single-line manner, then a single peak waveform was obtained. However, the energy output of this single-line laser was too weak for our purposes.

In order to define the damage flux of the laser pulse we constructed an equivalent pulse having a single-peak waveform with its maximum equal to that of the second peak and with leading and trailing edges drawn to average out the enclosed area under the original waveform. This equivalent waveform is indicated by the dashed curve in figure 1. It contains 50% of the energy that was in the pulse and has a full width at the half maximum of 75 ns.

We monitored the waveforms of both the incident and transmitted pulses in the manner described in reference [1]. The transmitted pulse was attenuated when damage occurred as shown in figure 2. Near threshold, the attenuation occurs at the peak of the second pulse while above threshold it occurs at the peak of the first pulse. This is evidence for the importance of the peak intensity in the damage process. It is also one rationale for constructing the equivalent pulse as described above in order to define the damage flux.

2.2 Focal Spot Diameter

Another problem encountered in our experiment was that due to the unstable resonator cavity configuration, the transverse mode output of the DF laser was an annular ring in the near field [2]. Only in the far field, about 10 meters away from the DF laser, would the mode consist of a near-diffraction limited central spot plus a series of weak secondary annular rings. The experiment in this work was located in the near field of the DF laser output because of limited laboratory space. As a result of placing a focusing lens in the near field, the determination of the focal spot diameter was more nontrivial than in other circumstances.

Three different approaches were used to estimate the focal spot diameter of the DF laser beam when focused by a 3.58 cm focal length lens. The results of these three approaches which agree very well with each other are summarized in table 2. In the first approach, the burn patterns produced by

Table 2. Determination of focal spot diameter for DF laser and 3.58 cm focal length lens

1.	By burn on anodized aluminum	130 μm
2.	By scanning 23 cm focal length lens focal spot and scaling according to the ratio of focal lengths	118
3.	By diameter of region of surface damage showing interference "ripples"	<150

the focused DF laser beam on an anodized aluminum block were measured. The laser energy was varied until the size of the burn pattern became constant, but before massive disruption occurred. Using this definition of the measured focal spot diameter we obtained a value of 130 μm. In the second approach, a small pin-hole of 35 μm in diameter was used to scan the focus of a long focal-length lens. The focus of the 3.8 cm focal length lens was not scanned because the focused laser beam readily damaged the pin hole. Instead, we scanned the focus of a long focal-length lens (f = 23 cm) and scaled the result to the short lens according to its focal length. The expected Gaussian spatial profile of the focused beam was observed at the focus of the long focal-length lens. The result of scaling to the short focal-length lens gave 118 μm for the diameter at the $1/e^2$ points of intensity. In the third approach, we measured the diameter of a surface damage site showing interference ripples [3]. These ripples are produced when dust particles, defects or inclusions, at or near the surface scatter light which then interferes with the incident light. The resulting interference pattern is seen in the damaged material only in the region directly exposed to the incident beam. The parts of the damage sites showing interference ripples were found to be less than 150 μm in diameter. This observation is illustrated in the micrographs shown in figure 3.

3. Damage in the 2-5 μm Optical Materials

3.1 Damage Morphology

Several types of damage morphology were observed on both the entrance and exit surfaces of

the tested samples. Figure 3 is a micrograph of a damage site located at the exit surface of a SrF_2 crystal. (Nomarski illumination was used to obtain the micrographs presented in this paper.) The central region in figure 3 contains interference ripples and is the area directly irradiated by the DF laser pulse. The diameter of this region in which the damaging interaction took place is ≈ 150 μm. The extended area showing massive disruption results from the response of the medium to the violent interaction that took place in the irradiated area.

Almost all damage sites on the surfaces of the alkaline-earth fluorides show aligned cracks corresponding to the cleavage planes of the crystals. Figure 4 shows a damage site at the entrance surface of a CaF_2 crystal. A distinctive family of aligned cracks can be seen oriented in a preferred direction within the site. However, on the same crystal, another damage site shows two sets of cracks having two different orientations as seen in figure 5. The dividing line which we thought was a polishing scratch is actually the edge of a twin plane. On one side of the edge, the cracks are oriented with respect to the cleavage plane of one twin, and on the otherside they are oriented according to the cleavage plane of the other twin. For a MgF_2 crystal, which has no well defined cleavage plane, no oriented cracks were observed as shown in figure 6.

Although no pictures are available to show the bulk damage morphology, we observed that for most of the fluoride materials the damage site locations varied along the axis of the incident laser beam. This suggests that the damage mechanism in the samples that we have studied is determined by the presence of defects or inclusions.

3.2 Some Properties of Potentially Useful 2-5 μm Materials

Several important physical properties of the 2-5 μm materials which we studied are listed in table 3. In general, the alkaline-earth fluorides have absorption coefficients of $\sim 10^{-4} cm^{-1}$. On the other hand, the absorption of sapphire is two orders of magnitude higher than that of the alkaline-earth fluorides.

Table 3. Some properties of potentially useful 2-5 μm materials

	Index of Refraction n	Average Sample's Absorptivity[a] $\beta(cm^{-1})$	Knoop Hardness	Melting Point °C
Alkaline-Earth Fluorides				
MgF_2	1.355	4.8×10^{-4}	415	1255
CaF_2	1.41	$\sim 3.5 \times 10^{-4}$	120	1395
SrF_2	1.41	$\sim 6 \times 10^{-4}$	130	1450
BaF_2	1.457	$\sim 18.5 \times 10^{-4}$	65	1355
Alkali-Halides				
LiF	1.353	25.5×10^{-4}	102	844
NaF	1.31	5.2×10^{-4}	60	1012
NaCl	1.52	4.2×10^{-4}	18	801
Al_2O_3	1.68	4×10^{-2}	~1700	2040

[a] These values are taken from references [4] and [5].

If damage in these samples is determined by the presence of defects or inclusions, one might expect low damage threshold to correlate with high scattering at the laser wavelength. Therefore, we measured the total scattering for these samples at four different wavelengths including 3.39 μm which is sufficiently close to the DF laser wavelength (~3.8 μm) to permit a comparison of scattering and damage. The results of our scattering measurements are given in table 4.

Table 4. Scattering* in 2-5 μm window materials ($\times 10^3$)

Material	λ(μm) = 0.4762		0.6471		1.15		3.39	
	Forward	Backward	Forward	Backward	Forward	Backward	Forward	Backward
MgF_2	2.23	1.62	1.68	9.00	0.554	0.282	0.404	0.0807
CaF_2	3.64	4.54	2.15	2.36	0.960	0.541	0.532	0.0943
BaF_2	2.43		1.41	1.47	0.455		0.157	0.0658
SrF_2	1.98	2.68	1.16	1.39	0.404	0.318	0.179	0.0495
NaF	14.1	13.8	7.64	8.53	1.75	2.30	0.184	0.210
LiF	4.14		2.29	3.03	0.564		0.0973	0.0700

* Scattering is the fraction of the light scattered into the forward or backward 2π steradians with respect to the total quantity of light transmitted through the sample.

3.3 Results of Damage Threshold Measurements

The bulk damage thresholds for the materials we studies are listed in table 5. Only single shot on single site testing is reported. For the interest of the readers, we also include the ratio of damage thresholds for different materials normalized to that of NaCl. All the samples were obtained from commercial sources and were specified as having "high-power laser" finishes.

Table 5. Threshold for bulk laser irradiation induced damage (DF laser light, λ = 3.8 μm)

Material	I_B(GW/cm^2)*	$R = I_B/I_B$(NaCl)
† MgF_2	18.5	1.19
CaF_2	25.5	1.65
SrF_2	28.5	1.84
BaF_2	27.5	1.77
† LiF	20.0	1.29
NaF	>30.0	>1.94
NaCl	15.5	1.00
Al_2O_3	25	1.61

* This table gives peak intensity on axis at the threshold for damage.
† These materials had nonuniform damage thresholds possibly due to inclusions.

The measured bulk damage thresholds do not correlate with the total scattering which we measured. On the basis of visual observation we conclude that most of the scattering was caused by the inadequate quality of the surface finishes. In fact, surface damage threshold for these samples was 5 to 10 times lower than the bulk damage threshold, and was determined by the low quality of the surface finishes. It is for this reason that we do not list the surface damage fluxes.

4. Conclusions

The alkaline-earth fluorides tested in this work have very similar bulk damage thresholds and the site morphology suggests that inclusions or defects are responsible for the damaging interaction. The surface damage thresholds for these samples are much lower than the bulk damage thresholds. This can be attributed to poor surface finish quality and leads us to recommend that improved polishing techniques be developed in order to make these materials applicable to high power laser systems.

We also found that sapphire has a very high bulk damage threshold, 25 GW/cm^2. Since sapphire is mechanically strong and readily available in large pieces, it should be considered for use in the 2-5 μm region.

5. Acknowledgements

The authors are grateful to Crystal Systems Inc. for providing one of the sapphire samples and also thank many individuals at NWC, China Lake, CA., for their technical assistance especially in the scattering measurements.

6. References

[1] Leung, K.M., Bass, M. and Balbin-Villaverde, A.G.J., in Proc. 7th ASTM/ERDA/NBS/ONR Symposium on Laser Induced Damage in Optical Materials: 1975, NBS Special Pub. 435, 107 (1975).

[2] Siegman, A.E., Proc. IEEE 53, 277 (1965).

[3] For example, see Temple, P.A. and Soileau, M.J., "Resonant Defects Enhancement of the Laser Electric Field," this Proceedings.

[4] Hass, M., Harrington, J.A., Gregory, D.A. and Davisson, J.W., Appl. Phys. Lett. 28, 610 (1976).

[5] Harrington, J.A., Gregory, D.A. and Ott, W., "Infrared Absorption in Chemical Laser Window Materials," Appl. Opt. (to be published).

7. Figures

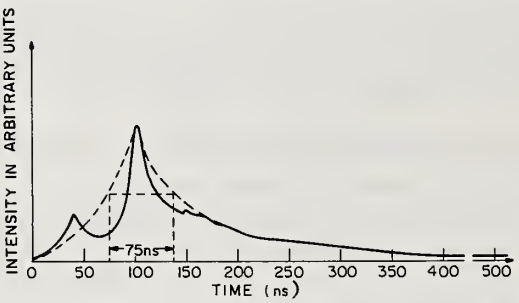

Figure 1. Temporal profile of a multi-line DF laser pulse. The dashed curve represents the equivalent pulse constructed in order to deduce a damage threshold intensity.

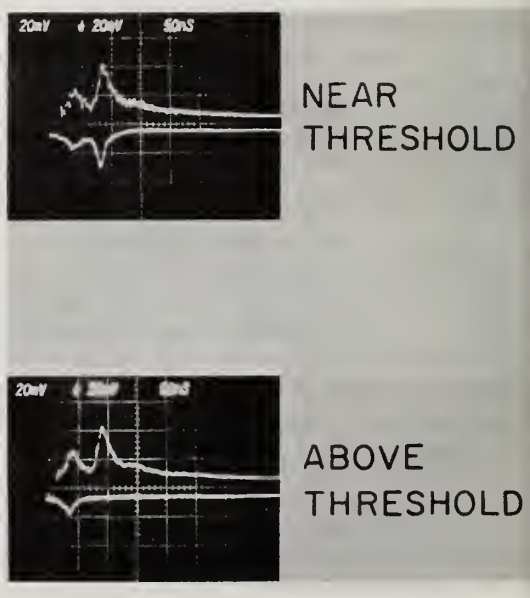

Figure 2. Typical oscilloscope traces for bulk damage in SrF_2 due to DF laser light. The upper trace is the incident pulse waveform and the lower trace is the transmitted pulse waveform. When damage occurs the transmitted pulse waveform is attenuated.

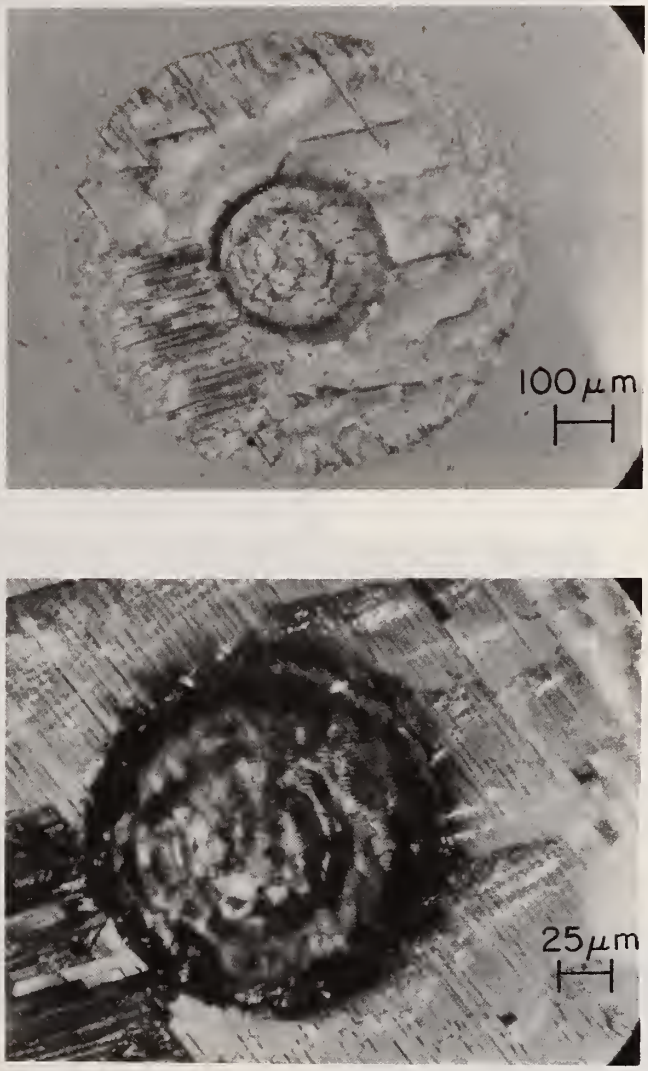

Figure 3. Nomarski micrographs of exit surface damage to SrF_2. The lower photograph is an enlargement of the central region of the irradiated site showing interference ripples.

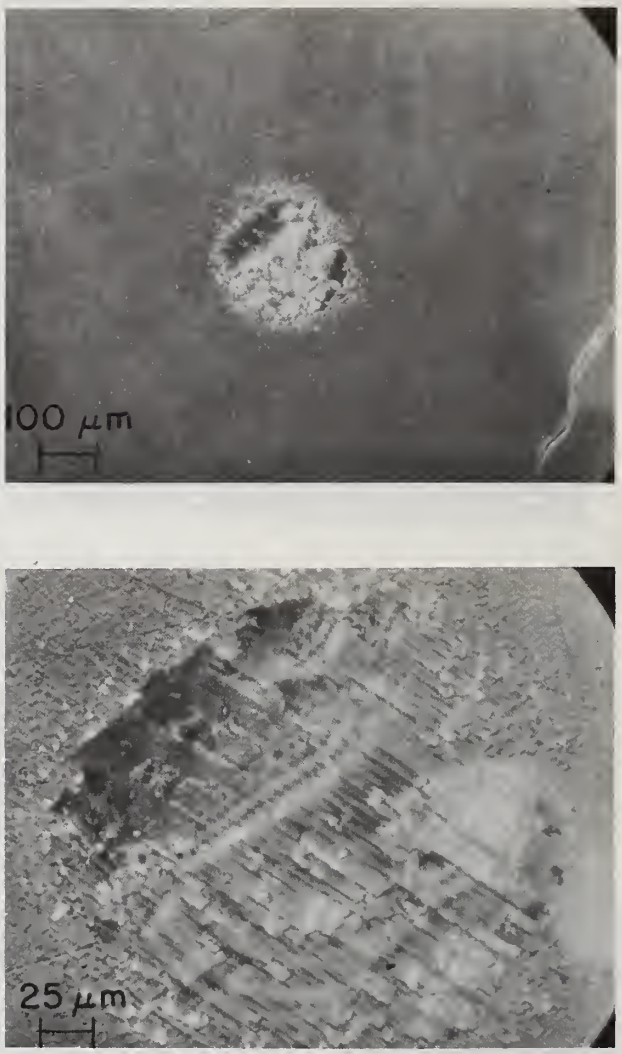

Figure 4. Nomarski micrographs of entrance surface damage to CaF_2. The lower photograph is an enlargement of the damage site showing the the aligned cracks.

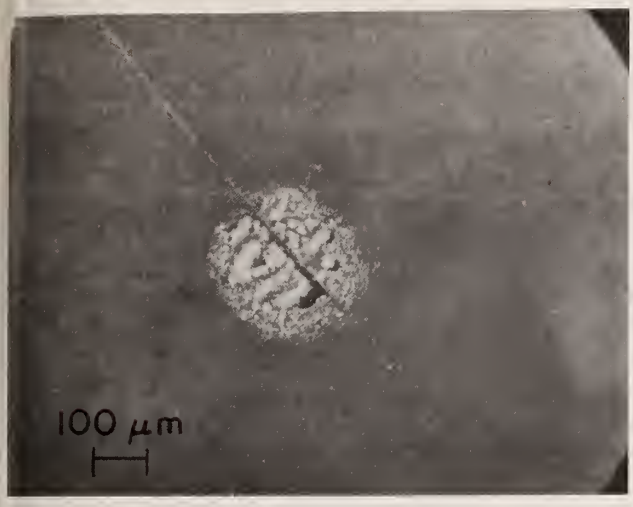

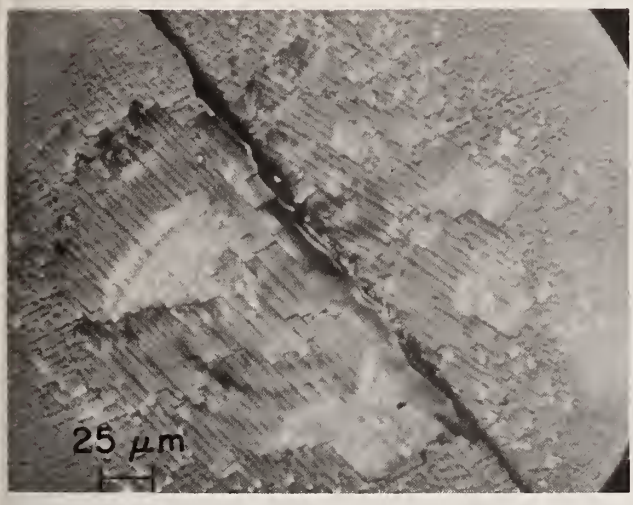

Figure 5. Nomarski micrographs of entrance surface damage to the same CaF_2 crystal as in figure 4. The enlarged picture shows clearly the edge of a twin plane which divides two sets of aligned cracks.

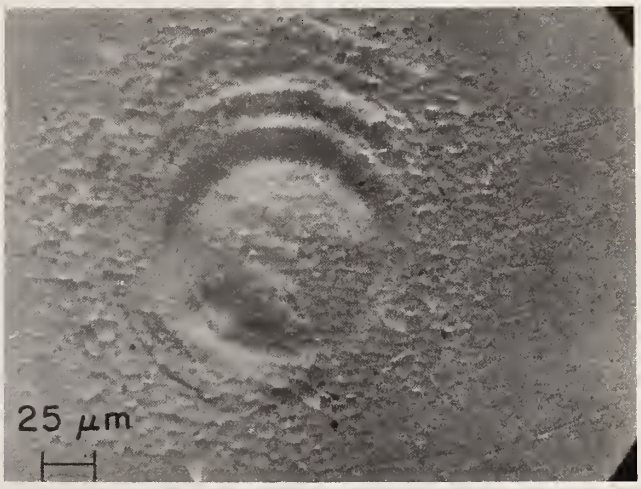

Figure 6. Nomarski micrographs of entrance damage to a MgG_2 single crystal. No aligned cracks are observed in this case since MgF_2 has no well defined cleavage planes.

COMMENTS ON PAPER BY BASS, LEUNG, TANG, AND SOILEAU

Due to the poor quality of the samples, no correlation between scattering and damage threshold could be observed.

2.1 NAVAL WEAPONS CENTER DIAMOND TURNED OPTICS FACILITY

D. L. Decker and R. E. Cram
Michelson Laboratories, Naval Weapons Center
China Lake, California 93555

The generation of optical surfaces by diamond single point turning or milling is of much current interest. This fabrication method can be cost effective and can readily produce very unconventional surfaces and components, allowing radically new system designs. In addition, this fabrication method can reliably produce optical components with superior characteristics including very low scatter, near intrinsic absorption and laser damage threshold. This paper will briefly describe the requirements and existing machines for diamond single point machining of high quality optics, and materials known to be amenable to this fabrication method. The characteristics of a new machine at NWC, which includes an air bearing spindle and carriage ways and closed loop interferometer control will also be discussed. The emphasis of the NWC effort is to explore selected areas of machine technology and to further explore the capabilities of diamond turned components.

Key words: Diamond single point turning; interferometric control; laser damage threshold; optical absorption; optical components; optical scattering.

1. Introduction

The fabrication of high quality optical components by diamond single point turning has been demonstrated in a number of laboratories, notably the Union Carbide Y-12 Plant [1][1] at Oak Ridge, Tennessee and the University of California, Lawrence Livermore Laboratory (LLL) [2], Livermore, California. These laboratories have extensively documented machine requirements and have explored machining conditions and machinability of a wide range of potentially useful materials. This work has been primarily done with an emphasis on superprecision machined mechanical parts, not optical components per se. With due respect, this paper summarizes these results and indicates some outstanding problems. This paper further presents ideas and hardware approaches based heavily on this information and Naval Weapons Center experience in conventional optics fabrication and characterization. Also included are details of a diamond turning facility being built up at NWC.

2. Background

Table 1 is a summary of present state-of-the-art optics machining capability [3]. The surface roughness values quoted for small samples are derived from total integrated scattered light measurements assuming the applicability of the simple scalar scattering theory [4]. The very best mechanically polished metal surfaces typically have roughness values in the range 25-40 Å rms. There are, however, significant differences between the diamond turned and mechanically polished surfaces--notably the type and scale of lateral structure. The diamond turned surface typically has residual periodic structure corresponding to the tool feed (typically 100 μin/rev) and sometimes also to lead screw or drive train irregularity, whereas only random structure is present on a mechanically polished surface.

Table 1. Physical characteristics of state-of-the-art diamond turned metal status as of 1976.

Part	Figure accuracy	Surface finish
Small diameter (< 6 in)		
Flat (one axis)	λ/4 (5.7 μin P-P)	< 40 Å rms (< 0.16 μin rms)
Contour (two axis)	λ/2 to λ/1	50 to 100 Å rms
Large diameter (80 in max)	λ/0.5	180 Å rms

Optical absorptance of diamond turned metal surfaces is typically nearly as low as the best evaporated films and much lower than for corresponding polished surfaces [5]. In addition, laser damage threshold values are high. Pulsed laser damage threshold values in many cases are nearly intrinsic [4]. A wide variety of metals and insulators have been successfully diamond turned as of 1976: metals including copper and several copper alloys including brass, gold, silver, aluminum, and various aluminum alloys, lead and nickel (electroless); insulators including NaCl, KCl, CaF_2, SrF_2, BaF_2, ZnS, ZnSe, MgF_2, and acrylic plastics. Several criteria determine the machinability of a material--absence of significant tool wear from chemical dissolution or from abrasive action of the workpiece and low friction between the tool and work. Excess friction is manifested primarily by the built-up edge resulting from cold

1. Figures in brackets indicate the literature references at the end of this paper.

welding of the work material to the tip of the tool. The formation of a built-up edge severely degrades finish quality and endangers the cutting edge of the tool. The machining action on materials like the alkaline earth fluorides whose range of ductile behavior is limited or nonexistent is clearly much different than experienced on say, OFHC copper. Regardlessly, very good surfaces can be generated on such materials [6]. It is possible to generate directly and easily components by turning which have nearly arbitrary surfaces of revolution. One is not limited to spherical or approximately spherical surfaces as in conventional pitch lap techniques. To generate an arbitrary surface of revolution, tool motion on two independent coordinate axes is required. Most common is a facing lathe arrangement, with two orthogonal linear slides [1,2], but other configurations have also been implemented [1]. Independently of the details of machine design, a number of general principles can be listed. Machine quality, meaning basic machine slideway and spindle accuracy and reproducibility of motion is paramount. A number of factors directly contribute: (1) the stability of the machine with time and with whatever temperature fluctuations may be present in the machine environment, (2) machine stiffness and absence of excessive sources of vibration. Also essential to satisfactory diamond turning results is a quality tool and proper workpiece composition and support. These requirements are discussed in greater detail in the following paragraphs.

James Bryan, of LLL and others have pointed out that vibration which is synchronous with spindle rotation does not contribute to workpiece roughness at least in first order [7]. Asynchronous sources are then particularly troublesome--coolant and airconditioning pumps, carriage drive motors, etc. Since there are no suitable zero temperature coefficient materials available for all critical machine parts, temperature control of the machine becomes essential. This problem can be ameliorated to some extent by using interferometric tool position determination, with temperature stabilization required for whatever machine elements exist between tool and its reference mirror(s) and between workpiece and its reference mirror(s). Much effort has gone into machine temperature stabilization, with several notable successes. The LLL approach using an extensive oil shower is particularly easy to implement in a machine shop environment, and provides a clean (absence of particulates), temperature stable environment [2]. However, in this approach it is difficult to explore the effect of machining fluid (necessarily the temperature stabilizing fluid) on the optical properties of the resulting work. Several outstanding problems, including reliable coatability of diamond turned surfaces remain to be solved. Other approaches to the machine temperature stabilization problem include the use of interferometric position measurement as an element in the carriage control feedback loop with a less extensive oil shower such as the approach which has been implemented, for example, at the Y-12 plant [8].

For materials which can be successfully diamond turned, there is minimal friction between the tool and work, minimal wear and no built-up edge. Hence, as the tool passes over the work, the tool imparts a surface finish which is a transfer of the finish of the tip of the tool. It is axiomatic that a very smooth, sharp and accurately shaped tool must be used. These tool requirements are met commercially for the most part in a satisfactory manner. Although, since machinability of a given material is determined by tool compatibility, it is quite possible that materials now considered unmachinable with diamond tools, e.g., iron and ferrous alloys, could be amenable to precision machining with tools of different composition. The last requirement indicated above is no less important than those listed first. It has long been appreciated in the optics fabrication community that nondistorting work support is required. For example, parts are commonly waxed down to support fixtures. However, in the case of the often complicated mechanical or very unconventional optical parts which are diamond turned, support can be a problem. A useful general solution has involved the use of a rubber potting compound, which since it cures from the liquid does not generate shear forces, and as a cured product has a modulus so low that no large tensile or compressive forces are exerted on the work [9]. Even so, uniform support (distribution of holding forces) is an essential feature in the design of a work support. The problems associated with existing machines can be summarized as follows: (1) failure of the tool to accurately track as a consequence of way friction, stiction, or irregularity or noise in the case of roller way systems, (2) large potential Abbe offset errors as a consequence of large separation between tool tip and the primary source of positioning accuracy (lead screw), and (3) constraints which item (2) places on the system--very tight temperature control of the entire machine, for example. These problems become more severe as machines are made larger. Of course, there are many other difficulties which are independent of machine design. For example, the problem of tool/material compatibility.

3. NWC Diamond Turning Facility

With these introductory remarks, this paper will now briefly describe a machine which is being built up at NWC. The design of this machine is intended to address many of the operational difficulties of existing optics turning machines. There is no claim that the design of this machine is unique, as it contains elements which have been developed and used extensively on other machines. However, it does combine many features and capabilities found only separately into one integrated system, designed from the very beginning as an optics turning machine. This machine is intended to fill a research role: (1) explore selected areas of machine technology, and (2) further explore the capabilities of diamond turned optics. The initial machine configuration will permit swinging parts up to 14 inches in diameter with a total chuck/part weight of greater than 100 lbs. The basic machine design includes a state-of-the-art air bearing spindle, and air bearing slide ways. Figure 1 is an isometric schematic of the NWC machine, showing the arrangement of the slides and spindle. The machine base is an air suspension

isolated black granite surface plate. This arrangement has several advantages over the most common machine configuration, namely, the Moore #3 conversions. All critical components are tied thermally and mechanically to the base in a similar manner, with all parts at essentially the same height from the floor. Vertical temperature gradients are thus less important. Also, the granite surface plate represents a very flexible two dimensional optical/mechanical bench, allowing changes in components or configuration to take place without extensive redesign or rework. For example, the incorporation of an interferometer to measure slide position is easily accomplished, as is shown in figure 1. It is relatively easy to have the interferometer beam at tool height, thus minimizing Abbe offset errors. It is in general not possible to gauge tool/work positions right at the tool tip. The present design calls for gauging on the back surface of the spindle faceplate through the spindle, and gauging tool position right at the tool holder. The Moore #3 conversion unfortunately does not conveniently permit use of a gauging/control interferometer at tool height. The carriage control loop will include a very high speed calculator or computer which will issue rate and position commands to the dc torque motor drive chassis. The interferometer will provide position correction via hard wired comparator. The feedback loop bandwidth including motor drive electronics will be in excess of 20 kHz_3. Table 2 indicates basic specifications for the NWC machine.

Table 2. Basic specifications and features of the NWC diamond turning machine.

Spindle	
Hydrostatically supported	
Axial and radial runout	3 μin TIR max
Angular (wobble) error	0.1 arc s max
Axial and radial stiffness	10^6 lb/in
Slides	
Hydrostatically supported	
Straightness (yaw) and flatness (pitch)	3 μin TIR max in any inch, 10 μin max in any 10 inches
Stiffness in pitch and yaw	10^6 lb/in
Other features:	
Flat belt spindle drive from vibration isolated variable speed motor	
Traction drive dc torque motor reduction, and possibly traction final drive to carriage	
Temperature stabilizing oil passages incorporated in slides, spindle and all critical members	
Closed loop interferometer positioning and control of slide motion with interferometer beam at tool post height	
Very high speed calculator or computer in control loop	

As has been extensively documented primarily by the Y-12 laboratory, the incorporation of a slide position interferometer will not solve all control problems. In particular, short period motion/position errors associated with slides or slide drives cannot be removed by interferometric control. Smooth, if not accurate,drives are mandatory. The NWC approach will use a traction drive reduction from an encoded dc torque motor to the final carriage drive, as has been suggested and experimented with by Y-12 [8]. It is quite possible the final connection to the carriage will be by traction drive also rather than the conventional lead screw drive. Hydrostatically supported slides also provide important improvements in slide position accuracy, especially for intermittent slide motion. This machine will be set up in February 1977.

4. Summary

The NWC machine then specifically addresses the following areas of machine technology: (1) slides and slide drives, (2) slide position/motion control, and (3) tool/workpiece position/motion errors as a consequence of Abbe offset errors. Some of the approaches suggested in this paper are admittedly relatively high risk, but such a course is appropriate for a research machine. The present goals of the NWC machine are summed up simply: to be able to machine a component requiring two axis motions to a quality equal or better than existing machines can produce with one axis motion alone, and to be able to readily vary machining parameters such as machining fluid to explore the effect of such changes on the ultimate optical properties of the part. It is clear why diamond turned optical components have created so much interest. It is the intention of the NWC effort to contribute in a significant way to this vital endeavor.

5. Acknowledgments

The authors of this paper acknowledge many valuable discussions with personnel at Lawrence Livermore Laboratory, notably Jim Bryan and with James Arnold, Dick Sladky, and Del Bender of the Union Carbide Y-12 plant. Also acknowledged is support from the U. S. Army Missile Command, and the Air Force Weapons Laboratory. Support was also provided by Naval Weapons Center Independent Research Funds.

6. References

[1] Arnold, J. B. and Steger, P. J., "Diamond Turning on Advanced Machine Tool Prototypes," presented at the SME Clinic on Industrial Application of Precision Machining and Gaging, November 19-21, 1974, San Francisco, CA. (Union Carbide, Inc., Oak Ridge, Tenn. 37830, Report Y-DA-5975, 1975.)

[2] Bryan, J. B., et al., "A Practical Solution to the Thermal Stability Problems in Machine Tools." (Society of Manufacturing Engineers, Dearborn, Mich. 48128, Technical Paper No. MR72-138, 1972.)

[3] Abstracted from numerous reports and publications, principally from Y-12 and LLL, and from NWC measurements of available diamond turned specimens.

[4] Decker, D. L., Soileau, M. J., Porteus, J. O. and Bennett, J. M., "Surfaces, Optical and Laser Damage Characteristics of Diamond-Turned Metal Mirrors," these Proceedings.

[5] Bennett, H. E., Soileau, M. J. and Archibald, P. C., in *High Energy Laser Mirrors and Windows* (Semi-Annual Report No. 6, ARPA Order 2175, Naval Weapons Center, May 1975), pp. 53-61.

[6] Arnold, J., Sladky, R. and Steger, P., "Machinability of Window Materials," presented at the ARPA Infrared Window Meeting, 12 July 1976.

[7] Bryan, J. B., Clauser, R. and Holland, E., "Spindle Accuracy," Amer. Mach. 111, No. 25, December 4, 1967, pp. 149-164.

[8] Arnold, J., et al., "Diamond Machining of Reflectors," Progress Report under AFWL Contract 75-343 and 76-114 period ending January 1976. (Union Carbide, Oak Ridge, Tenn. 37830, Y-12 Plant Document No. Y-DA-6681, February 1976.)

[9] Jones, W. F., "Part Support," presented at the SME Clinic on Precision Machining and Gaging, Oak Ridge, Tenn., November 14-16, 1972. (Union Carbide, Inc., Oak Ridge, Tenn. 37830, Preprint Y-DA-4841.)

7. Figure

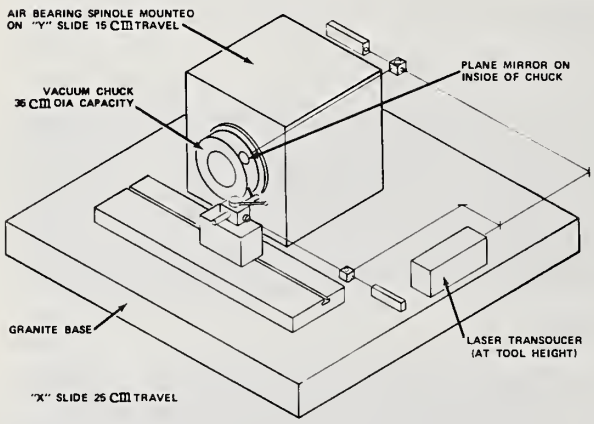

Figure 1. Isometric schematic of the NWC diamond turning machine. Shown are X and Y hydrostatic slides, hydrostatic spindle, and laser position/control interferometer with beam at tool height. All components mounted on granite surface plate base.

COMMENTS ON PAPER BY DECKER AND CRAM

No discussion.

2.2 10.6 μm PULSED LASER DAMAGE STUDIES OF DIAMOND TURNED KCl WINDOW SURFACES

M. J. Soileau, J. M. Bennett, J. O. Porteus,
W. Faith and J. Jernigan
Michelson Laboratories, Naval Weapons Center
China Lake, California 93555
and
T. T. Saito
Lawrence Livermore Laboratory
Livermore, California 94550

Laser damage measurements at 10.6 μm are presented for diamond turned surfaces of polycrystalline KCl. The two types of windows tested were hot-forged RbCl- and EuCl-doped KCl. Surface damage thresholds of the two materials range from 1.8 to 2.4 GW/cm^2. The optical properties of these specimens were measured after diamond turning and compared to chemically etched surfaces on the same specimens. RMS roughness, infrared scattering, and absorption at 10.6 μm were measured. The influence of the machining grooves on the character of the laser damage on the surfaces is discussed. The regularity of the surface defects produced by the diamond turning process offers a unique opportunity to study the effects of surface defects on the laser damage threshold of optical surfaces.

Key words: Diamond turning; KCl laser windows; laser damage; 10.6 μm laser.

Introduction

Surface finishing problems have severely limited the usefulness of KCl for laser windows. The major problem is to produce low scatter, low absorption, damage resistant surfaces with good optical figures. Many techniques have been tried with mixed results [1-5][1]. Standard lap polishing produces well finished surfaces having good optical figures, but the surfaces are highly scratched and have high absorption at 10.6 μm [1]. Chemical etching produces surfaces which are scratch free [2,3], laser damage resistant [3,4], with low surface absorption [4], but with poor optical figures [1]. Various combinations of chemical/mechanical techniques have produced surfaces with good optical figures and low absorption [1,5]. However, even with the best of such techniques, one is plagued by scratches, relatively poor damage thresholds, high cost of manufacture, and poor reproducibility in the results.

Single point diamond turning has been used to produce optical surfaces on metal mirrors. Mirrors produced using this technique have been shown to have high damage thresholds, low absorption, and good optical figures [6]. The purpose of this work was to determine if similar results could be obtained by diamond turning KCl. Measurements of pulsed laser damage thresholds, optical scattering, and absorption at 10.6 μm indicate that diamond turning is an attractive alternative to mechanical polishing and chemical etching for producing optical surfaces on KCl windows.

Experimental

The two specimens tested were doped, polycrystalline KCl. The KCl was grown (and doped during the growth process) by Harshaw, and hot-forged into polycrystalline form by the Honeywell Ceramics Center [7]. One specimen was doped with EuCl and the other with RbCl. These specimens will be referred to as KCl:EuCl and KCl:RbCl.

The samples were diamond turned on the same day at Union Carbide's Y-12 plant in Oak Ridge, Tennessee. Both were fly cut off center using a feed rate of 0.2 in/min, and a spindle speed of 1200 rpm. No lubricant was used to minimize surface contamination. Off center fly cutting was used since we have found in cutting single crystal windows that turning the window on center resulted in a rougher surface [8]. Some machined polycrystalline samples were found to be rougher than machined single crystal specimens. Repeated machining of the same part seemed to reduce the roughness of some crystals, but increased the roughness of others. We were not able to get a completely clear surface; the unclear areas may be related to the crystal orientation of the tool. Nomarski micrographs of typical areas on each specimen tested are shown in figure 1. As seen in the figure, the fly cutting off center produced machining grooves which were approximately straight and parallel (at least over the diameter of the laser probe used in the damage measurements).

---

1. Figures in brackets indicate the literature references at the end of this paper.

After diamond turning, the specimens were shipped to NWC, China Lake, California for optical characterization and pulsed CO_2 laser damage testing. The specimens were wrapped in tissue and sealed in a plastic bag for shipment. Our experience has been that any physical contact with a finished KCl surface raises the surface absorption and lowers the damage threshold. If the surfaces of the specimens had been coated with protective layers before shipment, the results of our measurements might have been better.

Laser absorption calorimetry was performed on each of the specimens on the same day they were received by NWC. These measurements were repeated after the conclusion of all damage testing on the specimens. The specimens were then chemically etched to remove any surface damage and surface contamination introduced by the diamond turning [1], and the absorption measurements were again repeated.

Total integrated scatter (TIS) in the forward and backward directions was measured as a function of wavelength using the NWC Optical Evaluation Facility [1,9]. This instrument uses a Coblentz sphere to collect the hemispherical scattering from the specimen and focus it onto a detector mounted at the conjugate point of the sphere. The TIS backscatter data for a wavelength of 6471 Å were used to compute an equivalent surface roughness for the two specimens.

Surface scans were made on both specimens using a Talystep surface profiling instrument. This instrument, manufactured by Rank Precision Industries Ltd., Leicester, England, uses a conical diamond stylus tip of approximately 8 μm radius to record variations in the surface height. The stylus loading is continuously variable from less than 0.5 mg to about 50 mg. A load of approximately 1 mg was used for the traces. This was about the smallest amount possible to keep the stylus from skipping. Some flattening of surface features was observed by comparing two traces made over the same track. However, the flattening was generally less than 40 Å on features having peak to valley depths of the order of 400 Å. (A previous experiment using stylus loadings of 0.6 mg and larger on a sputtered silver film showed no indentation for loadings under 4 mg when replicas of single traces were observed in the electron microscope. This result is in agreement with the previously observed phenomenon [10] that the hardness of materials can be much larger for very small loadings.) A scan speed of 3 μm/s on the sample surface was used, and the total distance covered by a scan was 61 μm. The lateral resolution of the stylus tip was checked by tracing over slip planes on (110) single crystal aluminum produced by laser pulses. Structure 0.7 μm wide having a slope of about 1° was well resolved.

The output of the Talystep (voltage variations of ± 1 volt, corresponding to height variations on the sample ranging from ± 5 μm to ± 250 Å depending on the gain used) was fed into a Hewlett-Packard Model 5480 B Signal Averager and thence into a Hewlett-Packard Model 2100A Minicomputer. The signal averager digitized the data at preset time intervals, so that an entire scan consisted of 1000 data points. In this way surface height information could be sampled at intervals as small as a few hundredths of a μm or as large as 1.5 μm. The sampling rate was chosen so that the curve formed by connecting adjacent points was a reasonable representation of the surface, commensurate with the limiting resolution imposed by the radius of the stylus tip.

A computer program originally written to determine surface statistics from surface scan data taken with the FECO Scanning Interferometer [11] was modified to calculate the same statistical quantities from the digitized Talystep data. These quantities are rms height, rms slope, height and slope distribution functions, and autocovariance function. The statistical quantities could be calculated for a single scan (1000 data points) or for averages of many scans.

The Talystep was equipped with two micrometers having least counts of 2 μm which moved the sample parallel and perpendicular to the direction of motion of the stylus tip. Thus a sample could be positioned as desired and a series of parallel, equally spaced scans could be made, for example, across a laser damage crater. This was done for a crater on the exit face of the KCl:EuCl sample.

Polarization interference photomicrographs were taken at the Y-12 Plant to estimate the peak-valley surface roughness for the two samples. If the peak-valley values are divided by $2\sqrt{2}$ to convert them to rms values, one obtains 177 Å rms for the KCl:RbCl and 205 Å rms for the KCl:EuCl. Diamond turned surface roughness measurements made with polarization interference microscopes have historically indicated somewhat rougher surfaces than FECO, light scattering, and stylus instrument measurements [12].

Damage testing was performed using the Naval Weapons Center's laser damage facility [4,13]. The experiments reported in this paper were conducted on a pulsed, single-mode CO_2 laser operating in the 10.6 μm wavelength region. It has reproducible temporal and spatial characteristics which are detailed in the following discussion. The laser is sealed with Brewster windows, resulting in a linearly polarized output beam (vertical polarization direction). Beam intensity is controlled by a rotating polarizer-analyzer combination, each consisting of two ZnSe plates tilted in opposite directions to minimize beam shift, as well as by CaF_2 attenuators. Following the attenuators, the energy in each pulse is measured by a pyroelectric energy meter which is calibrated using a thermopile calorimeter. The beam enters the test chamber through an NaCl window and is focused on the sample with a 2.54 cm diameter, 3.546 cm focal length ZnSe meniscus lens. (Focal length given is for 10.6 μm.) A meniscus lens was used in order to minimize spherical aberrations. A HeNe laser is used for convenience in aligning the optics.

The temporal beam characteristics are monitored with a photon-drag detector having a 1.5 ns rise time. Figure 2 shows the measured intensity as a function of time, together with an analytical expression which describes this dependence. As can be seen in figure 2, the laser output increases linearly to the peak and falls off as a steep exponential. The peak power, calculated in watts using the total output energy and temporal pulse shape, is 1.27×10^7 times the total output energy (in joules). From this expression we can define an equivalent pulse width of 78.7 ns; i.e., the total energy divided by 78.7 ns gives the peak power of the pulse. Note that the 1/e full width of the pulse is approximately 78.7 ns. The full width at half maximum (FWHM) of this pulse is approximately 60 ns.

The spatial profile of the beam as it enters the damage chamber was measured using a pinhole scanned across the beam, and can be represented by a Gaussian distribution to within 4%. The 1/e full width of the unfocused beam was 5.8 mm. The spot size for the 3.546 cm focal length ZnSe lens was determined by scaling the measured spot size using a 11.91 cm focal length lens [4] by the ratio of the focal lengths of the two lenses. This calculation yields a $1/e^2$ spot diameter of 59.5 μm for the 3.546 cm focal length lens. The effective f-number of this lens is approximately 6. The correct position for the ZnSe lens was determined using a technique previously described by Porteus et al [13]. This procedure allows us to set the position of the specimen surface to within 10 μm (the repeatability of the translation micrometer).

The test chamber and the analytical instrumentation used in this experiment have been described previously [14]. The chamber is designed for ultrahigh vacuum, including bakeout. However, the measurements reported in this paper were made at a base pressure better than 1×10^{-7} Torr without bakeout. Visible changes in the specimen (surface or bulk) were monitored by observing the scattered light with a 20-power optical microscope.

Results

The two specimens were examined using Nomarski microscopy to determine the qualitative nature of the surfaces and with a Twyman-Green interferometer to determine optical figure. The Nomarski micrographs of these surfaces showed indications of tool marks from the diamond turning process. However, the appearance of the tool marks varied greatly with position on the specimens, and as can be seen in figure 1, was quite different for the two specimens. Portions of the surfaces had a "cloudy" appearance when viewed with the unaided eye. The cloudy areas did not correlate with the areas of heavy tool marks and may be the result of improper handling or atmospheric attack.

Twyman-Green interferograms to show the optical figure of the surfaces were taken at the Y-12 Plant and are shown in figure 3. As can be seen in this figure, the KCl:EuCl specimen was flat to about two waves in the visible, and the KCl:RbCl specimen was flat to about six waves in the visible. In both cases the fringes show little irregularity, indicating that the figure errors may be caused by improper blocking procedure.

The results of the total integrated scattering (TIS) measurements at 10.6 μm are summarized in figure 4, and the backscatter is plotted in figures 5 and 6 as a function of wavelength. In figure 5 the backscatter of the KCl:EuCl specimen is compared to that of a mechanically polished Eu^{++} doped KCl surface. Note that the scattering levels and wavelength dependence of the two specimens are virtually identical. The scattering levels include bulk scatter which is quite large for small grain polycrystalline KCl such as these specimens. The rms roughness calculated from the TIS value at 6471 Å was 374 Å. The plot in the lower left of figure 5 is the theoretical scatter computed from the 135 Å rms roughness of this specimen as measured by the Talystep surface profiling instrument. In figure 6 the scattering from the machined sample is compared to that of an etched single crystal. In the visible the scattering from the machined sample is over an order of magnitude higher than that of the single crystal, but at 10.6 μm the scattering levels are virtually identical. The rms roughness of the machined surface is 326 Å as calculated from the 6471 Å TIS value.

The average absorption (surface plus bulk) at a wavelength of 10.6 μm was 12.6×10^{-4} for the machined KCl:EuCl specimen and 20.3×10^{-4} for the machined KCl:RbCl specimen; average deviation from these values were approximately ±30%. Both specimens were approximately 1 cm thick. After damage testing was completed, the samples were etched in concentrated HCl to remove any surface damage and surface contaminants associated with the diamond turning process, and the absorption was measured. The results for the KCl:EuCl sample are shown in figure 7. The average absorption of this sample after etching was approximately 5.2×10^{-4}, in good agreement with absorption measurements made on similar material etched using the same technique [1]. From the absorption measurements before and after etching we can infer an absorption of 3.7×10^{-4} per surface, which is an estimation of the surface absorption caused by the diamond turning process. Since the specimen experienced considerable handling in the interval between the time the diamond turning was completed and the first absorption measurement was made, the value 3.7×10^{-4} per surface represents an upper limit for the absorption caused by the diamond turning process.

The KCl:RbCl specimen could not be etched satisfactorily using our standard technique. Each attempt to etch the surface resulted in an increase in the total absorption of the specimen. This effect was probably due to the tendency of the material to undergo preferential etching, thus enhancing grain

boundaries. Because of this problem we were unable to obtain an estimate of the surface absorption of the KCl:RbCl specimen.

In order to determine surface profiles, ten Talystep scans were made on each side of each sample, in all cases perpendicular to the grooves. Five of the scans were made in a visually clear area and five in an obviously grooved area. There was no large difference between the rms roughness values for the different surfaces. However, the KCl:RbCl sample was slightly smoother than the KCl:EuCl sample (difference ~ 15 Å rms). There were definite roughness differences between the clear and grooved areas on a given surface (difference ~ 20 Å rms). Roughnesses in the grooved areas averaged about 148 Å rms, while those in the clear areas averaged about 128 Å rms. The smoothest area measured had a roughness of 102 Å rms. On a few scans there were positive spikes, as large as 1500 Å above the mean surface level, but no correspondingly deep grooves.

Eight scans were made parallel to the grooves on a visually clear area of the exit face of the KCl:EuCl sample. The rms roughness values for these scans were nearly identical on the average with those made perpendicular to the grooves on the same surface (134 Å rms as compared to 130 Å rms). However, the character of the roughness was different and the autocovariance functions were different for the two types of scans. In figure 8 are shown typical scans parallel and perpendicular to the grooves, and the corresponding autocovariance functions. On the surface scans, well resolved structure as closely spaced as 0.6 μm is shown, indicating that the stylus tip has at least this good resolution. This result is in agreement with the previously mentioned measurement of structure on an aluminum surface. Interesting differences can be observed between the two autocovariance functions: (1) Both curves have initial exponential shapes, but the scan parallel to the grooves has a larger correlation length. If both curves are extended uniformly down to zero, the crossing distances (or approximate correlation lengths) are about 1.6 μm for the scan perpendicular to the grooves and about 3.2 μm for the scan parallel to the grooves. (2) The periodicity of the autocovariance function for the scan perpendicular to the grooves is more definite than for the other one, and the separation between secondary peaks is ~ 5.5 μm, in good agreement with the value of 5.3 μm measured for the separation of the grooves on a Nomarski micrograph similar to the one shown in figure 1. (3) The rms slope is 2.1° for the scan perpendicular to the grooves and 1.7° for the scan parallel to the grooves. Although the above mentioned differences are small, there is evidence that roughness comes both from the grooves made by the cutting tool and also from tool chatter as the grooves are being cut. It is also possible that the stylus tip was not tracing exactly parallel to the grooves in the one case, since the grooves could only barely be seen during the alignment process.

After nondestructive optical characterization was completed, the laser damage thresholds of the specimens were determined at a wavelength of 10.6 μm. The single shot thresholds for the entrance and exit surfaces of each specimen were measured as a function of the angle between the electric field vector of the laser and the machining grooves; the results are summarized in figure 9. The power levels required for damage varied greatly and a "threshold" could not be determined. The power level which caused damage in 50% of the shots was arbitrarily defined as the "damage threshold" ($P_{50\%}$). Note the large spread in power levels from the lowest power which caused damage (P_L) to the highest power for which no damage occurred (P_H). This large variation in threshold for a given orientation relative to the machining grooves made it very difficult to see any dependence of the threshold on orientation angle. The entrance and exit damage thresholds for each orientation were averaged and the results are given in figure 10. The *average* thresholds thus computed compare quite well with previous measurements on similar material [4]. However, as previously indicated, these surfaces had very nonuniform surface quality, surface absorption, and damage threshold.

Typical Nomarski micrographs of entrance and exit surface damage sites are shown in figure 11. The exit surface damage is characterized by ripples whose spacing is nearly equal to the laser wavelength in the material. The ripples were most pronounced when the machine grooves were normal to or at large angles to the incident laser electric field. The ripple spacing and orientation in the exit surface damage sites are as predicted by the laser induced dipole theory [15]. However, this theory predicts that similar features should also be seen on the front surface damage sites, and none were observed. The reason for this apparent discrepancy is not clear and should be resolved in future work.

One of the exit damage sites in the KCl:EuCl specimen was scanned with the Talystep surface profiling instrument. The site chosen was produced with the laser electric field perpendicular to the machine grooves, and the scan was made parallel to the machine grooves. The scan was perpendicular to the ripples in the damage site. Three of the scans of this crater are shown in figure 12. The scan 80 μm from the crater center is comparable to the traces in the upper part of figure 8, but plotted on a greatly reduced vertical scale. The features to note in this figure are the symmetry of the crater and the "modulation" of the crater depth, corresponding to the ripples seen in the micrograph of the exit surface damage crater in figure 11. At the center of the crater the amplitude modulation is about 0.1 μm in a total depth of 2.5 μm. These scans show conclusively that the observed ripple pattern is removal and/or displacement of material and not simply changes in the refractive index in the damage region.

Discussion

The optical properties of surfaces produced by single point diamond turning of polycrystalline, doped KCl compare favorably with surfaces on similar materials generated by other techniques. However, the cosmetic quality of these surfaces is not as good as that which can be obtained by other techniques. Residual machine tool marks or grooves were apparent over much of the surface of the KCl:EuCl specimen, and neither specimen had completely clear surfaces. However, the scattering at a wavelength of 10.6 μm was as low as that from surfaces on similar materials generated by conventional techniques.

The surface absorption of the diamond turned specimens at a wavelength of 10.6 μm compared favorably to that measured for standard commercial surfaces on KCl. However, the surface absorption was five times higher than that which can be produced by chemical etching and approximately twice the absorption of the surfaces produced by the best chemical/mechanical techniques [1]. Part of the surface absorption measured in the diamond turned specimens may have been caused by contamination from handling and atmospheric attack. Reductions in surface absorption can be achieved with better handling techniques and improvements in the machining process such as chemically etching the specimen prior to the diamond turning. This step would ensure that surface damage and surface contamination caused by the grinding and shaping of the window would be removed. An initial chemical etch has resulted in a significant reduction in the surface absorption in KCl polished using abrasive polishing techniques [1].

The optical figure of the diamond turned surfaces was not as good as can be achieved by lap polishing of KCl, but was superior to the figure of surfaces on KCl produced by etching or cloth polishing. The figure errors of the diamond turned specimens had little irregularity, indicating that they may have been caused by an improper blocking technique, and could probably be reduced considerably by improving the blocking technique.

The damage thresholds were quite good as compared to those of mechanically polished and chemically etched surfaces on similar material (fig. 10). The fact that the diamond turned surfaces had higher thresholds is probably not significant since the previous data were taken with a 200 μm spot size ($1/e^2$ diam.) and these data were taken with a 59.5 μm spot size ($1/e^2$ diam.). Thus, the higher damage threshold could be simply a spot size dependence. What is significant is that the thresholds for the diamond turned surfaces are the same order of magnitude as the thresholds for surfaces prepared by more conventional techniques. Diamond turning of KCl is at an early stage of development and significant improvements can be expected.

Exit surface damage seems to be associated with defects, as evidenced by the ripple structure in the damage craters. The ripple structure is strongly correlated with the direction of the diamond turning grooves for sites illuminated with the laser electric field normal to the grooves. However, we were unable to show correlation of the thresholds with the angle between the electric field and the grooves. This is not too surprising since little long term correlation of surface roughness was found in the surface scans made parallel to and perpendicular to the machine grooves. There was such a large variation in the thresholds for a given groove orientation that all but a very large orientation dependence would probably have been masked by the variations caused by surface quality variations.

Future work on diamond turned KCl surfaces should be performed on surfaces having more uniform quality. Presumably as the diamond turning technology is improved, uniform quality surfaces will be available. Hopefully the effects of specific surface defects and their orientation with respect to the incident laser field can then be determined.

Conclusions

Diamond turning offers an attractive alternative to abrasive polishing and chemical etching of KCl surfaces. These surfaces are comparable in optical figure, roughness, and absorption at 10.6 μm to good commercial finishes on KCl. The scattering at 10.6 μm and laser damage threshold of diamond turned surfaces are essentially equivalent to those of the best surfaces on KCl produced by chemical/mechanical techniques. The results reported in this paper are extremely encouraging considering the limited experience in diamond turning of KCl.

The nonuniformity of the surfaces tested prevented any definitive determination of the effect of machine groove orientation on the laser damage threshold. However, the presence of ripples in the exit surface damage craters is suggestive that defects are important in the laser damage process, since such ripples are produced by the laser interaction with surface defects. The laser damage resistance of diamond turned KCl surfaces should increase, surface uniformity should improve, and surface defects should be reduced as more experience is gained in the machining of KCl.

Acknowledgments

This work was supported by the Defense Advanced Research Projects Agency, the Air Force Weapons Laboratory,and Naval Weapons Center Independent Research funds. The authors are grateful to the Y-12 Division of Union Carbide, particularly to R. E. Sladky and J. B. Arnold for providing the specimens used in these experiments. We are also grateful to P. Archibald of NWC for making the scattering measurements.

References

[1] Soileau, M. J., et al., in *Laser Induced Damage in Optical Materials: 1975*, A. J. Glass and A. H. Guenther, eds. (NBS Spec. Publ. 435, 1976), pp. 20-28.

[2] Davisson, J. W., in *Proceedings of Third Conference on High Power Infrared Laser Window Materials, 1973*, C. A. Pitha and B. Bendow, eds. (AFCRL-TR-74-0085, Special Report 174, 1974), pp. 525-534.

[3] Allen, S. D., et al., in *Laser Induced Damage in Optical Materials: 1974*, A. J. Glass and A. H. Guenther, eds. (NBS Spec. Publ. 414, 1974), pp. 66-75.

[4] Soileau, M. J., et al., in *Proceedings of Fifth Annual Conference on Infrared Laser Window Materials, 1975*, C. R. Andrews and C. L. Strecker, eds. (Defense Advanced Research Projects Agency, Arlington, Va., 1976), pp. 391-417.

[5] Turk, R., et al., in *Proceedings of Fifth Annual Conference on Infrared Laser Window Materials, 1975*, C. R. Andrews and C. L. Strecker, eds. (Defense Advanced Research Projects Agency, Arlington, Va., 1976), pp. 103-112.

[6] Saito, T. T., in *Laser Induced Damage in Optical Materials: 1974*, A. J. Glass and A. H. Guenther, eds. (NBS Spec. Publ. 414, 1974), p. 227.

[7] Harrison, W. B., et al., in *Proceedings of Fourth Annual Conference on Infrared Laser Window Materials, 1974*, C. R. Andrews and C. L. Strecker, eds. (Defense Advanced Research Projects Agency, Arlington, Va., 1975), pp. 599-610.

[8] Arnold, J. B., et al. "Diamond Machining of Reflectors," Report Y-DA-6681, Union Carbide, Y-12 Plant, Oak Ridge, TN 37830.

[9] Bennett, H. E., et al., in *Proceedings of Fifth Annual Conference on Infrared Laser Window Materials, 1975*, C. R. Andrews and C. L. Strecker, eds. (Defense Advanced Research Projects Agency, Arlington, Va., 1976), pp. 910-916.

[10] Whitehouse, D. J., in *Characterization of Solid Surfaces*, P. F. Kane and G. B. Larrabee, eds. (Plenum Press, New York, 1974), pp. 49-73.

[11] Bennett, J. M., "Measurement of the rms Roughness, Autocovariance Function and Other Statistical Properties of Optical Surfaces Using a FECO Scanning Interferometer," Appl. Opt. 15 (November 1976).

[12] Sladky, R. E., et al., in *Laser Induced Damage in Optical Materials: 1975*, A. J. Glass and A. H. Guenther, eds. (NBS Spec. Publ. 435, 1976), pp. 57-65.

[13] Porteus, J. O., et al., "Focusing Method Used in Laser Damage Experiments," Appl. Opt. 15, 2024 (1976).

[14] Porteus, J. O., et al., in *Laser Induced Damage in Optical Materials: 1975*, A. J. Glass and A. H. Guenther, eds. (NBS Spec. Publ. 435, 1976), pp. 207-215.

[15] Temple, P. A., and Soileau, M. J., "Resonant Defect Enhancement of the Laser Electric Field," these Proceedings.

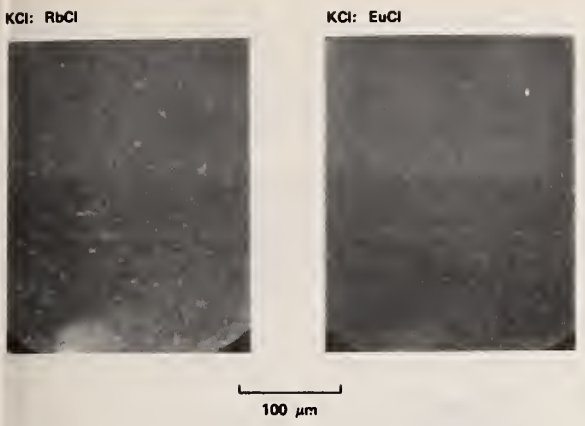

Figure 1. Nomarski micrographs of the surfaces of diamond turned KCl. Note that the visibility of the grooves differs greatly in the two specimens and varies with position on a given speciment.

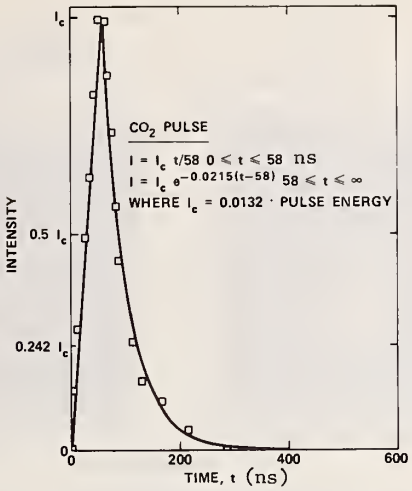

Figure 2. Temporal profile of the Co_2 laser output.

Figure 3. Twyman-Green interferograms of the diamond turned KCl surfaces.

	KCl:EuCl		KCl:RbCl	
WAVELENGTH	FORWARD SCATTER	BACKSCATTER	FORWARD SCATTER	BACKSCATTER
0.4762	6.0×10^{-2}	3.6×10^{-2}	4.0×10^{-2}	3.0×10^{-2}
0.6471	4.5×10^{-2}	2.3×10^{-2}	2.2×10^{-2}	1.7×10^{-2}
1.15	1.8×10^{-2}	8.4×10^{-2}	5.8×10^{-3}	4.8×10^{-3}
3.39	1.6×10^{-3}	1.5×10^{-3}	7.0×10^{-4}	4.7×10^{-4}
10.6	3.5×10^{-4}	1.5×10^{-4}	5.7×10^{-4}	6.8×10^{-5}

Figure 4. Total integrated scatter (TIS) in the forward and back directions for various wavelengths (in μm). The values are the ratios of the total hemispherical scatter to the incident beam intensity.

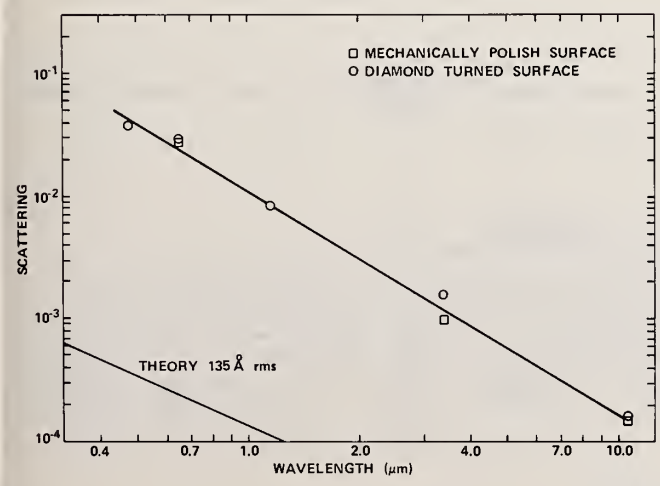

Figure 5. Backscatter as a function of wavelength for a diamond turned KCl:EuCl window and a mechanically polished sample of similar material. The roughness used in the theoretical curve was measured on the diamond turned sample with a surface profiling instrument.

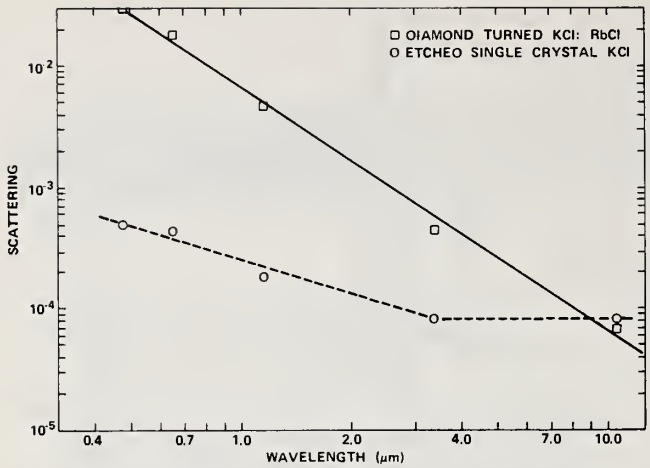

Figure 6. Backscatter as a function of wavelength for a diamond turned KCl:RbCl window and an etched single crystal sample.

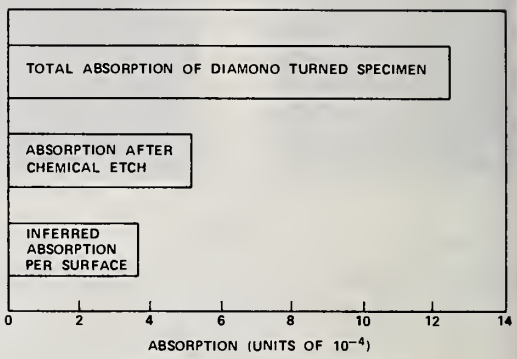

Figure 7. Absorption measurements at a wavelength of 10.6 μm on diamond turned KCl:EuCl before and after etching.

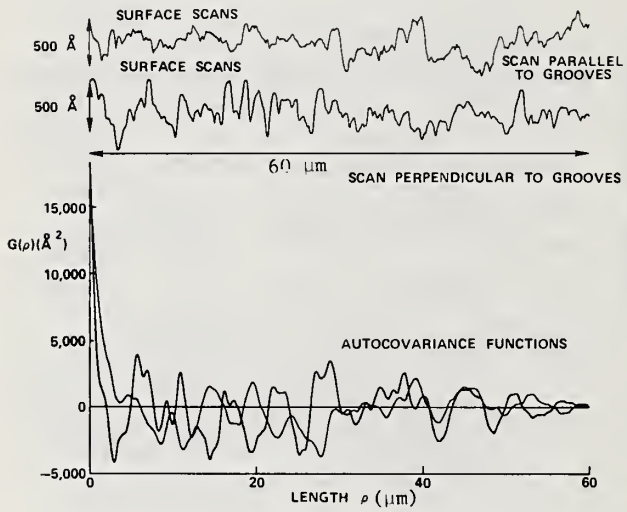

Figure 8. Typical surface scans made parallel and perpendicular to the grooves on the exit face of the KCl:EuCl diamond turned sample. The rms roughnesses are 127 Å rms parallel to the grooves and 135 Å perpendicular to the grooves. The autocovariance functions calculated from the scan data are shown below; the curve with the steeper initial slope and more periodicity is for the scan perpendicular to the grooves.

SPECIMEN	SURFACE	ORIENTATION ANGLE (DEGREES)	$P_{50\%}$ (GW/CM²)	P_L (GW/CM²)	P_H (GW/CM²)
KCl:EuCl	EXIT	89	1.98	1.49	2.11
		50	2.61	1.85	2.77
		3	1.35	1.17	2.34
	ENTRANCE	84	2.03	1.90	2.16
		32	3.98	1.01	4.35
		8	2.62	1.60	4.09
KCl:RbCl	EXIT	90	1.87	0.87	2.13
		81	1.58	1.42	3.50
		18	1.51	0.91	1.92
	ENTRANCE	84	1.77	0.65	2.65
		66	1.78	1.01	2.55
		13	2.48	0.37	2.51

Figure 9. Pulsed damage thresholds for the diamond turned KCl samples. The values are peak on-axis intensities. P_L is the lowest power which produced damage, P_H the highest power which did not produce damage, and $P_{50\%}$ the power which produced 50% of the time.

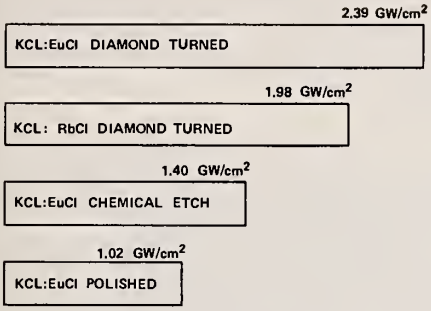

Figure 10. Average damage threshold for diamond turned, etched, and polished KCl. The diamond turned specimens were damaged with a 59.5 μm spot ($1/e^2$ diam.), and the other specimens with a 200 μm spot ($1/e^2$ diam.). All values are peak on-axis intensities.

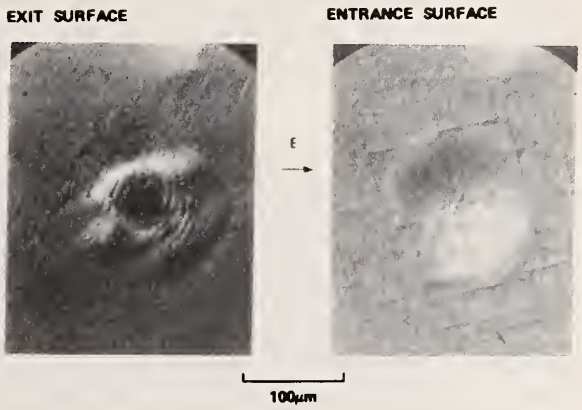

Figure 11. Nomarski micrographs of entrance and exit surface damage sites on KCl:EuCl.

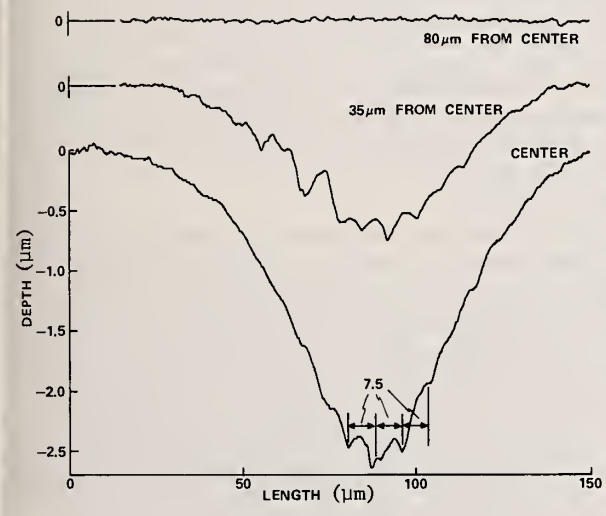

Figure 12. Selected surface profiles made on an exit surface damage crater in the KCl:EuCl specimen. The scans were made parallel to the machining grooves and perpendicular to the ripples in the damage site.

COMMENTS ON PAPER BY SOILEAU, BENNETT, PORTEUS, FAITH, JERNIGAN, AND SAITO

No short-term degradation of chemically etched surfaces has been observed, even for periods up to one week, when the sample was maintained in a controlled, dry atmosphere. Other environmental stability tests have not been made on these samples. The speaker emphasized that the laser beam used in the studies was carefully diagnosed, and was very nearly Gaussian in profile. He further commented that the surfaces tested were within a factor of two in surface roughness of the test available from industry.

2.3 SURFACE, OPTICAL AND LASER DAMAGE CHARACTERISTICS OF DIAMOND-TURNED METAL MIRRORS

D. L. Decker, M. J. Soileau, J. O. Porteus and J. M. Bennett
Michelson Laboratories, Naval Weapons Center
China Lake, California 93555

Diamond turning, in addition to its attractive manufacturing advantages, can produce superior optical components. Low scattered light, low absorption, and high damage threshold can be reliably realized with present technology. This paper intercompares the surface and optical characteristics of a large number of diamond-turned metal mirrors, including bare, electroplated, and sputtered substrates. Many diamond-turned specimens display near intrinsic pulsed laser damage threshold values, often accompanied by slip banding. This phenomenon has been previously observed only on atomically clean, well ordered single crystal surfaces of aluminum. In contrast, however, some electroplated specimens fail catastrophically by delamination. Regardless of sample type, most sites fail by melting initiated by localized absorbing centers.

Key words: Auger analysis; diamond-turned metal mirrors; laser damage; light scattering; optical absorption; surface roughness.

1. Introduction

Diamond turning, in addition to its attractive manufacturing advantages, can produce superior optical components. Low scattered light, low absorption, and high laser damage threshold can be reliably realized with present technology. This paper intercompares the surface and optical characteristics of a number of diamond-turned metal mirrors, including bare and electroplated substrates. The data presented include selected high resolution profilometer traces with autocovariance function and height and slope distributions computed from these traces. Many diamond-turned specimens display what can be described as intrinsic laser damage behavior, often accompanied by slip banding. This phenomenon has been previously observed only on clean, well ordered single crystal surfaces of aluminum. In contrast, however, diamond-turned electroplated surfaces can fail catastrophically by delamination. Auger studies of such a disrupted surface are presented with some surprising conclusions. In the same section some preliminary Auger data taken during ion profiling are given.

2. Surface Characterization

The most striking features of diamond-turned surfaces are the residual machining grooves left as the tool passes over the work. It has been shown that magnitude of the surface structure can be predicted to a large degree from an idealized view of the machining process, given values of tool nose radius, and tool feed rate [1,2][1]. Figure 1 is a Nomarski micrograph of a Lawrence Livermore Laboratory diamond-turned copper surface, denoted Cu 95. The apparent spacing between grooves in this photograph is 7 μm. However, since the Nomarski microscope is slope sensitive, the actual period of this structure is 14 μm. Also visible in this micrograph are the boundaries of individual crystallites in addition to a myriad of small "particulate" appearing structures which are often seen on diamond-turned surfaces. If we examine the same surface with a diamond stylus profilometer [3], scanning perpendicular to the groove structure, the periodicity is very obvious, together with much random excursion including relatively sharp, narrow valleys that may correspond to the grain boundaries, as shown in figure 2. The autocovariance function, derived from an analysis of the digitized profilometer data, readily shows the large correlation associated with a repeat distance of 14 μm and again at two and three times this value, but the correlation for higher multiples of the fundamental is nonexistent. Figure 3 shows the corresponding height and slope distribution functions. Both height and slope distributions can be reasonably approximated by Gaussians, in contrast to the autocovariance function, which includes a contribution from the periodic grooves in addition to the more or less Gaussian short range order. The values of rms height and slope are somewhat typical for a diamond-turned surface, although significantly lower values have been measured on some specimens. Note then the rms slope is twice that associated with the residual machining grooves per se as a consequence of the occurrence of other much steeper structures.

The presence of periodic structure means that the surface will scatter light in preferential directions in the manner of a diffraction grating, although a poor one, as a consequence of lacking long range order [2,4]. The magnitude of the total scattering from this surface is much lower in the visible than one would predict from simple scalar scattering theory and the profilometer-measured rms roughness. For example, in the case of Cu 95 the rms roughness inferred from measured scattered light values in the visible is ~ 35 Å, a factor of over two lower than directly measured. Since the scattered light intensity varies as the square of the rms roughness, the measured scattered light intensity is a factor of over four lower than one would expect. Taking into account only the spatial frequencies important to visible light scattering helps, but does not remove this discrepancy [4]. Most surfaces,

1. Figures in brackets indicate the literature references at the end of this paper.

including mechanically polished and diamond turned, follow the wavelength dependence of the scalar scattering theory in the visible, but lie above theoretical values in the infrared, often by several orders of magnitude (fig. 4). It has been conjectured that the scattering mechanism in the infrared involves poorly correlated, but very effective scattering centers, which have been given the name "particulates" [5]. A proper theoretical explanation of the scattering in the infrared from these surfaces remains unresolved.

3. Laser Damage Studies

Pulsed laser damage to these surfaces is a closely related problem. Whatever damage mechanisms exist are tied directly to the energy deposited in, or to the electric fields at, the metal surface. Electric field interference effects associated with the polarizability of structure on KCl [6] and metal [7] surfaces have been observed. There is obvious influence on laser damage structure by the machining grooves and by crystallite grain boundaries on the diamond-turned metal samples of this study. Figure 5 is a Nomarski micrograph of a laser damage site on LLL Cu 95, showing the effect of the machining grooves in defining the upper and lower edges of the crater just at melt threshold (56 J/cm^2) [8]. Note that this crater is entirely within the boundaries of a single crystallite. Theoretical calculations indicate an intrinsic threshold on copper of about 55 J/cm^2 for the 100 ns pulse length used in these experiments [9]. This calculation assumes room temperature values of the absorptance, thermal diffusivity, and heat capacity. This good agreement may be fortuitous as all pertinent quantities are temperature dependent, especially the absorptance. This calculation should be performed as an integration over temperature with appropriate temperature-dependent variables in the integrand. The melt crater shown in figure 5 is very uniform by comparison to the damage crater on Cu 95 (fig. 6). The small circular structures are melt pits initiated by localized absorbing centers in contrast to the uniform, intrinsic absorption demonstrated in the melt crater of figure 5. The structure of figure 6 is further complicated by the influence of grain boundaries. Note the ripples associated with the nearly horizontal grain boundary in the upper center of this photograph. The laser electric field is in the vertical direction. The crest-to-crest spacing is 10 μm, which suggests a standing wave interference effect [7]. Also obvious in the lower center of this damage site is a patch of extensive slip banding with different orientation on either side of a slip vertex or grain boundary. Slip banding has previously been observed only on very clean surfaces of single crystal aluminum [10]. Figure 7 is a damage site on LLL Cu 8B at 54 J/cm^2. The slip bands are more or less equally spaced about 8 to 9 μm apart. The energy density of the pulse initiating the slip banding in this case was essentially identical to that which generated the melt pit in figure 5. Since no melting is involved in slip banding, it could conceivably occur at lower energy and may be a significant effect below catastrophic damage, especially in a repetitively pulsed system. Figure 8 is a Nomarski micrograph of another damage site on diamond-turned LLL Cu 8B, and obviously considerably above threshold for that site. The very nonuniform crater is defined in part by melt puddles. Grain boundary influence is also obvious, but it is not clear whether we are seeing cause or effect here. There is an apparent tendency for melt puddles to congregate on grain boundaries, presumably a result of contaminants more or less permanently located at grain boundaries (e. g., oxide particles) or else swept to that location during "cleaning."

Figure 9 is a damage site on LLL Cu 8B which was repolished at NWC after a damage series was performed on the initial diamond-turned surface. The polished surface displayed a quite sharply-defined threshold value of about 36 J/cm^2. The particular crater in figure 9 was produced at 59 J/cm^2 and very closely resembles the crater in the previous figure on a diamond-turned surface. Diamond-turned bare copper surfaces can display damage characteristics which can be described as intrinsic. In the case of the melting threshold, such a surface (if clean and free from defects) can yield threshold values in excellent agreement with simple theory. However, there are many sites on a diamond-turned bare copper surface which do not damage either in appearance or threshold differently from a polished copper surface. Figure 10 shows a damage site on a bare copper diamond-turned sample supplied by Heliotrope, Ltd. of England. The surface of this sample has a much different appearance in the Nomarski microscope, and the proprietary surface appears to have been ion or chemically polished after diamond turning, displaying an extremely poor figure. It was of considerable interest to examine the damage characteristics of this surface, since it was possibly "cleaner." This surface, however, behaved very much like the polished LLL Cu 8B surface with a reasonably sharp melt threshold at 40 J/cm^2 as determined by extrinsic absorption at localized points.

Since grain boundaries play a role in defining a relatively low extrinsic threshold, a microcrystalline surface with its necessarily smaller scale grain boundary structure might provide a significantly higher *average* threshold. Such a surface is provided by electroplating. However, the results obtained to date on diamond-turned electroplated gold and silver show about the same relative spread in threshold values from site to site compared to the bare copper results. In some cases spectacularly poor results were obtained for LLL Au 50 (see fig. 11). This coating catastrophically delaminated at an energy density of only 37 J/cm^2, 20% above the value which universally produced damage at all sites. The delamination may have been related to the negative 75 V bias on the sample relative to the faraday cup ion/electron collector. The origin of such an effect is unknown. This delamination site was atypical, most sites being much less spectacular and more like those seen on bare copper. Figure 12 shows a more typical melt crater on LLL Au 50 occurring at 30 J/cm^2.

4. Auger Surface Analysis

The battery of characterization instruments which are incorporated into the NWC UHV damage chamber includes an ion sputtering gun and an Auger spectrum analyzer. This paper presents some preliminary

Auger results on two sample types: diamond-turned bare copper and electroplated silver. Figure 13 indicates the Auger spectrum obtained on the Heliotrope copper surface before and after ion-milling away 40 Å of the material. The initial sulfur, chlorine, and carbon peaks are not present after sputtering. Figure 14 shows the time evolution of the copper, carbon and oxygen peaks. Carbon definitely seems to be associated only with the surface. Although oxygen initially decreases, the peak-to-peak intensity resumes its initial value (before sputtering) after sputtering ceases. A probable explanation is preferential sputtering of oxygen from the surface region [11] and subsequent diffusion of oxygen from the bulk, perhaps along grain boundaries. A depth profile study on LLL Ag 14 shown in figure 15 indicates the presence of sulfur and oxygen contamination limited to within 20 Å or so of the surface. The silver and copper intensities increase in figures 14 and 15 as surface contaminating atoms are removed which are absorbing copper or silver Auger electrons. An interesting discovery was made on LLL Au 50: Nowhere in the area of the delamination could any evidence of copper from the substrate be found. The delamination occurred entirely within the gold electroplated coating.

5. Summary and Conclusions

Figure 16 is a summary of properties of several diamond-turned and polished samples discussed in this paper. The surface roughness values are derived from scalar scattering theory using visible light scattering values. The actual topography measured by a diamond profilometer is much rougher than these numbers indicate with rms values in some cases, e. g., the Heliotrope sample, nearly an order of magnitude larger. In fact, the roughness values inferred from infrared scattering more nearly agree with the profilometer roughness values. The values of E_{D0}, E_{D50}, and E_{D100} are, respectively, damage thresholds in J/cm^2 indicating some statistics of the damage threshold from site to site; e. g., 0, 50, and 100 percent of the sites examined would damage at the energy density indicated. There is little difference among the LLL diamond-turned bare copper samples in values of E_{D0} and E_{D50}. Variation in E_{100} is probably not significant either due to so few data points even with several dozen damage sites and shot energies. One conclusion which can be clearly stated, however, is that the great majority of sites examined showed damage at energy densities much less than the intrinsic melt threshold as a consequence of absorbing centers and/or field enhancement due to polarizable structure. Both macroscopic grain boundaries and perhaps some sort of particulates are involved. LLL 8B and 2D are identical except that 2D was vapor degreased with Freon as a final cleaning step. Since there are no observable damage differences in these two samples, one concludes that whatever comprises the particulate contamination is not so removed. Since values of E_{D50} lie 20% or so below the intrinsic melt threshold, a very significant increase in operational mirror flux loading could be accomplished if the nature of the localized extrinsic absorption on these surfaces were understood and could be eliminated. The observation of intrinsic damage at a significant fraction of sites examined on diamond-turned surfaces is a good indication of the likelihood of improving the cleanliness and perfection of the surface overall, with a corresponding increase in average threshold.

6. Acknowledgments

The authors of this paper acknowledge the contributions of several coworkers at NWC: P. Archibald, E. Ashley, W. Faith, and J. Jernigan. We thank J. Bryan of the Lawrence Livermore Laboratory, T. Saito of the Air Force Weapons Laboratory, and I. M. H. Pagden of Heliotrope, Ltd. for samples. This work was carried out under sponsorship of the U. S. Army Missile Command and with NWC Independent Research funds.

7. References

[1] Donaldson, R. R., "Nomograms for Theoretical Finish Calculations with Round Nose Tools," presented at the Society of Manufacturing Engineers Conference, San Francisco, Ca., November 19-21, 1974.

[2] Sladky, R. E. and Dean, R. H., in *Laser Induced Damage in Optical Materials: 1975*, A. J. Glass and A. H. Guenther, eds. (NBS Spec. Publ. 435, 1976), pp. 57-65.

[3] Bennett, J. M., in *High Energy Laser Mirrors and Windows* (Semi-Annual Report No. 7-8, ARPA Order 2175, Naval Weapons Center, 1976), in press.

[4] Stover, J. C., in *Laser Induced Damage in Optical Materials: 1974*, A. J. Glass and A. H. Guenther, eds. (NBS Spec. Publ. 414, 1974), pp. 163-168.

[5] Bennett, H. E. and Archibald, P. C., in *High Energy Laser Mirrors and Windows* (Semi-Annual Report No. 6, ARPA Order 2175, Naval Weapons Center, 1975), pp. 145-155.

[6] Soileau, M. J., Porteus, J. O., Faith, W. N., Jernigan, J. L. and Saito, T. T., "10.6 μm 100 ns Laser Damage Studies of Diamond-Turned KCl Window Surfaces," these Proceedings.

[7] Temple, P. and Soileau, M. J., "Resonant Defect Enhancement of the Laser Electric Field," these Proceedings.

[8] The damage studies reported in this paper were carried out in the NWC laser damage chamber, at 10^{-7} Torr using a Lumonics CO_2 TEA laser with a 5-inch focal length ZnSe lens. The focal spot is 200 μm in diameter at the $1/e^2$ points on the Gaussian beam profile, and the pulse length is 100 ns.

[9] Bennett, H. E., "Thermal Distortion Thresholds for Optical Trains Handling High Pulse Powers," these Proceedings.

[10] Porteus, J. O., Soileau, M. J., and Fountain, C. W., "Character of Pulsed Laser Damage to Al at 10.6 μm as Inferred from Single-Crystal Targets in Vacuum," these Proceedings.

[11] Wehner, G. K., in *Proceedings of the Sixth Annual Scanning Electron Microscopy Symposium, 1975.* O. Johari and I. Corvin, eds. (IIT Research Institute, Chicago, Il. 1975), pp. 133-139.

8. Figures

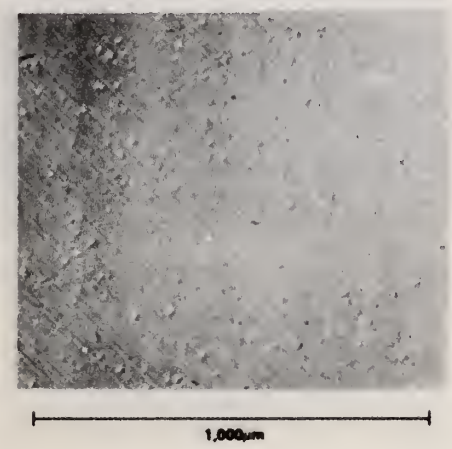

Figure 1. Nomarski micrograph of a diamond-turned copper surface (LLL Cu 95).

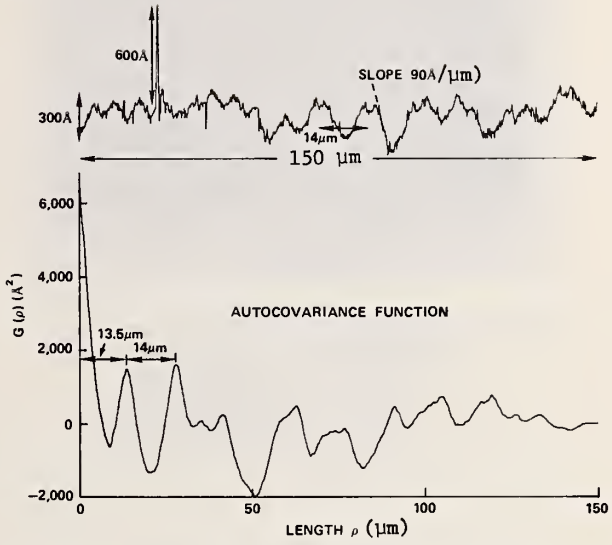

Figure 2. Diamond stylus profilometer scan of LLL Cu 95, together with the computed autocovariance function.

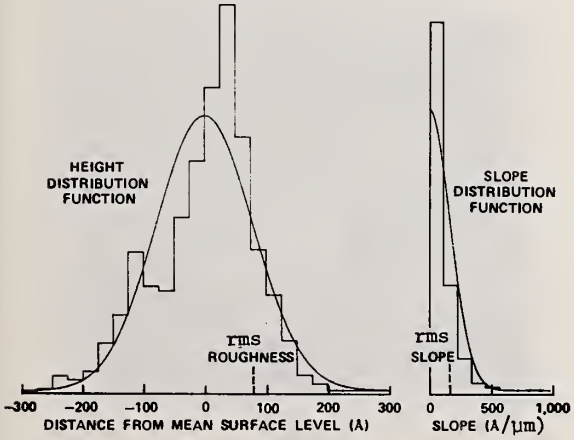

Figure 3. Height and slope distribution functions computed from the profilometer trace of figure 2.

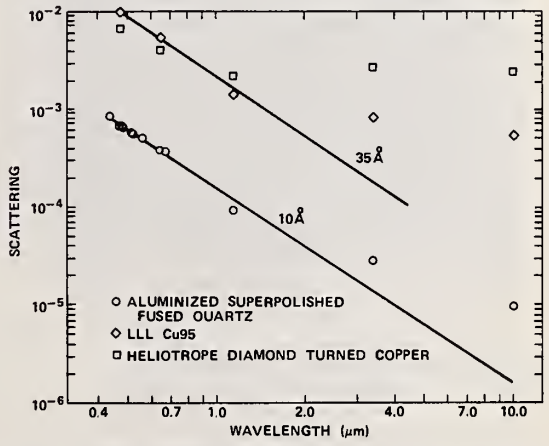

Figure 4. Total integrated backscattered light as a fraction of the incident beam intensity vs wavelength for two diamond-turned samples, and an aluminized supersmooth polished fused quartz flat. Straight lines are theoretical best fits of the aluminized and diamond-turned surface scattering data.

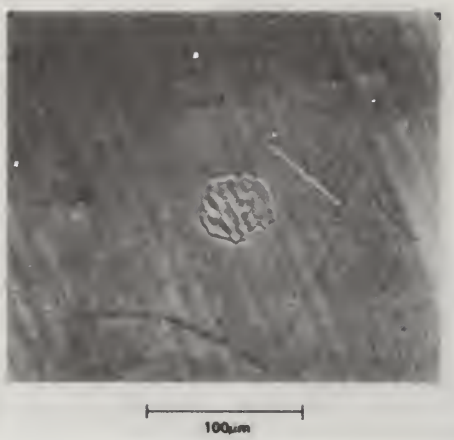

Figure 5. Nomarski micrograph of a laser damage size on LLL Cu 95, just at melt threshold. Note the effect of the machining groves in defining the upper and lower edges of the crater.

Figure 6. Nomarski micrograph of another damage crater on LLL Cu 95, considerably above threshold for this site. Very complicated effects are present and described in the text.

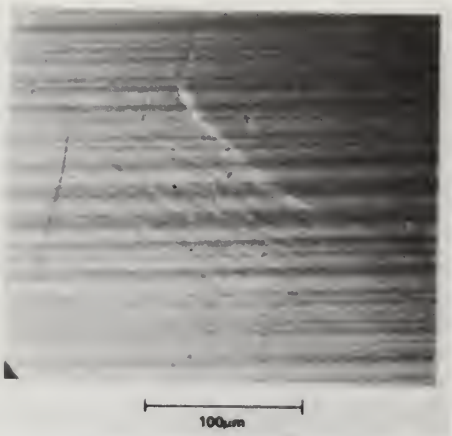

Figure 7. Nomarski micrograph of a damage site on LLL Cu 8B, with very striking slip banding. This effect was produced at a loading more or less identical to the melt threshold, 54 J/cm^2.

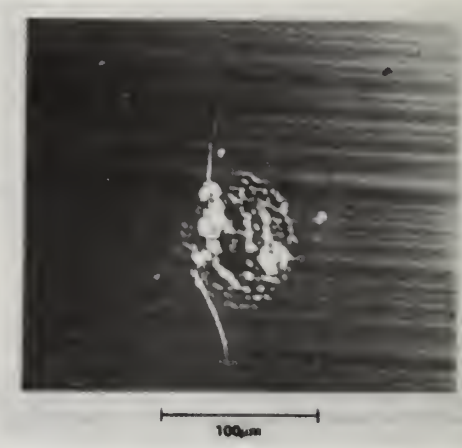

Figure 8. Nomarski micrograph of another damage site on LLL Cu 8B, considerably above threshold for that site.

Figure 9. Nomarski micrograph of a damage site on LLL Cu 8B, after being mechanically polished at NWC following an initial series of damage tests on the diamond-turned surface.

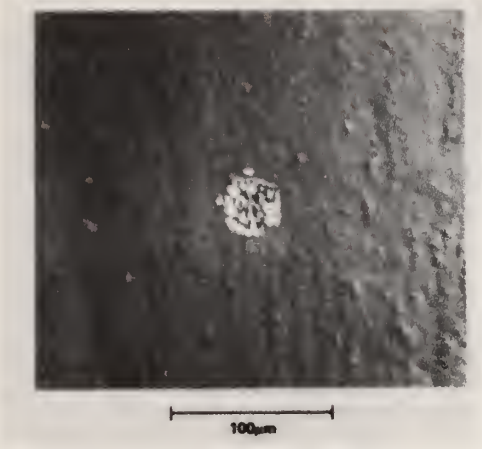

Figure 10. Nomarski micrograph of a damage site on a diamond-turned copper surface supplied by Heliotrope, Ltd. of England.

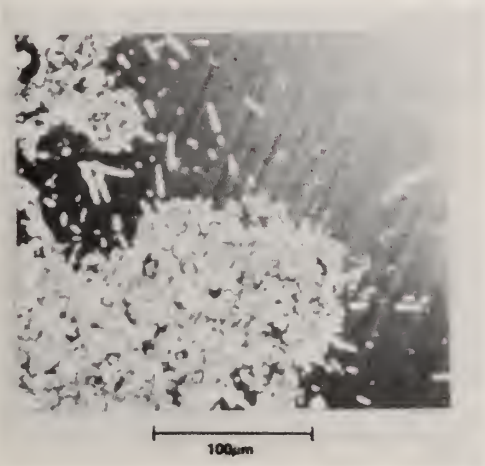

Figure 11. Nomarski micrograph of a damage site on LLL Au 50. Delamination was atypical and may have been related to bias conditions on sample. Additional details are provided in the text.

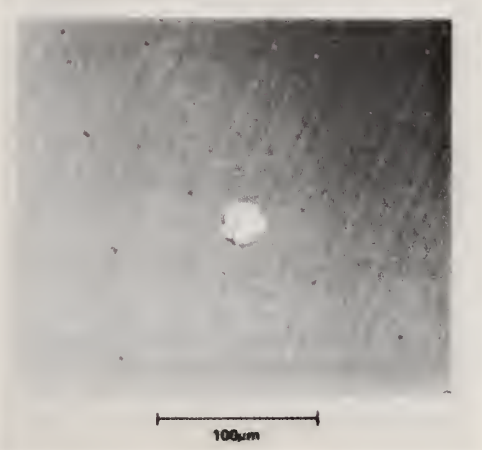

Figure 12. Nomarski micrograph of a more typical damage crater on LLL Au 50, constrasted with the site shown in figure 11.

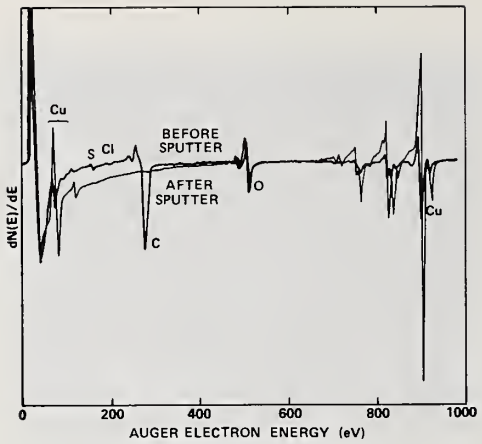

Figure 13. Auger electron spectrum obtained on the Heliotrope, Ltd. sample before and after sputter-etching away 40 Å of material.

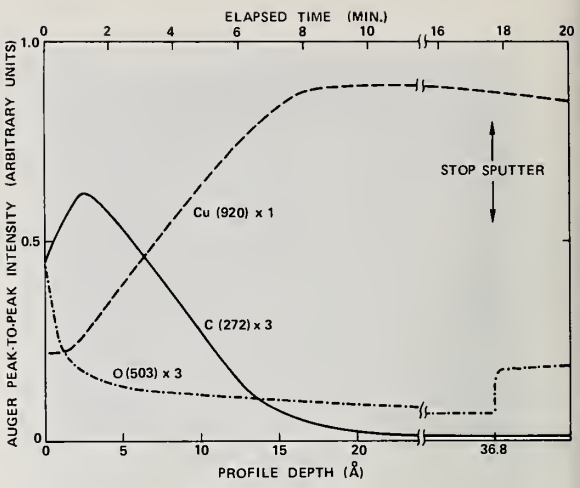

Figure 14. Auger electron spectrum showing time evolution of the copper, carbon, and oxygen peaks during sputter etching.

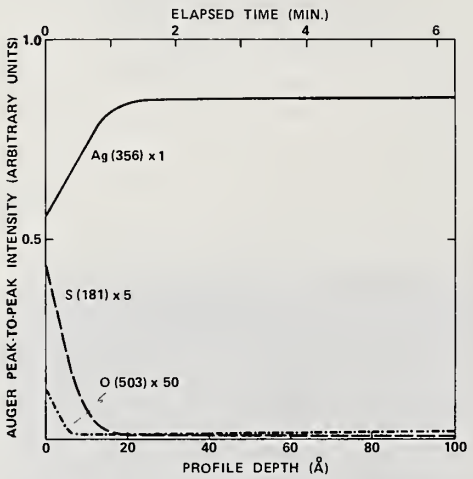

Figure 15. Auger electron spectrum taken during sputter etching of LLL Ag 14, showing decrease of sulfur and oxygen concentration away from the surface.

SAMPLE	SURFACE ROUGHNESS (Å RMS)	SCATTERING AT 10.6μm x 10^{-4}	REFLECTANCE AT 10.6μm	E_{D0}	E_{D50}	E_{D100}
HELIOTROPE 1 IN. DIA	30	25		34	40	47
LLL Cu95	38	6	0.9923	40	46	52
AFTER "CLEANING"				37	40	49
Cu2D	36	9	0.9931		39	60
Cu8B	39	9	0.9931	42	45	66
REPOLISHED					35	51
Ag14	29	6	0.9934	28	49	57
Au50	29	5	0.9884	20	25	30

Figure 16. Summary of optical and laser damage characteristics for several diamond-turned metal mirrors. E_{D0}, E_{D50}, and E_{D100} are, respectively, the energy densities such that 0, 50, and 100% of the sites examined would damage at that energy. Other details are provided in the text.

COMMENTS ON PAPER BY DECKER, SOILEAU, PORTEUS, AND BENNETT

R. Sladky of ORNL commented that diamond-turned surfaces exhibit two scales of periodic structure. The actual tooling grooves are spaced at about 2.5 to 3.8 μm (100 to 150 microinches). Many diamond-turning machines also generate a periodic surface wave of about 25 to 30 μm spacing. The latter can often be eliminated by improving the machine itself.

Discrepancies exist among surface characterizations obtained by different means, such as light scattering, FECO measurements, Nomarski microscopy, and Tallystep profilometry. Each technique is sensitive to a different range of spatial frequencies. The speaker commented that they have been unable to resolve discrepancies between light scattering and Tallystep measurements.

R. Wood of General Electric, Ltd. commented on the low damage threshold of copper mirrors made with hard drawn copper rather than OFHC due to oxide decoration at grain boundaries. He expanded on this point in his subsequent paper.

2.4 CHARACTER OF PULSED LASER DAMAGE TO Al AT 10.6 μm INFERRED FROM SINGLE-CRYSTAL TARGETS IN VACUUM

J. O. Porteus, M. J. Soileau and C. W. Fountain
Michelson Laboratories, Naval Weapons Center
China Lake, California 93555

Pulsed laser-induced stress can produce permanent damage to metal surfaces, even in the absence of melting. Possible causes of such damage in Al are differential expansion resulting from thermal gradients and compression resulting from vaporization. By using single-crystal targets in which plastic deformation can be observed in the form of slip bands, one may obtain information on the direction, magnitude, and thus on the origin of stress. Targets having (111), (001), and (110) surface plane orientations were prepared and tested under oxide-free, ultrahigh vacuum conditions, using well-characterized 100 ns, 10.6 μm focused laser pulses. Vapor particle emission was monitored to provide an indication of vaporization pressure. At energy densities $\gtrsim$ 37 J/cm^2 the results indicate the dominance of evaporative compression. At energy densities near and below the threshold for melting (14.2 J/cm^2) the interpretation of the observed slip banding is less clear, apparently due to the combined effects of thermal and evaporative stresses.

Key words: Laser-induced stress; plastic deformation; single-crystal aluminum; slip bands; vaporization.

Introduction

The orderly development of laser-hardened materials requires an understanding of basic failure modes and their relative importance. In metals plastic deformation from pulsed laser-induced thermal stress may be important well below the melting point [1][1]. An alternative source of stress at high temperatures is evaporative compression, i.e., the reaction pressure on the target produced by the ejection of vapor [2]. Because of the complex characteristics of the target and its environment, and the complexity of the laser source, it is usually difficult to distinguish between surface damage due to thermal expansion, melting, and vaporization. By using pure, annealed single-crystal Al targets, whose plastic response to a given stress is sensitive, predictable and easily recognized, we can make this distinction and obtain other valuable information on laser-induced stress fields. The target surfaces are cleaned and shot in ultrahigh vacuum to avoid possible complications resulting from the presence of air or an oxide film. Vapor particle emission is monitored on each pulse to provide an indication of vaporization pressure. Finally, the laser has simple, reproducible spatial and temporal characteristics which permits accurate thermal modeling.

Plastic deformation is indicated by the formation of slip bands peculiar to the crystallographic orientation of the target and the direction of laser-induced stress. In general, planes with the densest packing, and directions with the smallest interatomic spacing offer the least resistance to slip. In Al these are the {111}-type planes and ⟨110⟩-type directions, respectively [3]. The intersection of the slip planes with the target surface form slip traces. If the slip direction in these planes is entirely parallel to the surface plane, i.e., along the slip traces, no slip bands appear, provided the surface is reasonably smooth. This situation has been reported for a Cu(111) surface exposed to pulsed 1.06 μm laser radiation [4]. Slip was detected by etch pits indicating accumulations of dislocations along slip traces. If the slip has a component normal to the target surface, slip bands appear along the slip-trace directions. This effect, which requires no etching for its observation, is the main subject of this report.

Damage Test Facility

The general layout and operation of the damage test facility has been previously described [5,6]. The source is a CO_2 TEA laser which operates single-line single-mode. The pulse envelope is a sharp spike of approximately 100 ns duration, which decays rapidly to zero. The target lies at the focal point of a 24 cm ZnSe lens, where the spatial profile of beam intensity as a function of the distance r from the beam axis is represented by $\exp[-(r/225.5\ \mu m)^2]$. The use of this lens, instead of the 12 cm lens used in previous work [5,6], permits mounting the lens outside the ultrahigh vacuum test chamber, where it can be removed for bakeout.

---

1. Figures in brackets indicate the literature references at the end of this paper.

Sample Preparation

The single-crystal targets are identical to specimens previously used in low energy electron diffra tion experiments [7]. The samples were spark-cut, oriented, mechanically polished and electropolished before being placed in the test chamber. Final cleaning was performed by Ar-ion sputtering after bake-out. To remove residual Ar, the targets were annealed for 1 hour at 500°C; they were then allowed to cool to room temperature. Surface cleanliness was verified by Auger analysis. To produce lightly oxidized surfaces (less than 50 Å of oxide) the chamber was subsequently filled with bottled N_2 for a few minutes and then repumped. Surfaces produced by these procedures have the "orange peel" type of roughness characteristic of etched surfaces, and are not of optical quality. Targets having three different surface plane orientations were prepared: (111), (001), and (110).

Damage Thresholds

Thresholds for damage due to melting, as indicated by visible crater formation, were measured. Threshold energy densities were found to be 14.2 ± 0.6 J/cm^2 for all targets, with no significant dependence on orientation or light surface oxidation. Evidence of plastic deformation in the form of surface "haze" is always seen when the threshold for melting is approached, as discussed below. However, viewing limitations of the 20X microscope used for damage monitoring would make damage thresholds based on plastic deformation much more subjective.

It is instructive to compare this result with that obtained on a more conventional target under equivalent conditions. We, therefore, measured the threshold for crater formation on a polished 2024 Al target from a previous study [5,6] using the 24 cm lens. The value of 8.3 ± 1.3 J/cm^2 is significantly lower than that measured on the relatively clean single-crystals, probably indicating a higher surface absorption. Embedded contaminants are apparently responsible for the localized pitting observed on this sample, as the threshold for cratering is approached. This, combined with the higher background scattering, precluded the immediate detection of evidence for plastic deformation of the matrix although a surface roughening can be observed with Nomarski.

Damage Above Threshold

To interpret the observed slip banding one must be able to identify slip systems in the face-centered cubic lattice. Figure 1 shows perspective diagrams of the preferred slip planes, directions, and traces in relationship to the (111)-oriented target surface. The laser beam is indicated by the heavy vertical arrow. In the (111) target the slip systems may be conveniently classified into three types as represented in the figure. Slip into or out of the surface may occur in $\{1\bar{1}\bar{1}\}$ planes inclined away from the beam axis, as in (a), or inclined toward the beam axis, as in (b). The same sets of planes and directions are involved in both (a) and (b), but the position of the planes with respect to the beam axis is reversed. The reversal manifests itself in the orientation of the equilateral triangle corresponding to the slip traces, as shown in the figure. Figure 1(c) represents slip in planes intersecting the surface plane and in directions parallel to the surface plane. This type of slip cannot be observed unless the surface is irregular, or has been etched [4].

Figure 2(a) is a Nomarski micrograph of a portion of the (111)-oriented target after exposure to two laser pulses, each producing an energy density of approximately 37 J/cm^2. Surrounding the resulting crater, and extending out to a distance r equal to 2-3 crater diameters are prominent slip bands exhibiting the threefold symmetry characteristics of the (111) orientation. Figure 2(b) is a perspective diagram of the associated slip systems. The orientation of the triangle formed by the slip bands typifies figure 1(b), which is reproduced here. The bands show no evidence of cross slip which would indicate the type of slip indicated in figure 1(c). The relationship of the direction of illumination to bright lines and shadows produced by the slip bands, both in optical (fig. 3), and in scanning electron micrographs, shows that the slip bands form terraces which are stepped toward the laser as the beam axis is approached.

Slip-banding on the (001)-oriented target, produced by a single 28 J/cm^2 pulse, is shown in figure 4(a) and analyzed in figure 4(b). A fourfold slip band pattern surrounds the crater corresponding to the four {111} planes which make equal angles with the (001) surface. The preferred slip may be classified into three types in analogy with figure 1. However, because of the fourfold symmetry we cannot distinguish between (a) and (b). Type (b) is more probable because of its similarity to the (111) case. The bands are again found to be stepped toward the laser. This, combined with the fact that the bands are visible in dark field micrographs, also favors the indicated interpretation.

The corresponding result on the (110) target is shown in figure 5, where the slip banding was produced by a single 47 J/cm^2 pulse. Here slip in {111} planes making a dihedral angle of 35.3° with the surface (110) plane supersedes slip in {111} planes perpendicular to the surface. In contrast to the (111) and (001) targets the bands are stepped *away* from the laser.

Laser-Induced Stress

It is possible to use the foregoing observations to arrive at a result for the direction of the laser-induced stress. The combined results from figures 2-5 are summarized schematically in figure 6. The approximate direction of the stress component in an azimuthal plane has been inferred by applying the following criteria to be projected slip directions shown in the figure: (1) The stress has a shear component along the active slip planes, whose direction agrees with the observed direction of slip. (2) Slip is preferred along planes which are subjected to the maximum resolved shear stress, i.e., which are inclined most nearly at 45° to the direction of applied stress [8]. An exact analysis, in which resolved shear stresses in the actual, rather than the projected slip directions are considered, should yield qualitatively similar results.

The inferred stress in figure 6 must be associated with a thermal and/or a vaporization effect. Radiation pressure, which may influence the distribution of molten material near the damage threshold [5, 6], is well below the critical shear stress and may be ignored. Thermal stresses produced by short laser pulses are predominantly parallel to the surface plane [1,4]. In the azimuthal planes a compressive radial component dominates, which is not reconcilable with present results. Evaporative compression on the crater and surrounding area, resulting in a predominantly normal stress, is the alternative mechanism. Supporting evidence for the latter mechanism comes from measurements of vapor particle emission, which is discussed in a later section.

Damage Near Threshold

At energy densities insufficient to produce melting Nomarski micrographs reveal a surface roughening on polycrystalline, as well as single-crystal samples. Figure 7 shows this effect on two different areas of the Al(111) target, for which both Nomarski and dark-field micrographs are presented. Except for magnification, the dark field images correspond more closely to what is seen with the 20X microscope mounted on the test chamber. Thus the energy density represented in (a) is below, and that in (b) is just above the threshold for crater (dark circle at lower right) formation. The Nomarski micrographs show that the roughening consists of slip bands along the three ⟨110⟩-type crystallographic directions. However, the bands show a sixfold, rather than the threefold symmetry apparent in figure 2. Because of this and the difficulty in determining the slip direction here, the possible importance of thermal stress cannot be excluded in this situation. In the Nomarski photograph at the upper right, the roughening inside the cratered area indicated by the dark field photograph shows little correlation with crystallographic direction, confirming that the cratered area corresponds to a melt zone. The conclusion is that the roughening, which is observed with Nomarski both in single-crystal and polycrystalline Al, is plastic deformation, possibly resulting from thermal stress.

The slip banding is faintly visible in the dark field photographs, and undoubtedly accounts for the surface haze observed in the test-chamber microscope as one approaches the threshold for cratering. This can be seen more clearly on the (110) target, as shown in figure 8. Here the energy available for plastic deformation is concentrated in a single slip direction, providing greater sensitivity. The sequence of events is also unmistakable here. That is, slip banding occurs *before* the crater is formed.

Vaporization

An indication of the stress available for evaporative compression can be obtained from the intensity and energy of vapor particles emitted by the target. Figure 9 shows schematically the detector used for monitoring particle emission. The collector is typically biased at either + or -12.6 V, while the grid is grounded. Typical signals developed across the 50 Ω input of a Tektronix 7844 oscilloscope are shown in figure 10. With the negative bias one observes a positive signal showing two prominent, and numerous smaller peaks. With the positive bias one observes a negative-going peak which is about ten times as great as the largest positive going peak. The positive peaks are undoubtedly due to positive ions. The origin of the negative-going peak is less certain, but is believed to be due to secondary electrons generated at the grid by a large flux of high energy neutrals. The arrival time excludes an explanation of the signal in terms of photo-electrons, while plasma conduction is excluded on the basis of the relatively small magnitude of the signal with negative bias.

The energy of the ions or neutrals can be obtained from the time of flight, provided the particle mass is known. In figure 11 we have plotted the arrival time of the most intense ion peak from the clean targets vs the energy density of the pulse. The ion energies are given by the scale on the right, assuming the mass is that of a single Al atom. Corresponding information for the neutrals is given in figure 12. Here the energy is found to vary more strongly with pulse energy than for the ions.

The emission density of the ions at the target can be obtained from the collected ion signal if the charge per ion is known. In figure 13 we have plotted the maximum ion signal vs the pulse energy density. The scale on the right gives the corresponding emission density computed from the collector geometry, assuming uniform emission with a cosine-squared angular distribution over a 451 μm diameter illuminated area and unit ionic charge. The corresponding plot for the neutrals is given in figure 14. Unfortunately, it is impossible to put a reliable emission density scale on this figure, since very

little is known about the secondary yield γ for neutral atoms. The only estimate available [9] indicates a yield ~0.1 for 100-200 eV neutrals. Using this value and the fractional opaque area of the grid (~20%) we find that the neutral emission density is ~300 times the ion emission density at a pulse energy of 37 J/cm^2. Thus the reaction pressure due to vaporization is predominantly due to neutrals. Assuming that the neutrals are accelerated to their full energy within the 100 ns duration of the laser pulse yields a value ~150 bars (10^5 N/m^2) for the reaction pressure. This is in satisfactory agreement with published values measured under similar conditions with a piezoelectric gauge [2]. The critical yield stress of our target is estimated at $\lesssim$ 20 bars [10], which implies that the evaporative mechanism is feasible at the energy densities represented in figures 2-6. Near, and below threshold the signal from emitted vapor particles is unobservable, although in the case of neutrals this may be associated with a rapid decrease in γ with reduced particle energy. These results, therefore, also admit the possible significance of thermal stress near threshold.

Summary and Conclusions

In summary, we have made pulsed laser-damage measurements at 10.6 μm on clean and lightly oxidized single-crystal Al targets in ultrahigh vacuum. We find no significant dependence of the threshold for melting on crystallographic orientation, or on the presence of a thin oxide layer. We also find that the threshold for crater formation is almost twice as high on these surfaces than it is on polished 2024 polycrystalline targets. Microscopic analyses of the laser-damaged single-crystals reveal slip bands, which provide detailed information on laser-induced stress fields and their effects on the target. For example, the roughening observed on polycrystalline targets below the threshold for crater formation can now be assigned to plastic deformation. At higher intensities the slip patterns observed on the differently oriented targets permit determination of the stress direction. Monitoring of the particle emission energy and intensity accompanying damage permits an estimate of the reaction pressure induced by vaporization. The evidence from slip banding and vapor particle emission implies that evaporative compression is dominant at intensities well above the threshold for crater formation, while thermal stresses may be important at lower levels.

Acknowledgments

Various aspects of this program were supported by Naval Air Systems Command, Office of Naval Research, Army Missile Command, and Navy Independent Research Funding. The authors are grateful to Drs. H. E. Bennett and K. H. Westmacott for helpful comments and criticism, to W. N. Faith for preparing the samples, and to J. H. Dancy for electron microscopy.

References

[1] Apollonov, V. V. et al., Sov. J. Quantum Electron. 5, 216 (1975).

[2] McMordie, J. A. and Roberts, P. D., J. Phys. D: Appl. Phys. 8, 768 (1975).

[3] Hirth, J. P. and Lothe, J., *Theory of Dislocations* (McGraw-Hill, New York, 1968), pp. 255-257.

[4] Haessner, F. and Seitz, W., J. Materials Sci. 6, 16 (1971).

[5] Porteus, J. O., Soileau, M. J. and Bennett, H. E., in *Laser Induced Damage in Optical Materials: 1975*, A. J. Glass and A. H. Guenther, eds. (NBS Spec. Publ. 435, 1976), pp. 207-215.

[6] Porteus, J. O., Soileau, M. J., Bennett, H. E. and Bass, M., in *High Energy Mirrors and Windows* (Semi-Annual Report No. 7-8, ARPA Order 2175, Naval Weapons Center, 1976), in press.

[7] Porteus, J. O. and Faith, W. N., Phys. Rev. B 12, 2097 (1975).

[8] See Ref. 3, pp. 269-270.

[9] Rostagni, A., Z. Phys. 89, 55 (1934); see also Levine, L. P., Ready, J. F. and Bernal G., E., IEEE J. Quantum Electron. QE-4, 18 (1968).

[10] Lücke, K. and Lange, H., Z. für Metallkunde 43, 55 (1952).

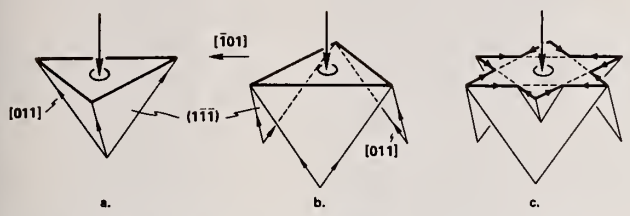

Figure 1. Preferred slip systems in Al(111) target. Slip planes are $\{1\bar{1}\bar{1}\}$. Slip directions are $\langle 011 \rangle$ in (a) and (b), and $\langle \bar{1}01 \rangle$ in (c). Slip traces (heavy lines) are $\langle \bar{1}01 \rangle$.

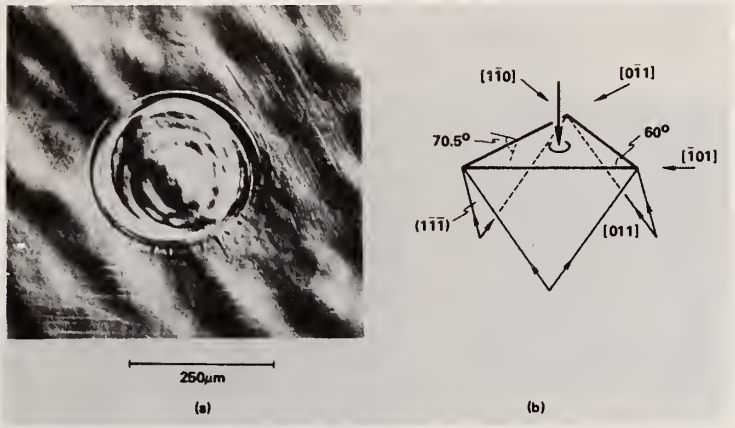

Figure 2. (a) Nomarski micrograph of pulsed laser damage on Al(111) target at 37 J/cm^2 (max. of 2 pulses), showing triangular slip banding in [$\bar{1}$01], [1$\bar{1}$0], and [0$\bar{1}$1] directions. (b) Diagram showing slip (arrows near bottom) associated with banding in (a). Corresponding slip traces are indicated by heavy lines lying in the direction indicated near the top of the diagram. The heavy vertical arrow represents the laser beam.

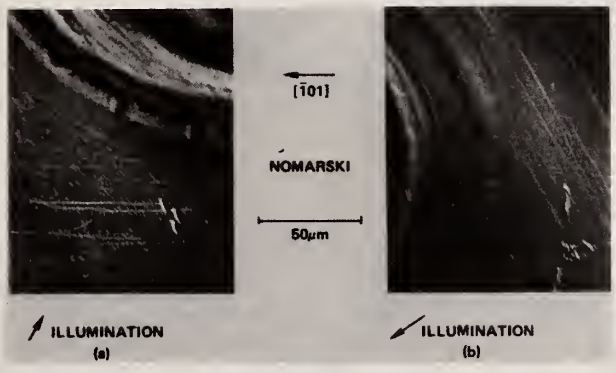

Figure 3. Slip-band terraces of Al(111) target near edge of damage crater. Risers between terraces show as bright lines when facing direction of illumination. Exposure is 37.0 J/cm^2 (max. of 3 pulses) in (a) and 31.6 J/cm^2 (max. of 3 pulses) in (b).

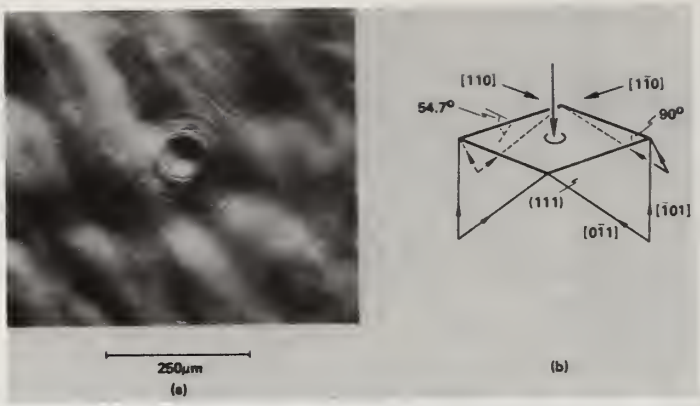

Figure 4. (a) Nomarski micrograph of pulsed laser damage on Al(001) target at 28 J/cm^2 (one pulse), showing fourfold slip banding. (b) Perspective diagram similar to figure 1(b), showing slip produced in the (001) target.

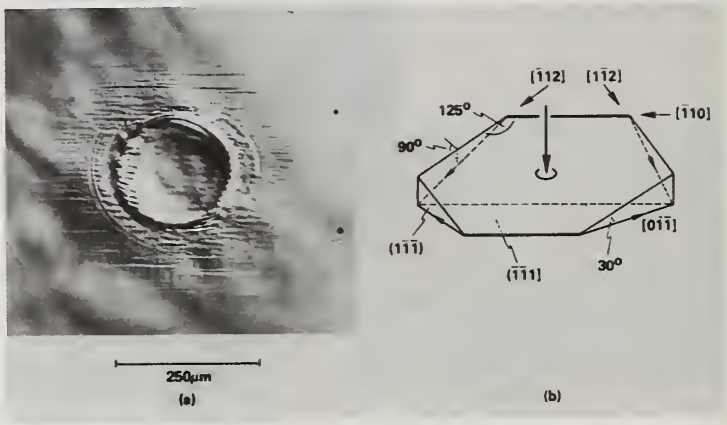

Figure 5. (a) Nomarski micrograph of pulsed laser damage on Al(110) target at 47 J/cm^2 (one pulse) showing slip banding in [$\bar{1}$10] direction.
(b) Analysis of slip shown in figure 3(a). Banding along [$\bar{1}$10] directed slip traces (heavy lines) is much more pronounced than along traces lying in [$\bar{1}$12] and [1$\bar{1}$2] directions.

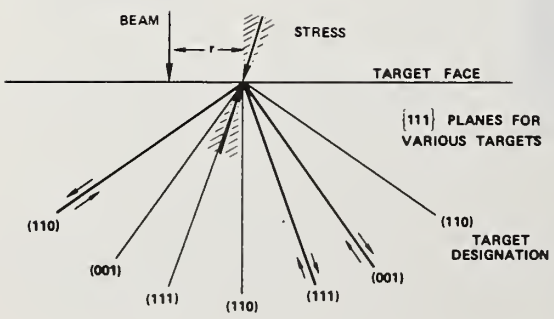

Figure 6. Summary of slip-banding results at energy densities $\lesssim$ 37 J/cm^2. Diagonal lines at the bottom of the figure represent the dihedral inclinations of available {111} slip planes to the target face in all three targets, which are identified in each case. Active planes are designated by heavy lines and arrows showing the projected direction of slip. The direction of the compressive stress component indicated by the shaded arrows is consistent with the observed slip, according to the criteria given in the text.

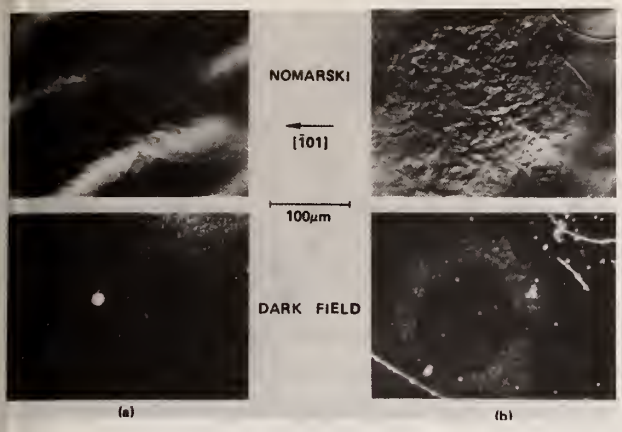

Figure 7. Damage on Al(111) target below (a) and just above (b) the threshold for crater formation. Corresponding areas are shown in Nomarski and in dark field micrographs. The bright spots in the dark field micrographs are dirt specks. Exposure is 8.0 J/cm^2 (one pulse) in (a) and 15.3 J/cm^2 (one pulse) in (b).

Figure 8. Damage on the Al(110) target below (a) and above (b) the threshold for crater formation, as seen in dark field micrographs. Exposure is 12.2 J/cm^2 (max. of 2 pulses) in (a) and 16.9 J/cm^2 (one pulse) in (b).

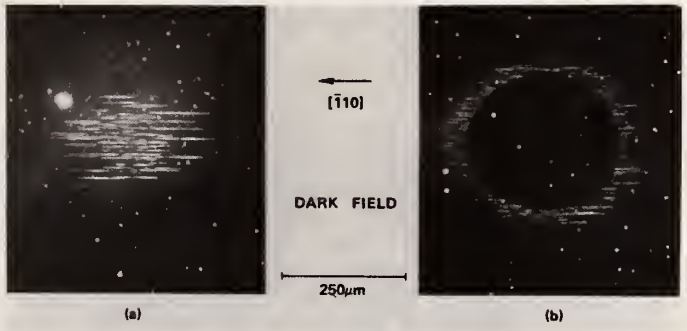

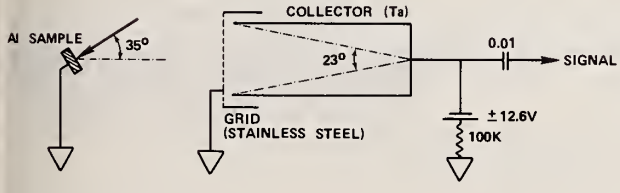

Figure 9. Charged particle detector, showing relationship of Al target sample and laser beam. Distances are on the same relative scales. Collector diameter is 2.5 cm.

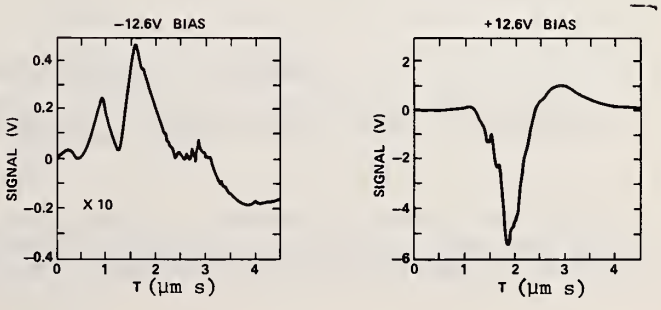

Figure 10. Time spectra of vapor particle emission observed with different collector biasing at 33.3 J/cm^2.

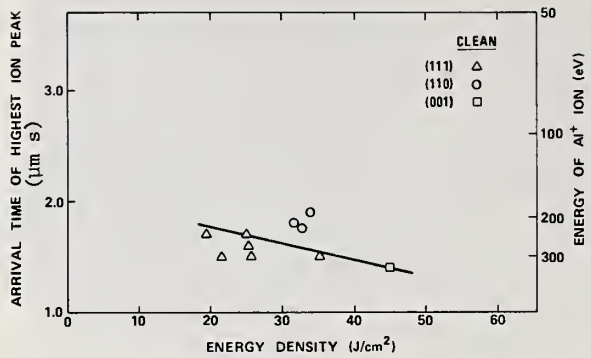

Figure 11. Arrival time of emitted ions vs pulse energy density, showing computed particle energies. Results are from differently oriented, clean targets.

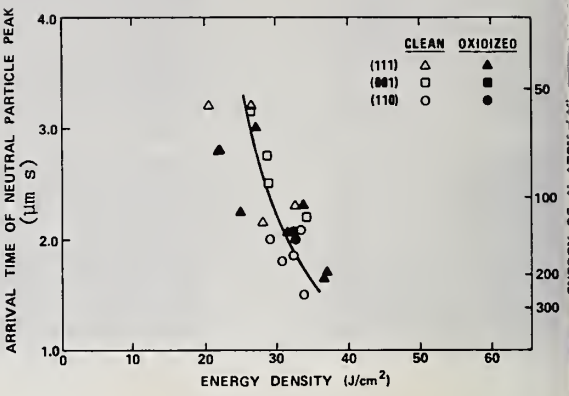

Figure 12. Arrival time of emitted neutral particles vs pulse energy density, showing computed particle energies. Results are shown from both clean and lightly oxidized targets of different orientation.

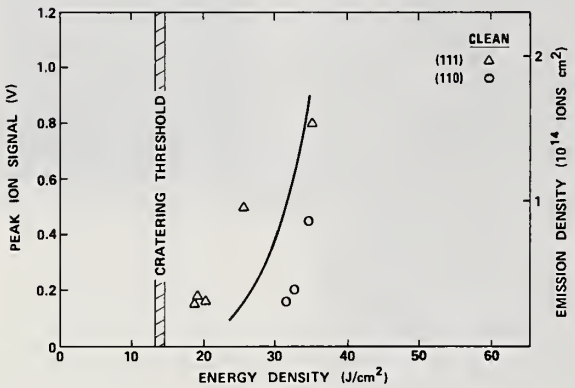

Figure 13. Peak signal of emitted ions vs pulse energy density, showing computed emission densities. Results are from clean targets.

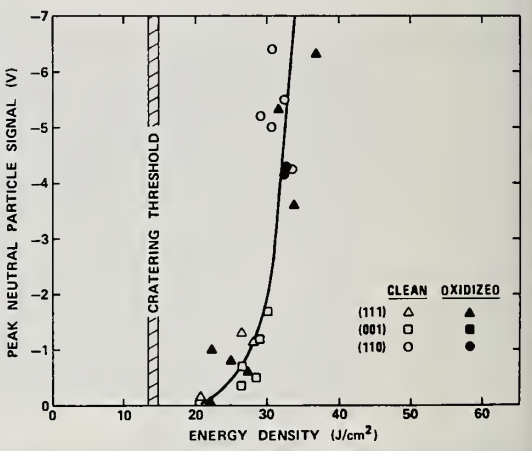

Figure 14. Peak signal due to emitted neutrals vs pulse energy density. Results are from both clean and oxidized targets.

COMMENTS ON PAPER BY PORTEUS, SOILEAU, AND FOUNTAIN

It was emphasized that slip planes could be generated by thermoelastic stresses at power levels well below the levels required to produce local melting of the surface.

2.5 MEASUREMENTS AT 10.6 μm OF DAMAGE THRESHOLD IN GERMANIUM, COPPER, SODIUM CHLORIDE, AND OTHER OPTICAL MATERIALS AT LEVELS UP TO 10^{10} W/cm^2*

J. J. Hayden and I. Liberman**
University of California
Los Alamos Scientific Laboratory
Los Alamos, NM 87545

We have measured the damage threshold levels in various optical materials useful as mirror surfaces and windows at 10.6 μm. Typical values range from .73 J/cm^2 for a micro-machined aluminum mirror up to 12.6 J/cm^2 for a micro-machined OFHC copper mirror. Materials tested include: ZnSe, conventionally polished copper mirrors, micro-machined aluminum and copper mirrors, uncoated and AR coated NaCl windows, polished germanium flats and tungsten mirrors. Tests have been done in air and vacuum, at different angles of incidence, and at different angles with respect to the plane of polarization of the incident light.

Key words: Beam quality; damage threshold; Gaussian beam; peak energy density; pulse width 1.4 nanoseconds (FWHM).

1. Experimental Setup

The laser system used to obtain these measurements is a mode-locked TEA double-discharge laser system illustrated in figure 1. An oscillator with a mode-locker and Pockels cell is used to generate a 1.4 ns (FWHM) pulse containing 5 mJ. The beam passes through a 2:1 beam expander, which utilizes a spatial filter at the focus to improve beam quality. The beam is then amplified to the 2 J level by pre-amplifiers 1 and 2. The prepulse absorption cell is an SF_6 cell which removes precursors of the main pulse. Oriented polyester films (.0064 mm to .051 mm thick) were used as attenuators to provide a variable laser output. The beam then passes through a pick-off pellicle (0.0064 mm thick) which is used to reflect a portion of the beam into a calorimeter. The beam is focused with a 30 meter radius mirror and a spatial filter is placed at the focal spot. The expanding beam is again focused with a 5 meter radius mirror onto the test sample.

2. Analysis

For a Gaussian beam, the energy density at a given radius can be expressed in the form

$$I = I_o \exp\left(-\frac{2r^2}{w^2}\right) \tag{1}$$

where I = energy density at radius r, I_o = peak energy density, w = spot radius at $1/e^2$ intensity. The total energy, J_o, can be expressed as

$$J_o = \int_0^{\infty}\int_0^{2\pi} I\, r\, dr\, d\theta = \frac{\pi w^2 I_o}{2} \tag{2}$$

Solving for I_o

$$I_o = \frac{2J_o}{\pi w^2} \tag{3}$$

Substituting this expression for I_o into eq. (1) we obtain

$$I = \frac{2J_o}{\pi w^2} \exp\left(-\frac{2r^2}{w^2}\right) \tag{4}$$

A pyroelectric detector array was used at the sample position to determine the energy distribution in the beam. Figure 2 shows the output of the pyroelectric detector array. Figure 3 shows how the individual detector outputs match a Gaussian. The beam is a Gaussian, and the $1/e^2$ diameter as determined from the detector array is 0.36 cm. Since w = .18 cm, we determine from eq. (3) that

$$I_o = \frac{2J_o}{\pi(.18)^2} = 19.6\ J_o$$

To calibrate the pick-off pellicle a calorimeter is inserted after the 5 meter radius focusing mirror. A shot is taken and the calibration factor of total joules in the beam per mV of pick-off calorimeter response is calculated. Thus the peak energy density delivered to the sample is the calibration factor times the mV from the pellicle calorimeter times 19.6.

3. Other Considerations

The energy densities necessary to damage copper mirrors is great enough to cause a plasma to be formed on the mirror surface. In order to make sure that this plasma did not affect the energy density actually arriving at the mirror surface, measurements were also made in a vacuum (pressure $\approx$ 1 torr absolute).

Damage threshold was determined visually. An argon-ion laser was injected collinear with the CO_2 beam. The scattering of the argon-ion beam was observed during exposure and was observed to change dramatically when damage occurred. Additionally, a very bright visible light source was used on the optical surfaces during laser light exposure. When damage occurred, the reflective character of the sample surface was observed to change. Damage threshold was arbitrarily defined as the minimum peak energy density at which a sample damaged in three exposures (or fewer) on the same spot.

The angle of exposure of surfaces was varied during these experiments. In the following tables, 90° indicates the surface was normal to the laser beam. An angle indicated "in plane of incidence" means the surface was tilted in the p plane of polarization. An angle "out of plane of incidence" was tilted in the s plane of polarization.

Several spots were tested on most samples. The energy density was progressively increased on a single spot until damage was observed. Then another spot was tested at an exposure level nearly as high as the damage threshold first observed, and exposure raised until damage occurred. Threshold values are listed in two columns. The first column "Highest J/cm^2 without damage," indicates the highest exposure level used (three shot exposures) which did not cause damage. The second column "Lowest J/cm^2 with damage," lists the lowest value of damage threshold which was observed. The actual "average" damage threshold is approximately the arithmetic mean of the values in the two columns.

4. Results

Table 1 shows the damage threshold of conventionally polished and micro-machined (diamond turned) OFHC copper mirrors.

Unexpectedly high damage thresholds were measured for OFHC copper mirrors. Micro-machined mirrors had a slightly higher damage threshold than conventionally polished mirrors in both air and vacuum. At the 45° angles no increase was noted in damage threshold, contrary to what might be expected by increasing the exposure area by a factor of 1.414.

The most significant point to note in table 1 is that for all conditions tested, the damage threshold was 10.1 J/cm^2 ± 25%. This uniformity indicates good reproducibility of surface which can be expected of good quality copper mirrors.

Figure 4 shows a photomicrograph of an undamaged micro-machined OFHC copper mirror (80x). Note the machining marks and the crystal boundaries. Figure 5 shows the same mirror at a damage site (80x). Note that the grain boundaries have melted together and the surface appears to be smoother. Figure 6 shows a conventionally polished OFHC copper mirror (80x). It appears to have a much smoother surface than the micro-machined mirror. Figure 7 shows a damage site on the conventionally polished OFHC mirror. The character of damage is different than the micro-machined mirror in that small "pits" are blasted out of the surface.

Table 1. Damage Threshold for 1.4 ns pulse at 10.6 μm on OFHC copper mirros.

Material	Medium	Angle	Highest J/cm^2 without damage	Lowest J/cm^2 with damage
OFHC Copper Mirror Conventionally Polished	Air	90°	10.8	8.8
OFHC Copper Mirror Micro-machined	Air	90°	11.3	9.3
OFHC Copper Mirror Conventionally Polished	Air	45° in Plane of Incidence	8.8	9.7
OFHC Copper Mirror Conventionally Polished	Air	45° out of Plane of Incidence	8.9	9.8
OFHC Copper Mirror Micro-machined	Vacuum	90°	11.3	12.6
OFHC Copper Mirror Conventionally Polished	Vacuum	90°	7.3	10.5
OFHC Copper Mirror Micro-machined	Vacuum	45° out of Plane of Incidence	7.3	7.4
OFHC Copper Mirror Conventionally Polished	Vacuum	45° out of Plane of Incidence	9.9	11.0
OFHC Copper Mirror Micro-machined	Vacuum	45° in Plane of Incidence	7.1	7.6

Table 2 shows the damage threshold of NaCl windows, both AR coated and uncoated.

The damage threshold for NaCl windows which were AR coated was considerably (almost a factor of 2) higher than for uncoated samples. All samples were very good quality single crystal NaCl with "high power laser finish." The vendor would not reveal what AR coating was used. Analysis of the coating by an electron microprobe indicated that it was most likely a single layer CaF_2 coating. Transmissions were measured for the uncoated (T = 91.5%) and AR coated both surfaces (T = 98%) samples. Other poor surface quality NaCl samples (uncoated) have damaged as low as 1 J/cm^2. Figure 8 is a photomicrograph of damage to AR coated NaCl (320x). Notice that the damage appears to be mainly in the coating. Figure 9 shows uncoated NaCl (200x). The damage here appears to be a fracture pattern in the NaCl crystal.

Table 2. Damage Threshold for 1.4 ns pulse at 10.6 μm on NaCl.

Material	Medium	Angle	Highest J/cm^2 without damage	Lowest J/cm^2 with damage
NaCl Window uncoated-uncoated	Air	90°	5.7	5.7
NaCl Window AR - AR	Air	90°	10.8	9.9
NaCl Window AR - uncoated	Air	90°	9.6	7.7
NaCl Window uncoated-uncoated	Vacuum	90°	5.4	5.4
NaCl Window AR - AR	Vacuum	90°	6.1	8.2

Table 3 lists damage threshold for several other materials of interest.

The sample of copper electroplated on a SiC substrate was, without question, the best of all samples tested. Repeated shot at 11.4 J/cm^2 failed to produce damage. The SiC substrate is a potentially useful substrate material for large diameter mirrors because of its high stiffness to weight ratio.

Table 3. Damage threshold for 1.4 ns pulse at 10.6 μm for other materials.

Material	Medium	Angle	Highest J/cm^2 without damage	Lowest J/cm^2 with damage
Aluminum Mirror Micro-machined	Air	90°	-	0.7
Germanium Polarizer Plates, Polished, uncoated	Vacuum	70° in plane of incidence	4.1	4.6
ZnSe Window uncoated-uncoated	Air	90°	1.5	1.9
ZnSe Window AR - AR	Air	90°	1.9	1.4
Copper Electroplated SiC Substrate Conventionally Polished	Air	90°	11.4	11.4
Tungsten Mirror Conventionally Polished	Air	90°	-	2.44
Tungsten Mirror Conventionally Polished	Vacuum	90°	1.6	2.26

5. Summary

Copper mirrors, both micro-machined and conventionally polished have been measured to have a high damage threshold. Both types of copper mirrors are suitable for most high peak power applications because beam quality deterioration resulting from plasma formation will generally occur before mirror damage occurs (in air).

The peak energy density at which NaCl windows can be used without damage is improved by almost a factor of 2 by using an AR coating of CaF_2.

*Work performed under the auspices of the U. S. Energy Research and Development Administration.

**Westinghouse Research Laboratories, Pittsburgh, PA.

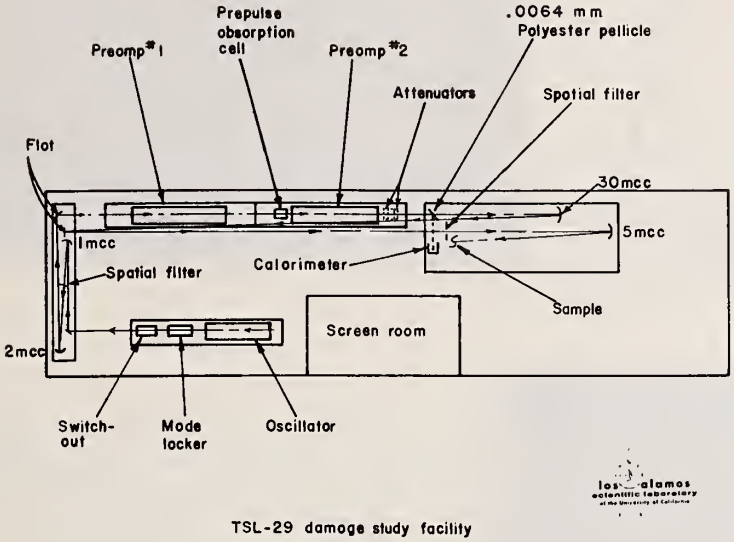

Figure 1. TSL-29 damage study facility.

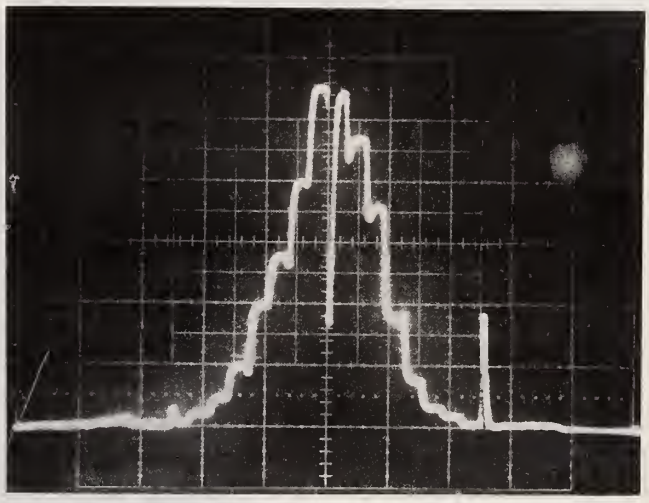

Figure 2. Output of the pyroelectric detector array.

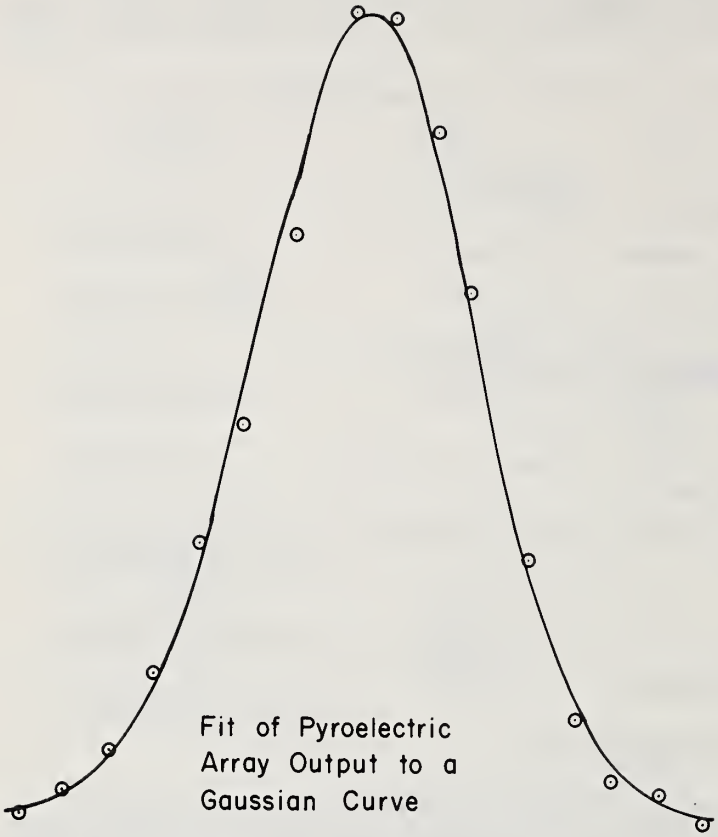

Figure 3. Fit of pyroelectric array output to a Gaussian curve.

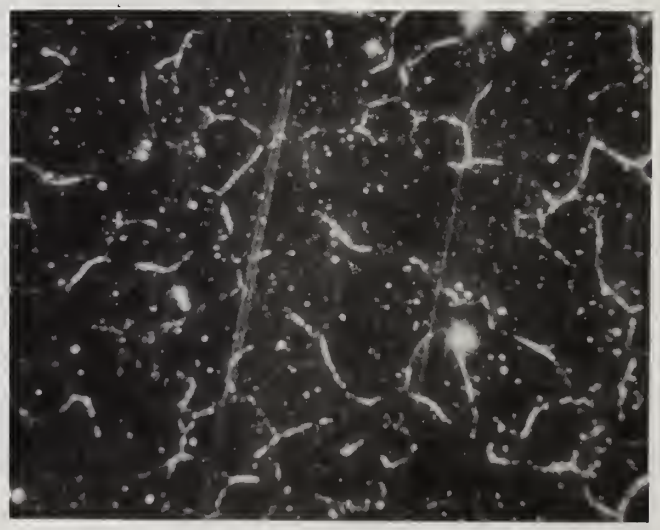

Figure 4. Photomicrograph of an undamaged micro-machined OFHC coppor mirror (80x).

Figure 5. Same mirror as figure 4 at a damage site (80x).

Figure 6. Conventionally polished OFHC copper mirror (80x).

Figure 7. Damage site on the conventionally polished OFHC mirror.

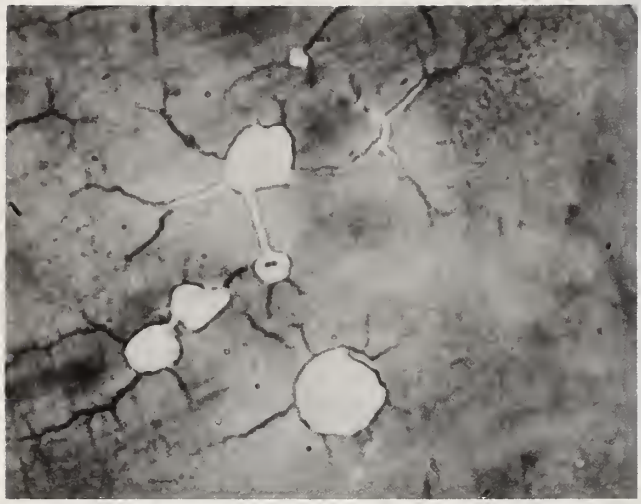

Figure 8. Photomicrograph of damage to AR coated NaCl (320x).

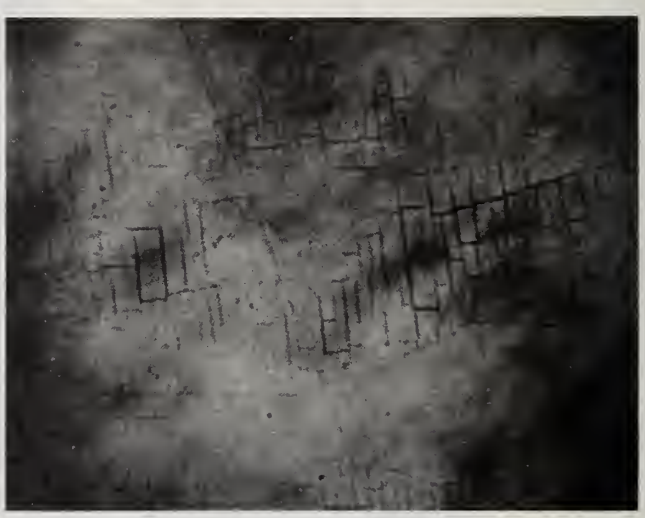

Figure 9. Uncoated NaCl (200x).

COMMENTS ON PAPER BY HAYDEN AND LIBERMAN

In response to a question concerning the character of the surfaces of the NaCl samples, the speaker commented that the samples were free of haze, and had excellent surface properties. The coated and uncoated surfaces were treated identically except for the coating process. The observed damage on coated elements always occurred at the uncoated surface, whether it was the exit surface or the entrance surface. This may be a standing wave effect. The coatings were suspected to be CaF_2, but the supplier had not identified the coating material. The session chairperson entered a plea for coating vendors to identify the materials of their coatings, to avoid the necessity of destructive analysis by the user.

2.6 LASER-INDUCED DAMAGE OF MIRROR AND WINDOW MATERIALS AT 10.6 μm

R. Gibbs and R.M. Wood
The General Electric Co. Ltd.
Hirst Research Centre
Wembley HA9 7PP, England

Pulsed laser-induced damage thresholds (CO_2 TEA laser, 60 ns FWHH) and 10.6 μm absorption measurements have been made on a wide variety of mirror and window materials. The effects due to different methods of substrate preparation and coating of metal mirrors have been studied, and as a result, mirrors of higher damage threshold have been manufactured. Front surface damage thresholds of uncoated windows have been measured and correlated with microscopically visible surface features. Improvement has been achieved by ion-beam etching of single-crystal materials. The damage threshold of dielectric coatings, both reflecting and anti-reflecting, has been found to be limited by microscopically visible coating defects.

The absorption and damage measurement techniques will be discussed together with the details of the power and energy measurement programme. The measured results will be presented, and in the case of metal mirrors, compared with computed values of damage threshold derived from the measured values of absorptivity.

Key words: Dielectric coatings; infrared laser windows; laser heating of metal surfaces; laser mirrors; pulsed CO_2 laser damage; surface damage; 10.6 μm absorption; 10.6 μm optical components.

1. Introduction

A programme of research was commenced in 1974 under DCVD sponsorship at the Hirst Research Centre of The General Electric Company, with the aid of studying 10.6 μm laser-induced damage and distortion in optical components for use with a variety of laser systems. This paper reports work on pulsed, 60 ns, laser damage threshold measurements, absorption measurements, surface improvement, and accurate power energy measurement.

The components studied include a range of window materials, metal mirrors, and dielectric coated substrates.

2. Damage Threshold Measurement

A sealed-off CO_2 TEA laser [1][1] was used in the damage studies. The advantage of using this type of laser is its pulse to pulse repeatability. The output of this laser consists of 50 mJ pulses in a 60 ns FWHH main pulse and a 0.7 μs tail. The tail, although of low power, contains two-thirds of the pulse energy (see fig. 1). The spatial intensity distribution of the pulsed laser beam is Gaussian in the TEM_{00} mode, with a 1/e diameter of 4.5 mm. More recent development of this laser, developed by RSRE, Baldock and Marconi-Elliott Avionic Systems Ltd., Borehamwood, has concentrated on increasing the peak power/unit volume in order to make an even more compact device and to simultaneously increase the percentage of energy in the main pulse.

The damage measurement apparatus is shown diagrammatically in figure 2. The beam is focused to 100 μm, 1/e intensity diameter, using a 64 mm focal length germanium meniscus lens. The beam power may be varied by means of thin polythene attenuators. The power is monitored using a Rofin model 7443 germanium photon drag monitor in conjunction with a Tektronix 585A oscilloscope with type 82 plug-in.

Damage sites are observed in situ under ×100 magnification and the sample is scanned in the focal plane of the lens. This methodolgy has been built up in order to study the effects of surface defects and is analogous to the raster-scan method previously used at HRC to examine surface variation of 1.06 μm damage thresholds [2].

3. Beam Characterisation

Calibration of the photon-drag monitor was obtained by comparison with a black-painted disc calorimeter. The black paint (3M black suede) has been shown to have a spectrally flat absorption out to 10.6 μm by measurement of diffuse reflectivity at the National Physical Laboratory [3]. The calorimeter was calibrated against an NPL secondary standard in the visible (0.69 μm) and near I-R (1.06 μm).

[1]Figures in brackets indicate the literature references at the end of this paper.

Beam profiles were measured by measuring the transmission through a set of calibrated circular apertures. For a Gaussian beam profile, log (1-transmission) is proportional to the diameter squared. The optical distortion produced by the attenuators was shown to be negligible by measuring the focused beam profile with and without the attenuators.

4. Absorption Measurement

A calorimetric absorption measurement has been developed which can measure a total absorptivity less than 10^{-4} in either windows or mirrors at normal incidence.

The apparatus (fig. 3) consists of a matched pair of copper blocks with thermistors embedded in them, to one of which is clamped the sample. The blocks are mounted in a thermally insulated environment such that cooling times are in excess of twenty minutes. A 10W CO_2 laser is used to irradiate the sample, whose temperature rise is displayed on a pen recorder, via a dc bridge circuit and voltage amplifier. A small correction for cooling [5] is applied (fig. 4). Calibration was obtained by substituting a black-painted brass disc, whose absorptivity is taken to be 98% [3], for the test sample. By deliberately using a large sample holder, problems commonly encountered with thermal isolation, the contacting of thermocouples to samples and thermal stability are avoided while achieving enough sensitivity to accurately measure the smallest absorption so far encountered.

5. Damage to Metal Mirrors

The damage thresholds and absorptivities of a wide range of metal mirrors have been measured (table 1). Visible surface features which correlated with lowered damage thresholds were observed on all polished surfaces, but not on diamond-turned surfaces. The latter were also found to have low absorptivity compared with the conventionally polished surfaces.

Correlation between damage thresholds and absorptivity and thermal properties has been found. Theory [4] predicts that the damage threshold intensity, I_D, is proportional to

$$(Tm - To)\ \frac{\sqrt{k\rho s}}{\alpha}$$

where Tm = melting temperature
To = ambient temperature
k = thermal conductivity
ρ = density
s = specific heat
α = 10.6 μm absorptivity

For a mirror with a thin gold coating, α is that of gold, k, ρ and s refer to the substrate. Tm refers to the material with the lower melting point. If only the 'clear' areas of mirrors are considered, then the damage threshold is related to the absorptivity of a comparable but scratch-free surface. This may be taken as a diamond-turned surface in this context, as diamond-turned mirrors have the same damage threshold as clear areas of polished mirrors, but with no site-to-site variation (see table 1).

Good correlation is found between experimental damage thresholds and theory for a selection of mirrors including plated ('hard') gold surfaces (fig. 5). Evaporated gold-coated mirrors have a lower threshold than predicted, and this is thought to be related to the poor adhesion of the films.

Simplified theory predicts that the damage threshold, T_D, is related to pulse length, τ, by the relationship

$$I_D \propto \frac{1}{\sqrt{\tau}}$$

and this may be used to compare results measured with different pulse length lasers.

6. Damage to Window Materials

Front surface damage thresholds have been measured for a wide variety of window materials. These are summarized in table 2.

By using the scanning technique and simultaneously observing the focal area for signs of damage, it was found that in all materials tested, lowered damage thresholds could be correlated with visible surface defects, i.e., polishing scratches, pits, and absorbing surface inclusions. With practice and patience, it was found to be possible to pre-select defect-free areas on a given surface, whose damage threshold represents the highest measured on that surface. The scanning technique allowed the lowest defect-limited threshold to be measured accurately, ensuring that damage occurred only at the centre of the focused spot, i.e., at the measured power density.

It was observed that not all defects affected the damage threshold equally, and that those which had the greatest effect were the sharpest discontinuities. Ion beam etching techniques were used in an attempt to smooth out such discontinuities, and met with some success in single crystals (fig. 6) raising the defect-limited damage threshold of the surface up towards its intrinsic value.

7. Damage to Coatings

Damage thresholds of multilayer mirror coatings and anti-reflection coatings on germanium have been measured (table 3). Results are presented on representative coatings from two suppliers.

The dominant effect in mirror coatings is due to 1-10 μm coating defects which damage at a much lower power density than the rest of the coatings (fig. 7). The sample (A) coatings had a high defect density and it was difficult to find a defect-free area to irradiate with the 100 μm spot used. The sample (B) coating had a much lower defect density.

Defects in single-layer AR coatings have much less effect on the damage threshold than those in mirror coatings, and the effect is of the same order produced by normal polishing imperfections in substrate finish.

8. Conclusions

Surface variations in damage threshold have been shown to correlate with microscopically visible features, of roughly 1-10 μm dimension. These features are typically polishing scratches in windows and metal mirrors, and absorbing defects in dielectric coatings. The effect of coating defects has been found to be most catastrophic in highly-reflecting mirrors, lowering the damage threshold by a factor of ten or more, whereas in $\lambda/4$ layers the threshold lowering factor is less than two.

Scratch effects in copper mirrors have been eliminated by the adoption of diamond-turning instead of conventional polishing techniques and hence good correlation has been found between measured damage thresholds and theory based on surface melting.

Plated god surfaces have been found to have significantly higher damage thresholds than evaporated gold coatings on identical substrates, as well as having higher reflectivity and greater durability.

9. Acknowledgment

This work has been carried out with the support of Procurement Executive, Ministry of Defence, sponsored by DCVD.

10. References

[1] Stark, D.S., Cross, P.H. and Foster, H., IEEE J.Q. Elec., QE.11(9), 774 (1975).

[2] Wood, R.M., Taylor, R.T., and Rouse, R.L., Optics & Laser Technology, 105 (June 1975).

[3] Edwards, J.G., Private Communication (1976).

[4] Ready, J.F., J. App. Phys., 36(2), 462 (1965).

[5] Hass, M., Davisson, J.W., Rosenstock, H.B., and Babiskin, J. App. Opt., 14(5), 1128 (1975).

11. Tables & Figures

Table 1. Damage thresholds - metal mirrors.

Description	α	Damage threshold MW mm^{-2}	
		worst	scratch-free
evaporated Au/polished Ni/Cu	1.8	0.7	1.2
plated Au/polished Ni/Cu	1.4	2.0	2.7
plated Au/polished Ni/Cu	3.0	0.7	1.0
diamond turned (d-t) Au	1.2	-	5.5
d-t thick plated Au/Cu	1.0	-	7.0
evaporated Au/d-t Cu	1.3	-	2.0
plated Au/d-t Cu	1.0	-	8.0
polished Cu	1.1	6.0	9.0
d-t Cu	0.8	-	9.0

Table 2. Front surface damage thresholds - windows

Material	β cm^{-1}	Damage threshold	
		worst	clear area
Ge	0.032	0.7	4.0
etched Ge	-	3.0	5.0
GaAs	0.011	1.6	3.2
etched GaAs	0.011	2.5	4.0
CdTe	-	1.0	1.5
CVD ZnSe (Raytheon)	0.0049	3.0	7.5
CVD ZnSe (Raytheon)	0.0049	2.8	6.2
CVD ZnSe (UK)	-	0.8	4.5
CVD ZnS (UK)	0.35	0.6	6
KCl (Harshaw)	-	5.0	12
NaCl (Harshaw)	-	15	>17

Table 3. Damage thresholds - dielectric coatings

Description		Damage threshold MW mm^{-2}	
		defect	clear area
Single-layer AR			
ZnS on Si	(A)	0.4	1.2
ZnS on Ge	(B)	1.4	2.8
ZnS on Ge	(B)	2.8	4.0
ThF_4 on ZnSe	(B)	3.0	>6
R = 85%			
ZnS/ThF_4 on Ge	(B)	5	10
R ≈ 100%			
on Si	(A)	<0.2	1.2
ThF_4/ZnS on fused SiO_2	(B)	0.8	3.8

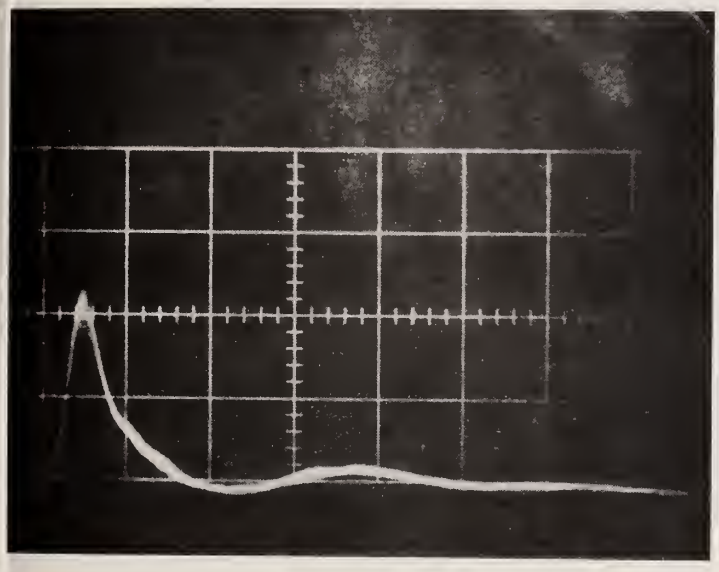

Figure 1. TEA laser pulse (timescale 100 ns/1 div).

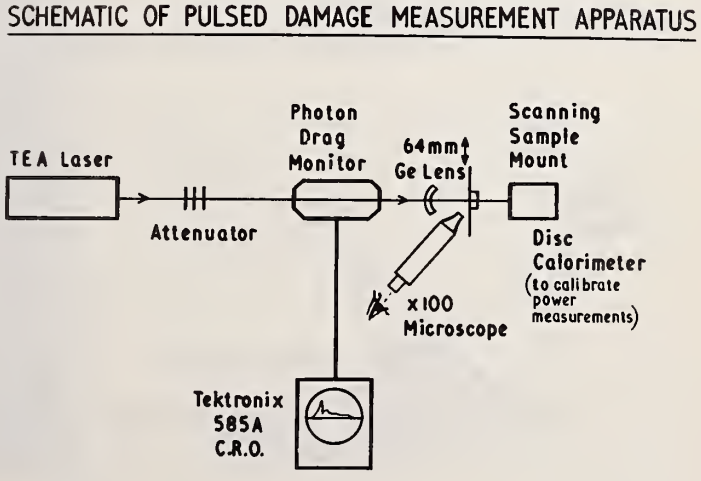

Figure 2. Schematic of pulsed damage measurement apparatus.

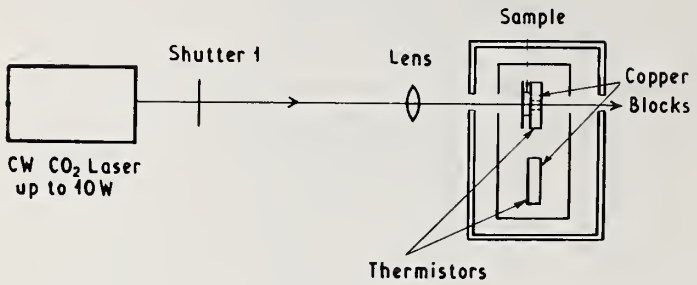

Figure 3. Schematic of absorption apparatus.

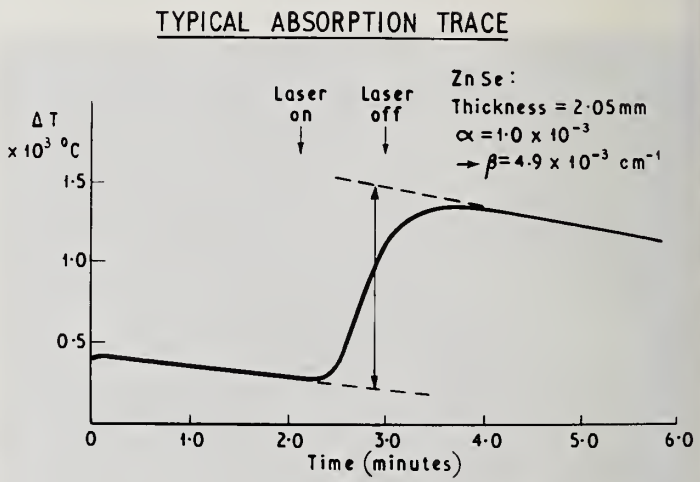

Figure 4. Typical absorption trace.

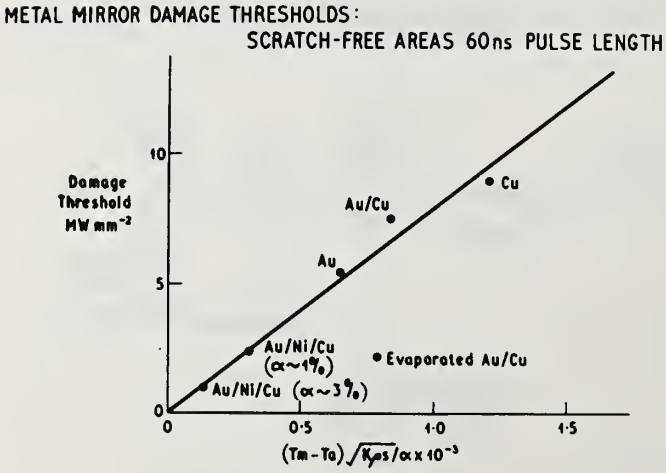

Figure 5. Metal mirror damage thresholds (scratch free area).

(a) Ge

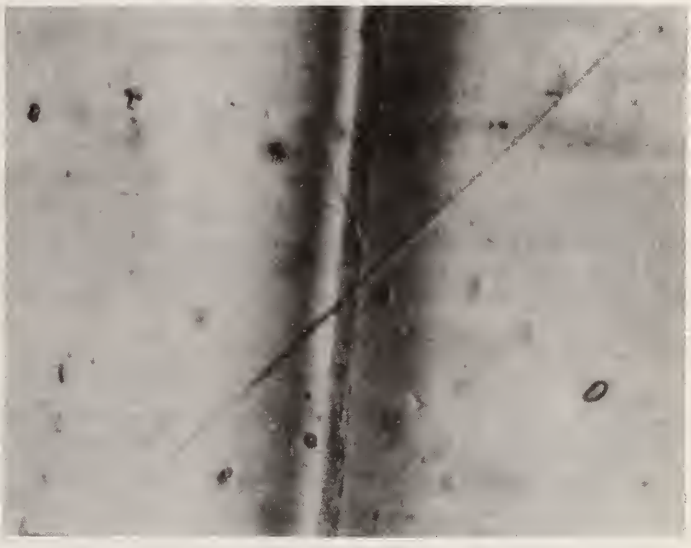

(b) GaAs

Figure 6. Surface improvements by ion-beam etching (left-hand side unetched, right-hand side etched).

Figure 7. Damage at defects on multilayer dielectric coatings due to a single pulse.

COMMENTS ON PAPER BY GIBBS AND WOOD

The speaker commented on the effect of material removal by ion-beam etching. He indicated that up to 1 μm of removal improved the optical quality of the surface, but removal of 1 - 10 μm increased the scattering at the surface. In ZnSe the damage threshold was increased by removal of up to 1 μm of material, but further removal lowered the damage threshold. In germanium and CdTe, however, the damage threshold continued to improve with continued material removal up to 10 μm of removed material. This may be due to the removal of deeply imbedded polishing material.

It was noted that the observed surface damage thresholds were well below reported bulk values. The speaker commented that due to the thin samples used (about 5 mm), bulk damage thresholds were difficult to measure.

The speaker indicated that the ZnO impurity seen in ZnSe was in the form of subsurface microcrystallites. Identification was by x-ray fluorescence spectroscopy.

2.7 ABSORPTANCE OF DIELECTRIC ENHANCED MIRRORS AT 5.3 μm*

P. Kraatz, J. R. Buckmelter, and S. J. Holmes
Northrop Corporation
Northrop Research and Technology Center
Hawthorne, California 90250

The absorptance of a variety of dielectric-enhanced mirrors has been measured in the 5.3 μm region using CO laser calorimetry. The samples comprise nineteen designs fabricated from ten dielectric material combinations deposited on thirteen basic mirror types (i.e., four substrate materials with a total of six metallic coating combinations). Thirty-two samples were fabricated by six vendors without duplications of any complete mirror design among any two (or more) vendors.

Results are grouped according to dielectric material combinations and design. Effects of substrate material selection and metallic coatings (if any) are discussed. The precision (i.e., standard deviation) of all absorptance measurements is presented. Accuracy, relative to (1-R) obtained from standard reflectometer measurements, is evaluated for selected mirrors.

Key words: Absorptance; CO laser calorimetry; CO laser mirrors; dielectric-enhanced mirrors; infrared laser mirrors; metal mirrors; reflectance.

1. Introduction

A wide array of designs and materials is available for dielectric enhancement of metal mirrors used in lasers operating in the mid-infrared. In order to quantitatively evaluate the absorptance and reflectance of a number of such designs for the CO laser wavelength region centered at ~5.3 μm, a systematic investigation has been carried out using CO laser calorimetry as the primary tool. Results are reported here.

2. Experimental

In order to make accurate and reproducible measurements of the absorption of multilayer dielectric mirrors, it is necessary to measure a quantity which is proportional to the absorption. On this basis a calorimetric technique is chosen in which one measures the temperature rise of the coated mirror subjected to illumination from a laser.

The system configuration for measurement of absorptance in partial or total reflectors is shown in figure 1. In this mode of operation, the power reflected from the sample S is monitored by the cone R, referenced to a cone r_1 having identical thermal mass. The power absorbed by the sample is calculated from the sample temperature rise monitored by the thermocouple A referenced to a thermocouple r_2 affixed to the reference cone r_3. The transmitted power is monitored by a cone T, referenced to the cone r_3 of identical thermal mass. The power output of the laser is monitored by a power meter and calibrated beam splitter. The calorimeter cones R, T, r_1, and r_3 are of identical design, thermal mass (within 1%) and mounting within the chamber so that their increases in temperature are comparable for a given energy input; heating and cooling behavior is also very similar, precluding difficulties in interpretation of the resultant curves.

The raw data obtained from the system thus comprise the incident power P_I, the power reflected from the sample surface P_R, the power absorbed by the sample P_A, and the power transmitted through the sample P_T. The data can be checked for self-consistency using the relation,

$$P_I = P_R + P_A + P_T \quad (1)$$

* Work supported by AFSWC Contract No. F29650-75-M-D707.

provided that P_R, P_A and P_T are of comparable magnitude. If $P_R \gg P_A$, P_T as in mirrors reflecting >99% of the incident power, $P_I = P_R$ within the precision of power measurements using a calibrated aluminum cone or a ballistic thermopile (typically ±5%). The fractional power absorbed (absorptance) of an opaque reflector ($P_T = 0$) with negligible scatter is then

$$A = P_A/(P_A + P_R) \quad , \tag{2}$$

and the reflectance is

$$R = P_R/(P_A + P_R) \quad . \tag{3}$$

Hence, results can be verified by comparison with values of R and (1 - R) obtained using a reflectometer [1][1].

All samples were measured in this system with the vacuum in the chamber maintained between 40 and 125 millitorr, using the multiline output of the longitudinal discharge CO cw laser. A gas mix comprising helium, oxygen, carbon monoxide, and nitrogen was used to produce an output spectrum centered at a wavelength of ~5.3 μm with the shortest wavelength lines at ~5.05 μm and the longest at ~5.7 μm. The beam diameter is approximately 8 mm, limited by a variable intracavity iris; total power is ~7W.

The beam is incident upon the mirror sample at an angle of approximately 10° ; the distance from the mirror surface to the aluminum calorimeter cone monitoring reflected power is ~19 cm. A variable diameter iris is placed between the mirror surface and the calorimeter cone to limit pickup of spurious multiply reflected or scattered radiation. With this iris set at a diameter of 10 mm (to avoid clipping the beam) the acceptance cone seen by the reflected power monitor has an included angle of ~3° .

Alignment of the sample and reflected power cone is achieved first with a Helium-Neon laser coaxial with the CO laser and calorimeter chamber. This alignment is subsequently checked with the CO laser beam and a fluorescent screen before pumping down the sample chamber, since alignment of reflecting optics is quite critical to absorptance measurements.

Absorptance and reflectance of a mirror is calculated from eqs. (2) and (3) using the temperature rise of the sample and calorimeter cone as raw data, where the mass and heat capacity of each is known. The "peak method" as adapted by Saito, et al., [1] is used to determine the sample temperature rise, except as noted. The peak method previously described by Kraatz and Mendoza [2] for measuring transmitted power in window absorption measurements is employed in the determination of reflected power from the temperature-time trace generated by the monitor cone. The heat capacity of aluminum (calorimeter cone) and molybdenum (sample substrates) were taken as 0.215 cal/g°K and 0.0597 cal/g°K, respectively, from the AIP Handbook [3] in the present measurements.

3. Results and Discussion

Results of the study are detailed in figures 2-7, grouped according to coating materials and design. All absorptance and reflectance values presented in the figures were obtained calorimetrically through eqs. (2) and (3). A total of thirty-two mirror samples from six vendors, and one diamond turned single crystal CaF_2 substrate obtained from T. Saito of Lawrence Livermore Laboratories, were measured in the study. The six vendors were OCLI, Perkin-Elmer, CVI, Spectrum Systems, Coherent Radiation Laboratories, and Northrop.

Results for the ThF_4/ZnS combination are listed in figure 2. It is clear that optimum reflectivity is obtained with three or four pairs of these materials and little improvement is to be expected with additional layers. Addition of a half-wave thickness of ThF_4 (presumably to reduce electric field strength and increase damage threshold) does not appreciably affect absorptance. The effect of addition of a quarter wave thickness of ZnS for the same purpose cannot be established unequivocally from the present data. Substitution of PbF_2 for ThF_4 results in very low reflectance, since the difference in refractive indices is too low ($n_{PbF_2} \cong 1.73$, $n_{ZnS} \cong 2.21$) for effective enhancement with a minimum number of pairs.

---

1. Figures in brackets indicate the literature references at the end of this paper.

Figure 3 lists results obtained with another popular material combination for this wavelength region (ThF_4/ZnSe). Inspection of the first five entries in the figure show an increase of 0.0004 in R or a decrease of ~30% in absorption with addition of one pair. However, the use of seven pairs as an all-dielectric stack on molybdenum (with poor base reflectivity) results in relatively low total reflectance.

Effects upon absorption of addition of half waves of ThF_4 or quarter-waves of ZnSe to the dielectric stack are again unclear from the present data. Substitution of CaF_2 for ThF_4 in the design appears to result in decreased reflectance, as indicated by the last two entries in the figure. Similarly, reflectance of CaF_2 or CerVit mirrors is less than that of molybdenum mirrors with identical coating designs.

In summary, it appears that this material combination is most successful in terms of low absorptance and high reflectance, with three samples from three different vendors having absorptances of less than 1×10^{-3} (i.e., reflectances greater than 0.9990). This performance is unequalled by any other material combination.

Designs employing SiO combined with Si or Ge are listed in figure 4. The first four entries and last entry in the figure illustrate the importance of careful control of the thickness of the chromium layer used to promote adherence of the SiO to the metallic layer. Although this Cr layer has a nominal thickness of only 50 Å or less, it is apparent that reflectance has been impaired by it, especially in the last entry in the figure. Comparing this result with the identical design deposited on a silver layer shows the effect of the poor base reflectivity of the Cr layer. On the other hand, no real conclusion can be drawn regarding the effect of micromachined copper substrates upon absorption in mirrors where other materials and the design is unchanged. One example exhibits an appreciable increase in absorptance, while the other shows no significant difference.

With regard to the number of pairs required for optimum reflectance, it appears that one pair is not adequate and three pairs may not be at the saturation point. Substitution of Ge for Si as the high index layer apparently does not alter this conclusion.

Results for designs employing (Al_2O_3/Si) listed in figure 5 indicate that this is not a particularly successful combination. The three-pair designs on copper and molybdenum should yield higher reflectance values if problems with deposition parameters have not occurred. High absorptance in the sapphire layers, due to entrapped water or non-stoichiometry, or low refractive index of silicon, due to excessive defect concentrations, could explain these results.

Results for various combinations of materials with germanium are listed in figure 6. Comparing the second and third designs indicates that a saturation of the enhancement effect occurs at about six pairs, bearing in mind that the base reflectivity of the silver used in the second design is higher than that of the Mo substrate. Poor consistency of results is indicated for both the first and third designs, wherein two samples were fabricated by the same vendor (the vendors of the first and third designs are different). The most obvious explanation for these inconsistencies is poor control of optical thickness of the various layers, leading to an offset from the design wavelength. Addition of a half wave ThF_4 layer for greater resistance to pulsed laser damage, as shown in the last two entries in the figure, does not appear to affect absorptance appreciably. It is also interesting to note that the choice of substrate (CaF_2 or Mo) has little effect upon absorptance.

Results of absorptance measurements on uncoated CaF_2 substrates finished by micromachining or polishing to a low scatter finish are listed in figure 7. Unfortunately, the comparison is not as meaningful as it might be, since the bulk absorptance of the micromachined sample is not known. The temperature time trace from the calorimeter run on this sample indicated heavy direct scatter to the sensing thermocouple, probably as a result of the surface finish. The beam was offset from the sample center to avoid the worst areas for this.

An indication of the overall accuracy of the calorimetric results, relative to standard reflectometer measurements, is provided by the data of figure 8. The reflectance of four mirrors measured in the calorimetric study was subsequently measured in a standard reflectometer at the Michelson Laboratory, NWC, China Lake, California, at 5.2 μm, 5.4 μm, and 5.6 μm. Since the center of the CO laser spectrum employed in calorimetry is between 5.2 μm and 5.3 μm, calorimetric results are correlated with reflectrometer data taken at 5.2 μm. With the exception of the second entry in the figure, the results are encouraging. A similar comparison of absorptance (A) with ($1-R_R$) by Saito et al., [1] at 10.6 μm showed agreement within 18 - 20%, with the calorimetric results indicating the

lower value for absorptance as in the present work. With respect to reflectance, the results are quite encouraging. Three of the four calorimetric reflectance values are within 0.0004 or less of the reflectometer values, while the fourth deviates by 0.002.

Reasons for these discrepancies are difficult to determine. Possible problem areas include the bandwidth of the laser and reflectometer spectra, the acceptance cone of the reflectometer and calorimeter, and the reflective bandwidth and homogeneity of the coated sample.

4. References

[1] Saito, T. T., Callender, A. B., and Simmons, L. B., "Calorimeter to Measure the 10.6 μm Absorption of Metal Substrate Mirrors," Appl. Opt., Vol. 14, p. 721, 1975.

[2] Kraatz, P. and Mendoza, P. J., "CO Laser Calorimetry for Surface and Coating Evaluation," Proc. Fourth Conf. on Infrared Laser Winder Materials, p. 77, 1975.

[3] Gray, D. E., Ed. American Institute of Physics Handbook, 3rd. Ed., McGraw-Hill, N. Y.

5. Figures

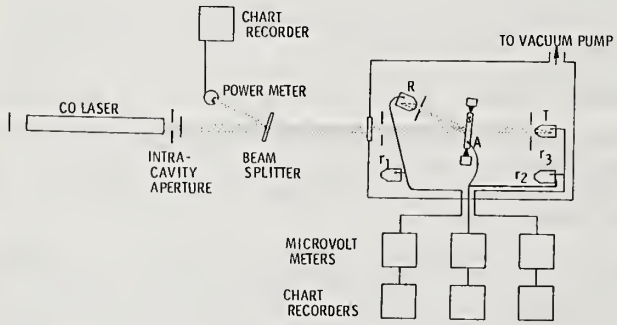

Figure 1. Schematic of calorimeter measurement system for partially transmitting/reflecting optics.

SUBSTRATE	COATING MATERIALS & DESIGN	A	R
Mo	$(ThF_4/ZnS)^2 + ZnS$	$3.191 \pm 0.144 \times 10^{-3}$	0.9968
Mo	$Ag + (ThF_4/ZnS)^3$	$1.740 \pm 0.048 \times 10^{-3}$	0.9983
CerVit	$Ag + (ThF_4/ZnS)^3$	$1.840 \pm 0.124 \times 10^{-3}$	0.9982
CaF_2	$Cr-Au+(ThF_4/ZnS)^4 + ThF_4$	$5.954 \pm 0.263 \times 10^{-3}$	0.9940
Mo	$Cr-Au+(ThF_4/ZnS)^4 + ThF_4$	$1.302 \pm 0.046 \times 10^{-3}$	0.9987
Mo	$(PbF_2/ZnS)^2 + ZnS$	$2.520 \pm 0.156 \times 10^{-2}$	0.9748

Figure 2. Dielectric enhancement designs utilizing (ThF_4/ZnS) and (PbF_2/ZnS).

SUBSTRATE	COATING MATERIALS & DESIGN	A	R
Mo	$Ag + (ThF_4/ZnSe)^3$	$9.620 + 0.427 \times 10^{-4}$	0.9990
CerVit	$Ag + (ThF_4/ZnSe)^3$	$1.459 + 0.044 \times 10^{-4}$	0.9985
Mo	$Cr\text{-}Au + (ThF_4/ZnSe)^3 + ThF_4$	$6.988 + 0.284 \times 10^{-4}$	0.9993
CaF_2	$Cr\text{-}Au + (ThF_4/ZnSe)^3 + ThF_4$	$1.489 + 0.103 \times 10^{-3}$	0.9985
Mo	$Ag + (ThF_4/ZnSe)^4$	$6.160 + 0.256 \times 10^{-4}$	0.9994
Mo	$(ThF_4/ZnSe)^7 + ZnSe$	$1.237 + 0.036 \times 10^{-3}$	0.9988
CaF_2	$(ThF_4/ZnSe)^1 + (CaF_2/ZnSe)^2 + ThF_4$	$2.191 + 0.102 \times 10^{-3}$	0.9978
Mo	$(ThF_4/ZnSe)^1 + (CaF_2/ZnSe)^2 + ThF_4$	$2.006 + 0.087 \times 10^{-3}$	0.9980

Figure 3. Dielectric enhancement designs utilizing (ThF_4/ZnSe) and CaF_2/ZnSe).

SUBSTRATE	COATING MATERIALS & DESIGN	A	R
Cu[1]	$Cr + Ag + Cr + (SiO/Si)^1$	$(9.619 \pm 0.121) \times 10^{-3}$	0.9904
Mo	$Cr + Ag + Cr + (SiO/Si)^1$	$(9.752 \pm 0.309) \times 10^{-3}$	0.9902
Cu[1]	$Cr + Au + Cr + (SiO/Si)^1$	$(1.526 \pm 0.0455) \times 10^{-2}$	0.9847
Mo	$Cr + Au + Cr + (SiO/Si)^1$	$(5.293 \pm 0.107) \times 10^{-3}$	0.9947
Mo	$Ag + (SiO/Si)^3$	$(1.391 \pm 0.066) \times 10^{-3}$	0.9986
		$(1.966 \pm 0.059) \times 10^{-3}$	0.9980
Mo	$Ag + (SiO/Ge)^3$	$(1.395 \pm 0.042) \times 10^{-3}$	0.9986
Mo	$Cr + (SiO/Si)^3$	$(8.811 \pm 0.325) \times 10^{-3}$	0.9912

1. MICROMACHINED COPPER SUBSTRATE FURNISHED BY T. SAITO AND LAWRENCE LIVERMORE.

Figure 4. Dielectric enhancement designs utilizing SiO in combination with Si and Ge.

SUBSTRATE	COATING MATERIALS & DESIGN	A	R
Cu[1]	$Cr + (Al_2O_3/Si)^3$	$2.000 \pm 0.0525 \times 10^{-2}$	0.9800
Mo	$Cr + (Al_2O_3/Si)^3$	$2.405 \pm 0.102 \times 10^{-2}$	0.9760
Mo	$(Al_2O_3/Si)^5 + Si$	$5.504 \pm 0.175 \times 10^{-3}$	0.9945

1. MICROMACHINED COPPER SUBSTRATE FURNISHED BY T. SAITO AND LAWRENCE LIVERMORE.

Figure 5. Dielectric enhancement designs utilizing Al_2O_3 and Si.

SUBSTRATE	COATING MATERIALS & DESIGN	A	R
Mo	$(ZnS/Ge)^2 + Ge$	$(9.753 \pm 0.453) \times 10^{-2}$	0.9025
		$(5.773 \pm 0.158) \times 10^{-3}$	0.9942
Mo	$Ag + (ZnS/Ge)^4$	$(9.550 \pm 0.500) \times 10^{-4}$	0.9990
Mo	$(ZnS/Ge)^6$	$(6.951 \pm 0.358) \times 10^{-4}$	0.9993
		$(4.948 \pm 0.121) \times 10^{-3}$	0.9950
CaF_2	$Cr\text{-}Au + (ThF_4/Ge)^3 + ThF_4$	$(1.690 \pm 0.053) \times 10^{-3}$	0.9983
Mo	$Cr\text{-}Au + (ThF_4/Ge)^3 + ThF_4$	$(1.374 \pm 0.066) \times 10^{-3}$	0.9986

Figure 6. Dielectric enhancement designs utilizing germanium in combination with various materials.

SUBSTRATE	COATING MATERIALS & DESIGN	A
CaF_2[1]	UNCOATED (MICROMACHINED)	$(4.358 \pm 0.203) \times 10^{-4}$
CaF_2[2]	UNCOATED (NRTC POLISH)	$(4.050 \pm 0.260) \times 10^{-4}$

1. MICROMACHINED SINGLE CRYSTAL CaF_2 SUBSTRATE FURNISHED BY T. SAITO AND LAWRENCE LIVERMORE. $L = 0.947$ cm $\beta_T = 4.60 \times 10^{-4}$ cm^{-1} (SURFACE AND BULK).

2. SINGLE CRYSTAL CaF_2 SUBSTRATE POLISHED AT NRTC. $L = 0.715$ cm $\beta_T = 5.664 \times 10^{-4}$ cm^{-1} (SURFACE AND BULK). $\beta = 3.0 \times 10^{-4}$ cm^{-1} (BULK), $\beta_S = 9.5 \times 10^{-5}$ PER SURFACE.

Figure 7. Absorptance results for uncoated single crystal CaF_2 substrates.

MIRROR DESIGN	CALORIMETER ($\lambda \cong 5.3$ μm)		REFLECTOMETER[a] ($\lambda \cong 5.2$ μm)		ΔA[b] (%)	ΔR[c] (%)
	A	R_C	R_R	$(1-R_R)$		
Mo + Ag + $(ThF_4/ZnSe)^4$	6.16×10^{-4}	0.9994	0.9991	9.0×10^{-4}	-31.5	+.03
Mo + Ag + $(SiO/Si)^3$	1.39×10^{-3}	0.9986	0.9970	3.0×10^{-3}	-53.7	+.16
Mo + Ag + $(SiO/Ge)^3$	1.40×10^{-3}	0.9986	0.9982	1.8×10^{-3}	-22.2	+.04
Mo + Ag + $(ZnS/Ge)^4$	9.55×10^{-4}	0.9990	0.9991	9.0×10^{-4}	+ 6.1	-.01

a. REFLECTOMETER MEASUREMENTS PERFORMED AT MICHELSON LABORATORY, NWC, CHINA LAKE, CALIFORNIA.

b. $\Delta A = \frac{A - (1-R_R)}{(1-R_R)} \times 100$

c. $\Delta R = \frac{R_C - R_R}{R_R} \times 100$

Figure 8. Comparison of measurement techniques.

COMMENTS ON PAPER BY KRAATZ, BUCKMELTER, AND HOLMES

No discussion on this paper.

2.8 OPTICAL PROPERTIES OF MIRRORS PREPARED BY ULTRACLEAN dc SPUTTER DEPOSITION

P. A. Temple, D. K. Burge, and J. M. Bennett
Michelson Laboratories, Naval Weapons Center
China Lake, California 93555

Sputter deposition is a method for producing mirror surfaces. However, the sputtering gas is generally incorporated in the metal film. This investigation was undertaken to determine the amount of gas trapped and the effect this gas had on film optical properties. Thin film mirrors of aluminum, silver, copper, and gold were prepared by dc sputter deposition under ultraclean conditions using argon or xenon as the sputtering gas. The sputtering gas entrapment was measured by a flash desorption technique. Film reflectance was correlated with preparation conditions and gas entrapment. In general, the film reflectance was reduced by the presence of sputtering gas. The gas trapped was a function of the metal being sputtered, the sputtering gas type, and the sputtering gas pressure. For example, the gas content of silver films could be varied over nearly two orders of magnitude. In some cases, films with reflectances as high as the best UHV evaporated films were prepared.

Key words: Aluminum; copper; flash desorption spectroscopy; gold; reflectance; silver; sputter deposition.

Introduction

Although it is an accepted method for preparing thin films, particularly in the microelectronics industry, little has been done with sputtering in making high quality optical films for mirror coatings. We wish to report on the method of preparation and on the properties of high quality optical thin films for copper, gold, silver, and aluminum deposited by dc diode sputtering under ultraclean conditions. Films were prepared using either xenon or argon as a sputter gas. There is evidence that a fairly high atomic percentage of the sputtering gas is trapped in the films prepared by dc diode sputtering [1][1]. Therefore, in this report an effort will be made to correlate film gas content with film reflectance. The sputtering gas content was determined by a flash desorption technique.

Description of Sputtering System

The dc sputtering source (fig. 1) consisted of a dc diode sputtering gun especially designed for use in an UHV system by Sputtered Films, Inc. [2]. This gun used 12.7 cm diameter annular ring targets surrounding an insulated center anode and employing a magnetic field to increase the path length of the sputter gas ions and confine them to the target region. The sputter target was water cooled. A substrate holder designed to expose any one of five sets of substrates was positioned 15 cm above the upward-looking sputter gun. Each set of substrates consisted of one 3.86 cm diameter and two 0.95 cm diameter polished fused quartz substrates. The larger substrate was used for reflectance and scattering measurements while the smaller substrates were used for electron microscopy. A Sloan Technology Corporation Model DTM-4 deposition rate monitor [3] was located adjacent to the rotatable substrate holder and allowed for continuous monitoring of film thickness. A shutter was placed just above the sputter source and made it possible to adjust the plasma current prior to actual deposition.

This apparatus was placed in an all-stainless-steel vacuum system pumped with a 500 ℓ/s Varian VacIon pump and was capable of a base pressure in the 10^{-11} Torr range. A residual gas analyzer (RGA) was attached to the chamber, so that the residual gas in the system could be monitored prior to admitting the sputtering gas. Care was taken to minimize the amount of water vapor and hydrogen present in the system by initially rough-pumping the system using a Gast Manufacturing Corp. oilless reciprocating pump [4] followed by two backfillings with dry nitrogen (boiloff from a liquid nitrogen tank) and pumpings. The system was then baked for two to four hours while being pumped sequentially by three Varian VacSorb pumps. During this initial baking and pumping, no hot filaments were present in the system, and the ion pump was not turned on. It is well known that hot tungsten causes the formation of carbon monoxide from hydrocarbons and water, with the subsequent release of hydrogen [5].

The entire system was further baked, with the ion pump on, for at least 24 hours at approximately 200°C and allowed to cool for another 24 hours. Prior to the admission of the sputtering gas, titanium was evaporated from a sublimation gun to produce a fresh gettering surface. Since the ion pump could not be operated in the pressure range required for sputter deposition, a liquid nitrogen trap was used instead. It was cooled for one-half hour prior to turning off the ion pump. With the ion pump shut off, but the liquid nitrogen trap operating, the chamber pressure would rise very slowly to about

1. Figures in brackets indicate the literature references at the end of this paper.

1×10^{-9} Torr by the end of a 30-minute period. Generally, sputter deposition required less than one-half hour, and if begun immediately after the ion pump was turned off, it was assumed that the residual gas pressure remained below 1×10^{-9} Torr. RGA analysis showed that this remaining gas consisted mainly of helium, hydrogen, and argon while the active gases were unchanged from the pump-on amounts and evidently were either being gettered on the fresh titanium surface or condensed in the cold trap. Previous experience with the growth of silver films under various evaporation conditions indicated the importance of having low residual amounts of oxygen and water vapor present during deposition [6]. Since some of the films produced during this investigation were grown over an extended period and had exceptionally good optical properties, the quantities of active gases were apparently being kept at very low levels.

Research-grade argon and xenon (impurities less than 5 ppm for argon and 50 ppm for xenon) were used for the sputtering and were admitted through a Varian leak valve. The minimum pressure at which the plasma arc would form was 2-3 mTorr as monitored with a Varian Millitorr Gauge. Unlike most sputtering systems which use continuously flowing gas, a fixed quantity of gas was admitted to the sputtering chamber and then the gas source was valved off. When necessary to replace gas that had been implanted in the target or trapped in the film, fresh gas was leaked in to return the chamber to the desired pressure. The loss rate of gas was noted and used as a rough measure of the relative gas entrapment by the various films prepared. However, since the substrate represented only a small percentage of the total area available for trapping, this method gave only a very rough indication of gas entrapment.

The arc power, supplied by a Hitran Corporation Model DCS-3000L power supply, could be varied from 190 to 2370 watts, and gas pressures were in the 2 to 40 mTorr range. Deposition rates were found to be nearly linear with power. For example, the deposition rates for aluminum at 5 mTorr argon pressure were 9.5 (Å/s)/kW. Only at very low power settings did this relationship change. At the lowest gas pressures, the mean free path of the metal atoms was comparable to the source-to-substrate distance, so that metal atoms primarily traveled in straight lines from the target to the substrate. At higher pressures the mean free path was reduced and metal atoms impinged on the substrate from all forward directions. This led to reduced film thicknesses at the edges of the sample because of shadowing by the sample holder. In particular, difficulty was experienced with the Sloan thickness monitor, and in some cases, actual film thicknesses in unshadowed areas on the sample were as much as 30% greater than those indicated by the thickness monitor. While the holder for the quartz crystal in the monitor was modified to minimize this effect, it was necessary to also use a calibration appropriate to the pressure involved. Actual film thicknesses were determined interferometrically [7].

Results

Aluminum, copper, gold, and silver films were prepared under different conditions by varying the sputtering rate, gas type and gas pressure. Normal incidence reflectance [7,8] was measured from 0.26 to 20 μm, and film roughness was determined from scattered light measurements [7,9]. Reported below are data on the spectral reflectance of films produced by choosing the parameters listed above such that the highest deposition rates were obtained for the two sputtering gases used. Table 1 shows the conditions under which these films were produced and the reflectance at a wavelength of 10 μm.

Aluminum

Figure 2 shows the reflectance of aluminum films prepared using argon or xenon as a sputtering gas. Also shown is the reflectance of an evaporated film deposited under UHV conditions. It is evident from this figure that films of optical quality equal to that of UHV evaporated films may be produced by rapid deposition using argon as a sputtering gas.

Copper

Figure 3 shows the reflectance of copper films produced by sputter deposition and UHV evaporative deposition. Deposition by both argon and xenon sputtering produced films of reflectance slightly higher than those produced by UHV evaporative deposition.

Gold

Figure 4 shows the reflectance of gold films produced by sputter deposition along with the reflectance of an UHV evaporated gold film. In the case of gold, the films produced by xenon sputtering were of the same quality as those produced by evaporation. The argon-produced films were approximately 1% lower in reflectance throughout the spectrum.

Silver

Figure 5 shows the reflectance of silver films produced by sputter deposition along with the reflectance of a UHV evaporated silver film. The xenon sputtered film shows a reflectance nearly as high as UHV evaporated silver, while the argon sputtered film has a lower reflectance everywhere, with the visible reflectance falling particularly low.

Gas Entrapment

Several authors [10] have studied argon trapping rates occurring during sputter deposition and have found that the trapping rate varies widely, depending upon the material being sputtered. Lee and Oblas have proposed a model which describes a mechanism for the generation of fast neutral gas atoms (by reflection from the sputtering target) which can travel to the substrate and embed themselves in the film as it is being formed. However, they suggest the existence of a threshold kinetic energy for the atoms below which they will not stick in the film. For example, this threshold kinetic energy for silver is 110 eV [1]. Lee and Oblas predicted in their model that the percentage of trapped gas will increase when the target material has high atomic mass, the sputtering gas has low atomic mass, and the sputter gas pressure is low. Their data verify the dependence on target mass. We have found that the dependence on gas atomic mass does not follow such a simple model, but that the dependence on gas pressure is as predicted by the model.

Figure 6 shows the atomic percentage of gas trapped in films sputtered under the conditions given in table 1. As predicted and demonstrated [1], sputtering gas content does decrease with decreasing target atomic mass. However, since xenon is so much more massive than argon, one might expect that the atomic percentage of xenon trapped in the films would be well below the atomic percent of argon trapped in films prepared under similar conditions. As figure 6 shows, the atomic percent of xenon present in gold is lower than the atomic percent of argon in gold. However, the silver films showed essentially identical atomic percentages of argon and xenon, and the copper films showed more xenon than argon. These results are not wholly consistent with the model of Lee and Oblas which would anticipate a lower xenon content for all metals.

A further consequence of the Lee-Oblas model is that films made with high sputtering gas pressure would have less trapped gas than those films made under lower gas pressure. Figure 6 also shows the argon content of silver films deposited at 3, 20, and 40 mTorr pressures. The amount of argon trapped using 40 mTorr argon pressure is almost two orders of magnitude less than when deposited with 3 mTorr of argon pressure. As suggested by Lee and Oblas, high kinetic energy neutral argon atoms are reflected from the target and impinge upon the substrate and growing films. The number of collisions suffered between the target and the growing film will determine the kinetic energy of gas atoms upon reaching the film. In general, the higher the kinetic energy, the greater the probability of capture. The presence of gas will increase the number of collisions suffered by gas atoms and therefore reduce their kinetic energy. The results shown in figure 6 are consistent with this view.

Reflectance versus Gas Content

Figure 7 shows the reflectance of two silver films produced at 3 mTorr and 40 mTorr argon pressure. It would appear from these data that the films with the least amount of argon entrapment produce the highest reflectance films.

In the case of gold, the argon-produced film contained a higher percentage of gas than did the xenon produced film. Figure 4 shows the high gas content film again having lower reflectance.

Figure 3 shows the reflectance of copper films produced by both argon and xenon deposition as having the same reflectance. Figure 6 indicates that both films contained approximately the same atomic percent of sputtering gas.

At this time insufficient data exist to determine the relationship between gas content and reflectance of aluminum. However, data reported elsewhere [11] do indicate that those aluminum films which were deposited at a low argon pressure exhibited the highest reflectance. Deposition at low pressure generally results in a higher percentage of gas entrapment, and it would be expected that aluminum would follow this trend. Figure 6 indicates that the argon content of aluminum films is in the ppm range, and any modification of optical properties due to argon content is not expected. A more likely explanation of the lower reflectance of xenon sputtered films (fig. 2) and of high pressure argon sputtered films [11] relates to the *rate* of deposition. In all cases the reflectance of aluminum films is lower for slowly deposited films and higher for the rapidly deposited films. Aluminum is highly reactive, and it is likely that impurities present in the system--particularly oxygen containing compounds--may be adding impurities to the films.

Figure 5 shows the reflectance of silver films sputtered using both argon and xenon. Figure 6 shows that these two films contain essentially identical atomic percentages of gas. The reduced reflectance of argon sputtered films and the unaffected reflectance of xenon sputtered films seem to indicate that xenon does not affect the reflectance of silver in the same way that argon does. It is not clear at this time the reasons for this occurrence.

Conclusions

We have prepared thin films of aluminum, copper, gold, and silver by dc sputter deposition which have a reflectance as high as, or in some cases higher than, the reflectance of UHV evaporated films. These films were deposited using argon and xenon as sputter gases. The resultant sputtering gas content of all films was determined by a flash desorption technique. The measured gas content was compared to the (relative) content predicted by a gas entrapment model suggested from Lee and Oblas. Our results were substantially in agreement with this model.

The reflectance of these films was correlated with sputter gas content. In the case of gold and silver the reflectance of films with high gas content was less than the reflectance of films with low gas content. This was most striking in a study of silver deposited with argon as the sputter gas. It would appear, however, that other effects such as impurities incorporated into aluminum are present and may play a stronger role in the final reflectance than does sputter gas incorporation.

Table 1. Sputter Deposition Conditions and Measured Reflectance at 10 μm.

METAL	GAS	ARC VOLTAGE (kV)	CURRENT (A)	PRESSURE (mTorr)	RATE (Å/s)	REFLECTANCE (at 10 μm)
Aluminum[a]	Argon	0.710	3.00	3.0	25.0	0.988
Aluminum	Xenon	1.000	0.35	5.7	3.5	0.984
Aluminum (UHV evaporated)		--	--	--	--	0.988
Copper[b]	Argon	1.000	1.00	2.0	21.0	0.994
Copper	Xenon	1.000	0.45	5.7	8.5	0.992
Copper (UHV evaporated)		--	--	--	--	0.992
Gold[c]	Argon	1.000	1.00	8.0	30.0	0.981
Gold	Xenon	1.000	0.10	5.7	5.0	0.992
Gold (UHV evaporated)		--	--	--	--	0.992
Silver[d]	Argon	1.000	1.50	3.0	67.0	0.993
Silver	Xenon	1.000	0.45	5.7	22.0	0.994
Silver (UHV evaporated)		--	--	--	--	0.995
Silver[e]	Argon	1.000	1.50	3.0	67.0	0.993
Silver	Argon	0.500	2.00	40.0	28.5	0.994

[a] See figure 2.

[b] See figure 3.

[c] See figure 4.

[d] See figure 5.

[e] See figure 7.

Acknowledgments

This work was supported by ERDA, ARPA, AFWL and NAVWPNCEN Independent Research funds. One of the authors (P. A. Temple) was a NRC-NWC Postdoctoral Fellow during the period this work was done and wishes to acknowledge the support of the NRC-NWC postdoctoral program.

The authors are grateful to Mr. Richard Smith, Mrs. Verla Walker, and Ms. Jane Williams for their invaluable assistance in preparing the artwork and manuscript for publication.

Appendix

The apparatus used to determine the sputter gas content of sputter-deposited films is shown in figure 8. A linear feedthrough held three 0.95 cm diameter quartz substrates on which films had been deposited. The feedthrough allowed the selection of any vertical position on the three substrates. The entire chamber was mounted on a translation stage which allowed for horizontal motion.

A RGA was used to monitor the argon or xenon content of the small vacuum chamber (the total volume was 1×10^{-3} m^3). The RGA was set at mass 40 for argon and mass 129 for xenon. Pulsed, 10.6 μm laser radiation entered the chamber through a NaCl window and was focused on the film. Sufficient laser energy was available to totally evaporate the metal in a small circular spot on the film. The typical spot size was 0.9 mm in diameter, and all films tested were 2000 Å thick. The evaporated spots were subsequently photographed, and the area of each spot was determined using a planimeter.

Prior to the laser evaporation, the ion pump attached to the chamber was valved off. The laser was then triggered and the increase in RGA current caused by the released gas was recorded on an x-y recorder.

The RGA was used in the faraday cup mode whenever possible. The RGA sensitivity was determined by measuring the response of the RGA when a known pressure of argon or xenon was present. The argon and xenon pressures were measured using a Varian nude ion gauge and the calibration adjustment for argon and xenon published by Varian. These numbers are considered to be accurate to 20% which limits the accuracy of the flash desorption apparatus to no better than 20%. The calibration procedure was carried out while the RGA head was attached to the sputter chamber (fig. 1).

References

[1] Lee, W. W. Y. and Oblas, D., J. Appl. Phys. 46, 1728 (1975).

[2] Sputtered Films, Inc., 725 E. Yanonali St., Santa Barbara, Cal. 93103.

[3] Sloan Technology Corp., Santa Barbara, Ca.

[4] Gast Manufacturing Corp., P. O. Box 97, Benton Harbor, Mi. 49022.

[5] Tharp, L. N. and Scheibner, E. J., J. Appl. Phys. 38, 3320 (1967).

[6] O'Handley, R. C. et al., Surf. Sci. 50, 407 (1975).

[7] Bennett, H. E. and Bennett, J. M., "Precision Measurements in Thin Film Optics," in *Physics of Thin Films*, G. Hass and R. E. Thun, Eds. (Academic Press, New York, 1967), Vol. 4, pp. 1-96.

[8] Bennett, H. E. and Koehler, W. F., J. Opt. Soc. Am. 50, 1 (1960).

[9] Bennett, H. E. and Porteus, J. O., J. Opt. Soc. Am. 51, 123 (1961).

[10] See Ref. 1, references.

[11] Temple, P. A. et al., in *High Energy Laser Mirrors and Windows* (Semi-Annual Report No. 7-8, ARPA Order 2175, Naval Weapons Center, NWC TP 5845, 1976), pp. 35-53.

Figures

Figure 1. Photograph of the sputter chamber showing the central anode (held in place by three cap screws) surrounded by the cathode (target) made of the material which is to be sputtered. Outside of the target is a shield which contains magnets which cause ions to spiral toward the cathode. Above the sputter gun is a substrate holder which is designed to expose any set of three substrates simultaneously. Adjacent to the substrate holder is a quartz crystal deposition monitor.

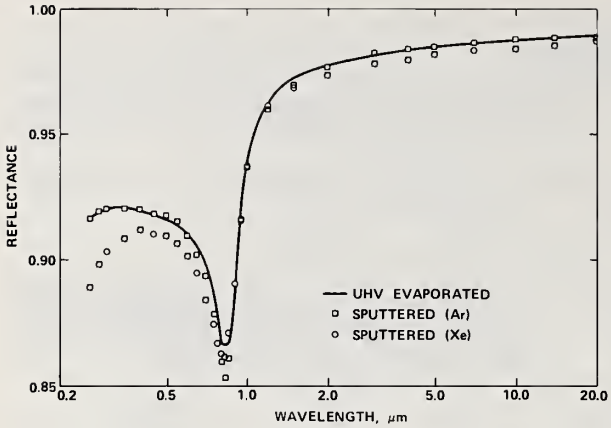

Figure 2. The spectral reflectance of sputter deposited aluminum. The conditions under which the films were deposited are shown in table 1. The reflectance of UHV evaporated aluminum is shown for comparison.

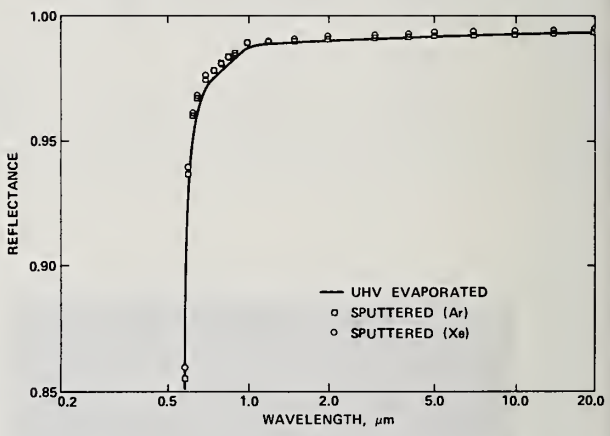

Figure 3. The spectral reflectance of sputter deposited copper. The conditions under which the films were deposited are shown in table 1. The reflectance of UHV evaporated copper is shown for comparison.

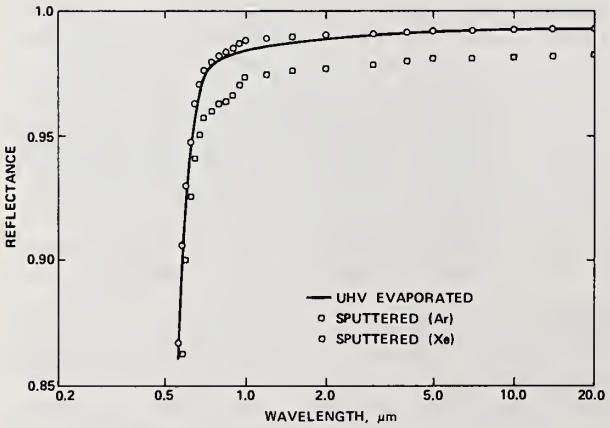

Figure 4. The spectral reflectance of sputter deposited gold. The conditions under which the films were deposited are shown in table 1. The reflectance of UHV evaporated gold is shown for comparison.

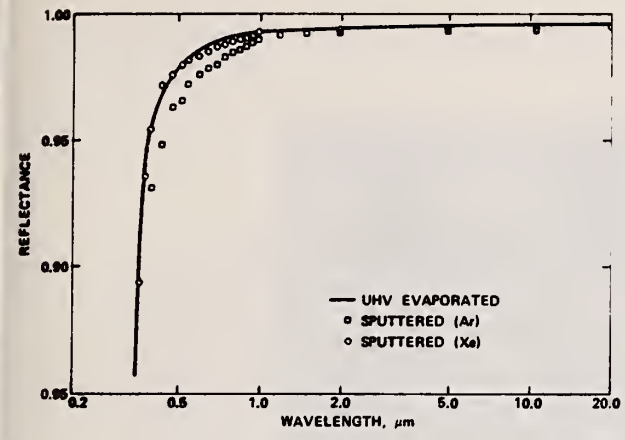

Figure 5. The spectral reflectance of sputter deposited silver. The conditions under which the films were deposited are shown in table 1. The reflectance of UHV evaporated silver is shown for comparison.

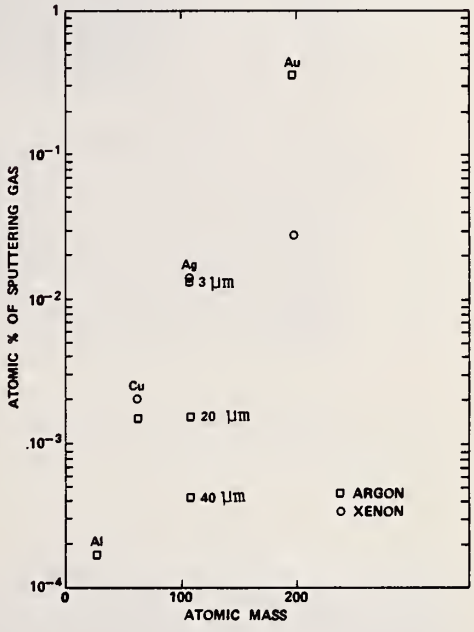

Figure 6. The atomic percentage of trapped sputtering gas in thin films of aluminum, copper, silver, and gold. Two sputtering gases, argon and xenon, were used. Also shown is the argon content in silver films when the deposition was made at three different pressures. The gas content was determined using a flash desorption technique. The absolute accuracy is approximately 25% while the precision is at least 10%.

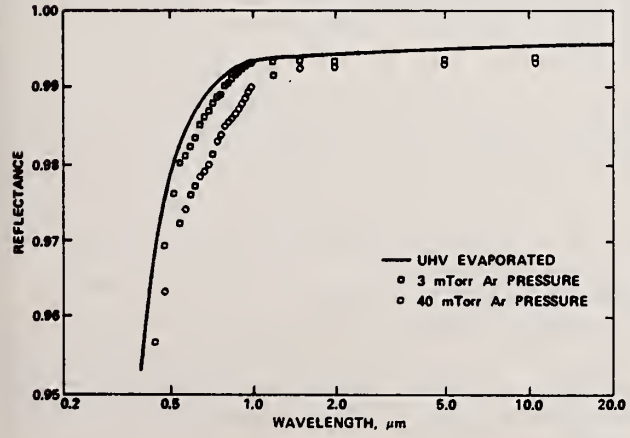

Figure 7. The spectral reflectance of silver films sputter-deposited using argon at 3 mTorr and at 40 mTorr pressures. Also shown is the spectral reflectance of UHV evaporated silver. The conditions under which the films were deposited are shown in table 1.

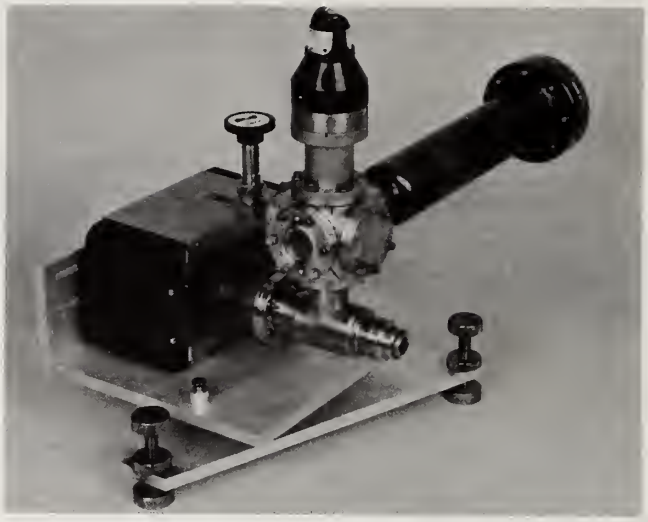

Figure 8. A photograph of the flash desorption apparatus used to determine the atomic percentage of sputtering gas present in thin sputter deposited films. The entire top half of the apparatus is mounted on a translation stage which allows for horizontal motion of the laser beam across the sample. A NaCl window is visible in the foreground.

COMMENTS ON PAPER BY TEMPLE, BURGE, AND BENNETT

The speaker noted that it was hard to carry out consistent parametric studies of the sputter process due to the interdependence of the variables, such as sputter gas, deposition rate, and impurity level. It was observed that argon sputtering led to higher deposition rates than xenon, for example. Aluminum films, which are highly reactive, exhibited much better quality when laid down quickly. Using argon sputtering, but maintaining a slow deposition rate, yielded Al films of poor quality.

3.1 Materials for High-Power Window and Mirror Coatings and Multilayer-Dielectric Reflectors*

M. Sparks

Xonics, Incorporated, Santa Monica, California 90401

Antireflection coatings and reflectors having lower values of absorptance than are presently available are needed for high-power, and even some low-power, applications. Intrinsic values of absorptance of antireflection coatings, multilayer-dielectric reflectors, and metallic-reflection-enhancing coatings are orders of magnitude lower than current experimental values A_{exp}. A major factor limiting the values of A_{exp} is that a given coating material usually has orders of magnitude greater absorption when deposited as a film than when grown as a bulk crystal. The most likely source of this extra film absorptance A_f is contamination of the film. Numerous contaminants include water, HCO_3, ClO_3, NO_3^-, OH^-, and CN^-. Contamination can occur before or during deposition, upon exposure to the atmosphere (where absorption by porous films and surface adsorption are important), or during use or storage. At 10.6 μm only two molecular layers of water or a packing density of 99.95% are formally required to give $A_f = 10^{-4}$, which is a typical desired value. High-packing-density films should be vacuum vapor deposited using ultraclean deposition conditions including thorough baking of the entire system, high-purity single-crystal starting materials, special care in evaporation, state-of-the-art substrate preparation, and ultrahigh vacuum. Spectroscopic and calorimetric measurements of $A_f(\omega)$ on very thick films and on normal-thickness films, both deposited on attenuated-total-reflection plates, should be made. Material-selection guidelines, including a bulk absorption coefficient less than 0.5 cm^{-1} and a value of the index of refraction in the required range, are developed and used to select the following 10.6 μm candidate materials: ThF_4, NaF, BaF_2, SrF_2, NaCl, KCl, $KGaF_4$, As_2S_3, As_2Se_3, ZnS, ZnSe, and TlI. Distinguishing absorption on the coating surface from that in the bulk of the coatings by utilizing the nearly zero electric field on the surfaces of certain coatings is proposed. Inclusion damage is expected at ~1-10 J/cm^2 for nanosecond pulses or ~10 to several hundred J/cm^2 for microsecond pulses. Intrinsic damage is expected by heating at ~100 J/cm^2 for a 10 μs pulse and $A_f = 10^{-3}$, or by such nonlinear processes as electron-avalanche breakdown at ~10 J/cm^2 (i.e. $I \cong 10$ GW per cm^2) for a 10 ns pulse. Strongly absorbing 1-μm-radius inclusions spaced 175 μm apart in the coating give rise to absorptance $A_f \cong 10^{-4}$. Thermally induced stresses in a 2 mm-diameter detached film segment may be sufficient to cause additional detachment and a runaway process.

Key words: Attenuated total reflection spectroscopy; dielectric coatings; infrared lasers; laser damage; thin films.

1. Introduction

Deposition of thin dielectric films is of great interest for (1) antireflection coatings, where the reflectance is to be reduced, and for (2) multilayer-dielectric reflectors, and (3) metallic coatings, where the reflectance is to be increased. Some high-power systems of current interest cannot be operated without antireflection coatings on the windows. The best uncoated metallic mirrors have high intrinsic values of normal incidence absorptance, ranging from approximately one-half percent at 10.6 μm, to approximately two percent at 500 nm, to approximately 10 percent from 400 nm to 100 nm (12.5 eV). Much lower values of absorptance are needed in some high-power systems. By contrast, multilayer-dielectric reflectors (and window and mirror coatings) have much lower intrinsic values of absorptance, probably less than 10^{-8} in many cases, for all wavelengths from the vacuum ultraviolet through the infrared to ~10 μm. Since the lowest current experimental values of absorptance are a few times 10^{-4} for window and mirror coatings and multilayer-dielectric mirrors, it is possible that technical improvements in film deposition techniques could result in lower absorptance for all three of the film devices.

In view of the current difficulties in obtaining satisfactory coatings for high-power infrared windows and mirrors, a study of the problems of these coatings was made [1][1]. The present paper is a summary of the results,

*This research was supported by the Defense Advanced Research Projects Agency

[1]Figures in brackets indicate the literature references at the end of this paper.

most of which also apply to multilayer-dielectric reflectors and to wavelength regions other than the infrared. It is emphasized that the study was limited to a near-term program of obtaining coatings in a research-laboratory environment in the shortest period of time for the lowest cost. Fundamental investigations and manufacturing of field-use components were not explicitly included in the study, although it is necessary to keep the ultimate use in mind even during the research-laboratory stage of the investigation.

2. High Absorptance of Films

In addition to the already stringent requirements of coatings for low-power use, the high-power coatings must have low optical absorptance. Required values for the film absorptance per surface A_f have not been established for any of the major systems of interest. A typical desired value is $A_f = 10^{-4}$, which is chosen to make the absorptance of two coated surfaces equal to that of the window for the typical case of a 2 cm-thick window with absorption coefficient $\beta_b = 10^{-4}$. The value of the film absorption coefficient β_f corresponding to $A_f = 10^{-4}$ and a typical thickness of 2 μm is $\beta_f = 0.5\ cm^{-1}$. Since much greater values of absorption coefficient can be tolerated in the film ($\sim 0.5\ cm^{-1}$) than in the bulk ($\sim 10^{-4}\ cm^{-1}$), it would appear that obtaining materials for films should be much easier than for windows. However, the absorption coefficient of a given material usually is much greater when deposited as a thin film than when grown as a bulk crystal. As a typical example, a material with a bulk value of $\beta_b = 10^{-4}\ cm^{-1}$ may have a film value of $\beta_f = 10\ cm^{-1}$. This much greater absorptance in film form than in bulk form is one of the most serious coatings problems, though by no means the only one.

In general the source of the extra absorptance in films is not known. It is suggested that contamination of the film is by far the most likely candidate for explaining this extra absorptance. Water is the most important contaminant for the 2 to 15 μm wavelength region, but there are many others. The contamination can be in the bulk of the film, adsorbed on the surface of the film, or in pores in the film. The contamination can occur during deposition, from the residual gas for example, after deposition, by surface adsorption or by absorption into the pores for example, or before deposition, by substrate contamination for example.

As seen in figure 1a, liquid water absorbs strongly from 2 μm through 15 μm. The absorption coefficient at 10.6 μm is $\sim 10^3\ cm^{-1}$, and the values at the other prominent laser frequencies are shown by the vertical lines. In passing notice that this top figure illustrates the invalidity of the myth that the frequency must be near an absorption line in order to have great absorptance. From ~6.5 to 10.5 μm there is very little structure in the absorption spectrum, but the absorption coefficient has the very large value of $10^3\ cm^{-1}$. The broad absorption from ~11 to 15 μm results from the hydrogen-hydrogen interactions in the liquid water, and this absorption is missing in the water-vapor spectrum, which is shown in figure 1b. In fact, careful measurements [3] indicate that the absorption coefficient of water vapor at 10.6 μm may be orders of magnitude smaller than that of liquid water.

For adsorbed water, only 1 nm is required formally (using $\beta = 10^3\ cm^{-1}$ for liquid water) to give 10^{-4} absorptance. Pores in films are known to readily absorb water from the atmosphere on removal from the vacuum-deposition chamber, and a fraction of 5×10^{-4} of pores filled with water formally gives an absorptance of 10^{-4}.

At 10.6 μm, molecules containing O_3 are particularly offensive since they usually absorb near 10.6 μm. There are many known molecules that are strongly absorbing in the infrared. Deutsch [4] observed molecular absorption on sample surfaces in attenuated-total-reflection studies. Duthler [5] showed that molecular-ion absorption was an important source of bulk absorption, pointed out the relation to matrix-isolation spectroscopy studies, and catalogued strongly absorbing molecular ions. Phil Klein [6] has argued that molecules containing carbon probably cause a wide absorption band extending from ~2 to ~5 μm.

There are absorption bands of molecules and molecular ions extending throughout the range from 2 to 12 μm as seen in figure 2. These and other film contaminants include the following:

- Water
- Other molecules and molecular ions such as CHO_3, ClO_3, NO_2, CO_2, CO, N_2O, DHO, SO_4, and CH_4
- Other hydrocarbons
- Cleaning materials
- Rinses
- Residues from plastic containers
- Macroscopic inclusions
- Particles spattered from the starting material
- Dirt, dust, pollen
- Residual gas contamination
- Diffused ions or molecules
- Fingerprints.

It is not surprising that film contamination is important since current film-deposition processes are simply very dirty methods of growing crystals. The deposition process should be cleaned up by pushing the process to the current ultimate limit. It is known that some films that cannot be deposited under ordinary deposition conditions can be deposited successfully with sufficient care including long baking of the complete system at high temperatures. Reduction of film contamination by the ultraclean deposition conditions described below is important in obtaining strong adhesion of the film to the substrate and in reducing film stress as well as in lowering the film absorptance. The ultraclean deposition conditions include use of state-of-the-art substrates, experimental determination of the optimum substrate temperature and careful subsequent control of this temperature, baking of the entire system at the highest practical temperature for long periods of time, use of spattering filters, use of high-purity single-crystal starting materials, and use of state-of-the-art ultrahigh vacuum techniques. At the present stage of the program, in which the goal is to obtain satisfactory research-laboratory films, it is important to have all these conditions met absolutely perfectly. Once satisfactory coatings are obtained it is hoped that some of the stringent deposition conditions may be relaxed. Indeed, it may not be currently feasible to manufacture coatings for the large optical elements needed in some systems unless some of these conditions are relaxed.

Only vapor vacuum deposition should be used in the near-term program. Other deposition techniques may be interesting, promising, and important, but not for the near-term program.

3. Suggested Measurements

Just as for windows, the measurement of small values of absorptance is a problem. Measurements of absorptance values in the range of 10^{-4}, and as a function of frequency, are needed. The frequency dependence is of course one of the most useful clues in determining the source of absorptance. Recall that by normal transmittance spectroscopy, measurements of values of absorptance of $\sim 10^{-2}$ can be made. For the films of usual thickness, say 2 μm thick, this is not sufficient since values of 10^{-4} are of interest. For films that can be deposited as very thick layers, say 200 μm thick, normal spectroscopic measurements could be useful. Calorimetric measurements are the most useful for measuring small values of absorptance, and it is believed that absorptance values of 10^{-4} can be measured with confidence. However, the complete frequency dependence cannot be determined since there is not a continuous range of wavelengths at which sufficiently high power is available.

Attenutated-total-reflection (ATR) spectroscopy is another important method. The film is deposited on the surfaces of an ATR plate, which is a substrate constructed such that the beam makes a number of total internal reflections in traversing the plate. Since the beam samples the surface at each of approximately 50 total internal reflections in a typical plate, 50 times smaller values of surface absorptance can be measured. Thus, a film absorptance of $\sim 2 \times 10^{-4}$ can be measured. The frequency dependence can also be determined since this is a spectroscopic measurement. The main difficulty is in interpreting the experimental results, and in particular in obtaining the numerical value of the absorptance.

Figure 3a is an illustration of the liquid-water absorption spectrum for a water-contaminated thorium-tetrafluoride film deposited on a zinc-selenide ATR plate. This spectrum leaves little doubt that there is water contamination in this sample. Figure 3b illustrates one of the difficulties in extracting the value of film absorptance from the curves and in interpreting the ATR spectrum results in general. Here the transmittance increased when the film was deposited. Thus, even a rough estimate of the absorptance cannot be obtained.

An important factor that has not been emphasized in previous ATR measurements of film absorptance is that the angle of the ATR plate should be adjusted for the particular film-substrate combination, rather than using such a fixed angle as 45 degrees for all measurements. A simple calculation illustrates that for barium fluoride the index of refraction is very close to the value at which total internal reflection occurs for a 45 degree plate. In fact at a wavelength value near 5 μm the index of barium fluoride drops to the value at which total internal reflection is no longer possible, and some leakage out of the ATR plate is expected. It seems likely that the reduction in transmittance from approximately 4 to 8 μm in figure 3b is due to this lack of total internal reflection.

In general the total internal reflection can occur either at the surface of the film or at the interface of the film and the substrate. The angle of the ATR plate should be chosen such that the total internal reflection is at the film surface in order to give the greatest electric field and the greatest absorptance in the film. The conditions on the angle, which are easy to derive and are discussed elsewhere, [1] are as follows: For the case of $n_f > n_s$, where n_f is the index of refraction of the film material and n_s is the index of refraction of the substrate, total internal reflection is possible only at the film surface. In this case the ATR plate angle θ must satisfy the inequality $\theta > \sin^{-1}(1/n_s)$, which is the general condition for total internal reflection (for arbitrary values of n_s and n_f). For the case of $n_f < n_s$, total internal reflection is possible at either the film surface or at the substrate-film interface. As mentioned above, in order to have the maximum absorptance in the film the total internal reflection should occur at the film surface. This requires that θ satisfies the double inequality $\sin^{-1}(1/n_s) < \theta < \sin^{-1}(n_f/n_s)$.

There is a possibility of distinguishing between absorption on the surface of the film, at the film-substrate interface, or in the bulk of the film. The reason is that at the surface of a metal the electric field is very small, as illustrated schematically in figure 4. For a dielectric coating that is one-half of an optical wavelength thick, the electric field is also nearly equal to zero on the outside surface of the coating. For a quarter-optical-wavelength-thick dielectric coating the electric field has a large value at the surface, and for a dielectric coating deposited on a dielectric substrate the electric field is not equal to zero at either the interface or the surface. Thus, by measuring the absorptance under various conditions it is possible in principle to distinguish between absorption at the interface, absorption at the surface of the film, and absorption in the bulk of the film. In particular, distinguishing optical absorption by adsorbed layers from that by other sources should be possible. Either ATR or calorimetric measurements could be used.

This measurement technique is included in the category of measurements which are interesting, but not for the near-term program. There are many promising methods of measuring absorptance including ellipsometry, emissivity, surface acoustical-wave-type measurements, low-temperature measurements, alpha phones, and a number of others. Even the simplest sounding of these methods has turned out in the past to be technically difficult, and the development of new measurement techniques should not be included in the near-term program.

4. Material Selection Guidelines and Suggested Materials

Since there are no coatings available with $A_f = 10^{-4}$ for any of the infrared frequencies of interest and only a small handful of coating materials have been investigated, it is important to select new candidates with the highest probability of success. For window materials, values of the total power through a window under various conditions were convenient figures of merit [8,9]. The dependence $P(\beta, \sigma, C, K, \cdots)$ of the power P, calculated by making simplifying assumptions, on such parameters as the absorption coefficient β, material strength σ, heat capacity C, and thermal conductivity K clearly shows the relative importance of these parameters. For example, diamond is a

good material in some applications because its great strength and thermal conductivity more than compensate for its high 10.6 μm absorption coefficient. Coatings on the other hand must satisfy a number of independent requirements. For example, coatings must have good adhesion to the substrate, homogeneity, stability in the atmosphere, and low absorptance, reflectance, and scattering. Failure to achieve any one of these properties makes the coating unacceptable, no matter how good the other properties are. An absorptance of 10^{-10} would not compensate for the inability to adhere to the substrate. Thus the figures of merit are replaced by a set of guidelines for selecting candidate materials:

- The value of the bulk absorption coefficient β_b must be less than a required value such as 0.5 cm^{-1}. (Large measured values of film absorption coefficient do not preclude the use of a material since a major goal of the program is to reduce the values of film absorptance.)
- The value of the index of refraction n_r must be within the required range. In multilayer coatings, at least one low-index and one high-index material is required.
- The thermal-expansion-mismatch contribution to the film stress must be sufficiently small to prevent failure. Other information on stress should be used when available.
- Nonhygroscopic materials are desirable, although it may be possible that hygroscopic materials can be used as an inside layer of a multilayer stack.
- High-purity, single-crystal starting materials must be available. The single-crystal requirement may be relaxed later in the program.
- Materials must be nonradioactive and nontoxic for some applications.
- The hardness of the outside materials should be great for coatings that must withstand abrasion.
- Previous experience with the materials in question should be considered, but caution is required to avoid misleading negative results.
- The following properties are desirable, but are difficult to predict for new materials that have not been previously deposited successfully in thin-film form:

  film packing density

  stability (water or other chemical attack, thermal or photo decomposition)

  deposition compatibility in multilayer coatings

  adhesion to substrate

  stoichiometry in thin-film form

  no adverse diffusion effects at interface

  homogeneity.

By using these guidelines, the following best candidates were chosen for 10.6 μm use:

- ThF_4
- Na (F, Cl) [10]
- KCl
- (Ba, Sr) F_2
- $KGaF_4$ and other Cryolite-type materials
- $As_2(S_3, Se_3)$
- Zn (S, Se)
- TlI.

The fluorides and chlorides are low-refractive-index materials, and the remaining five materials at the bottom of the list are high-index materials. These candidates are discussed, and a list of other good candidate materials and a preliminary discussion of materials for use at 2 to 6 μm are given elsewhere [1].

Of the unacceptable and unlikely candidates for 10.6 μm coatings, the following are important: Materials containing the light elements H, He, Li, Be, C, N, and O. The light masses are expected to give rise to a fundamental resonance too near 10.6 μm, making $\beta_b > 0.5$ cm^{-1}. Note that the vast number of materials containing oxygen and carbon are expected to be unsatisfactory. Many oxides are known to have $\beta_b > 0.5$ cm^{-1} at 10.6 μm. Although it is not certain that some oxides and carbon-containing materials will not have a sufficiently low absorption coefficient, the generally high absorption at 10.6 μm of these materials make them less likely candidates.

The absorption coefficients of the fluorides are marginal. Fluorides that are known to have too great absorptance at 10.6 μm include LiF, $(Ca, Mg)F_2$, AlF_3, and $NaAlF_4$ (cryolite). Potassium fluoride is more hygroscopic than KCl or KBr. Lead fluoride would have to be deposited with greater packing density than that which has been obtained previously (0.9). Thallium fluoride is a less desirable candidate since thallium is toxic. The rare-earth fluorides $(Ce, La, Nd, Pr, Yb)F_3$ probably will not have $\beta_f < 0.5\ cm^{-1}$, although this is not certain. Other unlikely and unacceptable materials are listed elsewhere [1].

5. Protective Coatings

Protective coatings for such hygroscopic window and coating materials as alkali halides have been discussed in the literature for some time [11]. In addition to the prevention of water-vapor penetration, it may become extremely important to develop a thin coating to reduce adsorption of water and other contaminants on the surface of optical components. It was shown [1] that information in the literature suggests the following results: (a) It is not likely that polycrystalline films can protect large areas of alkali halides from moisture attack [11]; (b) It is possible, though not certain, that polycrystalline films can be sufficiently dense and sufficiently hydrophobic to allow $A_f = 10^{-4}$ to be attained in carefully prepared films [11]; (c) Very thin glassy films were found not to protect alkali halides [11]; (d) Thick glassy films, say 1 μm thick on well polished substrates, did protect alkali halides. However, on long exposure to humidity, moisture attack that started at the edges of the sample eventually covered the entire substrate under the coating [11]; (e) Polymer films will be considered further in order to determine the possibility of their providing sufficient moisture protection in spite of the known great moisture vapor transmission rates and to determine the possibility of reducing their normally great optical absorption to acceptably low values. (f) The possibility of using very thin polymer films as hydrophobic outside layers over antireflection coatings to reduce adsorption on the surface will also be investigated. (g) Priority of future research on such amorphous semiconductors as germanium is low since the likelihood of obtaining β_f less than $0.5\ cm^{-1}$ is small.

The main concern about polymer coatings in the past was that of obtaining pin-hole-free coatings in order to prevent moisture attack of the underlying antireflection coating or substrate. This is indeed important since it is known that moisture will attack underlying substrates through pin holes in polymer films. Unfortunately, in addition to this technical problem there are two fundamental properties of polymer films that possibly could prevent their use as moisture-protection films.

First, the rate at which moisture vapor permeates through a polymer is one of the routinely measured properties of polymers. Formally using the measured values of this moisture-vapor transmission rate through unsupported (i.e., not deposited on substrates) polymer films suggests that pin-hole-free polymer films would not be useful in preventing water from penetrating through the polymer to a substrate or an antireflection coating. However, the moisture-vapor transmission rate could be drastically different for a polymer deposited on a solid from that of an unsupported polymer film. The results from the literature and from workers in the field are conflicting, in some cases suggesting that moisture-vapor protection is possible and in other cases suggesting that it is not. We suspect that inhibition of the moisture-vapor transmission at the polymer-substrate interface is important if polymers do indeed provide sufficient moisture-vapor protection.

In considering the problem of moisture-vapor transmission through polymer coatings, it must be recalled that these coatings are extremely thin and that only two monolayers of water transmitted through the film could cause unacceptably great optical absorptance. According to available data, absorption of water by plastic films (as opposed to water-vapor transmission through the films) probably will be tolerable at 2.8, 3.8, 5.3, and 10.6 μm.

The second fundamental problem with polymer coatings is that the published infrared spectra of all polymers that we have found to date show values of absorptance that are too great to allow $A_f = 10^{-4}$ for either antireflection coatings or for very thin protective coatings. Professor M. Shen and coworkers at the University of California at Berkeley have deposited polyethane coatings by a plasma deposition method which is believed to give pin-hole-

free coatings. [12] Measurements of the absorption coefficient of these coatings made at the Hughes Research Laboratory gave values of β_f = 3-7 cm^{-1}. Shen and coworkers plan to reduce the contamination of the film in the hopes of reducing this value of the film absorption coefficient.

6. Stresses

The stress in a thin film is believed to consist of three components, one from the mismatch of the thermal expansion coefficient of the film and the substrate, one from contaminants in the film, and one from an intrinsic contribution. The contribution from the mismatch of the thermal expansion coefficient is well understood, and very simple calculations give the observed values of this component of stress. For any proposed film-substrate combination this thermal-expansion mismatch component of stress should be calculated in order to determine if the film can withstand this stress. Examples are given in the complete report [1], Unfortunately, the thermal-expansion mismatch contribution to the stress is often less than that of the other two contributions.

Film contamination typically leads to compressive stresses. Campbell [13] states that, "In impure films in which oxygen and other materials are incorporated into the structure during growth, the resultant stresses are usually sufficiently high to overshadow any of the "pure film" effects. The stresses are then usually compressive, at least in the initial stages of growth and provided that the reacting species migrate through growing film to the interface. Compressive stresses are observed in thermally grown, anodized, and certain sputtered and evaporated films. If the ion migration takes place from the interface to the film surface, tensile stresses will be observed." Of great importance for the power of stress are the packing density and the water vapor absorption. During exposure to atmosphere very often a stress relief takes place.

The intrinsic contribution to the stress in a film is not well understood. It is not possible to predict in advance what the stress will be in a new film material on a given substrate. However, for film materials that have been previously deposited it is possible to predict with a fair degree of success what the stress will be for a given film-substrate combination or for a particular multilayer coating on a given substrate.

7. Laser Heating and Damage

There are three damage or failure regimes of interest in general. The first is damage or optical distortion resulting from heating by ordinary linear absorption in the coating. The second is the absorption by macroscopic imperfections such as inclusions. It is well known that inclusions are extremely important in laser damage under short-pulse operation. It has also been pointed out [14] that inclusions can increase the average heating in addition to causing the well known damage. The absorption can, in general, be linear or nonlinear. The third is the intrinsic nonlinear damage mechanism such as electron-avalanche breakdown.

The results of the heating and damage studies are very briefly as follows:

- For $2A_f = A_b = 2 \times 10^{-4}$, the film and bulk contributions to the spatial average of the window temperature, which determines the thermally induced optical distortion, are equal and have a typical value T_{tot} = 1.0 K, which is sufficient to cause thermally induced optical-distortion failure in some cases.
- In a typical system with repeated short pulses, only the time-average heating need be considered (apart from inclusion damage, nonlinear effects and possible more stringent conditions of future systems).
- The linear absorption (below the damage threshold) by strongly absorbing ($\sigma_{abs} = \pi a^2$) one-micro-radius inclusions with an average spacing of 175 μm gives rise to absorptance $A_f = 10^{-4}$.
- Inclusion damage is expected to occur at energy densities $It_p \cong$ 1-10 J/cm^2 for nanosecond pulses or at $It_p \cong 10$ to several hundred joules per square centimeter for microsecond pulses. In principle, values of $It_p < 1 J/cm^2$ are possible for nanosecond through microsecond pulses.
- Intrinsic damage of coatings is expected to occur at $It_p \cong 10^3 J/cm^2$ for a pulse of duration t_p = 10 μs and $A_f = 10^{-3}$ as a result of linear heating of the coating, or at $It_p \cong 100 J/cm^2$ (or $I \cong 10$ GW/cm^2) for a 10 ns pulse of ~1 to 10 μm radiation as a result of electron-avalanche breakdown or perhaps another nonlinear process.

- The calculated value of 25 K temperature rise for a detached film segment of diameter D = 2 mm under continuous illumination at 10^3 W/cm^2 and $A_f = 10^{-4}$ is surprisingly small.
- The temperature is proportional to D^2 for a detached segment.
- The thermally induced stress corresponding to T = 25 K has a typical value of 20 MPa (3×10^3 psi), which may be sufficient to cause further detachment, then further temperature increase since $T \sim D^2$, and possibly a runaway condition resulting in damage.

In pulsed operation, for short pulse durations $t_p \ll \tau_\ell$, where $\tau_\ell \equiv C\ell_f^2/4K$ has a typical value of 0.4 μs, the detachment causes little additional temperature rise since thermal diffusion into the substrate already was negligible. For values of energy density near the threshold for failure (of the undetached areas of the film), the size of the detached area probably will be increased, and various types of fracture both in and out of the plane of the film could cause failure, especially in subsequent pulses.

For very long pulse durations $t_p \gg \tau_D$, where $\tau_D \cong C(D/2)^2/4K$ has a typical value of 2.5×10^{-2} s for detached diameter D = 1 mm, the above steady-state results are approached. For intermediate pulse durations $\tau_\ell < t_p < \tau_D$, the detachment causes a greater temperature rise $T \cong IAt_p/C\ell_f$ than the corresponding value $T = IAt_p/C\ell_{z=0}$, with $\ell_{z=0} = (\pi K t_p/4C)^{1/2}$, for unimpeded thermal diffusion into the substrate.

8. Acknowledgments

In preparing the report of which the present paper is a summary, comments were solicited from a representative sample of active workers in the field of coatings for high-power infrared optics. I am indebted to a number of people for a great amount of assistance, and I deeply appreciate the time and effort they have contributed. At the beginning of the program the current status of coatings of high-power infrared materials was discussed with the following investigators: Dr. R. R. Austin, Dr. H. E. Bennett, Dr. E. Bernal G., Mr. A. Braunstein, Mr. M. Braunstein, Dr. T. F. Deutsch, Dr. T. M. Donovan, Dr. C. J. Duthler, Dr. S. Geller, Dr. A. J. Glass, Dr. M. Hass, Dr. A. R. Hilton, Dr. T. D. Holstein, Dr. J. Kershenstein, Dr. G. E. Kuhl, Dr. J. R. Kurdock, Dr. J. Lehman, Dr. J. H. Marburger, Dr. D. Milam, Dr. P. A. Miles, Dr. T. Norwood, Dr. H. Posen, Dr. G. Ruse, Mr. C. S. Sahagian, Dr. M. Shen, Maj. J. L. Stapp, Dr. C. M. Stickley, Dr. L. Van Uitert, Dr. B. L. Weigand, Dr. R. W. White, and Capt. H. V. Winsor.

I want to thank the following for their comments on a preliminary draft of the report [1]: Dr. R. R. Austin, Dr. E. Bernal G., Mr. A. Braunstein, Dr. T. M. Donovan, Dr. M. Hass, Dr. L. P. Mott, and Dr. H. Posen. Dr. Guy Ruse, University of Colorado, stressed the importance of thorough baking of the entire system and pointed out that this was essential in attaining stable films of certain compounds.

9. References

[1] Sparks, M., Xonics, Inc. Sixth Technical Report, Contract DAHC15-73-C-0127, December (1975).

[2] Sadtler Standard Infrared Prism Spectra, Midget Edition (Sadtler Research Labs, Philadelphia, Pa., 1959).

[3] CRC Handbook of Lasers with Selected Data on Optical Technology, ed. R. J. Pressley (Chemical Rubber Co., Cleveland, Ohio, 1971).

[4] Deutsch, T. F., J. Electron. Matls. 4, 663 (1975).

[5] Duthler, C. J., J. Appl. Phys. 45, 2668 (1974); Proceedings of 4th Annual Conference on Infrared Laser Window Materials, Tucson, Ariz., Nov. 18-20, 1974 (January 1975).

[6] Klein, P., this proceedings (to be published).

[7] Willingham, C., Bua, D., Statz, H., and Horrigan, F., Raytheon Research Division Final Technical Report, Contract DAAH01-74-C-0719, August (1975).

[8] Horrigan, F., Klein, C., Rudko, R., and Wilson, D., Microwaves 8, 68 (1969).

[9] Sparks, M., J. Appl. Phys. 42, 5029 (1971).

[10] Such symbols as Na(F, Cl) denote the set of materials NaF and NaCl.

[11] Young, P. A., Thin Solid Films 6, 423 (1970).

[12] Reis, T. A., Hirtsuka, S., Bell, A. T., and Shen, M., this proceedings (to be published).

[13] Campbell, D. S. in Handbook of Thin Film Technology, ed. L. I. Maissel and R. Glang (McGraw-Hill, New York, 1970).

[14] Duthler, C. J. and Sparks, M., J. Appl. Phys. 44, 3038 (1973).

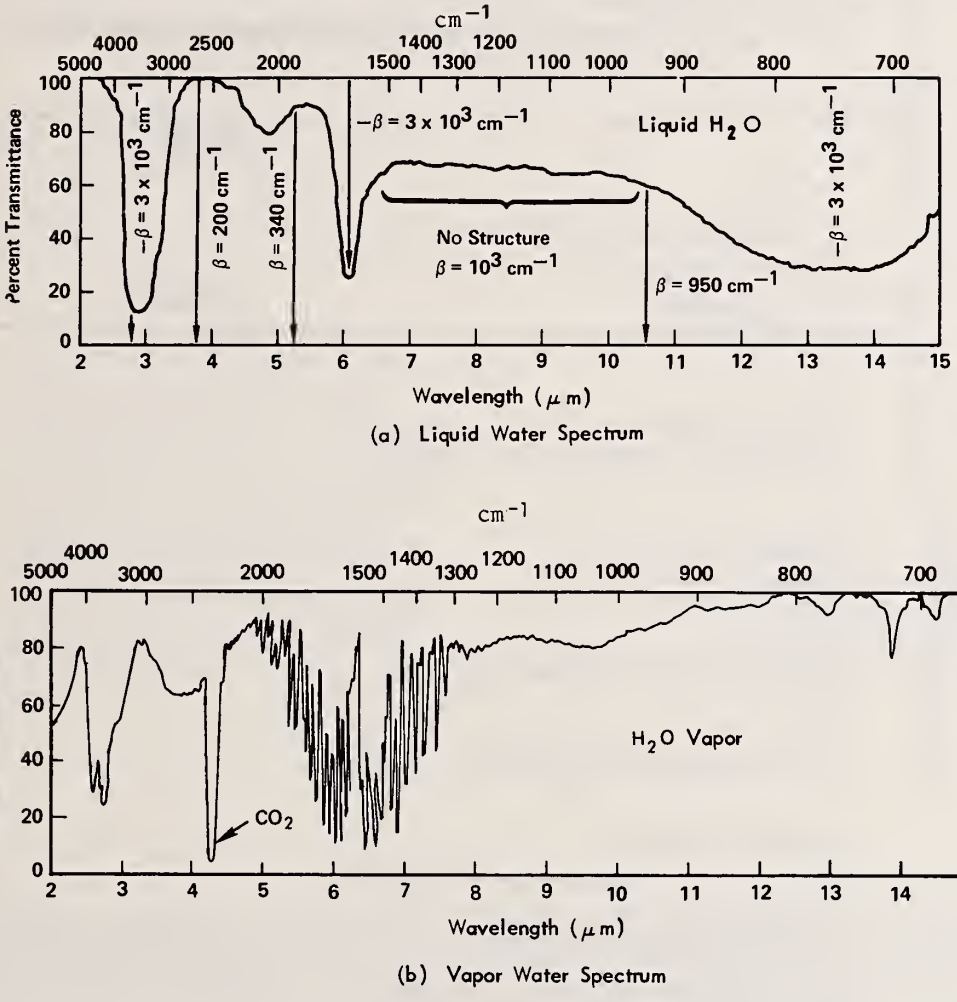

Figure 1. Transmission spectra of (a) liquid water and of (b) water vapor [2].

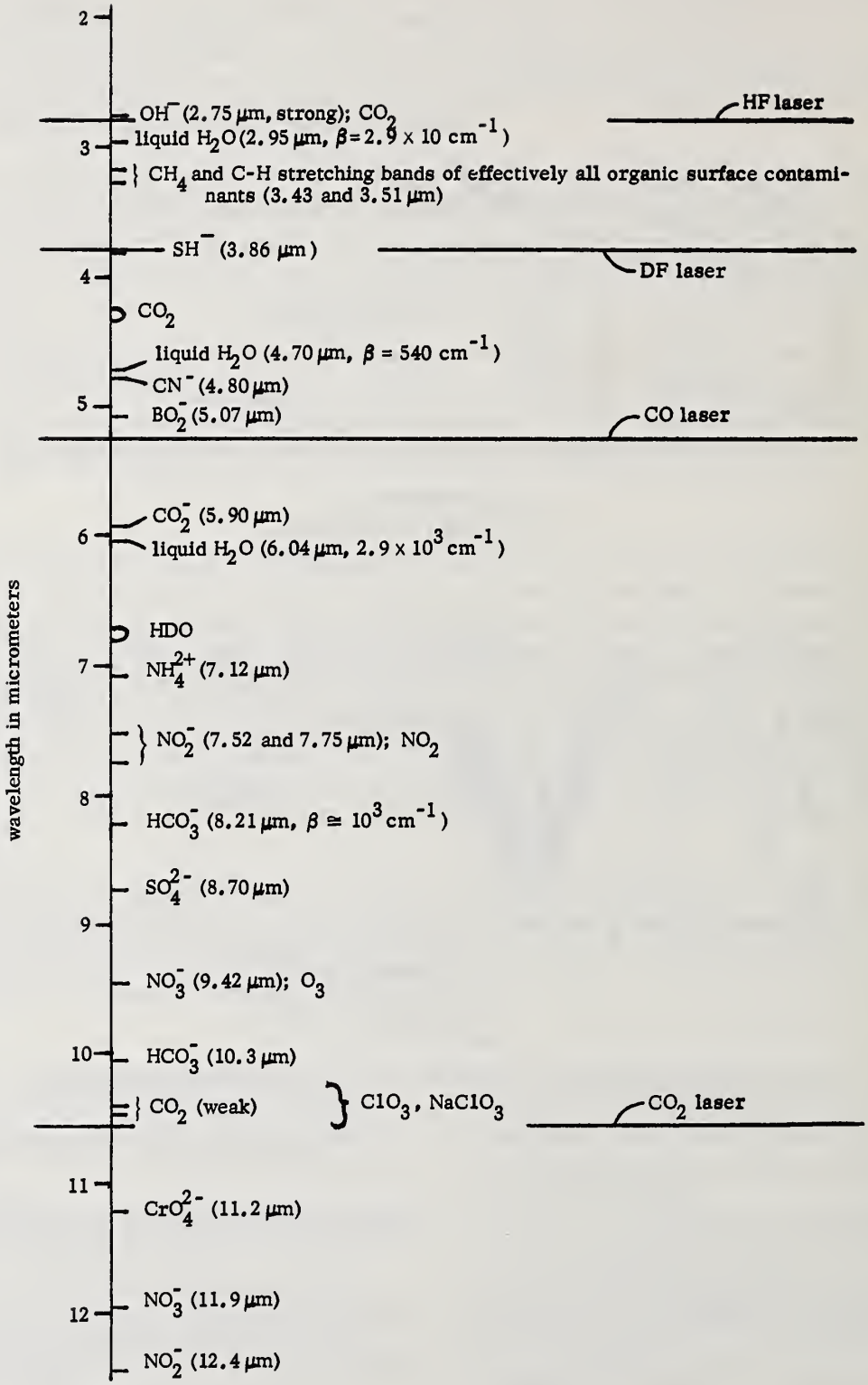

Figure 2. Positions of absorption peaks of some possible coating contaminants.

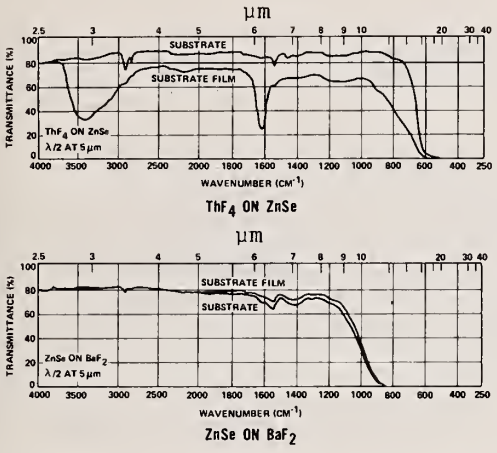

Figure 3. Attenuated-total-reflection spectra [7]. (a) This ATR spectrum for a ThF_4 coating deposited on a ZnSe substrate clearly shows the spectrum of contaminating water. (b) This ATR spectrum of ZnSe on BaF_2 illustrates the difficulty of interpreting ATR-spectrum results (an apparent <u>increase</u> in transmittance when the coating was deposited) and illustrates a decrease in transmittance with increasing wavelength probably resulting from a lack of total internal reflection.

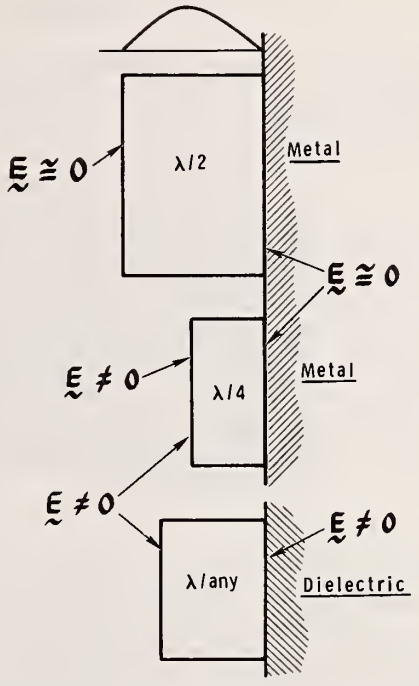

Figure 4. Schematic illustration of coatings used to distinguish between absorption at the film surface, in the bulk of the film, and at the film-substrate interface.

COMMENTS ON PAPER BY SPARKS

*The question was raised about evidence of water contamination in thin films, as a function of deposition conditions. Hal Bennett of the Michelson Laboratory indicated that by use of ellipsometry, one can detect a single monolayer of H_2O on films down to a vapor pressure of 10^{-3} torr of H_2O. This monolayer seems to be in equilibrium, and a second layer does not immediately form. He indicated that this observation is in substantial agreement with the Brunauer-Emmett-Teller theory.**

Morris Braunstein of Hughes Research Laboratory indicated that in a study of ThF_4 films carried out at Hughes by Dave Zuccaro, H_2O absorption was detected unless ultra-high vacuum deposition techniques were used. It was agreed that calorimetric or ATR measurements are much more sensitive than spectroscopy for detecting weak impurity absorption.

C. B. Willingham of Raytheon reported observable water absorption in the ZnS films detected by ATR. He also commented that the presence of impurities in the coating process can lead to alterations of the film structure, resulting in porous films.

* *Handbook of Physics*, 2nd Edition, E. U. Condon and H. Odishaw, Eds. (McGraw-Hill, New York, New York, 1967) pp. 5-96 to 5-115.

3.2 ALTERNATE MATERIALS FOR INFRARED WINDOW COATINGS

A. D. Baer, T. M. Donovan, A. K. Green and G. Turner
Michelson Laboratories, Naval Weapons Center
China Lake, California 93555

The results from studies of a number of new materials (NaF, SrF_2, and As_2Se_3) to be used in antireflectance coatings for KCl and NaCl windows are reported. The preparation and measured properties of thin films of these materials are reported. The properties studied include absorption at 10.6 μm, scattering, structure, index of refraction, and damage threshold. NaF is a promising material in that it has a relatively low absorption and high damage threshold and can be used as a single-layer antireflectance coating on NaCl. The properties of NaF films are good enough that this material can be used as a component of 10.6 μm coatings. SrF_2 films are higher absorbing, but less easily damaged than BaF_2 films. As_2Se_3 films are more easily damaged than As_2S_3 films.

Key words: Alkali halides; antireflectance coating; chalcogenide glasses; infrared optical properties; laser damage; optical absorption; optical scattering; thin-film coating.

Introduction

Laser systems utilize thin-film coatings to create high- and low-reflectance surfaces. At present, the performance of optical coatings in a system limits the power-handling capability of that system. Improvement in coating performance has been sought by investigating design [1-3][1], thin deposition [4-6], and the properties of new materials [7]. It is important to identify new materials with properties which can be used in optical coatings because it may be impossible to fabricate a viable coating with standard materials. The work reported here includes a study of thin films for some materials which have not been studied thoroughly heretofore, with special emphasis on the performance of these materials as composites of 10.6 μm antireflectance (AR) coatings for NaCl and KCl.

Thin films of only a few of many promising materials have been studied carefully [8]. An earlier study was performed on Ge, MgF_2, As_2S_3, BaF_2, and ZnS; results indicated that As_2S_3 and BaF_2 were the best choices for multilayer coatings at 10.6 μm wavelengths based on the protective and power-handling capabilities [9]. More recent work with 10.6 μm AR coatings has stressed the use of ThF_4, BaF_2, ZnS, ZnSe, As_2S_3 and TlI [10-14]. Thin films of the lanthanide fluorides have been studied very recently [7 Properties of NaF, SrF_2, and As_2Se_3 are discussed and compared in this paper with the properties of BaF_2 ThF_4, and As_2S_3 thin films.

Many of the properties of NaF are consistent with its use as an optical coating at wavelengths of 10.6 μm. Its index of refraction at 10.6 μm is 1.23, very close to the square root of the index of refraction for NaCl [15,16]. Consequently, a single layer of NaF, a quarter-wave thick, would almost totally eliminate reflections of 10.6 μm light from a NaCl surface. This is the simplest possible design for a broad-band AR coating. Moreover, NaF appears to perform well with high-intensity pulses of light; a study of the performance of NaF with 1.06 μm light in 30 ps pulses showed that the damage threshold of NaF is exceptionally high, and the nonlinear index of refraction is exceptionally low [17]. One possible disadvantage of NaF is its relatively high solubility in water; however, the solubility of NaF though large is only .12 of NaCl's [16], and NaF films can be used in applications where the humidity of the environment can be controlled.

Low water solubility is an important advantage of both As_2Se_3 and SrF_2. The solubility of SrF_2 is 0.1 that of BaF_2 and 3×10^{-4} that of NaCl [15,16] while As_2Se_3 is insoluble in water [18]. Moreover, As_2Se_3 and SrF_2 also seem promising because similar materials (As_2S_3 and BaF_2) have been used successfully as composites of AR coatings at wavelengths of 10.6 μm [9]. The indices of refraction for these materials are such that a zero-reflectance coating on NaCl or KCl must consist of two or more layers. In order to further verify the usefulness of these materials, low-absorbing three-layer coatings [1-3] composed of As_2S_3 and ThF_4, and of As_2Se_3 and NaF were designed, fabricated, and tested. An As_2Se_3/NaF/As_2Se_3 with 10.6 μm absorptance of .06% is reported below. This absorptance is lower than that of an $As_2S_3/ThF_4/As_2S_3$ coating (1.2%), because NaF is lower absorbing than ThF_4.

Experimental

Thin films of NaF, SrF_2, BaF_2, ThF_4, As_2S_3, and As_2Se_3 were deposited on NaCl and KCl windows, then evaluated with calorimetric and transmission measurements. Transmission electron microscopy, total integrated scatter, and laser damage measurements were performed on selected films. The measurements

1. Figures in brackets indicate the literature references at the end of this paper.

and sample preparation were standardized as much as possible to facilitate comparison of the performance of the various materials.

Single-crystal NaCl and KCl windows, 38.6 mm in diameter, were obtained from Harshaw Chemical Co. These windows were etched for three minutes in concentrated HCl prior to deposition. The absorptances of these windows after the etch, but prior to deposition, were 3-8 x 10^{-4} for the KCl windows and 7-15 x 10^{-4} for the NaCl. The [100] direction of the crystalline lattice in the windows was found to diverge at least 7° from the direction normal to the face of the window. All samples were handled and stored in the same way.

Depositions were performed in two different trapped, diffusion-pumped vacuum systems and an ion-pumped system according to the conditions outlined in table 1. The evaporators were loaded with materials from the following sources: pure As_2S_3 and As_2Se_3 provided by Cerac, and single crystals of NaF, SrF_2, and BaF_2 prepared by Harshaw Chemical Co. As table 1 shows, different sources and conditions were employed for different films. In order to compare pairs of materials, some As_2S_3 and As_2Se_3 films and some BaF_2 and SrF_2 films were deposited in the same systems under identical conditions. The properties of these paired films are those discussed in the following section. NaF was prepared in all three deposition systems with equivalent performance for films prepared in two of the systems, but with high absorptance for films prepared in the third system. Water absorption bands were visible in the transmittance traces of the highly absorbing films. Measurements on NaF films reported here were performed on those samples for which water absorption bands were not visible in the transmission traces.

Spectral dependence of transmission was measured using a Perkin-Elmer 180 spectrophotometer, a two-beam instrument. All but one of the transmittance measurements reported here are absolute. An uncoated KCl window was placed in the reference beam when the transmittance of the As_2Se_3 film deposited on a KCl window was measured. For this measurement, 100% transmittance is defined as the transmittance of an uncoated window.

Table 1. Deposition conditions for thin films.

Material	Source	Substrate Temperature	Base Pressure (Pa)	Deposition Pressure (Pa)	Deposition Rate (nm/s)
As_2S_3	Quartz Flask with Tantalloy Element, E Beam	75°C	$< 10^{-6}$	7×10^{-4}	0.5-2
As_2Se_3	Quartz Flask with Tantalloy Element, E Beam	75°C	7×10^{-6}	7×10^{-4}	0.5
ThF_4	Mo Boat 150 A	150°C	7×10^{-6}	1×10^{-4}	0.5-5
NaF	E-gun, Mo Boat, and Bn Crucible	75°C	7×10^{-6}	11×10^{-4}	0.1
SrF_2	C-Crucible	340°C	1×10^{-5}	7×10^{-4}	0.1
BaF_2	C-Crucible	150°C (25°-340°C)	1×10^{-5}	7×10^{-4}	0.3-3

Absorptances of the windows were measured calorimetrically before and after coatings were applied. This was done by measuring the rate of temperature rise due to power absorbed with a 60 watt beam of light in a 10.6 μm laser [10,14,19]. The beam, 6 mm in diameter, was shown through the center of the window. Absorptance measurements were performed three times, the window being rotated by 120° about its axis between measurements; the absorptance of the sample was taken as the average of these measurements and the uncertainty of the absorptance was defined as the standard deviation of the measurements. The spread in the three values of absorptance, 1-8 x 10^{-4} with typical values of 4 x 10^{-4}, appears to be due to nonuniformity in the windows. These uncertainties can amount to as much as 80% of the value of low absorptance coatings and are the primary limitation of the accuracy of the absorptance measurement. Consequently, the 1-2% corrections associated with the non-ideal heat flow in the 38.6 x 6 mm windows has been neglected [20]. In estimating the absorption constant from absorptance, interference effects have been included [10,21]. These estimates are accurate to 10% when not limited by substrate nonuniformity. When the standard deviation due to nonuniformity is significant, it will be given explicitly.

Laser damage measurements were performed using 100 ns pulses from a CO_2 TEA laser focused to a 200 μm spot as has been discussed elsewhere [22,23]. These data are included to illustrate their correlation with optical properties of the films. With the exception of NaF films where a range of damage thresholds are given, the laser damage and absorptance values reported below were measured on the same films.

Properties of Single Layers

Transmittance spectra of windows coated with thin films of NaF and As_2Se_3 are presented in figures and 2. The clean fringe patterns displayed by these curves show that the films are not heavily contaminated with impurities. The transmittance curves peak at the 100% line across the infrared band, indicating the films absorb less than 5×10^{-3} from 2.5 to 12 μm. The flatness of the NaF transmittance curve around wavelengths of 10.6 μm illustrates the broadband AR action for a single layer of NaF. Indices of refraction of BaF_2 and SrF_2 are close enough to those of KCl and NaCl that strong fringes are not present. Some of our BaF_2 and SrF_2 films showed water absorption bands. All films of these two materials were deposited in one particular deposition system. It may be that all films of these materials are significantly contaminated with water, even though structure indicating water absorption is not present on the transmittance spectra. Water contamination could be the source of the high absorption constant found here for BaF_2 and SrF_2 thin films.

The absorption constants of most films studied here were substantially higher than constants for bulk samples of the same material. Absorption constants at 10.6 μm have been reported to lie between 0.5 and 1.5 cm^{-1} for bulk samples of As_2S_3, NaF, and SrF_2. While the absorption constants shown in table 2 for the As_2S_3 are close to bulk values, the constants for the NaF and SrF_2 films are far higher than the bulk values. The extra absorption in all polycrystalline films including NaF may be due to contamination of the films or may be associated with the interfaces between crystallites in the layers; in either case, it may be possible to reduce absorption in the films by optimizing deposition parameters.

Even so, the absorption constant of the NaF films is almost low enough that coatings with absorptances less than 5×10^{-4} can be produced. Coatings with such low absorptances will be possible if films with absorption constants less than roughly 2 cm^{-1} can be deposited; that is, the absorption constants in the NaF films must be reduced only a factor of three, in order to obtain a film with completely acceptable performance.

Table 2. Absorption constants and damage thresholds. Measured with 10.6 μm laser radiation. The range given for the threshold of NaF films represents damage thresholds for several films.

FILM/WINDOW	INDEX	$\beta(cm^{-1})$	(J/cm^2)
NaF/NaCl	1.23	6.0 ± 0.4	38 ± 7
ThF_4/KCl	1.35	10-12	---
SrF_2/KCl	1.36	25	194
BaF_2/NaCl	1.38	15	76
As_2S_3/NaCl	2.37	1.2 ± 0.6	38
As_2Se_3/KCl	2.72	1.1 ± 0.4	12

The damage thresholds of most films listed in table 2 are high enough that the films could be used in practical coatings. Thresholds of all the films except As_2Se_3 are comparable in size to the thresholds found for the best polished surfaces of windows: KCl windows, 73 J/cm^2 and NaCl windows, 110 J/cm^2 [23]. The damage thresholds of SrF_2 and BaF_2 films are actually the same or larger than the polished surfaces, although thresholds of films of the other materials are lower and should be increased if possible.

The shape of the damage sites in the As_2S_3 films indicates a way in which the damage thresholds might be increased. At each damage site one or more damaged areas were present which were centered about small pits, the same size and density of μm-sized defects in the films. Apparently the defects nucleated the damage. It was difficult to determine the shape of the defects through a microscope; however, similar defects found in annealed As_2S_3 films were large enough to show facets characteristic of crystalline structure. Crystallites of As_4S_3 have been reported in As_2S_3 films grown by physical vapor deposition [26]. The μm-sized defects in our films may be of similar origin, but whatever the nature of the defects, their number and size is a strong function of deposition conditions and surface preparation of the window. Consequently, there is a good chance that a way can be found to produce films with fewer defects and which have a higher damage threshold.

A second interesting aspect of the data listed in table 2 is that the damage thresholds are not inversely correlated with linear optical absorption. If the films were damaged because of thermal effects associated with linearly absorbed power, one would expect that a high absorptance would produce

a low damage threshold. This is exactly opposite to the trend indicated by the data in table 2; high damage thresholds were found for films with high absorption constants. We interpret this as showing that pulse-damage thresholds are not related to linear absorption. Rather, the critical parameter is the magnitude of the electric field in the material as found by Bettis and coworkers in their 1.06 μm damage studies [24,25]; the damage thresholds at 10.6 μm do tend to be inversely correlated with index of refraction as suggested by these authors.

Optical scattering is another physical process which could limit the performance of coatings. This is a very real possibility for materials such as NaF which usually form polycrystalline thin films. Interfaces between the crystallites cause optical scattering. NaF films, 2.16 μm thick, were deposited on unoriented single-crystal windows and on windows oriented with their faces normal to the [100] direction. The performance of films deposited on unoriented windows is emphasized here; however, we did find that films deposited on oriented windows were not polycrystalline while those deposited on unoriented windows were polycrystalline with crystallite sizes on the order of 250 nm. These polycrystalline films scattered enough visible light that they had a hazy blue cast, but apparently the crystallites are small enough that the infrared light is not significantly scattered. Measurements of the total integrated scatter of NaF films deposited at two different temperatures are listed in figure 3. About 10^{-4} of the incident beam was scattered by the films deposited at 75°C. Consequently, for applications at wavelengths longer than 3 μm optical scattering does not appear to be a serious performance limitation of polycrystalline films.

Antireflectance Coatings

Two- and three-layer antireflectance coatings composed of the films studied here were deposited on KCl windows and the absorptance and transmittance of each window was measured. The measured absorptances are listed in figure 4 along with that of a single, quarter-wave thick layer of NaF and the calculated absorptance of the films. The calculations were performed assuming that the absorption constants of the layers in the multilayer coatings were equal to those measured for the same materials deposited as single layers [2]. Except for the $As_2S_3/ThF_4/As_2S_3$ coating, the calculated and measured absorptances are essentially equal. This shows that the films can be deposited in multilayer configurations with the same absorptive properties as in single layer configurations. The absorptance of a single NaF layer can be seen to be somewhat high. The advantage of the three-layer configurations is obvious; the actual absorptance of the three-layer coating is half that of the two-layer coating, and the theoretical absorptance is less than one-third that of the two-layer coating. The absorptance of the coating composed of As_2Se_3 and NaF is lowest because of the lower absorption constants of these materials.

Transmittance spectra measured on the two three-layer coatings are shown in figures 5 and 6. The clean shapes of these curves show that contamination of these coatings is low. By comparing these figures with figure 1, the bandwidth of the AR action of the three-layer coatings can be seen to be less than that of a single, quarter-wave layer of NaF.

Conclusions

Both SrF_2 and NaF show promise for applications as components of multilayer coatings for use with infrared lasers. SrF_2 films have a very high damage threshold and an absorption constant which can be reduced. NaF films function well as a single-layer AR coating on NaCl and have the damage threshold and absorption constant almost good enough; deposition conditions for improved NaF films may well be discovered. Optical scattering of the polycrystalline films is not an important limitation on performance of the films in the far infrared. The damage threshold of As_2Se_3 is quite low; unless a way is found to deposit As_2Se_3 films with a substantially higher damage threshold, As_2S_3 is a better material for high-index layers in multilayer coatings.

Acknowledgments

The authors gratefully acknowledge the technical assistance and advice of P. C. Archibald, E.J. Ashley, C. L. Barker, D. L. Burdick, J. H. Dancy, and M. J. Soileau as well as the suggestion that NaF films be studied by W. Reichelt. This work was supported by the Defense Advanced Research Projects Agency, the Energy Research and Development Administration, and the Naval Weapons Center independent research funds.

References

[1] Braunstein, M. et al. in *Proceedings of the Fifth Annual Conference on Infrared Laser Window Materials: 1975*, C. R. Andrews and C. L. Strecker, eds. (Defense Advanced Research Projects Agency, Arlington, Va., 1976), p. 135.

[2] Baer, A. D., "Design of Three-Layer Antireflectance Coatings," these Proceedings.

[3] Starling, J. et al. in *Proceedings of the Fifth Annual Conference on Infrared Laser Window Materials: 1975*, op. cit., p. 144.

[4] Golubovic, A. et al. in *Laser Induced Damage in Optical Materials: 1974*, A. J. Glass and A. H. Guenther, eds. (NBS Spec. Publ. 414, 1974), p. 76.

[5] Golubovic, A. et al. in *Laser Induced Damage in Optical Materials: 1975*, A. J. Glass and A. H. Guenther, eds. (NBS Spec. Publ. 435, 1975), p. 236.

[6] Baer, A. D. et al. in *Laser Induced Damage in Optical Materials: 1975*, op. cit., p. 244.

[7] Golubovic, A. et al. in *Proceedings of the Fifth Annual Conference on Infrared Laser Window Materials: 1975*, op. cit., p. 168.

[8] Black, P. W. and J. Wales, Infrared Physics 8, 209 (1968).

[9] Young, P. A., Thin Solid Films 6, 423 (1970).

[10] Willingham, C. B. et al. in *Proceedings of the Fifth Annual Conference on Infrared Laser Window Materials: 1975*, op. cit., p. 356.

[11] Braunstein, A. I. et al. in *Laser Induced Damage in Optical Materials: 1973*, A. J. Glass and A. H. Guenther, eds. (NBS Spec. Publ. 387, 1973), p. 151.

[12] Chaffin, J. H. and R. A. Skogman in *Proceedings of the Fifth Annual Conference on Infrared Laser Window Materials: 1975*, op. cit., p. 155.

[13] Donovan, T. M. and A. D. Baer in *Proceedings of the Fifth Annual Conference on Infrared Laser Window Materials: 1975*, op. cit., p. 291.

[14] Gibbs, W. E. K. and A. W. Butterfield, Appl. Opt. 14, 3043 (1975).

[15] Dickinson, S. K. in *Infrared Laser Window Materials Property Data for ZnSe, KCl, NaCl, CaF_2, SrF_2 and BaF_2* (Air Force Cambridge Research Lab, Bedford, Mass., AFCRL-TR-75-0318, 1975).

[16] Moses, A. J. in *Handbook of Materials Properties, Vol. 1* (Plenum Press, New York, 1971).

[17] Smith, W. L. et al. in *Laser Induced Damage in Optical Materials: 1975*, op. cit., p. 321.

[18] *Handbook of Chemistry and Physics*, R. C. Weast, ed. (Chemical Rubber Co., Cleveland, Ohio, 1969), p. B-83.

[19] Loomis, J. S. in *Laser Division Digest* (Air Force Special Weapons Center, Kirtland AFB, N. Mex., TR-LRD-72-1, 1972), p. 29.

[20] Bernal, Enrique G., Appl. Opt. 14, 314 (1975).

[21] Baer, A. D. in *High Energy Laser Mirrors and Windows* (Naval Weapons Center, China Lake, Ca., NWC-TP-5845, 1976), p. 120.

[22] Soileau, M. J. et al. in *Proceedings of the Fifth Annual Conference on Infrared Laser Window Materials: 1975*, op. cit., p. 391.

[23] Soileau, M. J. et al., "Laser Damage Studies of Low Index Coating Materials at 10.6 μm," these Proceedings.

[24] Bettis, J. R. et al. in *Laser Induced Damage in Optical Materials: 1975*, op. cit., p. 289.

[25] Bettis, J. R., et al. in *Laser Induced Damage in Optical Materials: 1974*, op. cit., p. 214.

[26] Braunstein, M. et al. in *Laser Window Surface Finishing and Coating Technology* (Hughes Research Laboratories, Malibu, Ca., AFCRL-TR-74-0425, 1974), pp. 15-19.

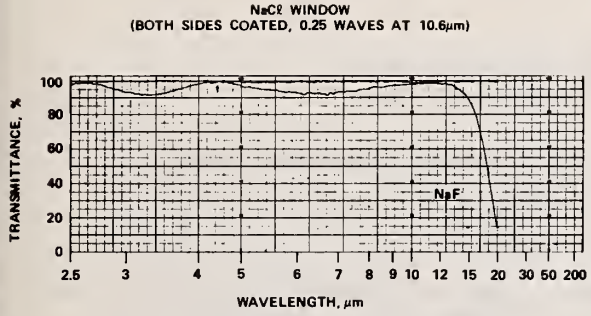

Figure 1. Absolute transmittance measured on a NaCl window coated with a 2.16 μm thick layer of NaF on both sides.

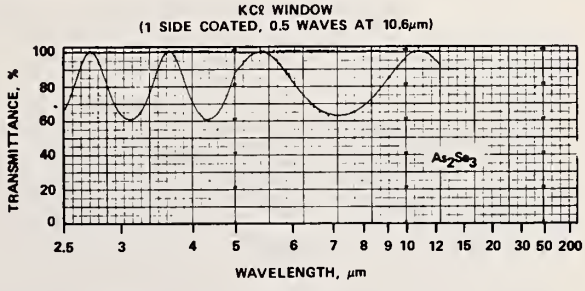

Figure 2. Relative reflectance of a KCl window coated on one side with a 2.24 μm thick layer of As_2Se_3. The transmittance is ratioed to that of an uncoated KCl window.

WAVELENGTH, μm	T, °C (DEPOSITION)	FORWARD
3.39	RT	5.49×10^{-4}
3.39	75°	1.06×10^{-4}
10.6	RT	5.28×10^{-3}
10.6	75°	1.33×10^{-4}

Figure 3. Total integrated scatter measured on KCl windows coated with a 2.16 μm thick layer of NaF. Films were deposited at room temperature (RT) and 75°C.

LAYERS	MATERIALS	ABSORPTANCE, 10^{-3} (MEASURED)	ABSORPTANCE, 10^{-3} (CALCULATED)
1	NaF	1.8	—
2	As_2S_3/ThF_4	2.5	2.5
3	$As_2S_3/ThF_4/As_2S_3$	1.2	0.7
3	$As_2Se_3/NaF/As_2Se_3$	0.6	0.5

Figure 4. Calculated and measured absorptance of 10.6 μm light for various types of antireflectance coatings. The multilayer coatings were deposited on KCl windows and the NaF coating was deposited on an NaCl window.

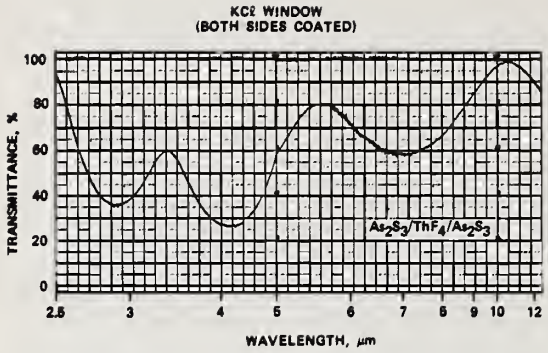

Figure 5. Absolute transmittance measured on a KCl window coated on both sides with an $As_2S_3/ThF_4/As_2S_3$ coating.

Figure 6. Absolute transmittance measured on a KCl window coated on one side with an $As_2Se_3/NaF/As_2Se_3$ coating.

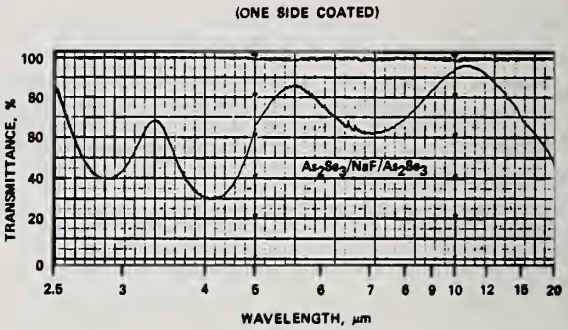

COMMENTS ON PAPER BY BAER, DONOVAN, GREEN, AND TURNER

It was pointed out that low intensity absorption measurements need not correspond to the absorption which causes damage at high intensity. Nonlinear absorption processes may play an important role.

3.3 DESIGN OF THREE-LAYER ANTIREFLECTANCE COATINGS

A. D. Baer
Michelson Laboratories, Naval Weapons Center
China Lake, California 93555

Design constraints are less stringent for three-layer coatings than for two-layer coatings. Mathematical relationships which govern the design of three-layer antireflectance coatings are presented. These new relationships are analogous to those governing the design of two-layer coatings; however, a continuous range of solutions exists. Three-layer solutions are represented by closed curves in coating-thickness space, while two-layer solutions are represented by two discrete points. Armed with a knowledge of the performance of similar designs with similar materials, one can select the three-layer solution with lowest absorptance (within 10%). Three-layer coatings offer greater design flexibility than two-layer coatings not only because of the wider-range of solutions, but also because of a wider choice of viable materials. Three-layer antireflectance coatings can be formed entirely of low-index materials (BaF_2, NaF), or with the low index material next to the window (As_2S_3, NaF).

Key words: Absorptance; antireflectance coating; bandwidth; coating design; multilayer coating.

1. Introduction

Three-layer antireflectance coatings have been receiving attention recently because, at infrared wavelengths, the coatings have lower absorptances than do other antireflectance coating [1-3][1]. For example, consider coatings composed of NaF and As_2Se_3 thin films. The calculated absorptance is 0.2% for the best two-layer coating, but only 0.05% for the best three-layer coating. The absorptance of the three-layer coating is lower because the third layer makes it possible to partially compensate for the high NaF absorption [1,2]. As illustrated by this example, design flexibility is the primary advantage of three-layer coatings, although the nature of the flexibility is not well understood. The present work aims to clarify three-layer design by detailing the properties of solutions of the three-layer design problem, and by showing how the performance of the various three-layer coatings can be systematically investigated.

Three-layer antireflecting coatings have been designed using several approaches. One approach sets the thicknesses of the layers equal to a quarter wavelength, and determines conditions on the indices of refraction which must be satisfied for the reflectance to be zero [4,5]. It is usually not possible to find a set of materials for which these conditions are satisfied exactly, so that in practice the reflectance of the coatings will not be zero, although it may be quite small. This method of design is at a disadvantage if only a few viable coating materials are available, and if coatings with extremely low loss must be produced. Coatings with lower loss can be obtained if the thicknesses of the layers are not restricted *a priori*. Design without such restrictions has been done using two approaches: a computer optimization method [1,2], and the Thetford method [5,6]. The computer optimization method determines layer thicknesses for which loss in the coatings is minimized; this method has the advantage that a minimum-loss design can be determined even if a zero reflectance solution does not exist. The Thetford method determines layer thicknesses for zero reflectance by utilizing vector calculations, an approximate method, and a systematic trial-and-error approach. A third method, used here, is based on closed form equations not previously published, which give solutions for zero reflectance at one wavelength; the advantage of this method is that a single calculation gives a layer thickness, and that all solutions which exist can be determined and examined.

2. Design Equations

The following development of three-layer design parallels the textbook developments of two-layer design [4,5]. The materials are assumed to be lossless, and two equations are derived which must be true if the reflectance of the coating is to be zero. A zero-reflectance requirement sets two conditions because both the real and imaginary components of the Fresnel coefficient must vanish. The two conditions are expressed in the form of two equations which determine families of solutions; solutions with layer thicknesses differing by a half-wavelength belong to the same family. Layer thicknesses for

1. Figures in brackets indicate the literature references at the end of this paper.

each family of solutions are determined by a three-step calculation which utilizes the two equations. The following symbols will be used in the design equations:

$i = \sqrt{-1}$	
n_j	index of refraction of layer j
r	Fresnel reflection coefficient
r_{jk}	Fresnel coefficient of isolated interface
δ	phase of Fresnel coefficient
λ	wavelength in free space
t_j	thickness of layer j (meters)
X_j	optical thickness of layer j (wavelengths)

The Fresnel coefficient for an isolated interface is [5]

$$r_{jk} = (n_j - n_k)/(n_j + n_k). \tag{1}$$

The optical thickness is

$$X_j = n_j t_j/\lambda. \tag{2}$$

The various media associated with the three-layer configuration will be numbered as shown in figure 1. The two equations to be derived will relate X_2 and X_1 (or equivalently t_2 and t_1) in terms of X_3 and the r_{jk} for the three interfaces shown in figure 1.

These equations follow directly from Smith's theorem [5-8]. This theorem is derived by asking what conditions must be satisfied in order for the transmission of a multilayered structure to be unity. The structure is divided conceptually into two parts and the Fresnel coefficients for reflections from each part are examined. Reflectance will be zero only if the magnitudes and phases of the two coefficients are related as shown in figure 2. Derivation of design equations will consist of determining r_a and r_b, and then using the relationships in figure 2 to establish the equations.

In invoking Smith's theorem we are already assuming that the various materials are lossless. If this is a bad assumption, the thicknesses we calculate will be wrong, and the reflectance of the coating will not be close to zero when the materials have their normal amount of absorption. A coating of particular design can be tested by calculating the reflectance of the coating, putting in reasonable values for the absorption constants. This has been done for several designs using standard computer programs; the reflectance at the chosen wavelength was less than 10^{-5} for these designs. For the low loss materials used in these designs (absorption constant less than 10 cm^{-1}), design errors due to the assumption of losslessness are completely negligible. Losses will be neglected throughout the development of the design equations, and added back in later when performance is calculated.

In applying Smith's theorem, we will conceptually divide the three-layer coating at its center layer. The structure remaining on either side consists of a single thin film separating two media. The formula for the Fresnel coefficient of this kind of structure is well known [4,5], and in the notation used here gives

$$r_a = \frac{r_{21} + r_{10}\exp(-4\pi X_1 i)}{1 + r_{21}r_{10}\exp(-4\pi X_1 i)} \tag{3}$$

$$r_b = \frac{r_{23} + r_{34}\exp(-4\pi X_3 i)}{1 + r_{23}r_{34}\exp(-4\pi X_3 i)}. \tag{4}$$

Smith's theorem states that the magnitudes of r_a and r_b must be equal. If one equates the square of the magnitude of these coefficients as given by eqs. (3) and (4), and then solves for X_1, he finds

$$X_1 = \pm \frac{1}{4\pi} \arccos\left[\frac{r_{21}^2 + r_{10}^2 - |r_b|^2 (1 + r_{21}^2 r_{10}^2)}{2r_{21}r_{10}(|r_b|^2 - 1)}\right]. \tag{5}$$

The phase constraint shown in figure 2 is a simplification of the requirement.

$$\cos(\delta_a + \delta_b - 4\pi X_2) = 1 \tag{6}$$

which reduces to

$$X_2 = \frac{1}{4\pi}(\delta_a + \delta_b + 2\pi m)$$

$$m = 0, \pm 1, \pm 2, \ldots \tag{7}$$

Equations (5) and (7) are the design equations which make it possible to compute the thicknesses of the layers in a three-layer antireflectance coating.

Before attempting to apply these equations, visualize the solutions plotted in three-dimensional space. The thickness of each layer is represented by a point. There are a series of solutions, the points falling on a line in layer-thickness space. Consequently, a range of solutions exists. In applying these equations, we will have to deal with the half-wavelength ambiguity of sinusoidal functions, and the sign ambiguity of an arc cos function, and the range of solutions. In order to select a single solution on a line, we will begin by picking a value for X_3.

The three steps in the calculation of layer thicknesses are as follows: (1) Select a value for X_3. (2) Use this value of X_3 and eq. (4) to compute r_b, then substitute the magnitude of r_b into eq. (5) and compute the two possible values of X_1. (3) Select one of the values of X_1 and compute r_a using eq. (3), then compute X_2 using the phases of r_a and r_b and eq. (7). In performing these calculations, make the X's lie between 0 and 0.5. This can be done by adding or subtracting 0.5 to the values. By keeping the X's between 0 and 0.5 we are selecting two lines of solutions, and in step (3) we select one of these two lines. The recipe given here will produce all solutions, (X_1, X_2, X_3), with layer thicknesses between 0 and 0.5. Because of the sinusoidal ambiguity, solution space has the same sort of symmetry as a crystal with translational periodicity of 0.5 wavelength. Consequently, solutions for values of X larger than 0.5 can be found by increasing the approximate X's an appropriate number of half wavelengths.

Half wavelength manipulation of solutions is possible because of a well-known property of lossless thin films: The reflectance of a stack of thin films does not change when the thickness of one of the films in the stack is changed by exactly half a wavelength. In the present case this effect manifests itself by the way X_1, X_2, and X_3 are involved in eqs. (4), (5), and (7). As far as these equations are concerned, $(X + 0.5)$ is the same as X. This is true because the equations are based on the reflectance of thin films of lossless materials at one wavelength.

If one considers absorption and spectral dependence in addition to the reflectance at one wavelength, then the solutions are no longer equivalent. Clearly, increasing the thickness of a layer by half a wavelength increases its absorption, and this increase will be at least $(\beta\lambda/2n)$, where β is the absorption constant of the material [9]. Solutions with the lowest absorptance must belong to the set of solutions with the thinnest layers, those with X between 0 and 0.5. Only these solutions will be considered in the remaining sections. Even without absorption, the spectral dependence of different thickness is different. This follows from eq. (2) which shows that a particular change in wavelength produces a change in X which is proportional to thickness. Reflectance is determined by the X's. Therefore, because $(dX/d\lambda)$ is smallest for the thinnest layers, coatings with the thinnest layers have the largest bandwidth.

3. High-Low-High Coatings

In this section solutions are presented for coatings with the indices of refraction of the layers ordered higher, lower, and higher than that of the window. Figure 3 shows an example of this class of coating; it is typical of the three-layer coatings reported which have been studied for use on infrared windows. Although the equations derived in section 2 are quite general, only examples of coatings for which the outer and innermost layers are composed of the same materials will be presented here. Solutions for these examples are expected to be very similar to solutions for coatings composed of three different materials.

The graph in figure 3 is a plot of layer thicknesses for various solutions. This plot was created by selecting a value for X_3 and then calculating X_1 and X_2 using the recipe of section 2. Both X_1 and X_2 are plotted on the same graph as a function of X_3, X_2 being represented by the closed curve in the center of the graph, and X_1 being represented by the curves at the top and the bottom of the graph. For each choice of X_3 there are two choices for the pair, (X_1, X_2); the dashed lines in figure 3 represent one set of values, and the solid lines the other set of values. As an example of the use of these curves, we will find a solution for a coating with X_3 equal to 0.3, selecting the solution represented by the dashed lines, the values of the dashed curves at 0.3 gives X_2 equal to 0.04, and X_1 equal to 0.13. The graph in figure 3 represents every possible solution for which the X's are positive, but less than 0.5.

Since two-layer coatings are just special cases of three-layer coatings with a zero thickness for one layer, the two-layer solutions must be included with those plotted in figure 3. Examining figure 3, one finds that the X_1 curve crosses zero at two different values of X_3. It happens that the X_2 curve is single valued at this value of X_3, so that there are exactly two points (X_2, X_3) for which X_1 is equal to zero. These points are represented by triangles in figure 3, and are the solutions to the two-layer problem.

The solutions for a different high-low-high coating are shown in figure 4. Even though these solutions are for a different wavelength and different materials, the shapes of curves in figure 4 are strikingly similar to those of the curves shown in figure 3. There are two reasons for the similarity:

First, by dealing with X instead of t, we have eliminated all wavelength effects except changes in the index of refraction; and second, high-low-high coatings have similar solutions. Since solutions for high-low-high antireflectance coatings are so similar, one can obtain a good general understanding of the solutions and their performance by examining only a few examples.

Performance can be readily examined by using thickness of a layer to label a particular solution. Specification of the dashed or solid lines and specification of X_3 completely specifies the solution. In the performance studies which follow, X_3 will be used to label solutions, and a particular line of solutions will be examined.

The performance studies will be formulated as design problems. The first design problem is to select the solution with the lowest absorptance. If the typical coating materials are to be used (the low-index materials are most highly absorbing), an almost optimum coating can be selected using figure 4. The absorption constant of ThF_4 is six times that of As_2S_3 so that the solution with the lowest absorptance must be one in which the ThF_4 is thin. According to figure 4, X_2 is thinnest for solution 0.32 and this solution should have low absorptance, although it may not have the lowest possible absorptance because of absorption in the As_2S_3, and interference effects. The importance of these factors can be seen by examining the actual absorptance of the coating. Absorptances of the solutions represented by the dashed curves in figure 4 were calculated and plotted in figure 5. This was an exact calculation of absorptance, using realistic absorption constants for the materials. As shown in figure 5, the absorptance of solution 0.29 is lowest, although that of solution 0.32 is not much higher. Evidently the thickness of the highly absorbing middle layer is the factor which is most important in determining the absorptance of the coating.

In order to guess which solution has the lowest absorptance, one must know in a qualitative way how the absorptance depends on X_3. This dependence is determined by the refractive and absorptive properties of the materials. For the materials discussed above, the dependence of absorptance can be investigated by examining the dependence of X_2 on X_3, because X_2 is closely related to the absorptance. In figures 3 and 4, X_2 depends on X_3 in much the same way. With increasing X_3, X_2 decreases and reaches a broad minimum between 0.3 and 0.4. Moreover, the equations of section 2 show that the dependence of X_2 is determined by the relative sizes of the indices of refraction. This shows that the dependence of X_2 will be similar to that shown in figures 3 and 4 for any high-low-high coating, and if the low-index layer is highly absorbing, the dependence of the absorptance will be very similar to that shown in figure 5. The absorptance will reach a minimum for values of X_3 near 0.3, and will be close to minimum for a wide range of values of X_3 around the minimum. In particular, if X_3 is chosen to be 0.3, the absorptance will be close to minimum. Given this relationship, one does not have to perform an extensive calculation in order to identify the solution with the lowest absorptance. For all practical purposes, solution 0.3 will have the lowest absorptance. Of course this applies only to the absorptance of high-low-high coatings in which the absorption constant of the middle layer is substantially higher than those of the other layers.

The second design problem considered here is to select the solution with minimum absorptance, but which also has certain minimum bandwidth. Bandwidth is defined here in terms of loss due to reflectance and absorption in the coating. The spectral dependence of the loss of solution 0.3, dashed line of figure 4, is plotted in figure 6. The curve labeled "reflectance" includes only losses due to reflections while that labeled "total" includes loss due to absorption as well as reflection. Bandwidth will be defined as the width of the spectral region for which the total loss is less than 0.5%. A solution is to be found for which the bandwidth is larger than 1 μm.

The bandwidth of various dashed-line solutions from figure 3 were calculated using existing compute programs and plotted in figure 7. All effects, absorption and interference, are included in these calculations. Bandwidth is plotted as a function of X_3. As can be seen in figure 7, the bandwidth is greater than 1 μm for X_3 less than 0.095 and greater than 0.48. The optimum solution is the one for which X_3 falls in these ranges and has the lowest absorptance. According to figure 5, solution 0.095 has the lowest absorptance, 0.15%. The bandwidths calculated for the solid-line solutions are much narrower than those of the dashed-line solutions. As argued previously, any solution with X greater than 0.5 has a narrower bandwidth than that of a thinner, half-wave-equivalent solution. Therefore, solution 0.095 is the answer to the second problem.

The two design problems just discussed illustrate how performance can be systematically optimized using X_3 as a label. A second advantage to the present approach is that all three-layer solutions for which reflectance is zero are displayed. This makes it possible to determine the existence of solutions to various problems. For example, suppose that given the materials in figure 4, one were attempting to design a symmetrical three-layer combination with a Herpin equivalent index such that the combination would serve as an antireflectance coating for the window [4]. The critical requirement is that X_1 and X_3 be equal. Since there is no solution in figure 4 for which X_1 is equal to X_3, no perfect symmetrical antireflection coating exists. As another example, suppose that one were attempting to design a three-layer coating such that the reflectance is zero at two different wavelengths. Figure 3 and 4 show that the solutions have only one degree of freedom. Since the requirement of zero reflectance at a second wavelength sets two additional constraints, the problem is overconstrained and there is no general

solution. Solutions exist only for particular choices of the indices of refraction. This analysis suggests that there are no solutions for which the reflectance is exactly equal to zero in either of these examples. These problems are best approached using some sort of computer program which determines solutions for minimum loss, given certain constraints.

4. Existence of Solutions

The existence of solutions help determine which mathematical approach will be most fruitful, and which materials can be used. In this section, degrees of freedom and constraints are discussed. Conditions on the index of refraction for existence of solutions will be set forth for three-layer coatings in which the outer and inner layers have the same index of refraction. These existence conditions are compared with those for two-layer antireflectance coatings composed of the same materials. With some materials combinations, it proves possible to form a three-layer antireflectance coating, but not a two-layer antireflectance coating. Solutions for a coating with one of these extra materials combinations are presented and discussed.

Each layer of a coating has two degrees of freedom, one degree for the index and one degree for the thickness of the layer. As discussed previously, the requirement that reflectance vanish at some wavelength eliminates two degrees of freedom. A one-layer antireflectance coating has two degrees of freedom and two constraints, leaving zero degrees of freedom. A solution exists only for a particular index and thickness. A two-layer antireflectance coating has four degrees of freedom and two constraints, leaving two degrees of freedom. If the thicknesses of the layers in the coating are not fixed, then solutions exist for pairs of indices of refraction which range over two-dimensional areas of layer-index space. This is utilized in the Schuster plot, discussed below, in which the two indices of refraction corresponding to a two-layer coating are plotted in order to determine whether a solution exists [4,5]. If, on the other hand, one fixes the indices of refraction by choosing materials, then there are zero degrees of freedom and the solutions are represented by points in layer-thickness space. A three-layer antireflectance coating has six degrees of freedom and two constraints, leaving four degrees of freedom. Even if the indices of refraction are fixed by choosing the materials, one degree of freedom remains and the solutions are lines in layer-thickness space. If the layer thicknesses are not fixed, then solutions exist over three-dimensional regions of layer-index space. In what follows, our attention will be limited to only those three-layer coatings for which the inner and outermost layers have the same index of refraction. In this case one degree of freedom has been eliminated as the existence of solutions to this three-layer problem can be determined using a two-dimensional plot directly analogous to the Schuster plot.

In order for a solution to exist, it must be possible to meet the requirements of Smith's theorem. These requirements are related to the indices of refraction by way of the various r_{jk} which appear in eqs. (3) and (4). Since the thickness of the middle layer can always be chosen so that eq. (7) is satisfied, the critical requirement is

$$|r_a| = |r_b| \ . \tag{8}$$

According to eqs. (3) and (4), the magnitudes of r_a and r_b vary periodically with X_1 and X_3, respectively. Each Fresnel coefficient assumes a range of values with the maximum and minimum value determined by the indices of refraction. If it is ever going to be possible to make eq. (8) true, then these ranges must overlap; that is, eqs. (9) and (10) must hold.

$$|r_a|_{max} \geq |r_b|_{min} \tag{9}$$

$$|r_b|_{max} \geq |r_a|_{min} \ . \tag{10}$$

When the magnitudes of r_a and r_b are maximum or minimum, they are real functions of the indices of refraction. Equations (9) and (10) can be reduced to a collection of simpler inequalities involving the indices of refraction. The derivation is lengthy and will not be reproduced here. Rather a graphical summary of the results will be presented.

Two-layer coatings and the class of three-layer coatings considered here are composed of two materials. Each set of materials is represented by a point on the graph of figure 8, with the ordinate given by the index of the material in the innermost layer, and the abscissa given by the index of the other material. Various lines divide the graph into regions. Most of these lines apply to both three- and two-layer coatings, but one line applies to only three-layer coatings. Existence of a solution depends on whether the point representing the coating falls into an appropriate region. When applied to two-layer coatings, this type of graph is the Schuster plot [5]. Two-layer coatings do not exist in the region marked with a question mark, but we have not determined whether three-layer coatings exist in this region. The inequalities required by eqs. (9) and (10) reproduce all the lines which apply to the two-layer coatings, but a third line, given by

$$n_o = \sqrt{n_m \sqrt{n_w}} \tag{11}$$

with the n's defined as shown in figure 8. This line and the horizontal dashed line define new regions in which three-layer solutions exist, but two-layer solutions do not exist. New combinations of viable

coating materials fall into one of these regions; that is, practical three-layer coatings can be formed from materials that cannot be used to form two-layer coatings.

Coatings composed of various practical infrared coating materials are represented by points on figure 8. The standard high-low-high coatings are represented by the three horizontal lines at values of n_o corresponding to ZnS, As_2S_3, and As_2Se_3. Points on these lines represent specific low-index materials. There are new combinations for which n_o must be less than the index of the window. Any high- or low-index material is suitable for the middle layer as long as its index is a bit larger than that of n_o Points falling on the line in the new region of figure 8 represents the combination of a variety of low-index materials with NaF. These low-medium-low combinations represent a new class of coating with new combinations of materials, and a different form of solution.

Solutions for one of the low-medium-low coatings are plotted in figure 9. The dependence of the thickness of the middle layer on X_3 is much the same as that of the solutions shown in figures 3 and 4. On the other hand, the dependence of X_1 on X_3 is quite different for the two types of coating. The "outer layer" curve in figure 9 never crosses the axis so that there is no solution for which the thickness of any layer vanishes. As advertised, there is no two-layer solution for this combination of coating materials.

The preceding discussion points out that additional materials combinations are possible with three-layer coatings and offer a guide to determining which particular combinations will work. Low-medium-low combinations may prove useful at infrared wavelengths because the damage threshold of low-index is higher than that of high-index materials. The combinations may also prove useful at ultraviolet wavelengths where transparent, high-index materials do not exist.

5. Acknowledgments

The author gratefully acknowledges the contribution of Dennis Burge and Joe Haberman, who employed their computer programs to calculate absorption, reflection and transmission of various optical coatings. This work was supported by the Defense Advanced Research Projects Agency, the Energy Research and Development Administration, and the Naval Weapons Center.

6. References

[1] Braunstein, M., et al., "Laser Window Surface Finishing and Coating Science," Semi-Annual Technical Report 2, AFCRL-TR-76-0048, Hughes Research Laboratories (1976).

[2] Braunstein, M., et al., in *Proceedings of Fifth Annual Conference on Infrared Laser Window Materials: 1975*, C. R. Andrews and C. L. Strecker, eds. (Defense Advanced Research Projects Agency, Arlington, VA., 1976), pp. 135-42.

[3] Baer, A. D., et al., "Alternate Materials for Window Coatings," these Proceedings.

[4] Cox, J. T. and Hass, G., "Antireflectance Coatings for Optical and Infrared Materials," *Physics of Thin Films*, Vol. 2, G. Hass and R. E. Thun, eds. (Academic Press, New York, 1964), p. 239.

[5] Macleod, H. A., *Thin Film Optical Filters* (American Publishing Co., Inc., New York, 1969).

[6] Thetford, A., Optica Acta 16, 37 (1969).

[7] Smith, S. D., J. Opt. Soc. Am. 48, 43 (1958).

[8] Smith's theorem is nowhere articulated in precisely the form used here, but is used in all the references cited. Following Macleod, we ascribe the theorem to Smith. It can be derived by writing down the expression for transmission in the lossless case, and determining the conditions which r_a and r_b must satisfy if the transmission is unity.

[9] Baer, A. D., "Absorption in Optical Coatings: Interference Effects," in *High Energy Laser Mirrors and Windows* (Semi-Annual Report No. 7-8, ARPA Order 2175, Naval Weapons Center, NWC TP 5845, 1976), pp. 128-35.

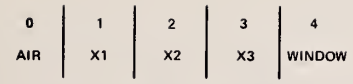

Figure 1. Numerical labels of the media associated with a three-layer coating. These labels are used in subscripts to denote layers or interfaces.

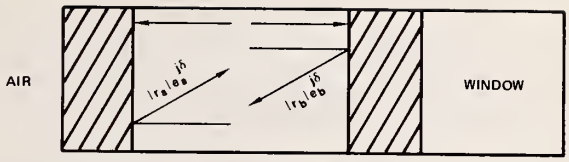

TRANSMISSION WILL BE 100%
IF AND ONLY IF

$$|r_a| = |r_b| \; ; \; 2\pi\left(\frac{nt}{\lambda}\right) = \frac{(\delta_a + \delta_b)}{2}$$

AND MEDIA ARE LOSSLESS

Figure 2. Mathematical conditions which must be satisfied for a coating to have no loss due to reflection or absorption of light.

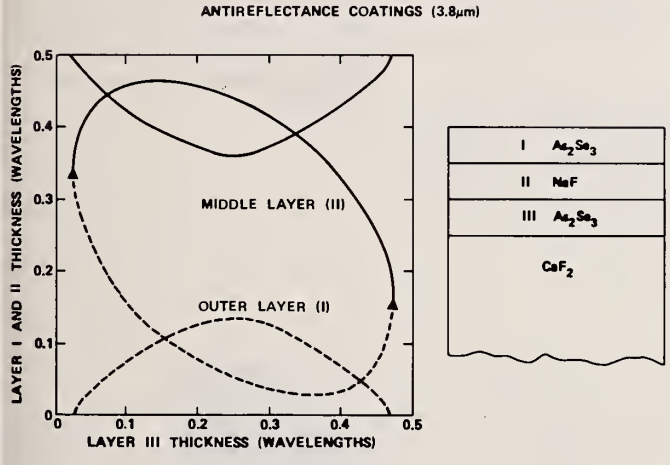

Figure 3. Antireflectance solutions for an $As_2Se_3/NaF/As_2Se_3$ coating deposited on a CaF_2 window. The wavelength of zero reflectance is 3.8 μm, and the indices of refraction were assumed to be 2.72 for As_2Se_3, 1.32 for NaF, and 1.41 for CaF_2.

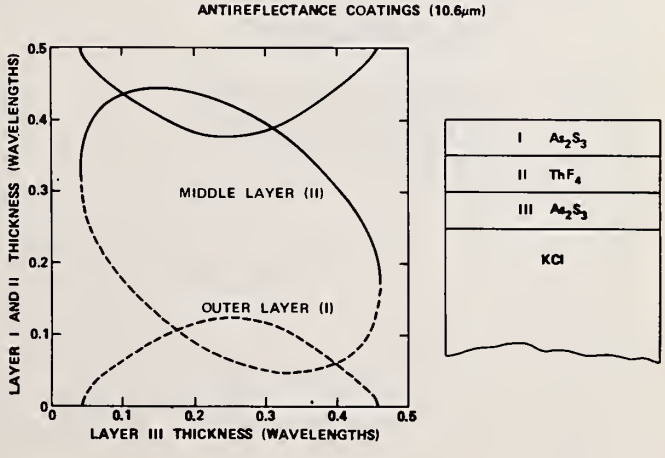

Figure 4. Antireflectance solutions for an $As_2S_3/ThF_4/As_2S_3$ coating deposited on a KCl window. The wavelength of zero reflectance is 10.6 μm, and the indices of refraction were assumed to be 2.37 for As_2S_3, 1.35 for ThF_4, and 1.46 for KCl.

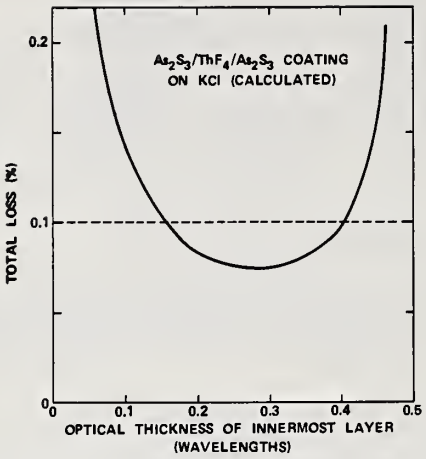

Figure 5. Calculated loss of the solutions plotted in figure 4. Reflectance losses were less than 10^{-5}. The absorption constants were assumed to be 1.7 cm^{-1} for As_2S_3 and 10 cm^{-1} for ThF_4.

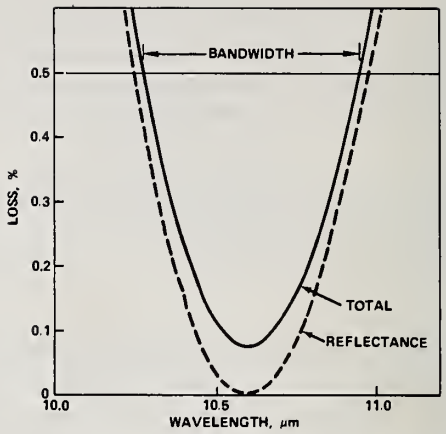

Figure 6. Spectral dependence of the total loss and the reflective loss of solution 0.3, dashed line, of figure 4. Transmission handwidth is defined as shown.

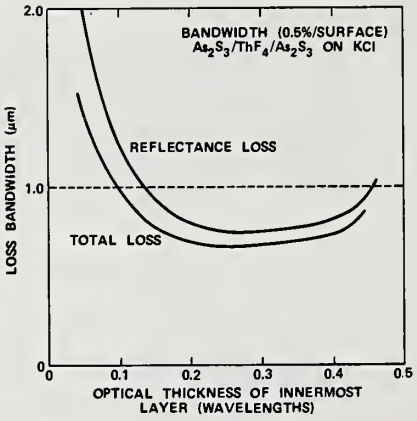

Figure 7. Transmission bandwidth of the solutions represented by the dashed lines in figure 4.

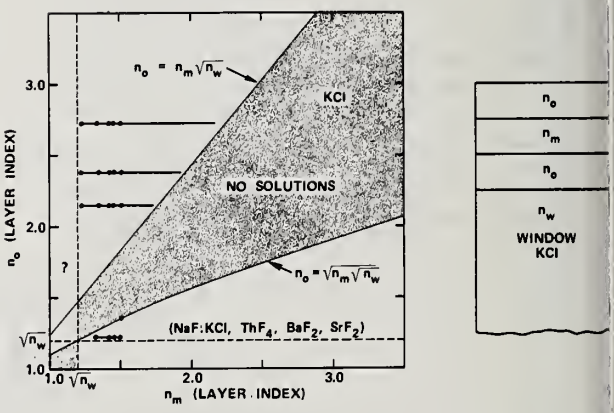

Figure 8. Plot for determining the existence of solutions to the three-layer problem for various combinations of coating materials. The window is KCl. The index of refraction of the outer and inner layers is n_o; the middle layer, n_m; and the window, n_w. Solutions exist when a point falls in one of the unshaded areas.

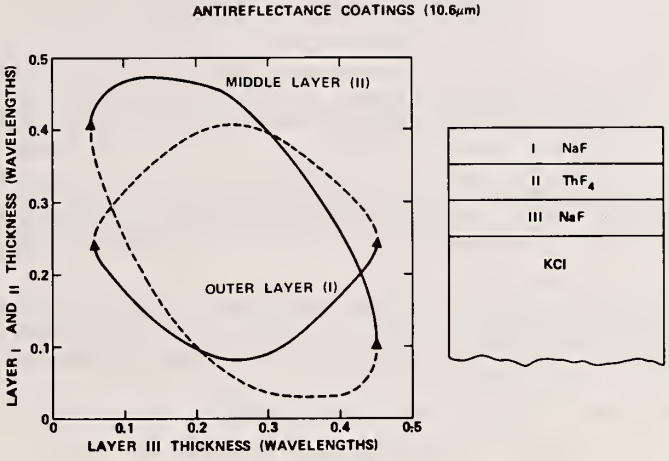

Figure 9. Antireflectance solutions for a NaF/ThF_4/NaF coating deposited on a KCl window. The wavelength of zero reflectance is 10.6 μm and the indices of refraction were assumed to be 1.32 for NaF, 1.35 for ThF_4, and 1.46 for KCl.

COMMENTS ON PAPER BY BAER

No discussion on this paper.

3.4 CHARACTERISTICS OF PLASMA POLYMERIZED ETHANE FOR LASER WINDOW COATING*

T. A. Reis, H. Hiratsuka, A. T. Bell, and M. Shen
Department of Chemical Engineering
University of California
Berkeley, California 94720

Thin film coatings were produced by passing ethane through a radiofrequency glow discharge in a tubular plasma polymerization reactor. Infrared absorption characteristics of the plasma polymerized ethane (PPE) depends on the reactor conditions. Absorptions are large for C-H stretching (3.5 μm) and bending (7.0 μm) frequency regions. However, outside of these regions the absorptions are low. Under appropriate polymerization conditions, the absorption coefficient at 10.6 μm for PPE film on polished, finished KCl crystal is 4-7 cm^{-1}. The refractive index for PPE is 1.51 (at sodium D line), which is higher than that of KCl. Thus the use of multilayer coating for good antireflection is indicated. Moisture resistance was tested by exposing the coated crystals at room temperature and 84% relative humidity for 100 hours.

Key words: Laser window coating; plasma polymerized.

1. Introduction

In the search for optical coatings for high energy infrared laser windows, most of the attention has been directed toward the inorganic materials. The requirements for such a coating are that it has low absorption characteristics in the 10.6 μm and 3-5 μm regions, is antireflective, and moisture resistant. Most organic polymers have not been considered viable candidates for such coatings because of their generally high absorptions in the infrared region, and the difficulty of depositing very thin and adherent films on the alkali halide substrate. However, it has recently been pointed out that by the use of plasma polymerization such difficulties can be circumvented [1][1]. By passing an organic vapor through a cold plasma generated by a radiofrequency glow discharge, thin, adherent, and pinhole free films can be readily deposited on a variety of substrates. These plasma polymerized materials are generally highly crosslinked amorphous networks. By carefully controlling the molecular structure, it is possible to produce coatings that have low absorptions in much of the infrared region. The purpose of this paper is to present some of our most recent results in the studies of plasma polymerization of simple hydrocarbons and of the properties of the resulting films.

2. Experimental

Tubular flow plasma polymerization reactors were used in this work. The design of a glass tubular flow reactor has already been described previously [2]. We have now constructed another tubular flow reactor out of Lucite. Although most of the data here were collected from the Lucite reactor, the glass reactor was also used. Plasma polymers of similar structure and properties can be prepared by either reactor using the appropriate reaction parameters.

Figure 1 shows that the Lucite tubular flow plasma reactor consists of a rectangular channel, which is the reaction chamber, surrounded by a protective cylinder and held in place end plates. Two parallel plate electrodes are inserted inside the reaction chamber with a fixed separation of 3 cm. Sample substrates are placed on a slide-in-plate which can be easily introduced into and removed from the bottom electrode. Both electrodes can be cooled by circulating fluids. The discharge is at 13.56 MHz. CP grade ethane gas was purchased from the Matheson Gas Company and

---

* Work supported by the Defense Advanced Research Projects Agency, monitored by the Air Force Cambridge Research Laboratory.

1. Figures in brackets indicate the literature references at the end of this paper.

was used as received. Before use the reactor effluents from air and inert gas discharges were analyzed by mass spectrometry. The composition was found to be nearly identical to that of the glass reactor, indicating the essential inertness of Lucite to the plasma conditions.

Mechanically polished crystals of potassium chloride were purchased from Harshaw Chemical Company. No further treatments were applied before use. The KCl crystals were placed on the bottom electrode in the reactor where the plasma polymerized film was deposited. Deposition rates were determined by weighing methods [3]. Film thickness was estimated by assuming the density of the polymer to be unity. Infrared spectroscopic analysis of the coated crystal was conducted with a Perkin-Elmer 467 spectrophotometer.

Humidity-resistance testing was carried out by exposing the crystals to the constant humidity atmosphere produced over an aqueous salt solution. After 100 hours, crystal surfaces were examined by optical microscopy to determine the effects of the exposure.

Refractive indices were determined on an Abbe refractometer by depositing the plasma polymer on a cut glass (n = 1.518). 1-Bromonaphthalene was used as matching liquid, which has a refractive index of 1.658.

3. Results and Discussion

3.1. Plasma Polymerization of Ethane

The form of the plasma-polymerized materials can be a film, an oil, or a powder. The general form of the polymer is related to the polymerization rate and whether the reaction occurs in the gas phase or on a surface. A powder generally results from a rapid gas phase reaction, while a film is generally the result of a slower surface reaction [3]. Thus, prior to any routine film depositions for any application, it must be determined under what reaction conditions that a good film can be produced for a particular reactor configuration. These conditions can best be summarized on plots known as characteristic maps [2-4]. The usual system variables that are chosen in the development of the characteristic map are the monomer flow rate and the total system pressure with the power as the parameter.

The characteristic map was constructed by depositing the polymer on an aluminum foil substrate attached to the slide-in-plate. The polymer coated foil was examined visually and tactilely after the deposition of polymer in order to qualitatively characterize the form of the polymer, and to determine the amount of the foil covered by the polymer. Characteristic maps for the Lucite tubular reactor at two different powers using pure ethane are shown in figure 2. Increasing the power from 200 watts to 300 watts shifts the boundaries and increases the regions somewhat, but the basic form of the characteristic map remains unchanged.

After the characteristic map was constructed for this particular reactor, the reaction conditions for the production of a good film could be determined, and the deposition rate of the film as a function of the various system variables could be explored. The variables of interest are the monomer flow rate, the total system pressure, and the deposition power.

The effect of the monomer flow rate on the deposition rate is shown in figure 3. The existence of a maximum in such a plot is characteristic of plasma polymerization [2]. The deposition rate of polymer as a function of the total system pressure is shown in figure 4. The corresponding weight of film deposited is also shown in the same figure. Film as well as oil and powder form part of the polymer deposited above a pressure of about 1.5 torr. This is the form of polymer observed on the characteristic map at lower flow rates and above that pressure (see fig. 2). The effect of the deposition power on the deposition rate was investigated from a threshold power of about 50 watts to about 450 watts, which is near the maximum output of the RF generator. From figure 5 it can be seen that even with reaction conditions that produce a maximum deposition rate, an 800% increase in the deposition power results in only about a 35% increase in the deposition rate. The corresponding weight of film deposited is also shown in the same figure, revealing that the corresponding increase is about 40%.

3.2. Moisture Resistance Studies

The plasma-polymerized ethane films deposited on KCl crystal surfaces were tested for moisture resistance by exposing the film coated surface to a controlled humidity environment for 100 hours. The coated and uncoated crystal surfaces at various conditions of exposure were examined and photographed at 256X magnification using a standard transmission binocular microscope. The photographs that were taken are shown in figure 6(a)-(d). Figure 6a shows the surface of a new, uncoated, and unexposed crystal that may be used as a comparison standard. The crystal was mechanically polished, but not etched by HCl [5-7], thus surface scratches are numerous. The surface on which plasma polymerized ethane (~ 1 μm thick) has been deposited is seen to be very similar to the original surface (fig. 6b). Exposure of a film coated crystal to room humidity (55-60% RH) for 100 hours does not appear to deteriorate the film surface as shown in figure 6c. A definite film deterioration is evident when a film of about the same thickness (~ 1 μm) is exposed to 84% RH in the constant humidity chamber for the same length of time as shown in figure 6d.

Comparison of figures 6a and 6d shows that most of the deteriorations of the crystal occur at the scratches and imperfections. It has been demonstrated in a previous electron microscopic study [8,9] that while more gentle variations on the surface of substrate can be evenly coated by a plasma polymerized film, sharp edges and small holes cannot. Thus the surface imperfections on these unpolished crystals are in fact not protected by the plasma polymerized film, thereby resulting in the observed deteriorations. Studies of plasma polymer coated crystals that have been finished are now underway.

3.3. Infrared Absorptions of Plasma Polymerized Ethane

Figure 7 shows an example of the infrared spectrum of plasma polymerized ethane. The strong absorptions at 3.4 μm, 6.9 μm, and 7.3 μm are, respectively, due to C-H stretching, C-H bending in CH_2, and C-H bending in CH_3. Ideally if the polymer consists of completely saturated aliphatic chains, then these characteristic bands would be the only absorbing regions. The absorptions in the region of 7.5 μm to 12 μm, which covers the 10.6 μm wavelength, may be ascribed to two types of non-aliphatic, non-hydrocarbon structures in the polymer. The first type may have resulted from molecular rearrangement in the plasma. In a recent paper we have demonstrated that plasma polymerized materials produced from unsaturated hydrocarbon monomers also contain double bonds and aromatic groups not originally present in the monomer [10]. These functional groups strongly absorb infrared radiation. To wit C=C stretching frequencies are in the region of 5.0 - 6.2 μm, out of plane C-H deformations in unsaturated hydrocarbons are between 10-11 μm, and C-H vibrations of mono-substituted phenyl groups are near 14 μm. The second type of structures may be attributed to the oxygenated groups. It has been shown that initiation of plasma polymerizations in a radiofrequency discharge is dominated by the free radicals, some of which are trapped in the polymer matrix and cannot readily terminate. These radicals are long-lived and are easily oxidized to form hydroxyl, carbonyl, and other oxygenated functional groups, which also contribute strongly to the infrared absorption [11]. For example, the O-H stretching is at 3.0 μm and the carbonyl stretching at 5.9 μm. In addition, increased absorption in the 8 - 10 μm region can be expected as a result of O-H deformation and C=O stretching vibration in alcohols and alkyl ketones.

In order to minimize these undesirable side effects, plasma conditions (slower rate of deposition) are used to minimize molecular rearrangement and radical trapping. A completely linear hydrocarbon polymer would have a chemical structure of $\{CH_2\}$, with a H/C ratio of 2.0. Increased crosslinking and unsaturation would decrease this ratio. Figure 8 shows that in fact the H/C ratio is quite low at high deposition rates, but increases rapidly with decreasing deposition rate to approach 2.0. In addition, the reduced rate of polymer deposition also favors the recombination of radicals. The annihilated radicals will render the polymer less susceptible to oxidation. Figure 9 shows that absorption due to the oxygenated group C=O (at 5.9 μm) continually decrease with decreasing rate of depositon, and at low rates the absorption at 5.9 μm falls below the limits of detectability of the spectrometer. Both these factors combine to reduce the absorption at 10.6 μm (fig. 9).

The best PPE film was shown in figure 9 to have an absorbance of about 0.5% per μm thickness at 10.6 μm. These results were, however, obtained on the infrared spectrometer using polished, but unfinished crystal substrates. A more sensitive and

elegant technique to detect low absorptions is microcalorimetry. PPE was deposited in this laboratory on the surface of a finished KCl crystal kindly supplied by Dr. M. Braunstein of Hughes Research Laboratory and then was returned to his laboratory for microcalorimetric measurements. Preliminary results indicate an absorption coefficient (β) of 4 - 7 cm^{-1}, and an absorption index (k) of 3.5 - 6 x 10^{-4} for our PPE film. By comparison we note that k = 2 x 10^{-3} for SrF_2, 5 x 10^{-4} for BaF_2 and 1 x 10^{-4} for ThF_4. These results are gratifying in indicating that plasma polymerized ethane film is in fact a viable candidate for optical laser window coatings.

Further improvement in lowering the infrared absorption may still be possible using the pulsed plasma technique. It is hoped that radical concentration may be further decreased through recombination during the pulsed periods when the plasma is turned off, thereby resulting in simpler polymer structures. As we have just discussed, reduction in the number of unsaturated and oxygenated groups will lower the absorption in infrared radiation.

3.4. Antireflection Characteristics

The reflectance (R) of a KCl substrate coated with PPE can be computed using the following equation [12]:

$$R = |r|^2 = \frac{r_1^2 + r_s^2 + 2r_1 r_s \cos 2\phi_1}{1 + r_1^2 r_s^2 + 2r_1 r_s \cos 2\phi_1} \qquad (1)$$

where r_1 and r_s are the Fresnel coefficients of the coating and the substrate, respectively:

$$r_1 = (n_o - n_1)/(n_o + n_1)$$

$$r_s = (n_1 - n_s)/(n_1 + n_s)$$

$$\phi_1 = 2\pi n_1 d_1/\lambda$$

and n_o, n_1, and n_s are the refractive indices of the air, coating and substrate, d_1 is the thickness of the coating and λ is the wavelength. By using the Abbe refractometer, the refractive index (n_1) of plasma polymerized ethane was found to be 1.51 at sodium D line. For λ = 10.6 μm and n_s = 1.49 (KCl), the reflectance of plasma polymerized ethane coated potassium chloride is calculated as a function of ($n_1 d_1$), the results of which are shown in figure 10. It is not surprising that PPE actually increases the reflectance of KCl, since in this case the condition of $n_o < n_1 < n_s$, is not satisfied. To achieve low reflectance, PPE must be used as a coating for substrates with higher refractive indices. Figure 11 shows that n_s should be around 2 in order for PPE to act as an antireflection coating.

An alternative consideration is to use multilayer coatings [13,14]. For a two layer coating, the reflectance is (for $n_1 d_1 = n_2 d_2$) [12]:

$$R = \frac{S_1 + a\cos 2\phi_2 + b\cos^2 2\phi_2}{S_2 + a\cos 2\phi_2 + b\cos^2 2\phi_2} \qquad (2)$$

where

$$S_1 = r_1^2 + r_2^2 + r_s^2 + r_1^2 r_2^2 r_s^2 - 2r_1 r_s (1 - r_2^2)$$

$$S_2 = 1 + r_1^2 r_2^2 + r_2^2 r_s^2 + r_s^2 r_1^2 - 2r_1 r_s (1 - r_2^2)$$

$$a = 2r_1r_2(1+r_s^2)+2r_2r_s(1+r_1^2)$$

$$b = 4r_sr_1$$

$$r_1 = (n_o-n_1)/(n_o+n_1)$$

$$r_2 = (n_1-n_2)/(n_1+n_2)$$

$$r_s = (n_2-n_s)/(n_2+n_s)$$

$$\phi_1 = \phi_2 = 2\pi n_2 d_2/\lambda.$$

Subscript 1 refers to the coating exposed to the air and 2 to that adjacent to the substrate s. The reflectance changes with ϕ as follows:

$$\frac{dR}{d(2\phi_2)} = J \frac{(n_1-1)(S_2-S_1)}{(n_2+n_s)(n_1+1)(S_2+a\cos 2\phi_2+b\cos^2 2\phi_2)^2} \qquad (3)$$

where

$$S_2-S_1 = (1-r_1^2)(1-r_2^2)(1-r_3^2) > 0.$$

The sign of this slope is determined by the discriminator J:

$$J = (n_2-n_s)(\cos 2\phi_2 - Q) \sin 2\phi_2 \qquad (4)$$

where

$$Q = \frac{(n_1-n_2)(n_2^2-n_1^2n_s^2)}{(n_1+n_2)(n_2^2-n_s^2)(n_1^2-1)}. \qquad (5)$$

We can now apply the preceding results to our plasma polymerized coatings on KCL for any fixed wavelength. In the case of PPTFE/PPE/KCl, $n_1 = 1.38$, $n_2 = 1.51$, $n_s = 1.49$, therefore, $Q = 1.615$. The value of the refractive index for plasma polymerized tetrafluoroethylene (PPTFE) was taken from the work of Hollahan, et al., [15]. The dotted line in figure 10 shows that a minimum reflectance of 0.012 can be expected theoretically at quarter wavelength. However, for the case of PPE/PPTFE/KCl (where the order of the layers is reversed), $n_1 = 1.51$, $n_2 = 1.38$, and thus $Q = 0.352$. Now it can be seen in figure 10 (broken line) that minimum reflectance occurs at a much thinner layer of coating ($\sim\lambda/12$). These results indicate that it is possible to obtain low reflectance in double layer coatings much less than the quarter wavelength thickness. In addition, it is apparent that the parameter Q is very useful in designing coatings for optical applications.

4. Acknowledgments

We are indebted to Drs. M. Braunstein, S. D. Allen, and J. E. Rudisill of Hughes Research Laboratories, Malibu, California for the microcalorimetric measurements.

5. References

[1] Tibbitt, J. M., Bell, A. T. and Shen, M., Proc. Fifth Annual Conference on High Power Infrared Laser Window Materials, Air Force Cambridge Research Labs., 1975, p. 205.

[2] Kobayashi, H., Bell, A. T. and Shen, M., J. Macromol. Sci.- Chem., A10, 123 (1976).

[3] Kobayashi, H., Bell, A. T. and Shen, M., J. Appl. Polymer Sci., 17, 885 (1973).

[4] Kobayashi, H., Shen, M., and Bell, A. T., J. Macromol. Sci. Chem., A8, 1345 (1974).

[5] Davission, J. W., Proc. 2nd Conf. on High Power Infrared Laser Window Materials, Air Force Systems Command, 1972, p. 525.

[6] Allen, S. D., Braunstein, M., Giuliano, C. and Wang, V., Proc. Symp. Damage in Laser Materials, 1974.

[7] Turk, B. R., Pastor, R. C., Timper, A. J., Braunstein, M. and Heussner, G. K., Proc. Fifth Annual Conf. on High Power Infrared Laser Window Materials, Air Force Cambridge Research Laboratories, 1974, p. 103.

[8] Niinomi, M., Kobayashi, H., Bell, A. T. and Shen, M., J. Appl. Phys. 44, 4317 (1973).

[9] Niinomi, M., Kobayashi, H., Bell, A. T. and Shen, M., J. Appl. Polymer Sci., 18, 2199 (1974).

[10] Tibbitt, J. M., Shen, M. and Bell, A. T., J. Macromol, Sci.- Chem., in press.

[11] Tibbitt, J. M., Bell, A. T. and Shen, M., J. Macromol. Sci.- Chem., A10, 151 (1976).

[12] Cox, J. T. and Hass, G., in G. Hass And R. E. Thun, eds., Physics of Thin Films, Vol. 2, Academic Press, New York, 1964, p. 239.

[13] Braunstein, M., Braunstein, A. I. and Rudisill, J. E., Proc. 2nd Conf. on High Power Infrared Laser Window Materials, Air Force Systems Command, 1975, p. 777.

[14] Loomis, J. S., Proc. 2nd Conf. on High Power Infrared Laser Window Materials, Air Force Systems Command, 1972, p. 799.

[15] Hollahan, J. R., Wydeven and Johnson C. C., Appl. Opt., 13, 1844 (1974).

6. Figures

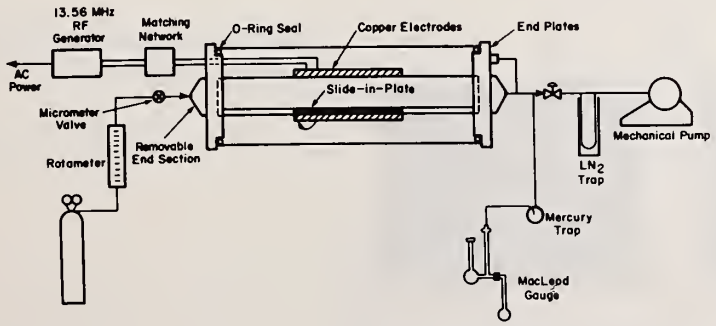

Figure 1. Schematic diagram of the tubular plasma polymerization reactor.

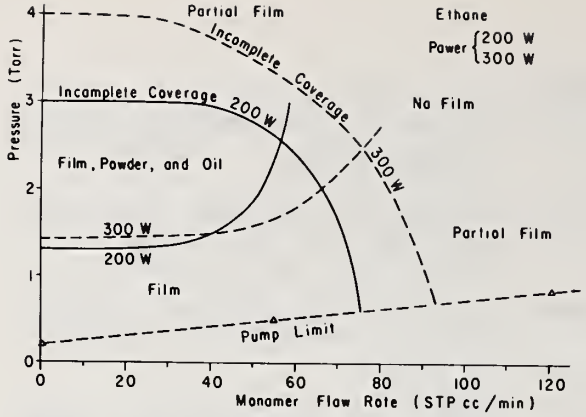

Figure 2. Characteristic map for plasma polymerization of ethane in the Lucite tubular plasma polymerization reactor.

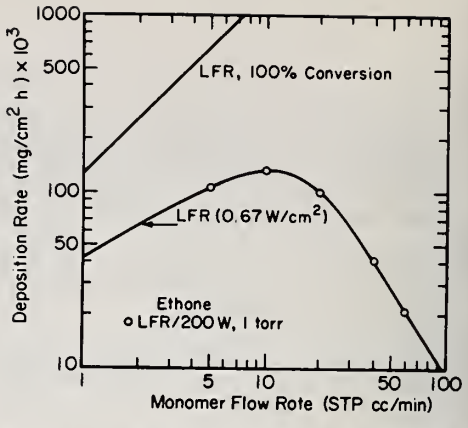

Figure 3. Deposition rate of ethane as a function of monomer flow rate.

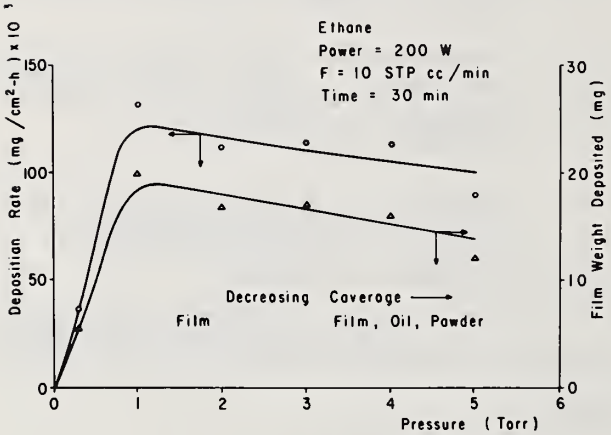

Figure 4. Deposition rate of ethane as a function of pressure.

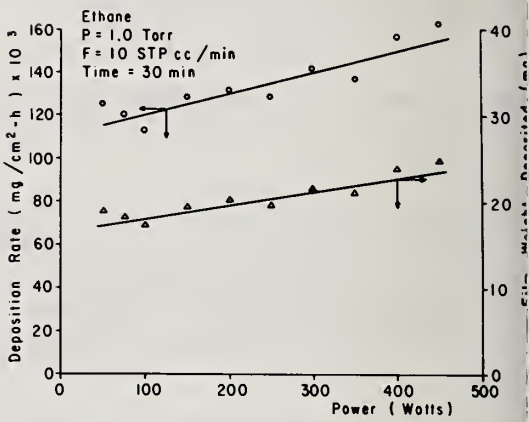

Figure 5. Deposition rate of etnane as a function of power.

Figure 6. Photomicrographs of (a) uncoated KCl crystal unexposed to humidity; (b) plasma polymerized ethane coated KCl crystal unexposed to humidity; (c) plasma polymerized ethane coated KCl crystal exposed to 55% humidity for 100 hours; (d) plasma polymerized ethane coated KCl crystal exposed to 84% humidity for 100 hours (coating thickness ∿ 1 μm).

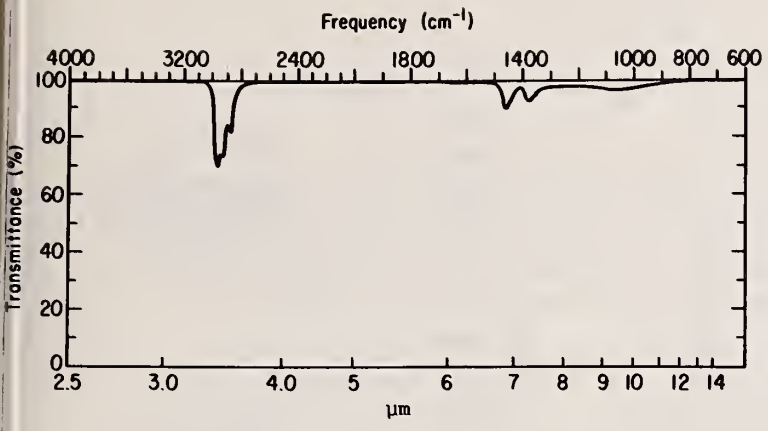

Figure 7. Infrared spectrum of plasma polymerized ethane.

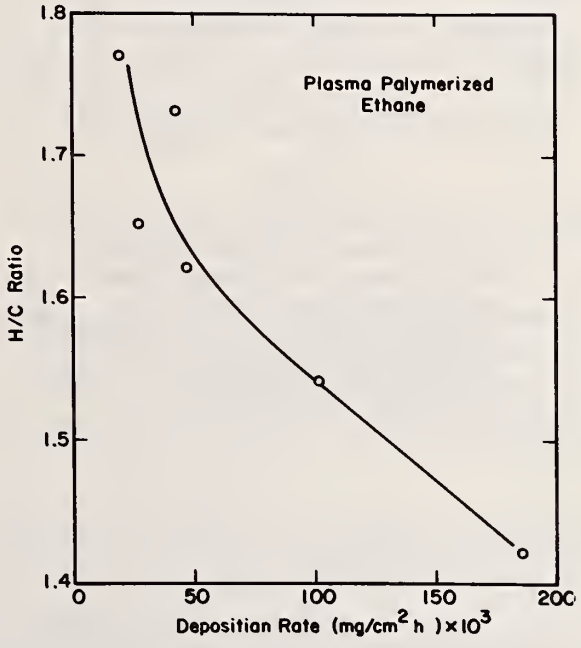

Figure 8. Hydrogen/carbon ratio as a function of deposition rate of plasma polymerized ethane.

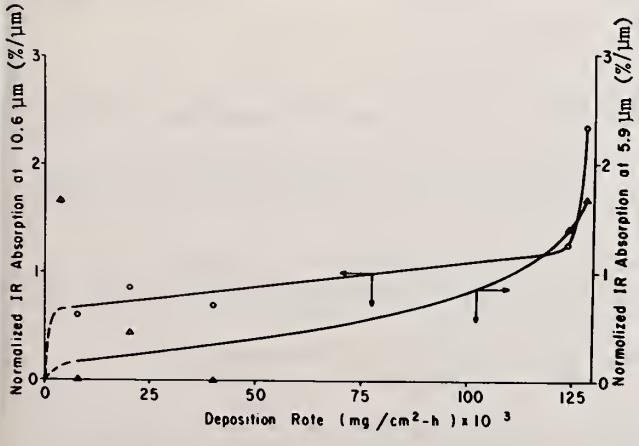

Figure 9. Infrared absorbance at 10.6 μm as a function of deposition rate for plasma polymerized ethane.

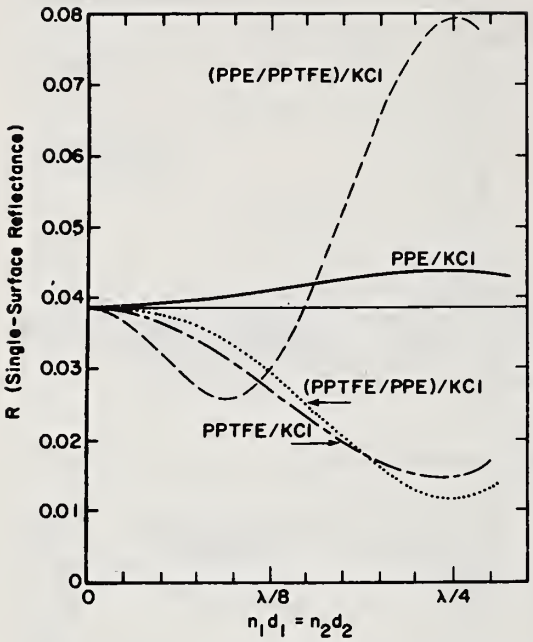

Figure 10. Calculated reflectance of single layer plasma polymerized ethane coated KCl (solid line), single layer plasma polymerized coated tetrafluoro-ethylene KCL (chain line), double layer PPTFE/PPE/KCl (dotted line) and PPT/PPTFE/KCl (broken line) as a function of optical thickness.

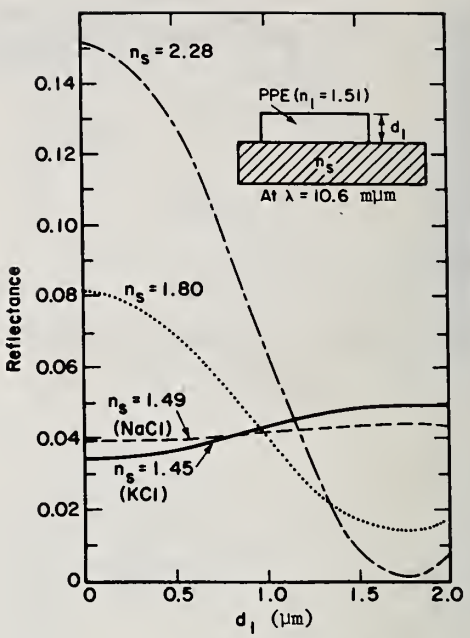

Figure 11. Reflectance of plasma polymerized ethane coated crystals of various refractive indices as a function of coating thickness.

COMMENTS ON PAPER BY REIS, HIRATSUKA, BELL, AND SHEN

It was suggested that to test for the absence of pin-holes in films, one should not rely only on the absence of electrolytic conduction when the film is immersed in a fluid, but should test the films for gas permeability as well.

3.5 EPITAXY AND OPTICAL SCATTERING IN TlI FILMS*

R. A. Skogman
Honeywell Corporate Research Center
Bloomington, Minnesota 55420

Thallium iodide has been identified as a protective high index coating material for potassium chloride laser windows. TlI has a high refractive index and an optical absorption of less than 1 cm^{-1} at 10.6 μm. The protective quality of TlI lies in its insolubility and remarkable adhesion to potassium chloride. This adhesion is due, in part, to the epitaxial growth of TlI on KCl. TlI microstructures resulting from different epitaxial growth habits are responsible for the optical scattering observed in films grown on certain KCl orientations.

We have found that the alignment of the TlI b_o axis parallel to the KCl <110> direction nearest the substrate surface determines the epitaxial growth habit. On the precise KCl (100) orientation, for example, two KCl <110> directions lie in the surface. This causes the TlI to nucleate in two orientations rotated 90° from one another. This unusual microstructure results in scattering by the diffraction of light passing from one biaxially birefringent orientation to another.

This model has been demonstrated for all KCl orientations and is well supported by x-ray data and polarized light microscopy. A practical solution to this problem has been found which routinely yields visibly clear TlI coatings.

Key words: Biaxial birefringence; epitaxial microstructure; optical scattering.

1. Introduction

TlI has been demonstrated as an excellent protective high index coating material for KCl laser windows.

Humidity resistance of TlI is excellent and films adhere extremely well to KCl substrates. TlI films have absorptions of less than 1cm^{-1} at 10.6μm and coatings of TlI have withstood 9 seconds of 80 kW cm^{-2} of CO_2 radiation without damage [1]! Anti-reflection coatings prepared with TlI have met reflectivity requirements. TlI is a biaxially birefringent material, but the effects are negligible at 10.6 μm[2]. Cloudiness in certain TlI films, though not considered a factor at infrared wavelengths, is of concern because of its unpredictable occurrence. An investigation of the causes of cloudiness was performed along with the investigation of the material's other properties.

The results of this investigation fall into two categories. The first category includes the cloudiness caused by the usual deposition process variables, i.e., substrate cleanliness, source contamination, etc. The second category consists of cloudiness caused by an interesting phenomenon unique to birefringent materials capable of epitaxial growth.

Cloudiness due to process variables will not be discussed here. It should be stated, however, that state-of-the art thin film evaporation procedures and newly developed KCl substrate preparation techniques will routinely yield clear TlI films. The exception to this statement is the subject of this paper.

2. Optical Scattering in Epitaxial TlI

It has been determined that certain KCl orientations produce cloudy TlI films independent of the cloudiness mechanisms related to process variables.

Unique microstructures developed during the epitaxial growth of birefringent TlI on certain KCl orientations are responsible for this cloudiness. Figure 1 shows a KCl substrate coated with TlI. The cloudy areas in the TlI correspond to different KCl subgrain orientations.

Figure 2 shows a microstructure typical of a cloudy TlI film of this type. The boundaries are visible only between crossed polarizers suggesting that they are very narrow and by themselves are not the source of scattering.

In order to determine the KCl orientations responsible for this peculiar microstructure, single crystals of KCl were shaped and polished to expose a wide range of orientations to the condensing TlI.

*Work supported by Defense Advanced Research Projects Agency under contract DAHC15-73-C-0464.
1. Figures in brackets indicate the literature references at the end of this paper.

Figure 3 is a photo of two such crystals. The cylindrical crystal contains all orientations normal to the KCℓ <100> axis which coincides with the axis of the cylinder. The other crystal in the figure is a plano-convex shaped lens coated on the convex side. The KCℓ <100> axis here is parallel to the axis of the lens.

Cloudiness in films on these crystals occurs in specific crystallographic regions. The lens-shaped crystal, for example, is cloudy along the two KCℓ <100> directions projected from the KCℓ <100> pole. These cloudy regions contain the microstructure mentioned previously and divide the lens into four quadrants.

Figure 4 is a macrograph of the entire lens as seen between crossed polarizers. With the KCℓ <100> directions parallel to the polarizer axes only the microstructural boundaries are extinguished. As the crystal is rotated with respect to the polarizers the entire film is extinguished when the KCℓ <110> directions become parallel to the polarizer axes. This implies that the TℓI contains, at most, two orientations, both of which have their optic axes parallel to the two KCℓ <110> directions. The fact that boundaries appear means that there are indeed two TℓI orientations.

X-ray Laue photos shown in figure 5 taken on both sides and in the middle of the cloudy region along the KCℓ <100> direction confirm the existence of the two TℓI orientations. The Laue spots from either side of the cloudy area are mirror images of those from the opposite side implying a 90^{o} rotation between the TℓI orientations. The Laue photo taken in the center (cloudy) area contains both sets of spots which means that both orientations occur in the cloudy area.

Scattering results as low incident light is refracted between these TℓI grains whose optic axes are rotated 90^{o} from one another. The axes in this case are aligned slow to fast and fast to slow; a situation of maximum refraction. This scattering causes the films to appear cloudy to the eye. At 10.6μm, of course, the birefringence is small and since the beam is normal to the film no scattering will occur.

3. The Epitaxial Habit of TℓI on KCℓ

The discrete spots on the Laue photos are sufficient evidence of the epitaxial growth of TℓI on KCℓ. Further x-ray analysis details this epitaxy and provides a model for the observed microstructures.

Figure 6 includes the results of x-ray analysis. In every case the TℓI b_o axis is aligned parallel to a KCℓ <110> direction. This suggests the importance of the KCℓ <110> direction that was noted under polarized light. Observation of orientations away from the principle orientations reveals that the TℓI b_o axis aligns itself with the KCℓ <110> direction nearest the substrate surface. Recalling the lens shaped crystal we realize that this alignment is the cause of the two orientations and their intersection along the <100> projection on the lens. This intersection has both KCℓ <110> directions equally near the surface. On exact KCℓ (100), which includes cleaved KCℓ, both <110> directions are in the surface plane and films on these surfaces contain the duplex microstructure and are cloudy.

Figure 7 is a model of the microstructure seen in the lens-shaped crystal. The TℓI b_o directions are parallel to the KCℓ <110> direction nearest the surface and there is a mixture of the two TℓI orientations along the KCℓ <100> directions.

On KCℓ (111) which has three <110> directions, three TℓI orientations are observed. Since the <110> directions here are 120^{o} from one another, only one orientation of TℓI can be extinguished between crossed polarizers at a time. Films on KCℓ (111), as observed, can never be completely extinguished in polarized light. These films, as would be expected, scatter less than films on KCℓ (100) which contain the orthogonally oriented grains.

Finally, since there is only one KCℓ <110> direction in the KCℓ (110) plane, TℓI grown on that surface is of a single orientation and does not scatter light.

To complete the study of TℓI epitaxy on KCℓ we examined the lattices involved in the epitaxy. Since both TℓI and KCℓ are ionic materials cation-anion alignment must be considered. Figures 8, 9, and 10 are scale drawings of the KCℓ (100), (110), and (111) lattice planes, respectively. Figures 11 and 12 are scale drawings of the TℓI (004) and (200) planes, respectively. Examination of the alignments of planes (as determined by x-ray analysis) shown in figures 13, 14, and 15 reveals an excellent ionic interaction in all cases. A lattice mismatch of only 3% between the TℓI b_o and the KCℓ d (110) helps account for the alignment of the TℓI b_o and KCℓ <110> directions on all KCℓ orientations.

Having established that epitaxial TℓI microstructures on certain KCℓ orientations are the source of cloudiness in some TℓI films two solutions become apparent. One solution, of course, is to use only KCℓ orientations which yield clear films i.e., without the peculiar microstructures. This means using orientations on or near the KCℓ (110) or orientations near, but not on the KCℓ (100). A more practical solution, however, is to eliminate the epitaxial growth entirely.

We have found that when TℓI is condensed in its cubic (β) phase on KCℓ and allowed to transform to

its stable orthorhombic (α) phase a clear, polycrystalline, randomly oriented film develops independent of substrate orientation.

The condensation of the β phase is accomplished by holding the substrate at 140°C or above during the deposition. The phase change occurs during substrate cooling with the α grain size being dependent on the condensation temperature and cooling rate.

At elevated substrate temperatures and low deposition rates, however, TlI will not condense on the KCl. Use of higher evaporation rates solves this problem. By using a graphite Knutsen style evaporation source we have achieved more uniform heating of the TlI and are able to successfully deposit films at rates over 3000Å per minute.

Films prepared in this manner at an arbitrary rate of 2000Å/min are not cloudy, have low absorptions, and have withstood the laser damage tests mentioned previously.

This fabrication technique is especially compatible with the subsequent high temperature deposition of low index coatings.

4. Conclusion

This investigation has furthered the fundamental understanding of TlI whose qualities as a protective laser window coating have already been exhibited.

5. Acknowledgments

I gratefully acknowledge C. I. Knudson for the excellent x-ray analysis and E. Bernal G. and R. J. Stokes for their valuable discussions and encouragement.

6. References

[1] Detrio, J. A.; Petty, R. D.; Ohmer, M. C. and Swenson, O. F., from "AR Coated KCl Damage at 10.6μm" presented at 8th Laser Damage Symposium.

[2] Chaffin, J. H. and Skogman, R. A., Proc. of 5th Annual Conf. on Infrared Laser Window Materials. 1976, p. 156.

7. Figures

Figure 1. Polycrystalline KCl coated with TlI.

Figure 2. Microstructure typical of cloudy TℓI.

Figure 3. Cylindrical and lens shaped single crystal KCℓ coated with TℓI.

Figure 4. Lens shaped KCℓ coated with TℓI with KCℓ <100> parallel to crossed polarizers.

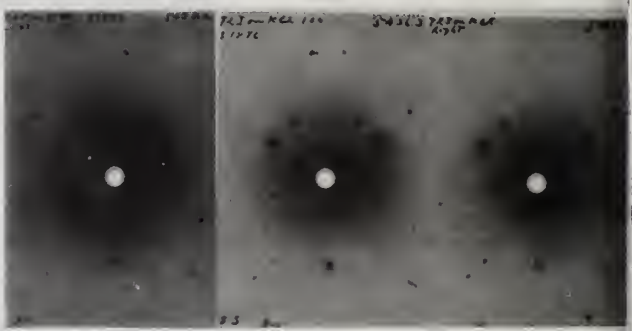

Figure 5. X-ray Laue photos of area on both sides of cloudy zone (left and right) and <u>in</u> the cloudy zone (center).

X - RAY OBSERVATIONS

KCℓ SUBSTRATE	TℓI FILM
(110)	(200) TEXTURE AND TℓI b. PARALLEL TO KCℓ (110).
(100)	(004) TEXTURE AND TℓI b. PARALLEL TO KCℓ (110).
(111)	(004) TEXTURE ANO TℓI b. PARALLEL TO KCℓ (110).

LATTICE MATCHING

TℓI b. 4.58 Å

KCℓ d(110) 4.448 Å

~3% MISMATCH

Figure 6. X-ray data.

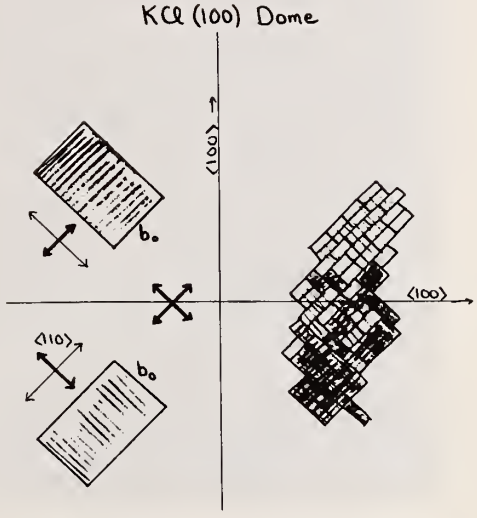

Figure 7. Model of TℓI orientations on KCℓ (100) lens-shaped crystal.

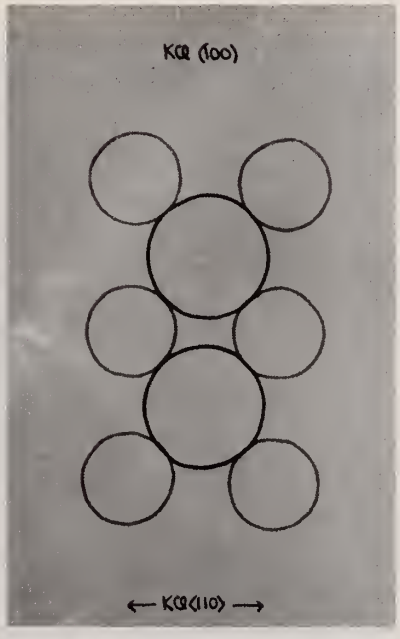

Figure 8. KCℓ (100) plane.

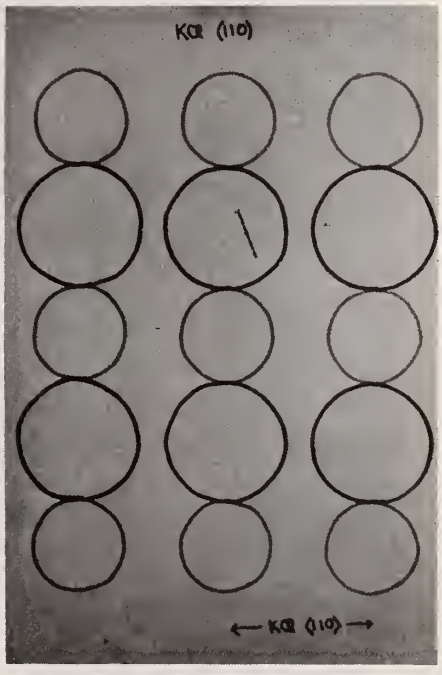

Figure 9. KCℓ (110) plane.

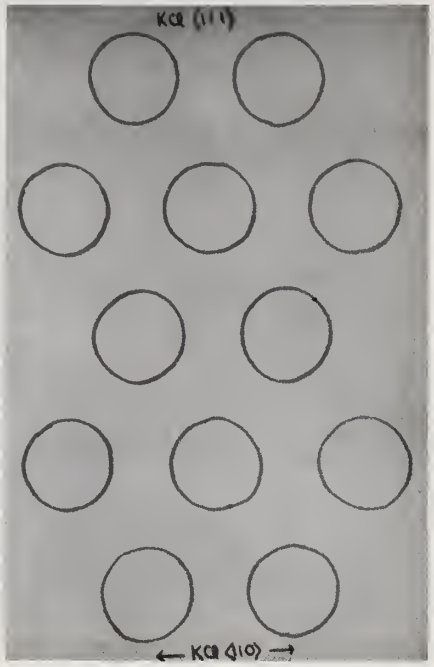

Figure 10. KCl (111) plane.

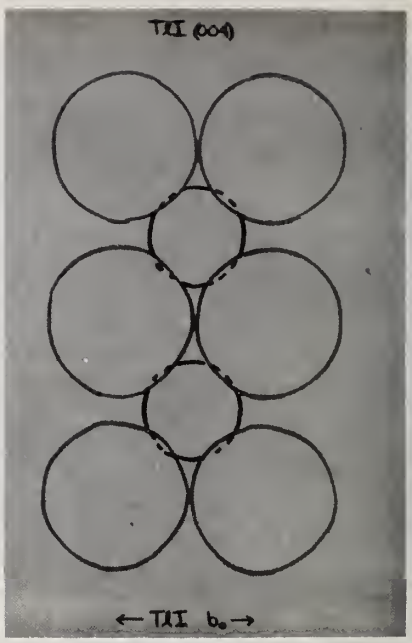

Figure 11. TlI (004) plane.

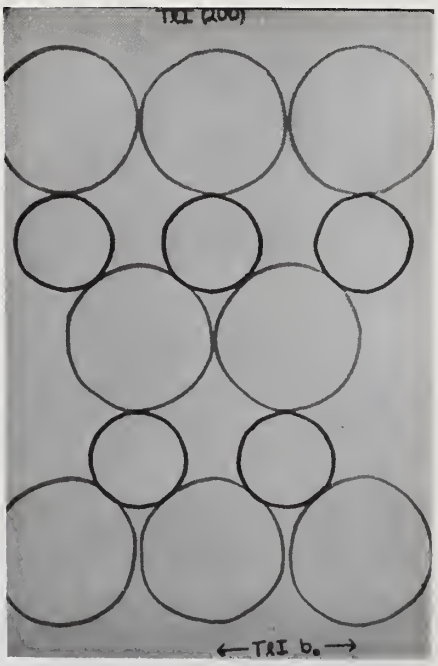

Figure 12. TlI (200) plane.

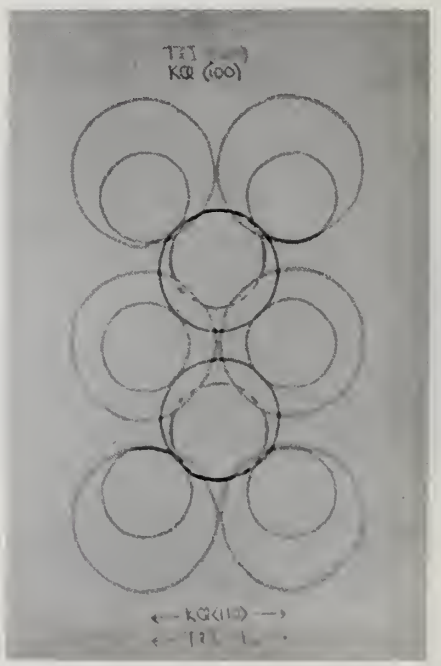

Figure 13. TlI (004) on KCl (100).

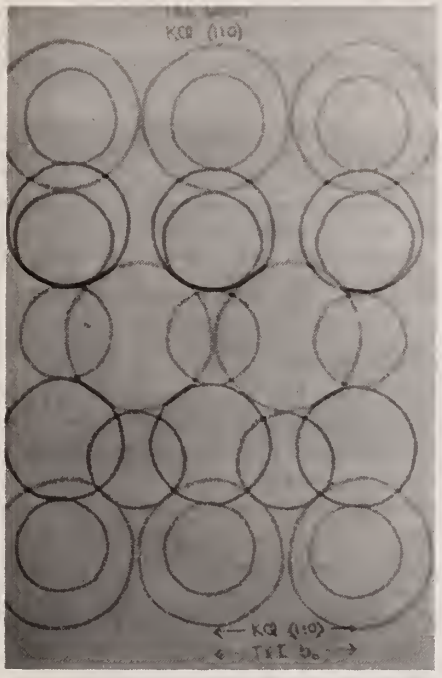

Figure 14. TlI (004) on KCl (111).

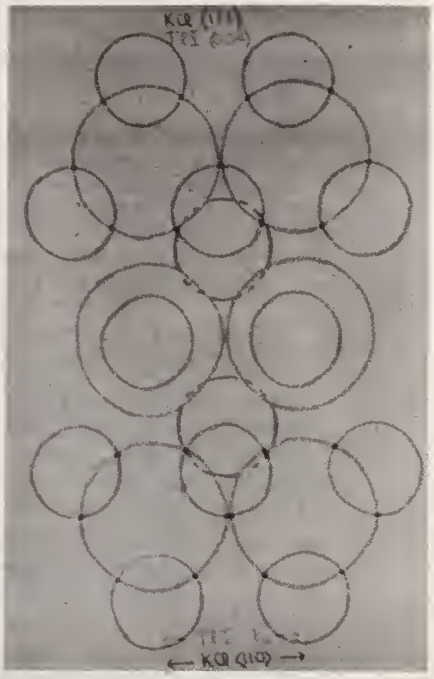

Figure 15. TlI (200) on KCl (110).

COMMENTS ON PAPER BY SKOGMAN

The speaker noted that no degradation of Tl1 films was seen upon several days exposure to 100% relative humidity.

3.6 THIN-FILM COATING EVALUATION BY ATTENUATED TOTAL REFLECTION

R. T. Holm and E. D. Palik
Naval Research Laboratory
Washington, D. C. 20375

Attenuated total reflection (ATR) is a particularly attractive technique for the determination of absorption constants of thin-film coatings because a wide spectral range can be studied in a relatively simple way. Calculations of ATR spectra have been made for typical thin-film laser-window coatings, e.g., ZnSe on BaF_2 and ThF_4 on ZnSe. With the aid of such calculations, it is possible to establish the optimum ATR trapezoid geometry, angle of incidence, and film thickness for particular film-substrate configurations to maximize the sensitivity of the experiment to the absorption constant. ATR has potential applications in thin-film characterization for large-window coatings, as examination of an ATR sample coated at the same time would enable rapid quantitative evaluation of resulting coatings.

Key words: Absorption; antireflection coatings; attenuated total reflection; laser windows; spectroscopic.

1. Introduction

One of the important properties of an antireflection coating that must be determined is its absorption constant. This can be accomplished either calorimetrically or spectroscopically. Although calorimetric techniques are very sensitive, they are not readily amenable to the measurement of absorption bands. Standard reflection and transmission experiments can be used to determine absorption bands, but suffer from lack of sensitivity, especially for thin coatings and low absorption. One technique that is both sensitive and spectroscopic is attenuated total reflection (ATR).

2. Discussion

We have made a series of detailed calculations to elucidate the general features of ATR as applied to antireflection coatings and also to determine the optimum conditions for doing the measurements. The ATR technique [1][1] is shown schematically in figure 1(a). A trapezoid is made from the laser-window material. Thin films of the antireflection-coating material of thickness d are evaporated on both sides of the trapezoid. Light is multiply reflected down the trapezoid at an angle of incidence θ which results in total reflection. If there is no absorption in the film, the total reflection is unity. When absorption is present in the film, the total reflection is less than unity, or, in other words, is "attenuated." The difference from unity is a direct measure of the absorption in the film. With θ and d fixed, the frequency of the light can be varied to measure the absorption bands in the film. The ATR technique is more sensitive than standard reflectance/transmittance measurements because the light undergoes absorption each time it is reflected as it transverses down the trapezoid. The ATR technique has been used by a group at Raytheon who studied a variety of film-window combinations with $\theta = 45^{\circ}$ [2].

We have calculated the reflectance R for a single reflection as a function of θ, d, and film absorption constant α for both s- and p-polarized light. These calculations are based on Wolter's reflectance equations for M layers [3] and, as such, will be applicable to multilayer coatings. We consider here only one layer. In the calculations we assume that the window material is nonabsorbing and that the refractive indices of the window and film are constant. The overall reflectance for N reflections is R^N.

An expanded view of the window-film-air interface region is shown in figures 1(b) and (c). Two different window-film configurations are considered: a high index film (HIF) on a low index window (LIW) and the reverse, a low index film (LIF) on a high index window (HIW).

1. Figures in brackets indicate the literature references at the end of the paper.

For the case of a HIF on a LIW, we have chosen ZnSe (n = 2.435) on BaF_2 (n = 1.458), as indicated in figure 1(b). Total reflection cannot occur at the window-film interface, but only at the film-air interface. The critical angle θ_c is 24.2° which corresponds to an angle of incidence of 43.3°. Thus, for $\theta >$ 43.3° total reflection occurs, giving rise to an evanescent wave in the air contiguous with the film. Since the total reflection takes place at the film-air interface, the light propagates back and forth across the film, sampling the whole film. Whenever there is loss in the film, interference effects arise because the reflectance is less than unity.

In figure 2 the reflectances R_s and R_p for s- and p-polarization as a function of the angle of incidence θ are shown for ZnSe on BaF_2 for a film thickness d = 2 μm at a frequency ω = 2632 cm^{-1} (3.8 μm) with a film intensity absorption constant α = 3 cm^{-1}. At θ = 43.3°, both R_s and R_p increase very rapidly to about 0.999, rather than 1.0 because α is nonzero. As θ increases beyond 43.3°, both R_s and R_p exhibit a minimum due to interference effects in the film and this minimum is related to θ and d. For maximum sensitivity, an ATR measurement should be made with the polarization having the lower reflectance and at an angle of incidence corresponding to a minimum of that polarization. In this case it would be s-polarization at θ = 70°. It must be kept in mind, however, that the total number of reflections in the is reduced as the angle of incidence is increased.

To demonstrate the spectroscopic features of ATR, we put into the film a frequency dependent, Lorentzian absorption band centered at 3.8 μm with a peak absorption of 10 cm^{-1} and a full width at half maximum of 200 cm^{-1}, as shown in figure 3(a). In figures 3(b) and (c) we show the reflectances as a function of frequency for p- and s-polarization, respectively, for angles of incidence of 50 and 70° with d = 2 μm. Also given on the ordinate is R^{50}, corresponding to fifty reflections. The minimum of R_s at 70° is about 0.98 giving an R_s^{50} of less than 0.4. The very weak fringes and the asymmetry of the absorption lines are caused by interference effects. A molecular absorption band with a peak absorption of 0.1 cm^{-1} would correspond to a minimum R_s^{50} at 70° of 0.99, which should be measurable.

The second case, a LIF on a HIW, is exemplified by ThF_4 (n = 1.45) on ZnSe (n = 2.435), as shown in figure 1(c). In this case, total reflection can occur at either interface, depending on the angle of incidence. The critical angle for the film-air interface is θ_{c1} = 43.6°, corresponding to θ = 24.2°. The critical angle for the window-film interface is $\theta = \theta_{c2}$ = 36.5°. For θ between 24.2 and 36.5° total reflection occurs at the film-air interface, and the ATR situation is identical to that discussed in connection with ZnSe on BaF_2. For θ greater than 36.5° total reflection occurs at the window-film interface. Now the evanescent wave associated with total reflection exists in the film, with the depth of penetration into the film decreasing as θ increases. With this dependence of penetration depth on angle of incidence, the absorption in the film can, in principle, be probed as a function of distance from the window-film interface.

The reflectance as a function of θ for ThF_4 on ZnSe with d = 2 μm, α = 3 cm^{-1} and ω = 2632 cm^{-1} is shown in figure 4 for s- and p-polarization. At θ = 24.2°, R_s and R_p abruptly increase to about 0.999. As θ increases, R_s exhibits a strong interference minimum at θ = 31.5° and R_p a weaker minimum at a slightly larger value of θ. When θ goes beyond 36.5°, R_s and R_p both increase rather quickly.

Figures 5(b) and (c) show the reflectances as a function of frequency when the film absorption is given by the Lorentzian absorption band of figure 5(a) for p- and s-polarization, respectively, for θ = 31.5 and 45° with d = 2 μm. At θ = 31.5° the minimum value of R_s is almost 0.97, resulting in an R_s^{50} of less than 0.3.

The reason why the reflectance at 31.5° is so much less than at 45° is explained by figure 6, which shows the reflectance as a function of the film thickness for 31.5

and 45^{o} for p-polarization with $\alpha = 3\ cm^{-1}$ and $\omega = 2632\ cm^{-1}$. At 45^{o} the penetration depth of the evanescent wave into the film is about 0.8 μm. As the film thickness increases, the reflectance at 45^{o} saturates at $d \approx 2$ μm. Any further increase in d beyond 2 μm is not "seen" by the evanescent wave. At 31.5^{o}, however, the light samples the whole film, no matter how thick it is. Thus, the reflectance decreases as the film thickness increases, asymptotically approaching the value of R_p obtained when the film thickness is semi-infinite. The interference fringes in the 31.5^{o} reflectance are readily evident.

3. Conclusion

In order to evaluate antireflection coatings while developing growth procedures, a simple and routine technique to spectroscopically measure absorption bands in the coating is needed. As we have shown, attenuated total reflection appears ideal for this purpose for absorption constants of approximately 1 cm^{-1} or greater. The ultimate sensitivity of an ATR experiment is controlled by the film thickness, the polarization and angle of incidence of the light, and the total number of reflections in the trapezoid. ATR apparatus is available commercially and fits many infrared spectrometers.

4. Acknowledgments

The authors thank M. Hass of the Naval Research Laboratory for helpful discussions and suggestions.

5. References

1 Harrick, N. J., Internal Reflection Spectroscopy (Interscience, New York, 1967).

2 Willingham, C. B., Bua, D., Statz, H. and Harrigan, F., "Laser Window Studies", Final Technical Report under Contract DAAH01-74-C-0719, Raytheon Research Division, Waltham, Mass. (August 1975), and Deutsch, T. F., J. Elect. Mater. 4, 663(1975).

3 Wolter, H., in Handbuch der Physik, S. Flugge, ed. (Springer - Verlag, Berlin, 1956), Vol. 24, p.461.

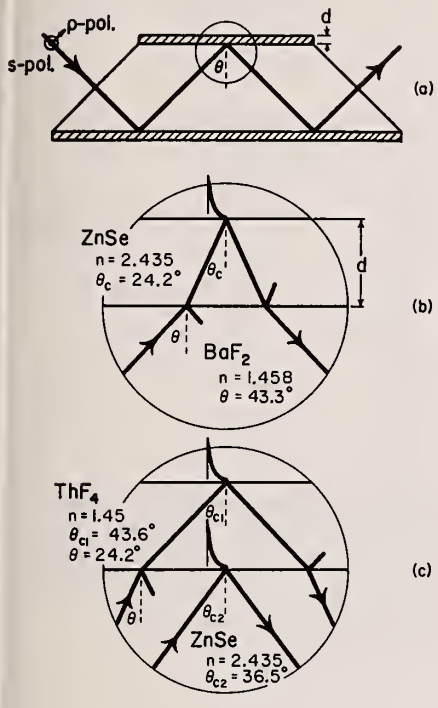

Figure 1. (a) Schematic illustration of ATR technique showing light transversing down a trapezoid of the window material with antireflection coatings of thickness d at an angle of incidence θ. Expanded view of encircled region in (a) showing details of the light propagation for (b) a high index film (ZnSe) on a low index window (BaF_2) and (c) a low index film (ThF_4) on a high index window (ZnSe).

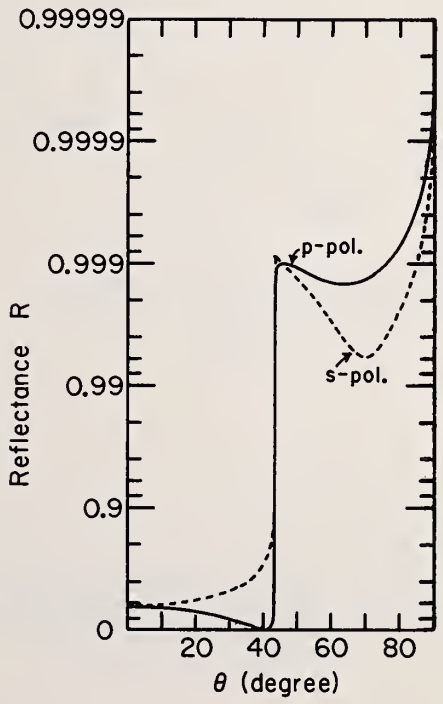

Figure 2. Calculated reflectance R as a function of the angle of incidence θ for ZnSe on BaF_2 with $\omega = 2632\ cm^{-1}$, $\alpha = 3\ cm^{-1}$ and $d = 2\ \mu m$ for s- and p- polarization.

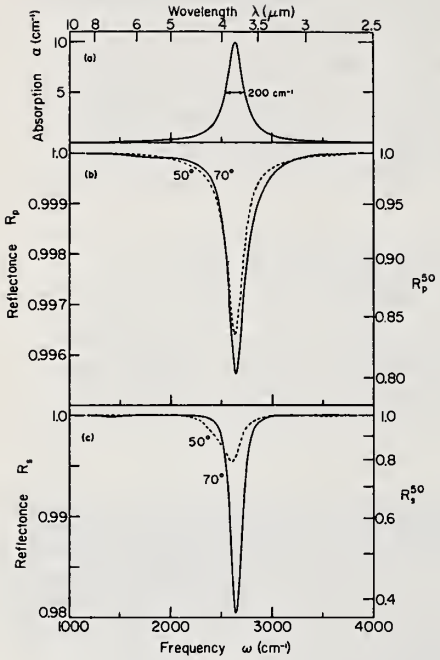

Figure 3. Frequency dependent, Lorentzian absorption band for the film used in the calculation of (b) and (c). Calculated reflectance R as a function of frequency ω for ZnSe on BaF_2 for (b) p-polarization and (c) s-polarization for d = 2 μm and θ = 50 and 70°. The ordinate in (b) and (c) also shows R^{50}, corresponding to fifty reflections.

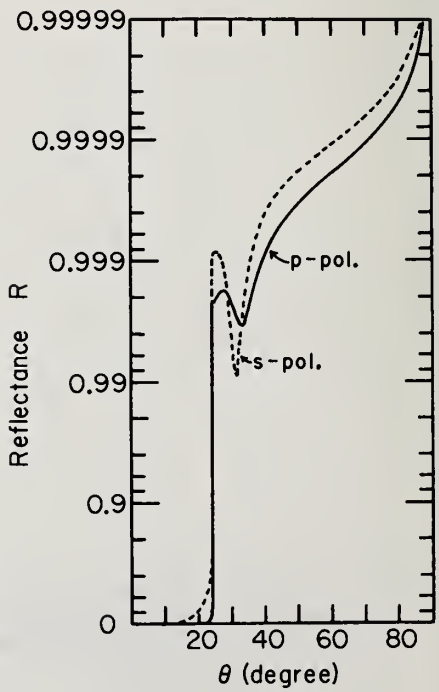

Figure 4. Calculated reflectance R as function of the angle of incidence θ for ThF_2 on ZnSe with ω = 2632 cm^{-1}, α = 3 cm^{-1} and d = 2 μm for s- and p-polarization.

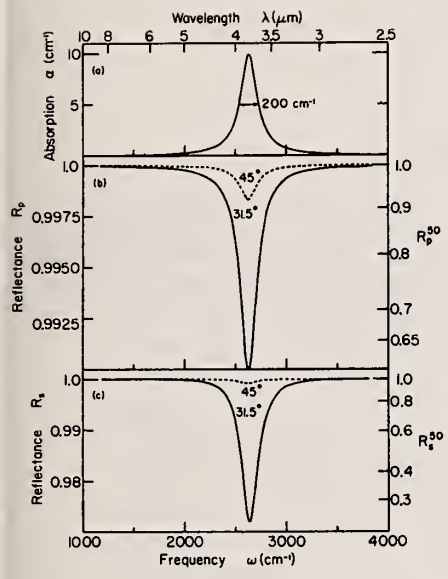

Figure 5. (a) Frequency dependent, Lorentzian absorption band used in the calculations of (b) and (c) for the film. Calculated reflectance R as a function of frequency ω for ThF_4 on ZnSe for (b) p-polarization and (c) s-polarization for d = 2 μm and θ = 50 and 70°. The ordinate in (b) and (c) also shows R^{50}, corresponding to fifty reflections.

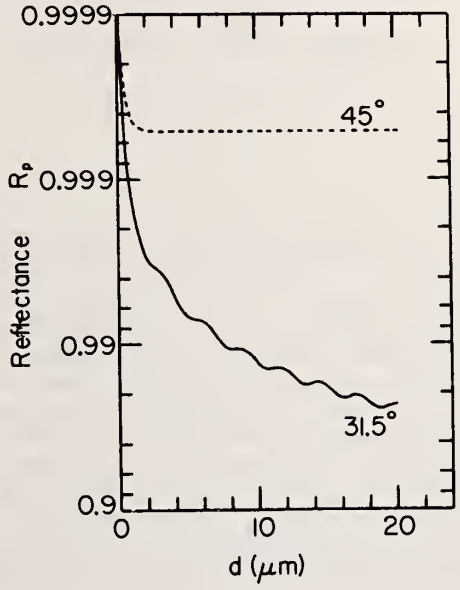

Figure 6. Calculated reflectance R as a function of film thickness d for ThF_4 on ZnSe for ω = 2632 cm^{-1}, α = 3 cm^{-1} and p-polarization for θ = 31.5 and 45°.

COMMENTS ON PAPER BY HOLM AND PALIK

As a demonstration of the sensitivity of ATR techniques, the speaker mentioned that they had detected a 50 Å layer of carbon at a SiO_2 - Si interface by ATR. He was not sure what the effect of scattering would be on ATR measurements. It did not appear that the extension of the ATR measurement to multilayer films or inhomogeneous films has been fully analyzed, but in the evanescent wave case, it does seem possible to probe multilayer thin films as a function of depth.

4.1 ZnSe SPUTTERED COATINGS*

David A. Walsh
John A. Detrio

University of Dayton
Research Institute
Dayton, Ohio 45469

The sputter deposition of ZnSe for laser window coating preparation has been studied using substrates of ZnSe and KCl. Sputtering targets made from CVD ZnSe and commercially hot pressed material were also compared. Self films of ZnSe on ZnSe were studied for absorption versus thickness using films of $\lambda/4$, $3\lambda/4$, and $5\lambda/4$ at 10.6 μm. Calorimetric absorption measurements showed the HP target material produced coatings with 3 to 6 times greater absorption. Auger analysis indicated the presence of sulfur in the HP films, but none in films made with the CVD target. Both types of coatings appeared to be non-stoichiometric. Film and substrate inhomogeneity prevented reliable measurements of the film absorption coefficient. ZnSe on KCl coatings were investigated with Auger Spectroscopy in order to distinguish between target material effects and the influence of surface preparation methods. As-polished material showed Al and oxygen present at the interface which indicate a residue of polishing compound. The residue was readily removed by etching in concentrated HCl. Damage measurements were also made on the ZnSe coatings.

Key words: Absorption damage levels; CVD; coatings; hot pressed; sputtered.

1. Introduction

This work represents the continuation of efforts to investigate the properties of sputter deposited ZnSe as a potential laser window coating. Previous work was directed at the modification of sputtering equipment to allow convenient optical monitoring of the film thickness [1][1], and attempts to obtain uniform coating thickness over practical dimensions [2]. The deposition of ZnSe on KCl as a test vehicle for evaluating the potential for depositing compact, pinhole-free, and tightly adherent coatings was reported previously [3]. During this latter study the effect of sputtering process variables (voltage, current, spacing, argon pressure) was further investigated. Mechanical strength problems associated with the thermal expansion mismatch between coating and substrate greatly reduced the survival of thick coatings of ZnSe on KCl. However, our experience indicated that the sputtered films were probably superior to thermally evaporated films with respect to environmental durability and we have continued to investigate this coating process for application to other substrates and for KCl coating designs which do not require a thick first layer of ZnSe. In this paper we report some of our initial attempts to understand the source of the 10.6 μm absorption in sputtered ZnSe films and the role of sample surface treatment in the production of low absorbing coatings.

2. Experimental

Two ZnSe targets have been used in the current investigation. One is composed of hot-pressed (HP) Kodak Irtran IV material; the other of chemical vapor deposited (CVD) Raytheon ZnSe. Previous evaluations have shown that there is a trend toward lower absorption in the coatings deposited from the CVD material, however, these differences were not defined well enough to make reliable judgements regarding the optimization of the individual coating parameters involved. The present work has included samples for Auger analysis of the film/substrate combinations and more sophisticated polishing methods were employed to allow more precise optical characterization.

---

* Work supported by Air Force Materials Laboratory Contract F33615-76-C-5093.

1. Figures in brackets indicate the literature references at the end of the paper.

2.1. Auger Analysis of Sputtered ZnSe

To evaluate the relative purity of coatings deposited from the two target materials, four sets of 6 mm square by 1 mm thick substrates were prepared from commercial ZnSe and KCl bulk material. For KCl, a freshly polished surface was generated by rough lapping with 9 μm SiC on a glass flat followed by pad polishing with 3 μm and 1 μm aluminas. The ZnSe samples were prepared from optically polished specimens. These surfaces were used as-received from the polishing vendor.

The finished surfaces were covered with a layer of Spawr "Opticoat" [4] to protect them during subsequent wire saw cutting and dicing operatings. Two of the KCl sample sets were then etched for 2 min in concentrated HCl to permit a comparison with the polished-only surface. As shown in table 1, two types of rinsing following the etch were evaluated to determine whether denatured ethanol would produce a cleaner surface than the 2-propanol customarily used. Some workers have employed an ethanol rinse prior to the 2-propanol since the KCl is slightly soluble in ethanol which prevents the recrystallization of dissolved KCl on the etched surface [5]. Samples were dried in a warm air stream during a slow withdrawal from the final 2-propanol bath. Both the polished-only and polished/etched specimens were stored in an evacuated dessicator prior to coating. Final cleaning of the ZnSe samples consisted of washing with a cotton swab in a mixture of "Micro" [6] detergent and deionized water followed by rinsing in running deionized water and immersion in three successive rinses of reagent grade 2-propanol with warm air drying. Samples were then dessicator-stored until coated.

Table 1. Preparation and coating results: CVD vs hot-pressed sputtering targets

Runs: 196 through 199

Variables: Target Materials, Argon Purity

Sample Coding:

KCl: Pol = Polished only

Eth = 2 min HCl etch + rinse in Ethanol + 3 rinses in 2-propanol

2-prop = As above with 2-propanol rinsing (3x) only

ZnSe Zn = Polished + detergen + 3 rinses in 2-propanol

Sputtering Conditions: 1000V (260 W), 8 μm, 2" spacing

Thickness measurements for ZnSe coatings:

Run No.	ZnSe Target	Argon Treatment	Coating Th'k Å
196	CVD	None	7,000
197	H/P	"	9,100
198	CVD	Purif.	9,500
199	H/P	"	10,200

Target materials were cleaned prior to film coating by pre-sputtering for 30 minutes onto a dummy substrate platen. Pre-sputtering conditions were the same as those used for the experimental films. These were held constant in all of the runs with R F voltage at 1000V (260 watts), argon pressure at 8 μm and target to substrate spacing of two inches. The depositions were duplicated from each of the targets using in one case the grade 5 argon as-received and in the second case the same argon further purified by passing it through a dessicant drying column followed by a G.E. "Go-Getter" catalytic Titanium gas purifier.

The results of Auger analysis of the sputtered ZnSe target materials on the ZnSe substrates are shown in figure 1. Sulfur contamination in the amount of approximately 1 At% is detected in the coatings deposited from the hot-pressed target. No contaminants were detected in the films deposited from the CVD material. Compositional shifts at the film/substrate interface are indicated for the hot-pressed target coatings where the sulfur concentration drops to a background level and there is an apparent shift to the Se-rich condition within the substrate. This is probably due to the normalization of the curves since the substrates are also CVD ZnSe. This Se-rich indication may also be seen in the film deposited from the CVD target in the plasma of as-received argon, while the gettered argon and CVD target produce a film which varies in intensity, but remains stoichiometric.

The presence of sulfur is also seen in figures 2 and 3, the Auger traces of films deposited from the hot-pressed ZnSe target onto the KCl substrates. Scans of CVD ZnSe coatings on similar substrates again indicate that this target material is free of sulfur contamination.

Additional contamination is indicated by the detection of Al and oxygen as the coating is penetrated and the substrate surface is approached. These signals are absent from the films deposited on the etched substrates. Since the intensity of both Al and oxygen reach a maximum intensity just below the interface, it is apparent that these peaks are due to imbedded Al_2O_3 polishing abrasive. This is confirmed by their absence at the interface of the etched KCl where the polished surface has been dissolved by the concentrated HCl.

In previous work, it was found that the sputtering rate of the more dense CVD target is appreciably higher than the lower density hot-pressed target. This has been observed again during this study as shown in table 2. The difference in sputtering rates would imply a more efficient energy transfer between the argon ions and the target surface.

Table 2. Sputtering rate of target materials vs argon treatment*

Argon Treatment	Sputtering Rate Å/min	
	Hot-Pressed	CVD
None	376	422
Gettered	352	420

*All other conditions held constant at 1000V RF, 8 μm Ar pressure, 2" spacing 250 watts.

It was also observed that the film tends to be Se-rich at the interface. Changes in the sputtering rates and variations in Ar pressures during the runs will be carried out to investigate if this is actually occurring or whether it may be due to the Auger measuring procedure.

Finally, it was concluded that the gettering of the 99.999% pure Argon used in the sputtering procedures results in no significant changes in the films which could be detected by Auger spectroscopy.

2.2. Absorption of ZnSe Target Materials

Two experiments were designed to measure the differences in absorption in films deposited from the hot-pressed and CVD ZnSe targets. In the first, several previously coated 1" ZnSe specimens were repolished in our laboratory. These were then coated with films of equal thicknesses from the hot-pressed and CVD targets with and without argon gettering and the coating absorption evaluated at 10.6 μm. In the second experiment, β vs coating thickness tests were carried out on similarly re-cycled window specimens in a quadrant format to provide uncoated, $\lambda/4$, $3\lambda/4$, and $5\lambda/4$ thick segments for 10.6 μm calorimetry.

a. Absorption of Sputtered ZnSe Films of the Same Thickness

The 1" witness plate samples were rough ground to identical thicknesses then polished and figured on a pitch lap to a flatness of ≈ 3 fringes. Surface finish on one of the samples from the block was determined to be 60 Å by T.I.S. evaluation.

Samples were cleaned after deblocking by immersion in trichloroethylene to remove residual wax followed by a detergent washing and 2-propanol rinsing using the same procedures as for the Auger samples. Sputtering conditions were held the same in these runs as in the coatings for Auger evaluation.

Results are shown in table 3. It was found that for both CVD sputtered films, the absorption is much less than in similarly deposited coatings from the hot-pressed target. This higher absorption correlates with the sulfur contamination detected by Auger analysis.

As in the case of the specimens prepared for Auger analysis, efforts to further purify the argon gas by gettering produced no significant influence on the coating performance.

Table 3. Absorption of ZnSe coatings on ZnSe substrates.

Target	Argon	Coating Rate Å/min	Coating Thickness Å	Coating Absorption $B_c \times 10^3$	Coating Absorption B_c cm^{-1}
H/P	as rec'd	380	10,500	4.04	28.4
"	gettered	385	10,000	2.60	26.0
CVD	as rec'd	491	10,500	.68	6.5
"	gettered	488	10,000	.97	9.7

b. Absorption vs Thickness of Sputtered ZnSe Coatings

In this evaluation absorption versus coating thickness for both the CVD and hot-pressed targets was investigated. Samples of $1\frac{1}{2}$" diameter were repolished following the same procedure outlined above. The same sputtering conditions were used to permit a direct comparison with the previous results. Optical thicknesses of $\lambda/4$, $3\lambda/4$, and $5\lambda/4$ were sputtered onto three 90^o quadrants of each sample with the fourth quadrant left uncoated as a control.

The absorption of each quadrant was measured calorimetrically at 10.6 μm and the results are shown in table 4. Absorption, in general, is again seen to be lower for the CVD target material than for the hot-pressed, however, the measured values for the $\lambda/4$ coating is much higher than in the previous evaluation and an inconsistency can be noted in the case of the $\lambda/4$ coatings with an apparent reversal in relative absorption to what would be expected: the hot-pressed material showing a much lower β and the CVD film much higher. The cause of this result is presently unclear. Calculations of refractive index based on observation of the thickness monitor interference fringe peaks at 6328 Å also indicates an anomalous value for the $\lambda/4$ coating. Measurement of a witness plate coated in the same run indicates that the proper physical thickness had been deposited. Measurement of the scattering of HeNe laser radiation at the same absorption site tends to exclude the possibility that an inclusion within the film has produced this reading.

Table 4. Summary of sputtered ZnSe coating absorption vs thickness

Hot-Pressed Target

Run No.	Thickness Optical	Thickness Calc. Å	Thickness Obs. Å	Absorption $B_c \times 10^{-3}$	Absorption B_c cm^{-1}	$n_{calc.}$ [a]	Scatter
206-1	$\lambda/4$	11,050	11,000	1.08	9.8	2.44	0.053
206-2	$3\lambda/4$	33,150	36,600	5.65	15.4	2.39	0.097
206-3	$5\lambda/4$	55,250	55,200	5.71	10.3	2.54	0.066

CVD Target

Run No.	Thickness Optical	Thickness Calc. Å	Thickness Obs. Å	Absorption $B_c \times 10^{-3}$	Absorption B_c cm^{-1}	$n_{calc.}$ [a]	Scatter
207-1	$\lambda/4$	11,050	11,050	3.54	32.2	2.18	0.053
207-2	$3\lambda/4$	33,150	34,000	4.23	12.4	2.48	0.052
207-3	$5\lambda/4$	55,250	55,300	3.53	6.4	2.48	0.069

[a] $n_{calc.} = q\lambda/2\ell$

$n_b = 2.40$

c. Focused CO_2 Laser Damage Tests

The damage resistance of these films to focused CO_2 laser radiation was measured. The details of the experiment are described elsewhere in these proceedings [7]. The results of the tests are somewhat surprising as shown in figures 4 and 5 which show the sequence of 3 s laser irradiations at various sites on the samples. The hot-pressed materials produced a coating which had some very tough spots which survived repeated irradiation while the CVD material coatings in general had lower damage levels. The CVD coatings were more uniformly damage resistant, however.

In summary, the CVD coatings had a higher threshold and were more homogeneous with respect to damage while the HP material was capable of with standing high power densities in selected areas. In general, the samples developed a residual strain at powers substantially below (30-50%) the level of catastrophic damage. Because these coatings were quite thick they suffered crazing and spontaneous destruction over much of their surface when first removed from desiccator storage just prior to irradiation. The damage results are subject to considerable uncertainty due merely to the variation in coating coverage. The power density corresponding to the average level of irradiation which produced catastrophic damage is 63 ± 32 kW/cm^2 for the HP target coatings and 51 ± 11 kW/cm^2 for the CVD material.

d. Water-Immersion Test: ZnSe on CaF_2

A test for the environmental stability of ZnSe coatings on CaF_2 substrates has been developed by Major D. O'Brien of AFML/LPO for evaluation of e-gun deposited films. By immersing the coated sample in deionized water and observing the elapsed time required to delaminate the coating, a qualitative measure of durability has been obtained. For most of these coatings, survival times have been fairly short; on the order of seconds up to a maximum of one to two minutes.

To compare sputtered ZnSe coatings to those fabricated by e-gun evaporation, coatings were deposited onto two pad-polished CaF_2 samples comparable to those used in the previous absorption work. Sputtering was done with the CVD target under the standard conditions of 1000V RF, 8 μm Ar pressure and 2" target to substrate spacing. Two thicknesses were deposited. One of these was 7800 Å which approximated the thickness of those being produced by Maj. O'Brien. The other was 29,000 Å to observe the effect of this testing scheme on a thicker coating. A 1/8" stripe across the sample face was masked during film deposition to allow for coating thickness determination.

Following 5 minutes immersion of the two samples in deionized water at 25°C the thicker film was observed to be developing a very fine crazing pattern about 1/32" wide at the edges of the masked area. The thinner film was unaffected at 5 minutes, but by 15 minutes it too had developed a similar crazing adjacent the masked area. At the end of 45 minutes, the crazing had spread to approximately 1/8" wide into the coating around the masked area and 1/32" around the outer edge of the thick coating sample. The thinner sample had developed a crazing only about 1/32" wide in the masked area during this same time interval. At the end of 75 minutes the test was terminated, but the samples were allowed to remain immersed overnight to observe the effect of this long exposure. At this elasped time the thicker film had crazed over about 50% of its area; the thin coating remaining unchanged with crazing limited to about 1/32" at the masked stripe. At a total immersion time of 17 hours, the thicker coating was completely crazed. The thinner film was crazed over about 60% of its area.

While not originally intended as part of the evaluation, it was observed that a portion of the coated specimens survived intact throughout the entire 17 hours. The samples used in the test were approximately equal halves of a 51 mm diameter by 10 mm thick KCl disc which had been fractured during prior handling; the fractured surface planes being at an angle of $\approx 45^\circ$ to the polished faces. During the coating procedures these areas also received a layer of ZnSe deposited at this oblique angle. It was in these portions of the samples that both of the sputtered coatings were unaffected by the immersion procedure. No special effort had been made to prepare these surfaces prior to deposition. Immersion in the detergent and water solution and a 2-propanol rinsing being the only cleaning they received.

This severe moisture resistance evaluation indicates that the integrity and bonding of the sputtered ZnSe is definitely superior to e-gun deposited coatings when applied to polished surfaces. Where the latter were completely crazed in minutes, the sputter deposited films remained intact for a much longer time and the crazing progressed at a slow rate from an area of exposed substrate surface where the solvent was able to penetrate under and lift the coating. It is possible that had the polished face received a continuous deposition over its entire surface the test results may have been more favorable. This implication is supported by the apparent durability of the coating sputtered onto the fractured surface.

It is of interest to note that in spite of the critical thermal shock characteristics of CaF_2 material, the temperature changes which are inherent in the sputtering process incurred no damage to the substrates used in this work.

3. References

[1] Walsh, D.A., Pukite, G.U., Fenter, J.R., Rev. Sci. Instr., 47, 8 (1976)

[2] Johnston, G.T., Walsh, D.A., Harris, R. J., and Detrio, J.A., UDRI-TR-75-23, 30 June 1975

[3] Walsh, D.A. and Bertke, R.V., Proceedings of the Fifth Laser Window Conference, p. 139, 1976

[4] Trademark, Spawr Optical Research, Inc., Corona, California

[5] Turk, Roger, Priviate communication, Feb. 1976

[6] Trademark, International Products Corp., Trenton, New Jersey

[7] Detrio, J.A. and Petty, R. D., Laser Induced Damage in Optical Materials; 1976, to be published.

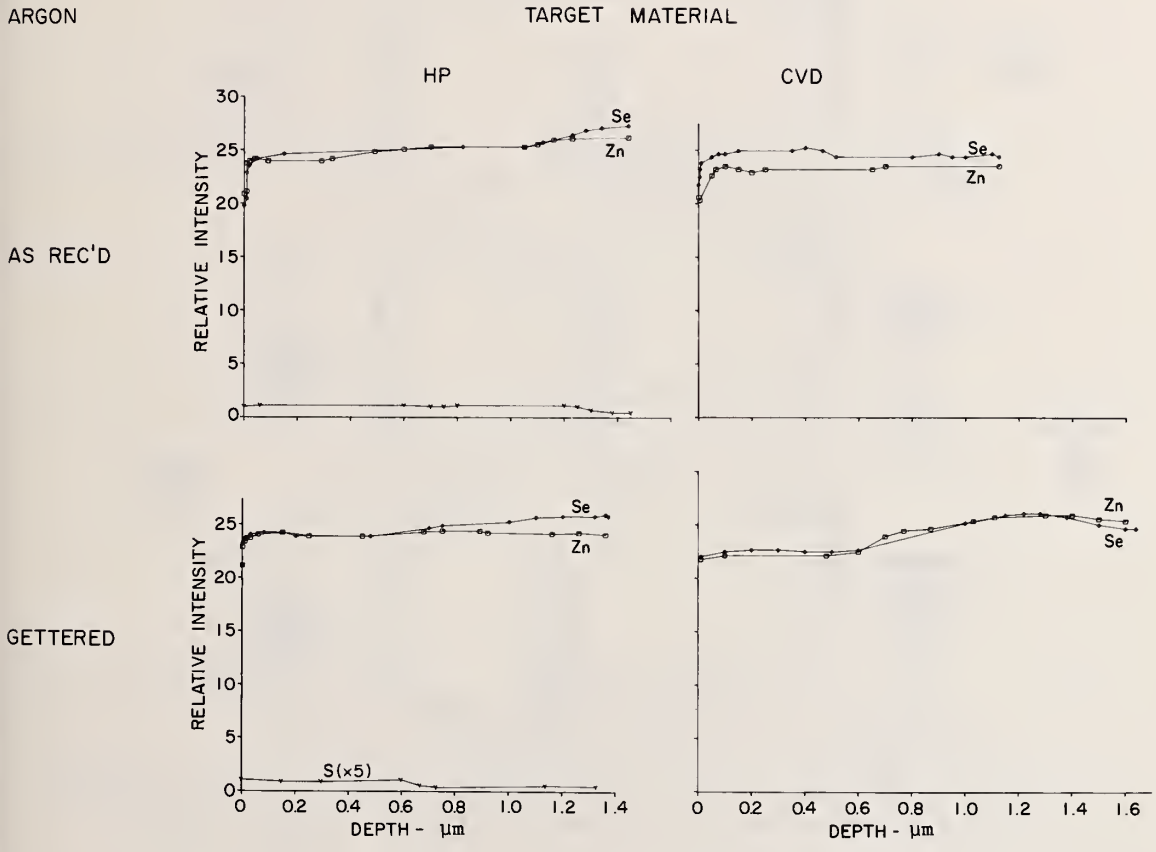

Figure 1. Auger spectra of ZnSe coatings on ZnSe substrates.

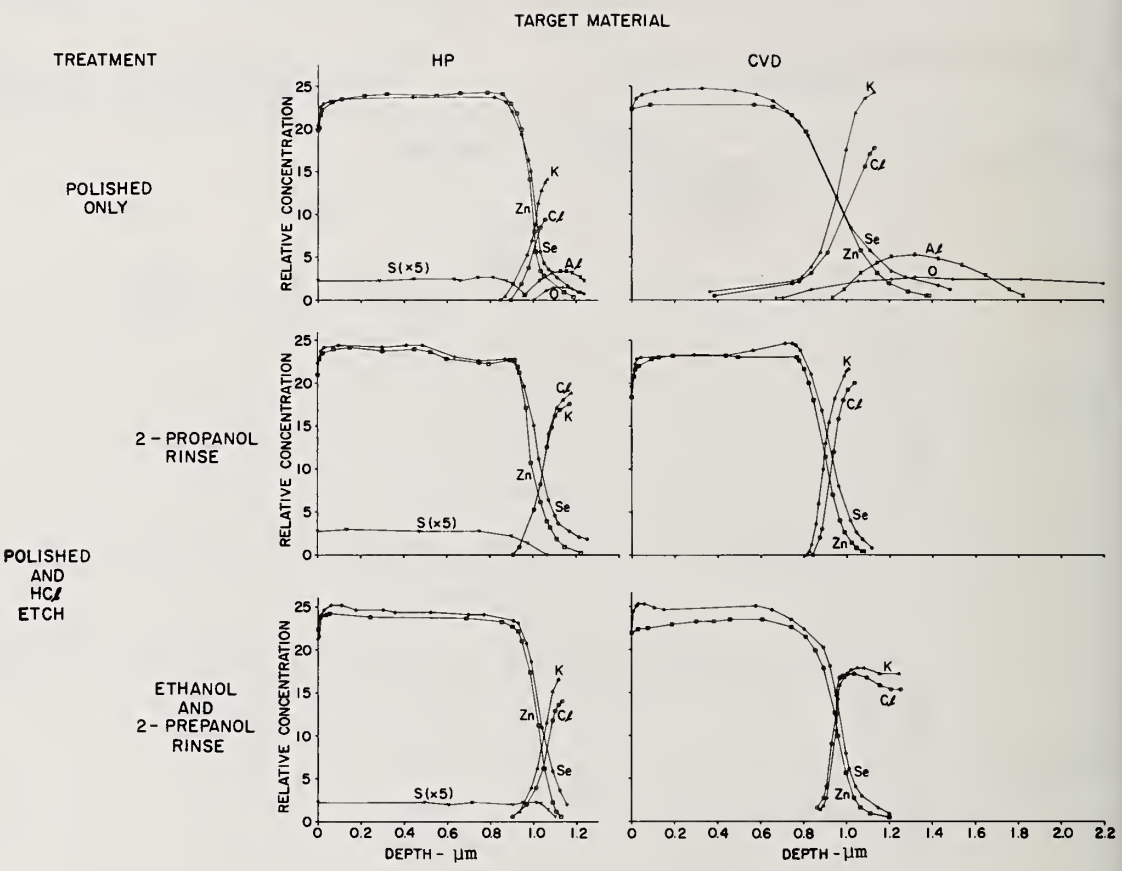

Figure 2. Auger spectra of ZnSe coatings on KCl substrates: argon gas as-received.

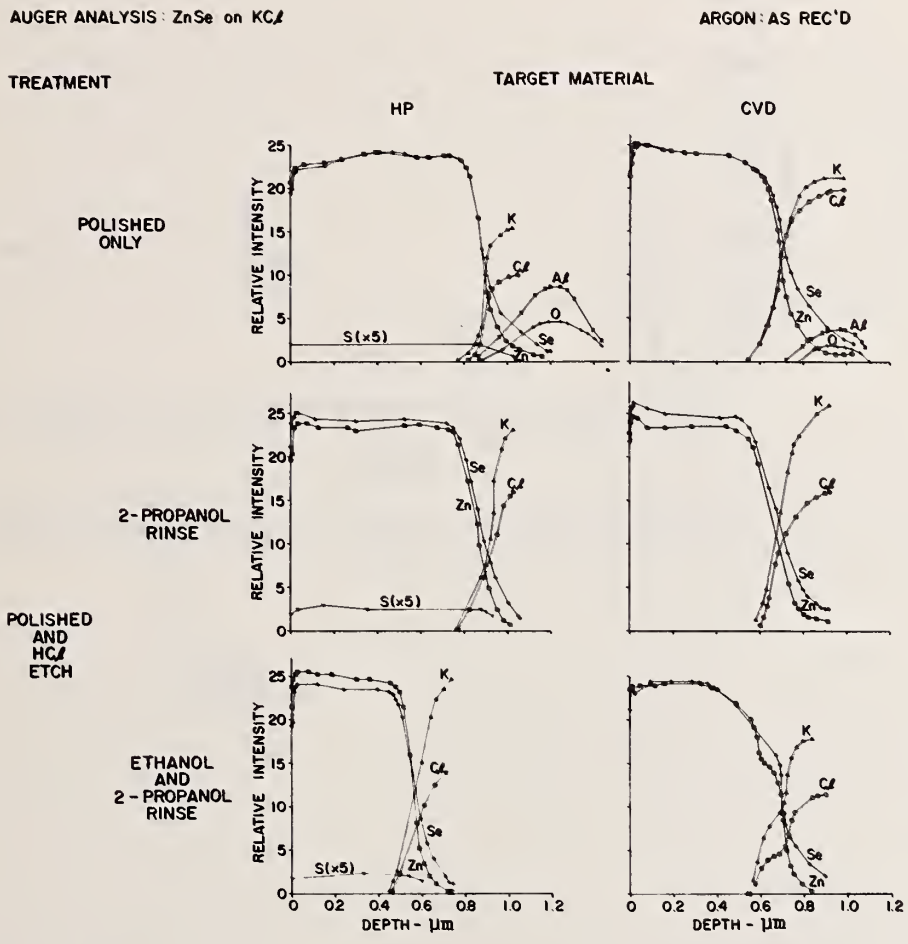

Figure 3. Auger spectra of ZnSe coatings on KCl substrates: gettered argon gas.

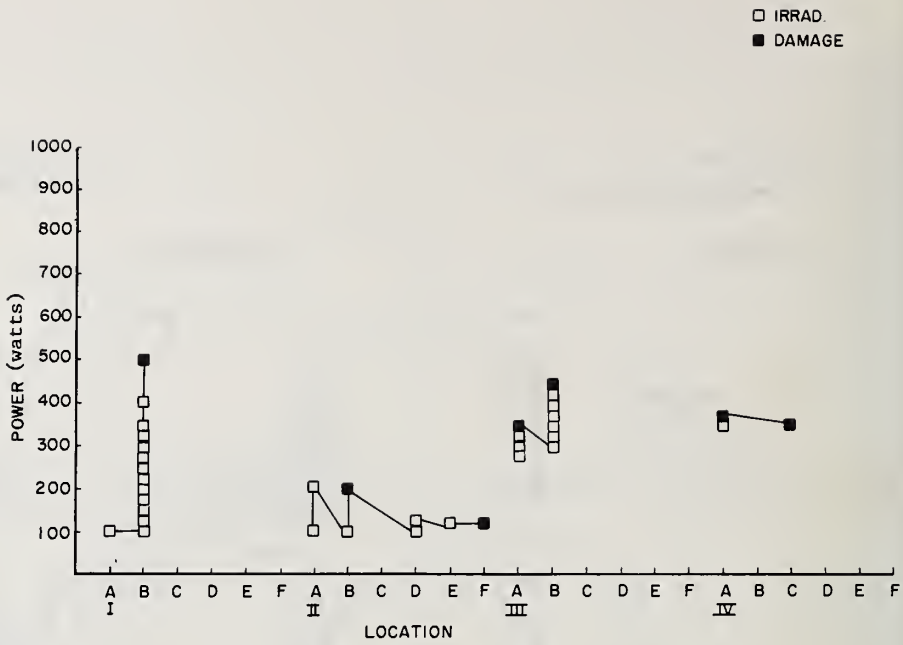

Figure 4. Irradiation sequence - ZnSe (HP) on KCl substrate.

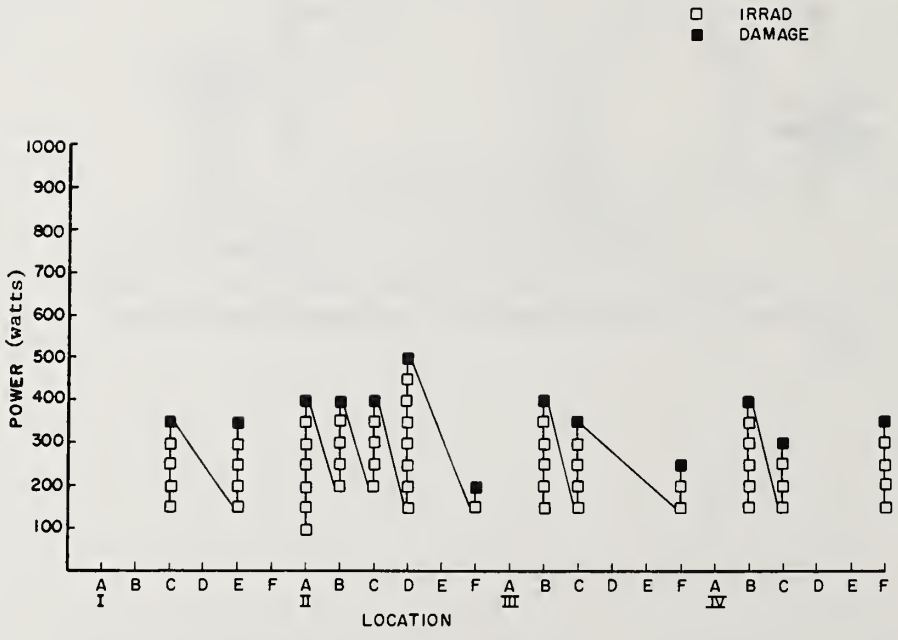

Figure 5. Irradiation sequence - ZnSe (CVD) on KCl substrate.

COMMENTS ON PAPER BY WALSH AND DETRIO

It was pointed out that in general, ZnSe coatings on CaF_2 substrates did not survive very long, but in one case where the coated surface was freshly cleaved rather than polished, the coating seemed to survive indefinitely.

4.2 LASER DAMAGE STUDIES OF LOW INDEX COATING MATERIALS AT 10.6 μm

M. J. Soileau, A. D. Baer, J. O. Porteus, J. L. Jernigan,
W. N. Faith, T. M. Donovan, and A. K. Green
Michelson Laboratories, Naval Weapons Center
China Lake, California 93555

The 10.6 μm laser damage thresholds were measured for a variety of promising low index coating materials. Coatings deposited on KCl and NaCl windows were studied. Measurements on NaF, BaF_2, and SrF_2 indicate that all these materials have thresholds in excess of 1 GW/cm^2 when properly deposited. A comparison of the bulk and thin film threshold of these materials will be given. Our results indicate that NaF is an attractive alternative to ThF_4 since it has reasonably low absorption, a high damage threshold, and can be used as a single layer antireflection coating on NaCl. The primary mechanism of failure in the coatings tested was found to be coating delamination associated with defects on the substrate surfaces.

Key words: Coatings; laser damage; laser windows; 10.6 μm lasers.

Introduction

Windows in most laser systems require antireflection (AR) coatings to reduce Fresnel losses and feedback to the laser's oscillator-amplifier chain. Infrared systems utilizing NaCl or KCl windows have the additional requirement that the exposed window surfaces be protected against attack from the atmosphere. As an illustrative example consider a CO_2 laser fusion system that uses an oscillator and five amplifier stages with two NaCl windows on each amplifier. Antireflection coatings on these windows could increase total system output by a factor of two (assuming 20 surfaces with 4% reflection loss per surface for uncoated windows) while minimizing the problems of isolating the oscillator from back reflections and protecting the windows from atmospheric moisture attacks.

In order to realize such improvements in systems performance one must have low index coating materials to use as single layer or components of multilayer AR coating designs. Such materials must have reasonably low absorption at the optical frequency of use, must be compatible with the window substrate and must be able to survive the extreme flux from the laser. In this paper pulsed laser damage studies on low index coating materials are presented. Materials studied were NaF, BaF_2, and SrF_2. These materials were chosen because they all have reasonably good transmission at 10.6 μm ($\beta < 1$ cm^{-1} in bulk form) and have excellent transmission in the 3-5 μm region [1,2][1]. NaF is of special interest since its index of refraction is almost exactly equal to the square root of the index of NaCl at 10.6 μm. NaF can therefore be used as a single-layer (quarter wave) AR coating for NaCl at 10.6 μm.

Experimental

Films of NaF, SrF_2, and BaF_2 were deposited on NaCl or KCl substrates. All films were an optical thickness of one quarter wave at 10.6 μm. The films were deposited in a standard oil-pumped vacuum system in the manner described by Baer et al. [2]. The 10.6 μm absorption of the films was determined by laser calorimetry [3,4]. The total absorption of the uncoated windows was measured before coating deposition, and the total absorption of the window/coating combination was measured after coating deposition. The differences in the two absorption values were attributed to the particular coatings involved.

Damage testing was performed using the Naval Weapons Center's laser damage facility [5]. The experiments reported in this paper were conducted on a pulsed, single-mode CO_2 laser operating in the 10.6 μm region. It has reproducible temporal and spatial characteristics which are detailed in the following discussion. Beam intensity is controlled by a rotating polarizer-analyzer combination, each consisting of two ZnSe plates tilted in opposite directions to minimize beam shift, as well as by CaF_2 attenuators. After the attenuators, the energy in each pulse is measured by a pyroelectric energy meter which is calibrated using a thermopile calorimeter. The beam enters the test chamber through a NaCl window and is focused on the sample with either a 5.08 cm diameter, 11.91 cm focal length or a 2.54 cm diameter, 3.546 cm focal length ZnSe meniscus lens. The meniscus lens was used in order to minimize spherical aberrations. Focal lengths given are for 10.6 μm. A HeNe laser is used for convenience in aligning the optics.

---

1. Figures in brackets indicate the literature references at the end of this paper.

The temporal beam characteristics are monitored with a photon-drag detector having a 1.5 ns rise time. Figure 1 shows the measured intensity as a function of time, together with an analytical expression which describes this dependence. As can be seen in figure 1 the laser output increases linearly to the peak and falls off as a steep exponential. The peak power, calculated in watts using the total output energy and temporal pulse shape, is 1.27×10^7 times the total output energy (in joules). From this expression we can define an equivalent pulse width of 78.7 ns; i.e., the total energy divided by 78.7 ns gives the peak power of the pulse. In previous work [5,6] we described this pulse as being approximately 100 ns wide and having peak power 1.27 times the power calculated by dividing the total output energy by 100 ns. The peak power calculated using either technique is the same. However, the 78.7 ns width is more meaningful since it and the total energy yield the peak power directly. Note that the *1/e* full width of the pulse is approximately 78.7 ns. The full width at half maximum (FWHM) of this pulse is approximately 60 ns.

The spatial profile of the beam as it enters the damage chamber was measured using a pinhole scanned across the beam and can be represented by a Gaussian distribution to within 4%. The *1/e* full width of the unfocused beam was 5.8 mm. When focused by the 11.91 cm focal length ZnSe lens the spatial profile, as measured using a scanning slit, can be represented by $exp[-2(r/100)^2]$ where r is the half width of the Gaussian in μm. Thus, the $1/e^2$ spot diameter for this lens is 200 μm. The focused beam width was measured as a function of the ZnSe focusing lens position. From this measurement the depth of field of this lens was determined to be approximately 3 mm [5,6]. The approximate effective f-number of the lens, i.e., the focal length divided by the *1/e* beam width, is ~ 20 and helps to explain the large depth of focus which was observed. The spot size for the 3.546 μm focal depth was determined by scaling the measured spot size of the 11.91 cm focal length lens as the ratio of focal lengths to the two lenses. This calculation yields a $1/e^2$ spot diameter of 59.5 μm for the 3.546 cm focal length lens. The effective f-number of this lens is approximately 6.

The correct focal position for the lens was determined using a technique previously described by Porteus et al. [7]. This procedure allows us to determine the focal position of the specimen surface to within 10 μm (the repeatability of the translation micrometer).

The test chamber and the analytical instrumentation used in this experiment have been described previously [6]. The chamber is designed for ultrahigh vacuum, including bakeout. However, these measurements were made at a base pressure below 1×10^{-7} Torr without bakeout. Visible changes in the specimen (surface or bulk) were monitored by observing the scattered light with a 20-power optical microscope.

Results

Bulk thresholds for single crystal NaF, BaF_2, and SrF_2 were measured to determine if intrinsic 10.6 μm damage limits would prohibit the use of these materials as coatings for NaCl or KCl windows. The single crystal materials were acquired from the Harshaw Chemical Company. The 3.546 cm focal length lens was used in this part of the experiment to minimize the problem of surface damage. The results of these measurements are summarized in figure 2. As can be seen in this figure all of the bulk values are quite high. The values given are for the peak on-axis intensity at the focal plain of the lens (approximately 0.5 cm into the bulk of the 1.0 cm thick specimens) and includes the effects of attenuation of the beam by these weakly absorbing materials. The high number for the BaF_2 threshold may be due to the fact that it is an n-on-one number and the other numbers are for single shot damage. The one-on-one (single shot) damage threshold for the BaF_2 could not be determined because of the very low surface damage threshold for this specimen. By preconditioning the surface (successively higher energies after initial illumination applied below the single-shot threshold) we were able to transmit sufficient energy into the material to cause bulk damage without damaging the front surface.

The bulk threshold for Harshaw Chemical Co.'s single crystal NaCl was determined using the same experimental arrangement described above (the same lens, focusing procedure, detector calibration, and data reduction techniques). The threshold for breakdown thusly determined was 1.92×10^6 V/cm, which is quite close to values of 2.02×10^6 V/cm measured in similar material in our laboratory with the same laser, the 11.91 cm focal length lens [6], and the value of 1.95×10^6 V/cm reported by Yablonovitch [8].

The NaCl breakdown threshold from this work and the breakdown thresholds for the BaF_2, SrF_2, and NaF are compared in figure 3. Note that the measured thresholds for the proposed coating materials are all significantly higher than that of NaCl. The ratios of field strengths given in figure 3 agree quite well with values obtained at other wavelengths [9,10] and in the case of NaF, with the ratio of the dc thresholds [11]. The relatively large discrepancy (~14%) between the 10.6 μm and 3.8 μm ratios for BaF_2 is probably due to the fact that the 10.6 μm threshold for BaF_2 was determined for the n-on-one case and ratioed to the one-on-one threshold for NaCl.

The implication of these results is that coatings of NaF, BaF_2, and SrF_2 on NaCl will not be limited by intrinsic processes. Films of one quarter-wave optical thickness (for $\lambda = 10.6$ μm) were deposited on substrates of NaCl and KCl in the manner described by Baer [2] and the total 10.6 μm of the films determined using laser calorimetry. The results of the absorption measurements are given in figure 4. The absorption values given are the fraction of the total incident power absorbed by the films. The

substrates on which these films were deposited all had total absorption $< 10^{-3}$ each at 10.6 μm prior to coating deposition. Therefore, the film absorption values computed by subtracting the initial substrate absorption from the total absorption of the substrate/coating combination should be reasonably accurate. The accuracy of each absorption measurement is ± 10%; thus, ± 20% would be the accuracy of the difference if the coating and substrate absorption were equal. Since the substrate absorption was always less than the coating absorption the uncertainty of the numbers in figure 3 should be less than ± 20% and greater than ± 10%.

These films were damage tested, and the results are summarized in figure 5. As can be seen in these data, the thresholds for NaF, BaF_2, and SrF_2 are all significantly greater than values measured for ThF_4 by other workers [12]. Then, from a pulsed laser damage standpoint, these materials offer a significant advantage over ThF_4 films. The numbers given in figure 5 are peak-on-axis intensities (single shot) which produced damage 50% of the time. The NaF data were taken with the 11.91 cm focal length lens ($1/e^2$ spot diameter equal to 200 μm), and the BaF_2 and SrF_2 data were taken with the 3.546 cm focal length lens ($1/e^2$ spot diameter equal to 59.5 μm).

Discussion

Simple one-dimensional heat flow calculations indicate that the temperature of the films tested increased approximately 1000°, 640°, and 170°C for the SrF_2, BaF_2, and NaF, respectively, for power densities equal to the damage thresholds. Temperature increases were calculated using room temperature thermal properties. Since the heat capacity of these materials increases with temperature, these temperature rises represent an upper limit, assuming the average absorption of the films are as given in figure 4. From this we conclude that the films did not fail due to thermal evaporation or linear absorption in the films.

Micrographs of the damage sites and comparisons with uncoated window surface damage data suggest that the coatings failed due to substrate surface limitations. Figure 6 is a Nomarski micrograph of a typical damage site on the SrF_2-coated specimen. Failure appears to have been by massive or explosive fracturing of the KCl substrate which was chemically etched [4] prior to coating deposition. Previous work indicated that the one-on-one threshold of etched KCl surfaces is 67% [6] of the bulk value reported by Yablonovitch [8]. This measured threshold is very close (1.13 MV/cm compared to 0.97 MV/cm) to the expected value for an uncoated etched surface. From this evidence we conclude that the SrF_2/KCl combination failed due to dielectric breakdown of the KCl surface.

Figure 7 is a Nomarski micrograph of a typical damage site for BaF_2 on a NaCl substrate. The laser spot size was 59.5 μm ($1/e^2$ diameter). The laser was linearly polarized with the electric field vector in the vertical direction. The damage threshold given in figure 5 for this coating is 1.22 times that measured for an uncoated NaCl window with a similar surface finish [6], a standard commercial polish from Harshaw Chemical Co. Several defects can be seen in the damaged area in figure 7. Close inspection of this micrograph reveals a ripple pattern associated with the coating delamination or removal and similarly with the large defect that is evident. The ripples are due to resonant effects for polarizable elements (defects) on the surface [13]. The presence of these defects and the associated ripple patterns, combined with the nearness of the threshold to values measured for similar uncoated surfaces, strongly suggests that damage to this film was initiated by defects on the NaCl surface.

Figure 8 is a Nomarski micrograph of a typical damage site on NaF-coated NaCl substrate. The laser spot size was 200 μm ($1/e^2$ diameter). The laser was linearly polarized with the electric field vector in the vertical direction. Note the defects in the damage area and their associated ripple patterns. The illuminated area contained many defects, and the specimen damaged at this point with an incident power level approximately 40% below the power level which produced damage 50% of the time in this specimen.

The average threshold for NaF on NaCl was 77% of the value measured for another commercially polished surface (Harshaw Chemical Co.) using the same laser, focusing lens and diagnostic facilities [6]. This decrease may be due to the introduction of defects in the coating process (either on the surface or in the coating). However, it is equally likely that this 23% difference is due to variations in surface quality from specimen to specimen.

The effects of surface defects on laser damage to surfaces and coatings are illustrated in figure 9. Note that the coating "separation" line has a set of ripples which contour it. These ripples are in the coating material and are separated by one wavelength in the NaF coating. The ripples on the uncoated surface are on spacings of one wavelength in NaCl. The ripples in the coated area and the uncoated area are physical variations on the surface and not just density or index variations. The micrograph in figure 9 was taken after the area was silvered. The only effect of the silver coating was to enhance the visibility of the ripples. The micrographs in figures 6, 7, and 8 are of unsilvered surfaces.

It is not clear whether the ripples associated with the coating separation line are "cause" or "effect." The separation line itself could be a source for the ripples or it may represent the point where the intensity of the interference between the incident beam and the dipole field from a surface defect has decreased to the point that sufficient energy for coating removal is not available. Since there seems to be a reasonable correlation with the ripples in the uncoated area, the latter case seems more likely.

A NaCl window was coated on each side with a quarter-wave optical thickness of NaF. Since the square root of the index for NaCl is almost exactly equal to the index of NaF, this window was effectively AR-coated on both sides. The window was placed in the damage chamber, and the entrance and exit surface (or coating) damage threshold was measured. The two thresholds differed by about 15%. The window was then turned over so that the side that was the exit was now the entrance surface and vice versa. The result of this experiment was that a given side (i.e., coating plus surface) had the same threshold for the entrance and exit surface case. This is as expected for an AR coating since the coating/window system is symmetric with respect to electric field strengths and total transmitted energy; this result is summarized in figure 10.

Conclusions

NaF, SrF_2, and BaF_2 offer attractive alternatives to ThF_4 as low index coatings for windows in the 10.6 μm range. NaF is particularly attractive since it can be used as a single layer AR coating at 10.6 μm. The bulk damage mechanism for these materials is intrinsic dielectric breakdown, and the breakdown thresholds are considerably above those of the NaCl and KCl windows on which coatings are to be deposited. Thus, coatings of these materials should not be limited by intrinsic properties.

Coatings of NaF, SrF_2, and BaF_2, deposited using state-of-the-art techniques in conventional vacuum systems, exhibit absorption of a factor of 10 to 200 times that of the bulk single-crystal material. However, this relatively high absorption does not limit the use of these materials for low average, high peak power pulsed applications. In order to be useful in systems with high average power outputs this extrinsic absorption in these materials in thin film form must be reduced.

The peak power handling capability at 10.6 μm for thin films of NaF, SrF_2, and BaF_2 on NaCl and KCl is limited by the substrate surfaces. Surface defects interact with the incident beam to produce optical interference in the substrate surface and/or in the film. Evidence for such interference is seen as permanent damage to the surfaces and coatings that have periodic structure with spacing of one wavelength in the material.

NaF is an excellent material for use as an AR coating for NaCl windows in pulsed laser applications. Since it is a square root of the index match for NaCl, AR coatings can be formed using a single quarter-wave layer. For an AR-coated window the entrance and exit surface damage thresholds are equal. Such a window/coating system is symmetric with respect to electric field intensity and power transmission.

Acknowledgments

This work was supported by ERDA, ARPA, and NAVWPNCEN Independent Research funds. The authors are grateful to Mr. Richard Smith, Mrs. Verla Walker, and Ms. Jane Williams for their invaluable assistance in preparing the artwork and manuscript for publication.

References

[1] Sparks, M., "Coatings for High-Power Infrared Optics," these Proceedings.

[2] Baer, A. D., et al., "Alternative Materials for Laser Window Coatings," these Proceedings.

[3] Loomis, J., Appl. Opt. 12, 877 (1973).

[4] Soileau, M. J., et al., in *Laser-Induced Damage in Optical Materials: 1975*, A. J. Glass and A. H. Guenther, eds. (NBS Spec. Publ. 435, 1976), pp. 20-28.

[5] Porteus, J. O., et al., *op. cit.*, pp. 207-15.

[6] Soileau, M. J., et al., in *Proceedings of Fifth Annual Conference on Infrared Laser Window Materials: 1975*, C. R. Andrews and C. L. Strecker, eds. (Defense Advanced Research Projects Agency, Arlington, Va., 1976), pp. 391-417.

[7] Porteus, J. O., et al., "Focusing Method Used in Laser Damage Experiments," Appl. Opt., in press.

[8] Yablonovitch, E., Appl. Phys. Lett. 19, 495 (1971).

[9] Bass, M., et al., "Pulsed Laser-Induced Damage at the DF Wavelengths," these Proceedings.

[10] Fradin, D. W., et al., Appl. Opt. 12, 700 (1973).

[11] Von Hipple, A., J. Appl. Phys. 8, 815 (1937).

[12] Wang, V., et al., in *Laser-Induced Damage in Optical Materials: 1974*, A. J. Glass and A. H. Guenther, eds. (NBS Spec. Publ. 414, 1974), pp. 59-65.

[13] Temple, P. A. and Soileau, M. J., "Resonant Defect Enhancement of the Laser Electric Field," these Proceedings.

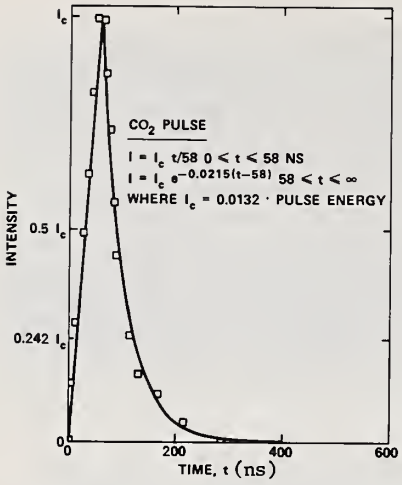

Figure 1. Temporal profile of laser output. The peak power in this pulse is 1.27×10^7 times the total energy in the pulse. The 1/e full width of the pulse is approximately 78.7 ns. The FWHM pulse width is approximately 60 ns.

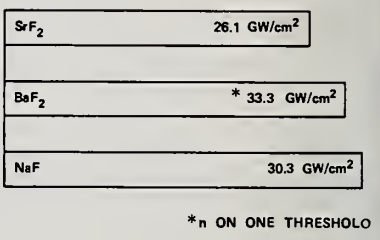

Figure 2. 10.6 μm bulk thresholds single crystal NaF, SrF_2, and BaF_2. The powers given above are peak-on-axis intensities. The high value for the BaF_2 threshold is probably due to the fact that it is an n-on-one number, and the others are for single-shot damage.

RATIOS OF DAMAGE FIELDS IN NaF, SrF_2 AND BaF_2 TO NaCl

	10.6 μm	3.8 μm	1.06 μm	dc
NaF	1.57	>1.51	1.64	1.60
SrF_2	1.39	1.41	---	---
BaF_2	1.55	1.36	---	---

Figure 3. Ratios of damage fields in NaF, SrF_2, and BaF_2 to NaCl. The 10.6 μm ratios were all obtained with the same experimental setup. The 3.8 μm, 1.06 μm, and dc values were obtained from other work [10,11].

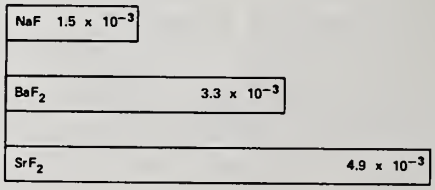

Figure 4. 10.6 μm absorption for quarter-wave coatings of NaF, BaF_2, and SrF_2. The NaF and BaF_2 films were deposited on NaCl, and the SrF_2 was deposited on KCl.

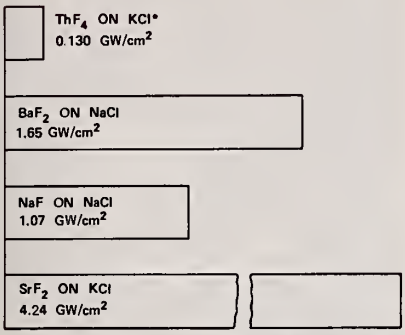

Figure 5. Summary of 10.6 μm damage data for low index coating materials. The power densities given above are the peak-on-axis intensities which produced damage 50% of the time. The NaF data were taken with the 11.91 cm focal length ZnSe lens ($1/e^2$ spot diameter equals 200 μm), and the BaF_2 and SrF_2 data were taken with the 3.546 cm focal length ZnSe lens ($1/e^2$ spot diameter equals 59.5 μm).

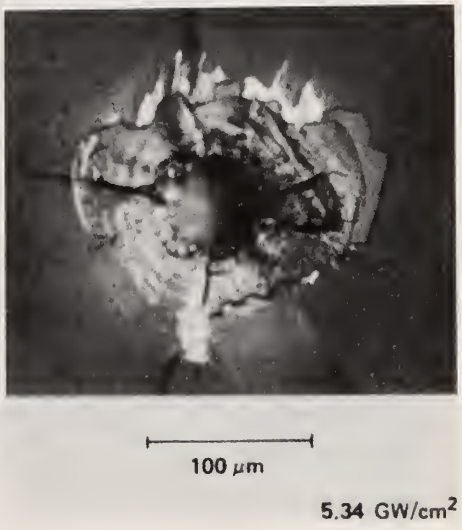

Figure 6. 10.6 μm laser damage to a SrF_2 on KCl (exit surface). This site is typical of all damage to the SrF_2 film. Failure appears to have been initiated at the KCl surface.

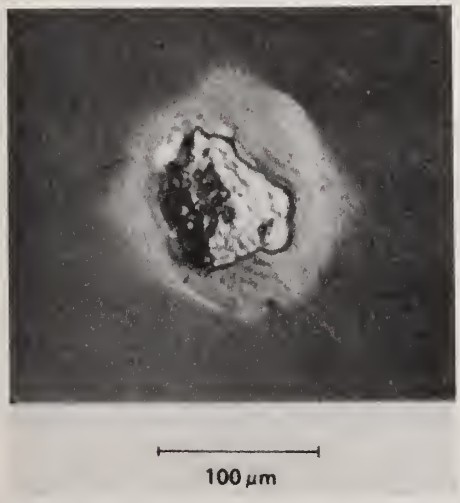

Figure 7. 10.6 μm laser damage to a BaF_2 coating on NaCl (exit surface). This site is typical of all damage to the BaF_2 film. Failure appears to be initiated at defects on the NaCl surface. The laser is polarized in the vertical direction in this picture. The line in upper right represents coating delamination; a large defect can be seen in lower right corner.

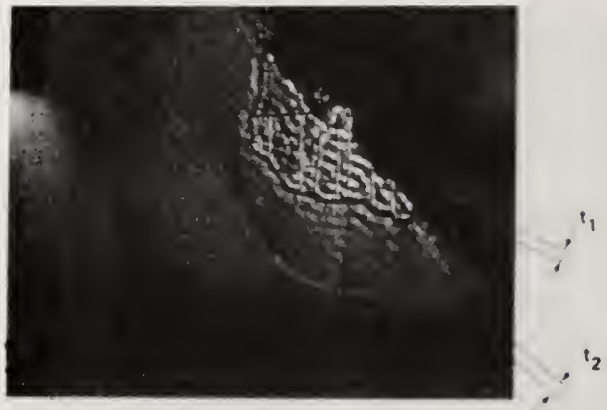

Figure 8. Exit surface damage to NaF-coated NaCl. Note ripple structure associated with surface defects. The laser spot $1/e^2$ diameter was 200 μm.

Figure 9. Effects of surface defects on window coating damage (exit surface). Note that the ripple pattern is associated with the coating separation line. The laser spot $1/e^2$ diameter was 200 μm. As in all the micrographs presented here, the incident laser electric field is in the vertical direction.

NaF COATING No. 1

EXIT SURFACE	760 MW/cm²
ENTRANCE SURFACE	740 MW/cm²

NaF COATING No. 2

EXIT SURFACE	872 MW/cm²
ENTRANCE SURFACE	870 MW/cm²

Figure 10. Entrance and exit surface damage on AR-coated NaCl. Threshold values given are peak-on-axis intensities. The $1/e^2$ spot diameter was 200 μm. Coatings No. 1 and No. 2 refer to AR coatings of NaF on either side of a NaCl window.

COMMENTS ON PAPER BY SOILEAU, BAER, PORTEUS, JERNIGAN, FAITH, DONOVAN, AND GREEN

Damage in these experiments was invariably accompanied by the emission of a flash of light, indicative of plasma formation. Near threshold, the light emission was less intense. The defects observed in this study were always on the substrate, and were attributed to the surface polishing process. The speaker indicated that the homogeneity of the fluoride films had not been investigated thoroughly.

4.3 THE USE OF RARE EARTH FLUORIDES AS 10.6 μm ANTIREFLECTIVE COATINGS

A. Golubovic, J. Fitzgerald, I. Berman, J. Bruce
R. Bradbury, J. J. Comer, W. S. Ewing and H. G. Lipson
Deputy for Electronic Technology (RADC)
Solid State Sciences Division
Hanscom AFB, MA 01731

The rare earth fluorides have been evaluated as possible antireflective laser window coatings at 10.6 μm. Emphasis was placed on SmF_3, EuF_3, and GdF_3 as a single layer coating for ZnSe and as the low index material in a 2-layer design with ZnSe on KCl substrates. The chemistry, structure and texture of the coatings were examined by several techniques including electron and optical microscopy, x-ray diffraction, Auger spectroscopy,and optical spectroscopy. Pulsed laser damage studies at 10.6 μm were performed to evaluate the relative merits of these coatings. As expected, the damage threshold for the single layer fluoride coatings as ZnSe were found to exceed the threshold of the 2-layer designs on KCl substrates.

Key words: Laser antireflective coatings; materials purification requirements; pulsed laser damage; rare earth fluorides; zinc selenide coatings.

1. Introduction

In a previous paper [1][1] we reported on the optical, mechanical and structural properties of several rare earth fluorides, namely LaF_3, NdF_3, CeF_3,and GdF_3, for use as antireflective coatings at 10.6 μm. There it was noted that these materials might serve as alternatives to ThF_4 as low index coating materials for HEL application. It is the purpose of this paper to report on a continuation of that study and to present the results of recent investigations on several more rare earth fluorides namely SmF_3, EuF_3, GdF_3,and PrF_3.

For this investigation we have considered the fluorides as antireflective coatings for use on ZnSe as a single layer $\lambda/4$ design and for the alkali halides as a double-layer coating together with ZnSe as the high index first layer. These designs represent practical applications for these low index materials and provide a realistic means for evaluating their performance in HEL applications. Pulsed laser damage threshold is used as a diagnostic tool in the overall evaluation of these coatings in addition to the structural and chemical analysis by various techniques.

2. Experimental

The potassium chloride substrates used in this investigation were (100) oriented Czochralski grown crystals obtained from Optovac, Inc. as 2.5 cm diameter x 1.25 cm thick rough polished blanks. Prior to final polishing, each substrate was checked for proper orientation by x-ray diffraction. The mechanical-chemical polishing procedures used for these substrates has been described in an earlier paper [1] and is similar to that described by NRL [2]. The substrates used in this investigation were subject to pitting during mechanical polishing and were judged inferior to those used in previous investigations. When etched, a slight mosiac structure was observed for these crystals.

The ZnSe substrates were fabricated from Raytheon CVD material obtained from Dr. J. Pappis. Substrate blanks were cut 2.5x2.5x0.300 cm by Manlabs, Inc. and then polished and etched according to the method described by Hughes [3].

The two layer antireflective coating designs for KCl were based on ZnSe as the high index (n = 2.42) coating together with the low index fluorides. Coating designs were computer optimized for the individual fluoride coatings based on experimentally measured indicesfrom single layer fluoride coatings on ZnSe substrates. The coating design for SmF_3 (n = 1.59) is given in figure 1 together with the theoretical and experimentally measured spectral response for this coating pair. All of the two layer designs have the some broad band response at 10.6 μm.

For the two layer coatings on KCl the ZnSe first layers were deposited by both thermal and R F sputter deposition techniques. The R F sputter deposited samples

1. Figures in brackets indicate the literature references at the end of this paper.

were produced from a pressed powder ZnSe target in a Randex turbo pumped system in an ultrapure argon atmosphere. R F power levels between 50 and 250 watts were used to determine optimum deposition parameters for these coatings which are given in table 1. The samples were ion etched prior to deposition for 30 seconds at 50 watts power for improved film adherence. The sputter system did not have provision for in-situ thickness monitoring, but careful control of pressure and R F power provided accurate, reproducible calibration of rate. Thus, film thickness was controlled by time of deposition at a calibrated rate. The final thickness for each coating was determined by measurement of the interference maxima in the spectral scan between 1 and 15 μm.

The thermally deposited ZnSe coatings were produced in a VEECO VE-400 medium high vacuum system. Prior to deposition each sample was glow discharge cleaned for a period of 10 minutes in research grade argon gas at a pressure of 150 µm. The starting material for these depositions was scrap Raytheon CVD ZnSe remaining from substrate preparation. Early depositions used a quartz crucible source, however, the films produced with this crucible material showed unidentifiable lines in powder x-ray analysis For later depositions Al_2O_3 crucibles were used eliminating this contamination. For these depositions, rate and thickness control were maintained by an Inficon XMS-3 quartz crystal monitor which allowed rate control to ±0.1 nm/s. In addition, substrate temperature was controlled by a quartz iodine lamp behind the substrate. The deposition parameters for the thermally deposited ZnSe coatings are shown in table 1.

All of the rare earth fluoride coatings reported in this investigation were thermally deposited in either medium high vacuum or in special cases ultra high vacuum. The medium high vacuum depositions were performed in a LN_2 trapped NRC-801 bell jar system equipped with an Inficon quartz crystal monitor and quartz iodine heating lamp. Substrate temperatures were continuously monitored during deposition by a chromel-alumel thermocouple in direct contact with the substrate fixturing. For these depositions no in-situ cleaning was performed, however, prior to deposition the substrates were heated to 373°K for at least one hour to eliminate water adsorption.

The ultrahigh vacuum depositions were performed in a General Electric all stainless steel ion pumped system equipped with quartz iodine heaters, a quartz crystal monitor and a UTI 100 c precision mass analyzer. No provision was made for in situ cleaning in this system, however, a 525°K bakeout of the entire system insured elimination of adsorbed water from the substrate prior to deposition.

The starting materials for the fluoride depositions were either Cerac/pure (99.9%) or Ventron optical grade. No detectible difference were observed from these different starting materials. Each starting material was powder x-ray analyzed to determine rare earth oxide content. In the case of PrF_3, PrOF was detected as a major contaminant of the starting material. In those cases where powder (-325 mesh) starting material was used, it was necessary to vacuum press the material to prevent spatter as the source was heated.

The deposition parameters for each of the fluoride materials is summarized in table 2 together with the measured indices for the coatings. For the EuF_3 deposition, the parameters given are for the cubic difluoride EuF_2. The preliminary depositions of EuF_3 were found to be erratic, leading to a two stage deposition beginning with the trifluoride and finishing with the difluoride. The initial stages of these depositions were characterized by rapid pressure and deposition rate fluctuations. The coatings produced from this stage were found to be unstable and very highly stressed. The second stage of these depositions was controlled and required additional source power to establish rate. Coatings produced from starting material after taken completely through stage one, or using already sublimed material were found to be stable, clear and adhered well to all substrate combinations. The trifluoride and difluoride structures were identified by x-ray and reflection electron diffraction of stage one and stage two material.

3. Characterization

The structure and chemistry of the coatings studied in this investigation were characterized by a variety of techniques. X-ray and electron diffraction were used to determine the crystallinity, preferred orientation and composition of the coatings. Powder x-ray diffractrometry was used to determine the gross composition of the starting material. X-ray diffractrometry scans of the coated samples were used to determine preferred orientation where possible. Reflection and glancing angle electron diffraction patterns were also used to establish structure and preferred orientation of the coatings prior to removal from substrates. Reflection electron diffraction patterns were also made for several films at the substrate-film interface by

floatation of the films from the substrates. Identification was made of the various structures by comparison with the ASTM Powder Diffraction File. For the ZnSe coatings, Auger spectroscopy was used to determine the relative stochiometry of the films by profiling techniques. Surface topology was studied by Nomarski interference contrast microscopy as well as both scanning and transmission electron microscopy. Spectral scans from 1-15 μm were made of each coated sample as well as laser calorimetric absorption measurements at 10.6 μm. Finally, pulsed laser damage measurements at 10.6 μm were used to evaluate and compare the various coatings and coating parameters. The results of these various analyses are summarized below.

The sputtered ZnSe coatings on KCl were identified as cubic with a strong preferred orientation of the {111} planes parallel to the substrate surface. This same preferred orientation was observed on glass monitor slides and is the same as reported earlier [4] for ZnS sputter deposited coatings. Figure 2 shows an electron micrograph of a surface replica of a typical sputtered ZnSe coating together with a reflection electron diffraction pattern of the surface. The microcrystals visible in this micrograph are believed due to dust falling from the pressed ZnSe sputtering target during deposition. Finally, the dark artifacts which appear in the coating are believed to be non stochiometric inclusions of ZnSe, however, no free zinc or selenium was detectable by powder x-ray diffraction techniques.

The thermally deposited ZnSe was also found to be cubic with a preferred (111) orientation as determined by x-ray diffraction. Figure 2 shows an electron micrograph of a surface replica of the thermally deposited ZnSe together with a reflection electron micrograph of this surface. The diffuse electron diffraction pattern suggests a somewhat less ordered surface than the sputtered ZnSe coating. The overall smoothness of this coating is superior to the sputtered coating surface with only small micro crystals interupting the texture.

The quality of the thermally deposited coatings was strongly dependent on deposition rate. High rate depositions produced highly stressed films which crazed immediately when removed from the deposition chamber. In addition, the high rate films tended to have a deep orange color suggesting decomposition, however, no deviation from stochiometry could be detected by Auger spectroscopy measurements of these films.

The sputtered ZnSe coatings were more adherent than the thermally deposited films. None of the thermally deposited films survived the high humidity of our laboratories without crazing. However, the sputtered films of ZnSe were not masked and the coating extended over the edges of the substrate as well as the surface, which allowed all but the most highly stressed films to adhere to the substrate without crazing. All of the two layer coatings reported on here had sputtered ZnSe first layers.

The surface textures for the four fluorides deposited on ZnSe are shown in the electron micrographs of figure 3. The hexagonal structured SmF_3 and PrF_3 are smoother with fewer surface features than the cubic EuF_2 or the orthorhombic GdF_3. X-ray diffraction measurements showed preferred orientation for all of the fluorides on both ZnSe and KCl substrates. For the hexagonal structures this preferred orientation was easily identifiable as (100). However, the orientation of the GdF_3 and the EuF_2 could not easily be determined from the limited x-ray data available.

The transmission spectral scans for 1 μm films of each of the fluorides deposited on KCl are shown in figure 4. The absorption peaks at 3 and 6 μm seen in all of these coatings is presumed to be due to OH. It is of note that hexagonal structures show greater absorption at these wavelengths than either the cubic or orthorhombic materials. In an attempt to eliminate these absorption bands, two experiments were performed for LaF_3 to reduce the OH in the deposited films: 1) a codeposition experiment involving a simultaneous deposition of Ca metal during the fluoride deposition, and 2) deposition in ultra high vacuum with known low H_2O and OH residual gas pressures. For experiment 1, a second filament deposition arrangement was installed in the NRC medium high vacuum system with a pyrex glass shield around the filament. This allowed a continuous evaporation of Ca metal without contaminating the system. A few minutes before depositing the fluoride coating, the Ca source was brought to deposition temperature and a low rate deposition was established. During the fluoride deposition the Ca deposition remained continuous providing a continuously replenished getter for OH and other getterable materials. This procedure reduced the 3 and 6 μm OH bands in LaF_3 by 40% using a normal deposition as a reference. The second experiment involved deposition of LaF_3 in well characterized ultra high vacuum using the ion pumped system described above. During the deposition the residual gases present in the system were continuously monitored between mass 2 and mass 70. At no time did the residual gas pressure of H_2O exceed 7×10^{-8} pascal during the LaF_3 deposition. The effect of the ultra high vacuum on this deposition was dramatic, with an 86% reduction of the 3 and

6 μm absorption bands in this material. The transmission spectral scans resulting from these experiments is shown in figure 5 together with the spectra for LaF_3 from a medium high vacuum deposition. Ultra high vacuum depositions were also tried for SmF_3 and CeF_3, however no effect was seen for these materials. It was also determine that the fluorides with less OH absorption had greater indices of refraction. This effect has been reported elsewhere [5].

10.6 μm laser calorimetry measurements were made for each of the fluorides deposited on KCl. The results of these measurements are summarized in table 3 and are expressed in terms of the ratio of power absorbed by the coating to the power transmitted. These absorption measurements are relatively high yielding film absorption values between 100 and 200 cm^{-1}. The Fourier spectral scans of these materials (see figure 6) suggest residual contamination of the substrate as the cause of this high absorption.

Pulsed laser damage measurements at 10.6 μm were used for the final evaluation of these coatings for HEL application. The experimental arrangement used is identical to the one described in an earlier paper [4] and is shown diagramitically in figure 7. The characteristics of the TEA CO_2 laser used are given in table 4. The incident energy density was controlled by placing calibrated CaF_2 absorbers in the beam between the laser and the GaAs focussing lens. For all of these measurements a 180 μm spot size was used. Ten selected sites on each coating were irradiated at each energy density (one on one firings are reported here). Damage was evaluated by Nomarski microscopy and statistically analyzed to determine the damage threshold for each coating. In most cases a minimum of two samples of each coating design were analyzed. The results of these measurements are given in table 5, and as expected, the damage thresholds were the highest for the single layer coatings on ZnSe. The damage threshold for the sputtered ZnSe coating on KCl is particularly interesting. The threshold of 20 J/cm^2 reported here is comparable to the threshold of thermally deposited ZnSe on KCl and indicates that for this material sputter deposition is a viable alternative to thermal deposition.

The damage thresholds for the fluorides reported here are lower than the value measured for CeF_3 coatings (35 J/cm^2) reported in an earlier paper [4]. The double layer damage thresholds are all similar and indicate that interfacial damage between coatings is the limiting factor for this design. Of particular interest is the damage threshold for EuF_2 on ZnSe which was the lowest threshold reported for the fluoride single layers. This is surprising since the absorption coefficient at 10.6 μm was the lowest for the fluorides reported and additionally this material was cubic (and thus isotropic) with only small 3 and 6 μm absorption bands.

4. Discussion

The rare earth fluorides under consideration are the compounds of the form XF_3 where X is a metal anion with atomic number between 57 and 71. Three of the fluorides of this series are also known to have stable di-fluorides namely EuF_2, SmF_2 and YtF_2. The europium difluoride has been reported on here. These fluorides are all low index materials with useful transmission between the near UV and the infrared to a least 15 μm. The stable crystal structures of the rare earth fluorides reported are either hexagonal or orthorhombic in the tri fluoride form and cubic (fluorite structure) in the difluoride form. The hexagonal fluorides tend to be susceptible to water absorption when deposited as thin films. This may be due to a fairly open structure for these films, and the results of the ultra-high vacuum deposition for LaF_3 seem to support this hypothesis since for at least this material water absorption was partially eliminated. A final test of the absorption mechanism will require in situ measurements of the 3 and 6 μm absorption bands for these films.

The structural stability of these films has not been treated here. There is evidence that the fluorides are structurally unstable when measured over long time periods [6]. Thin films of those fluorides which are known to have both hexagonal and orthorhombic structures have been found to be of the stable hexagonal form. Obviously, more work is needed in this area.

The starting materials used in this investigation were of the highest comercial purity available. The heavy metal impurity levels have not been established for these materials and for most of them only x-ray diffraction has been used to evaluate presence of contamination. The chemical nature of the rare earths makes it difficult to prepare ultra pure starting material and further work is needed in this area. It is clear from the work on ThF_4 [3] that ultra pure starting materials are necessary for the optimization of the fluorides for use as HEL coatings.

References

[1] Golubovic, A. et al., Proceedings of the Fifth Annual Conference on Infrared Laser Window Materials, 1976, C. R. Andrews and C. L. Strecher, Editors.

[2] Davisson, J. W, Proceedings on High Power Infrared Laser Window Materials, 1972, C. A. Pitha, Editor.

[3] Braunstein, M., Braunstein, A. I., Zuccaro, D. and Hart, R. P., Proceeding of the Fourth Annual Conference on Infrared Laser Window Materials, 1974, C. R. Andrews and C. L. Strecher, Editors.

[4] Ewing, W. et al., Proceedings of the Fifth Annual Conference on Infrared Laser Window Materials, 1976, C. R. Andrews and C. L. Strecher, Editors.

[5] Bananova, L. P. and Grigor'Eva, G. N. Izvestha Sibirskogo Otdeleni'a Akad. Nauk SSSR 2, 115 (1962).

[6] Holmes, S. J. and Kraatz, P., AFML Technical Report No. AFML-TR-75-188, January 1976.

Tables and Figures

Table 1. Deposition parameters for ZnSe on KCl sputtered coatings.

Sputter Etch	P = 50 watts	- 60 s
Deposition	P = 100 watts	- 1 hour
	Argon pressure	1.3×10^{-2} torr

Thermal Deposition

Glow discharge cleaning - Argon Gas - 10 minutes

Deposition: Rate = 2A°/S T_s = 70°C

Source: Al_2O_3 crucible

Table 2. Deposition parameters for fluoride coatings.

Coating	Substrate	T_s(°C)	Rate
SmF_3 (Cerac/Pure) n = 1.59 - 1.60	KCl	150°	0.5A°/S
	ZnSe	150°	0.5 - 1.0A°/S
	(KCl) ZnSe/	100°	0.5A°/S
EuF_3 (EuF_2) (Cerac/Pure) n = 1.59 - 1.60 (n = 1.55 - 1.56)	KCl	150°	0.5A°/S
	ZnSe	120°-150°	0.5 - 1.0A°/S
	(KCl) ZnSe/	100°	0.5A°/S
GdF_3 (Cerac/Pure) n = 1.56	KCl	150°	0.5 - 1.0A°/S
	ZnSe	150°	0.5 - 1.0A°/S
	(KCl) ZnSe/	90° - 120°	0.5A°/S

Table 3. 10.6 μm absorption data for single layer coatings on ZnSe.

Coating	P_o (watts)	Thickness (μm)	P_{abs}/P_o (coating)
GdF_3	2.50	1.75	0.062
SmF_3	2.55	1.40	0.054
EuF_3 (EuF_2)	5.00	2.19	0.032

Table 4. Characteristics of TEA CO_2 laser pulses.

PULSE ENERGY	65 MILLIJOULES
REPETITION RATE	1 PPS
SPATIAL MODE	TEMoo, GAUSSIAN TO I/Io ≤ 0.01
MODE DIAMETER	5.5 mm
LONGITUDINAL MODES	MANY
PULSE WIDTH	100 ns FWHM

Table 5. 10.6 μm pulsed laser damage for reported fluoride coatings.

COATING	SUBSTRATE	THRESHOLD (J/cm²)
EuF_2	KCL	--
	(KCL) ZnSe/	6.5
	ZnSe	14.6
GdF_3	KCL	14
	(KCL) ZnSe/	6.5
	ZnSe	18
SmF_3	KCL	10.5
	(KCL) ZnSe/	6.0
	ZnSe	20
PrF_3	(KCL) ZnSe/	7.0
ZnSe	KCL	20.0

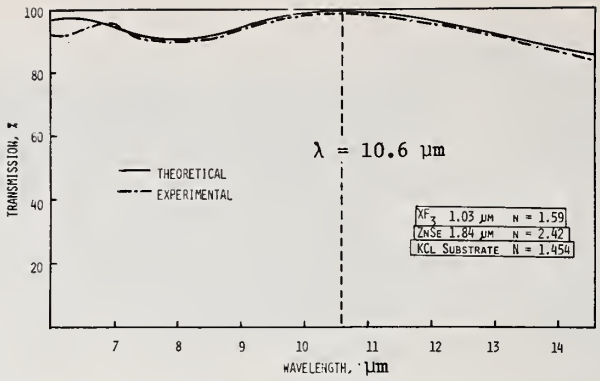

Figure 1. Spectral response of $ZnSe/XF_3$ antireflective coated KCl.

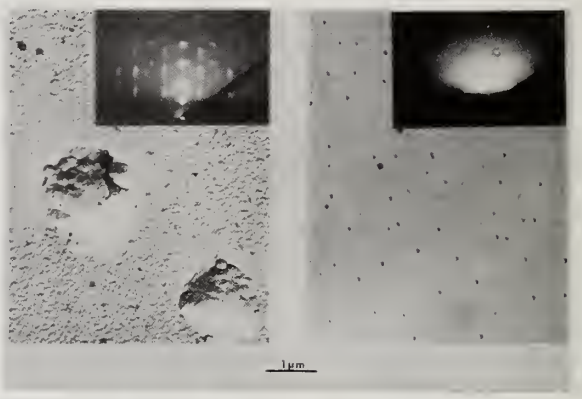

Figure 2. Electron micrographs comparing texture of sputtered and evaporated ZnSe on KCl.

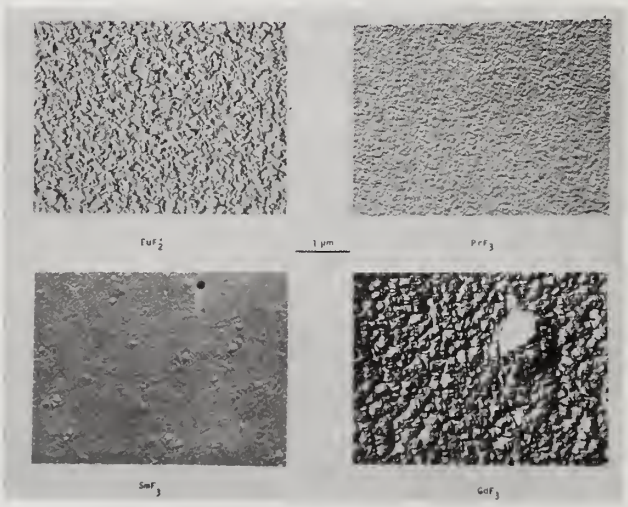

Figure 3. Electron micrographs comparing texture of evaporated fluorides on ZnSe.

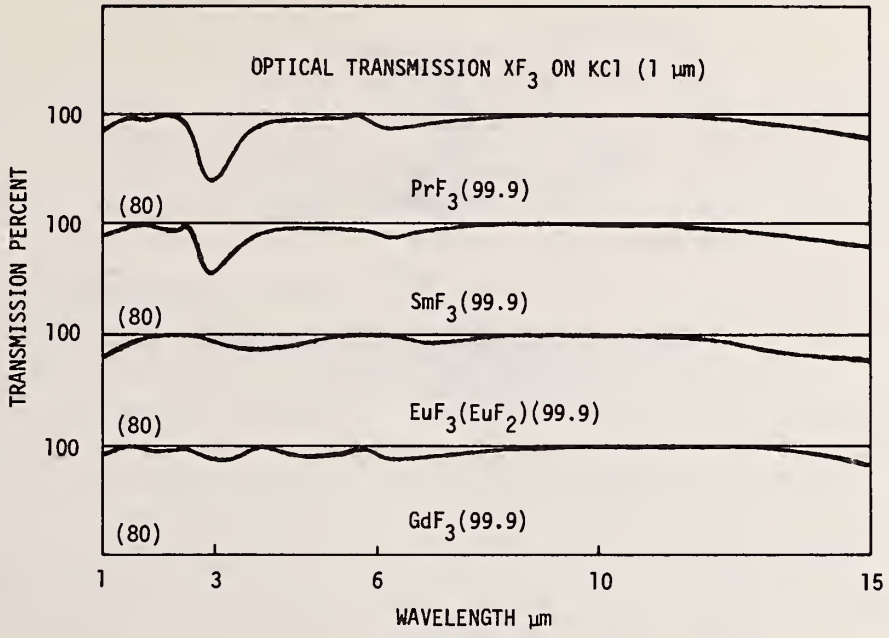

Figure 4. Optical transmission of XF_3 on KCl.

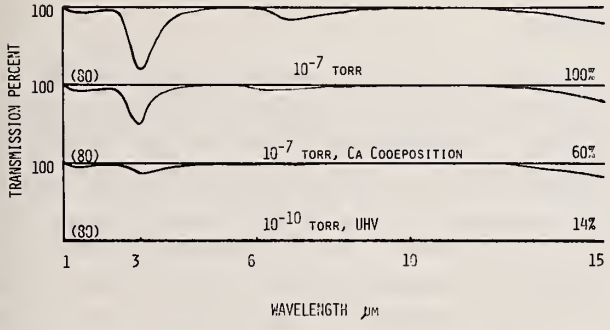

Figure 5. Transmission spectra of LaF_3 vs deposition vacuum integrity.

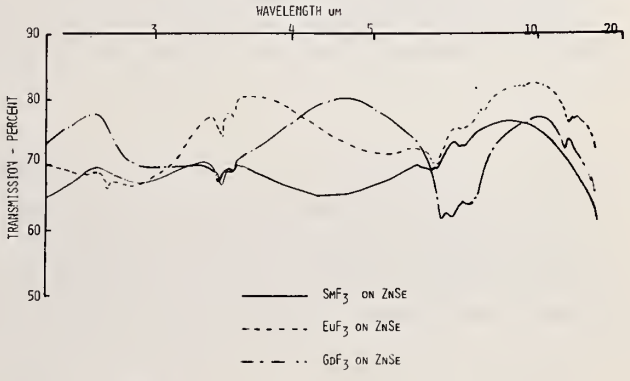

Figure 6. Fourier spectral response of fluoride films.

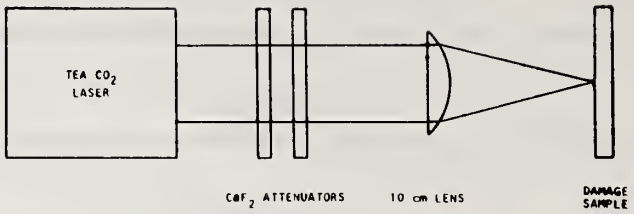

Figure 7. Experimental set-up for pulsed CO_2 laser damage experiments.

COMMENTS ON PAPER BY
GOLUBOVIC, FITZGERALD, BERMAN, BRUCE, BRADBURY, COMER, EWING, AND LIPSON

No discussion on this paper.

4.4 PERFORMANCE OF $Ge_{0.45}Se_{0.55}/As_2S_3$ ANTIREFLECTION COATINGS AT 3.8, 5.3, and 10.6 μm

John F. Lewis and Melvin C. Ohmer
Air Force Materials Laboratory
Wright-Patterson AFB, OH 45433

Transparent vitreous films of Ge_xSe_{1-x} have been grown by conventional evaporation techniques whose refractive index can be varied from 2.5 to 3.1 by varying x from .35 to .5. For x=.45 it is possible to construct a two-layer double-quarter wave AR coating where $Ge_{.45}Se_{.55}$ is the layer nearest the substrate and As_2S_3 is the outer layer. In a cooperative program, AR coatings of this type were synthesized at the Materials Research Laboratories, Victoria, Australia, and evaluated at the Air Force Materials Laboratory. AR coatings were deposited on Eu^{++} doped KCl (10.6 μm), BaF_2 (5.3 μm), and CaF_2 (3.8 μm). The coatings were characterized with regard to absorption, transmission, and bandwidth. For the KCl sample, the cw CO_2 damage threshold was determined. The absorption per surface for all wavelengths was less than .1%. Absorption bands at the shorter wavelengths were not visible in the spectrophotometer data.

Key words: Absorption; antireflection coatings; germanium selenide; infrared laser windows.

INTRODUCTION

The infrared properties of Ge_xSe_{1-x} alloy films have been investigated extensively by Butterfield [1][1] and Gibbs and Butterfield [2]. Films containing up to 50% germanium can be produced by evaporation from carbon boats and the film composition is identical to that of the initial alloy. The index of refraction of these films may be varied from 2.5 to 3.1 by varying x from .35 to .5. The films show no evidence of crystallinity and have no absorption bands between 2.0 and 15 μm. The extinction coefficient [2] for GeSe films at 10.6 μm is of the order of 1.4×10^{-3}, corresponding to a beta of 16 cm^{-1}. The beta value is comparable to that of good ThF_4 at 10.6μm. The films are reported to be physically robust and to adhere strongly to many substrates. Therefore, Ge_xSe_{1-x} films are promising as components of antireflection (AR) coatings for infrared lasers.

In an exchange program, AR coatings were deposited by the Materials Research Laboratories [3] on CaF_2, BaF_2, and Eu^{++} doped KCl substrates supplied by AFML for, respectively, 3.8, 5.3 and 10.6 μm. All substrates were polycrystalline. The coatings were in the half aperture format and on one side only. The coated substrates were returned to AFML and characterized with regard to absorption, peak transmission, bandwidth, physical thickness, and transmision in the visible. For the KCl sample, the cw CO_2 damage threshold was determined.

AR DESIGN

The AR design was the two-layer double-quarter type where $Ge_{.45}Se_{.55}$ is the layer nearest the substrate and As_2S_3 is the outer layer. The indices nearly satisfy the relationship $n_1=n_2\sqrt{n_s}$ where n_1 is the layer nearest the substrate and n_s is the substrate index. The design indices [4] for 10.6, 5.3 and 3.8 μm were, respectively, for As_2S_3 2.376, 2.395, 2.397, and for $Ge_{.45}Se_{.55}$ 2.866, 2.886, 2.896. The calculated reflectivity for all three wavelengths is less than .001.

1. Figures in brackets indicate the literlature references at the end of this paper.

ABSORPTION

The absorption was determined by vacuum laser calorimetry. The laser beam was incident on the coated surface. The absorption values at 5.3 μm and 10.6 μm were obtained from the University of Dayton Research Institute (UDRI) and at 3.8 μm from the University of Alabama at Huntsville. The results of these measurements are summarized in table 1. The substrates were nominally 1 cm thick. The absorption per surface was .1% or better at all three wavelenths. At 10.6 μm, this is the best result ever attained in a two layer coating on KCl. The value of the AR coating absorption at 3.8 μm indicates that the materials incorporated into the design are not plagued by water absorption bands. While the coating absorption at 5.3 μm is very low there are harder coatings designs [5] with lower absorptions.

LASER DAMAGE THRESHOLD AT 10.6 μm

A Sylvania 971 CO_2 one kilowatt laser was utilized to determine the damage threshold of the coated KCl sample. The beam was focused to a diameter of .8mm and the power varied from 100-900 watts. The coating displayed a conditioning effect. Without conditioning, the coating would fail at 300 watts corresponding to a respectable threshold value of 60 kW/cm^2. With conditioning, a level of 500 watts was observed. The threshold is defined in terms of the average power (the total power divided by the area of the beam at the $1/e^2$ point). However, irreversible strain was introduced in the coatings at a level of 100 watts. Since only one sample was available these damage measurements should be considered as preliminary.

SPECTRAL TRANSMISSION

The spectral transmission of each AR coating was obtained on a Perkin-Elmer 621 spectrophotometer. The transmission vs wavelength for the 10.6 AR coating is shown in figure 1. The experimental peak transmission for the 10.6, 5.3 and 3.8 μm coating occurred at, respectively, 10.6, 5.5, and 4.1 μm. The bandwidth, the wavelength region over which the transmission is within .5% of the peak value, was .2, .37 and .3 μm for, respectively, the 10.6, 5.3, and 3.8 AR coatings. The coating thicknesses were controlled by a 1.55 μm laser optical thickness monitor. For the 10.6 μm coating the required thickness, compensation for dispersion, corresponded to an integral number of fringes (seven). Therefore, it was easier to accurately control the thickness for the 10.6 AR coating. The total physical thicknesses of the two layer coatings were determined on a Sloan Dektak and are listed in table 2. The theoretical thickness was determined from the AR design. The experimental peak transmission and the experimental thickness were used to calculate the expected theoretical spectral response for the 3.8 AR coating. The reduced optical thickness for each coating at 3.8 μm was .27 instead of .25 and the peak transmission was 4.1 μm. An 8% thickness error in each coating thickness shifts the transmission peak from 3.8 to 4.1 μm.

OPTICAL DENSITY

It is very desirable that infrared laser windows be transparent in the visible for ease of alignment. The optical density (OD = $\log_{10} I_0/I$) of AR coatings was determined at 6328Å. The OD was 1.0, 1.4 and 2.9 for, respectively, the 3.8, 5.3 and the 10.6 AR coatings. These OD's correspond to 10%, 4% and .1% transmission. The 10.6 coating appears opaque and metallic, and the other coatings appeared reddish. The coatings showed no stress induced birefringence even though they were deposited on polycrystalline substrates.

CONCLUSIONS

The $Ge_{.45}S_{.55}$- As_2S_3 AR coating absorption was the lowest ever measured for a two layer AR coating on potassium chloride at 10.6 μm and its damage threshold is acceptable. Many coating materials considered for application at 2-6 μm have water absorption bands at 2.9 and 6.1 μm. $Ge_{.45}Se_{.55}$-As_2S_3 AR coatings do not have that problem resulting in a very low coating absorption at 3.8. On the negative side the 10.6 μm coating is not transparent in the visible. It would be interesting to investigate two layer AR coatings which utilize appropriate GeSe alloys for each layer.

ACKNOWLEDGMENTS

The authors would like to thank William C. Schoonover of the Air Force Avionics Laboratory for arranging the substrate and sample exchanges.

REFERENCES

[1] A. W. Butterfield, Thin Solid Films, 23, 191 (1974).

[2] W. E. K. Gibbs and A. W. Butterfield, Applied Optics, 14, 3043 (1975).

[3] Materials Research Laboratories, Cordite Avenue, Maribyrnong, Victoria, P.O. Box 50, Ascot Vale, Vic., 3032.

[4] A. D. McLachlan, Private Communication.

[5] Melvin C. Ohmer, AFML-TR-76-103.

Table 1. Absorption of Anti-Reflection Coatings Determined By Calorimetry

Substrate	Wavelength	$A_o \div 10^{-4}$	$A_o \div 10^{-4}$	% per surface
KCl	10.6	8.9	19.5	.11%
BaF_2	5.3	11.9	19.0	.07%
CaF_2	3.8	51.3	56	.05%

Table 2. Comparison of Theoretical and Measured Coating Thickness

Substrate	Theoretical Thickness	Experimental Thickness	% Error
CaF_2	7,244 Å	7,875 Å	8.7
BaF_2	10,124	10,500	3.7
KCl	20,400	21,060	3.2

Figure

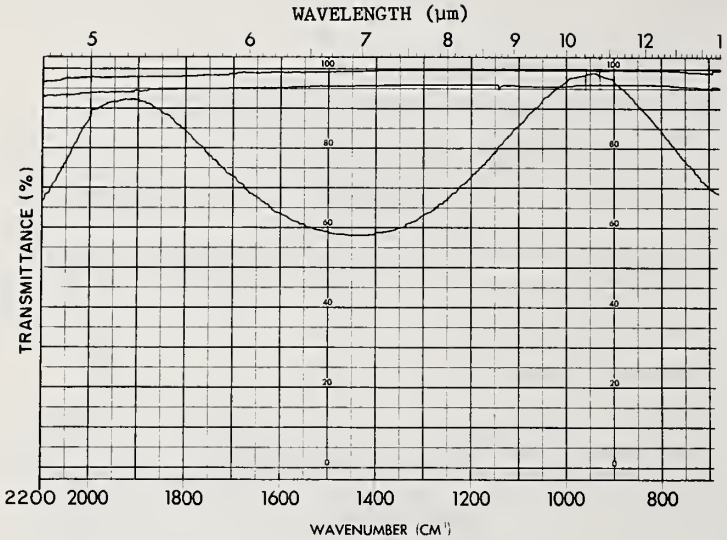

Figure 1. Transmission vs wavelength for $Ge_{.45}Se_{.55}$-As_2S_3 AR coating designed for 10.6 -(single surface).

COMMENTS ON PAPER BY LEWIS AND OHMER

No discussion on this paper.

4.5 AR-COATED KCl DAMAGE AT 10.6 μm*

John A. Detrio and Roger D. Petty
University of Dayton Research Institute
Dayton, Ohio 45469
and
Melvin C. Ohmer and Orven F. Swensen
Air Force Materials Laboratory
Dayton, Ohio 45433

Antireflection coatings on KCl windows for high power CO_2 lasers have been studied using focused radiation to establish relative damage thresholds. Single layer coatings composed of TlI, multilayer designs employing TlI and either KCl or ThF_4 were capable of withstanding 9 seconds irradiation at an average power density of nearly 130 kW cm^{-2}. Two definitions of the onset of mechanical damage were used; physical degradation including thermally induced fracture, and the first appearance of permanent residual strain as observed in a plane polariscope. Nomarski microscopic observations were also utilized to search for subtle signs of damage. Data were taken to detect any "conditioning" effects due to below-threshold irradiation. Conditioning was found to be negligible in all coatings studied except possibly one. No special handling precautions were taken and therefore these values represent the inclusion of ordinary laboratory environmental degradation. Correlations between damage levels and factors such as absorption were investigated.

Key words: Alkali halides; antireflection coatings; coatings; KCl; laser damage.

1. Introduction

In order for alkali halide materials such as KCl to be practical windows for high power infrared lasers, it is essential that they be antireflection (AR) coated both for the control of reflected energy and for environmental protection. Several promising AR coating designs employing TlI on KCl have been evaluated. The coatings have low absorption at 10.6 μm and low scatter also. In order to assess the power handling capability of these coatings they were tested in the focused beam from a 1 kW CO_2 laser. Since this study represents an initial survey of such materials, the damage tests were structured so that the effect of "conditioning" and subtle forms of damage could be investigated following the tests. The paucity of samples leads to a restricted definition of damage thresholds which does not permit any statistically sound comparison or evaluations.

2. Experimental

The basic experimental apparatus is that described in previous CW laser damage work conducted at our laboratories [1][1]. The test plan employed in this study represented a considerable compromise in obtaining data on the various parameters which might be used to characterize the laser-induced damage of AR coatings. The parameter of greatest interest is the so-called "damage threshold" (kW/cm^2). Radiation densities above this threshold always destroy the coating. Because the damage can be initiated by defects in any practical window it is also of interest to obtain damage data as a function of area, either by using a variable beam size or by multi-point sampling. Certain other systematic aspects of the damage testing must be understood and controlled in order to obtain meaningful damage data. These effects include the influence of focused radiation, temporal effects in both irradiation and storage times, and the existence of "conditioning" [2] effects in which prior irradiation below threshold tends to improve the material's damage resistance. The physical format of

* This work was supported by the Air Force Materials Laboratory, Wright-Patterson Air Force Base under contract no. F33615-76-C-5092.

1. Figures in brackets indicate the literature references at the end of this paper.

the coatings (full aperture both sides, half aperture one side, quadrant coated one side, etc.), and a desire to search for the existence of subtle damage indicators or precursors has greatly complicated the testing. The influence of coating design (thickness and order in multilayer designs) and the influence of coating deposition parameters and correlations between nondestructive measurements such as absorption and damage levels are very desirable.

Our approach to these varied requirements has been to divide the 1-1/2" diameter circular samples into four quadrants to conform to the quadrantly coated sample format. The irradiation site location is shown in figure 1. Six locations are generally available for irradiation in each of the four quadrants. When the sample fractures or otherwise degrades, there is a chance that the damage may extend into another site and thereby reduce the total number of test locations available. To minimize the potential impact of this problem, the sample is flooded with a stream of dry nitrogen from below and an exhaust system is set up over the sample to collect any debris or smoke and draw it upward. Depending on the coating format, either of the upper quadrants I or II was tested first. A series of exposures starting at 100 W, the lowest power available, were made with increments in power up to the maximum available--about 1 kW. If the sample is damaged, the second location, B was irradiated at a power 20-30% below that which produced damage at the first position, A. If damage is observed a further reduction in power below the damage threshold is made and a new location is tested. If no damage occurs, the power is increased at suitable increments (50-300 watts) until damage is again observed. If no damage is observed the remaining locations are each irradiated at different power levels below threshold to permit post-test investigations of more subtle forms of degradation. With this strategy, conditioning, damage threshold, and subtle forms of damage can be simultaneously searched for. Not all sample formats permitted this same strategy to be employed with equal success nor did all of the samples cooperate in the tests by maintaining their physical integrity after the first damage occurred.

The samples were irradiated for times of 9, 3, or 1 second required to obtain damage within the power levels available. Generally, 9 seconds is considered sufficient for these tests based on peak temperature and stress considerations and the spacing between the irradiation sites. Longer times will tend to raise the average temperatures without significantly changing the local temperature and stress gradients. For focused damage tests, we therefore elected to utilize the longest times consistent with the test requirements.

The spot sizes and powers were measured before or after a given exposure. The power is read with a CRL Model 213 power meter which has been checked against a total capture ballistic calorimeter. The spot size measurements were made using burn patterns in plastic blocks. The spot size was found to be somewhat irregular with a 0.075 cm ± 0.012 cm diameter, full width at half maximum (FWHM) measured at power levels from 100 to 500 watts. The spot size did not appear to be sensitive to the incident power, but the depth of penetration was linear with incident power only up to 500 watts (see figure 2). The spot size (FWHM) used in reporting these data is 0.08 cm and has a standard deviation of about ± 20%. The spot size data are probably the weakest part of a good power density measurement and therefore only average powers are given. The average power will be defined as the total power divided by the area of the beam at the $1/e^2$ point. The $1/e^2$ diameter is $\sqrt{2 \ln 2}$ times the FWHM or 0.094 cm.

The experiments were conducted in much the same way as our previous KCl window damage tests with all observations being made through polariscopes. The value of the polariscopes was greatly diminished in the case of TlI coatings where natural birefringence dominated the observed behavior over any induced strain effects.

Photographs were made before and after each exposure using 35 mm film (KODAK TRI-X) and a dark field linear polariscope. The exposure is 1/2 second for the entire field with a strobe supplying light for the polariscopic observations. This arrangement gave the most consistent results with respect to exposure times through the telephoto lens system. The aperture was set at f/11 to insure sufficient depth of field. Following development, the film rolls were contact printed for ease of study. The samples were also photographed in polarized light before and after completion of the entire test.

The damage threshold is defined as the lowest power at which damage was observed. This definition is not consistent with our previous definition which would be the power half-way between the level at which damage is observed and the next lowest level at which no damage occurs. Sufficient data do not exist for these samples to use Loomis' criteria [3] for damage threshold.

3. Data

The data for damage threshold, as defined above is summarized in table 1 including the first appearance of residual strain and the detection of physical degradation. The number of damage sites on each sample or quadrant are also given in table 1. The photographs of the samples taken after completion of the testing are shown in figure 3 and also serve to summarize the strain and visible damage. In those cases in which the coatings are on both sides of the sample, the data may include information on the damage to each side. In general, the incident side is the primary side being tested. In several cases the first side tested had a higher damage threshold; therefore, the exit side damage defined the damage limit at a given location.

The exposure data for the various coatings tested are summarized graphically in figures 4 through 7. The sequence of "shots" is shown by the open squares and circles for radiation incident on "Side 1" and "Side 2", respectively. If only one side was irradiated, the coated side is designated as "Side 1". To avoid the repetitious appearance of the damage test sequence graphs, only representative data are shown. Additional data concerning the thin films are listed in tables 2-4.

A Nomarski microscope was utilized to search for subtle forms of surface damage or deformation. No useful information was gathered by this technique since the appearance of strain in the polariscopic photographs is the most subtle form of degradation observed.

4. Discussion of Results

Earlier studies [1, 2] have shown a quadratic relationship between damage and absorption for alkali halide materials. The damage resistance of these materials is dominated by their surface absorption [1] and it is reasonable to examine these data for such a relationship. The absorption data shown in figure 8 were taken in our laboratory. The curve does not show a clear trend since the coating absorption data are not equally distributed along the abscissa nor did the samples all suffer damage. There is a general trend for highly absorbing samples to damage more easily. Too few data exist in this study to provide a sound basis for any empirical or theoretical relationship between damage and absorption. In most cases these absorption data have been in excellent agreement with

Table 1. Coated KCl 10.6 μm data summary.

Sample No.	Location Quad	Location Side	Coating Design Sub/C_1/C_2/C_3	Coating Format	Damage Level and No. of Damage Sites Strain kW/cm^2	Strain (No.)	Decomposition kW/cm^2	Decomposition (No.)	Absorption (percent)
8A5	I & II	1	KCl/TlI	Half Aperture	>144	(0)	>144	(0)	
8C6	I & II	1	KCl/TlI	Half Aperture	> 91	(0)	> 91	(0)	
8B5	I	1	KCl/TlI/KCl/TlI	Full	57	(13)	>129	(0)	0.07
8B5		2					129	(3)	0.07
8A7	I	1	KCl/TlI/ThF_4/TlI	Quadrant	>136	(0)	>136	(0)	0.20
8A7	II	1	KCl/TlI		>129	(0)	>129	(0)	0.14
8A7	IV	1	KCl/ThF_4		29	(4)	115	(1)	0.12
8B2	II	1	KCl/TlI/ThF_4/TlI	Quadrant			86	(1)	0.21
8B2	III	1	KCl/TlI				126	(2)	0.18
8B2	I	1	KCl/ThF_4				57[a]	(3)	0.20
8B6	I	1	KCl/TlI	Half	>115	(0)	>115	(0)	0.03
8A6	I	1	KCl/TlI	Half	>137	(0)	>137	(0)	0.03
8B4		1	KCl/ZnSe/KCl/ZnSe		> 86	(1)	129[b]	(2)	0.09
8B4		2					43	(3)	0.09
8D2	I	1	KCl/As_2S_3/KCl/As_2S_3	Full			< 14	(3)	3.0
8D2	II	2					< 14	(3)	3.0
8C2		1	KCl/TlI/AgCl/TlI	Full Both Sides			21.5	(11)	0.28
8C2		2					< 14	(13)	0.28

a Sample fractured on initial exposure
b Showed conditioning.

Table 2. TlI coating design data.

Sample[a]	Materials	Thickness (Micrometers)	Refractive Index	Coating Absorption (Percent)
8A5	TlI	1.03 (λ/4)	2.4	0.1
8A6	TlI	1.10 (λ/4)	2.70	0.09
8B6	TlI	1.08 (λ/4)	2.41	0.03
8C6	TlI	1.77 (λ/2)	2.47	0.03

a Substrate designations are, A and C Eu:KCl; B and D Rb:KCl.

Table 3. Two-layer coatings design data.

Sample	Materials	Thickness (Micrometers)	Refractive Index	Coating Absorption (Percent)
8A7-I	TlI/ThF_4	2/1.2 (AR)		0.20
8A7-II	TlI	2.57 -	2.43	0.14
8A7-IV	Th_4	1.30 -	1.35	0.12
8B2-II	TlI/ThF_4	2/1.2 (AR)		0.21
8B2-III	TlI	2.55 -	2.51	0.18
8B2-I	ThF_4[a]	1.33 -	1.35	0.20

a This layer failed the "Scotch tape" test.

Table 4. Three-layer coatings design data.

Sample	Materials	Thickness (Micrometers)	Reflectance	Coating Absorption (Percent
8B5	TlI/KCl/TlI	(0.88/0.81/0.48)[a]	5.5% R	0.07
8B4	ZnSe/KCl/TlI	(0.88/0.81/0.48)[a]	7.0% R	0.09
8C2	TlI/AgCl/TlI	(1.0/1.25/0.12)[a]	4.5% R	0.28

a These are full aperture coatings and the designed thicknesses are shown.

that obtained by the supplier. We have observed an increase in the absorption of uncoated samples exposed to the laboratory environment. This atmospheric degradation will probably adversely affect the data for samples that are partially coated or coated only on one side.

The coating damage observations will be discussed in three categories of coatings: TlI in single layers, TlI/ThF_4 two-layer designs, and three-layer designs.

The TlI coatings of both λ/4 and λ/2 thickness were very damage resistant to focused CO_2 radiation. The absorption is also low in these coatings as shown in table 2. The film's microstructure and composition were investigated with x-ray techniques and light microscopy. The films are shown at low magnification in figure 9 which serves to illustrate the wide variations in the apparent structure of the TlI film--yet all were quite damage resistant. X-ray diffraction studies showed that the KCl substrates for samples 8A5 and 8C6 were polycrystalline but highly textured with the (220) approximately parallel to the surface. The coating was also identified as TlI with an orthorhombic structure. No evidence was found of CoCl or NaCl type lattice forms or of the iodine rich Tl_3I_4 or TlI_3 phases.

The TlI/ThF_4 two-layer coatings were observed to damage when the ThF_4 coated quadrant was irradiated. The two-layer AR design quadrant was destroyed by a "Scotch tape" test of adhesion prior to the laser damage tests. Thus, only the TlI layer was available for study. Previous experience in our laboratories with ThF_4 coatings has shown that the high 10.6 μm absorption of these films is related to the presence of oxygen. Consequently Auger spectroscopy was used to study the chemical composition as a function of thickness through the ThF_4 film. The in-depth profile plots for samples 8B2 and 8A7 are shown in figure 10. Although the fluorine deficiency seen in these graphs is partially an artifact of the sputter-etch procedure used to profile the coating in depth the changes in oxygen content are real. The chemistry of the two samples is not the same, nor is the chemistry of each quadrant the same. Sample 8B2 showed an increase in oxygen content at the ThF_4-KCl interface, while the same quadrant of 8A7 showed no similar increase at the coating substrate interface. Sample 8A7 was also profiled in the two-layer region in which iodine contamination was found in the ThF_4. The unexpected presence of copper at the ThF_4-TlI interface was not found elsewhere.

The three-layer AR designs were not as damage resistant as the other coatings reported upon here. At this time, no chemical studies have been conducted on these multilayer samples. With such a limited sample population and with little information on the status of attempts to optimize the three-layer coatings for low absorption it is not prudent to draw conclusions concerning the relative merits of these designs with respect to their damage resistance.

5. Acknowledgments

The Auger spectra were taken by Messrs. Tom Wittberg and James Hoenigman and interpreted with the help of Dr. William Moddeman of the University of Dayton. The x-ray analysis and microstructural evaluations were contributed by Dr. Richard Harmer also of the University.

It is a pleasure to acknowledge the assistance of Ms. Marile McMahon and Mr. Douglass Sauer in obtaining these damage data, Ms. Mary Wendeln for computational support and data reduction, and Mr. Donald Stevison of AFML/LPE for the use of the 1 kW laser.

The samples were all prepared by Honeywell under contracts with the Air Force Materials Laboratory, Wright-Patterson Air Force Base, Ohio.

6. References

[1] Detrio, J., Petty, R., Fox, J., Larger, P. and Fenter, J., Fifth Conference on Infrared Laser Window Materials. Compiled by C. Robert Andrews and Charles L. Strecker, 389-390 (1976).

[2] Loomis, J.S. and Saito, T.T., "Third Conference on High Power Infrared Window Materials," Vol. 3, Air Force Cambridge Research Labs, AFCRL-TR-0084(III) (1973).

[3] Huguley, C.A. and Loomis, J.S., Proc. 7th NBS, ASTM, ONR, ERDA Symposium on Laser Induced Damage in Optical Materials, NBS Spec. Pub. 435, 187-201 (1975)

7. Figures

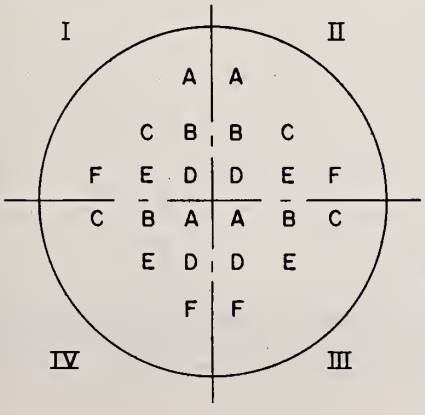

Figure 1. Sample irradiation site format. The quadrants and site locations are shown for the normal orientation of the sample in its mount with quadrants I and II at the top, and radiation incident upon the front of the sample.

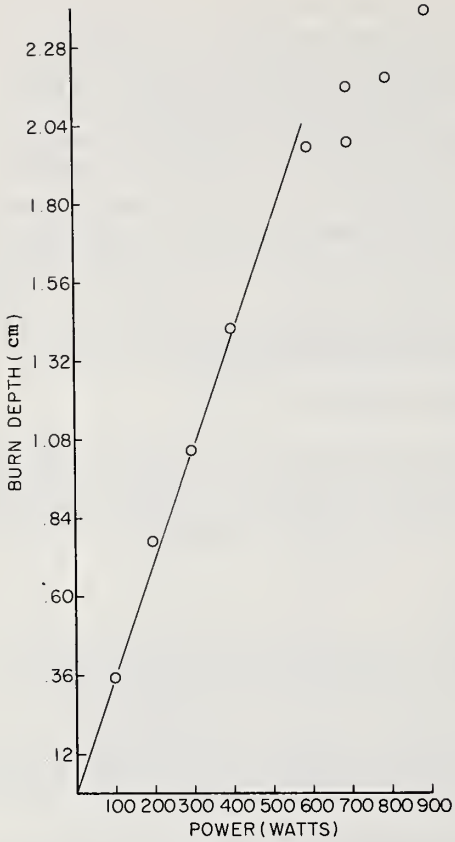

Figure 2. Depth of pentration and power of CO_2 radiation near the focus of a 1 m focal length mirror. All points were irradiated for the same time interval -- 0.1 s.

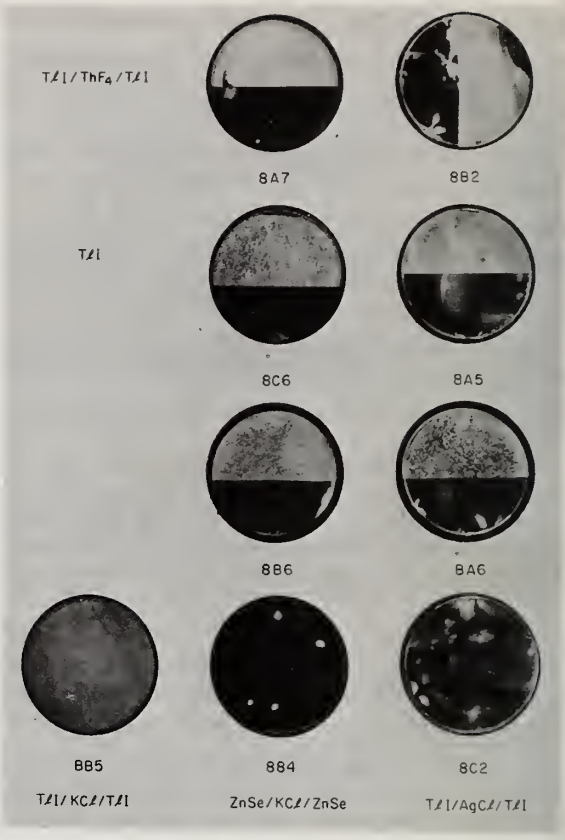

Figure 3. Composite polariscopic photograph of the coatings made upon completion of the tests.

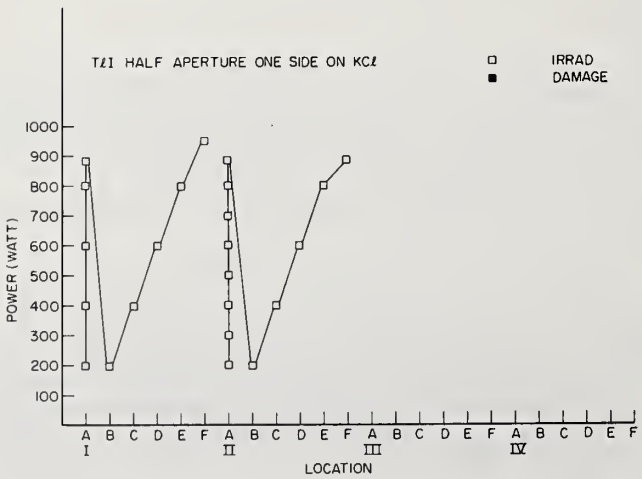

Figure 4. Damage test sequence for sample 8B6 which is representative of the TII on KCl coatings studied.

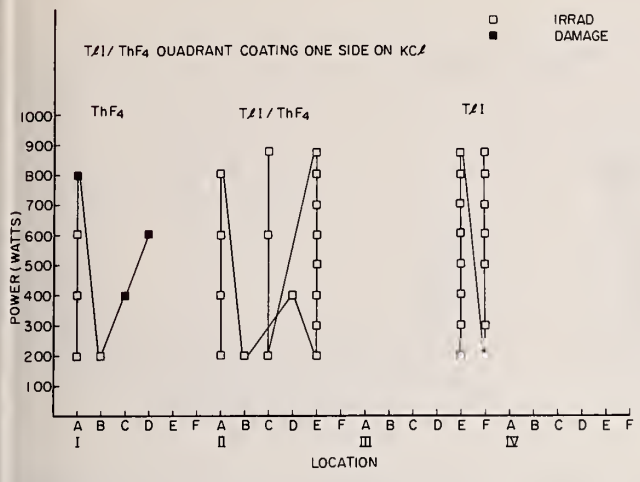

Figure 5. Damage test sequence for TII/ThF_4 quadrantly coated sample 8B2 showing the effect of sample damage on the subsequent test procedure which deviated significantly from our initial plan.

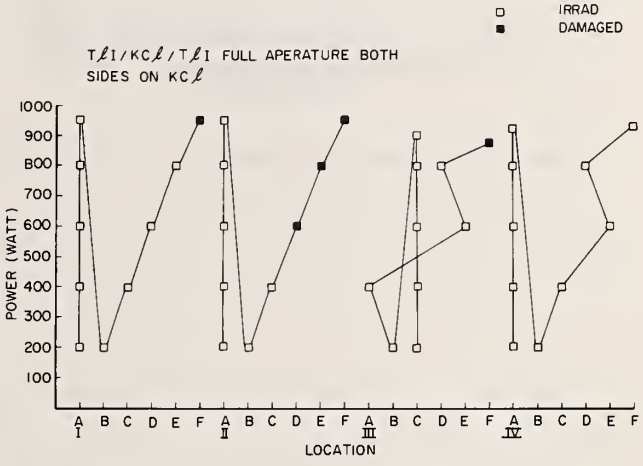

Figure 6. Damage test sequence for TII/KCl/TII coated KCl sample 8B5.

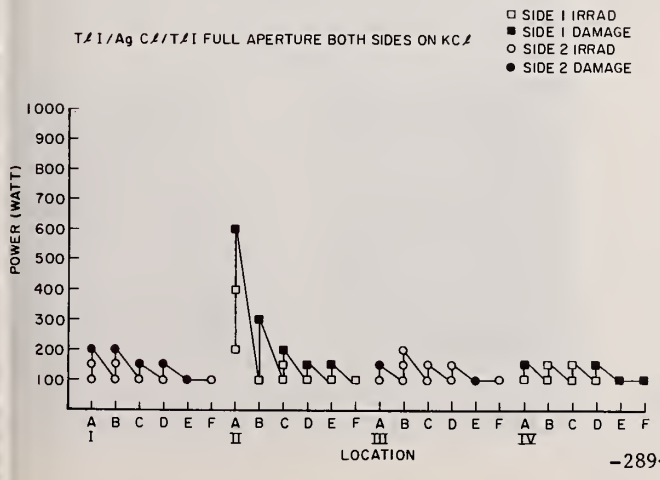

Figure 7. Damage test sequence for TII/AgCl/TII coated KCl showing the influence of irradiation from different sides.

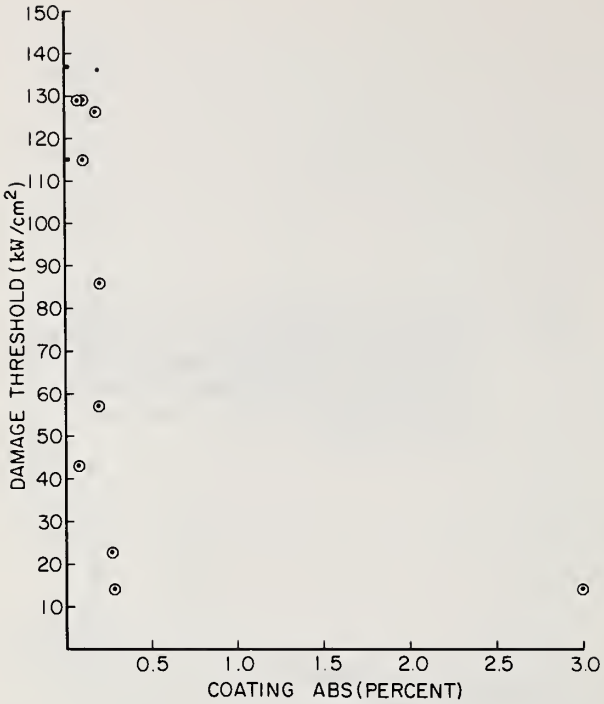

Figure 8. Measured damage threshold versus coating absorption measured for the samples in this study. The data show all samples tested. The circled data represent samples for which damage was observed. Each quadrant of the quadrantly coatings are plotted separately. The correlation between the two quantities exists, but its functional dependence cannot be deduced from these data.

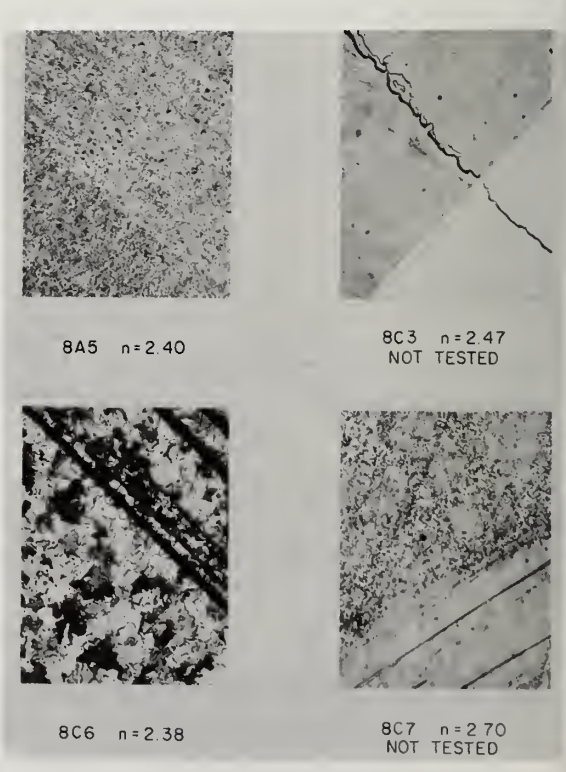

Figure 9. Low power magnification micrographs of some of the TII coatings investigated.

AUGER IN-DEPTH PROFILE OF ThF_4/TℓI COATED KCℓ

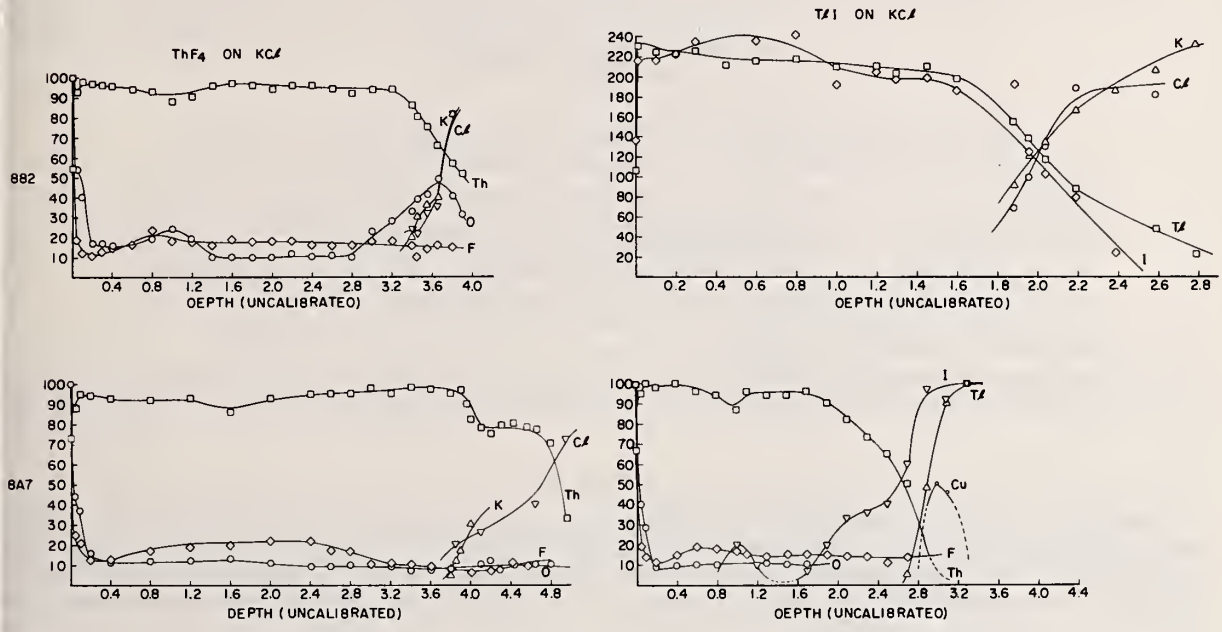

Figure 10. Auger profile scans of the TII/ThF_4 coatings showing the presence of oxygen in the ThF_4.

COMMENTS ON PAPER BY DETRIO, PETTY, OHMER, AND SWENSEN

Permanent residual strains were observed in many samples at illumination levels well below the threshold for catastrophic damage. These observations were made by means of a polariscope.

4.6 SPECTRAL DEPENDENCE OF DAMAGE RESISTANCE OF REFRACTORY OXIDE OPTICAL COATINGS*

Brian E. Newnam and Dennis H. Gill

University of California
Los Alamos Scientific Laboratory
Los Alamos, NM 87545

The laser damage thresholds of three refractory oxide material coatings (TiO_2, ZrO_2, and HfO_2) and SiO_2 were measured at three wavelengths (355, 532, and 1064 nm). For each wavelength, quarter-wave thick films were deposited on fused silica substrates by three manufacturers using electron-gun evaporation. Samples were irradiated with the primary, doubled and tripled frequency of a mode-locked Nd:YAG laser with pulse duration 20-30 ps. An increase of the threshold electric field from 1064 to 532 nm was measured, which was consistent with that predicted for electron-avalanche breakdown. Reduced thresholds at 355 nm indicated dominance of two-photon absorption.

Key words: Damage thresholds; electron avalanche; picosecond pulses; refractory oxides; standing-wave fields; thin films; two-photon absorption.

1. Introduction

The damage resistance of optical thin film components has proven to be a major limitation on the peak intensity attainable for laser fusion experiments at 1064 nm. The desire to conduct future fusion experiments at visible and ultraviolet wavelengths has prompted the anxious suspicion that optical coatings may become an even more limiting factor. This is due to the probable onset of multiphoton absorption as a mechanism leading to early damage at short wavelengths and high intensity. In addition, laser isotope separation has posed severe endurance requirements for multilayer reflections for submicrosecond pulses in the ultraviolet.

Previous laser damage experiments at 1064 and 694 nm have provided a useful, if not satisfactorily complete, characterization of various thin film materials. However, no reports of controlled tests below 694 nm have been found by these authors. The present experiments at 355, 532, and 1064 nm were thus strongly motivated.

2. Test specimens

The refractory oxides TiO_2, ZrO_2, and HfO_2 were chosen for evaluation because they have been successfully used as the hard, high-refractive-index components of multilayer stacks for 694 and 1064 nm. Also, SiO_2 films, often used as a hard, low-refractive-index component, were selected for evaluation. Single-layer films of TiO_2, ZrO_2, and SiO_2 were evaporated onto fused silica substrates (Optosil I) by two commercial vendors who represented the state-of-the-art of electron-gun technology. The HfO_2 films were deposited on Ultrasil substrates by electron-gun evaporation by P. Baumeister and O. Arnon at the University of Rochester. Film thicknesses of one quarter-wave (QW) at 355, 532, and 1064 nm were obtained. Spectral transmission curves for these films are shown in figure 1.

HfO_2 was considered of special interest because of its short wavelength cutoff at 230 nm. Although the HfO_2 films we tested showed absorption at 260 nm (unbaked), heating to 400° C in air would have shifted the edge to 230 nm[1]. There are a few reports of rf sputtering[2] and electron-gun deposition [3] of this material, but its damage resistance has not been published previously.

3. Experimental procedure

The experimental apparatus and techniques were similar to those described previously[4]. A schematic of the apparatus is shown in figure 2. For these experiments KDP-I and KDP-II frequency doubling and tripling crystals were used with overall energy efficiencies of 45% and 20%, respectively. The samples were placed near the focus of a 50 cm focal-length, fused silica lens for the 355 nm tests. The spot size radius (at I_0/e^2) incident on the lens was approximately 1.2 mm. A 100 cm lens was used for the 532 and 1064 nm tests where the incident radii were 1.5 mm and 2 mm, respectively.

* Work supported by the Energy Research and Development Administration.

1. Figures in brackets indicate the literature references at the end of this paper.

The laser pulse profile was measured on every shot (see fig. 3) by a linear Si diode array (RL512C) with resolution of 25 μm manufactured by Reticon Corporation. The spot-size radius was 0.12 mm for both 355 and 532 nm and 0.22 mm for 1.064 nm. This device was suitable for use at all three test wavelengths due to the adequate sensitivity of silicon from the UV to 1.1 μm. The experimental parameters are listed in table 1.

Table 1. Experimental parameters

A. Wavelength = 1064 nm, 532 nm, 355 nm
B. Pulsewidth = 30 ps, 20 ps, 17 ps
C. Spot-size radius = W = .12 - .22 mm
D. Single shot per irradiated site
E. 40 shots (average) per threshold
F. Normal incidence

For laser irradiation at 1064 and 532 nm, laser-induced-scatter (LIS) and spark detection were used simultaneously to monitor film disruption. Irradiation at 355 nm, however, caused fluorescense in all the materials studied, so that our standard method of detecting spark emission at 420 nm could not be used here.

As shown in figure 4, the damage threshold is evaluated as a range of values rather than a single number. The range indicates the variability of the damage resistance over the sample surface and is not related to the accuracy of the measurements. The upper end of the threshold range was defined as the maximum pulse energy density for which neither visible film disruption nor spark radiation of a minimum value was detected. The lower end was defined as the minimum energy density for which damage was detected either by the LIS method or by the occurrence of a spark radiation with at least the prescribed energy.

4. Spot-size tests

Before measuring thresholds versus wavelength, preliminary tests were conducted to determine an approximate range of spot-size radii. A large irradiation spot-size was desired to sufficiently average over film densities, being mindful of the limited laser energy available at 355 nm. By irradiating a TiO_2 film with 30-ps pulses at 1064 nm, we found that the damage threshold did not change significantly for radii ranging from 70 to 500 μm. This evidence suggested that the separation of defects most easily damaged by 30-ps pulses was very much smaller than 70 μm, possibly even less than one μm.

5. Spectral test results

A list of the damage thresholds measured in this study is given in table 2. The results for 1064 nm are typical of commercially-available coatings, with the exception of the low value for one of the TiO_2 samples. In addition, the threshold energy densities for each film material for a selected manufacturer are plotted versus wavelength in figure 5. Between the wavelengths of 1064 nm and 532 nm, it may be seen that the damage thresholds of TiO_2 and ZrO_2 increase, whereas that of HfO_2 is rather constant and that of SiO_2 decreases. The thresholds for all four materials decrease rapidly between 532 and 355 nm.

Now, representing the results in terms of incident energy density does not give the complete picture for thin films. It has been established that the standing-wave (SW) electric field must be taken into account when evaluating damage resistance[4,5]. In particular, the fields in a QW thick film of HfO_2 at 355 nm are quite different for 532 and 1064 nm irradiation (see fig. 6). The same is true for TiO_2 (fig. 7) and ZrO_2. Of course, minimal electric-field variations occur in SiO_2 films on fused silica substrates. Moreover, the damage resistance may be dependent on the pulsewidths which varied for each laser wavelength.

A more absolute measure of damage resistance is the rms electric field $\bar{E}$ at breakdown which most likely occurs at the location of the SW maximum in the film[6]. The threshold field in a thin film is computed using the relation

$$\bar{E} = (377\ I_0)^{1/2} \left| \frac{E}{E_0^+} \right|_p \qquad (1)$$

Table 2. Damage thresholds of single layer refractory oxide coatings

Film Material	Manufacturer	Film Thickness, λ/4 @ (nm)	Laser Wavelength (nm)	Damage Threshold	
				Peak Energy Density (J/cm^2)	Peak Intensity (GW/cm^2)
TiO_2	A	532	355	0.14-0.26	7.6-14.1
	"	532	532	3.0 -4.4	134-196
	"	532	1064	1.8 -2.6	56-81
	B	532	532	2.4 -3.4	107-151
	"	1064	1064	3.5 -5.5	110-172
ZrO_2	A	355	355	1.7 -2.7	92-147
	"	532	532	4.1 -5.0	182-220
	"	1064	1064	3.6 -4.2	113-132
	B	355	355	1.4 -2.2	76-119
	"	532	532	3.1 -4.7	138-210
HfO_2	U.R.	355	355	2.1 -3.0	114-163
	"	355	532	3.0 -4.2	133-187
	"	355	1064	3.6 -4.2	113-131
	"	1064	355	1.5 -1.6	81-87
SiO_2	B	532	355	2.3 -3.2	125-174
	"	532	532	3.7 -4.9	165-220
	"	532	1064	5.5 -6.0	172-188
	A	532	532	6.2 -7.0	280-310

where 377 ohms is the free space impedence, I_0 is the incident peak intensity (GW/cm^2) and $|E/E^+_0|_p$ is the peak electric field normalized to the incident field.

Figure 8 shows the spectral dependence of the threshold electric field in MV/cm. For each material the threshold field increases from 1064 nm to 532 nm before falling from 532 nm to 355 nm.

6. Discussion

The increase of the threshold field from the near infrared through the visible region would be unexpected if absorption processes initiated laser damage. However, for an electron avalanche, the qualitative expression for the frequency dependence of the breakdown field is[7]

$$\bar{E}(\omega) = (1+\omega^2 \tau_r^2)^{1/2} E_{dc}, \qquad (2)$$

where τ_r is a relaxation time determined principally by phonon collisions and is a characteristic of each material. When ω is comparable to $1/\tau_r$ then frequency dispersion should be noticed. This is just what is seen in figure 8. A similar increase in thresholds between 1064 and 694 nm was reported by Bass and Barrett[8] for surface damage of several crystals. Smith, et al.[9], have also reported a qualitative increase in the bulk thresholds at 532 nm over that at 1064 nm for several alkali halide crystals and fused quartz irradiated by 30-ps pulses. For wavelengths longer than approximately 532 nm, it is not possible from the present experiments to say at what wavelength the maxima of the thresholds are reached. However, it is apparent that linear or multiphoton absorption are not the dominant processes in the visible region from 1064 to 532 nm. The rapid decrease that was measured below 532 nm does suggest that multiphoton absorption is dominant in the ultraviolet region. A comparison of the absorption edge energies of the films with the multiphoton laser energies (see table 3) suggests that resonant absorption by a single photon at 355 nm is the damaging mechanism in TiO_2, and that two-photon absorption is very possible at that wavelength for ZrO_2, HfO_2, and SiO_2 for these short (~ 17 ps) pulses.

Table 3. Comparison of multiphoton energies and film properties

Laser Wavelengths and Photon Energies

$\lambda(\mu m)$	ν (μm^{-1})
0.355	2.82
0.532	1.88
1.064	0.94

Material	Bandgap Energy (μm^{-1})	Resonant Absorption by
TiO_2	2.9	one photon at 355 nm two photons at 532 nm
ZrO_2	4.1	two photons at 355 nm three photons at 532 nm
HfO_2	4.4	two photons at 355 nm three photons at 532 nm
SiO_2	~ 5.6	two photons at 355 nm three photons at 532 nm

The threshold fields for 532 and 355 nm plotted in figure 8 were measured with shorter laser pulsewidths (~21 and ~17 ps, respectively) than the nominal 30 ps of the 1064 nm fundamental. It is of interest to consider the possible pulsewidth influence on the results. Bettis, et al. [10], have recognized a $\tau^{-1/4}$ dependence of the threshold electric field in the data reported by several researchers in crystals and glasses. This is consistent with the avalanche breakdown mechanism, and it should be noted, is the same as for metal surfaces.

A pulsewidth effect on the threshold of thin films has also been reported by a few workers. The spark thresholds of a ZrO_2 film measured between 10 and 35 ns at 694 nm by Newnam and DeShazer[11] fit the $\tau^{-1/4}$ dependence, but the lower LIS thresholds measured simultaneously showed a much weaker pulsewidth dependence. The thresholds at 694 nm for several multilayer reflectors reported by Bliss, et al. [12], also exhibited a pulsewidth dependence roughly comparable to $\tau^{-1/4}$.

To normalize the present results all to 30 ps using a $\tau^{-1/4}$ law the data in figure 8 would be multiplied by 0.95 and 0.87 at 532 and 355 nm, respectively. However, the effect of two-photon absorption at 355 nm would be less at 30 ps than 17 ps which might affect the above factor. Finally, the presence of film defects may well override any pulsewidth dependence, especially at subnanosecond pulses. Obviously, further experiments versus pulsewidth would be necessary for satisfactory clarification of this matter.

7. Conclusions

The electric fields at the damage thresholds of TiO_2, ZrO_2, HfO_2, and SiO_2 have been determined to increase between 1064 and 532 nm for 20-30 ps pulses, which is consistent with an avalanche breakdown process. The sharp reduction in thresholds at 355 nm indicates the probable presence of two-photon absorption except for TiO_2, for which resonant linear absorption is identified.

8. Acknowledgments

The authors are grateful to John McLeod for numerous helpful discussions, and to George Faulkner for help in taking and analyzing the data.

9. References

[1] Baumeister, P., Univ. of Rochester, private communication (1976).

[2] Motovilou, O. A., Optics and Spec. 22, 537 (1967).

[3] Icenogle, W., Spectra Physics Corp., private communication (1976).

[4] Newnam, B. E., Gill, D. H. and Faulkner, G. E., Laser Induced Damage in Optical Materials: 1975, NBS Spec. Pub. 435, 254 (1975).

[5] Boling, N. L., Crisp, M. D. and Dube, G., Appl. Opt. 12, 650 (1973).

[6] Apfel, J. H., Matteucci, J. S., Newnam, B. E. and Gill, D. H., presented at 1976 Symposium on Optical Materials for High Power Lasers, Boulder, CO., July 13-15, 1976.

[7] Bloembergen, N., IEEE J. Quant. ELECT, QE-10, 375 (1974).

[8] Bass, M. and Barrett, H. H., Appl. Opt. 12, 690 (1973).

[9] Smith, W. L., Bechtel, J. H. and Bloembergen, N., NBS Spec. Pub. 435, op. cit., 321 (1975).

[10] Bettis, J. R., House, R. A. and Guenther, A. H., presented at the 1976 Symposium on Optical Materials for High Power Lasers, op. cit.

[11] Newnam, B. E. and DeShazer, L. G., Laser Induced Damage in Optical Materials: 1972, NBS Spec. Pub. 372, 123 (1972).

[12] Bliss, E. S. and Milam, D., Laser Induced Damage in Optical Materials: 1972, NBS Spec. Pub. 372, 108 (1972).

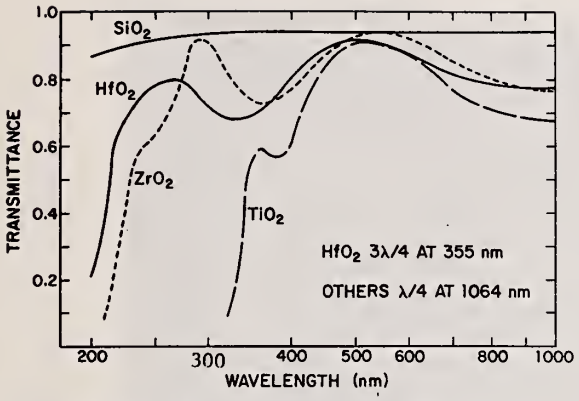

Figure 1. Spectral transmission curves for test samples. The peak values for HfO_2 and TiO_2 are low due to a wedge in the samples.

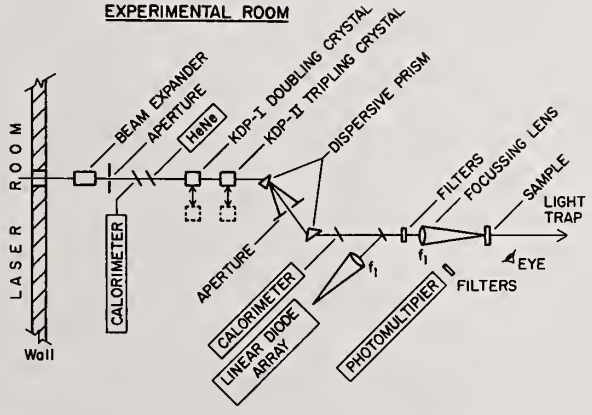

Figure 2. Experimental setup for laser damage threshold measurements.

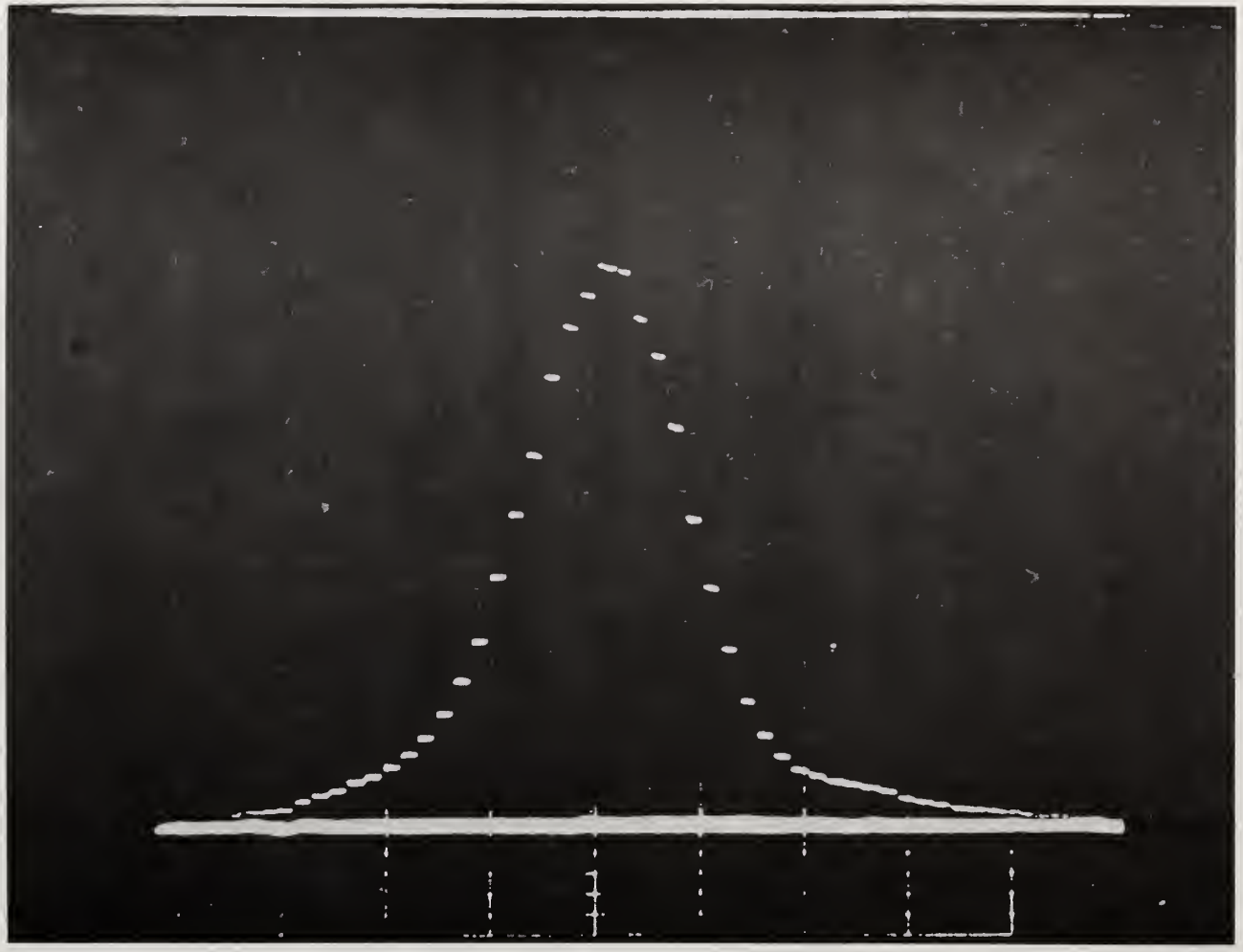

Figure 3. Output of Reticon linear Si diode array used to measure laser beam profile at the sample. Beam profile was measured on every shot.

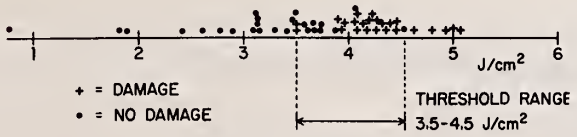

Figure 4. Scatter plot of laser damage data showing how the quoted threshold range is determined.

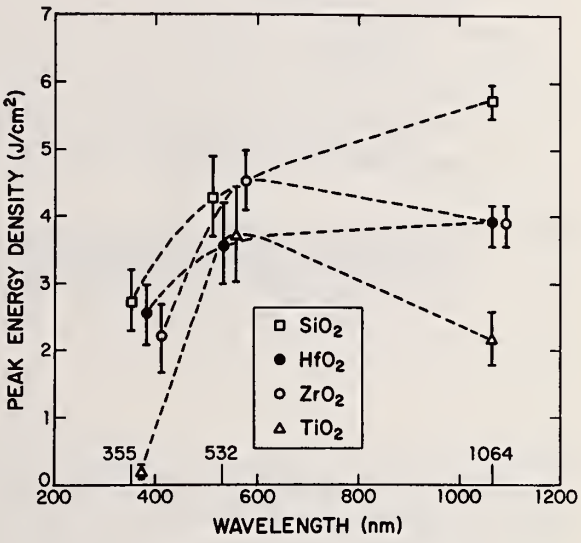

Figure 5. Threshold energy densities versus wavelength for each of the film materials tested.

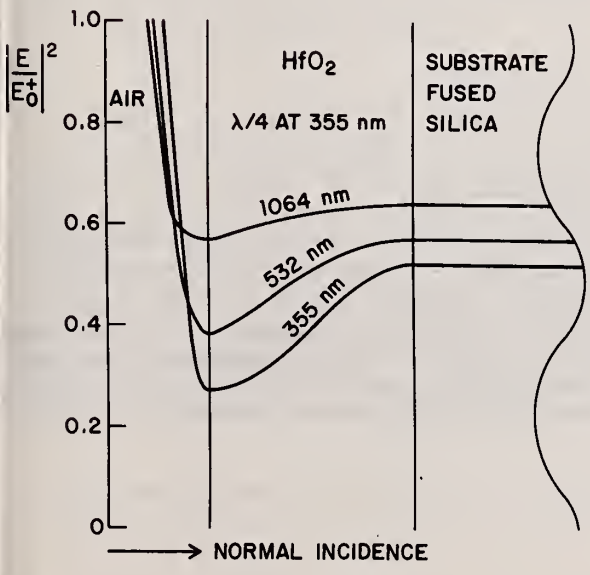

Figure 6. Standing wave electric field pattern in a single layer of HfO_2, $\lambda/4$ thick at 355 nm, used at three different wavelengths: 355, 532, and 1064 nm.

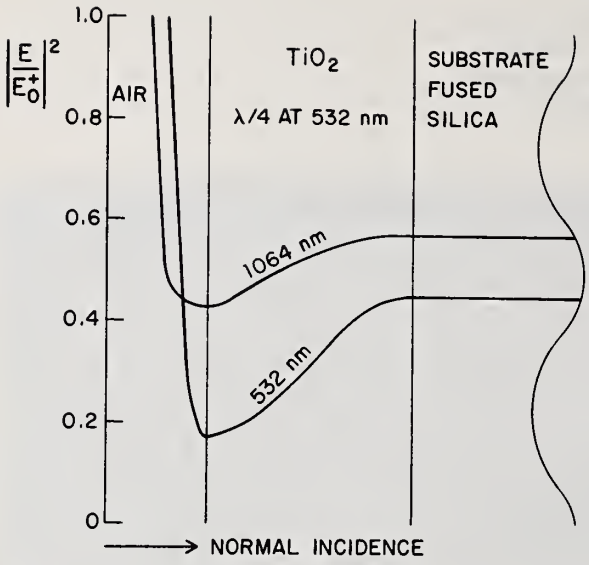

Figure 7. Standing wave electric field pattern in a single layer of TiO_2, λ/4 thick at 532 nm, used at two different wavelengths: 532 and 1064 nm.

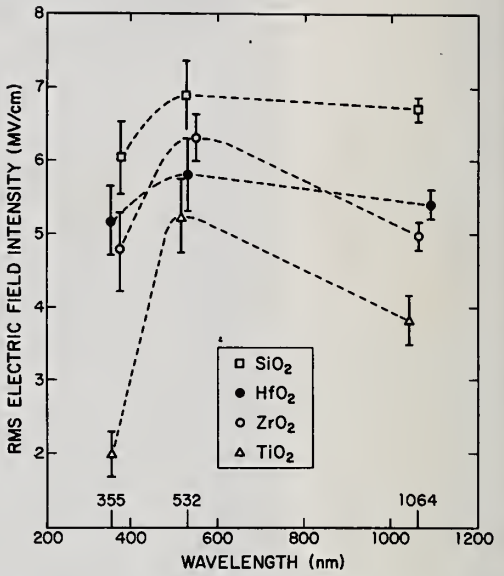

Figure 8. Threshold electric fields versus wavelength for each of the film materials tested.

COMMENTS ON PAPER BY NEWNAM AND GILL

The speaker emphasized that the absorption measurements were taken on the thin film samples themselves. He remarked that on HfO films, those with higher linear absorption showed a higher damage threshold, indicating that two-photon absorption, rather than linear was causing the observed damage. When asked about spark detection, he pointed out that all the samples fluoresced when illuminated at 0.335 μm, so that spark detection of plasma was not possible for the UV damage studies. He stated that since no spot size dependence could be observed, either no inclusions or widely distributed very small inclusions were responsible for the damage. The morphology of the damage at short wavelength has not been investigated in this work, but others have reported no difference between short wave length damage morphology and that seen at 1.06 μm.

4.7 THE ROLE OF ELECTRIC FIELD STRENGTH IN LASER DAMAGE OF DIELECTRIC MULTILAYERS

Joseph H. Apfel and John S. Matteucci
Optical Coating Laboratory, Inc.
Santa Rosa, California 95402

Brian E. Newnam and Dennis H. Gill
University of California
Los Alamos Scientific Laboratory
Los Alamos, New Mexico 87545

The intensity of the local electric field within a multilayer illuminated by a laser beam is determined by the vector addition of forward and reverse flowing waves as a result of interference. The profile of the electric field intensity will therefore depend upon the multilayer design and can have a peak value which is more or less than the peak field of the incident beam. We have examined four multilayer designs, each composed of approximately equal numbers of high and low index films arranged so that the electric field profiles are significantly different. Laser damage thresholds for these coatings were compared with calculated electric field strength profiles.

For electron-gun evaporated titania/silica coatings damaged by 30 picosecond pulses of 1.064μm radiation the damage threshold is dictated by electric field intensity in the titania layers.

Key words: Dielectric films; electric fields; laser damage; optical coatings; standing-waves.

Introduction

Precision determination of laser damage thresholds is possible, yet among workers there is still uncertainty regarding the damage mechanisms. Several workers have reported experiments which support the expected relationship between damage and local electric field strength [1-3][1]. However, in multilayer coatings, the variations of material thresholds due to processing by different or common manufacturers may be masking the field strength dependence. In these studies four multilayer designs with widely different electric field enhancement factors were prepared simultaneously in one coating operation. The results of laser damage threshold experiments are then compared with calculated field strengths.

Description of the Experiments

Figure 1 describes the multilayer designs which are composed of eight or nine layers of titanium dioxide and silicon dioxide deposited onto fused silica substrates. Design A is a simple quarter-wave stack of nine layers beginning and ending with high index (TiO_2) films. In Design B the centermost layer of the quarter-wave stack was omitted resulting in an eight-layer design with a central, half-wave optically thick, low index (SiO_2) layer. In Designs C and D the fourth or sixth layer was omitted in similar fashion.

The spectral plot of figure 1 shows that the peak transmittance of Designs B, C, and D is not precisely centered at 1.064μm. From the scan it can be inferred that the optical thicknesses of the individual layers vary by less than one percent and that both coating materials have an extinction coefficient (imaginary part of the complex refractive index) of less than 0.001.

---

1. Figures in brackets indicate the literature references at the end of this paper.

For laser radiation incident on the coated surface of the substrate the four designs are specified as A, B, C, and D (see fig. 1). For laser radiation incident from the reverse direction, i.e., incident upon the multilayer from the substrate side, the designs are specified A', B', C', and D'. When the laser beam which is incident on the substrate at 8° passes into the fused silica it is refracted to an incident angle of 5.51°. For the reverse (primed) exposures the incidence angle onto the multilayers is therefore 5.51°.

Figure 2 and figure 3 show the computed profiles of the time averaged square of electric field strength ($\overline{E^2}$) for each of the designs [4]. In figure 3 where radiation is incident upon the multilayer from the reverse or substrate side (primed), the incident field intensity has been adjusted to represent the same beam intensity used for the other cases (unprimed). Thus, the profiles represent the field in the various designs with equal beam energy densities incident on the samples. In these figures the high and low index layers are distinguished by thickness. Since the optical thickness of all layers is equal, the high index layers have smaller physical thicknesses.

The coatings were prepared in a multiple spindle coating machine equipped with externally actuated masks which permit the omission of any one or more layers from substrates mounted in each spindle rack. Thus, all four designs were prepared in a single run and have minimum differences attributable to process variation.

The four 38mm diameter by 7mm thick fused silica substrates were cleaned by gentle scrubbing in a hot solution of detergent in deionized water, rinsed with deionized water and then immersed into the vapor of an alcohol dryer. Electron beam heated evaporation sources with copper rotary hearths were used for deposition. The titanium dioxide films were deposited at 80Å/min and the silicon dioxide at 175Å/min onto substrates held at $225^{\circ}C$.

The completed coatings were exposed to 30ps pulses of 1.064μm radiation as described previously [1]. Each sample was tested with radiation polarized in the *s* plane and incident on the coated side of the substrate, and from the reverse direction at an angle of 8°.

Results

Table I and figure 4 include the measured laser damage threshold ranges. The top end of the threshold range was defined as the maximum pulse energy density for which neither visible damage nor spark radiation of a minimum value was detected. The lower end was defined as the minimum pulse energy density for which damage was detected either by the LIS method or by the occurrence of a spark with at least the prescribed radiant energy. An average of 68 laser shots was made for each range determination; the number for each is shown in figure 4.

Table I. Damage thresholds of TiO_2/SiO_2 multilayer designs.

Design	Incident From Air	Incident From Substrate*
A	4.8 - 7.4 J/cm^2	3.6 - 4.4 J/cm^2
B	3.5 - 4.5	2.9 - 3.3
C	4.4 - 5.6	1.58- 1.85
D	1.46- 1.68	2.1 - 2.8

*Pulse energy densities incident upon the multilayer from within the fused silica substrate.

Discussion of results

We have attempted to fit the experimental threshold range determinations to computed values for three models of electric field dependence. It is assumed that the damage will correlate with field strength in either the high (TiO_2) or low (SiO_2) index layers. Although we have plotted damage threshold as a function of $\overline{E^2}$, these experiments do not allow us to identify the power n in the hypothesized E^n dependence of damage. With the large spot-size used for irradiation, these experiments may show that damage threshold at a particular damage site is reached when E reaches a certain level.

Model 1 assumes that damage occurs in either material when the local field exceeds a threshold value. This is the simplest model and probably the most applicable. If damage results from homogeneous absorption or from pure avalanche breakdown, this model should apply. The predicted thresholds for the two materials in the eight configurations will be proportional to the reciprocals of the peak $\overline{E^2}$ values (see figs. 2,3, and 5). Figure 6 (Model 1) shows the result of a least squares fit[2] of the mean value of the experimental ranges to the predicted thresholds for both high (TiO_2) and low (SiO_2) index failure.

High index failure is the best fit as indicated by a standard deviation[3] of 0.43 compared to the next lowest value of 0.60 for Model 2 (see below). The slope of the best fit line for high index failure corresponds to an RMS electric field of 7.9MV/cm.

In Model 2 it is assumed that damage occurs when the volume integral of the time average squared field over one layer equals the threshold value. This integral is proportional to the area on the $\overline{E^2}$ plots (see figs. 2,3, and 5). The model would apply if damage results when the total homogeneous absorption in a layer reaches threshold value. Since the layers have equal thickness, the value of the integral is proportional to the average value of $\overline{E^2}$. Figure 7 is a plot of the least squares fit of experimental data to Model 2. High index failure is again a better fit with the data.

Model 3 is similar to Model 2 except that the total integral of $\overline{E^2}$ is taken over all layers of the same material throughout the multilayer. The fit between experiment and model shown in figure 8 is not very good.

Failure due to peak electric field in the high index layers is indicated by these results. The fact that Model 2 is close to Model 1 is consistent with the shape of the profiles (see figs. 2,3, and 5) because the area under each layer profile is approximately proportional to the peak height of the profile.

Sample B (Designs B and B') are critical to the separation of failure due to high or low index materials. In the other three samples the peak fields are equal for both materials so the experiments will not distinguish which fails. Only when data from Sample B are included can we distinguish the materials.

Figure 9 shows the electric field profiles for the eight designs with incident intensities adjusted to equal the upper and lower ends of the experimental threshold ranges. On each profile small horizontal lines have been added to indicate the best fit solution of Model 1. These lines correspond to an internal RMS electric field of 7.9MV/cm.

If we assume that thresholds are correlated with the peak electric field in the high index (TiO_2) layers, then it is interesting to speculate about the discrepancies in the fit of Model 1. The fit is improved if the threshold data from Sample A are omitted. Table II shows how the peak field locations are distributed throughout

---

2. The least squares fit was made by minimizing the square of the deviations of the mean threshold values from a straight line through the origin.
3. The standard deviation is here defined as the square root of the mean squared deviation.

various designs. Notice that Sample A (Designs A and A') have peak fields in the outermost and innermost layers, whereas Samples B, C, and D have peaks confined to the four central layers.

Table II. Identification of layer in which the peak electric field occurs for both materials.

		Designs							
Layer*		A	B	C	D	A'	B'	C'	D'
1	H					H			
2	L			L		L		L	
3	H		H	H			H	H	
4	L		L	O	L		L	O	L
5	H		O	H	H		O	H	H
6	L		L	L	O		L	L	O
7	H		H		H		H		H
8	L	L			L				L
9	H	H							

O indicates an omitted layer *Count layers from substrate

On the assumption that the outer and innermost pairs of layers may have different thresholds than the others, Model 1' is presented (see fig. 10). Here the experimental threshold ranges are fit only to Samples B, C, and D. The comparable data for Designs A and A' are shown, but they were not used in determining the least squares fit The standard deviation, calculated for the six data points, is 0.24 for the high index failure and shows improvement compared to 0.43 for Model 1. The slope of the best fit line for high index failure in Model 1' corresponds to an RMS electric field of 8.3MV/cm.

In Model 1' (fig. 10) the experimental threshold is below the predicted value for high index failure in Design A'. Perhaps this indicates that the first layer adjacent to the substrate is induced to lower threshold by a phenomenon not considered in this analysis. A simple explanation of this discrepancy is not likely to also cover the case of Design B' in which the threshold range is slightly higher than prediction.

The peak fields in the low index (SiO_2) layers numbered 4 and 6 of Sample B are very high when damage occurs. According to the computation, the peak time average square of field in the low index layers is 2.3 times the peak in the high index layers, therefore, the central low index layers of Sample B are experiencing an RMS field of 12MV/cm at the threshold of damage.

In their damage studies of sputtered single TiO_2 layers, Gill, Newnam, Hartman, and Coleman [5] found a threshold range of 8-11.3 J/cm^2 for 30 ps pulses. The RMS field within the film, computed from an electric field profile, was 6.9 to 8.3MV/cm. Smith, Bechtel, and Bloembergen [6] found an RMS breakdown field strength of 11.7MV/cm for fused silica window material.

Conclusions

We have investigated the laser damage for several multilayer designs produced under identical conditions. For the materials studied in these experiments, there is a definite correlation between the peak field in the weak component and pulsed laser induced damage thresholds. The results indicate that the peak pulse energy density at threshold produces an RMS electric field about 8MV/cm in the high index titanium dioxide layers of each design. This compares with the field in the most damage resistant films previously reported. The field in the low index silicon dioxide layers varies between 8 and 12MV/cm and is felt not to induce failure.

There is an indication that the first high index layer coated on the fused silica substrate may have a lowered threshold. This could be due to coating process variation or to substrate induced defects.

Acknowledgments

The authors are grateful for the skilled technical assistance of George Faulkner (LASL) in conducting the damage experiments and William Klapp (OCLI) in preparing the coatings.

References

[1] B.E. Newnam, D.H. Gill, and G. Faulkner, "Influence of Standing Wave Fields on the Laser Damage Resistance of Dielectric Films", NBS Special Publication No. 435, 254 (1976).

[2] N.L. Boling, M.D. Crisp, and G. Dubé, "Laser Induced Surface Damage", Appl. Opt. 12, 650 (1973).

[3] B.E. Newnam and D.H. Gill, "Laser Damage Resistance and Standing-Wave Fields in Dielectric Coatings", J. Opt. Soc. Am. 66, 166 (1976).

[4] J.H. Apfel, "Electric Fields in Multilayers at Oblique Incidence", to be published in Applied Optics, Oct. 1976.

[5] D.H. Gill, B.E. Newnam, J.S. Hartman, and W.J. Coleman, "Super-High Damage Thresholds for RF-Sputtered TiO_2 Films", J. Opt. Soc. Am. 66,78 (1976).

[6] W.L. Smith, J.H. Bechtel, and N. Bloembergen, "Picosecond Breakdown Studies", NBS Special Publication No. 435, 321, (1976).

Figures

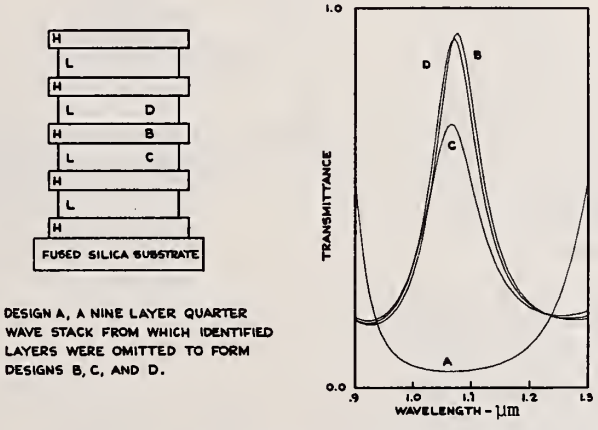

Figure 1. Schematic description and spectral transmittance plots of the four multilayer designs.

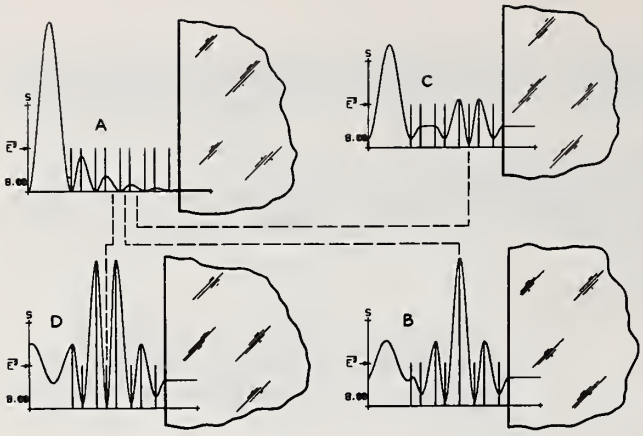

Figure 2. Electric field profiles for the four designs for s plane radiation incident at 8° from the air side. The abscissa is physical thickness measured normal to the layers and the ordinate is the computed value of the time average of the square of the electric field. Each profile is shown for an optical half-wave distance in the incident medium and for a short distance into the substrate where there is no standing wave. The field intensity of the incident beam is indicated by the arrow on each plot. The dotted lines connect the location of omitted layers with sample A.

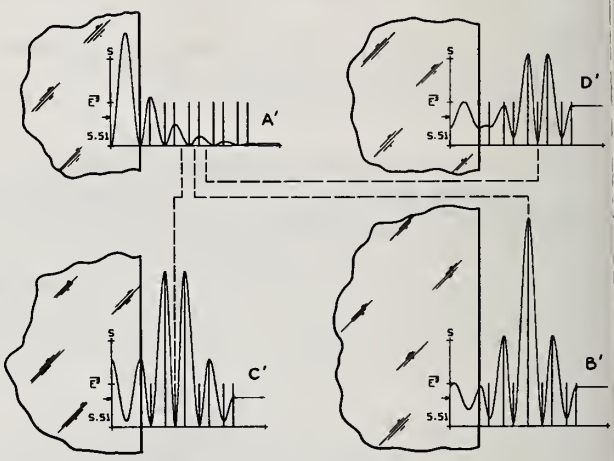

Figure 3. Similar to figure 2 except the radiation is incident on each design at 5.51° from the sybstrate side. The incident field intensity has been adjusted for first surface reflection and for substrate refractive index so that profiles can be compared with figure 2 for equal laser pulse energy density.

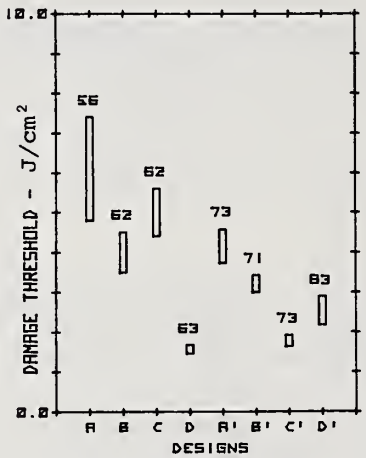

Figure 4. Experimental laser damage thresholds for the four multilayer designs. Data from table 1 for the samples irradiated from substrate side (primed) have been corrected for first surface reflection loss before inclusion in this plot. The number of laser shots is given in each test.

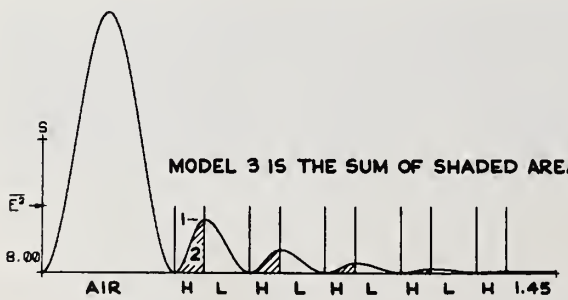

Figure 5. Graphical description of the models used for prediction of damage thresholds attributable to high index layers. Model 1 uses the peak value, Model 2 used the peak volume integral represented by indicated shading, and Model 3 uses the total volume integral of $\overline{E}^2$.

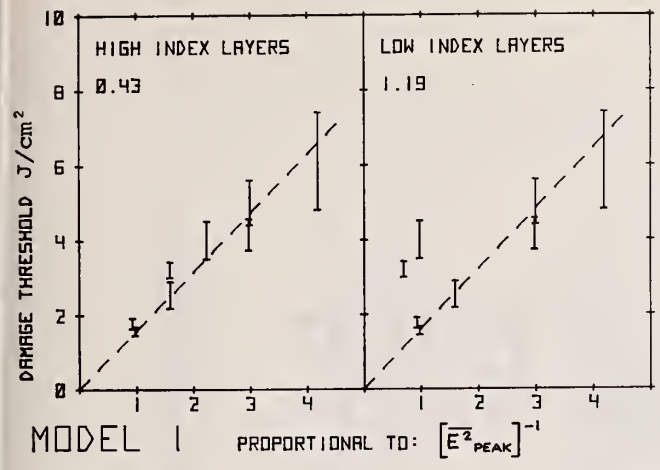

Figure 6. Model 1. Best fit of experimental results to prediction if threshold is proportional to the reciprocal of the peak $\overline{E}^2$ in the multilayers. The numbers are standard deviations of the plotted lines relative to the mean values of the threshold ranges.

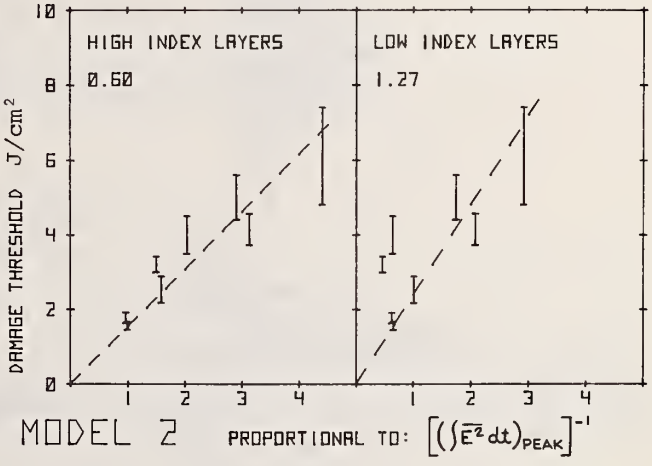

Figure 7. Model 2. Best fit of experimental results to prediction if threshold is proportional to the reciprocal of the maximum integrated time averaged square of electric field over one layer. The numbers are the standard deviations of the plotted lines relative to the mean values of the threshold ranges.

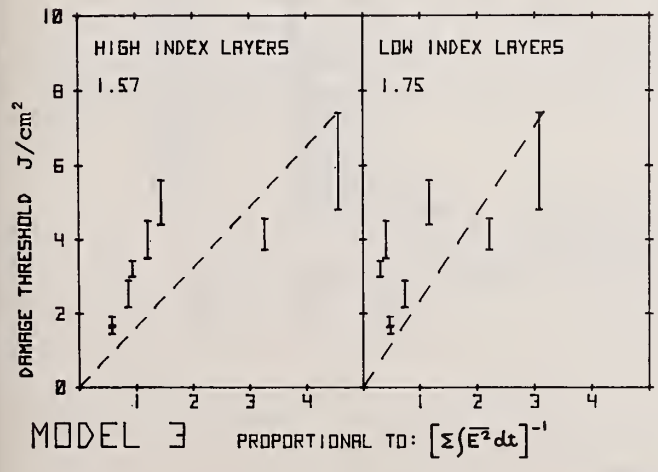

Figure 8. Model 3. Best fit of experimental results to prediction if threshold is proportional to the reciprocal of the sum over all layers of similar index of the integrated time averaged square of the electric field. The numbers are the standard deviations of the plotted lines relative to the mean values of the threshold ranges.

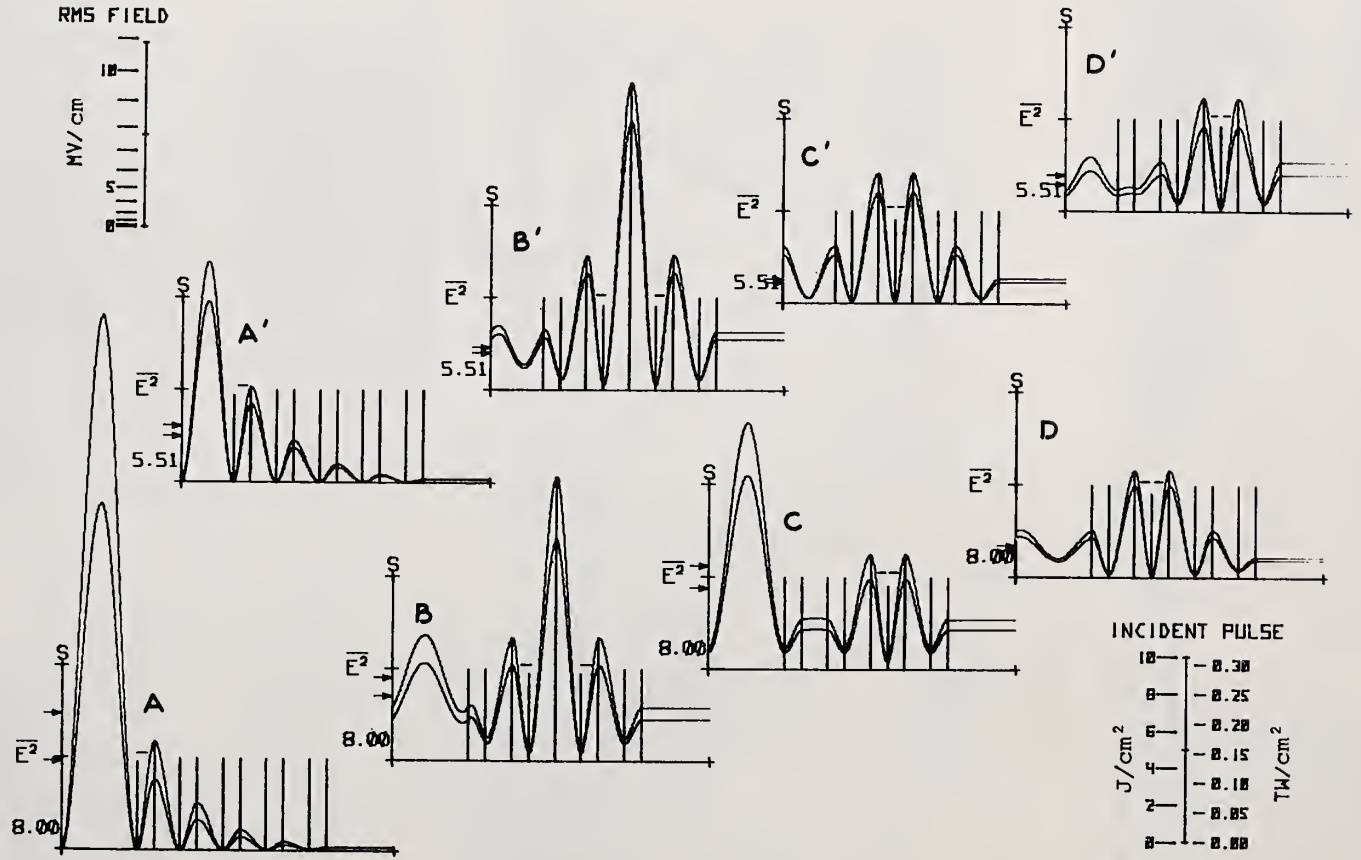

Figure 9. Electric field profiles for the four designs with incident intensities adjusted to equal the extremes of observed laser damage ranges for radiation incident from air side and from substrate side (primed). The short horizontal lines indicate the RMS field of 7.9 MV/cm.

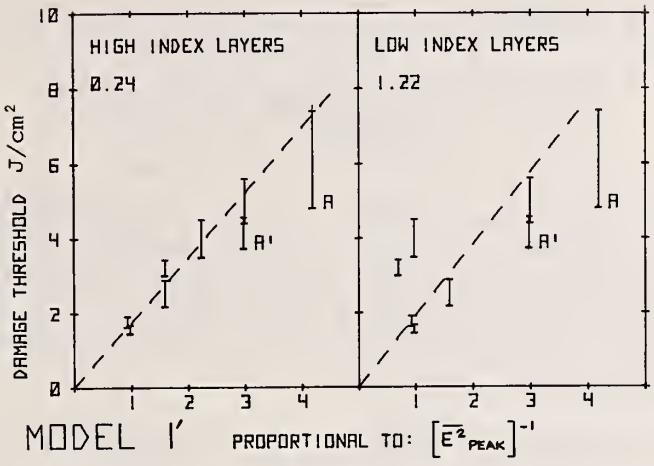

Figure 10. Model 1'. Best fit of experimental results to prediction if threshold is proportional to the reciprocal of the peak $\overline{E}^2$ in the multilayers. Only samples B, C, and D were used in establishing the best fit, otherwise this is similar to Model 1.

COMMENTS ON PAPER BY APFEL, MATTEUCCI, NEWNAM, AND GILL

Threshold values which were reported in this paper were higher than those reported in the previous paper. This was the result of improvements in the fabrication process used in making these films. The speaker emphasized that due to the coating design, it was not possible to exceed the anticipated damage threshold in the low index material without exceeding it first in the high index material. Consequently, damage was always expected to occur in the latter material.

Morphological examination has not yet been carried out on these samples since other tests are planned for them and morphological investigation being usually destructive. It was pointed out that even if post-mortem tests show that damage is localized in the vicinity of inclusions, that does not suffice to isolate the mechanism of damage, since all damage mechanisms are enhanced near an inclusion or imperfection.

It was further emphasized that light scattering measurements on multi-layer dielectrics are an unreliable test of damage levels. If the scattering occurs in the low index material, for example, that might not affect the damage threshold. Obviously, in multi-layer films, scattering and damage results can only be correlated if carried out at the same wavelength and angle of incidence, as the film designed for, to create the same standing wave pattern. Imperfections at regions of zero field will not lead to scattering increases.

4.8 Preparation Techniques and Hydroxyl Concentration vs. Surface Damage Threshold*

R. A. House II, J. R. Bettis, and A. H. Guenther
Air Force Weapons Laboratory
Kirtland AFB, NM 87117

A previous study on pulsed laser-induced damage on fused silica and other optical materials indicated that the damage threshold E (in V/cm) depended upon the RMS surface roughness σ (in A) as follows: $E\sqrt{\sigma} \sim$ const. Application of this relationship to previously measured thresholds affords a measure of the efficacies of various surface preparation techniques in improving surface damage thresholds, allowing a quantitative comparison. We have, in addition, observed an apparent correlation between thin film damage threshold and hydroxyl concentration in fused silica substrates. Depending on the particular film materials, the results imply that hydroxyl ions on the surface of silica substrates can be either beneficial or deleterious.

Key words: Damage threshold; etching; flame polishing; fused silica; hydroxyl; ion polishing; polishing; roughness; surface damage; thin films; threshold.

1. Introduction

In 1975, House et al.[1]**, reported preliminary results of an experimental study on pulsed laser-induced damage to optical surfaces. The experiments were accomplished at a wavelength of 1.06 micrometers and a pulse length of 40 ns (full width at half maximum) using a TEM_{oo} beam focused by a 50 cm lens to an effective spot size of 147 μm at the $1/e^2$ points. A major result for fused silica was the following relationship:

$$E \sqrt{\sigma} \sim \text{const.}$$

where E (in V/cm) is the macroscopic, threshold electric field and σ (in Å) is the RMS surface roughness. The constant depends upon the surface preparation technique used; hence, comparison of the quantities $E\sqrt{\sigma}$ (termed normalized thresholds) affords a way to directly and quantitatively relate various preparation techniques. This results since the normalized threshold explicitly accounts for the gross effect of roughness and separates that effect from the effect of the preparation technique. The roughness/threshold relationship has been found to hold for roughness values from about 10 Å to about 350 Å. In addition, data on samples of fused silica overcoated with either MgF_2 or SiO_2 show correlations with the transmittance of the substrate at 2.2 and 1.4 micrometers and in the ultraviolet. These correlations appear consistent with the interpretation that the hydroxyl concentration of the substrate affects the damage resistance of the film by oxidizing it - promoting the formation of MgO or SiO_2 rather than MgF_2 or SiO.

2. Data

2.1 Surface Preparation Techniques

Samples of fused silica were prepared to various final values of surface roughness by the following procedures: conventional polishing with barnesite (CB); CB plus etching in dilute nitric acid; CB plus half-wave overcoat of either SiO_2 or MgF_2; CB plus flame polishing; conventional rouge polishing followed by ion polishing using H^+, Ar^+, and Xe^+, and bowl-feed polishing with rouge. Details on the preparation techniques and experimental procedures are given elsewhere [1].

The figure presents a graphical summary of the data, using a log-log plot of breakdown electric field versus surface roughness. The types of surface preparation are identified by the symbols indicated; and the least-squares, best-fit lines are also depicted. The datum on the bulk threshold value of fused silica determined by Fradin [2] has also been plotted, assuming a hypothetical surface roughness equal to the average interatomic spacing of fused silica. The approximate spreads of breakdown values exhibited by the ion polished and bowl-feed polished samples are shown as hatched-in areas. The 100 Å surface roughness limit of Bloembergen [3] has also been identified to explicitly indicate that much of the present data fall below that limit.

*Based on portions of dissertations submitted by the first two authors in partial fulfillment of the requirements for the PhD at the Air Force Institute of Technology.

**Figures in brackets indicate literature references at the end of the paper.

A comparison of the effectiveness of each technique in improving damage threshold is presented in table 1. The first column lists the particular techniques, T_i, used in the experiment. The average $< E\sqrt{\sigma} >_i$ of the normalized threshold values was computed for each data set, and the results are shown as E_i' in the second column. These averages have an accuracy of ± 18% of the listed values, resulting from the measured accuracies of the field values and the roughness values. Column three shows a normalized comparison of the various techniques to the conventional polishing technique.

Table 1. Technique vs Average Normalized Threshold

Technique	E_i' (MV/cm)	E_i'/E_1'
T_1: Conventional	5.18	1.00
T_2: Etching	5.47	1.06
T_3: Ion Polish (H^+)	6.82	1.32
T_4: Ion Polish (Xe^+)	8.08	1.56
T_5: Ion Polish (Ar^+)	10.61	2.05
T_6: Flame Polish	10.97	2.12
T_7: SiO_2 Coat	4.06	0.78
T_8: Bowl-Feed	3.29	0.64
T_9: MgF_2 Coat	2.40	0.46

(Data taken from [1])

Note: T_1, T_2, T_6, T_7, T_9 barnesite polished

Note: T_3, T_4, T_5, T_8 rouge polished, absorbing rouge

Contamination of the samples T_3, T_4, T_5 has obviously been reduced by subsequent ion polishing.

It is evident that techniques 3, 4, 5, and 6 resulted in significantly improved thresholds, that techniques 7, 8,and 9 resulted in significantly reduced thresholds, and that technique 2 resulted in a possible improvement. If we exclude the probably erratic data point at $\ln \sigma = 4.4$ in the figure, then E_2' becomes 6.27 and E_2'/E_1' becomes 1.21 and technique 2 can then be said to have improved the damage resistance significantly.

Since nitric acid is not believed to attack fused silica [4], the improvement due to etching is attributed to the removal of surface contamination. The effect of contamination due to rouge [5] is very evident in the result for bowl-feed polishing. This result leads to a significant conclusion regarding the ion polished samples. Although all the ion polished samples had previously been rouge polished, it is clear from table 1 that the ion technique effectively removed the deleterious effect of the rouge. In addition, it is to be noted that it was the intermediate-mass ion (rather than the light or heavy ions) which gave the greatest improvement for the ion polishing procedure.* As readily observed, the flame polishing technique yielded the highest thresholds. It seems clear, that while the flame technique indeed smoothed the surfaces, a subtle change in the character of the surfaces must also have occurred. The evidence is the great difference in slope for these samples as compared to the other samples and the fact that the fit of the data to a straight line was five times better than for any of the other techniques. Not surprisingly, the overcoated samples exhibited reduced thresholds. However, it was surprising that the MgF_2 overcoated samples not only had lower thresholds than the SiO_2 overcoated samples, but also these thresholds were lower than those of the rouge-contaminated, bowl-feed polished samples. On theoretical grounds, Bettis et al.[6],have predicted that the damage threshold of a material should be proportional to the following quantity:

$$\frac{N}{n^2 - 1}$$

where N is the atomic number density and n is the index of refraction. The ratio of this quantity for MgF_2 to that for SiO_2 is 1.6, so that the MgF_2 overcoated samples should be expected to have higher thresholds than the SiO_2 overcoated samples. Although the explanation for the lowered thresholds was not definitely attributable to film stress or film scattering, the MgF_2 films were observed to have an index inhomogeneity of about 7%. In addition,as pointed out below, there is a likelihood that the MgF_2 films were not atomically pure and were partly composed of MgO.

*Note: Four other materials - BX-7, Cer-Vit, ED-2, and ED-4 - were also subjected to ion polishing and bowl-feed polishing. In each case, the ion polished samples had higher thresholds. Ion energies ranged from 20-30 KV at close to grazing incidence.

2.2 Hydroxyl Concentration

A series of thin-film samples of MgF_2 and SiO_2 on fused silica was prepared by electron beam deposition with the angle of incidence of the coating material as the variable. These data are presented in table 2. As can be seen, there is no obvious correlation of breakdown threshold with angle of incidence. Taking into account the measured values of roughness (which were nearly the same for all the samples of each data set) did not explain the variations of threshold. However, comparison of the thresholds with the transmission of the substrates at 2.2 and 1.4 micrometers and in the ultraviolet did result in a definite correlation. Table 2 shows the comparison of threshold with the substrate transmission at 1.4 micrometers. The correlation coefficient for the SiO_2 samples is -0.96, and the correlation coefficient for the MgF_2 samples is +0.80. The handling history of the samples was traced. It was found that the fused silica substrates had not all been supplied to the coating company by the same vendor. In fact, the percent transmission at 1.4 and 2.23 micrometers was correlated with the values of hydroxyl concentration quoted in vendors' literature [7]. Since the correlations of threshold with transmission are high, it is believed that the present data imply that the thresholds of MgF_2 and SiO_2 films fabricated by electron beam deposition do not greatly depend upon the deposition angle of incidence. The signs of the correlation coefficients indicate that the presence of hydroxyl is beneficial in the fabrication of SiO_2 films and deleterious to the fabrication of MgF_2 films. It is hypothesized then, when depositing SiO_2 ($n = 1.45$) films,there is a tendency to produce some SiO ($n \sim 2.0$). Since SiO has a higher index, to a first approximation, it has a lower damage threshold than SiO_2. Thus increasing the oxidation of Si to SiO_2 by the presence of hydroxyl ion is beneficial, and more damage resistant films will result. On the other hand, if hydroxyl ions in the substrate leads to the production of some MgO when depositing MgF_2 films, a higher index material than the desired MgF_2 will be produced leading to a less damage resistant film. That this competition between SiO/SiO_2 and MgF_2/MgO exists is well known [8].

Table 2. Threshold vs 1.4 micrometer transmission

Film	E(MV/cm)	1.4μm Trans.	Inc. Angle
SiO_2	1.24	83%	25°
SiO_2	1.16	85	20.3
SiO_2	0.813	92.5	42
SiO_2	0.681	93	29.3
SiO_2	0.564	94	18.6
MgF_2	0.61	95	20.3
MgF_2	0.50	85	18.6
MgF_2	0.50	85	25
MgF_2	0.50	86	29.3
MgF_2	0.50	86	42

(Data taken from [6])

Note: Decreasing transmission associated with increasing hydroxyl concentration.

3. Conclusions

The roughness normalization of threshold which appears to be valid for a wide range of substrate and film materials [1, 6], provides a very useful method for comparing the relative merits of various surface preparation techniques in affecting surface damage threshold. The utility of the normalized threshold is that the gross effect of roughness is accounted for and separated from the gross effects of the preparation techniques themselves. As an aside, the most striking example of this that we have so far observed is the effect of ultrasonic cleaning [1]. Rouge polished fused silica was damage tested before and after a long period of ultrasonic cleaning. Identical thresholds were observed. However, when the fact that the roughness increased by a factor of five was taken into account (the final normalized threshold being more than twice the initial normalized threshold), it became clear that ultrasonic cleaning is very effective in removing contamination. This conclusion was not at all evident from the basic threshold data, because the effect was completely masked by the roughness change. We believe that the threshold/roughness relationship is applicable for materials other than fused silica. Its usefulness over a wide range of film and substrate materials was clearly demonstrated previously [6].

As for coating failure mechanisms, we believe that we have observed a strong indication that the chemical composition of the substrate (hydroxyl in fused silica in the present case) can significantly alter the damage threshold by affecting the character of the deposited film.

4. Acknowledgments

The authors gratefully acknowledge the assistance of R. Austin and J. Kurdock of the Perkin-Elmer Corp. for measurements pertaining to the hydroxyl ion concentration.

5. References

[1] House, R. A., Bettis, J. R., Guenther, A. H., and Austin, R., NBS Special Publication 435 (Glass, A. J. and Guenther, A. H., Eds.), U.S. Government Printing Office, Wash, D.C. (1976), p. 305; also House, R. A., Dissertation (1975), AF Institute of Technology, WPAFB, OH.

[2] Fradin, D. W. and Bass, M., Appl. Phys. Lett. 22, #4, 157 (1973).

[3] Bloembergen, N., Appl. Opt. 12, #4, 661 (1975)

[4] Ringlien, J. A., et al., Appl. Phys. Lett. 25, #10, 598 (1974).

[5] Boling, N. L., Dubé, G., and Crisp, M. D. in NBS Special Publication 387, (Glass, A.J. and Guenther, A. H., Eds.), U.S. Government Printing Office, Wash, D.C. (1973), p. 69.

[6] Bettis, J. R., House, R. A., Guenther, A. H., and Austin, R., NBS Special Publication 435, (Glass, A. J. and Guenther, A. H., Eds.), U. S. Government Printing Office, Wash, D.C. (1976), p. 289; also Bettis, J. R., Dissertation (1975), AF Institute of Technology, WPAFB, OH.

[7] Austin, R. private communication.

[8] Ritter, E. in Physics of Thin Films, (G. Hass, M. H. Froncombe, and R. W. Hoffman, Eds.), Vol. 8, p. 6, Academic Press, New York, NY (1975).

6. Figure

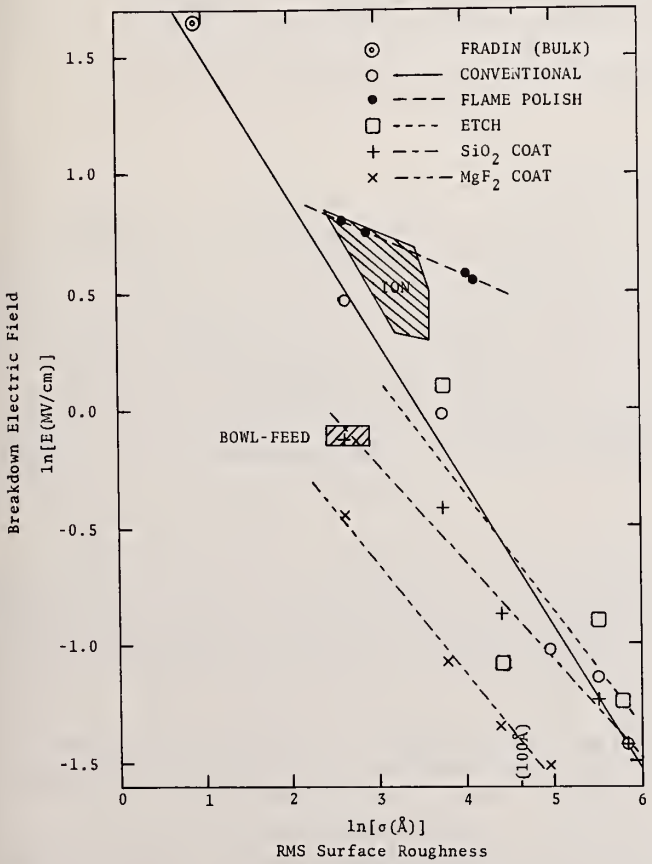

Figure 1. Threshold vs roughness for various surface preparation techniques.

COMMENTS ON PAPER BY HOUSE, BETTIS, AND GUENTHER

No discussion on this paper.

4.9 LASER INDUCED DAMAGE TO THIN FILMS INMERSED IN LIQUIDS

A. Balbin-Villaverde

Instituto de Física
Universidade Estadual de Campinas
Campinas S.P. 13100 - Brasil

L. G. DeShazer*

Center for Laser Studies
University of Southern California
Los Angeles, California 90007

A high power ruby laser system, operating in a single longitudinal and transverse mode was used to measured the damage threshold of a series of quarter-wave and half-wave single coatings, as well as for multilayer reflectors and antireflection "vee" coatings, inmersed in different liquids: water, carbon disulfide, nitrobencene, ethanol, methanol, acetone, and diiodometane. Coatings of TiO_2, MgF_2, SiO_2, ZrO_2, and ZnS on substrates of glass were studied. Liquids were chosen covering a wide range of their physical properties. A correlation is intended between the damage threshold of the coatings and liquid properties. It is found that the damage threshold for all the films increases steadily with the low frequency dielectric constant of the liquids. For multilayer reflectors is also observed a clear dependence of the damage threshold on the liquid index of refraction, through the modification of the electric field inside the films.

Key words: High power ruby laser damage; multilayer reflectors; single layer coatings; spark detection; thin films inmersed in liquids.

1. Introduction

Although up to the present time, the main effort was done on the damage study of solids, surface and bulk, caused by irradiation with high power lasers, several thorough studies of laser induced damage in thin films, were also undertaken. Among those, we can mention the work of A.F. Turner [1][1], who measured the damage threshold of single-double- and multi-layer coatings, using a high power ruby laser system, but because of the multimode operation of his laser, the thresholds reported by him might be considered as giving only relative values of the damage resistence of the different coatings tested. R. R. Austin and A.H. Guenther [2,3] determined the resistence of a set of AR coatings to irradiation by a high power neodymium laser. B.E. Newnam and L.G. DeShazer [4] reported a thorough and reliable study of the laser induced damage in thin films irradiated by a single mode ruby laser. That study comprised the measurement of damage thresholds for single-layer coatings of various thicknesses and materials, as well as antireflection "vee-coat" and multi-layer reflectors, being many of the films tested also in the reverse orientation.

In the present work is intended a different approach to the problem of the laser induced damage in thin films. D.W. Gregg and S.J. Thomas [5] have previously reported that inmersing two 99% dielectric mirrors (one "soft": zinc sulfide/thorium oxifluoride, and the other "hard": silicon oxide/titanium oxide) in nitrobenzene, their resistence to laser induced damage was greatly improved. They found that at the laser intensities for which the mirrors damaged in one or five shots in air, there was litlle damage in them, even for more than 50 laser shots, when they were inmersed in nitrobenzene. In that experiment the two mirrors under study were used as the back reflectos of the laser optical cavity.

Based in those results a sytematic study of this effect was undertaken. In our experiment the coatings were placed outside of the laser cavity, and in order to achieve the necessary laser intensities to damage them, a lens was used. A variety of coatings were tested, inmersed in liquids

---

* Present address: Office of Naval Research, 223 Old Marylbone Road, London NW1 5th, England.

[1] Figures in brackets indicate the literature references at the end of this paper.

with different physical properties, in an attempt to get a better understanding of this effect, and consequently, of the damage mechanism.

2. Test-samples.

The effect of liquid inmersion on the damage threshold was investigated for several single-films made of different materials, with thicknesses ranging from a quarter-wave up to three-quarter-wave as well as for multilayer reflectors, each made with various combinations of two different films materials. Most of the samples were tested in two ways: the first one with the liquid in front of the film facing the laser beam (which will be called forward orientation), whereas in the second way the sample was turned around with its substrate side towards the laser beam (reverse orientation). Likewise, a "vee-coat" sample was tested, this consisted of a bilayer coating with the layer in contact with the substrate made of a material of high index of refraction (of the order of 2 or higher), and the other layer of a low index material (about 1.4 or 1.5), with the thicknesses of both layers being designed to give a minimum of reflectance in air.

This thorough study of the damage threshold behaviour was done in order to have an extended basis for comparison between possible thin-film damage mechanisms, In table 1 and 2, all the cases investigated are enumerated, the first of these two tables is reserved for single-layer samples, whereas the second one is for multilayer reflectors and one "vee-coat". The nomenclature used specified the structure of the coatings when there are more than one layer, but made only with two different materials is as follows: for each layer of a quarter-wave thickness is used a capital letter H, if the material has the highest index of refraction or L, if it has the lowest one, raised to a symbolic power equal to the actual thickness of the layer expressed in units of a quarter-wave. The letter G stands for the substrate (BCS-2 glass), and A for the air. When some combination of layers is repeated itself, this is indicated through the use of the corresponding exponent. Letters are writen on a consecutive order starting from the substrate and ending with the air.

The substrate for all the samples is made of BCS-2 borosilicate glass, with an index of refraction of 1.513 at the wavelength of 694.3nm. The coatings were supplied by Optical Coatings Laboratory Inc. (O.C.L.I.), except for four of them which were made by Ray Owens at the University of Southern California. The index of refraction at a wavelength of 694.3nm for each material we used is as follows: TiO_2- 2.28, ZnS- 2.32, ZrO_2- 1.975, MgF_2- 1.38, SiO_2- 1.456, and for the sample 19: TiO_2- 2.35.

3. Liquid Selection for Inmersion Test

Eight liquids were tested in our experiment of laser induced damage in inmersed coatings. They were chosen according to the two following criteria:

1) wide range of refraction index values; because the electric field squared inside a film depends on the index of refraction of the liquid in which it is inmersed, we tested liquids covering the maximum available range of refractive indeceses, from water and methanol with n= 1.33 up to diiodomethane for which n= 1.72. Also a test in air (n=1) was included for the sake of completeness.

2) wide range of dielectric constant: because a preliminary test showed some dependence of the laser induced damaged threshold on the dielectric constant of the liquids, we selected them covering the whole available range of values of K, from air with K=1 up to formamide with K≈100.

Some of the most relevant physical properties of the liquids are listed in table 3. They are: [6,7,8,9]:

a) density (g/cm^3)

b) dielectric constant K, average value between low frequencies (audio) and radio-wave frequencies (400 MHz). The dielectric constant drops monotonously from dc up to about 500 MHz, depending on the liquid; for higher frequencies resonances begin to appear.

c) refraction index $n_{H\alpha}$, corresponding to the Hα line of the hidrogen spectrum at 656.3nm.

d) viscosity η (x 10^{-3} Pa.s)

e) heat of vaporization Δ H (KJ/g).

f) specific heat at constant pressure c_p ($W/cm^{o}K$).

g) thermal diffusivity D (cm^2 /ms).

Transmissivities were measured for all these liquids, at a laser power density of 2 GW/cm^2, with the same experimental arrangement used for the laser induced damage threshold measurements. Benzene, nitrobenzene, and carbon disulfide (which are very strong Raman and Brioullin actives) and diiodomethane, showed a loss of the order of 4%. For the other liquids the losses were negligible.

Table 1. List of tested thin films: single-layer

#	Material	Thickness	Orientation	Supplier
1,2	TiO_2	qw	forw.,rev	OCLI(0121)
3,4	TiO_2	hw	forw.,rev	OCLI(0123)
5,6	TiO_2	tqw	forw.,rev	OCLI(0137)
7,8	ZrO_2	qw	forw.,rev.	OCLI(0129)
9,10	ZrO_2	hw	forw.,rev.	OCLI(0131)
11,12	MgF_2	qw	forw.,rev.	OCLI(0133)
13,14	MgF_2	hw	forw.,rev.	OCLI(0135)
15	ZnS	qw	forw.	USC
16,17	ZnS	hw	forw.,rev.	USC
18	ZnS	tqw	forw.	USC

qw: quarter-wave; hw: half-wave; tqw: three-quarter-wave ; forw. : forwards; rev. : reverse.

Table 2. List of tested thin films: multi-layers*

#	Materials	# of layers	Structure	Supplier
19	TiO_2/SiO_2	20	$G(HL)^9HL^2A$	OCLI(0102)
20	ZrO_2/SiO_2	29	$G(HL)^{14}HA$	OCLI(0105)
21	ZrO_2/MgF_2	25	$G(HL)^{12}HA$	OCLI(0107)
22	TiO_2/SiO_2	2	$GH^{0.28}L^{1.32}A$	OCLI(0141)
23	ZnS/ThF_4	9	$G(HL)^4HA$	USC

*Samples were tested forwards.

Table 3. Physical properties of the liquids

Liquid	$n_{H\alpha}$	K	η	ΔH	ρ	c_p	D
Ethanol	1.36	25	1.19	0.85	0.791	2.40	0.89
Water	1.33_1	80	1.0	2.26	0.998	4.18	1.45
Methanol	1.32_7	33	0.58	1.10	0.826	2.51	0.96
Benzene	1.49_6	2.3	0.65	0.40	0.879	1.7	0.88
Formamide	1.44_5	100	3.36	----	1.133	2.31	----
Carbon Disulfide	1.62	2.6	0.37	0.35	1.26	0.97	1.31
Nitrobenzene	1.54_6	35	2.01	0.33	1.20	1.46	0.93
Diiodomethane	1.71_5	5.2	---	----	3.32_5	----	----

*Measured at 20 ^oC

4. Experimental apparatus

A schematic diagram of the experimental arrangement is shown in figure 1. The ruby laser oscillator operates in a single longitudinal and transverse mode TEM_{oo}. The transverse mode selection is achieved through the use of a intracavity aperture of 1 mm of diameter (Fresnel number of 0.4), whereas for the longitudinal mode selection we used an etalon as the output mirror. The shape of the output bean is monitored by making a spatial scan with a pinhole. The laser beam is Gaussian with a measured spot-size radius of 0.060 cm, at a distance of 100 cm from the aperture of the laser oscillator with a beam divergence of 1.3 mrad. A sample of the output beam, after to be delayed for about 30 ns, is displayed in the same oscilloscope than the transmitted beam for normalizing purposes. The photodetector system comprises a ITT F-4000 fast biplanar photodiode and a 519 Tektronik oscilloscope. A typical FWHM value for the pulse is 12 ns. Energy is measured using a RCA 7102 photomultiplier with an integrating circuit and a 555 Tektronix oscilloscope. The energy system is calibrated against a 102 thermopile from Hadron.

In order to achieve the neccesary power density to damage the samples the beam is focused with a lens of 10 cm focal length placed at 100 cm from the laser output aperture.

The cell for the thin-films damage studies is made with the sample as one of the windows, whereas the other one is an optical flat BCS-2 borosilicate glass, with a thickness of 6.2 mm. The windows are separeted by an O-ring teflon spacer, this material has the advantage to be resistent to the action of organic liquids. The spacer is made as thin as possible in order to reduce the losses by liquid absorption and stimulated scattering processes. The best thickness was found to be 3 mm. The cell is positioned non-normal to the beam to avoid the problem of the backscattered light.

The spark produced when the sample is hitted by the laser beam with an intensity above some threshold value was photo-electronically detected by using a 6199 RCA photomultiplier and recorded by a 555 Tektronix oscilloscope. The light emitted by the spark, corresponding to the black body emission at several thousands of degrees kelvin, has its peak in the visible region of the spectrum towards the violet. At the same time, the light emitted by the flash-tube and some small amount of ruby laser radiation, both scattered by the various optical components also reach the photodetector, giving signals of the same order or even greater than the corresponding to the spark emission. To overcome this problem we used a 6199 RCA photomultiplier with a peak of sensitivity at 400nm, a narrow-band uv filter and a high-frequency-pass RC filter in the output of the photodetector.

The duration of the spark emission pulses is of the order of 100 or 200 ns [10,11] for laser irradiated transperent solids, and thin-films, while on the other hand, the duration of the flash-lamp emission is about 1 ms. This difference in the frequency of both pulses of three or four orders of magnitude allows to the filter to cut-down the low frequency signal from the flash-lamp emission by a factor of 20, whereas only affect the spark signal by 20%. The spark detector is located off-axis of the laser and facing the back of the cell, in order to avoid the difference in the spark detection sensitivity, when this is observed through a layer of liquid.

5. Experimental Procedure.

The damage threshold was measured for each sample in air and when it was inmersed in different liquids. Between liquids the cell was rinsed with ethanol several times to avoid contaminations. We chose this liquid because of its solubility for all the liquids tested in our experiment. To keep the same all the experimental conditions the damage threshold in air was determinated with the sample mounted in the cell without any liquid. The effective thickness of the cell spacer, corrected for the index of refraction effect was: 3 mm for air, 2.4 mm for the liquid with the lowest index of refraction (n=1.33), and only 1.8 mm for diiodemethane (n=1.74). To overcome that source of error the cell was moved 1 cm far away from the lens, whenever a liquid was inserted into the cell. By turning around the cell the damage threshold of the thin-film samples were also measured with the laser beam irradiating them from the substrate side. In the last case, it is not neccesary a correction in the cell position when this is filled with different liquids.

For samples 1 through 14, their damage threshold was identified with the corresponding threshold for the spark detection. The same was done for the samples 18 to 23. The signal fron the spark detector was sent to one channel of a 555 Tektronik dual-beam oscilloscope, while on the other hand, the signal from the laser energy detector was displayed on the other channel. With this technique it is possible to measure for each laser shot its energy and the corresponding spark intensity. For each liquid between 10 and 20 shots were required to find the damage energy threshold. That was assumed to be the midpoint between the maximum energy for which there was a non-detectable spark and the minimum energy for which there was still a tiny spark. That energy interval was taken as the uncertainty associated with the measurement.

By moving the cell parallel to the lens we used different spots over the coating surface for each laser shot, measuring in that way the one-to-one damage threshold. The laser beam was

attenuated by means of a set of $CuCl_2$ cells. The distance lens-sample was kept constant throughout the whole set of liquids for each particular sample, in that way the effect of the beam spot-size on the damage threshold was avoided [12].

For samples 15 through 18 another damage threshold criterion was applied. There was a low power cw He-Ne laser beam superimposed to the ruby laser beam, irradiating boths the same spot on the sample surface. When some damage was produced in the coating, the scattering for the cw laser increased over its normal value, being that very small change detected visually. The same criterion as for the previous spark method was used to define the threshold, in this case will be called laser-induced-scatterer (LIS) threshold.

6. Experimental Results

Damage thresholds for the coatings inmersed in different liquids, relative to the corresponding value in air, are plotted in figures 2 and 13for all the samples tested as a function of the refractive index of the liquids, Open circles are used in those figures for the data corresponding to the liquids: formamide, water, and nitrobenzene. The first two liquids have the highest values of the low-frequency dielectric constant, K. The third one has a special interest, although having only a moderate value of K, it is the only liquid tested previously by D.W. Gregg and S.J. Thomas [5] and it will be used for later comparison. We also take into account the difference in the reflection losses in the window when the cell is filled with a liquid. The curves drawn in thoses figures only intend to visualize the apparent trend of the damage threshold.

The damage threshold in air for each sample is given in the figures mentioned above. They are expressed as the peak energy density ε_o (J/cm^2) and the corresponding peak power density P_o (GW/cm^2). It also includes the spot-size radius of the beam at the position of the sample ω_o. The laser pulsewidth fluctuated from 10 to 12 ns for different shots. Because in our study we are only interested in relative damage thresholds, the laser intensities are calculated aproximately by using only Dickson equations for the focusing of a Gaussian beam, without taking into account the effect of the truncation of the beam which is only severe near the focus of the lens.

The spark threshold criterion was applied for almost all the coatings because of the high initial scattering of the He-Ne laser by the films and by the liquids; that makes the LIS threshold measurement very difficult and inaccurate. Only for ZnS quarter- and half-wave films, with an initial very low laser scattering, the LIS threshold criterion was preferred to the spark method due to the fact that in this case the LIS threshold is between three and four times lower than the corresponding spark threshold. For a three-quarter-wave ZnS coating, being both thresholds very close to each other both were measured, that allows us to make a comparison of the effect of the liquid inmersion on each case.

The experimental results can be summarized in the following way:

1) There is definite dependence of the damage threshold on the index of refraction of the liquids, that relation depends on the film material, thickness and orientation of the samples. In some cases the threshold undergoes one hundread percent change, going from air to diiodomethane, whereas in some other cases the effect is almost null.

2) The damage threshold when the film is inmersed in a liquid with a high value of the dielectric constant K (open circles in figures 2 to 13) is higher than it corresponds from its index of refraction, increasing that difference with the value of K. Nevertheless, this effect is in average, only of the order of 20% for formamide which has the highest value of K. The effect is observed for all the films we tested regardless of the material,thickness and orientation of the samples. It is also found when the LIS criterion is applied.

7. Discussion of the experimenal results

In order to relate the observed differences in the behaviour of the costings when they are inmersed in liquids, it is neccesary to calculate in each case the real laser intensity that produces the damage, i.e., to take into account the interference effects in the coating. We calculate for each sample the electric field squared (EFS) at every point in the liquid, film, and substrate [13]. Because the incident laser intensity is measured in air, all the EFS values inside the sample should be normalized to the corresponding values for air, which will be called $[E_o^+]^2$. The index of refraction of the substrate is taken equal to 1.51, and furthermore, reflection losses were taken into account in the calculations.

Relative laser intensities are propertional to the quantity

$$n.|E/E_o^+|^2$$

where n and $|E|^2$ are the index of refraction and the EFS, respectively, in each medium. This last quantity unlike the EFS, is not continous across the medium boundaries. Relative laser intensities in each medium are given for all the samples in table 4, corresponding to the liquid refractive indeces of: n_1= 1.33, n_2= 1.50, and n_3= 1.72. For comparison, the inverse of the corresponding measured damage thresholds is included in the table. The possible correlations we found between damage threshold and laser intensity are summarized as follows:

1) Multilayer reflectors, the laser intensity in the liquid is independent of its refractive index and the changes in the damage thresholds are in agreement, within experimental errors, with the corresponding changes in the laser intensity in the coating for TiO_2/SiO_2, ZrO_2/SiO_2, and ZrO_2/MgF_2. For the ZnS/ThF_4 reflector is observed the same trend, but the effect is reduced.

2) TiO_2/SiO_2 "vee-coating", in this case the laser intensity in the coating does not depend on the refractive index of the liquids and the damage thresholds can be correlated with the laser intensities in the liquid at its interface with the coating where there is a minimum of the standing wave pattern.

3) Half-wave-layer coatings, three of them TiO_2, ZrO_2, and ZnS present the same trend, whereas for MgF_2 is the opposite one. In the coating the laser intensity is independent of the liquid in which it is inmersed. For the three coatings mentioned in first place, the change in the threshold can be correlated with the corresponding change in the laser intensity, averaged in the liquid, whereas for the last film of MgF_2 is with the laser intensity at the liquid-coating interface. Notice that for the MgF_2 film the laser intensity in the coating has a maximum, whereas for the other three films presents a mininum. Let us add that in ZnS is observed the same change in damage threshold than for TiO_2 (boths have almost the same index of refraction), although for the first film a LIS threshold criterion was used.

4) Half-wave-layer coating (reverse), all the samples show the same trend, even for ZnS for which the LIS criterion was applied; nevertheless, the intensity of the effect is different in each case. The best possible correlation, although poor, is with the laser intensities at the center of the film. Notice that for ZnS, TiO_2, and ZrO_2, there is a minimum of the laser intensity in that point, while for MgF_2 the intensity is a minimum or maximum depending of the index of refraction of the liquid. We can not find any correlation with the average intensity in the film. In these coatings the laser intensity in the liquid is the same for any liquid.

5) MgF_2 quarter-wave-layer, a fairly good agreement is found between damage threshold and the laser intensity in the liquid at its interface with the coating. In the film the laser intensity is almost independent of the liquid.

6) MgF_2 quarter-wave-layer (reverse), there is a good agreement with the laser intensities at the substrate-film interface and/or in the liquid. Notice that for the position mentioned in first place, there is a peak of the intensity, while the average intensity in the film does not depend on the liquid.

7) ZnS and TiO_2 quarter-wave coatings, boths show almost the same standing-wave pattern; nevertheless, they behave oppositely to each other, with regard to the damage threshold. In the first case we found a correlation with the peak laser intensity in the liquid, but for the second film there is not a simple correlation, probably because of the simultaneous changes of the laser intensity in the liquid (at the film-liquid interface) and in the film.

8) TiO_2 one-quarter and three-quarter layers (reverse), we found the same correlation for both with the laser intensity at the film-liquid interface (liquid-side) and in the liquid too. In this case the average laser intensity in the film is independent of the liquid.

9) ZrO_2 quarter-wave coating (forwards and reverse), for the two orientations we found an anomalous behaviour, the damage threshold presented a minimum for some value of the liquid index or refraction between n=1 and n=1.33, but the position of that minimum can not be determined precisely because there is not any liquid with a value of n between 1 and 1.33. The existence of that minimum was confirmed by repeting the measurements several times. By discounting that effect, it is possible to correlate the damage threshold with the peak laser intensity in the film. The laser intensity in the coating is almost independent of the liquid. That is also true for the average laser intensity in the film for the reverse orientation of the sample. In that last case, the best correlation is with the laser intensity in the film at the film-liquid interface.

10) TiO_2 and ZnS three-quarter-wave coatings, the measured damage thresholds are almost independent of the refractive index of the liquids, being the observed differences probably due to the

inherent fluctuations in the damage threshold measurements. That can also explain the slight differences observed for the ZnS when the two threshold criteria are used. No straight correlations can be found with either the EFS or laser intensity distributions.

Table 4. Comparison between the laser intensity and the inverse of the damage threshold for liquid inmersed coatings.

RELATIVE LASER INTENSITY/INVERSE DAMAGE THRESHOLD	n_1	n_2	n_3
QUARTER AND THREE-QUARTER LAYERS OF TiO_2 AND ZnS			
In the liquid (peak)	0.90	0.84	0.76
L-F interface (L-side)	1.58	1.89	2.31
L-F interface (F-side), film, F-G interface and substate	1.20	1.26	1.33
TiO_2 (λ /4)	1.07	1.12	1.78
ZnS (λ /4) (LIS threshold)	0.86	0.74	0.59
TiO_2 (3λ/4)	----	0.89	0.92
ZnS (3λ/4) (Spark threshold)	----	1.06	1.10
ZnS (3λ/4) (LIS threshold)	----	1.03	0.95
QUARTER AND THREE-QUARTER LAYERS OF TiO_2 (REVERSE)			
In the substrate (at λ/4)	0.87	0.81	0.74
G-F interface	1.53	1.81	2.22
In the film (mid-point for quarter-wave)	0.97	0.97	0.97
In the film (peak value for three-quarter-wave)	0.87	0.81	0.74
F-L interface (F-side)	0.87	0.81	0.74
F-L inter. (L-side) and liquid	1.15	1.21	1.28
TiO_2 (λ/4)	1.08	1.10	1.33
TiO_2 (3λ/4)	----	1.22	1.35
HALF-WAVE LAYER COATINGS			
In the liquid (at λ/4)	0.81	0.72	0.62
L-F interface (L-side)	1.43	1.63	1.87
L-F interface (F-side)	1.08	1.09	1.08
Film, F-G interface, substrate	1.08	1.09	1.08
TiO_2	0.88	0.85	0.77
ZrO_2	0.78	0.73	0.56
MgF_2	1.48	1.78	2.28
ZnS	0.90	0.85	0.74

Table 4. Continued

HALF-WAVE LAYER COATINGS (REVERSE)			
In the substrate (at $\lambda/4$)	1.38	1.57	1.81
G-F interface	0.78	0.70	0.60
In the film (mid-point)	1.38	1.57	1.81
F-L interface (F-side)	0.78	0.70	0.60
F-L interf. (L-side) and liquid	1.04	1.04	1.04
TiO_2	1.20	1.32	1.66
ZrO_2	1.11	1.24	1.36
MgF_2	1.33	1.42	2.09
ZnS	----	1.49	1.72
QUARTER-WAVE LAYER OF ZrO_2			
In the liquid (at $\lambda/4$)	0.87	0.80	0.71
L-F interface (L-side)	1.54	1.80	2.16
L-F interf. (F-side), film and substrate	1.61	1.21	1.24
ZrO_2	1.14	1.02	0.75
QUARTER-WAVE LAYER OF MgF_2			
In the liquid (at $\lambda/4$)	0.79	0.70	0.59
L-F interface (L-side)	1.40	1.57	1.78
L-F interface (F-side), film and substrate	1.05	1.05	1.03
MgF_2	1.24	1.50	2.18
QUARTER-WAVE LAYER OF ZrO_2 (REVERSE)			
In the substrate (at $\lambda/4$)	0.84	0.77	0.68
G-F interface	1.49	1.74	2.09
In the film (mid-point)	0.97	0.97	0.97
F-L interface (F-side)	0.84	0.77	0.68
F-L interface, (L-side) and liquid	1.11	1.15	1.19
ZrO_2	1.21	0.99	0.90
QUARTER-WAVE LAYER OF MgF_2 (REVERSE)			
In the substrate (at $\lambda/4$)	0.76	0.67	0.57
G-F interface	1.35	1.51	1.71
In the film (mid-point)	0.96	0.96	0.96
F-L interface (F-side)	0.76	0.67	0.57
F-L interface (L-side) and in the liquid	1.35	1.51	1.71
MgF_2	1.31	1.50	2.27

Table 4. Continued

MULTI-LAYER REFLECTORS			
In the liquid (peak)	1.04	1.04	1.04
H-Low interfaces (and at the center of the half-wave layer in TiO_2/SiO_2).....	1.38	1.56	1.80
TiO_2/SiO_2	1.30	1.34	1.64
ZrO_2/SiO_2	1.45	1.55	2.11
ZrO_2/MgF_2	1.53	1.62	2.21
ZnS/ThF_4	-----	1.12	1.24
TiO_2/SiO_2 VEE-COATING			
In the liquid	0.76	0.67	0.55
L-SiO_2 interface (L-side)	1.35	1.50	1.67
L-SiO_2 interface (SiO_2-side), SiO_2 film, SiO_2-TiO_2 interface, TiO_2 film, TiO_2-G interface, and substrate	1.02	1.00	0.96
TiO_2/SiO_2	1.53	1.62	2.26

F: film; L: liquid; G: BCS-2 glass substrate; H: high index material; Low: low index material

Liquid index of refraction: $n_1 = 1.33$ - $n_2 = 1.50$ - $n_3 = 1.72$

8. Discussion of laser induced damage mechanisms.

A comparison between the physical properties of the liquids listed in table 3, and the damage threshold of the coatings inmersed in those liquids shows no correlation at all for none of the properties, but with the low frequency dielectric constant. It is observed that when the films are inmersed in a liquid with a high dielectric constant, like water and formamide (and at less extent, nitrobenzene), their damage threshold data are not well fitted by the relative threshold vs index of refraction experimental curves, showing always higher values of the threshold. That effect is also observed when the films are tested in the reverse orientation, as well as when the LIS criterion is used.

A possible explanation of this effect of the laser induced damage dependence on the dielectric constant of the liquid can be as follows: there is a potential barrier at the film-air interface whose high controls the electron protoemission of the film surface when this is irradiated with the laser. The electrons emitted from the film surface, by absorbing energy from the laser beam, produced a "hot plasma" (with temperatures of the order of thousands of degrees, well above the melting point of any of the coatings). The exact form of that potential barrier is not known in general [14], being also afffected by the presence of inclusions, cracks, and pores on the film surface.

In spite of the fact that the exact shape of the potential barrier can not be calculated, we know that when a film is put in contact with a liquid, the height of the barrier at the new liquid-film interface should increase. That is due to the fact the positive image charges left in the film surface when the electrons are emitted, induce negative charges in the polarizable liquid at its interface with the film. Therefore, a new contribution is added to the interface barrier so its height increases, and acccording to that the electron photo-emission is reduced. That is in good qualitative agreement with the observed increase in damage threshold.

Let us also recall that the peak frequency in the Fourier transform of the laser pulse (about 10 ns) is of the order of 10^8 Hz, and consequently, this also should be the characteristic frequency for the induced charges. That supports the correlation we found with the dielectric constant of the liquids at low frequencies (up to about 5×10^8 Hz). The fact that the effect is observed also when the LIS criterion is used, means that the decrease in the electron photoemission not only affects the spark detectivity (reducing the size and/or the temperature of the spark plasma), but also acts on the intrinsic damage threshold of the films.

No definite correlations can be found for all the samples between the changes in the damage

threshold for different liquids and the corresponding change in laser intensity (or equivalently for the energy density of the laser). For some of the films the laser intensity has a different dependence on n (liquid index of refraction) in the liquid than in the film, and consequently, in those cases the lack of a correlation could be due to the combined changes in both regions. Only in those cases for which the standing-wave pattern is independent of n, either in the liquid or in the film, some degree of correlation can be found, like in the following cases:

For all the multilayer reflectors the laser intensity in the film controls the damage threshold, whereas for the bilayer "vee-coating" is the laser intensity in the liquid at the liquid-film interface which fixes the threshold. The same is also true for MgF_2 quarter-wave coating in both orientations, and for MgF_2 half-wave layer in the forwards orientation. For some other samples their damage thresholds are also related to the laser intensities in the liquid, not just at the interface, but to some average value in the liquid.

Let us also mention the fact that when the LIS criterion is used a similar behaviour is observed for the damage threshold as a function of the liquid index of refraction. All the facts previously discussed (including the dependence on the low frequency dielectric constant of the liquids) give us a strong evidence that the photo-electrons emitted by the film through the production of a "hot plasma", play an important role in the damage of the coatings, as well as the intensity of the beam in the liquid, by controling the formation of this plasma (which grows in size and temperature by absorbing energy from the laser beam). It is observed from the oscillograms of the transmitted beam, that the on set of the spark is accompanied by an absorption of the laser beam reaching a complete cutoff of the transmission for the laser intensities above damage threshold.

The possibility should be excluded of having only an "apparent change" in the damage threshold when different liquids are used due to the differences in the spark detectivity (by changing the size and/or the temperature of the spark), since a simmilar behaviour is observed for the LIS thresholds. Furthermore, as it was mentioned previously, the absorption of the laser beam by the liquids before damage takes place is negligible for all the liquids used in our experiment.

There is not evidence against the fact that some other mechanisms can also contribute simultaneously to the coating damage process. It is only found that when the conditions are the same for the mechanisms, the damage threshold is controlled by the photoemission of electrons from the films and the subsequent growing of the spark. Among those damage mechanisms we can mention; the electron avalamche induced by the intense optical field in the medium [15,16,17]; the heating of the films by linear absorption of the laser beam [1] and the induced stresses [2,3]. B.E. Newman discusses the possibility of the simultaneous action of those three different mechanisms of damage in thin films with their relative important depending of the coating material and the thickness [18].

D.W. Fradin and M. Bass [19] and N. Bloembergen [20] point out the important role played by the surface imperfections (micropores, cracks, inclusions) in the damage of solids. Simmilar discussion for the inclusion effect in thin film damage was carried on by L.C. DeShazer et al. [21]. In our case we have that the liquids, with their different values of n, should modify the degree of the optical electric field enhancement produced by the imperfections, and consequently, we are in presence of another mechanism by which the liquids can influence the damage threshold.

Finaly, a comparison between the results obtained in our experiment with the ones reported by D.W. Gregg and S.J. Thomas [5] shows a total disagreement, nevertheless, it has to be taken into account that different experimental procedures were followed in both cases. They used the dielectric mirror samples as the back mirror of the laser cavity inmersed in nitrobenzene, which also was used as the solvent for the Q-Switch dye. Another significant difference is that they do not measure the one-to-one damage thresholds, but the relative resistence of the samples to the laser induced damage with and without the liquid, after firing the laser many times.

9. Acknowledgements

The authors are grateful to Ray Owens for making some of the samples. We also thank B.E. Newman for providing the computer program for the determination of the standing-wave pattern in the bilayer "vee-coating".

10. References

[1] A.F. Turner, in Laser Induced Damage in Optical Materials: 1971, NBS Special Pub. 356, 119 (1971).

[2] R.R. Austin and A.H. Guenther, in Laser Induced Damage in Optical Materials: 1971, NBS Special Pub. 356, 137 (1974).

[3] R.R. Austin and A.H. Guenther, Appl. Opt. 11, 695 (1972).

[4] B.E. Newnam and L.G. DeShazer, in Laser Induced Damage in Optical Materials: 1972, NBS Special Pub. 372, 123 (1972).

[5] D.W. Gregg and S.J. Thomas, Appl. Phys. Lett. 8, 316 (1966).

[6] R.C. Weast, editor, Handbook of Chemistry and Physics, 53rd ed.(Chemical Rubber Company, Cleveland, 1972).

[7] C.J. West and C. Hull, editors, International Critical Tables of Numerical Data, Physics, Chemistry and Technology (7 vol., MacGrow-Hill, New York, 1933).

[8] A.A. Maryott and E.R. Smith, editors, Table of Dielectric Constants of Pure Liquids, NBS Circular 514 (1951).

[9] D.E. Gray, editor, American Institute of Physics Handbook, 2nd ed.(McGrow-Hill, New York, 1963).

[10] H. Dupont, A. Donzel and J. Earnst, Appl. Phys. Lett. 11, 271 (1967).

[11] L.D. Khazov, A.N. Shestov and G.P. Tikhomirov, Soc. Phys. Tech. Phys. 13, 1112 (1969).

[12] B.E. Newnam and L.G. DeShazer, IEEE J. Quantum Electron. QE-8, 611 (1972).

[13] O.S. Heavens, Optical Properties of Thin Solid Films (Dover Publications, New York, 1965).

[14] T.E. Fisher, J. Vac. Sci. Tech. 9, 860 (1972).

[15] B.S. Sharma and K.E. Rieckoff, Can.J. Phys. 45, 3781 (1967).

[16] B.S. Sharma and K.E. Rieckoff, Can J.Phys. 48, 1178 (1970).

[17] M. Bass and H.H. Barrett, in Laser Induced Damage in Optical Materials: 1971, NBS Special Pub. 356, 76 (1971).

[18] B.E. Newnam, Dissertation, University of Southern California (1973)

[19] D.W. Fradin and M. Bass, Appl. Phys. Lett., 22, 157 (1973).

[20] N. Bloembergen, Appl. Opt. 12, 661 (1973).

[21] L.G. DeShazer, B.E. Newnam and K.M. Leung, Appl. Phys. Lett. 23, 607 (1973).

11. Figures

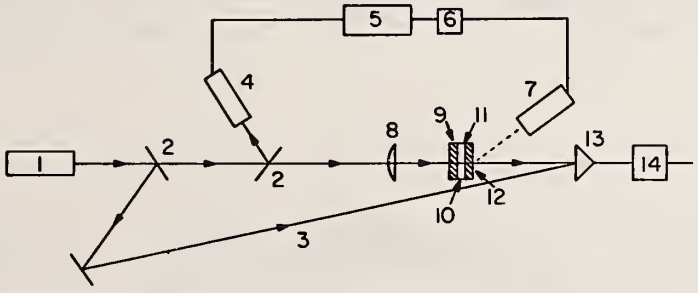

Figure 1. Schematic diagram of the setup for measurement of the damage threshold of liquid inmersed coatings: (1) single-mode ruby laser, (2) beam-splitter, (3) optical delay-line, (4) energy detector: RCA 7102 PM, (5) Tektronix 555 oscilloscope, (6) RC high-frequency-pass filter, (7) spark-detector: RCA 6199 PM, (8) focusing lens, (9) glass window, (10) liquid, (11) coating sample, (12) substrate, (13) ITT F-4000 PD, (14) Tektronix 519 oscilloscope.

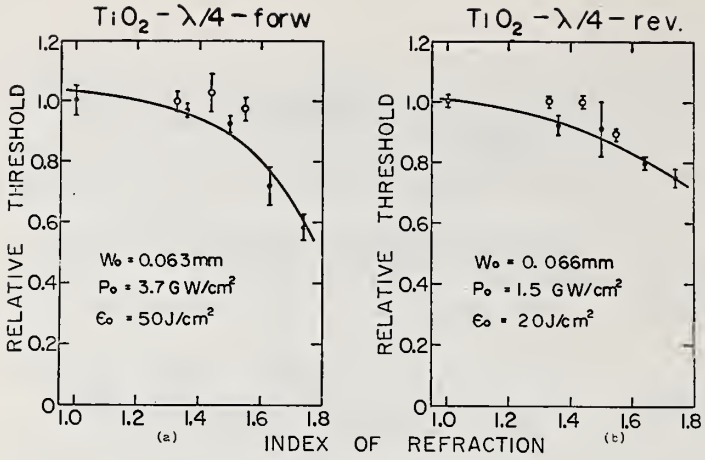

Figure 2. Relative spark threshold for a quarter-wave layer of TiO_2 vs index of refraction of the liquid, (a) forward orientation, and (b) reverse orientation.

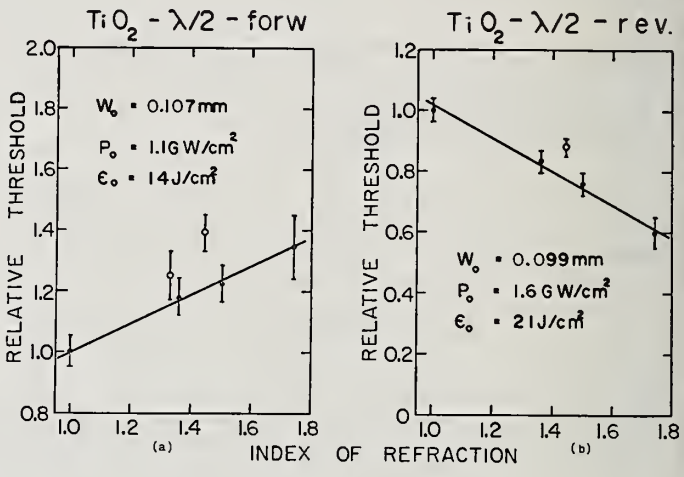

Figure 3. Relative spark threshold for a half-wave layer of TiO_2 vs index of refraction of the liquid, (a) forward orientation, and (b) reverse orientation.

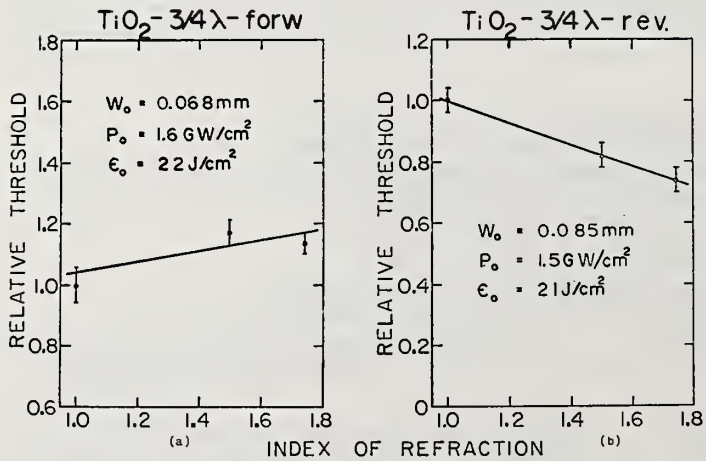

Figure 4. Relative spark threshold for a three-quarter-wave layer of TiO_2 vs index of refraction of the liquid, (a) forward orientation, and (b) reverse orientation.

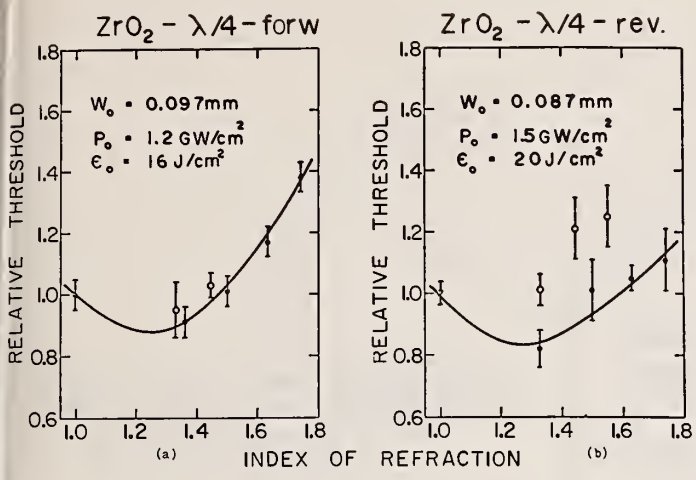

Figure 5. Relative spark threshold for a quarter-wave layer of ZrO_2 versus index of refraction of the liquid, (a) forward orientation, and (b) reverse orientation.

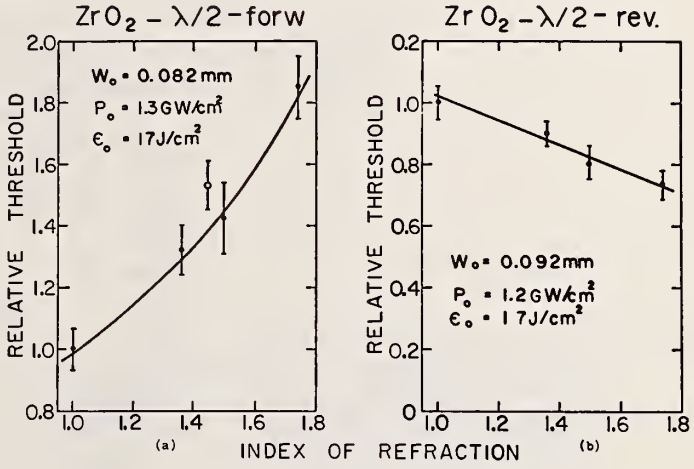

Figure 6. Relative spark threshold for a half-wave layer of ZrO_2 vs index of refraction of the liquid, (a) forward orientation, and (b) reverse orientation.

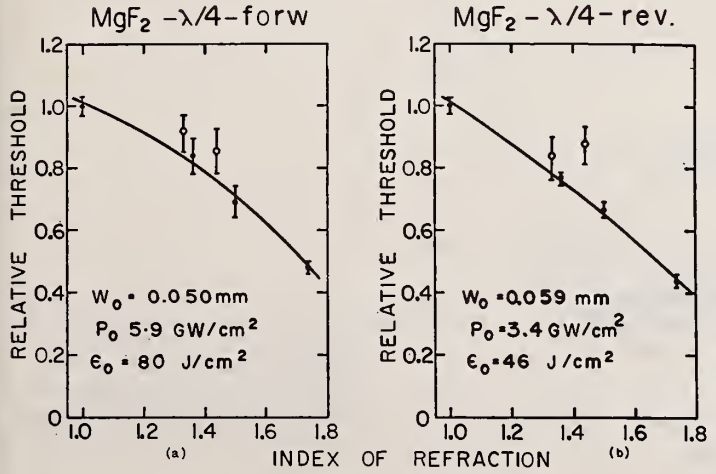

Figure 7. Relative spark threshold for a quarter-wave layer of MgF_2 vs index of refraction of the liquid, (a) forward orientation, and (b) reverse orientation.

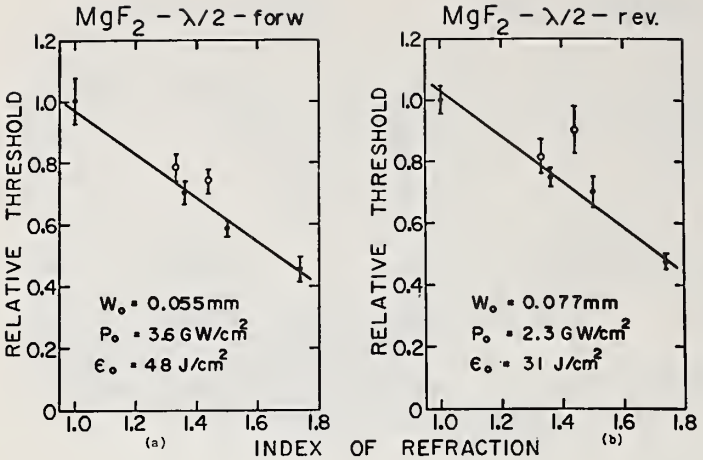

Figure 8. Relative spark threshold for a half-wave layer of MgF_2 vs index of refraction of the liquid, (a) forward orientation, and (b) reverse orientation.

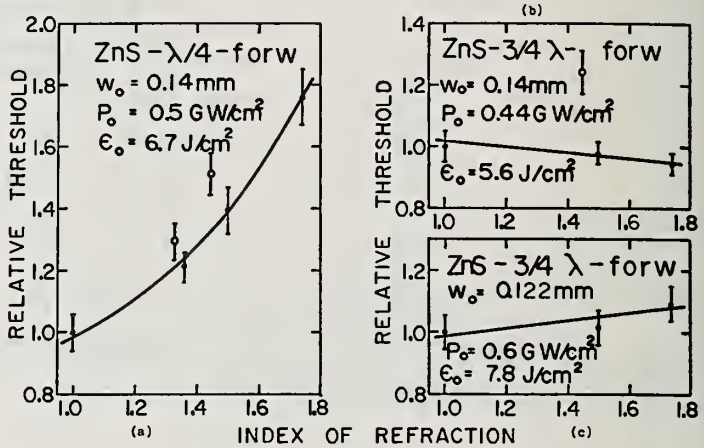

Figure 9. Relative threshold for a single-layer of ZnS, forward orientation vs index of refraction of the liquid, (a) LIS threshold for a quarter-wave, (b) spark threshold for a three-quarter-wave, and (c) LIS threshold for a threshold-quarter-wave.

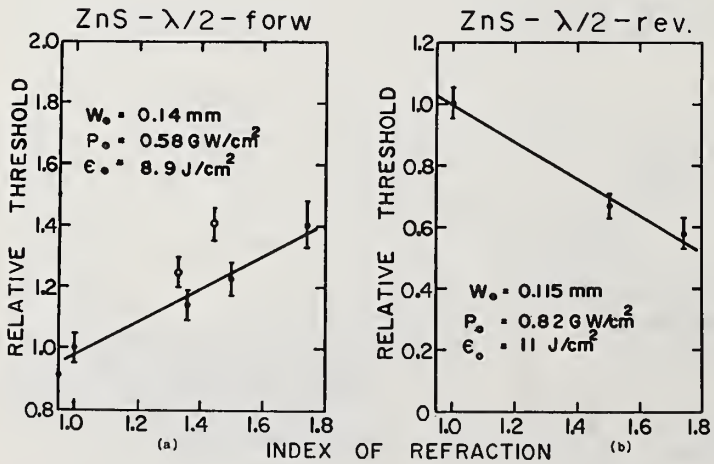

Figure 10. Relative LIS threshold for a half-wave layer of ZnS vs index of refraction of the liquid, (a) forward orientation, and (b) reverse orientation.

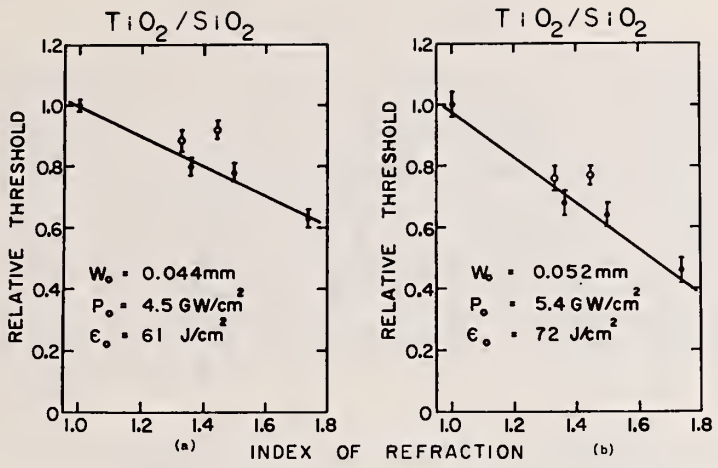

Figure 11. Relative spark threshold for TiO_2/SiO_2 coatings vs index of refraction of the liquid, forward orientation, (a) 20-layers reflector, and (b) bi-layer "vee-coating."

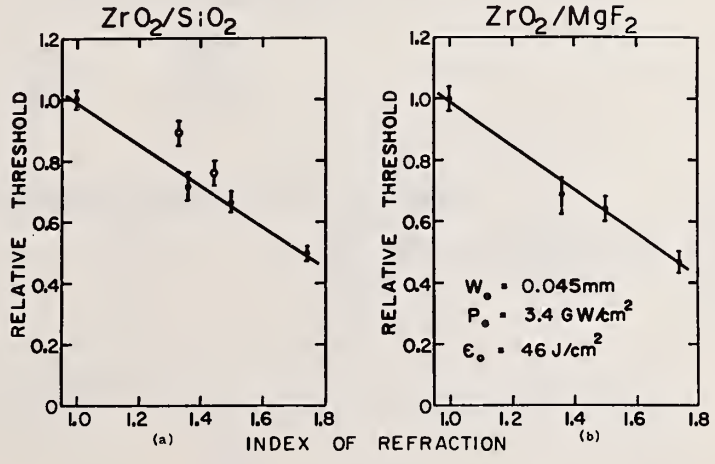

Figure 12. Relative spark threshold for multi-layer reflectors vs index of refraction of the liquid, forward orientation, (a) 29-layers ZrO_2/SiO_2 reflector, and (b) 25-layers ZrO_2/MgF_2 reflector.

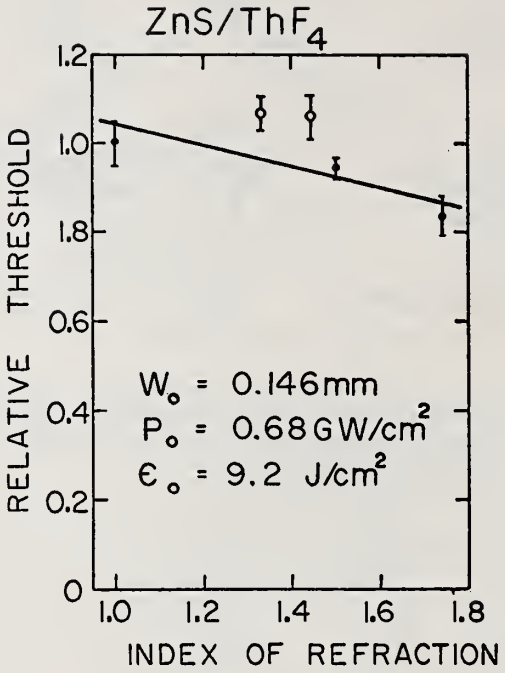

Figure 13. Relative spark threshold for a 9-layer ZnS/ThF_4 reflector.

COMMENTS ON PAPER BY BALBIN-VILLAVERDE AND DeSHAZER

No discussion on this paper.

4.10 DIELECTRIC COATINGS ON METAL SUBSTRATES*

S. S. Glaros, P. Baker and D. Milam
Lawrence Livermore Laboratory
Livermore, California 94550

Large aperture, beryllium substrate based mirrors have been used to focus high intensity pulsed laser beams. Finished surfaces have high reflectivity, low wavefront distortion and high laser damage thresholds. This paper describes the development of a series of metallic coatings, surface finishing techniques and dielectric overcoatings to meet specified performance requirements. Beryllium substrates were coated with copper, diamond machined to within 5 microinches to final contour, nickel plated and abrasively figured to final contour. Bond strengths for several bonding processes will be presented. Dielectric overcoatings were deposited on finished multimetalic substrates to increase both reflectivity and the damage thresholds. Coatings were deposited using both high and low temperature processes which induce varying stresses in the finished coating substrate system. Data will be presented to show the evolution of wavefront distortion, reflectivity, and damage thresholds throughout the many steps involved in fabrication.

Key words: Laser damage; laser fusion; metal mirrors; reflecting optics.

1. Introduction

The reflectors described in this paper were designed for use with the ARGUS laser. The system shown in figure 1 consists of a pair of nested ellipsoidal reflectors [1][1], coupled with an aspheric doublet refracting element, which provides uniform illumination of the specified laser beam profile. There are three distinct, but interrelated sections of this reflector design; the substrate choice, multi-metallic coating adhesion, and dielectric overcoating choice.

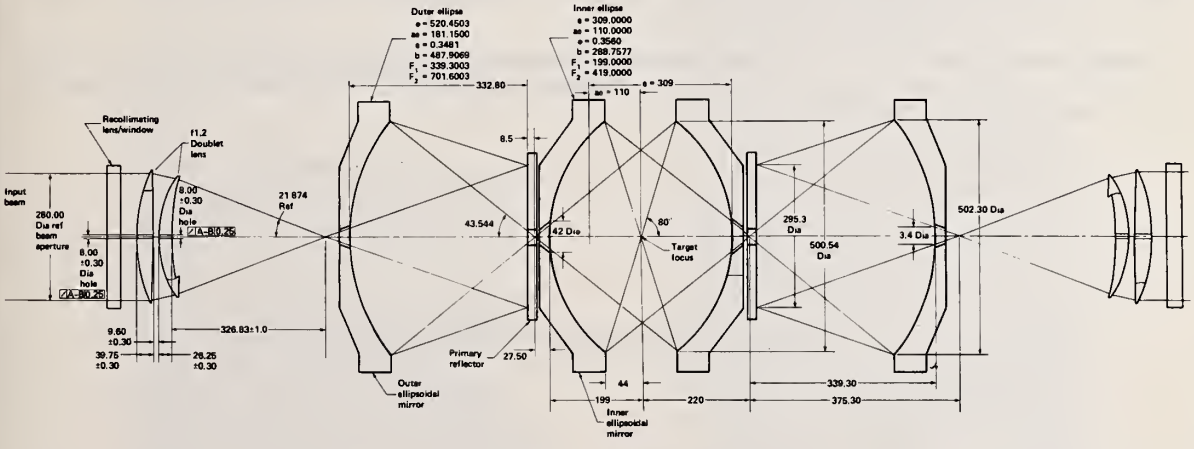

Figure 1. Argus optics parameters.

*Work performed under the auspices of the U.S. Energy Research and Development Administration under contract No. W-7405-Eng-48.

1. Figures in brackets indicate the literature references at the end of this paper.

2. Substrate Choice

The mirror substrate material choices were BK-7, Cervit and beryllium. There are four primary properties which determine the final choice since each of the four effect the substrate design [2] at different times during processing and final use.

The first property affecting substrate choice is strength and micro-yield strength. Macroscopic strength affects the shape of the substrate. Micro-yield strength describes local substrate strength. Here beryllium substrates are seven times stronger than those of BK-7 or Cervit thus giving superior rigidity for the same geometric dimensions as seen in table 1. The second property of interest is the modulus of elasticity which is the magnitude of stiffness. Again from table 2, beryllium is four times stiffer than BK-7 and three times stiffer than Cervit.

Due to the required high aspect ratio required in the geometry of the reflecting portion, both strength and stiffness necessitate thicker peripheral sections for BK-7 and Cervit than for beryllium substrates.

The third property affecting substrate choice is thermal diffusivity ($K/\rho C$). A certain amount of the laser pulse energy is absorbed in the coating and transmitted to the substrate. An excellent diffusivity such as that of beryllium, allows for rapid thermal equilibrium.

The fourth design property is thermal distortion which would be experienced in the final step of mirror processing, the dielectric overcoating. This overcoating subjects the substrate to temperatures of 200-300°C. BK-7 experiences nearly six times the distortion of Cervit while beryllium has only twice the distortion. The amount of distortion seen by beryllium substrates can be further reduced by coating both sides and by substrate stabilization where the substrate has been previously subjected to numerous cycles at these temperatures such that all creep has been accelerated prior to final lapping.

The logical choice based on the forementioned properties is beryllium [3], [4], [5], but even this material is subject to further choices. The desired high strength and low creep with relatively low cost and delivery time was met using ultra pure beryllium particles further shattered by impact with a beryllium target in an inert gas atmosphere. This material is subjected to a number of proprietary elevated temperature pressing and sintering operations to give the highest density with a maximum isotropy. The amount of beryllium oxide in the chosen material directly determines the strength and indirectly the amount of long term creep, hence long term dimensional stability. A number of different vendors processes will meet the forementioned criteria, but hot isostatic pressed beryllium was the least expensive and was available in shorter delivery times than some of the more exotic, but slightly superior processes.

Another factor which enters into the substrate choice is economics. Figuring a Cervit or BK-7 substrate is projected to be more expensive than diamond turning with final light lapping of the nickel coated beryllium substrate system.

Table 1. Mirror substrate design parameters.

MATERIAL ρ (gm/cm^3)	E MODULUS OF ELASTICITY ($10^6 N/cm^2$)	MYS MICRO YIELD STRENGTH (osi)	UTS ULTIMATE TENSILE STRENGTH (psi)	K THERMAL CONDUCT (Cal/cm-s C)	C SPECIFIC HEAT (Cal/gm C)	α COEF OF THERMAL EXPANS (10^{-6}/C)	D THERMAL DIFFUSIVITY K/ρC	THERMAL DISTORTION α/D (x 10^6)	T TRANSITION (C)
BK-7 2.200	7.00	1,500	-	0.0033	0.188	0.55	0.008	69.0	1,500
CERVIT 2.500	9.23	1,500	-	0.0040	0.217	0.10	0.008	14.0	800
BERYLLIUM (KBI HP-20) 1.852	28.00	3,000-10,000	55,200	0.3800	0.450	12.40	0.460	27.0	1,300

3. Multi-Metallic Coating

The proposed processing of the mirrors is detailed in table 2. In order to insure that this processing would yield the required diffraction-limited, high-damage threshold mirrors, a test program was instituted to investigate the variable parameters. Two inch diameter beryllium substrates were cut from KBI HP-20. The substrates were plated with best combination of metallic coating found in another sequence of ring shear tests shown in table 3. The copper plated samples were diamond turned after which interferograms were taken. The test samples were then nickel plated and another set of interferograms and capacitance noncontact measurement of figure. Polishing was by normal mechanical lapping on a conventional machine. The lap material was a soft pitch and beeswax compound. The abrasive was successive grades of synthetic Dupont diamond, the final grade being 0.1 μm size powder. The vehicle was distilled water with a small amount of liquid soap added as a wetting agent. The final surface was obtained by running speeds at the minimum range for the machine, 2-5 rpm on the rotational speed and 1-3 rpm on the reciprocal speed. The slow speeds cause less disturbance to the contacted lap surfaces.

Another set of interferograms was taken after polishing and then the specimens were sent to three different vendors. The processing up through dielectric coating is shown with its step by step interaction with substrate figure, in figure 2. A sample set of interferogram records is shown in figure 3. Since movement in either side indicates induced stress, interferograms of both sides of the sample are shown.

Table 2. Be substrate processing.

1. CUT ROUGH BLANKS 2mm OVER EACH DIMENSION EXCEPT 3mm OVER THE BEST FIT RADIUS ON THE ELLIPTICAL CONTOUR, OUT OF HP-20 MATERIAL.
2. VACUUM ANNEAL: HEAT AT LESS THAN 150°C/h UNTIL 900°C IS REACHED, HOLD FOR 1 h, COOL TO AMBIENT AT NOT MORE THAN 25°C/h.
3. ROUGH MACHINE UNTIL SURFACE IS 0.46mm OVER FINISH CONTOUR.
4. REPEAT VACUUM ANNEAL.
5. MACHINE IN CUTS NOT EXCEEDING 0.254,0127 AND 0.051mm IN THAT SEQUENCE UNTIL SURFACE IS 0.025mm BELOW THE FINISH CONTOUR.
6. REPEAT VACUUM ANNEAL.
7. CHEM MILL UNTIL ALL SURFACES ARE 0.152mm BELOW THE FINISH CONTOUR AND RINSE.
8. BAKE FOR 6 HOURS AT 100°C IN A CHAMBER EVACUATED BELOW 10^{-4}mm Hg.
9. AFTER MASKING, IMMERSE IN TURCO 4215, RINSE, IMMERSE IN BOILING DIST. H_2O FOR 5–10 min, ACTIVATE IN COMBINED SOLUTION OF 97g/l AMMONIUM SULFATE AND 51 ml/l SULFURIC ACID AT ROOM TEMP FOR 60 s, RINSE, IMMERSE IN A ZINCATE SOLUTION FOR 5 min, AT 80°C, RINSE, STRIP ZINCATE WITH NITRIC ACID AT ROOM TEMP, RINSE, REPEAT ACTIVATION THROUGH ZINCATE IMMERSION, APPLY SPECIAL COPPER STRIKE COATING AT 40.6°C FOR 5 min, RINSE, COPPER PLATE IN COPPER PYROPHOSPHATE TO A THICKNESS OF 0.300mm, RINSE, REMOVE MASKING.
10. REMACHINE HOLES AND TURN DOWN NON-FUNCTIONAL SURFACES UNTIL REQUIRED DIMENSION.
11. Y-12 R-O MACHINE TO SINGLE POINT DIAMOND TURN CONCAVE SURFACES OR FLAT ON PRIMARY REFLECTOR UNTIL FINAL CONTOUR IS ACHIEVED.
12. STABILIZE: COOL AT 2.3°C/min TO –70°C AND HOLD FOR 15 min, HEAT AT SAME RATE UP TO ROOM TEMP, HEAT AT NOT MORE THAN 150°C/h UP TO 200°C AND HOLD FOR 15 min, COOL AT 50°C/h DOWN TO ROOM TEMP AND HOLD 15 min, REPEAT COMPLETE CYCLE ONCE MORE.
13. FINAL DIAMOND TURN SURFACES TO 0.013mm BELOW FINAL CONTOUR.
14. INSPECT FIGURE FOR ELLIPSOIDAL MIRRORS; FIGURE, REFLECTIVITY AND WAVEFRONT DISTORTION FOR FLATS.
15. MASK, IMMERSE IN 60g/l ENTHONE ENBOND S-61 AT 82°C FOR 1–5 min, RINSE, IMMERSE IN 60g/l ENPLATE AD-480 FOR UP TO 1 min AT ROOM TEMP, RINSE, ACTIVATE USING 30ml/l ENPLATE 440 AT ROOM TEMP FOR UP TO 30 s, RINSE, PLATE WITH SHIPLEY'S NICULOY 22 AT 90.5°C AT A RATE OF 0.013 TO 0.018mm/h UNTIL 0.025mm PLATED ON, RINSE.
16. REMACHINE HOLES.
17. REPEAT STABILIZATION CYCLE.
18. LAP ELECTROLESS NICKEL TO REQUIRED FIGURE AND WAVEFRONT DISTORTION.
19. INSPECT FIGURE, WAVEFRONT DISTORTION AND SPOT SIZE.
20. DIELECTRIC OVERCOAT CONCAVE SURFACE FOR 99% REFLECTIVITY AT 1.064 μm DAMAGE THRESHOLD GREATER THAN 25GW/cm² FOR 100–150ps PULSES.

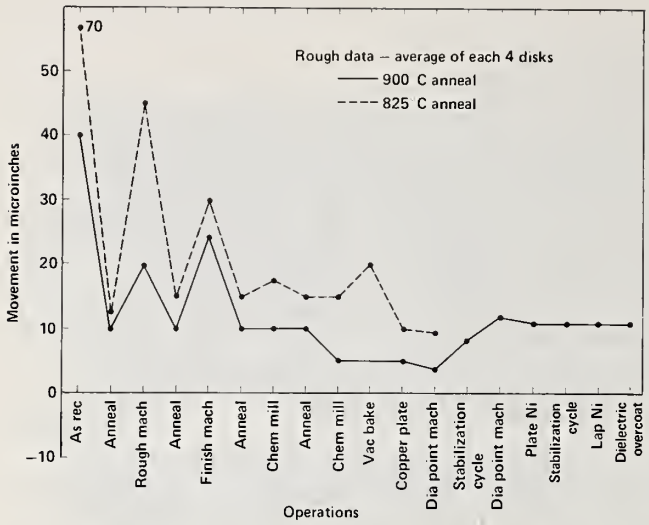

Figure 2. Non-contact interferometer results on HP-20 Be 2" disks.

Side A after Ni coating

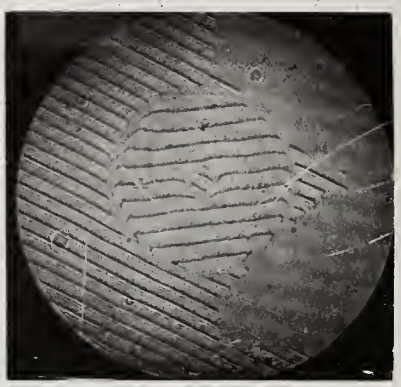

Side A after polish

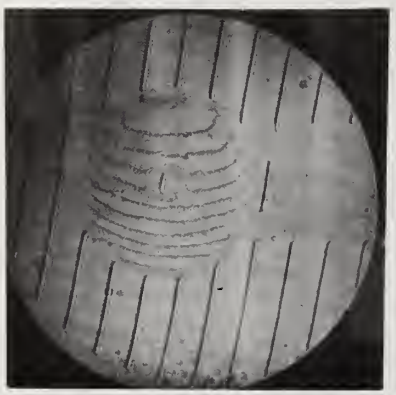

Side B after Ni coating

Side B after polishing

Figure 3. Interferograms during processing of a sample.

Table 3. Plating bond strengths.

PLATING BOND STRENGTHS

SAMPLE NO. LOC.	SINGLE ZINCATE Cu STRIKE Cu	DOUBLE ZINCATE Ni STRIKE Cu	DOUBLE ZINCATE Cu STRIKE Cu STABILIZED AT 100°	DOUBLE ZINCATE Cu STRIKE Cu STABILIZED AT 325°C
1 *RF	29,400 psi	4,400 psi	21,700 psi	25,900 psi
2 *RF	25,700	1,600	15,300	27,600
3 *RF	17,600	2,000	15,500	
4 *RF	16,600	1,700		
5 *RF	15,200	1,300		
6 *RF	15,100			
7 *RF	11,900			
8 *RF	11,300			
9 *RF	22,500			

	DOUBLE ZINCATE Cu STRIKE Cu	DOUBLE ZINCATE Ni STRIKE Cu (Ni 22)	DOUBLE ZINCATE Cu STRIKE Cu	DOUBLE ZINCATE Cu STRIKE HCl DIP Cu
1 LLL		2,389 psi	18,875 psi	11,011 psi
2 LLL		1,502	27,624	12,991
3 LLL		1,805	33,518	11,161
4 LLL		2,004 (Ni 22 + NiCl)	28,557	10,654
5 LLL		1,863		
6 LLL		6,054		
7 LLL		4,040		
8 LLL		10,595 (415 Ni)		
9 LLL		8,564		
10 LLL		4,390		
11 LLL		6,839		
12 LLL		3,341		

*ROCKY FLATS PLANT OF NORTH AMERICAN ROCKWELL

4. Dielectric Overcoating

A number of different dielectric coatings were deposited on the successful substrate system candidate. Additional coating runs were made at a number of temperatures since potential stress introduction was suspected at the elevated temperatures. Since the samples consisted of many coatings of dielectrics, metals and beryllium, there was good reason to expect the coefficients of thermal expansion to vary such as to induce stress hence change the final figure. Interferograms were taken after coating to determine whether stress induced figure changes had occurred. Table 4 shows the relationahip of the number of coatings on each sample, type of coating, application temperature, induced wavefront distortion, reflectivity, surface quality, and damage threshold.

Table 4. Dielectric coating parameters.

SAMPLES	REFLECTIVITY (%) AT 1.06 μm	SURFACE QUALITY (SCRATCH/DIG)	LAYERS	COATING	COATING APPLICATION TEMP (°C)	WAVEFRONT DISTORTION λ AT 1.06 μm	DAMAGE THRESH LD (J/cm² FOR) 125 ps
1	99.9		9	$Th(IO_3)_4$*	350	0.10	7.0 ± 1.5
2	99.8		9	$Th(IO_3)_4$*	300	0.05	6.5 ± 1.5
3	>99.0		20	$ZrO_2 + SiO_2$	275 ± 25	0.75	4.1 ± 0.5
4	>99.0		20	$ZrO_2 + SiO_2$	275 ± 25	0.05	3.6 ± 0.5
5	>99.0		12	$TiO_2 + SiO_2$**	275 ± 25	0	6.5 ± 1.5
6	>99.0		12	$TiO_2 + SiO_2$	275 ± 25	0	5.0 ± 1.0
7	>99.0		12	$TiO_2 + SiO_2$	175 ± 25	0	1.4 ± 0.4
8	99.6	80-50		$ZrO_2 + SiO_2$**	300	0	3.6 ± 0.5
9	99.7	80-50		$ZrO_2 + SiO_2$**	300	0.05	3.1 ± 0.5
10	99.9	80-50		$TiO_2 + SiO_2$**	300	0	3.3 ± 0.5
11	99.7	80-50		$ZrO_2 + SiO_2$**	200	0	2.3 ± 0.5
12	99.6	80-50		$TiO_2 + SiO_2$**	200	0	1.75 ± 0.5

* AUGER ANALYSIS OF TOP COATING
** AUGER ANALYSIS OF TOP TWO COATINGS

5. Dielectric Coating Damage Testing

Damage thresholds were measured using linearly polarized 1064 nm pulses 125 ± 25 ps in duration at nearly normal incidence. Peak energy density for each pulse was determined by reconstructing the spatial profile of the beam from a photograph, and normalizing the profile to agree with the energy contained in the pulse. A typical beam profile is shown in figure 4, with the associated isointensity contour plot. The circle scribed on the contour plot indicates the portion of the profile used in the normalization. On-axis integrated energy density can be determined to within ± 5-7%.

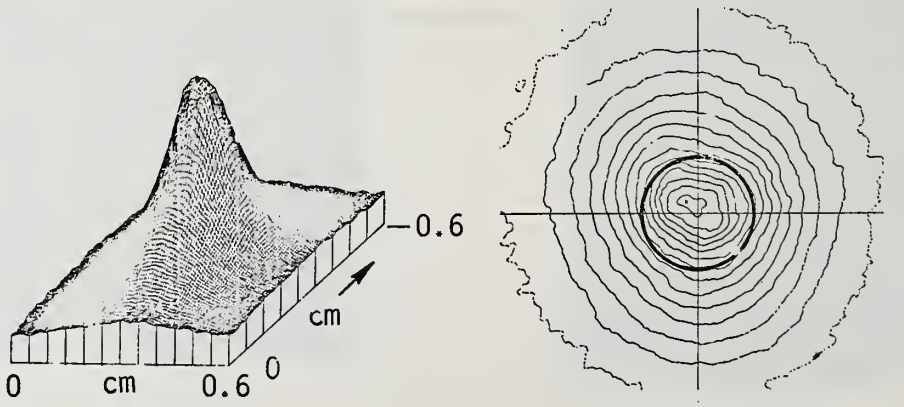

Figure 4. Laser pulse utilized in damage testing.

6. Summary

From the data collected in table 4, it becomes apparent that the higher coating temperature induces distortion into the coated substrate. The coating with neglible distortion and next to highest damage threshold was found in sampe #5. This sample was a 12 layer stack alternating TiO_2 and SiO_2 at 275°C temperatures resulting in no induced distortion and a damage threshold of 6.5 J/cm^2.

7. Conclusion

The beryllium substrate system with all of its complicated processing did prove to be about 50% less expensive than the comparable Cervit or BK-7 substrate system after coating.

The multi-metallic coatings applied to the substrate did provide bond strengths nearly equivalent to the beryllium substrate strength itself.

The dielectric overcoating developed for this substrate does provide a distortion free coating with as high a laser damage threshold as any glass substrate coated system.

8. Acknowledgments

The authors wish to acknowledge the extensive support of J. L. Emmett and H. G. Ahlstrom. The multi-metallic coating work was done by W. Kelly and E. Childs. The dielectric coatings were developed in conjunction with Coherent Radiation, OCLI and Spectra Physics.

9. References

[1] S. S. Glaros and A. J. Glass, "Compound Ellipsoidal Focusing System for Fusion Lasers", Sixth Symposium on Engineering Problems of Fusion Research, San Diego, Nov. 1975.

[2] R. R. Altenhof, "The Design and Manufacturing of Large Beryllium Optics", SPIE 19th Technical Symposium, San Diego, Aug. 1975.

[3] T. T. Saito and J. R. Kurdock, "Diamond Turning and Polishing of Infrared Optical Components", LLL document UCRL-77392, Oct. 1975.

[4] M. D. Guadagnoli and T. T. Saito, "Beryllium and its Optical Properties", App. Opt. 75.

[5] P. C. Baker, J. B. Sonderman and T. T. "Finishing of Precision Generated Metal Optical Components", SPIE 19th Technical Symposium, San Diego, Aug. 75.

COMMENTS ON PAPER BY GLAROS, BAKER, AND MILAM

No discussion on this paper.

5.1 Spot Size and Pulse Duration Dependence of Laser-Induced Damage

J. R. Bettis*, R. A. House II, and A. H. Guenther
Air Force Weapons Laboratory
Kirtland AFB, NM 87117

The threshold electric field for laser-induced damage in transparent dielectrics is shown to follow an inverse relation with the fourth root of the pulse duration. Preliminary analytical studies suggest the process involves the free-free plasma heating rate. The relationship is demonstrated for pulse durations ranging from a few picoseconds to several tens of nanoseconds. Furthermore, from considerations of total energy deposition, it is proposed that the threshold electric field follows an inverse relation with the square root of the damaging spot size. The results are compared to measured values with acceptable agreement.

Key words: Frequency dependence; laser damage; spot size dependence; time dependence.

1. Introduction

It has been proposed that there are three main processes involved in the pulsed laser-induced damage of optical components. Although we primarily consider in this paper pulsed laser effects, thermal cw-like damage is not completely ruled out. The three principal steps as given by Milam [1][1] are: (1) creation of an initial low-density free electron concentration, (2) buildup of this electron concentration until a density of 10^{18} to 10^{19} cm^{-3} is reached, (3) absorption of the remainder of the laser pulse by the resulting plasma. The details of the first two processes as presented by the authors in the 1975 Damage Symposium [2] give the material-to-material variation of the threshold for laser-induced damage. In the present paper we will show that the details of step (3) explain the spot size and pulse duration dependence of the threshold for observed laser-induced damage. This paper proposes an explanation of the pulse duration dependence which is an alternative to that explanation presented by proponents of the purely electron avalanche model of laser-induced damage [3].

It is essentially universally agreed that laser-induced damage will not occur unless a critical number density of free electrons are created. In gaseous dielectric breakdown the accepted mechanism for reaching a number density of 10^{18} to 10^{19} cm^{-3} is cascade or avalanche ionization. This is a process whereby a free electron is accelerated by the applied field until it reaches ionizing energy and collisionally ionizes a neutral or ion. The process repeats until a critical number density of free electrons is reached. Such a process is possible although unlikely [4] for laser frequency electric fields if the free electrons undergo collisions which momentarily align the momentum of the electron with the oscillating field. Under these avalanche conditions the growth of ionization would follow

$$N_{cr} = N_o \exp [\alpha(E)t] \qquad (1)$$

where N_o and N_{cr} are the initial and critical free electron densities respectively, α (E) is the field dependent ionization coefficient of the material and t is the time. Thus for decreasing pulse duration, α (E) must increase in order to maintain the required critical electron density. Since α(E) is proportional to the electric field, one would expect an increase in the threshold optical electric field for decreasing pulse duration. Yablonovitch and Bloembergen [3] have used d c breakdown of dielectrics to obtain appropriate ionization rates which predict about an order of magnitude increase in threshold field for a 10 ps pulse compared to a 10 ns pulse. Because the observed increase [5] is only about half this prediction we sought an alternate explanation of the observed phenomena.

2. The Model

We propose an explanation of the observed pulse duration dependence on the basis of the absorption of the laser pulse by the resulting electronic plasma. The absorption of the laser pulse and the subsequent heating of the plasma melts, spalls, crazes and otherwise photo-degrades the surface of the surrounding dielectric. Although the model proposed herein was developed for surface damage we will subsequently attempt to show that both surface and bulk damage are adequately described by the suggested model. A crucial point to note is that it is the heating of the plasma which ultimately leads to permanent or catastrophic damage. The assumption is made that the total heating of the plasma must remain constant for a given material to damage as the pulse duration and spot size are varied.

---

*Based on portions of a Ph.D. Dissertation submitted to the Air Force Institute of Technology, Wright-Patterson AFB, Ohio.

1. Figures in brackets indicate the literature references at the end of this paper.

Laser-Plasma Heating. In a plasma (kT > 1eV) the absorption of the laser beam by the plasma is dominated by the "free-free" or inverse Bremsstrahlung process [6]. Consider a plasma of thickness dx with laser power density, S_o, incident. To a first approximation, by Beer's law, the power density at the exit of the plasma is

$$S = S_o \exp(-Kdx) \tag{2}$$

where K is the absorption coefficient. The absorbed energy is

$$d\mathcal{E} = \Delta S \, A dt = [S_o - S_o \exp(-Kdx)] A dt \tag{3}$$

with A the area of the laser beam and dt a differential element of time. Expanding the exponential for small Kdx values yields for the heating rate,

$$\frac{dQ}{dt} = \frac{d\mathcal{E}}{dt} = S_o [1-(1-Kdx+ \ldots)] . \tag{4}$$

Neglecting higher order terms gives

$$\frac{dQ}{dt} \approx A S_o Kdx . \tag{5}$$

A given material will damage when the total heat input is sufficient to cause localized melting. Thus, the total heating is a constant, or

$$t_p \frac{dQ}{dt} = t_p A S_o Kdx = \text{constant} . \tag{6}$$

The absorption coefficient for inverse Bremsstrahlung as given by Johnston et al. [6] is

$$K = \frac{3.08 \times 10^{-7} Z N_e^2 \ln \Lambda(\omega)}{\omega^2 (kT_e)^{3/2}} \frac{1}{(1 - \omega_p^2/\omega^2)^{1/2}} \tag{7}$$

where kT_e is in eV, $\Lambda(\omega) = V_T/(\omega_p P_{min})$. Here Zq_e is the ionic charge, T_e is the electron temperature, V_T is the thermal velocity of the electrons, N_e is the electron number density (we have assumed singly ionized species such that $N_i N_e = N_e^2$), and P_{min} is the minimum impact parameter for electron-ion collisions [P_{min} = maximum of Zq_e^2/kT or $(\hbar/mkT)^{1/2}$], and ω_p is the plasma frequency.

David et al. [7] has shown that both N_e and T_e obeyed a power law dependence with laser flux. Fauquignon and Floux [8] calculated and experimentally verified that $T_e \sim S^{2/3}$, while Boland et al. [9] showed that a laser-induced plasma expanding from the surface of a dielectric obeyed an adiabatic expansion law. They experimentally verified that

$$T_e = \text{const } N_e^{2/3} . \tag{8}$$

Then

$$\frac{N_e^2}{T_e^{3/2}} \sim S . \tag{9}$$

Thus for a given material at a fixed laser frequency and constant spot size equations (6) and (9) can be used to write

$$t_p S^2 = \text{const (recall } S \sim E_{th}^2) \tag{10}$$

or

$$E_{th} = \text{const}/t_p^{1/4} . \tag{11}$$

Likewise, for a given material at a fixed laser frequency and constant pulse duration one obtains

$$A S^2 = \text{const} \tag{12}$$

or

$$E_{th} = \text{const}/\sqrt{d} \qquad (13)$$

where d is the spot diameter.

Equations (11) and (13) indicate inverse relations between the threshold field and both the square root of the beam diameter and the fourth root of the pulse duration. These dependencies will be compared to several existing observations.

Both equations (11) and (13) are expected to exhibit ranges of applicability. For pulse durations less than tunneling times ($\sim 10^{-14}$ s) equation (11) will probably be invalid. This cannot now be checked since the shortest pulse duration data available are for pulses of the order 10^{-12} s. For pulse durations greater than typical electron recombination times (a few microseconds) the added loss mechanism of recombination will begin to affect the inverse pulse duration dependence. An additional loss mechanism will be thermal diffusion. The time needed for heat to diffuse out of a spot with diameter d is

$$t_D = d^2/4D \,. \qquad (14)$$

Where D is the material diffusion coefficient which has values between 1 and .10 cm^2/s. For pulse durations much less than the thermal diffusion time one can neglect this loss which puts an applicability constraint on pulse duration and spot diameter d of

$$t_p/d^2 < 1/4D \qquad (15)$$

For a 150μm diameter spot equation (15) implies that the pulse duration dependence should hold for pulses shorter than about 5.6 to 56μs depending on the value of D.

For large diameter spots or for long pulse durations, the relative field calculated from equations (11) and (13) will become too small to create a critical number density. Coupling this with appropriate loss mechanisms implies a leveling off of the dependencies given by (11) and (13).

3. Comparison with Experiments

As an indication of the validity of equations (11) and (13) we present data collated from various laser damage investigations. Figures 1 and 2 are results collected by DeShazer et al., [10]. In figure 1 the intensity necessary to damage the surface of TiO_2 crystals is plotted versus reciprocal spot diameter. In figure 2 the relative threshold intensity for λ/4 ZnS films is plotted against reciprocal spot diameter. The limited amount of data precludes one from choosing between the model expounded here and the explanation given by DeShazer [10] based on a statistical concentration of surface defects. Figure 3 presents the results of Wang et al., [11] in which seven different dielectric reflectors were damaged as a function of spot size. The fit to the predicted 1/d dependence is again no worse than the defect model relationship presented by Wang [11]. It should be noted here that Newnam [12] has recently presented results which showed no spot size dependence for picosecond pulsed laser-induced damage of thin films.

In 1970, Nesterov et al., [13] showed that for the surface of sapphire the spot size dependence followed $E_{th} \sim 1/d^{0.67}$. With this correction the pulse length dependence can be separated. In figure 4 we plot threshold field versus pulse duration for the data collected by Nesterov et al. For pulses from 15 ns to 1.8 μs the relationship is $E_{th} \sim t^{-0.251}$. We next consider the alkali halide work of Fradin [5] and Smith [14]. Using the same laser system and focussing arrangements they damaged several alkali halides while varying the pulse duration from 10.3 ns down to 15 ps. For NaCl, five pulse durations; 10.3 ns, 4.7 ns, 300 ps, 30 ps, and 15 ps were used. This data is presented in figure 5 where a variation of $E_{th} \sim t^{-0.257}$ is obtained with an experimental fit of ± 8.5%. Four other alkali halides were damaged at 4.7 ns [5] and 30 ps [14] with similar results.

In figure 6 we compare the results presented in figure 5 with those obtained by Penzkofer [15], Bass [16], and Allen [17]. The spot size dependence given by equation (13) has been accounted for in this graph. For pulse durations varying from 6 ps to 311 ns the relation is again remarkably secure. The 311 ns duration data point was determined from the pulse shape as recorded by Allen et al., by neglecting a long tail which has a much lower peak intensity than the initial portion of the pulse. As can be seen from the figure, laboratory-to-laboratory variation in techniques and reporting procedures may still make direct comparisons tenuous.

Finally in table I we present the data of figure 6 in tabular form along with selected other results. From equations (11) and (13) the expression $\sqrt{d}\, t^{1/4} E_{th}$ should be constant for a given material. The first three NaCl results obey this relationship quite well. Notice that the NaCl results of Smith and Fradin are quite close although a factor of three lower in value than the other

NaCl results. The ZnSe films tested by Wang et al.,[18] and Bettis et al., [2] are also amenable to this treatment. Finally the KCl results of Smith and Fradin agree with $\sqrt{d}\ t^{1/4}\ E_{th}$ = constant, whereas the results of Bass and Allen do not agree. The suggestion has been made that this negative result is due to material variations in the KCl.

Table 1. Spot Size and Pulse Duration Variation of Thresholds

Source	Material	Pulse Length	Spot Diameter	E_{th} (MV/cm)	$\sqrt{d}\ t^{1/4}\ E_{th}$	λ
Penzkofer [15]	NaCl	6 ps	60 μm	28.7	0.344	1.06
Bass [16]	NaCl	92 ns	107	1.83	0.33	10.6
Allen [17]	NaCl	311 ns	73	1.63	0.33	10.6
Fradin [5]	NaCl	15 ps	18	12.4	0.103	1.06
Smith [14]	NaCl	30 ps	18	7.34	0.073	1.06
Fradin [5]	NaCl	300 ps	18	4.7	0.083	1.06
Fradin [5]	NaCl	4.7 ns	18	2.3	0.08	1.06
Fradin [5]	NaCl	10.3 ns	18	2.1	0.09	1.06
Wang [18]	λ/4 ZnSe	311 ns	73	0.122	4.38×10^{-2}	10.6
Bettis [2]	λ/2 ZnSe	40 ns	147	0.14	4.27×10^{-2}	1.06
Smith [14]	KCl	30 ps	18	5.86	0.058	1.06
Fradin [5]	KCl	4.7 ns	18	1.31	0.046	1.06
Bass [16]	KCl	92 ns	107	0.9	0.162	10.6
Allen [17]	KCl	311 ns	73	2.05	0.413	10.6

5. Conclusions

A wide variety of data correlates well with the expression $\sqrt{d}\ t^{1/4}\ E_{th}$ = constant. Further comparisons are difficult due to the lack of complete data. Extension of these results as well as the refractive index and surface roughness results to CW operation is an intriguing possibility. The characterization of these variables may make a search for a frequency dependence a reliable venture.

6. Acknowledgments

The authors would like to express their sincere appreciation to Dr. Alex Glass of Lawrence Livermore Laboratory for critical and constructive discussions.

7. References

[1] Milam, David, elsewhere in these proceedings.

[2] Bettis, J. R., R. A. House, A. H. Guenther, and R. Austin, "The Importance of Refractive Index, Number Density, and Surface Roughness in the Laser-Induced Damage of Thin Films and Bare Surfaces," Laser Induced Damage in Optical Materials: 1975 (A. J. Glass and A. H. Guenther, Editors), NBS Spec. Pub. 435, p. 289 (1975).

[3] Fradin, D. W., N. Bloembergen, and J. P. Letellier, "Dependence of Laser-Induced Breakdown Field Strength on Pulse Duration," Appl. Phys. Lett. 22, pp. 635-7 (1973).

[4] Sparks, M., "Current Status of Electron-Avalanche-Breakdown Theories," Laser Induced Damage in Optical Materials: 1975 (A. J. Glass and A. H. Guenther, Editors), NBS Spec. Pub. 435, p. 331 (1975).

[5] Fradin, D. W., Laser Induced Damage in Solids, Harvard University, Cambridge, Mass. (1973).

[6] Johnston, Tudor Wyatt, and John M. Dawson, The Physics of Fluids, Vol. 16, No. 5, p. 722 (May 1973).

[7] David, C., P. V. Avizonis, H. Weichel, C. Bruce, and K. D. Pyatt, "Density and Temperature of a Laser Induced Plasma," IEEE J. of Quant. Elect., QE-2, no. 9 (Sep. 1966).

[8] Fauquignon, C. and F. Floux, "Hydrodynamic Behavior of Solid Deuterium Under Laser Heating," The Physics of Fluids, vol. 13, no. 2, p. 386 (Feb. 1970).

[9] Boland, B. C., F. E. Irons, and R. W. P. McWhirter, A Spectroscopic Study of the Plasma Generated by a Laser From Polyethylene, U. K. Atomic Energy Authority, Abingdon Berkshire (1968).

[10] DeShazer, L. G., B. E. Newnam, and K. E. Leung, "The Role of Coating Defects in Laser-Induced Damage to Thin Films," Laser Induced Damage in Optical Materials: 1973 (A. J. Glass and A. H. Guenther, Editors), NBS Spec. Pub. 387, p. 114 (1973).

[11] Wang, V., C. R. Giuliano, and B. Garcia, "Single and Multilongitudinal Mode Damage in Multilayer Reflectors at 10.6 μm as a Function of Spot Size and Pulse Duration," Laser Induced Damage in Optical Materials: 1975 (A. J. Glass and A. H. Guenther, Editors), NBS Spec. Pub. 435, p. 216 (1975).

[12] Newnam, B. E., Elsewhere in these proceedings.

[13] Nesterov, L. A., A. A. Poplavskii, I. A. Fersman, and L. D. Khazov, "Variation of Destruction Threshold of a Transparent Dielectric with Laser Pulse Length," Soviet Phys.-Tech. Phys., Vol 15, No. 3, p. 505 (Sep. 1973).

[14] Smith, W. L., J. H. Bechtel, and N. Bloembergen, "Picosecond Breakdown Studies: Threshold and Nonlinear Refractive Index Measurements and Damage Morphology," Laser Induced Damage in Optical Materials: 1975 (A. J. Glass and A. H. Guenther, Editors), NBS Spec. Pub. 435, p. 321 (1975).

[15] Penzkofer, A., Optics Comm, Vol. 11, p. 265 (1975).

[16] Bass, M., and K, M. Leung, "The Dependence of the Pulsed 10.6 μm Laser Damage Threshold on the Manner in Which a Sample is Irradiated," IEEE J. of Quant. Elect., p. 82 (Feb 1976).

[17] Allen, S. D., M. Braunstein, C. Giuliano, and V. Wang, "Pulsed CO_2 Laser Damage Studies of RAP Grown KCl," Laser Induced Damage in Optical Materials: 1974 (A. J. Glass and A. H. Guenther, Editors), NBS Spec. Pub. 414, p. 66 (1974).

[18] Wang, V., J. E. Rudisill, C. R. Giuliano, M. Braunstein, and A. Braunstein, "Pulsed CO_2 Laser Damage in Windows, Reflectors, and Coatings," Laser Induced Damage in Optical Materials: 1974 (A. J. Glass and A. H. Guenther, Editors), NBS Spec. Pub. 414, p. 59 (1974).

8. Figures

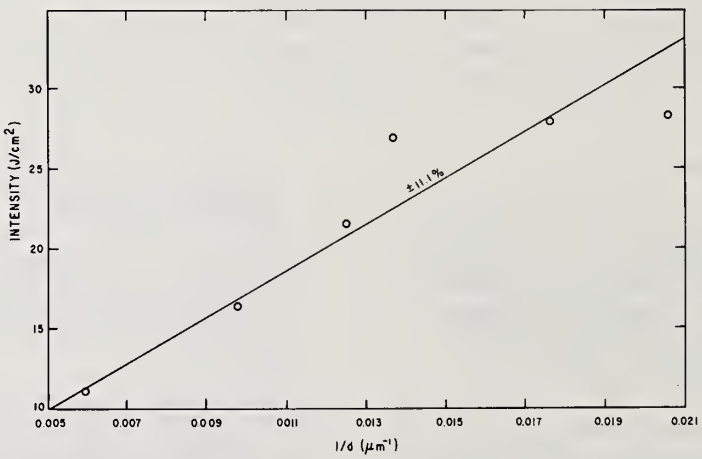

Figure 1. Threshold damage intensity versus reciprocal spot size for bare TiO_2.

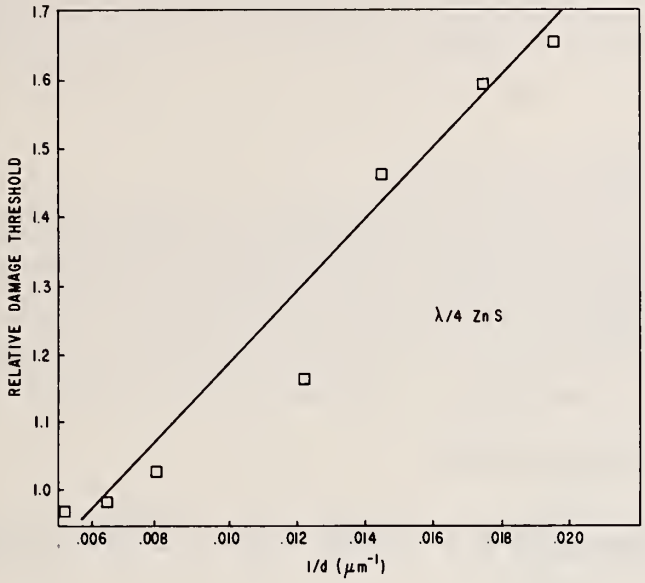

Figure 2. Threshold damage intensity versus reciprocal spot size for quarter-wave ZnS.

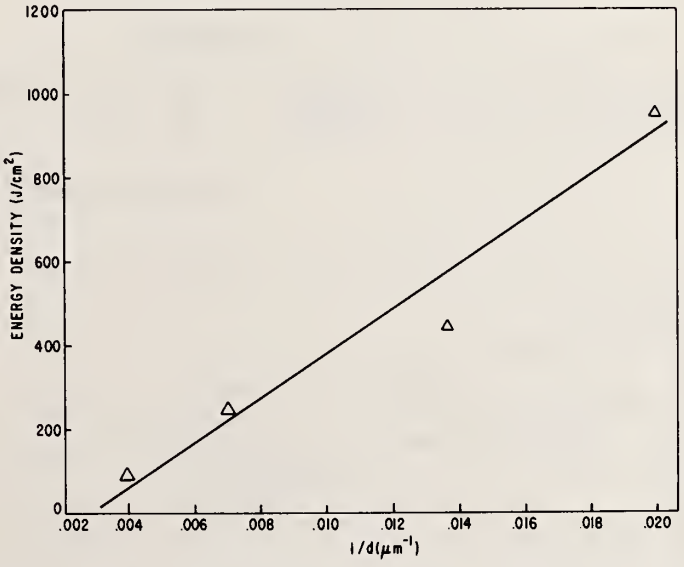

Figure 3. Threshold energy density versus reciprocal spot size for seven dielectric reflectors.

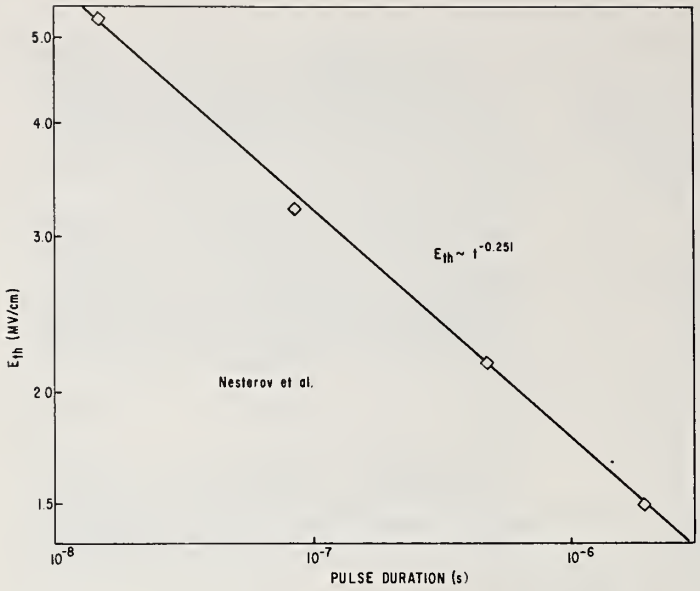

Figure 4. Threshold field versus pulse duration for the surface of polished sapphire.

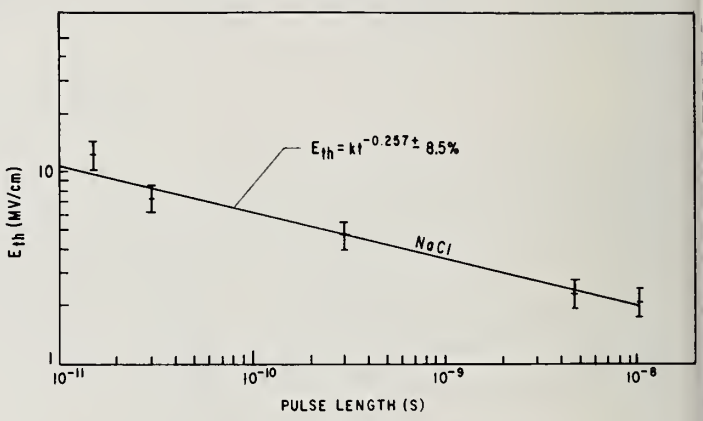

Figure 5. Threshold field versus pulse duration for NaCl.

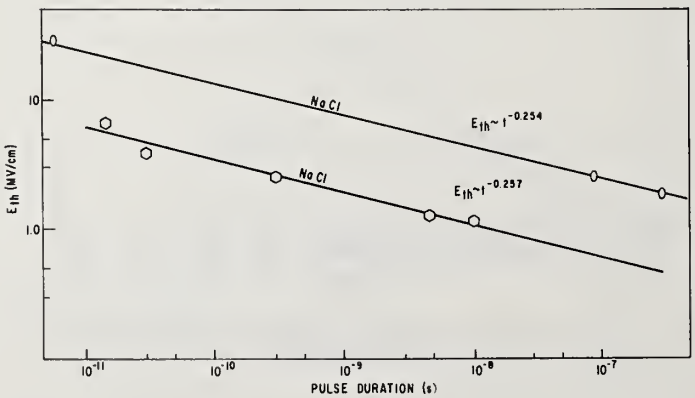

Figure 6. Threshold field versus pulse duration for NaCl.

COMMENTS ON PAPER BY BETTIS, HOUSE, AND GUENTHER

It is difficult to correlate results obtained by different experimenters on different samples for different pulse lengths or spot sizes, since the materials may exhibit radically different damage thresholds and may even be damaging due to different causes from one sample to another. It was pointed out that heat diffusion, which was not explicitly treated in this analysis, may be important at longer pulse durations.

NOTE ADDED IN PROOF

Since the preparation of this manuscript covering material presented at the Symposium, it has come to our attention through a more complete re-searching of the published literature that several other individuals have also investigated pulse length and spot size scaling of laser induced damage thresholds. The reported observations being accomplished primarily in the Soviet Union. It is indeed gratifying to note that there is excellent agreement with the proposed scaling relationships presented in our paper proper. Unfortunately, no detailed theoretical derivations of the scaling relationships was proposed in the earlier Soviet reports.

Verification of temporal scaling for damage thresholds in W/cm^2 (Q_{t_i}) as follows,

$$Q_{t_2} = Q_{t_1} (t_1/t_2)^{1/2} \tag{A}$$

for pulses t_1 between 9×10^{-11} s and 10^{-2}s is reported for the surfaces of several optical glasses [a]*. In addition, scaling of damage thresholds in W/cm^2 has been reported to follow a

$$Q \sim \frac{1}{d} \tag{B}$$

relationships for diameters (d) between 9 μm and 140 μm in bulk breakdown experiments [b] as well as between 190 μm and 10,000 μm at the surfaces of dielectrics.

If these relationships hold up under the test of time and repeated investigations, they will form a useful mechanism in which to correlate various reported damage measurements. They, together with already proposed scaling expressions for refractive index and surface roughness, afford the laser designer a powerful tool for selecting candidate optical materials. What is still lacking, however, is an appropriate scaling relation for the frequency dependence of laser induced damage. A simple frequency dependent relationship may be difficult to achieve due to non-linear behavior at high photon-fluxes, as well as the presence of resonances and other frequency specific properties of individual materials.

References

[a] Buzhinskii, I. M. and Pozdnyakov, A. E., Sov. J. Quant. Electron., 5, No. 7, (1975) 835-836.

[b] Nesterov, L. A., Poplavskii, A. A., Fersman, I. A., and Khazov, L. D., Sov. Phys. Tech. Phys., 15, No. 3, (1970) 505-507.

[c] Buzhinskii, I. M., Pozdnyakov, A. Ye., and Ushakov, S. A., Sov. J. Opt. Tech., 40, (1973) 335-336.

*Letters in brackets indicate the literature references at the end of this paper.

5.2

RE-EXAMINATION OF LASER INDUCED BREAKDOWN IN THE ALKALI HALIDES AT 10.6 μm *

C.C. Tang, K.M. Leung, and M. Bass
Center for Laser Studies, University of Southern California
Los Angeles, California 90007

Since the 10.6 μm bulk laser damage thresholds of alkali halides have been shown to depend on the experimental procedures used, we have remeasured the damage flux for these materials. Multiple shot per site thresholds were found to be higher than single shot per site thresholds for samples containing a large density of defects. By irradiating with two different spot sizes and observing an increase in damage threshold with decreasing spot size, a correlation between damage thresholds and the distribution of defects was determined. The single shot per site bulk breakdown electric field for NaCl using a 59 μm spot diameter was 1.8 MV/cm. Measurements made on conventional and RAP grown samples showed that both types of material preparation techniques are not yet able to produce samples with reproducible damage thresholds. Some, but not all, RAP grown samples are harder to damage than conventionally prepared materials.

Key words: Alkali halide crystals; laser induced damage; RAP grown materials.

1. Introduction

The laser induced bulk damage thresholds of IR materials have been shown to depend upon the manner in which the samples are irradiated [1][1]. In reference [1], it is reported that sites in a sample which have been pretreated by low laser intensities will have higher damage thresholds than unconditioned sites. Other investigators [2] have also observed this effect. Since the damage thresholds of alkali halides have been used to identify avalanche breakdown as the intrinsic damage mechanism [3], the results of references [1] and [2] indicate the need for remeasuring the damage properties of these materials. This requires re-examining the procedure of irradiation used by various researchers in measuring breakdown thresholds. In this paper, we will discuss the variations in damage thresholds between different samples of the same material. We present data which show that the dependence of the damage threshold on the method of irradiation is related to the presence of defects and inclusions in the medium. To determine the exact role of defects in laser induced breakdown of materials, a study was also made of 1) the relationship between the damage threshold and the size of the irradiated focal volume, and 2) the damage thresholds of recent conventional and RAP grown samples as compared to previous samples of the same materials.

2. Experimental

The experimental set up used has been described in detail earlier [4]. High speed photon drag detectors were used for comparing the incident laser pulse waveform with that transmitted through the sample. The occurrence of damage was visually determined during the experiment by the occurrence of a spark or by the appearance of residual damage following irradiation. An optical microscope was used later to examine the morphology of each irradiated site. Physical damage was accompanied by an attenuation of the transmitted pulse. The damage threshold was defined as the incident flux at which 50% of the irradiated sites damaged and its value was determined from the average of the results for 10 sites.

The important parameters of the TEA CO_2 laser system are summarized in table 1. The laser was operated in the fundamental TEM_{00} transverse mode in order to provide a well characterized beam spatial profile. This was focused into the bulk of the samples with lenses resulting in focal spot diameters of 59 μm or 89 μm. In our experiments, the diameter is defined as the diameter at which the intensity falls to $1/e^2$ of its peak value. Consistent with the notation used in the literature,

---

* Research sponsored by Defense Advanced Research Projects Agency, Contract No. F19628-76-C-0162, monitored by Air Force Cambridge Research Labs.

1. Figures in brackets indicate the literature references at the end of this paper.

Table 1. Summary of experimental parameters

Laser	CO_2 TEA
Wavelength	10.6 μm
Waveform	92 ns gain switched pulse with self mode locked spikes $\lesssim$ 2.5 ns duration and 8 ns interpulse spacing
Transverse mode	TEM_{00}
Attenuation	ZnSe beam splitter and two Brewster angle stacked plate polarizers
Focusing lens	Ge, 2.54 cm and 3.8 cm focal lengths, abberation free
Focal spot diameter	59 μm and 89 μm at $1/e^2$ in intensity
Detection system	Photon drag detectors and Tektronix 7844 oscilloscope. Risetime = 2.5 ns

this definition corresponds to the diameter at which the electric field falls into 1/e of its peak value. Since damage only occurs in the first half of the gain-switched CO_2 laser pulse as evidenced by observation of the transmitted waveform [4], the long tail of the pulse, containing 50% of the total energy, does not contribute to the breakdown mechanism of the material. The average energy flux $\tilde{\mathcal{E}}$ (J/cm^2) is given by

$$\tilde{\mathcal{E}} = \frac{\frac{1}{2}\mathcal{E}}{\pi w_0^2}$$

where $\mathcal{E}$ is the total energy contained in the entire pulse. The average power density P(W/cm^2) and the peak on-axis power density P_0(W/cm^2) are then related by

$$P_0 = 2P = 2\,\tilde{\mathcal{E}}/\tau$$

where τ is the full width at half maximum of the gain-switched part of the TEA laser pulse.

3. Comparison of N on 1 and 1 on 1 Damage Thresholds

An N on 1 measurement of the laser damage threshold has been defined as one in which a site is initially irradiated at a low intensity and the flux is increased by a small amount (5% in these experiments) on successive pulses until damage occurs [1]. This was the procedure used by Allen et al. [2] in reporting damage thresholds for RAP grown alkali halides. A more conventional threshold measurement is obtained in a 1 on 1 experiment where each site is irradiated only once and the intensity which produces damage 50% of the time is sought [1,3,4].

Our data for the N on 1 and 1 on 1 thresholds of several materials is summarized in table 2.

Table 2. Comparison of N on 1 and 1 on 1 laser damage thresholds

Material	10.6 μm Damage Threshold in GW/cm^2		Spot Size $2W_0 = 89\,\mu m$
	1 on 1	N on 1	$R = \frac{I_{Threshold}\ (N\ on\ 1)}{I_{Threshold}\ (1\ on\ 1)}$
NaCl (conventional)	9.83	9.89	1.00
NaCl (RAP)	<.38	<.38	- -
KCl (conventional)	.87	1.13	1.3
KCl (RAP)	<.38	<.38	- -
KBr (conventional)	<.38	<.38	- -
KBr (RAP)	7.23	15.35	2.12
NaF (conventional)	16.49	17.07	1.04
KI (conventional)	1.07	1.97	1.84

We note that the differences are not due to the difference in the definitions of the N on 1 and 1 on 1

thresholds because by increasing the incident flux by only 10% in a 1 on 1 experiment, we could produce damage on all sites. Thus, a difference greater than 10% is indicative of a conditioning effect due to the low intensity pulses in an N on 1 test.

Table 2 shows that the N on 1 experiment gives noticeably greater thresholds in the RAP processed KBr and the conventionally grown KI. The difference is less in KCl and in NaCl and NaF the two thresholds are the same. A few of the samples had very low thresholds due to high concentrations of inclusions and so in table 2 their damage fluxes are given as upper bounds. The presence of inclusions or defects in certain samples was detected by the observation that the positions of the damage sites varied randomly along the incident beam direction. In particular, this was seen in the RAP processed NaCl and KCl samples used in the present study. We note that as a result these samples had lower damage thresholds than conventionally prepared samples of NaCl and KCl. The reverse is true for the samples of KBr studied in this work.

4. Comparison of Materials

Upon comparing the thresholds of these materials with other samples investigated by Bass and Leung [1], a marked increase in damage thresholds for the conventionally grown NaCl and KCl samples was noted. The thresholds which they obtained for conventional NaCl and KCl were 6.10 GW/cm^2 and .65 GW/cm^2, respectively, as compared to 9.83 GW/cm^2 and 0.87 GW/cm^2 obtained herein. The previous RAP grown KCl had a threshold of 4.60 GW/cm^2 which is significantly higher than that of the sample studied in this work. This indicates that RAP grown materials are not necessarily always better than conventional materials. Clearly, they could be more damage resistant than conventional materials if they are inclusion and defect free.

A comparison of the breakdown electric fields of the recent samples with those obtained by Yablonovitch [3] at 10.6 μm is shown in table 3. The electric fields are normalized to that of NaCl.

Table 3. Relative breakdown fields at 10.6 μm - normalized to E_{NaCl}

Material	Current Results	Previously Published Results
NaCl	1	1
KCl	.573	.713
KBr	.309	.482
NaF	1.33	1.64 (@1.06 μm) [5]
KI	.440	.27

In the present work and for our particular sample of NaCl, the breakdown electric field was found to be (1.8 ± 0.18) MV/cm. Our experimental conditions were nearly identical to those of Yablonovitch who obtained (1.95 ± .2) MV/cm for the breakdown field of NaCl at 10.6 μm [3]. We can see that the two results agree within the experimental uncertainty of the measurements. Table 3 shows that there is general agreement in the breakdown field ratios for KCl and NaF. For the other samples, however, the ratios differ widely. Since the agreement of the results for NaCl indicates adequate experimental accuracy, we conclude that the discrepancies in the electric field ratios for the same materials are due to sample variations. This suggests that the damage threshold for any material should be obtained from the average of the value obtained for several samples.

5. Dependence of Damage Thresholds on Spot Size

DeShazer, Newnam, and Leung [6] have previously reported that the damage thresholds of thin optical coatings correlate strongly with the size and distribution of defects. Since the probability of hitting a randomly distributed defect is greater when a large cross-sectional area is irradiated than when a smaller area is irradiated, and since materials containing defects damage more easily than defect free materials, it is to be expected that large diameter beams, on the average, damage materials more easily than small diameter beams. The present work extends the results of [6] to bulk damage in transparent materials.

In order to investigate the role of defects in solids, the power density thresholds for damage to the materials shown in table 4 were determined using two lenses (their focal lengths were 25 and 38.0 mm) yielding focal spot diameters of 59 μm and 89 μm. The thresholds for NaCl, NaF, and RAP KBr did not depend noticeably on the focal spot diameter. For other samples, such as RAP NaCl and RAP KCl, the damage thresholds using the different lenses differed by an order of magnitude. Due to the smallness of the RAP KBr sample, only preliminary data consisting of a single site could be obtained using a 59 μm spot size. The presence of defects in RAP KCl and NaCl was verified by

Table 4. Comparison of damage thresholds for different spot sizes

Material	10.6 μm Damage Threshold in GW/cm^2	
	$2W_0$ = 59 μm	$2W_0$ = 89 μm
NaCl	13.21	9.83
NaCl - RAP	3.30	<.38
KCl	2.92	0.87
KCl - RAP	3.21	<.38
KBr	0.88	<.38
KBr - RAP	7.83*	7.23
NaF	19.02	16.50
KI	1.91	1.07

* preliminary data

morphological studies. The samples showing no dependence on focal spot diameter were either densely filled with small inclusions or relatively inclusion free and damaging due to an intrinsic process.

6. Conclusion

Our results indicate that the damage threshold depends on the manner of irradiation as shown by the N on 1 and 1 on 1 experiments. This effect appears to be caused by the presence of inclusions or defects in the materials. When inclusions or defects are present the damage threshold is dependent upon the particular sample studied and the volume of the site irradiated. A thorough study of a material must necessarily include measurements of several samples. Various focal spot sizes should be used with the intrinsic breakdown limit being approached for very small spot sizes.

7. Acknowledgments

The authors acknowledge the assistance of G.J. Benedict in this work as well as the Hughes Research Lab and the Naval Research Lab for supplying the RAP grown samples. Valuable conversations were held with M.J. Soileau who also arranged for the finishing of the RAP grown NaCl at the Naval Weapons Center.

8. References

[1] Bass, M., and Leung, K.M., IEEE J. of Quantum Electron. QE-12, 82 (1976).

[2] Allen, S.D., Braunstein, M., Giuliano, C., and Wang, V., NBS Special Publication No. 414, 66 (1974).

[3] Yablonovitch, E., Appl. Phys. Lett. 19, 495 (1971).

[4] Leung, K.M., Bass, M., and Balbin-Villaverde, A.G.J., NBS Special Publication No. 435, 107 (1975).

[5] Fradin, D.W., Yablonovitch, E., and Bass, M., Appl. Optics 12, 700 (1973).

[6] DeShazer, L.G., Newnam, B.E., and Leung, K.M., NBS Special Publication No. 387, 114 (1973).

COMMENTS ON PAPER BY TANG, LEUNG, AND BASS

It was pointed out that in order to verify the predictions of the statistical model, it is necessary to be able to detect threshold damage, i.e., damage occurring at a single defect. In actual fact, a distribution of defects, with varying thresholds, will occur. One must fold this distribution and the illumination distribution into the analysis.

The question was raised as to how far below the normal damage threshold one must lower the illumination level in order to achieve a specified life-time of a component. No convenient rule of thumb appears to be available. It was emphasized that questions of this sort are paramount for the system designer and that this kind of information is urgently needed by the optics community.

It was further emphasized that when results of different investigations are reported or compared, the spot size, pulse duration, peak intensity, focusing geometry, and Strehl ratio achieved in the experiment are all required to characterize the peak field.

5.3 CAN A MODEL WHICH DESCRIBES GAS BREAKDOWN ALSO DESCRIBE LASER DAMAGE TO THE BULK AND SURFACES OF SOLID DIELECTRICS

David Milam
Lawrence Livermore Laboratory
Livermore, California 94550

By assuming that laser-induced breakdown in highly transparent solids is a three-step process consisting of preionization, ionization growth, and absorption, it is possible to explain "explosive" threshold damage, typical surface damage morphology, the presence or absence of damage statistics, and the distribution of breakdown times. Special constraints on the preionization stage necessary to explain these phenomena are discussed.

Key words: Absorption; avalanche ionization; damage morphology; damage statistics; distribution of damage times; photo-ionization.

1. Introduction

Laser-induced gas breakdown experiments were recently performed [1][1] as a test of the lucky-electron hypothesis [2]. While these experiments were adequate to demonstrate the problems associated with that hypothesis, the data could not be readily explained by existing gas-breakdown theory. The intent of this paper is to suggest an alternate interpretation for those particular results, and to show that the same interpretation suffices to explain many results obtained in other laser damage experiments.

The proposed damage mechanism is valid only for highly transparent materials, and appears to be most functional as an explanation for results obtained at 1.06 μm and 0.69 μm. It is more difficult, but possible, to apply the mechanism to results obtained at 10.6 μm.

It is emphasized that the identification of highly transparent media can be done experimentally by using square-waveform pulses to induce damage. If a spatially homogeneous absorption is responsible for the damage, a well defined time of damage will be associated with a given intensity. The variation with intensity of the time required to induce damage indicates whether the absorption is linear or nonlinear. Induced effects such as free-carrier absorption can be identified by recording the waveform of the pulse transmitted through the sample. It is necessary in all cases, particularly in studies of dielectric films, to properly account for thermal diffusion [3] and effects due to standing-wave electric fields [4].

2. Review and Interpretation of Recent Gas Breakdown Data

Laser-induced gas breakdown is widely believed [5] to be highly analogus to microwave breakdown, consisting of three steps - preionization, ionization growth, and absorption. The first two steps are most important in determining whether or not breakdown will occur in a given set of circumstances. The second step, ionization growth, is believed to occur by impact ionization, and can only proceed if initial starting charge is supplied. The number of initial electrons will grow exponentially at a rate which depends linearly on the intensity and the ionization potential, and inversely on pressure and pulse duration [6].

Preionization can be externally supplied, or induced by heating particulates or by photo-ionization. Several experiments [7-10] have indicated that thermal mechanisms are the most important sources of seed electrons in 10.6 μm induced breakdown. Sources at 0.69 μm or 1.06 μm are not as well understood, but direct photoionization is the most probable source.

Several primary features of laser-induced gas breakdown are illustrated in figure 1, which gives the threshold for breakdown as a function of pressure. The data of Gill and Dougal [11] have been extended to lower pressures as indicated by the dashed portion of the curve. The low pressure regime has been reported by Krasyuk et. al. [12]. For moderate pressures, the breakdown threshold increases as the pressure decreases. At a lower pressure, which depends on pulse duration, direct photo-ionization becomes dominant over cascade ionization, and the threshold ceases to rise as the pressure is further reduced. This is because the photoionization rate is only weakly dependent on pressure [6]. The ionization rate is, however, highly nonlinear in intensity.

Consider now the application of these concepts to explain the experiments [1] used to test the lucky-electron theory [2]. These experiments consisted of measuring the distribution of breakdown times for Argon volumes irradiated by square-waveform ruby laser pulses. Data at two pressures, 20 psi and 500 psi, are shown in figure 2, where the fraction of volumes $N(t)/N_0$ which have not yet suffered breakdown is recorded as a function of time. At 20 psi, breakdown was deterministic, always occurring

1. Figures in brackets indicate the literature references at the end of this paper.

at the same time for a given input intensity, to within experimental error. At 500 psi, breakdown times were distributed throughout the laser pulse. The transition from deterministic to statistical behavior was readily mapped by studying intermediate pressures [1].

The statistical characteristics observed at the higher pressures could not be readily described by current gas breakdown theory, which assumes the existence of well defined rates for all processes. It was argued [1], however, that this behavior could be predicted if one allowed statistics in the start-up of the avalanche growth. At low pressures, ample photoionization was induced by the large fields necessary to cause ionization growth, and starting statistics were masked. At higher pressures, breakdown fields were lower, and photoionizations rare, so that statistics were observed.

Such an explanation does not depart significantly from the current understanding of laser damage. It keeps intact all debates concerning the number and origin of starting electrons, and the mechanisms by which statistics could be generated in the cascade process itself.

It will be demonstrated below that it is advantageous to assume that a major portion of the statistical nature of breakdown can be attributed to the preionization stage. Since even the smallest focal volumes studied contained > 10^{11} atoms, photoionization of the basic gas itself would have occurred at a well defined average rate even when that rate was small. Statistics are possible in photoionization only when a small number of atoms are irradiated. It will be asserted that the preionization at high pressures was due to photoionization of impurity ions present at a sufficiently low density that only a few such ions were in the focal volume. Note that the photoionization rate is greater when atoms are colliding than for individual atoms; such colliding atoms might serve as impurities.

3. Basic Damage Hypothesis

By analogy to the gas breakdown studies, the following hypothesis is suggested. Damage in solids for which absorption is not a problem is a sequence of the following three steps:

Preionization - This occurs by photoionization of isolated impurity ions for bulk damage, for surface damage induced by pulses < 200 ps in duration, and for most experiments with $\lambda < 0.69$ μm. Heating of particulates to obtain starting electrons will be important for surface damage by long pulses > 20 ns in duration, or in damage induced by wavelengths > 3-5 μm. The probability for direct photoionization is assumed to depend nonlinearly on intensity.

Ionization growth - By processes such as cascade ionization or vertical transitions which are described by probabilities which are linear in intensity.

Absorption - Which occurs when the electron population exceeds a critical density of about 10^{16}-10^{18} cm^{-3}. Linear absorption will always be present to some extent, and may become dominant for breakdown induced by very long duration pulses or by wavelengths near absorption maxima in the material.

4. Data Which Supports the Hypothesis
The Occurrence of Explosive Threshold Damage

When special techniques were used to prepare surfaces, it was frequently noted that the damage threshold on some sites increased greatly, and that damage when induced was explosive in nature. It was impossible to induce an arbitrarily small damage. This was observed in ion-beam polished sapphire [13] super-polished surfaces [14], leached ED-2 glass surfaces [15], ectched KCl [16], and in flame-polished surfaces [17,18].

It is important to note that such damage cannot be explained by any deterministic mechanism such as thermal absorption. Furthermore, the preionization/ionization growth/absorption sequence cannot explain explosive threshold damage if both growth stages are well represented by rates. In all these cases, the time required to induce damage is precisely calculable for a given laser pulse, and damage can be induced at an arbitrary chosen time, early or late, by adjusting the pulse intensity.

All reported explosive threshold damage occurred for pulses > 5 ns in duration, induced at 10^{9} - 10^{10} W/cm^2. Explosive damage has not been reported for damage by pulses < 200 ps in duration, which occurs at 10^{11} - 10^{12} W/cm^2. Instead, it has frequently been noted that short-pulse damage is very deterministic in nature. Abritrarily small damage could be induced in dielectric films [19-21], in the bulk of dielectrics [22] and on dielectric surfaces which had been polished [20], leached [20], or flame-polished [20]. It is important to note that such determinism in short pulse damage at 1.06 μm or 0.69 μm is not due to linear absorption. Absorbing filter glass, with absorption coefficients of 100-500 cm^{-1} have about the same damage threshold at 1.06 μm 100 ps as the best BK-7 glass. Only metal surfaces have been observed to undergo shot-pulse damage due to linear absorption.

The presence or absence of explosive threshold damage in solids appears to be closely analogous to the presence or absence of statistics in gas breakdown. When in gas breakdown the pressure is reduced, the breakdown field increases, photoionization becomes plentiful, and statistics disappear. In solids, reducing pulse duration increases breakdown fields and explosive thresholds disappear. The analogy suggests that explosive threshold damage occurred because a required trigger, an initial electron, was missing. Cleaning the surfaces by special techniques had removed the impurities and inclusions which were most readily ionized. The field required to ionize the remaining material exceeded the field required to produce ionization growth, and the growth was explosive once starting charge was obtained. Explosive threshold damage is not observed with short pulses because many atoms are subject to ionization by fields of 10^{11} W/cm^2, and starting charge is always provided.

It is important to note that the ionization growth stage appears to be dominant for short-pulse damage, and that the rate of growth depends lineary on intensity. Defects which only serve to furnish starting electrons will have almost no effect on short-pulse damage. Enhancement of the field at mechanical flaws will be important only as an aid to ionization growth. By contrast, damage induced by pulses > 5 ns in duration can be dominated by either preionization or ionization growth. Due to possible nonlinearities in the preionization, field enhancement, surface preparation, and impurity concentrations may be very important in setting long-pulse thresholds.

Consider now the application of the hypothesis as an explanation of a variety of experimental results.

5. Applications of the Hypothesis

5.1 Explanation of Surface Damage Morphology

5.1.1 Density of Damage Micropits vs. Pulse Duration

Threshold damage at 0.69 μm in thin films of refractory oxides produced randomly distributed micropits at three pulse durations [23]. The results are summarized in table 1.

Table 1. Density of Damage Micropits vs. Laser Pulse Duration

Pulse duration (ps)	Pit density (cm^{-2})	Avg. Pit diameter (μm)	Avg. Damage Threshold (W/cm^2)
20	10^7	0.1-0.3	10^9
1400	10^5	≈ 1.0	10^{10}
20000	10^4	3-5	10^{11}

The data is in reasonable agreement with calculations [24] which predicted that asorbing inclusions of one preferred size would be most readily heated by pulses of a given duration. This explanation was adopted [23], but inclusions in the sizes and spatial densities required to satisfy the hypothesis have not been located by any passive technique. An alternate explanation is suggested by the hypothesis of section 3. The pits are all due to micro-avalanches which do not connect into one common failure of sites irradiated at the threshold level. The pit size increases as the pulse duration increases due to longer "burn" times after pit formation at the temporal peak of the pulse, when seed ionization is produced. The spatial density of pits increases as the pulse duration decreases since more entities are available as sources of photo-induced starting charge in the larger breakdown fields associated with reduced pulse durations. An interesting test could be conducted by terminating long pulses (> 20 ns) at various times after the temporal peak to determine whether a relationship between "burn" time and pit size could be observed.

5.1.2 Relationship Between Surface Artifacts and Laser Damage

Flaws such as mounds or pits which are observable by microscopy on dielectric films have been identified as the cause of laser damage by Bradbury [25], who used the simple procedure of taking microphotographs before and after damage to ascertain that artifacts were weaker than the surrounding film. His experiments were done at 1.06 μm using pulses > 50 ns in duration with highly modulated waveforms. The same result has been inferred by deShazer et. al.[26] from measurements of the damage threshold as a function of irradiated spot size.

There is a fundamental problem with this assertion - the density of pits produced by laser damage depends on pulse duration [23] but the density of observable artifacts is clearly a constant for any given sample. There are additional problems with the technique described by deShazer et.al., which claims that measurements of the damage threshold as a function of focal spot size will yield (1) a damage threshold for the defects, (2) the spatial density of defects, and (3) the intrinsic damage threshold of the defect-free material. Only the defect damage threshold is gotten with any certainty. This comes from threshold measurements on large areas which always contain defects. The defect density and intrinsic threshold are to be obtained by fitting the data to a theoretical expersion for the spot size dependence of threshold. The derivation of that expression is itself in error;

it is for cylindrical beams, not beams of Gaussian spatial profile as asserted. Even when the corrected equation [27] is used there remains a fundamental ambiguity. As smaller beams are used, the probability of avoiding the irradiation of defects increases, and larger thresholds are measured on some sites. The maximum threshold observable on very small sites is possibly the intrinsic damage threshold. It could as well be the damage threshold for a second class of defects.

The model for damage given in section 3 suggests that artifacts may be important in setting damage thresholds for long pulses, in agreement with the observations of Bradbury [25]. Field enhancement at such artifacts will greatly aid preionization. The model also suggests that artifacts will be much less important for short-pulse damage, for which the linear electron growth process is dominant.

5.1.3 Cone-Shaped Damage to Polished Surfaces

Threshold damage on ED-2 glass surfaces polished with abrasives containing iron produced perfectly smooth, round microcraters [15]. These were explained [20] as a result of thermal expansion of absorbing particulates buried under the glass surface by cold-flow during polishing. It is equally plausible to assume that the craters are caused by microavalanches seeded by charge obtained from ionization or heating of the iron compounds, a process which would tend to produce identical craters by plasma absorption during the last portion of the pulse. Identical craters produced by thermal expansion of particulates requires identical particulates, which seems less likely.

5.1.4 Isolated Damage Micropits in the Bulk

Smith et. al. [22] have observed that threshold bulk damage induced by 30 ps 1.064 μm pulses results in isolated damages which they attribute to microavalanches formed about available electrons. This assertion was a valuable input to formulation of the hypothesis being advanced here, and is in keeping with the predictions of the hypothesis. The density of the pits, up to 10^9 cm^{-3}, results from the fact that many entities can be ionized by the large breakdown fields, and the sharpness of threshold follows from the assured supply of starting charge.

5.2 Damage Statistics

Statistics in laser damage have been observed in many experiments since they were first systematically studied by Bass and Barrett [2]. Statistics have been observed for breakdown on polished surfaces [2,29,30], in the bulk [29,31,32], in dielectric films [26,29], and in gases [1]. In all these instances, pulse durations exceeded 5 ns.

Statistics have not been reported for damage induced by pulses < 200 ps in duration.

These statistics follow from the hypothesis in section 3 as a close parallel to the occurrence of explosive threshold damage. For long pulses, at low field strengths, starting charge may not be reliably produced and statistics can be observed. For short pulses, in high fields,starting charge is always adequate.

It is probable that some statistical aspects of damage are due to the presence or absence of particulates. Thermal damage to inclusions could cause either temporal or spatial statistics [29]. There are only a few instances in which such particulates have been identified, and even when they are known to be present it is difficult to determine that they produce damage by some direct thermal process. The damage process near absorbing particulates should depend on the pulse duration. For long pulses, adquate time is available to allow thermal expansion or melting. With short pulses, electrons from the heated particle may lead to avalanche breakdown before simple thermal expansion is effective in destroying the sample. Some indirect support for this hypothesis is obtained by the behavior of the pole pieces in laser-triggered spark gaps. In gaps triggered by focusing 50 kW 20 ns ruby laser pulses onto one pole piece, the starting electrons are generated thermally. The pole piece erodes rapidly even on poles fitted with tungsten target areas [18]. The erosion creates thermal craters which grow progressively deeper with repeated firings. Gaps triggered by 100 ps 1.064 μm pulses require much less input laser energy and do not show the thermal cratering [18]. This suggests that nonlinear photoemission from metals may be more important in the very short pulse regime than thermal absorption and expansion. Care should be exercized in assuming that platinum or iron particulates will be a major cause of short pulse damage, even though they are known to be serious problems in long pulse damage [15,23].

5.3 Distribution of Breakdown Times

For nonabsorbing media, the experimental observations of the distributions of breakdown times are well summarized by the following:

With 5-20 ns Gaussian waveform pulses, threshold bulk breakdown is restricted to times near the temporal peak of the pulse [31]. Threshold breakdown in the bulk could be induced at any time during square-waveform ruby laser pulses [1,29]. In contrast, laser-induced gas breakdown could be induced

at any time during either Gaussian or square-waveform pulses [1,18]. In the last two observations, statistics were frequently seen, so that only a mean breakdown time could be associated with each input intensity. Nevertheless, the observations demonstrate that the strict exclusion of late breakdowns holds only for bulk breakdown of solids induced by ≃ Gaussian pulses.

Attempts have been made to calculate breakdown times by means of rate equations [34], as is done in gas breakdown. As expected, the calculation involving time-constant rates for electron production resulted in the prediction that a critical electron population could be generated at a specific time by a laser pulse of specific waveform and intensity. Breakdowns could be made to occur arbitrarily late in the pulse by adjusting pulse intensity. The authors complaint [34] that such late breakdowns have not been observed because of poor experimental control is unconvincing. Thousands of such breakdowns have been recorded. If late breakdowns were easily generated, they would have been observed by simple chance, particularly if experimental fluctuations were a problem.

The hypothesis advanced in section 3 suggests that the systematics in breakdown times are due to the dominance of preionization in the described experiments. With Gaussian waveform pulses of 5-20 ns, at threshold, preionization is restricted to the intense temporal peak of the pulse. The liberated electrons must be used immeidately or they are lost as seed charges by rapid recombination. Seed charge, and breakdown, can be produced at any time during a square-waveform pulse. Seed charge is produced most copiously at the peak of the pulse in gas breakdown, but the seed charges survive and remain available for production of late breakdowns.

6. Summary

A hypothesis for the breakdown in solids has been constructed by analogy to gas breakdown. The hypothesis does not differ markedly from existing schemes [2, 35],which generally assume that avalanche ionization is the failure mechanism in transparent materials. Rather, it is suggested that more attention must be given to the method by which starting charge is obtained.

The hypothesis was used to explain a wide variety of existing experimental data, and to suggest several experimental tests. Hopefully, a number of these tests can be conducted in the near future to refine, or if necessary, repudiate the hypothesis in an expedient manner.

7. Acknowledgments

The author gratefully acknowledges extensive and helpful conversations with M. J. Weber and A. J. Glass of Lawrence Livermore Laboratory, R. H. Picard and R. A. Bradbury of Rome Air Development Center (Hanscom Field, Mass.), N. Boling of Owens-Illinois Corporation, and M. Bass of the Center for Laser Studies, University of Southern California. He is further grateful for the continuing technical assistance of G. E. Murphy, and for the assistance of Patricia Page and Audrey Heine in preparation of the manuscript.

8. References

[1] Milam, D., Bradbury, R.A., and Picard, R.H., Laser-Induced Damage in Optical Materials: 1975, N.B.S. Spec. Pub. 435, pp.347, (1976).

[2] Bass, M., and Barrett, H.H., IEEE J. Quant. Electron., QE-8, 338 (1972).

[3] Picard, R.H., Milam, D., Bradbury, R.A., and Fan, J.C.C., Laser-Induced Damage in Optical Materials: 1975, N.B.S. Spec. Pub. 435, pp.272, (1976).

[4] Newnam, B.E., Gill, D. H., and Faulkner, G., Laser-Induced Damage in Optical Materials: 1975, pp. 254, (1976).

[5] Smith, D.C., Overview of Laser Radiation Induced Gas Breakdown, presented at First DOD Conference on High Energy Laser Technology, San Diego, CA., Oct. 3, 1974.

[6] Ready, J.F., Effects of High Power Laser Radiation, Chapter 5, Academic Press, New York, (1971).

[7] Canavan, G.H., and Nielson, P.E., Appl. Phys. Lett. 22, 409 (1973).

[8] Lencioni, D.E., Appl. Phys. Lett., 23, 12 (1973).

[9] Brown, R.T., and Smith, D.C., Appl. Phys. Lett., 22, 245 (1973).

[10] Smith, D.C., Berger, P. J., Brown, R.T., and Fowler, M.C., Investigation of Gas Breakdown with 10.6 Micron Wavelength Radiation, United Aircraft Research Laboratory Report L921104-6, (1972), Unpublished.

[11] Gill, D.H., and Dougal, A.A., Phys. Rev. Lett. 15, 845 (1965).

[12] Krasyuk, I.K., Pashinin, P.P., and Prokhorov, A.M., Soviet Physics J.E.T.P. 31, 860 (1970).

[13] Giuliano, C.R., Laser-Induced Damage in Optical Materials: 1972, N.B.S. Spec. Pub. 372, pp. 55, (1972).

[14] Fradin, D.W., and Bass, M., Appl, Phys. Lett., 22, 157 (1973).

[15] Boling, N.L., Ringlien, J.A., and Dubé, G., Laser-Induced Damage in Optical Materials: 1974, N.B.S. Spec. Pub. 414, pp.119 (1974).

[16] Allen, S.D., Braunstein, M., Giuliano, C.R., and Want, V., Laser-Induced Damage in Optical Materials: 1974, N.B.S. Spec. Pub. 414, pp. 66 (1974).

[17] Bettis, J.R., House, R.A., Buenter, A.H., and Austin, R., Laser-Induced Damage in Optical Materials: 1975, N.B.S. Spec. Pub. 435, pp.289 (1976).

[18] Milam, D., unpublished.

[19] Bliss, E.S., Milam, D., and Bradbury, R.A., Appl. Opt., 12, 602 (1973).

[20] Milam, D., Laser-Induced Damage at 1064 nm 125 ps, submitted to Appl. Opt. for publication.

[21] Newnam, B.E., private discussions.

[22] Smith, W.L., Bechtel, J.H., and Bloembergen, N., Laser-Induced Damage in Optical Materials: 1975, N.B.S. Spec. Pub. 435, pp. 321 (1972).

[23] Milam, D., Bradbury, R.A., and Bass, M., Appl. Phys. Lett. 23, 654 (1973).

[24] Hopper, R.W. and Uhlman, D. R., J. Appl. Phys., 41, 4023 (1970).

[25] Bradbury, R.A., unpublished.

[26] DeShazer, L.G., Newnam, B.E., and Leung, K.M., Appl. Phys. Lett. 23. 607 (1973).

[27] Picard, R.A., Milam, D., and Bradbury, R. A., Statistical Analysis of Defect-Caused Damage in Thin Films, submitted for publication to Appl. Opt.

[28] Duthler, C.J., Appl. Phys. Lett., 24, 5 (1974).

[29] Milam, D., Bradbury, R.A., Picard, R.H., and Bass, M., Laser-Induced Damage in Optical Materials: 1974.

[30] Wang, V., Giuliano, C.R., Allen, S.D., and Pastor, R.C., Laser-Induced Damage in Optical Materials: 1975, N.B.S. Spec. Pub. 435, pp. 118 (1976).

[31] Fradin, D. W., Yablonovitch, E., and Bass, M., Appl. Opt., 12, 700 (1973).

[32] Fradin, D.W., and Bua, D.P., Appl. Phys. Lett., 24, 555 (1974).

[33] To the author's best knowledge, the existence of platinum inclusions in glass was first demonstrated by R. F. Woodcock of American Optical Company.

[34] Kelly, P., Braünlich, P., and Schmid, A., Appl. Phy. Lett., 26, 223 (1975).

[35] Bloembergen, N., IEEE J. Quant. Elect., QE-10, 375 (1974).

9. Figures

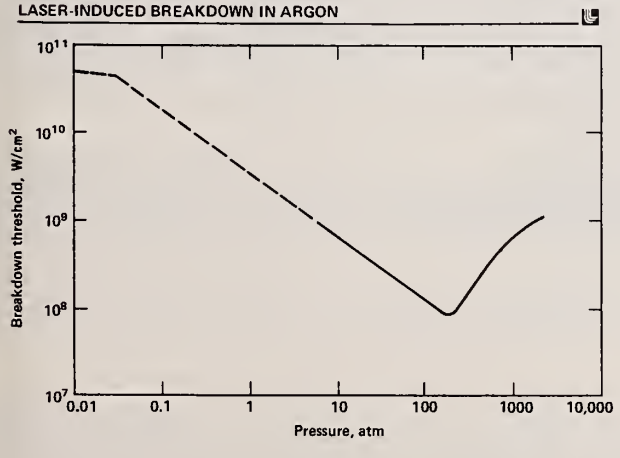

Figure 1. Breakdown threshold of Argon as a function of pressure. The data of Gill and Dougal [11] has been extrapolated using the pressure dependence found for avalanche ionization [6]. The low pressure region has been studied by Krasyuk, et al. [12], and shows the pressure dependence expected for dominance by direct photoionization.

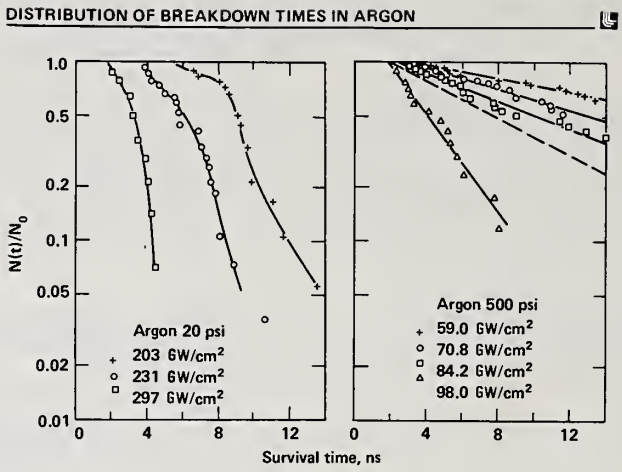

Figure 2. Distribution of breakdown times as a function of intensity. Argon volumes of about 10^{-9}cm^3 were irradiated by square-waveform ruby laser pulses [1].

COMMENTS ON PAPER BY MILAM

The speaker emphasized that although both photoionization and the avalanche process are manifestly nonlinear, the former depends on a much higher power of the intensity and so is far more dramatic in its nonlinearity. The question of looking for polarization dependence was brought up since the same energy density corresponds to a lower electric field value at circular polarization than at linear polarization. In argon gas, for example, higher thresholds were observed using circular polarization. B. Newnam of LASL indicated that he had not observed different thresholds for thin film damage at 30 ps, except for ZrO_2, in which two-photon absorption was expected to be operative. No polarization effect had been observed in 17 ns pulses in damage experiments carried out at Hughes Research Laboratories on solid materials.

B. Newnam also reported that he had seen explosive damage at 30 ps in one circumstance when high-damage threshold films were deposited on glass substrates and damage occurred at the substrate exit surface. This observation seems to contradict Milam's hypothesis.

5.4 LASER DAMAGE TO SEMICONDUCTOR MATERIALS FROM 10.6 μm CW CO_2 LASER RADIATION*

S. K. Gulati and W. W. Grannemann
Department of Electrical Engineering and Computer Science
The University of New Mexico
Albuquerque, New Mexico 87131

Damage thresholds for Si, Ge, GaAs, GaAsP, and GaP have been found experimentally. All the damage thresholds are of the order of KW/cm^2 for an irradiation time of 0.15 to 0.18 second. The damaged devices of Si and Ge show 30 to 50 percent decreases in carrier mobility at lower temperatures, thereby showing lattice damage. It is found that the experimental damage thresholds, surface and lattice damage can all be explained by applying the theory of parametric instability of the type formulated by DuBois and Goldman. The same theory is also applied to explain CW CO_2 damage thresholds for KCl windows as experimentally observed by Loomis and Huguly.

Key Words: Carrier mobility; damping rates; laser damage of semiconductors; parametric plasma instability; photon induced excitation.

Introduction

Damage thresholds for different semiconductors using pulsed laser radiation have been determined experimentally by several authors [1,2,3,4][1]. Different authors use different criteria for the occurrence of damage. However, the damage thresholds are all of the order of tens of MW/cm^2, which are about three orders higher than the damage thresholds in the present cw damage work. An attempt to explain the damage thresholds of semiconductors for pulsed lasers was recently make by Shatas, et al. [5], in which they used the theory of parametric instability as formulated by Gerstein and Tzoar [6]. These damage thresholds depend critically on carrier mobility and band gap. However, no such critical dependence is observed in the present work for cw CO_2 laser damage. Shatas, et al. in the same paper also applied the theory of modified two stream instability following Kaw and Dawson [7] in order to explain the observed damage thresholds. The damage thresholds in the present work are too low to be explained by any of these theories or the lucky electron theory of avalanche. Drude absorption is ruled out because the damage occurs at the same low power density in intrinsic GaAs. Simple Joule heating is insufficient to explain the observed damage. But the thresholds calculated by using the theory of parametric instability of DuBois and Goldman [8] are in a reasonable agreement with the experimental damage thresholds. The same theory also predicts correct damage thresholds for KCl windows as observed experimentally by Loomis and Huguly [9].

Experimental

The semiconductor chips which were irradiated were in the shape of a square of .25 cm x .25 cm. The cw CO_2 laser beam used was Gaussian in space with a diameter of 12 mm. A salt lens of 25 cm focal length was used to concentrate the beam. The sample was displaced from the focus to radiate it uniformly. The experimental arrangement is shown in figure 1. Mobility, resistivity, and carrier concentration measurements before and after damage were made over a temperature range of 20 °K to 300 °K using a CS-202 cryogenic refrigerator and applying Van der Pauw's [10] method. This apparatus is shown in figure 2.

Results

The damage thresholds were obtained by radiating the semiconductor until damage was visible on the surface. Different semiconductors with their solid-state parameters and experimental damage thresholds are listed in table 1.

The changes in mobility, resistivity, and carrier concentration in Ge and Si due to laser damage are shown in figures 3, 3a, 4, 5, and 5a, respectively. All of these show significant lattice damage.

---

*Work supported by Air Force Office of Scientific Research under Contract No. F44620-75-C-0077.

1. Figures in brackets indicate the literature references at the end of this paper.

Table 1. Different semiconductors with their solid-state parameters and experimental damage thresholds.

Semiconductor	Mobility $cm^2(V\text{-}s)^{-1}$	Carrier Concentration (cm^{-3})	Band Gap (ev)	Damage Threshold in W cm^{-2}
Ge (n-type)	2300	4×10^{14}	0.79	8.5×10^3
Si (n-type)	1200	6×10^{14}	1.11	1.1×10^4
Si (p-type)	300	3×10^{15}	1.11	2.2×10^4
GaAs (n-type)	3500	1×10^{16}	1.60	6×10^3
GaAsP (n-type)	2000	2×10^{17}	2.00	3.5×10^3
GaP (n-type)	110	1×10^{18}	2.4	1.33×10^3

Explanation of Damage Thresholds

The observed damage thresholds can be explained by using the theory of parametric instability of the type formulated by DuBois and Goldman [8]. This kind of instability can be excited in a system if the energy is fed into the solid-state plasma at a rate faster than the system can dissipate it.

The intense laser beam of frequency ω_o (2.83×10^{13} Hz in this case) interacts nonlinearly with the electron plasma, that has a resonance frequency given by $\omega_R = (\omega_e^2 + 3k^2\, Se^2)^{1/2}$ (where ω_e is the Langmuir frequency of the electron plasma and Se is the thermal velocity of the electron) and pumps the ion plasma at the beat frequency $(\omega_o - \omega_R)$. If ω_o and ω_R are very nearly equal, then $(\omega_o - \omega_R)$ is small and is characteristic of the ion acoustic frequency. Similarly, the laser beam can interact with the ion acoustic wave and pump the electron plasma. If this type of instability has a positive growth rate, then it can cause anomalous absorption and heating of the sample [11] with subsequent lattice damage.

The calculation of the damage thresholds is based on finding the nonlinear susceptibility in terms of the laser beam parameters (E_o, ω_o, k_o) and electron plasma parameters (n, T, ω_e).

It has been shown that

$$\varepsilon_L^{NL}(\vec{k},\omega) = \varepsilon_L(\vec{k},\omega) - \frac{\Lambda^2}{(k^2/k_D^2)\,\varepsilon_L(\vec{k},\omega-\omega_o)} \qquad (k \ll k_D) \tag{1}$$

where $\varepsilon_L(\vec{k},\omega)$ is the linear longitudinal dielectric constant of the electron plasma and $\varepsilon_L^{NL}(\vec{k},\omega)$ is the nonlinear dielectric constant under the action of the intense laser beam. Here

$$\Lambda^2 = \frac{1}{4}\left(\frac{\omega_p}{\omega_o}\right)^4 \frac{I_o}{nckT} \tag{2}$$

in which ω_p is the usual Langmuir frequency of the plasma and ω_o is the frequency of the incident laser field and I_o its intensity. n is the electron concentration of the plasma. Also, k_D is the inverse of the Debye-Huckel shielding length.

The nonlinear dielectric constant has two parts. The real part, when equated to zero, would give the resonance frequency of the plasma and is always very close to ω_o. The imaginary part gives the damping rate (γ^{NL}/ω_p)

$$\frac{\gamma^{NL}}{\omega_p} = IM\ \varepsilon_L^{NL}(\vec{k},\omega_L)$$

$$= \frac{\gamma_L}{\omega_p} - \Lambda^2\ Im\left(\frac{k_D^2}{k^2}\,\varepsilon_L^{-1}\ (\vec{k},\omega_L - \omega_o)\right), \tag{3}$$

where

$$\mathrm{Im}\left(\varepsilon_L(\vec{k},\omega_L)\right) = \frac{y_L}{\omega_p} \tag{4}$$

and is ordinary Landau damping. In the case of a solid-state plasma, it can be approximated as

$$\frac{y_L}{\omega_p} \simeq \frac{1/\tau_c}{\omega_p} = \frac{1}{\omega_p \tau_c} \tag{5}$$

where τ_c is the collision time of the carriers with the lattice phonons.

$\mathrm{Im}\left[\left(\frac{k_D}{k}\right)^2 \varepsilon_L^{-1}(\vec{k}, \omega_L - \omega_o)\right]$ can be estimated by $\left(\frac{\omega_i}{y_i}\right)\left(\frac{\omega_\ell}{y_\ell}\right)$

where y_i/ω_i and y_ℓ/ω_ℓ give the damping rates for acoustic and optical phonons, respectively.

Hence

$$\frac{y^{NL}}{\omega_p} = \frac{y_L}{\omega_p} - A^2\left(\frac{\omega_i}{y_i}\right)\left(\frac{\omega_\ell}{y_\ell}\right) .$$

This damping rate is negative (i.e., we have the growth of instability) if

$$A^2\left(\frac{\omega_i}{y_i}\right)\left(\frac{\omega_\ell}{y_\ell}\right) \geq \frac{y_L}{\omega_p}$$

or writing in terms of power threshold

$$P_{th} \simeq 4nckT\left(\frac{\omega_o}{\omega_p}\right)^4\left(\frac{y_L}{\omega_p}\right)\left(\frac{y_i}{\omega_i}\right)\left(\frac{y_\ell}{\omega_\ell}\right) \tag{6}$$

Now $\omega_o \simeq \omega_p$ and for this to be true the plasma concentration should be of the order of 10^{18} to 10^{19} cm^{-3}, but the starting carrier concentrations in our case are much less than this. Therefore, we propose a new excitation mechanism which alleviates enough electrons from the valence band to the conduction band via a continuous distribution of surface states within the band gap. This will be discussed at the end.

In a solid-state plasma Drude absorption causes the electron temperature to be higher than the ion bed temperature. Therefore, one can approximate [12]

$$\left(\frac{y_i}{\omega_i}\right) \simeq \frac{1}{2}\left(\frac{m_\ell}{m_i}\right)^{1/2}\left(\frac{\pi}{2}\right)^{1/2} \tag{7}$$

y_ℓ/ω_ℓ usually lies between 10^{-1} and 10^{-2} [13] depending upon the semiconductor. This mode is more readily damped in Si and Ge than in GaAs, GaAsP, GaP and salt windows.

Using appropriate values of the damping rates, and equation (6), we have calculated the damage thresholds for different semiconductors. The calculated values are compared with the experimental values in table 2.

The damping ratios used in the calculation are only approximate. These ratios are difficult to estimate from theories as well as from experiments.

Table 2. Calculated values are compared with the experimental values.

Material	Calculated Damage Thresholds in W cm^{-2}	Experimental Damage Thresholds in W cm^{-2}
Si (n-type)	7.2×10^4	1.1×10^4
Si (p-type)	9.8×10^4	2.2×10^4
Ge	4.08×10^4	8.5×10^3
GaAs	7.14×10^3	6×10^3
GaAsP	5.7×10^3	3.5×10^3
GaP	8×10^4	1.33×10^3
KCl	$10^4 \rightarrow 10^5$	$10^4 \rightarrow 10^5$ [9]

Photon Induced Excitation

It is well known that the width of the band gap for a semiconductor is much less near the surface as compared to within the bulk, e.g., the band gap for GaAs near the surface is 0.30 eV to 0.36 eV and 1.6 eV within the bulk [5]. Also within the band gap, there is a continuous distribution of surface states having a density of about 10^{12} to 10^{14} cm^{-2} $(eV)^{-1}$. The lifetimes for these states are 3 to 4 orders longer as compared to ω_o^{-1} for CO_2 laser. The electrons in the states near the Fermi level in an n-type semiconductor are almost resonantly excited to the conduction band. The emptied states are filled again by the electrons excited by the photons from the states lying below the Fermi level. This streaming process can produce electron concentrations of 10^{18} to 10^{19} cm^{-3} within milliseconds or less. The quantum yields and transition probabilities for such processes have been calculated by Kane [14] and experimentally verified by Gobeli and Allen [15]. The quantum yield has been shown to be of the order $\sim(h\nu-E_s)^n$ where n = 1 to 5/2, E_s is the separation between two surface states and $h\nu$ is the photon energy. This high quantum yield makes the proposed mechanism highly probable.

Conclusion

Damage thresholds of different semiconductors for CW CO_2 laser radiation have been found experimentally. It appears that the theory of parametric instability in solid-state plasmas explains the results satisfactorily. The same theory also seems to explain the observed damage thresholds for KCl laser windows.

Acknowledgments

We gratefully acknowledge very useful discussions with Dr. DuBois of the Los Alamos Scientific Laboratory and Drs. House and Bettis and Major J. L. Stapp of the Kirtland Air Force Weapons Laboratory. Our special thanks go to Mr. C. Huguly also of Kirtland Air Force Base for help in the experimental work.

References

[1] D. C. Emmony, R. P. Howson and L. J. Willis, Appl. Phys. Lett. 23, 598 (1973).

[2] M. Birnbaum, J. Appl. Phys. 36, 657 (1965).

[3] M. Bertolotti, L. Stagni, G. Vitali, S. L. Muzii, J. Appl. Phys. 42, 5843 (1971).

[4] J. L. Smith, N. B. S. - SP 414 Report, 200 (1974).

[5] R. A. Shatas, J. D. Stettler, L. M. Narducci, S. S. Mitra and H. C. Meyer, N. B. S. - SP 414 Report, 200 (1974).

[6] I. I. Gerstein and N. Tzoar, Phy. Rev. Lett. 27, 1650 (1971).

[7] P. K. Kaw and J. M. Dawson, Phys. Fluids 12, 2586 (1969).

[8] D. F. DuBois and M. V. Goldman, Phys. Rev. Lett. 14, 544 (1965).

[9] J. Loomis and C. Huguly, N. B. S. - SP 414 Report, 94 (1974).

[10] L. J. Van der Pauw, Phillips Res. Reports 13 (1958).

[11] J. Dawson and C. Oberman, Phys. Fluids 5, 517 (1962).

[12] D. F. Dubois in Statistical Physics of Charged Particle Systems, Eds. R. Kubo and T. Kihara, Syokabu and W. A. Benjamin, Inc. (1968).

[13] N. Tzoar, Phys. Rev. 164, 518 (1967).

[14] E. O. Kane, Phys. Rev. 127, 131 (1962).

[15] G. W. Gobeli and F. G. Allen, Phys. Rev. 127, 141 (1962).

Figures

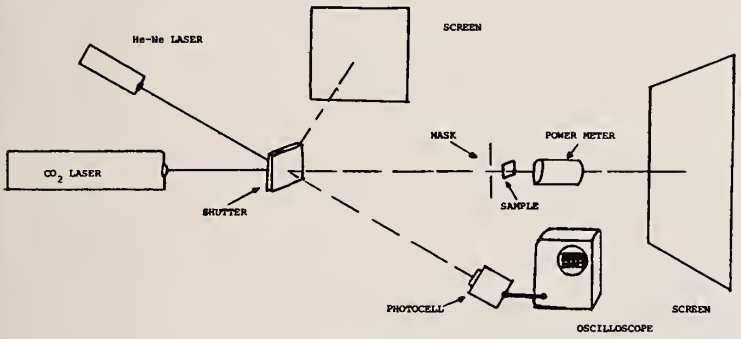

Figure 1. Laser setup.

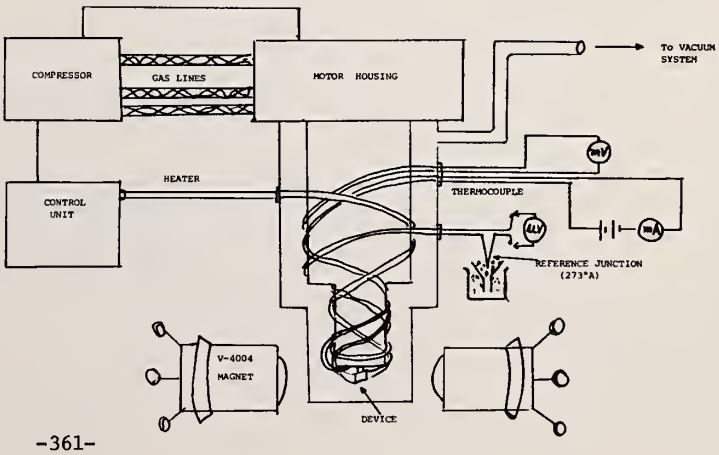

Figure 2. Mobility and resistivity measurement apparatus.

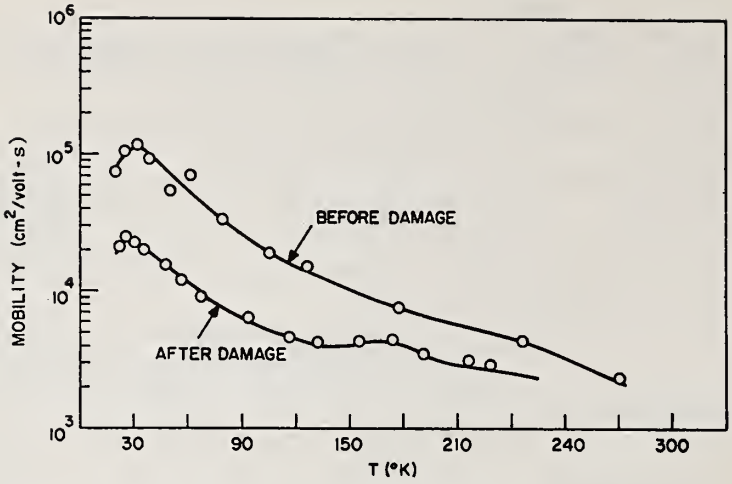

Figure 3. Electron mobility versus temperature for Ge before and after laser damage. The sample was radiated at 8.3×10^3 W/cm^2. The original electron concentration was $\sim 10^{13}$ at room temperature.

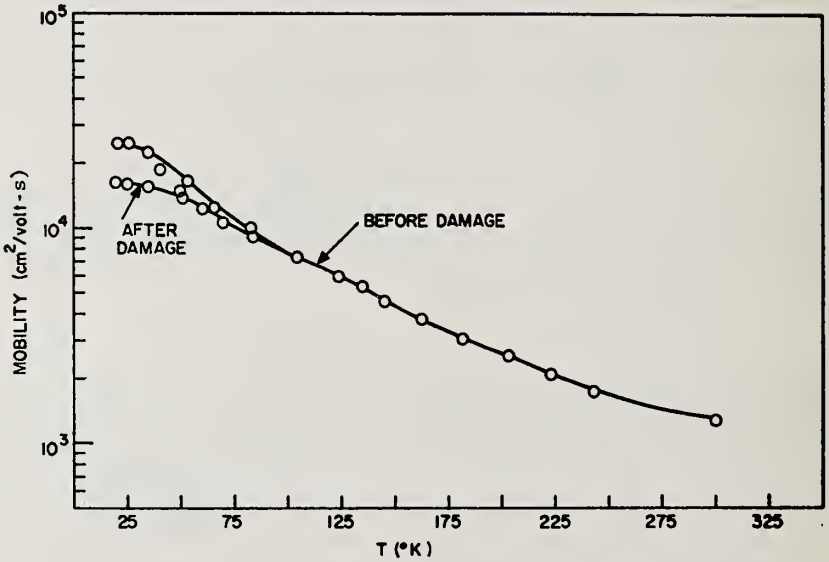

Figure 3(a). Electron mobility versus temperature for Si before and after laser damage. The sample was radiated at 0.96×10^4 W/cm^2. The original carrier concentration was $\sim 10^{15}$ cm^{-3} at room temperature.

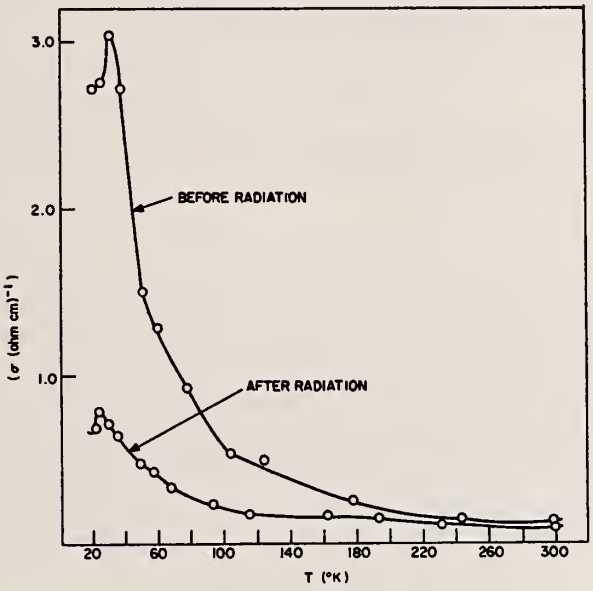

Figure 4. Conductivity versus temperature for Ge before and after laser damage for the same sample parameters as in figure 3.

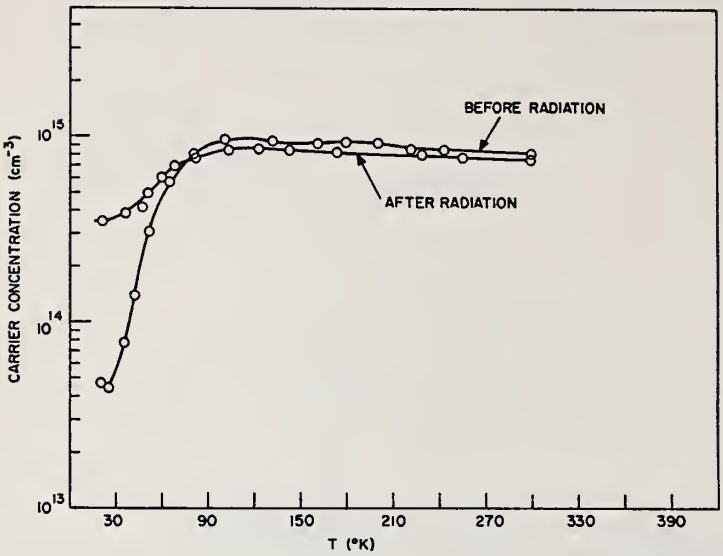

Figure 5. Carrier concentration versus temperature for Si before and after laser damage for the sample parameters as in figure 3(a).

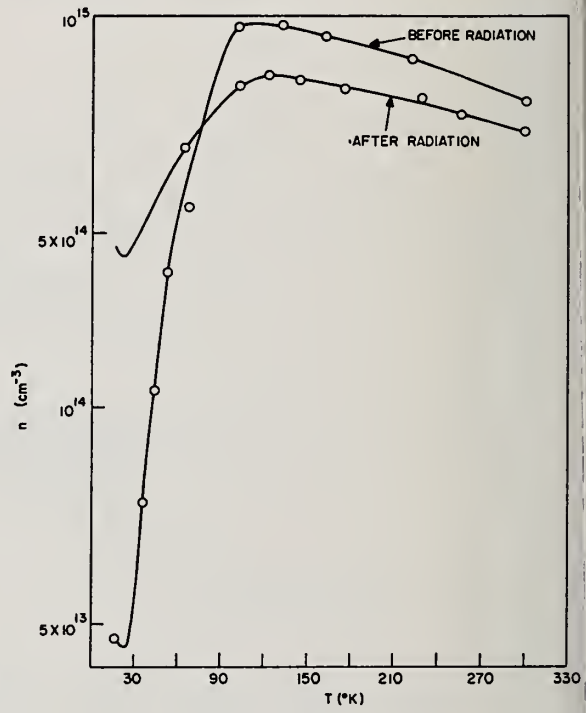

Figure 5(a). Magnified view of figure 5 to show the significant charge carrier removal due to laser damage.

COMMENTS ON PAPER BY GULATI AND GRANNEMANN

Several members of the audience noted the apparent discrepancy between the estimated density of surface states (10^{12} - 10^{14} cm^{-2}) and the apparent density of electrons generated (10^{19} cm^{-3}). The speaker argued that due to the long lifetime of electrons in the conduction band, the carrier concentration could grow to the required value during the laser pulse. This would require the continuous excitation of electrons from the valence band to surface states and thence to the conduction band during the period of illumination.

5.5 PHOTOTRANSPORT DAMAGE OF OPTICAL MATERIALS

Shew M. Wong
Rocky Flats Plant, Atomics International Division,
Rockwell International
and
David L. Olson
Rocky Flats Plant, Rockwell International
and
Colorado School of Mines
Golden, Colorado 80401

Described are well-established electrotransport phenomena which may serve as analogies for studies of laser-induced damage in optical materials through phototransport. Phototransport or photomigration relates to the segregation of ionic species or in vacancies in the optical materials caused by a competitive momentum transfer from the scattered photons to the specific ionic species of the optical material. Such microstructural changes in the material are expected to cause severe increases in localized absorption and enhance laser-induced damage.

Key words: Absorption; electrotransport; ionic segregation; laser; momentum transfer; phototransport; scattering; vacancies.

Introduction

Transport of specific atomic alloy components in both solid and liquid electrical conductors caused by a high-electrical direct current density has been well established [1, 2].* Much of this research effort has been performed to increase the service life of integrated circuits based on thin-film technology. Electrotransport in liquid alloys has had the interest of those investigators involved in purification technology, as well as those interested in exploring the electronic behavior of alloys. The concepts which have been established for the understanding of electrotransport and the resulting damage to electrical conductors should provide direct analogies to a phototransport phenomenon in optical materials which experience high-photon density. Phototransport or photomigration will be defined as the segregation of ionic species or vacancies in an optical material caused by a competitive momentum transfer from the scattered photons to the specific ionic species which are adjacent to the ionic vacancies. Given is a review of some electrotransport concepts based on momentum transfer and electronic scattering, and predictions are made as to the nature of phototransport damage in optical materials.

Electrotransport

Epstein and Paskin [3] have suggested a model for electrotransport behavior in liquid alloys which should be applicable to an ionic segregation phenomenon in optical materials caused by a high photon density or phototransport. Epstein and Paskin [3] assumed that the atomic alloy component which receives the largest momentum transfer from the scattered conduction electrons should be the atomic species that moves toward the anode. The atomic component of the alloy which receives the smallest momentum transfer would be expected to fall behind in this competitive process and thus concentrate at the cathode.

Epstein and Dickey [4] using the concept that the largest momentum transfer from the scattered conduction electrons should be with the alloy component that has the largest electronic scattering cross section, formulated the mechanics necessary to calculate the apparent electronic-scattering cross section of each of the alloy components as a function of the Fermi wave vector for the conduction electrons. This approach has been extended [5, 6] and experimentally verified [7, 8, 9] for a number of liquid alloys.

Figure 1 shows the calculated electronic back-scattering cross section (S) for the sodium-rubidium (Na-Rb) alloy system [8]. Notice that the Rb atom has the largest back-scattering cross section in Na-rich alloys, but with increasing Rb content there is a reversal and the sodium (Na) atom has the largest electronic back-scattering cross section. This reversal would suggest a change in which the alloy component rubidium or sodium (Rb or Na) goes to the anode as a function of alloy content. Figure 2 shows the results of measured electrotransport behavior of this Na-Rb alloy system. The drag coefficient is the quantity which measures the efficiency of the electrons in dragging with them a specific atomic-alloy species toward the anode. Notice that at the Na-rich side of the diagram, the drag coefficient for Rb is positive indicating that Rb is migrating toward the anode. In the Rb-rich side of the diagram, the drag coefficient for the Rb atom is found to be negative, which indicates that Rb atoms are migrating toward the cathode and confirming the predicted reversal behavior.

The electrotransport of vacancies must also be considered in solid electrical conductors. With high direct-current density, the metal atoms migrate toward the anode, while the vacancies migrate in the opposite direction. In an infinitely long and uniform conductor, electrotransport would not be expected to be destructive, but in situations where there is a divergence of the vacancy flux, localized high-vacancy concentration and void-formation results. Grain boundaries and surfaces are subject to a major

*Figures in brackets indicate the literature reference at the end of the paper.

nonequilibrium segregation of vacancies and void formation. Such defects have been found to enhance the failure of the metallization layers on integrated circuits.

Phototransport

One of the possible photon-scattering sites for optical materials is with the electronic defect structure associated with vacancies in nonstoichiometric optical materials. Figure 3 illustrates a cation sublattice in which two different types of cations (M^{++} and N^{++}), positioned around a cation vacancy, are in competition for successful migration into this adjoining vacancy. It is expected that the electronic defect region of these vacancies is sufficient in cross section to have photoelectric interactions which will scatter photons and transfer momentum. The ionic species, associated with this electronic defect which contributes the most to overall scattering phenomena, would be expected to receive the largest fraction of the transferred momentum, and the jump of this ionic species with the largest scattering cross section is expected to be the most probable.

The scattering phenomenon and the resulting momentum transfer can be analyzed with wave mechanics in the same manner as demonstrated for the electrotransport phenomenon [3-6]. With the determination of the proper interaction potential, the phase shifts for the scattered photon wave vectors can be calculated. Phase-shift data would allow calculation of the photon-scattering cross section as a function of the incident wavelength. With the photon-scattering cross section calculated for the specific ion-vacancy combinations of the optical material as a function of the wavelength of the incident radiation, predictions of the resulting mass-transport behavior can be made.

It will be assumed that the N^{++} ion adjacent to the vacancy has a larger photon-scattering cross section, S_N, than does the M^{++} ion, S_M, and will be transported in the direction of the photons in this competitive transfer process. This will leave the surface region of the optical material deficient in N^{++} ions and in excess of vacancies as illustrated in figure 4. If the phototransport results in large deviations from stable phase compositions of the optical material of interest, it is possible that the surface region, which is a subject to a large divergence in fluxes, may experience the precipitation of a second phase. Such localized microstructural changes will affect the optical behavior of the material. Also excessive transport of ions from the surface regions can produce a high vacancy concentration, such as is experienced in the failure mode of metallization on integrated circuits. Such localized high vacancy concentrations near the surface may result in void formation which would certainly influence the optical behavior of the material.

Consider the specific example of $LiNbO_3$ as the optical material. The equilibrium phase diagram [10] for the Li_2O-NbO_3 system is shown in figure 5. The Nb^{+5} ion adjacent to the cation vacancy is expected, with its more complex electronic structure, to have the largest photon-scattering cross section and thus contribute more to the photon scattering process than the Li^{+1} and O^{-2} ions. Further, it would be expected that the Nb^{+5} ion concentration near the surface of this optical material would decrease under high incident photon density. From the equilibrium phase diagram (fig. 5), it can be seen that excessive depletion of Nb^{+5} ions may result in the precipitation of a new phase (Li_3NbO_4) and thus cause major changes in optical behavior of the surface material.

With the assumption that the photon-scattering cross section is a function of the number of electrons associated with each of the ions, a prediction will be made as to which materials are most likely to receive phototransport damage. This assumption, known to be acceptable at the limit of small wavelengths, as elemental X-ray scattering, is cubic-power function of the number of electrons associated with each atomic species. Tables I, II, and III list possible optical materials with the number of electrons associated with each ion. For this competitive mass-transport process, materials with ions that have approximately the same number of electrons (table I) will not be subject to phototransport damage, but materials with large differences in the number of electrons (table III) for each ion are expected to be susceptible to phototransport damage. These predictions (tables I, II, and III) suggest that specific salts (NaF, KCl, AlF_3, MgF_2, SiF_4), and magnesium-aluminum silicates (spinel, enstatite, cordierite, sapphirine, and forsterite), should not experience phototransport damage. These calculations do raise concerns based on the experience with electrotransport, that phototransport damage would be expected in LiF, NaCl, TiO_2, AgCl, $LiNbO_3$, $LiIO_3$, and other materials with large differences in the number of electrons associated with each ion of the optical material.

Table I. Calculated predictions showing which optical materials should not experience phototransport damage.

Materials	Electrons per Ion	
	Cations	Anions
NaF	10	10
MgF_2	10	10
AlF_3	10	10
SiF_4	10	10
KCl	18	18
$CaCl_2$	18	18
RbBr	36	36
SiO_2	10	10
Al_2O_3	10	10
MgO	10	10
Magnesium-Aluminum Silicates:		
$MgAl_2O_4$ (spinel)	10, 10	10
Mg_2SiO_4 (forsterite)	10, 10	10
$MgSiO_3$ (enstatite)	10, 10	10
$Mg_2Al_4Si_5O_{18}$ (cordierite)	10, 10, 10	10
$Mg_4Al_{10}Si_2O_{23}$ (sapphirine)	10, 10, 10	10

Table II. Calculated predictions showing which optical materials may experience minor phototransport damage.

Material	Electrons per Ion	
	Cations	Anions
CdTe	46	53
GaAs	29	36
ZnSe	28	35
AgBr	46	36

Table III. Calculated predictions showing which optical materials should experience major phototransport damage.

Material	Electrons per Ion	
	Cations	Anions
LiF	2	10
LiCl	2	18
LiBr	2	36
BeO	2	10
B_2O_3	2	10
NaCl	10	18
RbF	36	10
AgCl	46	18
TiO_2	18	10
ZrO_2	36	10
CaF_2	19	10
$LiIO_3$	2, 46	10
$LiNbO_3$	2, 36	10
$CaCO_3$ (calcite)	18, 2	10

Acknowledgments

The authors acknowledge and appreciate support for the work performed under the U. S. Energy Research and Development Administration, Contract E(29-2)-3533.

References

[1] Rigney, D. A., *Electromigration in Metallic Systems,* Charge Transfer/Electronic Structure of Alloys, Ed. L. H. Bennett and R. H. Willers, AIME N.Y., N.Y., 87, 126 (1974).

[2] d'Heurle, F. M., Proc. IEEE 59, 1409 (1971).

[3] Epstein, S. G. and Paskin, A., Phys. Letter, 24A, 309 (1967).

[4] Epstein, S. G. and Dickey, J. M., Phys. Rev. B1, 2442 (1970).

[5] Olson, D. L., Blough, J. L., and Rigney, D. A., Scripta Met. 4, 1023 (1970).

[6] Olson, D. L., Blough, J. L., and Rigney, D. A., Acta Met. 20, 305 (1972).

[7] Blough, J. L., Olson, D. L., and Rigney, D. A., Mat. Sci. Eng. 11, 73 (1973).

[8] Lakshmanan, T. S., Olson, D. L., and Rigney, D. A., Scripta Met. 5, 1099 (1971).

[9] Lakshmanan, T. S. and Rigney D. A., Mat. Sci. Eng. 12, 285 (1973).

[10] *Phase Diagrams for Ceramists–1975 Supplement,* Ed. Levin, E. M. and McMurdie, H. F., Amer. Cer. Society, Columbus, Ohio, 86 (1975).

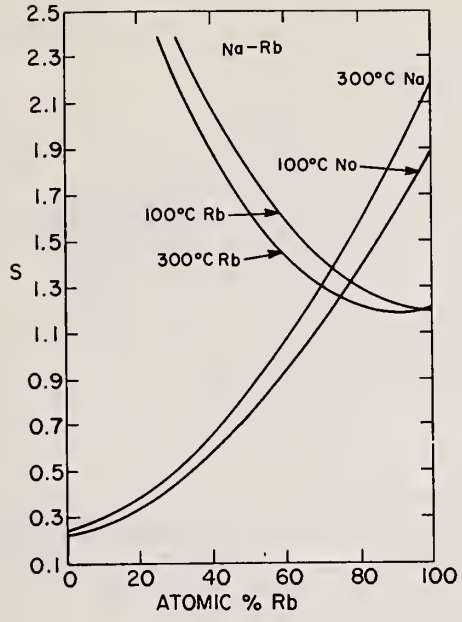

Figure 1. The electronic back-scattering cross sections for rubidium and sodium as a function of the rubidium content in sodium-rubidium alloys [8].

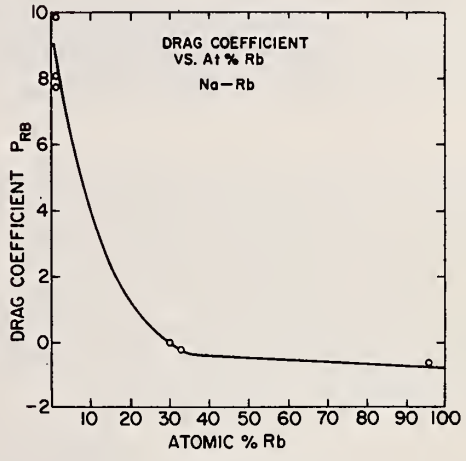

Figure 2. The electrotransport drag coefficient for rubidium as a function of the rubidium content in sodium-rubidium alloys [8].

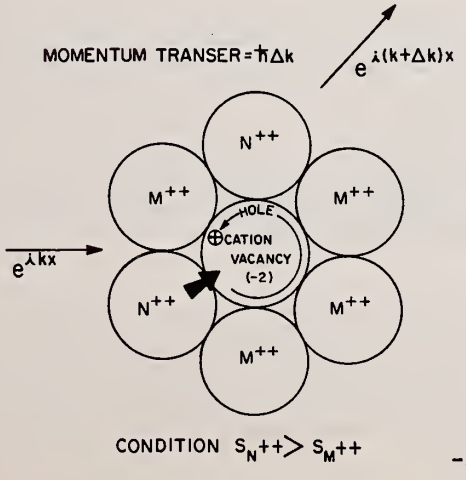

Figure 3. Photon scattering at the electronic defect structure associated with vacancies in nonstoichiometric optical material. Electronic defect structure is illustrated with cation sublattice.

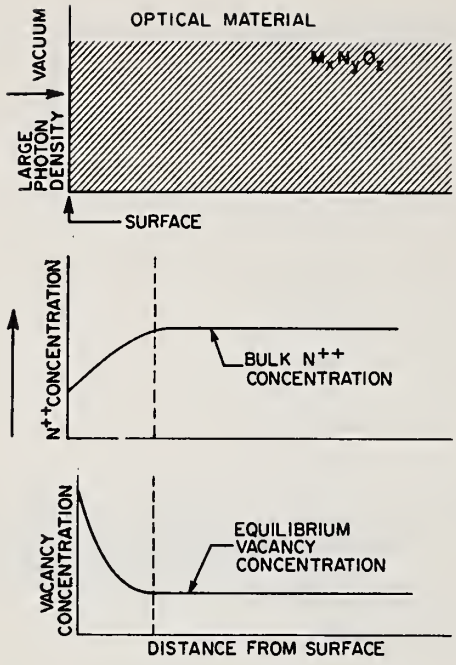

Figure 4. The ion and vacancy concentration near the surface of the optical material damaged by a phototransport process.

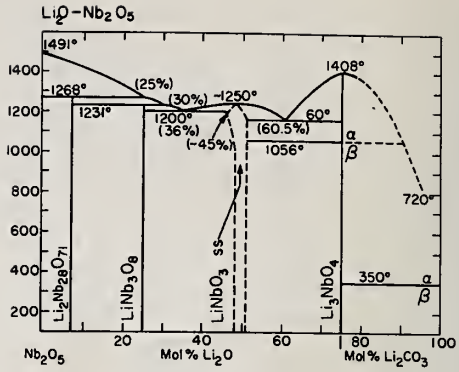

Figure 5. The equilibrium phase diagrams for the Li_2O - NbO_3 system [10].

COMMENTS ON PAPER BY WONG AND OLSON

It was pointed out that the momentum transfer from a photon to an atom is a maximum when the photon is resonantly absorbed or reflected from the atom and that the momentum transfer is just given by hν/c or 2 hν/c in that case. This is the basis of one proposal for laser isotope separation. The momentum transfer is small and increases with decreasing wavelength. The speaker felt that the effect might be much more significant at x-ray laser wavelengths. The effect is expected to be temperature dependent as well and one must examine whether the momentum obtained from the photons is sufficient to overcome the randomizing effect of the lattice phonon collisions. It is expected that the postulated effect, if it occurs, will be a cumulative effect leading to a net segregation and defect accumulation over a series of shots which in turn could lead to a higher probability of damage. Rates, being concentration dependent, will change during the cause of prolonged irradiation.

5.6 Resonant Defect Enhancement of the Laser Electric Field

P. A. Temple and M. J. Soileau
Michelson Laboratories, Naval Weapons Center
China Lake, California 93555

This paper describes a physical model for laser damage induced by surface defects. The model predicts that: (a) a polarizable defect will give rise to an electric field which can interfere with the laser field, (b) the interference pattern will be fixed in space along the direction of the laser beam polarization and with a spacing equal to the wavelength of the laser beam in the material, and (c) there is a strong defect size effect causing a significant increase in the field strength when the defect size is an odd number of half wavelengths. Experimental evidence supporting this model is presented.

Key words: Damage theory; laser damage; 10.6 μm laser.

Introduction

It has been observed that the laser damage thresholds of optical surfaces and thin films are reduced by defects [1,2][1]. This is to be expected since the electric fields are higher within defects [3]. A topological feature seen on laser-damaged surfaces is a wavelike set of ripples (figs. 1, 2) [4-6]. For the case of metals or semiconductors, the ripple spacing is λ, the free space laser wavelength. In the case of dielectrics, the spacing is $\lambda' = \lambda/n$, where n is the index of refraction of the material. These ripples are associated with surface defects, but the ripples occur away from the defect.

We wish to suggest an explanation for the ripple patterns. The patterns discussed in this paper were produced when the material was irradiated by a normally incident, linearly polarized, single-mode TEM_{00} laser pulse having a wavelength of 10.6 μm. The laser pulse width was approximately 60 ns full width at half maximum (FWHM). The ripples, such as those shown in figures 1 and 2, extend along the polarization direction (that is, the E vector is normal to the "waves" of the pattern) and are found to be associated with surface defects. While defects are generally recognizable as scratches, voids, etc., in the context of this paper a defect is any region of permittivity ε_2 which is different from the bulk permittivity ε_1.

Damage ripples are generated by a spatial modulation of the electric field intensity over the surface of the sample. The damage which occurs is a physical displacement and/or removal of material from the surface [7,8]. The spatial modulation in the electric field intensity will be shown to arise from the coherent interference of the incident laser field with the nonradiative longitudinal electric fields generated by the induced polarization charges present on the "boundaries" of defects within, or on the surface of the specimen. It will be shown that there is a definite size effect which causes an enhancement of the polarization-induced electric field and therefore, an increase in the modulation intensity when the defect diameter (or size) is an odd number of half wavelengths in the material. Finally, it is suggested that damage sites, once initiated as above, will act as new sources of electric field which then add in phase with the original defect field, resulting in a bootstrapping of damage ripple sites away from the original defect.

Electric Fields Caused by Defects

Figure 3 shows the surface polarization charge σ present when two dielectric materials of different permittivity are placed in a uniform electric field. If the electric field just within the defect is $\bar{E}_2'$, and the field is $\bar{E}_1'$ just outside the defect, then from the requirement that the normal components of the displacement vector be continuous across the boundary, it can be shown that the surface polarization charge density is

$$\sigma = \varepsilon_o \hat{n} \cdot (\bar{E}_1' - \bar{E}_2') \qquad (1)$$

where $\hat{n}$ is a unit vector normal to the defect and pointing away from it. In general the defect surface polarization charge will "follow" the incident (laser) electric field, and the magnitude of the polarization charge will be determined by the permittivities of the defect and host materials of the laser frequency.

A polarizable defect, for example a spherical particle, will generally reradiate energy with the familiar dipole radiation pattern when driven by a time-varying electromagnetic field. The maximum dipole radiation intensity is in the plane normal to the induced dipole axis. The dipole radiation intensity is zero on the line containing the induced dipole because the magnetic field is always zero on

1. Figures in brackets indicate the literature references at the end of this paper.

this symmetry axis, resulting in a zero Poynting vector. The electric field caused by the induced polarization surface charges, however, is not zero on this axis [9]. It will be shown that it is this time-varying "electrostatic" field which gives rise to surface ripples. The electrostatic fields resulting from induced surface charges will be calculated for two cases: a sphere, and a cylinder oriented with its axis normal to the incident laser polarization direction as well as normal to the laser radiation propagation direction. These two cases are simple models for pits or voids and scratches. In both cases we will only discuss the electric fields along the line which is parallel to the incident laser polarization direction and which passes through the center of the sphere or intersects, and is normal to, the axis of the cylinder. Along this "symmetry line" the induced electrostatic field is parallel to the laser field.

The defect electric field is time-varying as

$$\bar{E}(r,t) = \bar{E}(r) \sin 2\pi(\nu t + \Delta). \tag{2}$$

$\bar{E}(r)$, the maximum static defect field, is the electric field of the induced polarization charges generated by the peak electric field of the incident laser beam.

Sphere

The electrostatic field along the symmetry line of the sphere caused by the induced polarization charges is given by [10]

$$E(x)_{sphere} = 2a^3[(\epsilon_2 - \epsilon_1)/(\epsilon_2 + 2\epsilon_1)](E_1/x^3) \tag{3}$$

where a is the radius of the sphere, ϵ_1 the permittivity of the surrounding medium, E_1 the peak electric field of the laser beam in the defect-free surrounding medium, ϵ_2 the permittivity of the defect material, and x the distance from the center of the sphere to the field point. For example, for a spherical void in KCl of radius 2.5 μm, the static fields at distances of 10 μm and 30 μm from the void on the symmetry line are

$$E(10\ \mu m)_{sphere} = -6.7 \times 10^{-3}\ E_1; \quad E(30\ \mu m)_{sphere} = -2.5 \times 10^{-4}\ E_1 \tag{4}$$

and are parallel to the laser field. For a metallic defect we can assume that $\epsilon_2 >> \epsilon_1$, and eq. (3) then becomes a function of only a and x. For a particle of 2.5 μm radius the static fields are

$$E(10\ \mu m)_{sphere} = 3.1 \times 10^{-2}\ E_1; \quad E(30\ \mu m)_{sphere} = 5.8 \times 10^{-4}\ E_1. \tag{5}$$

Cylinder

The electrostatic field along the symmetry line (actually symmetry sheet) is given by [11]

$$E(x)_{cyl} = a^2[(\epsilon_2 - \epsilon_1)/(\epsilon_2 + \epsilon_1)](E_1/x^2) \tag{6}$$

where all the symbols have the same meanings as for the sphere. For a cylindrical void of radius 2.5 μm in KCl, the electric fields at distances of 10 μm and 30 μm from the cylinder are

$$E(10\ \mu m)_{cyl} = -2.2 \times 10^{-2}\ E_1; \quad E(30\ \mu m)_{cyl} = -2.5 \times 10^{-3}\ E_1, \tag{7}$$

again parallel to the incident laser field.

Interference with the Laser Field

The nonradiative electric fields expressed in eqs. (3-7) are time-varying with the frequency ν of the driving (laser) field. The net electric field intensity seen at any time and position along the symmetry line discussed previously is given by

$$E(x,t) = E(x)_{defect} \sin 2\pi\nu(t - x/c') + E_1 \sin 2\pi(\nu t + \delta) \tag{8}$$

where c' is the phase velocity of the electrostatic field of the induced polarization charges, and x is the position along the symmetry line from the defect to the field point; $E_1 \sin 2\pi(\nu t + \delta)$ is the electric field of the laser beam. Any time- and position-independent phase shift which may be present is given by δ.

At the time when $E_1 \sin 2\pi(\nu t + \delta) = E_1$, the field given by eq. (8) has the following characteristics (fig. 4a): Points A and C are positions of constructive interference, while points B and D are positions of destructive interference. One-half period later (fig. 4b), the positions of constructive interference, such as A and C, will again be positions of constructive interference, but with both the

laser electric field and the defect electric field being reversed in direction. Thus, when the defect field is added to the laser field, the resulting net field will exhibit maximal values spaced λ' apart along the symmetry line (points of constructive interference) and intermediate points with a field slightly lower than the laser field (points of destructive interference). The regions of constructive interference are fixed in space. The exact radial positions of the maximal points in the net electric field will depend on any time- and position-independent phase lags which exist between the induced polarization charges and the laser beam field, and on a 180° phase shift that may be present depending on which is larger, ε_1 or ε_2 (see eqs. 3,6). Point defects will exhibit fan-shaped ripple patterns when produced by linearly polarized light (fig. 2). Line defects will generate lines of ripples (fig. 1) which are parallel to the original defect.

The modulation in the electric field intensity resulting from the electrostatic field of a defect is on the order of ±2% adjacent to the defects (eqs. 4,7). It will now be shown that defects of certain sizes will result in a much larger modulation of the net field, particularly at points far from the defect.

Enhancement Caused by Propagation Delays

The instantaneous polarization charges generated in the above examples are distributed along the surfaces of the defect such that positive charge is along one side of the defect and negative charge is along the opposite side of the defect. The electric fields which are generated by these two sheets of charge and seen at some time t at a point P along the symmetry line are the result of the states of charge on the two sheets at two <u>different</u> earlier times. When the displacement of the two sheets of charge on the defect is on the order of one-half the wavelength of the incident laser radiation, a constructive interference condition will exist which will enhance the net defect-generated field as seen along the symmetry line.

Consider the field strengths E_1 and E_2 generated by two time-varying point charges, q_1 and q_2 at some time t (fig. 5). At a point P on the symmetry line, the fields seen at time t are

$$E_1(P,t) = \frac{q_o}{4\pi\varepsilon x^2} \sin 2\pi\nu \left(t - \frac{x}{c'}\right)$$

$$E_2(P,t) = \frac{-q_o}{4\pi\varepsilon (x+d)^2} \sin 2\pi\nu \left(t - \frac{x+d}{c'}\right) \qquad (9)$$

Case A

$d/c' = n\tau$, (or $d = n\lambda'$), where n is an integer and τ is the period of oscillation.

In this case $E_1 \approx -E_2$ and we have the usual near field "static" electric field due to a dipole.

Case B

$d/c' = n\tau/2$, (or $d = n\lambda'/2$), where n is an odd integer.

In this case $E_1 \approx +E_2$ as seen at point P, and the net electric field from the two point charges appears to be due to two charges of <u>like sign</u>. This case shows constructive interference, or resonance, with a resulting sinusoidally time-varying electric field which is the <u>sum</u> of two nearly identical electric fields rather than the difference of these two fields. As discussed above, this electric field will bear a fixed phase relation to the driving laser beam field independent of d and will give rise to a spatially modulated electric field on the symmetry line with maximal points spaced λ' apart (eq. 9). While the spherical and cylindrical defects do not give rise to the idealized dipole configuration used above, they do have well-separated charge distributions. The electric field for case B (resonant) will now be calculated.

Spherical Case, Resonant Condition

In the case of the sphere, charge is distributed on each hemisphere with charge density

$$\sigma = 3\varepsilon_o[(\varepsilon_2 - \varepsilon_1)/(\varepsilon_2 + 2\varepsilon_1)]\, E_1 \cos\theta \qquad (10)$$

where θ is the polar angle. The total charge on one hemisphere is

$$q = 3\varepsilon_o\, \pi a^2[(\varepsilon_2 - \varepsilon_1)/(\varepsilon_2 + 2\varepsilon_1)]\, E_1 \,. \qquad (11)$$

If we assume one-half the total charge on each hemisphere contributes to the constructive effect caused by propagation delay considerations, then we can approximate the field in the constructive case by considering +q/2 to be located as point charges on opposite sides of the sphere and on the symmetry line. A further simplification is to assume this net charge of q is located at the center of the sphere

rather than on opposite sides of the sphere. The field will then appear as the simple point charge field,

$$E(x) = q/4\pi\varepsilon_1 x^2 = [3\varepsilon_o a^2/4\varepsilon_1 x^2][(\varepsilon_2 - \varepsilon_1)/(\varepsilon_2 + 2\varepsilon_1)]\ E_1 \qquad (12)$$

which falls off as x^{-2} rather than as x^{-3} as in the static dipole case.

The fields for a spherical void in KCl having a radius a of 2.5 μm and distances x of 10 μm and 30 μm are

$$E(10\ \mu m)_{sphere} = -4.7 \times 10^{-3}\ E_1 \quad ; \quad E(30\ \mu m)_{sphere} = -5.2 \times 10^{-4}\ E_1 \quad . \qquad (13)$$

The field for a distance of 30 μm is significantly larger than the static field calculated for an identical distance and radius (eq. 4). For a metallic particle of similar size in KCl, the field can be calculated by assuming that $\varepsilon_2 >> \varepsilon_1$ in eq. (12). Then E(x) becomes independent of ε_2, $E(10\ \mu m) = 3.2 \times 10^{-2}\ E_1$ and $E(30\ \mu m) = 3.6 \times 10^{-3}\ E_1$. Again the field for a distance of 30 μm is significantly larger than the static field calculated for comparable conditions (eq. 5).

Cylindrical Case, Resonant Condition

In the case of the cylinder the polarization charge is distributed on each half cylinder with charge density,

$$\sigma = 2\varepsilon_o[(\varepsilon_2 - \varepsilon_1)/(\varepsilon_2 + \varepsilon_1)]\ E_1 \cos\theta \ . \qquad (14)$$

The total charge per unit length on each half cylinder is,

$$\tau = 4a\varepsilon_o[(\varepsilon_2 - \varepsilon_1)/(\varepsilon_2 + \varepsilon_1)]\ E_1 \quad . \qquad (15)$$

As in the resonant case for the sphere, we assume that the apparent charge density seen at P(x) is equivalent to that of a wire on the axis of the cylinder having charge per unit length τ. Then the field is

$$E(x) = \tau/2\pi\varepsilon_1 x = [2a\varepsilon_o/\pi\varepsilon_1 x][(\varepsilon_2 - \varepsilon_1)/(\varepsilon_2 + \varepsilon_1)]\ E_1 \qquad (16)$$

which falls off as x^{-1} rather than as x^{-2} as in the static cylinder case.

The fields for a particle radius a of 2.5 μm and distances x of 10 μm and 30 μm are

$$E(10\ \mu m)_{cyl} = -2.7 \times 10^{-2}\ E_1 \quad ; \quad E(30\ \mu m)_{cyl} = -9.0 \times 10^{-3}\ E_1 \qquad (17)$$

which for E(30 μm) is three times larger than the static field for a defect of the same dimension (eq. 7).

The strength of the additional fields discussed above are on the order of 2% of the incident field. If the incident laser beam intensity is sufficient to cause damage, then a ±2% modulation on the net electric field in the vicinity of the defect may well cause more damage in the regions of constructive interference and less damage in the regions of destructive interference. It will be shown in the next section that any damage which does occur will be spaced so as to cause additional fields of proper phase to add constructively with the original defect field. In this way, once initiated the damage pattern will tend to propagate in bootstrap fashion across the surface of the sample, with each successive damage site causing increased coherent scatter both back toward, and away from, the original defect.

Interference From Damaged Areas

Figures 1 and 2 show the appearance of typical ripple patterns as seen on the exit surfaces of KCl windows. Profilometry indicates that the patterns are actually undulations of the surface and not variations of the refractive index in the material [8]. A schematic diagram of this type of surface is shown in figure 6. In this figure the spacing between undulations is λ', the wavelength of the laser beam in the medium. While the damaged areas are shown as depressions, the only requirement is that they have a lower refractive index than the bulk material. When this lower refractive index appears, the sign of the polarization surface charge on each undulation corresponds to that shown in the figure. The charge distribution in each damage site is similar to the distribution in the original defect. However, each new "defect" is displaced an integral number of wavelengths from the original defect. Equation (9) indicates that the field at a point P and distance x from a defect is in phase with the field from another defect located $x + n\lambda'$ from the same point P, where n is an integer. Therefore, all the electric fields from all defects contribute in phase, resulting in a runaway situation once damage is initiated. The pattern finally dies away as the laser spot intensity falls off in the skirts of the beam.

The pattern, once initiated, will scatter both forward causing more damage ripples, and back causing increased damage to the already existing pattern. This scattering results in a larger net field for the constructive interference regions while the intermediate regions of destructive interference receive an ever decreasing net field. As the laser radiation continues, the pattern of ripples is therefore enhanced rather than washed out. Ripples having a peak-to-valley height of 0.1 μm have been observed in the bottom of a 2.5 μm deep damage crater in KCl [8].

Discussion

This paper presents a model for the interaction of a laser beam field with defects on optical surfaces. The model predicts that a nonradiative longitudinal electric field is generated by the laser-induced polarization charges at defect sites. The coherent interference of the induced field and the incident laser field results in a spatial modulation of the electric field intensity over the sample surface. This modulation of field intensity results in the ripple-like structure seen in laser-damaged surfaces. The sizes and orientations of the defects are found to be important. Maximum interaction with the defect occurs when the defect is an odd number of half wavelengths in width (or diameter), and in the case of a scratch, when the defect is normal to the polarization direction of the incident laser beam. Once generated, "ripples" on the surface become new defects of exactly the right spacing and orientation needed for maximum interaction with the incident laser beam. Thus, the ripples become self reinforcing and this bootstrap effect results in the production of more ripples. Near threshold, surface damage will be dominated by defects. Even very small defects become important because of the unstable condition produced by the induced electric field. All of these effects have been observed experimentally, and the details of two such observations are discussed in the following paragraphs.

Figure 1 shows the exit surface of a KCl window which was damaged by a single 60 ns pulse (FWHM) of polarized radiation having a wavelength of 10.6 μm. The damage pattern of ripples, spaced 7.5 μm apart, was propagated outward from a scratch. Notice that the scratch was enlarged and has the size and appearance of one of the damage ripples, indicating that the ripples have scattered the electric field back to the original defect. Once the damage pattern was established, the original defect was incorporated into the pattern as one more damage ripple. While other scratches exist on the window surface, the low polarizability of a defect whose axis is parallel to the laser polarization direction kept those scratches from generating damage patterns.

For a spherical defect (fig. 2) the pattern is fan-shaped. The orientation of ripples in this figure indicates that the longitudinal electrostatic field from the defect contributes to the damage and that the radiative electric field does not.

The phenomena discussed in this paper have direct bearing on the fabrication of optical components for laser use. Scratches normal to the laser field are to be avoided. Sharp surface discontinuities are more of a problem than are smooth ones. One should not use polishing or grinding particles of sizes near odd half-integral multiples of the laser wavelengths, and defects of these widths should be avoided. Surfaces produced by single point diamond turning have defects which are relatively well-oriented and have a relatively well-defined spacing which can be controlled by varying the machine parameters, such as spindle speed, feed rate, and tool-cutting angle. Deep chemical etches which enhance grain boundaries should be avoided, but light etches which tend to smooth defect edges could be very beneficial in raising surface damage thresholds. In summary, by controlling the shape, size, and orientation of defects on optical surfaces one can raise the damage threshold even if the total number of defects is not decreased.

Acknowledgments

This work was supported by the Energy Research and Development Administration, the Defense Advanced Research Projects Agency, the Air Force Weapons Laboratory, and Naval Weapons Center Independent Research Funds. The authors wish to acknowledge many helpful discussions with D. L. Decker concerning polarizable defects in optical materials.

References

[1] For example see A. J. Glass and A. H. Guenther, in *Laser Induced Damage in Optical Materials: 1974*, A. J. Glass and A. H. Guenther, eds. (NBS Spec. Publ. 414, 1974), pp. vii-xx.

[2] De Shazer, L. G., et al., in *Laser Induced Damage in Optical Materials: 1974*, A. J. Glass and A. H. Guenther, eds. (NBS Spec. Publ. 414, 1974), pp. 214-218.

[3] Bloembergen, N., Appl. Opt. 12, 661 (1973).

[4] Willis, L. J., and Emmony, D. C., Optics and Laser Technol. 7, 222 (1975).

[5] Soileau, M. J., et al., in *Proceedings of Fifth Annual Conference on Infrared Laser Window Materials: 1975*, C. R. Andrews and C. L. Strecker, eds. (Defense Advanced Research Projects Agency, Arlington, Va., 1976), pp. 391-417.

[6] Bass, M., et al., "Pulsed Laser-Induced Damage at the DF Wavelengths," these Proceedings.

[7] Soileau, M. J., et al., "Laser Damage Studies of Low Index Coating Materials at 10.6 μm," these Proceedings.

[8] Soileau, M. J., et al., "10.6 μm Pulsed Laser Damage Studies of Diamond Turned KCl Window Surfaces," these Proceedings.

[9] Jackson, J. D., *Classical Electrodynamics* (John Wiley & Sons, New York, 1962), p. 272.

[10] Stratton, J. A., *Electromagnetic Theory* (McGraw-Hill, New York, 1941), p. 204-205.

[11] Morse, P. M. and Feshbach, H., *Methods of Theoretical Physics* (McGraw-Hill, New York, 1953), p. 1184.

Figures

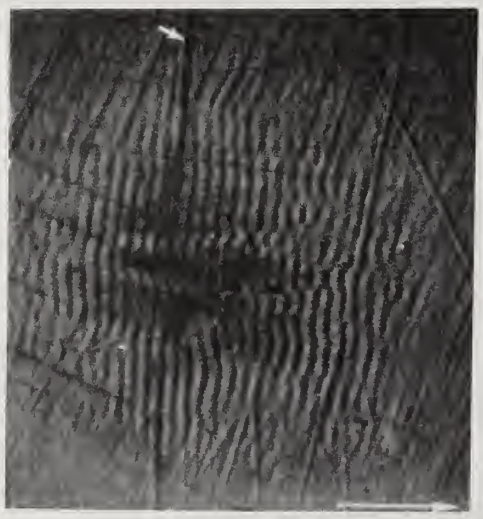

Figure 1. Nomarski micrograph of the exit surface of a KCl window which has been damaged by a single pulse of 10.6 μm laser radiation. The polarization direction is indicated by the arrow in the lower right corner of the figure. The spacing of the ripples is 7.5 μm. The upper arrow indicates the scratch which initiated the damage pattern.

Figure 2. Nomarski micrograph of the exit surface of a KCl window which has been damaged by a single pulse of 10.6 μm laser radiation. The polarization direction is indicated by the arrow. The damage was initiated by a particle defect and the spacing of the ripples is 7.5 μm.

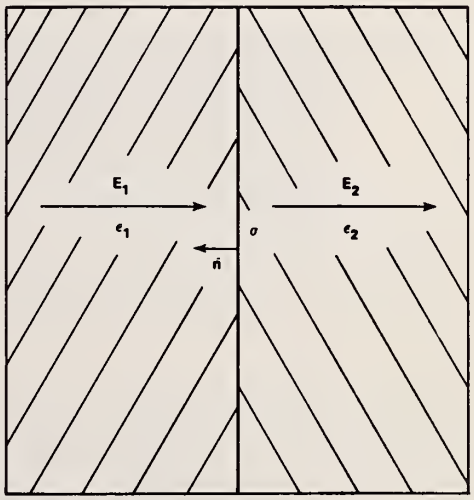

Figure 3. Schematic diagram showing the electric fields E_1 and E_2, the permittivities ε_1 and ε_2, unit normal $\hat{n}$, and surface charge density σ for two dielectrics in contact. Equation (1) gives the relationship between these variables.

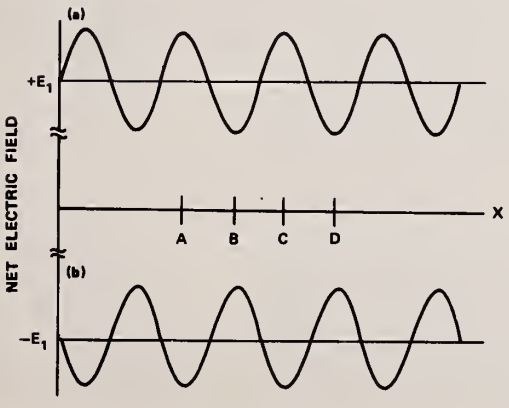

Figure 4. Electric field near a surface defect showing the spatial modulation in electric field intensity introduced by the defect. (a) The electric field is shown at time t, the time when the electric field of the laser beam is a maximum, E_1. (b) The electric field at time $t + \tau/2$, showing that points A and C, which were points of constructive interference at time t are also points of constructive interference one-half period later. Points B and D are points of destructive interference. The spacing A-C is λ', the laser wavelength in the medium.

Figure 5. Spatial arrangement of two point charges q_1 and q_2 separated by a distance d. The field point P is located directly above the two charges, a distance x from the top charge, eq. (9).

Figure 6. Schematic diagram of the original defect, such as a scratch, and the ripples caused by the enhanced electric field caused by the defect. The signs of the surface polarization charge produced by the laser beam electric field are indicated.

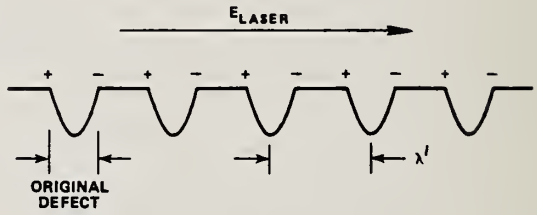

COMMENTS ON PAPER BY TEMPLE AND SOILEAU

It was anticipated that circularly polarized light would lead to a different kind of pattern, perhaps circularly symmetrical, but the analysis had not been carried out. The speaker cautioned that the process can propagate through the material since the ripple pattern set up by a scatterer leads to local index variations (due to the unspecified damage process) which in turn leads to further scattering.

APPENDIX I

PARTICIPANTS

A

C. M. Allred	Electromagnetics Division, National Bureau of Standards, Boulder, CO 80302
R. H. Anderson	Honeywell Corp. Res. Ctr., 10701 Lyndale Ave. So., Bloomington, MN 55420
J. P. Anthes	Sandia Labs, Laser Dev. Div., Albuquerque, NM 87115
J. H. Apfel	Optical Coating Lab., Inc., P. O. Box 1599, Santa Rosa, CA 95402
L. J. Aplet	Hughes Aircraft Co., M.S. E119, Centinela & Teale Sts., Culver City, CA 90230

B

A. D. Baer	Naval Weapons Center, Research, Code 6018, China Lake, CA 93555
A. Balbin-Villaverde	Instituto De Fisica-Universidade Estadual De Campinas, Campinas, Sao Paulo, Brazil 13100
N. Barnes	Los Alamos Scientific Labs., M/S 564, P. O. Box 1663, Los Alamos, NM 87545
M. Bass	U. of So. California, Center for Laser Studies, University Park, Los Angeles, CA 90007
H. E. Bennett	Michelson Lab., Naval Weapons Center, Code 6018, China Lake, CA 93555
E. Bernal G.	Honeywell Corp. Res. Center, Materials Sc. Dept., 10701 Lyndale Ave. So., Bloomington, MN 55420
J. R. Bettis	U. S. Air Force, AFWL/LRE, Kirtland Air Force Base, NM 87117
A. D. Blackburn	U. S. Air Force, AFWL/LRE, Kirtland Air Force Base, NM 87117
N. Boling	Owens-Illinois, Inc., 1700 No. Westwood, Toledo, OH 43666
W. T. Boord	Honeywell Systems & Res. Ctr., R2340, 2600 Rideway Pkwy., Minneapolis, MN 55413
G. H. Boultbee	Optical Coating Lab., 2789 Giffen Ave., Santa Rosa, CA 95404
H. S. Boyne	Electromagnetics Division, National Bureau of Standards, Boulder, CO 80302
M. Braunstein	Hughes Res. Labs., Chem. Physics Dept., 3011 So. Malibu Canyon Rd., Malibu, CA 90265
R. E. Brocklehurst	Wright-Patterson AFB, AF Materials Lab., AFML/LP, Dayton, OH 45433
R. R. Brown	Boeing Co., Res. & Eng. Div., MS 87/75, P. O. Box 3999, Seattle, WA 98006
J. Bruce	Hanscom Air Force Base, RADC/ETSO, Stop 30, Bedford, MA 01731
B. Burdick	United Technologies Res. Ctr-73, Silver Lane, East Hartford, CT 06108
M. W. Burnham	Rockwell International, Rocky Flats Plant, Box 464, Golden, CO 80401

C

R. M. Cannon, Jr.	Mass. Inst. of Technology, Dept. Mat. Sc. & Eng., Cambridge, MA 02137
G. E. Chamberlain	Electromagnetics Division, National Bureau of Standards, Boulder, CO 80302
J. Y. Chang	Grumman Aerospace Corp., Res. Dept., Plant 26, Bethpage, NY 11714
A. R. Cook	Electromagnetics Division, National Bureau of Standards, Boulder, CO 80302
V. Costich	Design Optics, 155 Moffett Park Blvd., Sunnyvale, CA 94086
F. K. Crosher	Optical Coating Lab., Inc., Adv. Prod. Dev., P. O. Box 1599, Santa Rosa, CA 95403

D

B. L. Danielson	Electromagnetics Division, National Bureau of Standards, Boulder, CO 80302
G. W. Day	Electromagnetics Division, National Bureau of Standards, Boulder, CO 80302
D. L. Decker	Naval Weapons Center, Code 6018, China Lake, CA 43555
L. Decker	Lockheed Res. Labs., Dept. 52-56, Bldg. 201, 3251 Hanover St., Palo Alto, CA 94304
J. A. Detrio	U. of Dayton, Res. Inst., 300 College Park, Dayton, OH 45469
M. J. Dodge	National Bureau of Standards, Div. 232.03, A251 Physics Bldg., Washington, D. C. 20234
C. J. Duthler	Xonics Inc., 6849 Hayvenhurst Ave., Van Nuys, CA 91406

E

F. L. Ebright	Science Applications, Inc., 201 S.W. Monterey Rd., Stuart, FL 33494
D. F. Edwards	Los Alamos Scientific Lab., MS/564, Los Alamos, NM 87545
R. Esposito	International Laser Systems (Kirtland AFB), 729 Sagebrush Trail, Albuquerque, NM 87123
W. S. Ewing	Hanscom Air Force Base, RADC/ETSO-30, Bedford, MA 01731

F

A. Feldman	National Bureau of Standards, A259, Materials Bldg., Washington, D. C. 20234
J. R. Fenter	Wright-Patterson AFB, AF Materials Lab., AFML/LPO, Dayton, OH 45433
D. G. Fischer	Coherent Radiation, 3210 Porter Dr., Palo Alto, CA 94304
A. M. Frank	Lawrence Livermore Lab., L-384 ME/Optics, P. O. Box 808, Livermore, CA 94550
D. L. Franzen	Electromagnetics Division, National Bureau of Standards, Boulder, CO 80302
W. G. D. Frederick	Wright-Patterson AFB, AF Materials Lab., AFML/LPO, Dayton, OH 45433
W. J. Fredericks	Oregon State University, Chem. Dept., Corvallis, OR 97331

G

D. E. Gilbert	Research Triangle Institute, P. O. Box 12194, Research Triangle Park, NC 27709
D. H. Gill	Los Alamos Scientific Lab., MS/552, Los Alamos, NM 87544
A. J. Glass	Lawrence Livermore Lab., L-547, P. O. Box 808, Livermore, CA 94505
A. Glassman	Spectra Physics, 1250 W. Middlefield Rd., Mountain View, CA 94042
G. A. Graves	U. of Dayton Research Inst., Rm 162, 300 College Pk., Dayton, OH 45469
P. M. Gruzensky	Electromagnetics Division, National Bureau of Standards, Boulder, CO 80302
A. H. Guenther	Air Force Weapons Lab/CA, Kirtland AFB., NM 87117
S. K. Gulati	U. of New Mexico, Dept. of Elec. Eng. & Computer Sci., Albuquerque, NM 87131

H

R. J. Harrach	Lawrence Livermore Lab., L-71, P. O. Box 808, Livermore, CA 94550
J. A. Harrington	U. of Alabama in Huntsville, Physics Dept., Huntsville, AL 35807
J. Hayden	Los Alamos Scientific Lab., MS-548, Los Alamos, NM 87545
K. Hebert	Design Optics, 155 Moffett Park Dr., Sunnyvale, CA 94086
D. Heiman	U. Southern California, Physics Dept., University Park, CA 90007
R. Hellwarth	U. Southern California, Physics Dept., University Park, CA 90007
G. L. Hennessey	Valtec Corp., Optical Coatings Div., 36 Pope Rd., Holliston, MA 01746
L. M. Hobrock	Hughes Aircraft Co., Optics Dept., Centinela & Teale Sts., Culver City, CA 90230
R. T. Holm	Naval Research Lab., Code 5233, Washington, D. C. 20375
S. J. Holmes	Northrop Research & Technology Center, 3401 W. Broadway, Hawthorne, CA 90250
A. Hordvik	Hanscom Air Force Base, RADC/ETSL, Bedford, MA 01731
R. A. House II	Air Force Weapons Lab/LRE, Kirtland AFB, NM 87117
J. E. Howard	U. of Wisconsin, Nuclear Eng. Dept., Madison, WI 53706
L. Huff	U. of Dayton Res. Inst., 300 College Park Ave., Dayton, OH 45469
C. A. Huguley	Air Force Weapons Lab/LRE, Kirtland AFB, NM 87111
G. J. Hutcheson	U. S. Army Missile Command, DRSMI/QRT, Bldg. 4500, Redstone Arsenal, AL 35809
T. V. Hynes	U. S. Army Materials & Mechanics Res. Ctr., Arsenal St., Watertown, MA 02173

I

W. Icenogle	Spectra Physics, 1250 W. Middlefield Rd., Mountain View, CA 94042

J

S. D. Jacobs	U. of Rochester, Lab for Laser Energetics, Hopeman Hall, River Station, Rochester, NY 14627
W. Q. Jeffers	Helios, Inc., P. O. Box 2190, Boulder, CO 80302
R. J. Jelly	E-A Industrial Corp., 4500 No. Shallowford Rd., Chamblee, GA 30341
G. T. Johnston	U. of Dayton Res. Inst., 300 College Park Ave., Dayton, OH 45469

K

M. A. Kahan	ITEK Corp., Optical Systems Div., Dept. 1-550/MS/K-346, 10 Maguire Rd, Lexington, MA 02173
T. Kardos	Broomer Res. Lab., 23 Sheer Plaza, Plainview, NY 11803
C. A. Klein	Raytheon Res., 28 Seyon St., Waltham, MA 02154
P. H. Klein	Naval Research Lab., Code 5222, Washington, D. C. 20375
A. Klugman	Northrop Research & Tech. Center, 374/61, 3401 W. Broadway, Hawthorne, CA 94304
B. Koepke	Honeywell Corp. Res. Center, 10701 Lyndale Ave., So., Bloomington, MN 55420
T. Kohane	Raytheon Res. Div., 28 Seyon St., Waltham, MA 02154
P. Kraatz	Northrop Res. & Tech. Center, 374/61, 3401 W. Broadway, Hawthorne, CA 90250

L

H. P. LeBodo	Laboratoire National d'Essais, Laser Div., 1 rue G-Boissier, Paris 75015, France
H. A. Lee	Owens-Illinois, Inc., Box 1035, Toledo, OH 43666
K. M. Leung	U. of So. California, Center for Laser Studies, 206 APL, University Park, Los Angeles, CA 90007
P. W. Levy	Brookhaven Nat. Lab., Physics Dept., 510-B, Upton, NY 11973
D. H. Liebenberg	Los Alamos Scientific Lab., MS/530, P. O. Box 1663, Los Alamos, NM 87545
R. M. F. Linford	McDonnell Douglas Corp., E-457, P. O. Box 516, St. Louis, MO 63166
H. G. Lipson	Hanscom Air Force Base, RADC/ESD, ETSS, Bedford, MA 01731
J. S. Loomis	U. of Arizona, Optical Sciences Center, Tuscon, AZ 85721
J. D. Lytle	Lockheed Res. Labs., Dept. 52-56, 3251 Hanover St., Palo Alto, CA 94304

M

R. W. MacPherson	Defence Res. Estab. Valcartier, Electro-Optics Div., P. O. Box 880, Courcellette, Quebec, GOA IRO
S. Manlief	Mass. Inst. of Technology, Lincoln Lab., Box 73, Lexington, MA 02173
D. Milam	Lawrence Livermore Lab., P. O. Box 808, Livermore, CA 94505
D. Morelli	Optical Coating Lab., P. O. Box 1599, Santa Rosa, CA 95403
D. L. Mullen	U. of Dayton Res. Inst., Kirtland AFB, AFWL/LRE, Albuquerque, NM 87117

N

B. E. Newnam	Los Alamos Scientific Lab., MS/552, P. O. Box 1663, Los Alamos, NM 87545
D. B. Nichols	Boeing Aerospace Co., MS/88-46, Box 3999, Seattle, WA 98055
W. P. Norris	Naval Weapons Center, Code-6056, China Lake, CA 93555

O

M. C. Ohmer	Wright-Patterson AFB, AF Materials Lab, Dayton, OH 45433
D. L. Olson	Colorado School of Mines, Dept. of Met. Eng., Hill Hall, Golden, CO 80421
D. R. Olson	Perkin-Elmer, MS/217, Main Avenue, Norwalk, CT 06856
R. M. Ono	Rocketdyne Div., Rocketwell Int., 521-197, 6633 Canoga Ave., Canoga Park, CA 91304

P

R. H. Picard	Rome Air Dev. Center, RADC/ETSL, MS/30, Hanscom AFB, Bedford, MA 01731
R. W. Pierce	Naval Weapons Center, Code-4051, China Lake, CA 93555
P. Pirooz	Owens-Illinois Co., Corp. Dev. Dept., P. O. Box 1035, Toledo, OH 43666
B. Platt	U. of Dayton Res. Inst., Kirtland AFB, AFWL/LRE, NM 87117
R. O. Pohl	Cornell U., Physics Dept., Clark Hall, Ithaca, NY 14850
J. O. Porteus	Naval Weapons Center, Code 6017, China Lake, CA 93555

R

W. L. Ramer	Rockwell Int'l., Dev. & Proj. Eng., P. O. Box 464, Golden, CO 80401
S. Refermat	U. of Rochester, Lab. for Laser Energetics, Hopeman 110, River Campus, Rochester, NY 14618
W. H. Reichelt	Los Alamos Scientific Lab., MS/532, Los Alamos, NM 87545
R. E. Rondeau	Wright-Patterson AFB, AF Materials Lab., AFML/LPJ, Dayton, OH 45433
T. Roszhart	TRW Systems, Inc., One Space Park, Redondo Beach, CA 90278
J. Rowe	Northrop Res. Tech. Center, 3401 W. Broadway, Hawthorne, CA 90250
A. M. Rubenstein	Inst. for Defense Analyses Res. Staff, Sci. & Tech. Div., 400 Army Navy Dr., Arlington, VA 22209
J. E. Rudisill	Hughes Res. Labs., 3011 Malibu Canyon Rd., Malibu, CA 90265
P. M. Rushworth	Martin-Marietta Corp-Orlando, MP/276, Box 5837, Orlando, FL 32808

S

T. T. Saito	Lawrence Livermore Lab., L-140, P. O. Box 808, Livermore, CA 94550
A. A. Sanders	Electromagnetics Division, National Bureau of Standards, Boulder, CO 80302
R. E. Seddon	Optical Coating Lab., Inc., Technical Div., P. O. Box 1599, Santa Rosa, CA 95401
M. Shen	U. of California, Chemical Eng., Berkeley, CA 94720
D. H. Sherman	II-VI, Inc., 207 Garden Lane, Glenshaw, PA 15116
A. R. Shimkunas	Optical Coating Lab., Inc., Research, P. O. Box 1599, Santa Rosa, CA 95402
R. A. Skogman	Honeywell Corp. Res. Ctr., 10701 Lyndale Ave. So., Bloomington, MN 55420
R. E. Sladky	Union Carbide Corp., Y-12 Plant, Bldg. 9998, Oak Ridge, TN 37830
R. L. Smith	Electromagnetics Division, National Bureau of Standards, Boulder, CO 80302
M. J. Soileau	Naval Weapons Center, Code 6018, China Lake, CA 93555
M. Sparks	Xonics, Inc., 1333 Ocean Ave., Santa Monica, CA 90401
W. Spawr	Spawr Optical Res., Inc., 1521 Pomona Rd., Corona, CA 91720
J. L. Stanford	Naval Weapons Center, Code 6018, China Lake, CA 93555
J. L. Stapp	U.S. Air Force, 2115 Carter Hill Rd., Mongtomery, Al 36617
J. Starling	Honeywell, Ceramics Ctr/V-1864, 1885 Douglas Dr., No., Golden Valley, NY 55422
T. G. Stoebe	U. of Washington, Dept. of Mining, Metallurgy & Ceramic Engr., Roberts Hall, FB-10, Seattle, WA 98195
R. Strandlund	Optical Coating Lab., Inc., P. O. Box 1599, Santa Rosa, CA 95401
C. L. Strecker	Air Force Materials Lab., WPAFB, LPO, Dayton, OH 54533
P. R. Stuart	National Physical Lab., Dov. of Mechanical & Optical Metrology, Teddington, Middlesex, England
O. F. Swenson	AF Materials Lab., AFML/LPO, WPAFB, Dayton, OH 45433
H. F. Swift	U. of Dayton Res. Inst., Dayton, OH 45469

T

C. Tang	U. of So. California, APL 211, Ctr. for Laser Studies, University Park, Los Angeles, CA 90007
P. A. Temple	Naval Weapons Center, Code 6018, China Lake, CA 93555
H. L. Tuller	Mass. Inst. of Technology, Dept. Materials Sci., Cambridge, MA 02139

W

V. Wang	Hughes Res. Lab., Opto Electronics Dept., 30-25, 3011 Malibu Canyon Rd., Malibu, CA 90265
R. Watt	L.A.S.L., P. O. Box 1663, Los Alamos, NM 87545
J. A. Weiss	Energy Res. & Development Admin., Div. of Laser Fusion, Washington, D. C. 20545
C. B. Willingham	Raytheon Co., Research Div., 28 Seyon St., Waltham, MA 02154
R. Windebank	Laser Optics, Inc., Mill Plain Rd., Danbury, CT 06810
I. M. Winer	Kirtland AFB, AFWL/ILS, Box 9316, Int'l. Airport, Albuquerque, NM 87117
H. V. Winsor	DARPA/MSO, 1400 Wilson Blvd., Arlington, VA 22209
R. M. Wolff	Valtec, Western Div., Box 2311, Newport Beach, CA 92663
S. M. Wong	Rockwell Int'l., Atomic Energy Div., Rocky Flat Plant, Bldg. 779, P. O. Box 464, Golden, CO 80401
R. M. Wood	Hirst Res. Centre, General Electric Co., Ltd., East Land, Wembley, Middlesex, England

Y

S. Yee	U. of Washington, Elec. Engr., Dept. FT-10, Seattle, WA 98105

Z

J. L. Zar	AVCO Everett Research Lab., Inc., Everett, MA 01845
R. W. Zimmerer	Scientech, Inc., 5649 Arapahoe Ave., Boulder, CO 80303
D. Zuccaro	Hughes Res. Labs., 3011 Malibu Canyon Rd., Malibu, CA 90265

NBS-114A (REV. 7-73)

U.S. DEPT. OF COMM. BIBLIOGRAPHIC DATA SHEET	1. PUBLICATION OR REPORT NO. Special Publication 462	2. Gov't Accession No.	3. Recipient's Accession No.

4. TITLE AND SUBTITLE

Laser Induced Damage in Optical Materials: 1976

5. Publication Date: December 1976

6. Performing Organization Code

7. AUTHOR(S)
Edited by Alexander J. Glass and Arthur H. Guenther

8. Performing Organ. Report No.

9. PERFORMING ORGANIZATION NAME AND ADDRESS

NATIONAL BUREAU OF STANDARDS
DEPARTMENT OF COMMERCE
WASHINGTON, D.C. 20234

10. Project/Task/Work Unit No.

11. Contract/Grant No.

12. Sponsoring Organization Name and Complete Address (Street, City, State, ZIP)
Electromagnetics Division, National Bureau of Standards, Boulder, CO 80302
American Society for Testing & Materials, Phila., PA 19103
Dept. of the Navy, Office of Naval Research, Arlington, VA 22217
Energy Research & Development Admin., Washington, D. C. 20234
Defense Advanced Research Project Agency, Washington, D. C. 20234

13. Type of Report & Period

14. Sponsoring Agency Code

15. SUPPLEMENTARY NOTES

Library of Congress Card Catalog Number: 76-600074

16. ABSTRACT (A 200-word or less factual summary of most significant information. If document includes a significant bibliography or literature survey, mention it here.) The Eighth Annual Symposium on Optical Materials for High Power Lasers, the Boulder Damage Symposium, was hosted by the National Bureau of Standards in Boulder, Colorado, from July 13th to 15th. The Symposium was held under the auspices of ASTM Committee F-1, Subcommittee on Laser Standards, with the joint sponsorship of NBS, the Defense Advanced Research Project Agency, the Energy Research and Development Administration, and the Office of Naval Research.

About 160 scientists attended the Symposium, including representatives of the United Kingdom, France, Canada, and Brazil. The Symposium was divided into five half-day sessions, concerning Bulk Material Properties and Thermal Behavior, Mirrors and Surfaces, Thin Film Properties, Thin Film Damage, and Scaling Laws and Fundamental Mechanisms.

As in previous years, the emphasis of the papers presented at the Symposium was directed towards new frontiers and new developments. Particular emphasis was given to new materials for use at 10.6 μm in mirror substrates, windows, and coatings. New techniques in film deposition, and advanced in diamond turning of optics were described. The scaling of damage thresholds with pulse duration, focal area, and wavelength are discussed.

Alexander J. Glass of Lawrence Livermore Laboratory and Arthur H. Guenther of the Air Force Weapons Laboratory were Co-chairpersons of the Symposium. The Ninth Annual Symposium is scheduled for October 4-6, 1977, at the National Bureau of Standards, Boulder, Colorado.

17. KEY WORDS (six to twelve entries; alphabetical order; capitalize only the first letter of the first key word unless a proper name; separated by semicolons)
Avalanche ionization; infrared windows; laser damage; metal mirrors; optical fabrication; optical materials; thin films.

18. AVAILABILITY

[X] Unlimited

[ ] For Official Distribution. Do Not Release to NTIS

[X] Order From Sup. of Doc., U.S. Government Printing Office Washington, D.C. 20402, SD Cat. No. C13.10:462

[ ] Order From National Technical Information Service (NTIS) Springfield, Virginia 22151

19. SECURITY CLASS (THIS REPORT)
UNCLASSIFIED

21. NO. OF PAGES
410

20. SECURITY CLASS (THIS PAGE)
UNCLASSIFIED

22. Price
$4.60

USCOMM-DC 29042-P74

SINGLE CRYSTAL DATA

REVISED! UPDATED!

In 1954, the first edition of CRYSTAL DATA (Determinative Tables and Systematic Tables) was published as Memoir 60 of the Geological Society of America. In 1960, the second edition of the Determinative Tables was issued as Monograph 5 of the American Crystallographic Association, and in 1967, the Systematic Tables were issued as Monograph 6. These editions proved extremely valuable to crystallographers throughout the world. Recognizing the need for updated crystallographic information, the National Bureau of Standards Office of Standard Reference Data has sponsored the issuance of a new edition.

This, the THIRD EDITION, should be of particular interest not only to crystallographers but also to chemists, mineralogists, physicists and individuals in related fields of study. The current edition, which comprises two volumes, Organic and Inorganic, is a thoroughly revised and updated work, containing over 25,000 entries.

The entries are listed, *within each crystal system*, according to increasing values of a determinative number: a/*b* ratio in trimetric systems, c/a ratio in dimetric systems, and cubic cell edge a, in the isometric system. In addition, the following information is given:

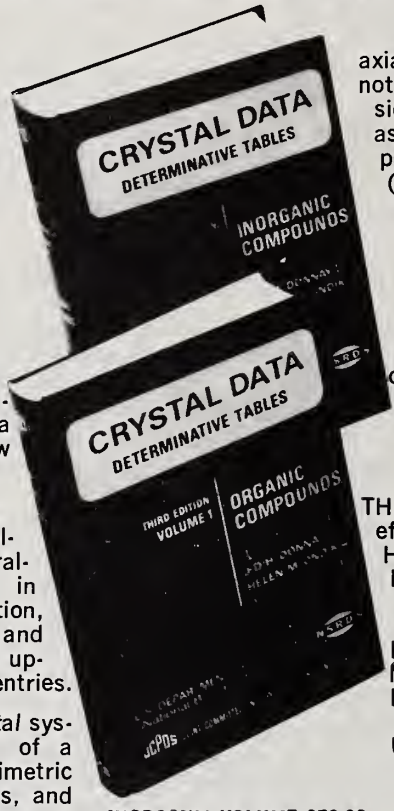

INORGANIC VOLUME $50.00

ORGANIC VOLUME $30.00

Plus shipping and handling

axial ratio(s) and interaxial angles not fixed by symmetry, cell dimensions, space group or diffraction aspect, number of formula units per unit cell, crystal structure, (whether determined), measured density and x-ray calculated density. Also listed is the name of the compound and synonym(s), chemical formula, literature reference and transformation matrix. When available, the crystal structure type, crystal habit, cleavages, twinning, color, optical properties, indices of refraction, optical orientation, melting point and transition point are also listed.

THIS EDITION culminates years of effort by J. D. H. Donnay, Johns Hopkins University, Helen M. Ondik, National Bureau of Standards, Sten Samson, California Institute of Technology, Quintin Johnson, Lawrence Radiation Laboratory, Melvin H. Mueller, Argonne National Laboratory, Gerard M. Wolten, Aerospace Corporation, Mary E. Mrose, U.S. Geological Survey, Olga Kennard and David G. Watson, Cambridge University, England and Murray Vernon King, Massachusetts General Hospital.

Shipments are made via insured parcel post. Additional charges for shipments by air or commercial carrier.
TERMS: Domestic—30 days Foreign—prepayment required. Address all orders to:
JOINT COMMITTEE ON POWDER DIFFRACTION STANDARDS 1601 Park Lane, Swarthmore, Pennsylvania 19081

Please accept my order for CRYSTAL DATA, DETERMINATIVE TABLES, Third Edition, Donnay/Ondik.

☐ **Organic Volume**

☐ **Inorganic Volume**

Ship to: _____

_____

Signature _____

NATIONAL STANDARD REFERENCE DATA SYSTEM
NSRDS

JCPDS

Time Was When Energy Was Cheaper

...but that's all changed now.

Today, increased energy costs—caused by increasing demand—boost the price of consumer goods, fuel inflation, and hurt our balance of payments.

That's why conserving energy is a must today, especially for you in the business and industry community which uses two thirds of our nation's energy.

Now . . . there's a book to tell you how to do it. It's called *EPIC—the Energy Conservation Program Guide for Industry and Commerce.* Prepared for you by the Commerce Department's National Bureau of Standards in cooperation with the Federal Energy Administration.

EPIC is a comprehensive handbook that can help you establish or improve an energy conservation program in your organization.

Not only industry and commerce but also hospitals, universities, research institutes, ANY organization that uses energy—and has to pay the bills—will want a copy of *EPIC.*

EPIC **outlines in detail the steps in setting up an energy conservation program.**

It contains a checklist of more than 200 Energy Conservation Opportunities—suggestions to save energy in a dozen different areas.

EPIC's actual case histories of energy saving actions help you estimate your potential for saving energy—and reducing costs.

And *EPIC* contains much more—financial analysis procedures to evaluate projects, sources of information on energy conservation, engineering data and factors, an energy conservation bibliography.

Make *EPIC* part of your plan to control energy use and costs. Make *EPIC* part of your contribution to using energy resources wisely . . . so we can keep America working and growing.

To order your copy of *EPIC*, send $2.90 per copy (check, money order or Superintendent of Documents Coupons) to Superintendent of Documents, U.S. Government Printing Office, Washington, D.C. 20402. Ask for NBS Handbook 115, EPIC, C13.11:115. Discount of 25% on orders of 100 copies or more.

ENERGY CONSERVATION PROGRAM GUIDE FOR INDUSTRY AND COMMERCE

U.S. DEPARTMENT OF COMMERCE / National Bureau of Standards
FEDERAL ENERGY ADMINISTRATION / Conservation and Environment

make color work for you

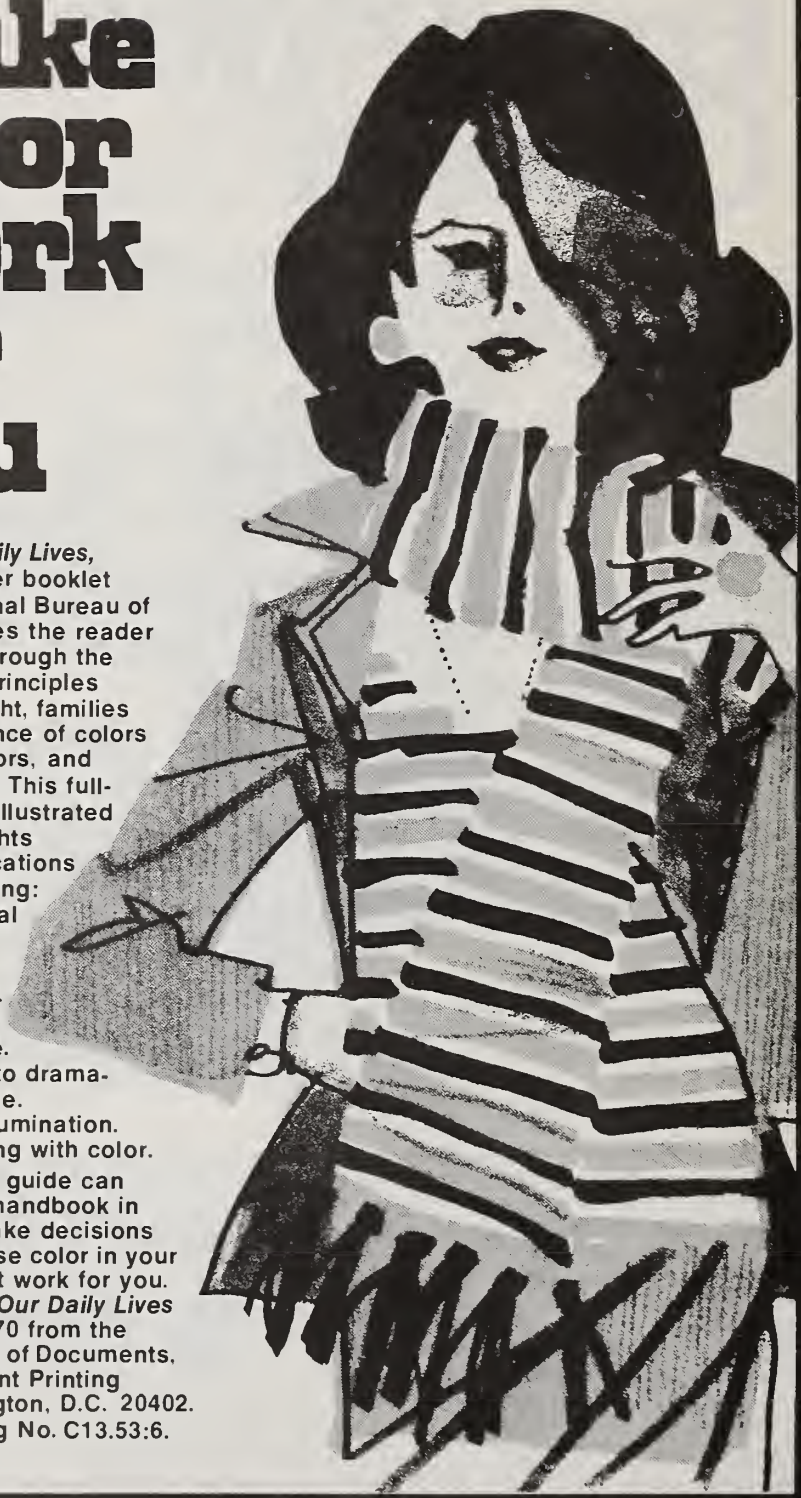

Color in our Daily Lives, a new consumer booklet from the National Bureau of Standards, takes the reader step by step through the fundamental principles of color and light, families of color, influence of colors upon other colors, and color harmony. This full-color, 32-page illustrated booklet highlights practical applications of color, including:

- Your personal color plan.
- Your color environment.
- Color plans for the home.
- Using color to dramatize or to hide.
- Color and illumination.
- Experimenting with color.

This new basic guide can serve as your handbook in helping you make decisions about how to use color in your life and make it work for you. Order *Color in Our Daily Lives* prepaid for $1.70 from the Superintendent of Documents, U.S. Government Printing Office, Washington, D.C. 20402. Use SD Catalog No. C13.53:6.

NBS TECHNICAL PUBLICATIONS

PERIODICALS

JOURNAL OF RESEARCH reports National Bureau of Standards research and development in physics, mathematics, and chemistry. It is published in two sections, available separately:

• **Physics and Chemistry (Section A)**
Papers of interest primarily to scientists working in these fields. This section covers a broad range of physical and chemical research, with major emphasis on standards of physical measurement, fundamental constants, and properties of matter. Issued six times a year. Annual subscription: Domestic, $17.00; Foreign, $21.25.

• **Mathematical Sciences (Section B)**
Studies and compilations designed mainly for the mathematician and theoretical physicist. Topics in mathematical statistics, theory of experiment design, numerical analysis, theoretical physics and chemistry, logical design and programming of computers and computer systems. Short numerical tables. Issued quarterly. Annual subscription: Domestic, $9.00; Foreign, $11.25.

DIMENSIONS/NBS (formerly Technical News Bulletin)—This monthly magazine is published to inform scientists, engineers, businessmen, industry, teachers, students, and consumers of the latest advances in science and technology, with primary emphasis on the work at NBS. The magazine highlights and reviews such issues as energy research, fire protection, building technology, metric conversion, pollution abatement, health and safety, and consumer product performance. In addition, it reports the results of Bureau programs in measurement standards and techniques, properties of matter and materials, engineering standards and services, instrumentation, and automatic data processing.

Annual subscription: Domestic, $9.45; Foreign, $11.85.

NONPERIODICALS

Monographs—Major contributions to the technical literature on various subjects related to the Bureau's scientific and technical activities.

Handbooks—Recommended codes of engineering and industrial practice (including safety codes) developed in cooperation with interested industries, professional organizations, and regulatory bodies.

Special Publications—Include proceedings of conferences sponsored by NBS, NBS annual reports, and other special publications appropriate to this grouping such as wall charts, pocket cards, and bibliographies.

Applied Mathematics Series—Mathematical tables, manuals, and studies of special interest to physicists, engineers, chemists, biologists, mathematicians, computer programmers, and others engaged in scientific and technical work.

National Standard Reference Data Series—Provides quantitative data on the physical and chemical properties of materials, compiled from the world's literature and critically evaluated. Developed under a world-wide program coordinated by NBS. Program under authority of National Standard Data Act (Public Law 90-396).

NOTE: At present the principal publication outlet for these data is the Journal of Physical and Chemical Reference Data (JPCRD) published quarterly for NBS by the American Chemical Society (ACS) and the American Institute of Physics (AIP). Subscriptions, reprints, and supplements available from ACS, 1155 Sixteenth St. N.W., Wash. D. C. 20056.

Building Science Series—Disseminates technical information developed at the Bureau on building materials, components, systems, and whole structures. The series presents research results, test methods, and performance criteria related to the structural and environmental functions and the durability and safety characteristics of building elements and systems.

Technical Notes—Studies or reports which are complete in themselves but restrictive in their treatment of a subject. Analogous to monographs but not so comprehensive in scope or definitive in treatment of the subject area. Often serve as a vehicle for final reports of work performed at NBS under the sponsorship of other government agencies.

Voluntary Product Standards—Developed under procedures published by the Department of Commerce in Part 10, Title 15, of the Code of Federal Regulations. The purpose of the standards is to establish nationally recognized requirements for products, and to provide all concerned interests with a basis for common understanding of the characteristics of the products. NBS administers this program as a supplement to the activities of the private sector standardizing organizations.

Consumer Information Series—Practical information, based on NBS research and experience, covering areas of interest to the consumer. Easily understandable language and illustrations provide useful background knowledge for shopping in today's technological marketplace.

Order **above** *NBS publications from: Superintendent of Documents, Government Printing Office, Washington, D.C. 20402.*

Order **following** *NBS publications—NBSIR's and FIPS from the National Technical Information Services, Springfield, Va. 22161.*

Federal Information Processing Standards Publications (FIPS PUBS)—Publications in this series collectively constitute the Federal Information Processing Standards Register. Register serves as the official source of information in the Federal Government regarding standards issued by NBS pursuant to the Federal Property and Administrative Services Act of 1949 as amended, Public Law 89-306 (79 Stat. 1127), and as implemented by Executive Order 11717 (38 FR 12315, dated May 11, 1973) and Part 6 of Title 15 CFR (Code of Federal Regulations).

NBS Interagency Reports (NBSIR)—A special series of interim or final reports on work performed by NBS for outside sponsors (both government and non-government). In general, initial distribution is handled by the sponsor; public distribution is by the National Technical Information Services (Springfield, Va. 22161) in paper copy or microfiche form.

BIBLIOGRAPHIC SUBSCRIPTION SERVICES

The following current-awareness and literature-survey bibliographies are issued periodically by the Bureau:

Cryogenic Data Center Current Awareness Service. A literature survey issued biweekly. Annual subscription: Domestic, $20.00; Foreign, $25.00.

Liquified Natural Gas. A literature survey issued quarterly. Annual subscription: $20.00.

Superconducting Devices and Materials. A literature survey issued quarterly. Annual subscription: $20.00.

Send subscription orders and remittances for the preceding bibliographic services to National Bureau of Standards, Cryogenic Data Center (275.02) Boulder, Colorado 80302.

U.S. DEPARTMENT OF COMMERCE
National Bureau of Standards
Washington, D.C. 20234

OFFICIAL BUSINESS

Penalty for Private Use, $300

POSTAGE AND FEES PAID
U.S. DEPARTMENT OF COMMERCE
COM-215